

Transactions of the ASME®

Technical Editor, **T. H. OKIISHI (1998)**
Associate Technical Editors
Aeromechanical Interaction
R. E. KIELB (1999)
Gas Turbine (Review Chair)
A. KIDD (1997)
Heat Transfer
M. G. DUNN (1999)
Power
D. LOU (1998)
Turbomachinery
R. A. DELANEY (1998)
A. STRAZISAR (2000)

BOARD ON COMMUNICATIONS
Chairman and Vice-President
R. MATES

OFFICERS OF THE ASME
President, **KEITH B. THAYER**
Executive Director, **D. L. BELDEN**
Treasurer, **J. A. MASON**

PUBLISHING STAFF
Managing Director, Engineering
CHARLES W. BEARDSLEY

Director, Technical Publishing
PHILIP DI VIETRO

Managing Editor, Technical Publishing
CYNTHIA B. CLARK

Managing Editor, Transactions
CORNELIA MONAHAN

Production Coordinator
VALERIE WINTERS

Production Assistant
MARISOL ANDINO

Transactions of the ASME, Journal of Turbomachinery
(ISSN 0889-504X) is published quarterly (Jan., Apr., July, Oct.)
for \$185.00 per year by The American Society of Mechanical
Engineers, 345 East 47th Street, New York, NY 10017.
Periodicals postage paid at New York, NY and additional
mailing offices. POSTMASTER: Send address changes to
Transactions of the ASME, Journal of Turbomachinery,
c/o THE AMERICAN SOCIETY OF MECHANICAL
ENGINEERS,

22 Law Drive, Box 2300, Fairfield, NJ 07007-2300.

CHANGES OF ADDRESS must be received at Society
headquarters seven weeks before they are to be effective.

Please send old label and new address.

PRICES: To members, \$40.00, annually, to nonmembers,
\$185.00.

Add \$40.00 for postage to countries outside the United States
and Canada.

STATEMENT from By-Laws. The Society shall not be
responsible for statements or opinions advanced in papers or
... printed in its publications (B7.1, Par. 3).

COPYRIGHT © 1998 by The American Society of Mechanical
Engineers. Authorization to photocopy material for internal or
personal use under circumstances not falling within the fair
use provisions of the Copyright Act is granted by ASME to
libraries and other users registered with the Copyright
Clearance Center (CCC) Transactional Reporting Service
provided that the base fee of \$3.00 per article is paid directly
to CCC, 222 Rosewood Dr., Danvers, MA 01923. Request for
special permission or bulk copying should be addressed to
Reprints/Permission Department.

INDEXED by Applied Mechanics Reviews and Engineering
Information, Inc.
Canadian Goods & Services
Tax Registration #126148048

Journal of Turbomachinery


Published Quarterly by The American Society of Mechanical Engineers


VOLUME 120 • NUMBER 2 • APRIL 1998

TECHNICAL PAPERS

- 205 1995 ASME Gas Turbine Award Paper: Development and Application of a Multistage Navier-Stokes Solver: Part 1—Multistage Modeling Using Bodyforces and Deterministic Stresses (95-GT-342)
C. M. Rhie, A. J. Gleixner, D. A. Spear, C. J. Fischberg, and R. M. Zacharias
- 215 1995 ASME Gas Turbine Award Paper: Development and Application of a Multistage Navier-Stokes Flow Solver: Part II—Application to a High-Pressure Compressor Design (95-GT-343)
C. R. LeJambre, R. M. Zacharias, B. P. Biederman, A. J. Gleixner, and C. J. Yetka
- 224 Stator Performance and Unsteady Loading in Transonic Compressor Stages
M. Durali and J. L. Kerrebrock
- 233 Effects of Inlet Distortion on the Flow Field in a Transonic Compressor Rotor (96-GT-547)
C. Hah, D. C. Rabe, T. J. Sullivan, and A. R. Wadia
- 247 Three-Dimensional Inverse Method for Turbomachinery Blading Design (96-GT-39)
A. Demeulenaere and R. Van den Braembussche
- 256 An Analysis of Axial Compressor Fouling and a Blade Cleaning Method (96-GT-363)
A. P. Tarabrin, V. A. Schurovsky, A. I. Bodrov, and J.-P. Stalder
- 262 Unsteady Flow in Oscillating Turbine Cascades: Part 1—Linear Cascade Experiment (96-GT-374)
L. He
- 269 Unsteady Flow in Oscillating Turbine Cascades: Part 2—Computational Study (96-GT-375)
L. He
- 276 On the Interpretation of Measured Profile Losses in Unsteady Wake-Turbine Blade Interaction Studies (96-GT-494)
H. P. Hodson and W. N. Dawes
- 285 Simulation and Validation of Mach Number Effects on Secondary Flow in a Transonic Turbine Cascade Using a Multigrid, $k-\epsilon$ Solver (96-GT-544)
M. Koiro and B. Lakshminarayana
- 298 Flow Development Through Interturbine Diffusers (96-GT-139)
R. G. Dominy, D. A. Kirkham, and A. D. Smith
- 305 Endwall Heat Transfer Measurements in a Transonic Turbine Cascade (96-GT-180)
P. W. Giel, D. R. Thurman, G. J. Van Fossen, S. A. Hippensteele, and R. J. Boyle
- 314 Discharge Coefficient of Turbine Cooling Holes: A Review (96-GT-492)
N. Hay and D. Lampard
- 320 An Experimental Investigation of the Velocity and Temperature Fields of Cold Jets Injected Into a Hot Crossflow (96-GT-491)
H. A. Rydholm
- 327 Flowfield Measurements for Film-Cooling Holes With Expanded Exits (96-GT-174)
K. Thole, M. Gritsch, A. Schulz, and S. Wittig
- 337 Characterization and Laboratory Simulation of Turbine Airfoil Surface Roughness and Associated Heat Transfer (96-GT-386)
D. G. Bogard, D. L. Schmidt, and M. Tabbita
- 343 Computational Prediction of Heat Transfer to Gas Turbine Nozzle Guide Vanes With Roughened Surfaces (96-GT-388)
S. M. Guo, T. V. Jones, G. D. Lock, and S. N. Dancer

(Contents continued on inside back cover)

This journal is printed on acid-free paper, which exceeds the ANSI Z39.48-1992 specification for permanence of paper and library materials. 

 85% recycled content, including 10% post-consumer fibers.

- 351 **An Unsteady Velocity Formulation for the Edge of the Near-Wall Region** (96-GT-478)
D. E. Wilson and A. J. Hanford
- 362 **Convective Heat Transfer of Cubic Fin Arrays in a Narrow Channel** (96-GT-201)
M. K. Chyu, Y. C. Hsing, and V. Natarajan
- 368 **The Effect of Periodic Ribs on the Local Aerodynamic and Heat Transfer Performance of a Straight Cooling Channel** (96-GT-541)
G. Rau, M. Çakan, D. Moeller, and T. Arts
- 376 **Rib Heat Transfer Coefficient Measurements in a Rib-Roughened Square Passage** (96-GT-356)
G. J. Korotky and M. E. Taslim
- 386 **LDA Study of the Flow Development Through an Orthogonally Rotating U-Bend of Strong Curvature and Rib-Roughened Walls** (96-GT-476)
H. Iacovides, D. C. Jackson, H. Ji, G. Kelemenis, B. E. Launder, and K. Nikas

ANNOUNCEMENTS

- 246 **Change of address form for subscribers**
- 392 **Information for authors**

Development and Application of a Multistage Navier–Stokes Solver: Part I—Multistage Modeling Using Bodyforces and Deterministic Stresses

C. M. Rhie

A. J. Gleixner

D. A. Spear

C. J. Fischberg

R. M. Zacharias

Pratt & Whitney,
United Technologies Corporation,
East Hartford, CT 06118

A multistage compressor performance analysis method based on the three-dimensional Reynolds-averaged Navier–Stokes equations is presented in this paper. This method is an average passage approach where deterministic stresses are used to ensure continuous physical properties across interface planes. The average unsteady effects due to neighboring blades and/or vanes are approximated using deterministic stresses along with the application of bodyforces. Bodyforces are used to account for the “potential” interaction between closely coupled (staged) rows. Deterministic stresses account for the “average” wake blockage and mixing effects both axially and radially. The attempt here is to implement an approximate technique for incorporating periodic unsteady flow physics that provides for a robust multistage design procedure incorporating reasonable computational efficiency. The present paper gives the theoretical development of the stress/bodyforce models incorporated in the code, and demonstrates the usefulness of these models in practical compressor applications. Compressor performance prediction capability is then established through a rigorous code/model validation effort using the power of networked workstations. The numerical results are compared with experimental data in terms of one-dimensional performance parameters such as total pressure ratio and circumferentially averaged radial profiles deemed critical to compressor design. This methodology allows the designer to design from hub to tip with a high level of confidence in the procedure.

Introduction

Compressors have traditionally been designed with many empirical assumptions defining blockage, loss, stator/blade turning, etc. The compressor flow field is highly three dimensional and highly viscous, often exhibiting relatively high losses in the endwall regions. Three-dimensional inviscid (Euler) approaches to design are rarely successful for compressor designs due to these effects (although they have had reasonable success for turbine applications). This viscous nature becomes more prevalent as the compressors are pushed to their operating limit (stall). Modern high-pressure compressor designs have narrower operating ranges and therefore the operating characteristics near stall must be predicted accurately. The viscous procedure outlined here will demonstrate the capability to predict the operating limits for compressors with excellent accuracy.

Recently, three-dimensional Navier–Stokes methods with eddy viscosity turbulence models have become practical using affordable computers [1–8]. The present authors [9] showed that the Navier–Stokes procedure was practical for fan design improvement, leading to substantially reduced development time and cost. The current work extends the previous isolated blade row procedure to multistage compressor applications.

The initial attempt at multistage modeling in the present work used the “mixing plane approach” [10]. In this procedure each

row is solved independently, passing information to adjacent rows at interface planes. These interface planes are approximately halfway between upstream trailing edges and downstream leading edges. Static pressure information is passed from the upstream interface plane of the downstream row to the downstream interface plane of the row of interest (i.e., potential bodyforces) and four independent tangentially averaged parameters (total pressure and temperature, meridional and radial flow angles) are passed from the downstream interface plane of the upstream row to the row of interest. The row of interest is the one that is being calculated. In very closely coupled compressors, these gridded domains offer little downstream extended region for resolving wakes, vorticity, etc. Nonreflecting plane procedures can theoretically account for this shortcoming [11]. Experimenting with this technique, however, showed serious lack of robustness for some cases (e.g., reverse flow). The mixing plane approach purposely exhibits jumps across these interface planes in static pressure, total pressure, etc., due to the upstream wake distortion being removed for the downstream row’s upstream boundary conditions (axisymmetric). This is the result of conserving momentum, continuity, and energy while removing wake distortion from the upstream flow. Obviously any blockage effect due to wake distortion on the downstream row is lost. The mixing plane procedure, while reasonably accurate for well-behaved compressors with little or no separation, breaks down at other conditions.

The shortcomings of the mixing plane approach motivated us to define a procedure that would allow for robust calculations that kept the features of the multistage physics deemed im-

Contributed by the International Gas Turbine Institute and presented at the 40th International Gas Turbine and Aeroengine Congress and Exhibition, Houston, Texas, June 5–8, 1995. Manuscript received by the International Gas Turbine Institute March 15, 1995. Paper No. 95-GT-342. Associate Technical Editor: C. J. Russo.

portant, i.e., potential bodyforces (including airfoil thickness) from neighboring rows, blockages from upstream row wakes and vorticity (in a form easily translatable between rotors/stators). The procedure deemed appropriate to achieve this was the average passage approach, employing bodyforces and deterministic stresses, outlined by Adamczyk [12, 13]. The concept of the bodyforce/deterministic stress approach is employed in the present work while the numerical procedure is a direct extension of the mixing plane approach. All of the mathematical terms present in Adamczyk's average passage equations are not modeled in the present work. While downstream bodyforces are approximated, no effects from upstream bodyforces are accounted for, as numerical studies have shown these effects to be very small for subsonic relative Mach inlet compressor applications. No attempt is made to account for "real" unsteady effects. For example, the potential circumferential nonuniformities imposed by the downstream stator as periodic circulation fluctuations on the upstream rotor are not rigorously accounted for.

The two-equation $\kappa-\epsilon$ turbulence model is modified to allow for the effects of turbulence decay/growth on a downstream row by keeping the production source terms from the upstream solution due to the circumferential distortion. This modeling assumption forces the solution to be corrected with the unsteady wake/vorticity produced from the upstream row.

This new approach has shown some substantial improvement over the initial mixing plane approach in multistage prediction capability, where the solutions have been run to near-stall conditions. The blockages (due to distortion from upstream rows or downstream rows) are passed through adjacent (downstream or upstream) blade rows. The radial transport resulting from these distortions is also maintained through the downstream rows. The most noticeable effect of this new modeling is the continuous nature of all parameters across the interface planes. The interface planes are no longer hard boundaries for row solutions. The present method is therefore termed the "continuous interface plane approach" from an interface boundary condition point of view. This coding viewpoint is quite a departure from Adamczyk's original multistage code where no interface is used (computational domain for each blade row encompasses the entire compressor domain).

The present paper will describe the basic multistage modeling and provide numerical substantiation by comparing results with experimental data. Validation of the present numerical procedure was established through a sequence encompassing increasing physical complexity. Numerous questions regarding the effect of the computational grid, boundary conditions, turbulence modeling, convergence, and design-turnaround time on the calculated flow field were answered during the validation process.

The current validation process required extensive computing resources with each blade row employing about 200,000 grid points to resolve viscous layers and tip clearance flows. The present validation/application study was made feasible through

the use of hundreds of networked workstations. This was a new less expensive computing resource to replace the supercomputer for large-scale execution of production, design-oriented, CFD analyses. The algorithms in the present Navier-Stokes solver, NASTAR, were modified so that the original domain could be divided into subdomains such that each subdomain could be solved as independently of the other subdomains as possible. Each subdomain is executed on a different workstation and exchanges boundary information with neighboring subdomains on other workstations.

The present paper demonstrates that the present scheme accurately predicts the compressor characteristics at the operating and near stall conditions. The use of this code, NASTAR, for the design of an 11-stage high-pressure compressor will be shown in a companion paper (Part II of this paper, [14]).

Theory

Navier-Stokes Computational Method. The governing equations for an isolated blade row calculation are the continuity equation, the Reynolds-averaged Navier-Stokes equations, and the Reynolds-averaged energy equation in mass-weighted variables. The turbulent viscosity and turbulent conductivity are introduced to model the Reynolds stress and the Reynolds heat flux terms. The turbulent viscosity and turbulent conductivity are determined by the two-equation $\kappa-\epsilon$ turbulence model. The near-wall regions are modeled by the VanDriest near-wall formulation of Dash et al. [15]. The flows are assumed to be fully turbulent in the present work. The limitations of the $\kappa-\epsilon$ turbulence model in an adverse pressure gradient are very well known. In general, the present calculations show slightly optimistic compressor behavior particularly for the compressors with higher pressure ratios even though trends are extremely well captured. Additional equations are the perfect gas and enthalpy-temperature relations.

Numerical modeling is based on the discretization of the fully conservative form of the transformation of the governing differential equations for arbitrary curvilinear coordinates. The formal discretization is second-order accurate using centered differencing. Numerical stability is ensured by using artificial dissipation. For the continuity equation, control volume face mass fluxes are constructed using pressure-weighted interpolation [16]. For other equations, locally varying second-order dissipation is used to stabilize the solution without sacrificing numerical accuracy. More details can be found in [17].

In the solution procedure, the momentum equations are solved first with a preliminary pressure field. Since this preliminary velocity field does not satisfy the continuity equation, pressure equations are solved to establish new velocity and pressure fields that satisfy the continuity equation. The momentum and continuity equations are coupled through this pressure correction procedure. A three-step pressure correction procedure [16] is used. The energy and turbulence scalar equations are each

Nomenclature

A = area
 D = laminar diffusion term
Diss = viscous dissipation term
 F = momentum bodyforce
 H = enthalpy
 P = pressure
 Q = energy source
 R = stresses for momentum equation
 r = radial coordinate
 T = temperature
 u, U = velocity
 x = axial coordinate

θ = tangential coordinate
 ρ = density
Subscripts
 dn = downstream blade row
 r = radial component
 s = static quantity
 t = stagnation quantity
 up = upstream blade row
 x = axial component
 θ = tangential component

Superscripts

\cdot = instantaneous quantity
 $-$ = time-averaged quantity
 $"$ = time-unresolved random fluctuation
 $'$ = periodic unsteady response fluctuation
 \wedge = primary time resolved periodic fluctuation
 \sim = aperiodic spatial fluctuation
 \sim = mixed quantity
p.a. = passage-to-passage averaging

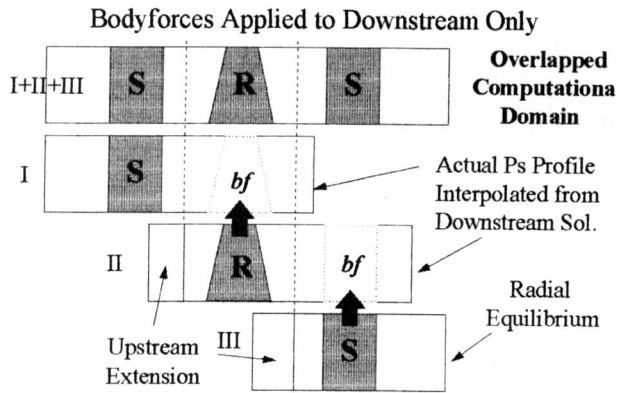


Fig. 1 Computational domain for one and half stage calculation

solved in turn. All equations are solved using the successive line underrelaxation procedure. This method had been demonstrated for a wide variety of flows ranging from low speed (incompressible) to high speed (hypersonic) flows [16, 17].

Multistage Modeling

1 Computational Domain/Grid. A typical computational domain for the current effort is shown in Fig. 1. Grids for individual blades overlap in order to pass bodyforces and deterministic stresses. The upstream extension is required to position the inlet axisymmetric boundary conditions (total pressure, total temperature, and circumferential velocity), transferred from the upstream blade row computation correctly. In other words, information from the interface plane is transferred upstream along inviscid streamlines. Without this extension, circumferentially nonuniform boundary conditions would have to be devised at the upstream interface plane. The radial flow angle at the upstream plane is assumed to be linearly distributed between endwall angles. An inviscid calculation within the upstream extension allows radial boundary condition profiles to be convected upstream from the interface plane allowing circumferential nonuniformities to develop. This interface plane is the coincident plane from the upstream row where all information is passed. The inlet radial flow angle is approximated to allow this convection. An exit static pressure boundary condition is obtained by a radial equilibrium assumption (for the last blade row) or by the static pressure profile interpolated from the actual downstream solution. Bodyforces are applied only in the downstream wake region while deterministic stresses are applied over the entire region.

For this study, H grids were used. A typical grid for a three-dimensional calculation used 120 nodes in the chordwise direction, 36 in the circumferential direction, and 47 in the radial direction for a total of approximately 200,000 grid points. The tip clearance grid is considered a subset of the normal H mesh. For each axisymmetric grid sheet, the interior of the airfoil is filled in with grid as shown in Fig. 2. The grid inside of the

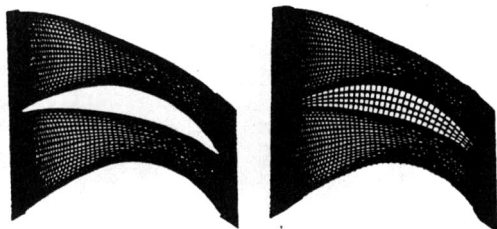


Fig. 2 Top view of a blade grid (blade is filled with grid)

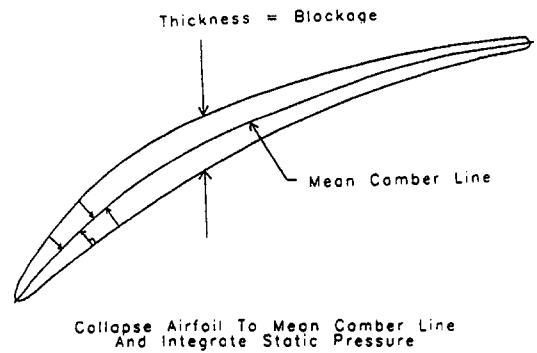


Fig. 3 Sketch of pressure integration over mean camberline

blade is "blocked out," and "activated" within the blade tip gap. The mesh point count dedicated to the tip clearance region is typically 60 chordwise by 5 circumferentially by 10 radial, or 3000 total.

2 Bodyforces. The bodyforce method used here is an extension from the mixing plane approach. The tangentially averaged static pressure at the interface plane (the plane halfway between the trailing edge and the following row's leading edge) observed in the following row, immediately downstream of the row of interest, is the "target" tangentially averaged static pressure for the upstream row. Blade forces will be imposed in the upstream row's extended grid section to "correct" its static pressure at its interface plane to coincide with that observed from the row immediately downstream at its interface plane. This is reasonable because the extended region is only required to allow solutions with separation (large reverse flow) and/or large tangential gradients. The potential bodyforces computed from the downstream row's surface static pressure as shown in Fig. 3 are just a first-pass guide to the bodyforces. The surface static pressure is projected to the camberline of the blade and the projected pressure force balances are computed as bodyforces. The tangential bodyforces produce the work/turning in a downstream rotor/stator, and are only necessary to prevent the calculation from choking in the downstream extended grid.

The interface plane static pressures can be matched by correcting the bodyforces in an iterative manner. However, all of the comparisons presented in this paper do not iterate on the interface plane static pressure as the first pass potential body forces were adequate.

Figure 4 shows the blade-to-blade view of stator wake velocity streaklines produced by bodyforces at the midspan loca-

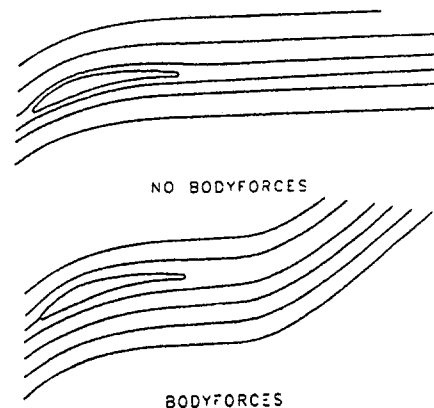


Fig. 4 Streaklines with and without bodyforces

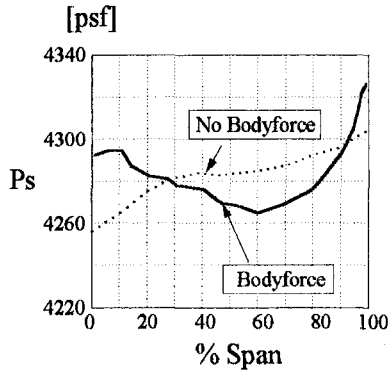


Fig. 5 Radial static pressures with and without bodyforces at interface plane

tion from a single-stage calculation.¹ The bodyforces introduce a potential interference effect by establishing a “target” radial static pressure profile at the interface plane, as shown in Fig. 5. Another numerical check is the U_x profile comparison at the interface plane. The U_x profiles are simply the outcome of the calculation since they are not enforced as hard boundary conditions at the interface plane. (Total pressure is the upstream interface boundary condition for the downstream row.) Figure 6 shows the improved profile match at the interface plane by introducing the proper “back-pressuring” effect. Ignoring these bodyforces (i.e., assuming radial equilibrium in a far downstream plane) leads to errors in multistage performance prediction. Figure 7 shows the improvement in a compressor stage performance prediction when employing bodyforces.

3 Deterministic Stresses. Recently, fundamental equation sets derived from the Navier–Stokes and energy equations that describe the average-passage flow field through a blade row have been reported by Adamczyk [12]. Adamczyk arrives at his average-passage equation sets by applying three operators to the describing equations. Ensemble averaging is first applied, identifying an unsteady mean velocity field wherein the effects of turbulence are represented in the familiar Reynolds stresses. This equation set retains the temporal derivatives. Time averaging is then applied to remove the periodic unsteadiness in the flow field. The third operator is “passage-to-passage” averaging. Effects of the spatially aperiodic components of the flow field are contained in a third correlation. As a result of these

¹ P&W’s 4KMS2 compressor rig last stage.

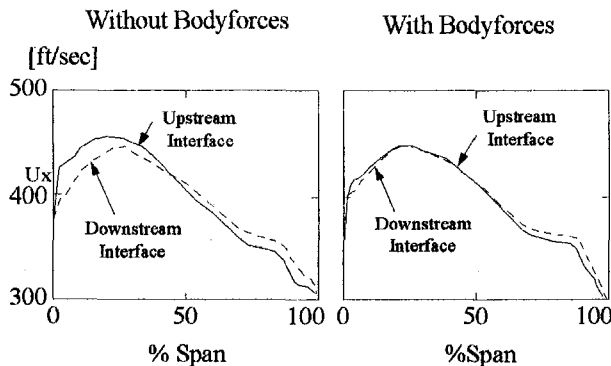


Fig. 6 Radial U_x profiles at the interface plane

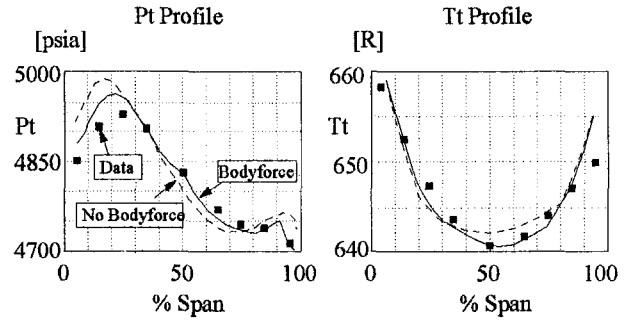


Fig. 7 Comparison of radial Pt and Tt profiles at the stage exit

averaging procedures, an additional term appears in the average-passage Navier–Stokes equations as:

$$R_{ij} = \text{Time-averaged Reynolds stresses} \\ + \text{Deterministic stresses} \\ + \text{Spatially aperiodic momentum flux correlations} \\ = \overline{[\rho u_i'' u_j'']} + [\overline{\rho \hat{u}_i \hat{u}_j} + \{\overline{\rho \hat{u}_i u_j'} + \overline{\rho u_i' \hat{u}_j} + \overline{\rho u_i' u_j'}\}]^{p.a.} \\ + [\overline{\bar{\rho} \hat{u}_i \hat{u}_j}^{p.a.}] \quad (1)$$

where u'' represents the time-unresolved fluctuations (noncorrelated with shaft speed), u' the periodic unsteady response of the blade to the wake, \hat{u} the primary time resolved periodic fluctuations, \bar{u} the spatially aperiodic fluctuations, ρ the instantaneous density, $\bar{\rho}$ the time resolved density, and $\bar{\rho}$ the time-averaged density. Among the deterministic stresses in the second bracket, only the first term, $\overline{\rho \hat{u}_i \hat{u}_j}$, is modeled in the present work. The rest of the terms, $[\{\overline{\rho \hat{u}_i u_j'} + \overline{\rho u_i' \hat{u}_j} + \overline{\rho u_i' u_j'}\}]$, are ignored in the present work and represent unsteady interaction terms, which have been studied by various researchers as unsteady mixing effects (e.g., see [18]). The spatially aperiodic momentum flux correlation in the third bracket due to the different airfoil counts is also ignored in the present work. The present approach does not model all of the mathematical terms but employs the “perceived” important deterministic stresses to represent wake blockage and mixing effects.

For example, the three-dimensional representation for the current multistage stator solution with the current approximations is expressed as:

$$\frac{\partial(\lambda \bar{\rho} \bar{u}_x \bar{u}_x)}{\partial x} + \frac{\partial(\lambda \bar{\rho} \bar{u}_\theta \bar{u}_x)}{r \partial \theta} + \frac{\partial(\lambda \bar{\rho} \bar{u}_r \bar{u}_x)}{\partial r} = -\frac{\partial \lambda \bar{p}}{\partial x} - \frac{\lambda \bar{\rho} \bar{u}_x \bar{u}_r}{r} \\ - \left[\frac{\partial(\lambda \overline{\rho u_x'' u_x''})}{\partial x} + \frac{\partial(\lambda \overline{\rho u_\theta'' u_x''})}{r \partial \theta} + \frac{\partial(\lambda \overline{\rho u_r'' u_x''})}{\partial r} + \frac{\lambda \overline{\rho u_x'' u_r''}}{r} \right] \\ - \left[\frac{\partial(\lambda \overline{\rho \hat{u}_x \hat{u}_x})}{\partial x} + \frac{\partial(\lambda \overline{\rho \hat{u}_\theta \hat{u}_x})}{\partial r} + \frac{\lambda \overline{\rho \hat{u}_x \hat{u}_\theta}}{r} \right] + D_{x,lam} + F_x \quad (2)$$

$$\frac{\partial(\lambda \bar{\rho} \bar{u}_x \bar{u}_\theta)}{\partial x} + \frac{\partial(\lambda \bar{\rho} \bar{u}_\theta \bar{u}_\theta)}{r \partial \theta} + \frac{\partial(\lambda \bar{\rho} \bar{u}_r \bar{u}_\theta)}{\partial r} = -\frac{\partial \lambda \bar{p}}{r \partial \theta} - 2 \frac{\lambda \bar{\rho} \bar{u}_x \bar{u}_\theta}{r} \\ - \left[\frac{\partial(\lambda \overline{\rho u_x'' u_\theta''})}{\partial x} + \frac{\partial(\lambda \overline{\rho u_\theta'' u_\theta''})}{r \partial \theta} + \frac{\partial(\lambda \overline{\rho u_r'' u_\theta''})}{\partial r} + 2 \frac{\lambda \overline{\rho u_x'' u_\theta''}}{r} \right] \\ - \left[\frac{\partial(\lambda \overline{\rho \hat{u}_x \hat{u}_\theta})}{\partial x} + \frac{\partial(\lambda \overline{\rho \hat{u}_\theta \hat{u}_\theta})}{\partial r} + 2 \frac{\lambda \overline{\rho \hat{u}_x \hat{u}_\theta}}{r} \right]$$

$$+ D_{\theta,lam} + F_\theta \quad (3)$$

Deterministic Stresses for X-Mom. Equation

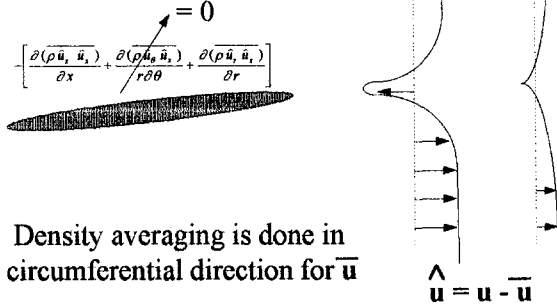


Fig. 8 Estimation of deterministic stresses

$$\begin{aligned} \frac{\partial(\lambda \bar{\rho} \bar{u}_x \bar{u}_r)}{\partial x} + \frac{\partial(\lambda \bar{\rho} \bar{u}_\theta \bar{u}_r)}{r \partial \theta} + \frac{\partial(\lambda \bar{\rho} \bar{u}_x \bar{u}_r)}{\partial r} = -\frac{\partial \lambda \bar{p}}{\partial r} - \frac{\lambda \bar{\rho} \bar{u}_r^2}{r} \\ + \frac{\lambda \bar{\rho} \bar{u}_\theta^2}{r} - \left[\frac{\partial(\lambda \bar{\rho} \bar{u}_x \bar{u}_r)}{\partial x} + \frac{\partial(\lambda \bar{\rho} \bar{u}_\theta \bar{u}_r)}{r \partial \theta} + \frac{\partial(\lambda \bar{\rho} \bar{u}_r \bar{u}_r)}{\partial r} \right] \\ + \left[\frac{\lambda \bar{\rho} \bar{u}_r^2}{r} - \frac{\lambda \bar{\rho} \bar{u}_\theta^2}{r} \right] - \left[\frac{\partial(\lambda \bar{\rho} \hat{u}_x \hat{u}_r)}{\partial x} + \frac{\partial(\lambda \bar{\rho} \hat{u}_\theta \hat{u}_r)}{\partial r} \right] \\ + \left[\frac{\lambda \bar{\rho} \hat{u}_r^2}{r} - \frac{\lambda \bar{\rho} \hat{u}_\theta^2}{r} \right] + D_{r,lam} + F_r \quad (4) \end{aligned}$$

where $D_{x,lam}$, $D_{\theta,lam}$, $D_{r,lam}$ represent the laminar diffusion terms, F_x , F_θ , F_r the bodyforces, and λ represents the weighting function related to airfoil blockage (unity means no airfoil thickness). Circumferential derivatives of deterministic stresses, $\bar{\rho} \hat{u}_i \hat{u}_j$, are zero and are dropped. The deterministic stress terms in the second bracket on the right side of the equations are evaluated from the current three-dimensional steady solutions. To evaluate deterministic stresses (i.e., $\bar{\rho} \hat{u}_i \hat{u}_j$) the circumferential direction is considered as a timelike dimension. The axisymmetric mean quantities are obtained by using density (or mass-weighted) averaging for all quantities and deterministic stresses are obtained by area averaging of the second-order correlations of gapwise fluctuations. The fluctuating quantities are the difference between the local solution and the axisymmetric solution (see Fig. 8). The energy equation has its own energy-velocity correlations employing a similar theoretical derivation;

$$\begin{aligned} \frac{\partial(\lambda \bar{\rho} \bar{u}_x \bar{H}_t)}{\partial x} + \frac{\partial(\lambda \bar{\rho} \bar{u}_\theta \bar{H}_t)}{r \partial \theta} + \frac{\partial(\lambda \bar{\rho} \bar{u}_x \bar{H}_t)}{\partial r} = -\frac{\lambda \bar{\rho} \bar{H}_t}{r} \\ - \left[\frac{\partial(\lambda \bar{\rho} \bar{u}_x \bar{H}_t)}{\partial x} + \frac{\partial(\lambda \bar{\rho} \bar{u}_\theta \bar{H}_t)}{r \partial \theta} + \frac{\partial(\lambda \bar{\rho} \bar{u}_r \bar{H}_t)}{\partial r} + \frac{\lambda \bar{\rho} \bar{u}_r \bar{H}_t}{r} \right] \\ - \left[\frac{\partial(\lambda \bar{\rho} \hat{u}_x \hat{H}_t)}{\partial x} + \frac{\partial(\lambda \bar{\rho} \hat{u}_\theta \hat{H}_t)}{\partial r} + \frac{\lambda \bar{\rho} \hat{u}_r \hat{H}_t}{r} + \frac{\lambda \bar{\rho} \hat{H}_t}{r} \right] \\ + D_{q,lam} + Diss + Q \quad (5) \end{aligned}$$

where $D_{q,lam}$ represents the laminar diffusion term, $Diss$ the viscous dissipation term, and Q the energy source term. These energy-velocity correlations are accounted for in the present work. The Reynolds stresses are still modeled within the framework of the $\kappa-\epsilon$ turbulence model. Interestingly, the $\kappa-\epsilon$ equations also have their own deterministic correlations. More turbulence modeling issues will be discussed in a later section.

4 Interface Boundary Conditions. Computations with deterministic stresses no longer use the mixing approach at boundary condition interfaces. The interface flux conservation difference between the mixing approach and the continuous interface plane approach with deterministic stresses is summarized in Table 1. Because the present work deals with compressible flows, the absolute total pressure, absolute total temperature, tangential velocity, and radial velocity obtained from the upstream blade row calculation using the relationships described in Table 1 are specified at the inlet, and the static pressure obtained from the downstream blade row calculation by interpolation is specified at the far downstream exit.

The main attraction in the continuous interface plane approach is that all of the flow variables are continuous at the interfaces. This is a major departure from the old mixing plane approach where all of the circumferential profiles are assumed to be mixed instantaneously at the interface. This instantaneous mixing at the interface plane changes blockage, which in turn causes Ps to increase across the plane, while the mixing loss causes a drop in Pt across the plane. The concept is sketched in Fig. 9. In practical compressor applications, the mixing loss is 0.5–1.5 percent of the average total pressure at the operating conditions.

The radial static pressure profiles at the stator-rotor interface from computations with and without deterministic stresses are plotted in Fig. 10. This case is a straight (unbowed) compressor and is chosen for the current discussion since the large corner separations highlight the importance of the deterministic stresses. The mixing approach without deterministic stresses shows a jump in static pressure proportional to the change in blockage across the interface due to the flow separation on the stator. The continuous interface plane approach with deterministic stresses shows nearly identical static pressure profiles at the interface plane. This convergence to a coincident tangentially averaged static pressure at the interface plane “assures” a continuous solution for the downstream row. The deterministic stresses from the upstream row are applied to the downstream row such that the interface plane for this row has the same “average” distortion as the upstream row at this location.

The U_x profiles at the interface plane with and without deterministic stresses are plotted in Fig. 11. The deterministic stresses produce a substantially improved U_x profile match. Perfect match is not sought in the present work since the first cut potential interference effects are of current interest as stated before.

To quantify the stresses, Fig. 12 shows the comparison of bodyforce, F_x , and the gradient of deterministic stresses, $-\left[\frac{\partial(\lambda \bar{\rho} \hat{u}_x \hat{u}_x)}{\partial x} + \frac{\partial(\lambda \bar{\rho} \hat{u}_r \hat{u}_x)}{\partial r} + \lambda \bar{\rho} \hat{u}_x \hat{u}_r / r\right]$, generated from the downstream stator at the midspan and the near endwall (hub) radial locations. It is shown that the deterministic stress magnitudes are significant within the endwall separated region. These forces are imposed on the upstream rotor’s extended wake region.

5 Radial Mixing With Deterministic Stresses. The deterministic stresses also produce radial mixing. The deterministic stress gradients for the X-momentum equation are: $-\left[\frac{\partial(\lambda \bar{\rho} \hat{u}_x \hat{u}_x)}{\partial x} + \frac{\partial(\lambda \bar{\rho} \hat{u}_r \hat{u}_x)}{\partial r} + \lambda \bar{\rho} \hat{u}_x \hat{u}_r / r\right]$, from Eq. (2). The first term in the bracket is primarily responsible for the blockage effect, the second term for the radial mixing, and the third term is for continuity. The second term for the radial mixing can be significant for flows with large flow separations. The resulting effect in the rotor can be visualized in the midpitch relative Pt contours in Fig. 13. The Pt contours with deterministic stresses clearly show the bending of contour lines due to the flow blockage and the radial mixing. These effects are important for flows with large separations or strong secondary flows. To quantify these effects further, the deterministic stresses, $\bar{\rho} \hat{u}_i \hat{u}_j$, and the Reynolds stresses, $\bar{\rho} u_i'' u_j''$, are compared in Fig. 14 for a compressor situation at the operating line and near-stall conditions at the rotor leading

Table 1 Interface flux conservation

	Mixing Approach		Continuous Interface Plane Approach	
	Upstream Exit	Downstream Inlet	Upstream Exit	Downstream Inlet
Continuity :	$\int (\rho U_x) d\theta = \bar{\rho} \bar{U}_x$		$\int (\rho U_x) d\theta = \bar{\rho} \bar{U}_x$	
Axial Momentum :	$\int (\rho U_x^2 + P) d\theta = \bar{\rho} \bar{U}_x^2 + \bar{P}$		$\int (\rho U_x^2 + P) d\theta = \bar{\rho} \bar{U}_x^2 + \rho \overline{U_x^2} + \bar{P}$	
Tangential Momentum :	$\int (\rho U_x U_\theta) d\theta = \bar{\rho} \bar{U}_x \bar{U}_\theta$		$\int (\rho U_x U_\theta) d\theta = \bar{\rho} \bar{U}_x \bar{U}_\theta + \rho \overline{U_x U_\theta}$	
Radial Momentum :	$\int (\rho U_x U_r) d\theta = \bar{\rho} \bar{U}_x \bar{U}_r$		$\int (\rho U_x U_r) d\theta = \bar{\rho} \bar{U}_x \bar{U}_r + \rho \overline{U_x U_r}$	
Energy :	$\int (\rho U_x T_t) d\theta = \bar{\rho} \bar{U}_x \bar{T}_t$		$\int (\rho U_x T_t) d\theta = \bar{\rho} \bar{U}_x \bar{T}_t + \rho \overline{U_x T_t}$	

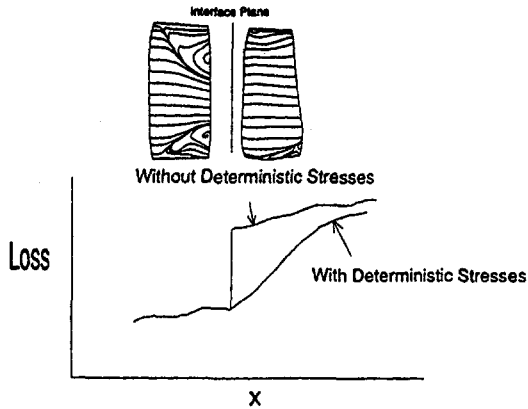


Fig. 9 Conceptual sketch of the streamwise loss distribution

edge and rotor midchord locations. The deterministic stresses produced by the upstream wake distortion can exceed the Reynolds stresses by an order of magnitude at the rotor leading edge and can be comparable to the maximum Reynolds stress magnitudes (within the tip clearance region) for a near-stall condition.

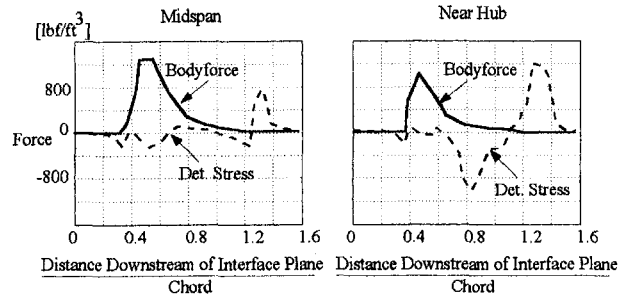


Fig. 12 Comparison of axial bodyforces and gradient of deterministic stresses

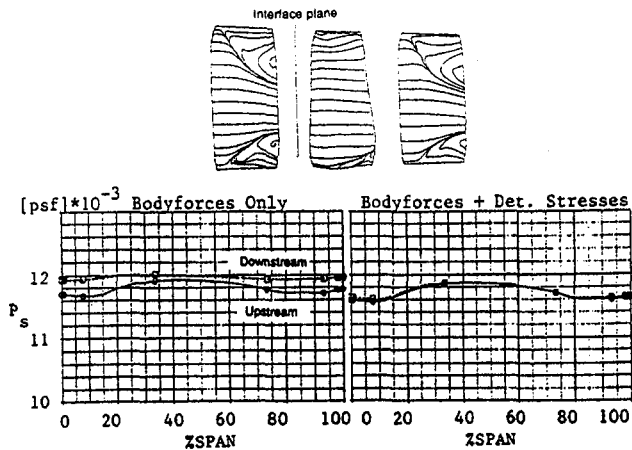


Fig. 10 Static pressure profiles at the boundary condition interface plane

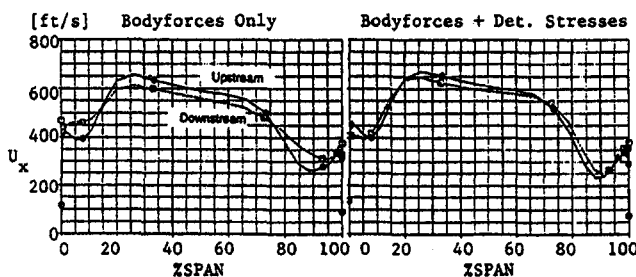


Fig. 11 U_x profiles at the boundary condition interface plane

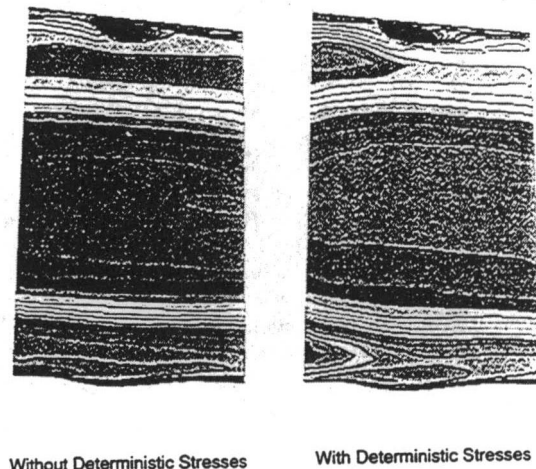


Fig. 13 Relative Pt contours at the midpitch location

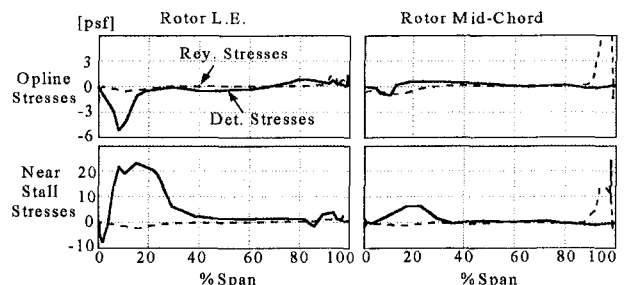


Fig. 14 Deterministic and Reynolds stresses comparison

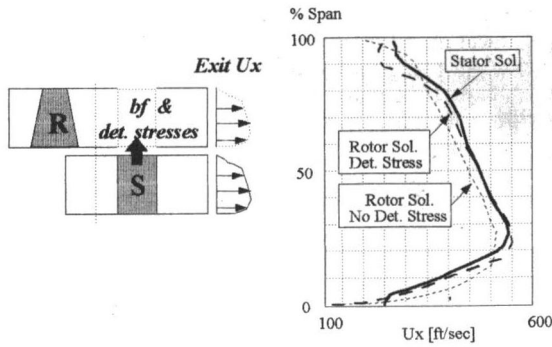


Fig. 15 Comparison of the exit plane U_x profiles

Another example that demonstrates the effect of deterministic stresses can be found in the wake computation. Figure 15 shows the calculated radial U_x profiles at the far downstream location in the wake of a rotor. The U_x profile shape with deterministic stresses closely represents the correct shape when compared with the actual downstream stator computation by introducing correct flow blockage and radial mixing through deterministic stresses. The discrepancy is due to grid resolution (i.e., truncation error) differences in the overlapped region. There is no attempt to force the exit of the row of interest to be identical with the downstream rows exit conditions as there is no need for this when the bodyforces/deterministic stresses are only necessary to line up tangentially averaged static pressures at the interface plane. Back pressure level at the exit of each blade row is adjusted while fixing the radial profile shape to drive the flow rate to the specified mass rate (see the later section on convergence). No information at the extended grid exit plane is directly used for the solution.

6 Incompressible Deterministic Stress Two-Dimensional Example. To explain the deterministic stresses, a two-dimensional incompressible case shown in Fig. 16 is considered as an illustrative example. The upstream stator wake profile is assumed to have a stepwise defect at the interface plane and static pressure is assumed to be constant. The areas A_1 and A_2 are assumed to be unity and the density is assumed to be unity for simplicity of discussion. As the calculation switches from the stator domain to the rotor domain, the wake profile is averaged and applied to the downstream calculation as a uniform inlet boundary condition (a constant U_x profile at the interface plane as shown in Fig. 16). The following simple analysis explains the effect of the deterministic stresses.

Without deterministic stresses:

Continuity:

$$\left[\int U_x dy \right]_{up} = (\bar{U}_{x_{dn}}) Area_{dn} \quad (6)$$

Momentum:

$$\left[\int (U_x^2 + P) dy \right]_{up} = (\bar{U}_{x_{dn}}^2 + \bar{P}_{dn}) Area_{dn} \quad (7)$$

From the continuity equation,

$$\bar{U}_{x_{dn}} = \frac{A_2 U_{x_{up}}}{A_1 + A_2} = \frac{U_{x_{up}}}{2} \quad (8)$$

From the momentum equation,

$$\bar{U}_{x_{dn}}^2 + \bar{P}_{dn} = \frac{A_1 P_{up} + A_2 (U_{x_{up}}^2 + P_{up})}{A_1 + A_2} \quad (9)$$

Therefore,

$$\begin{aligned} \bar{P}_{dn} &= P_{up} + \frac{A_2}{A_1 + A_2} \left(1 - \frac{A_2}{A_1 + A_2} \right) U_{x_{up}}^2 \\ &= P_{up} + \frac{1}{4} U_{x_{up}}^2 \end{aligned} \quad (10)$$

This shows that the static pressure instantaneously increases as mixed static pressure at the boundary condition interface plane with the lost wake blockage. Next, mixing loss is calculated:

$$[Pt_{up}]_{mass\ averaged} = P_{up} + \frac{1}{2} U_{x_{up}}^2$$

$$\begin{aligned} [Pt_{dn}]_{mass\ averaged} &= \bar{P}_{dn} + \frac{1}{2} \bar{U}_{x_{dn}}^2 = P_{up} + \frac{1}{4} U_{x_{up}}^2 + \frac{1}{2} \left[\frac{1}{2} U_{x_{up}} \right]^2 \\ &= P_{up} + \frac{3}{8} U_{x_{up}}^2 \end{aligned} \quad (11)$$

Therefore,

$$Pt_{mixing\ loss} = \frac{1}{8} U_{x_{up}}^2 \quad (12)$$

These quantities will be compared with the results of the deterministic calculation described below.

With deterministic stresses:

Continuity:

$$\left[\int U_x dy \right]_{up} = (\bar{U}_{x_{dn}}) Area_{dn} \quad (13)$$

Momentum:

$$\left[\int (U_x^2 + P) dy \right]_{up} = (\bar{U}_{x_{dn}}^2 + \bar{U}_{x_{dn}}^2 + \bar{P}_{dn}) Area_{dn} \quad (14)$$

In the deterministic stress method, all of the area-averaged (density-averaged in compressible flow) quantities are continuous across the interface plane:

$$\begin{aligned} \bar{U}_{x_{dn}} &= \bar{U}_{x_{up}} = \left[\int U_x dy / \int dy \right]_{up} = \frac{A_2 U_{x_{up}}}{A_1 + A_2} = \frac{1}{2} U_{x_{up}} \\ \bar{U}_{x_{dn}}^2 &= \bar{U}_{x_{up}}^2 = \left[\int (U_x - \bar{U}_{x_{up}})^2 dy / \int dy \right]_{up} \\ &= \frac{A_1 \left(\frac{A_2 U_{x_{up}}}{A_1 + A_2} \right)^2 + A_2 \left[\left(1 - \frac{A_2}{A_1 + A_2} \right) U_{x_{up}} \right]^2}{A_1 + A_2} \\ &= \frac{1}{4} U_{x_{up}}^2 \bar{P}_{dn} = \bar{P}_{up} = P_{up} \end{aligned} \quad (15)$$

The deterministic stress, $\bar{U}_{x_{dn}}^2 = (1/4) U_{x_{up}}^2$, represents the blockage and prevents the static pressure discontinuity seen in

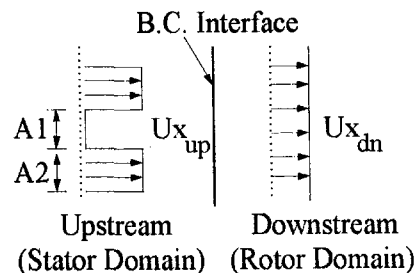


Fig. 16 Two dimensional incompressible flow example

the calculation without deterministic stresses (see Eq. (10)). This is an important characteristic for compressible flow since density and U_x are not affected. More importantly, the velocity triangles are preserved across the interface plane.

In the deterministic stress approach, the area-averaged total pressure is continuous:

$$\begin{aligned} [Pt_{up}]_{\text{area averaged}} &= P_{up} + \frac{1}{4}Ux_{up}^2 \\ [Pt_{dn}]_{\text{area averaged}} &= \tilde{P}_{dn} + \frac{1}{2}\overline{Ux_{dn}^2} + \frac{1}{2}\overline{\tilde{Ux_{dn}^2}} \\ &= P_{up} + \frac{1}{8}Ux_{up}^2 + \frac{1}{8}Ux_{up}^2 \\ &= P_{up} + \frac{1}{4}Ux_{up}^2 \end{aligned} \quad (16)$$

(One can show that mass-averaged total pressure is preserved also.) The deterministic stress term, $(1/2)\tilde{Ux_{dn}^2} = (1/8)Ux_{up}^2$, represents mixing loss and will approach zero at a far downstream location (compare with Eq. (12)). It is clear that the deterministic stresses represent both blockage and mixing loss. It is a logical way to overlap the solution domains without discontinuous representation of physical quantities between calculation domains. Discontinuities in the solution (without deterministic stresses) are less physical and alter the physical processes. These fine details become extremely important in multistage calculations where small errors accumulate through many stages.

7 Reynolds Stresses. The two equation κ - ϵ model is used to model Reynolds stresses. The density averaged κ - ϵ values are passed as boundary conditions at interfaces and the κ - ϵ equations have deterministic correlations similar to the momentum and energy equations. The production of kinetic energy due to the wake gradient must be accounted for. The gradients due to the steady wakes are lost across the interface plane but must be accounted for (see Ref. 19).

In the present work, the turbulence production term due to the circumferential distortion in the wake is passed to the downstream blade row κ - ϵ computation. (Reynolds stresses due to the circumferential distortion in the wake are also passed to the downstream momentum equation computations.) Otherwise the freestream kinetic energy will decay through the multistage computational domain as in a freestream calculation. The idea is to superimpose the turbulence production mechanism between blade frames of computation. However, this does not include the additional turbulence production effect due to the unsteady response effects such as wake chopping by downstream blades.

8 Convergence. Including more physics in modeling is not inexpensive. Early in the development effort, we experienced some significant convergence problems. The blade rows swing through enormous changes from choked to stalled conditions and vice versa. The numerical scheme has to be robust to accommodate these swings. The most important technique for enhancing the convergence in the present procedure is to specify

a target mass flow rate for each blade row as a constraint. Back pressure level at the exit of each blade row is independently adjusted while fixing the radial profile shape to drive the flow rate to the specified mass rate. At convergence, all boundary conditions at the interface planes are satisfied across interface planes. With this technique the convergence characteristic has improved significantly. A typical multistage calculation converges at about 4000 global iterations for an operating line point. A converged solution can be used as an initial condition for calculating the next point on a performance map. It takes approximately 2000 iterations to converge each additional point on a performance map.

Physical convergence criteria are used instead of absolute numerical convergence criteria. In a general sense, the physical aspects of the flow field are converged when they stop changing appreciably with iteration count. The compressor designers monitor the physical parameters in hierarchical order, beginning with the first-order parameters (mass flow, static pressure, etc.) and continuing through second-order parameters (total pressure, total temperature, efficiency, etc.). The designer normally monitors compressor exit total pressure and temperature and declares convergence when the mass-averaged total pressure and temperature no longer change with iteration. Typically oscillations in these parameters of less than 0.1 percent define convergence.

Validation

A three-stage high compressor rig for two different vane configurations known as the Straight HPC and Bowed HPC (straight and bowed vanes) compressors are computed and compared with experimental data.

Three Stage (Seven Airfoils) Calculation With Bodyforces and Deterministic Stresses. Two different multistage compressor results are presented to highlight the current computational capability in application to real world compressors. Both compressors represent the middle block of current large commercial engines (PW4000 series). The first compressor, Straight HPC,² features conventional straight vanes. Straight vanes typically have large corner separations at operating conditions. The second compressor, Bowed HPC,³ employs bowed vanes, which eliminate the corner separations at operating conditions for improved efficiency [20].

1 Compressor With Straight Vanes (Straight HPC). The computation was executed in two different ways for comparison. The first computation was done using the mixing-plane/no-bodyforce approach denoted as the NASTAR-I approach for the convenience of the following discussion. The second computation was done using the new deterministic stress approach with bodyforces denoted as NASTAR-II. The NASTAR-II computation accurately predicted the global total pressure ratio for this three-stage compressor, as seen in Fig. 17. It should be stressed here that this was a significant improvement over the NASTAR-I computation where the bodyforces and deterministic stresses were absent. The predicted total pressure and total temperature profiles at the compressor exit, normalized by the inlet values at the corresponding spanwise locations, using the NASTAR-II approach compare well with experimental data as shown in Fig. 18. The NASTAR-I computation produced a larger total pressure defect near the hub and underpredicted the overall total pressure and temperature ratios.

2 Compressor With Bowed Vanes (Bowed HPC). The NASTAR-II computation accurately predicted the speedline for this three-stage compressor as seen in Fig. 19. The NASTAR-I computation for the operating line was also reasonable since the flow separations were small. The bodyforces and determinis-

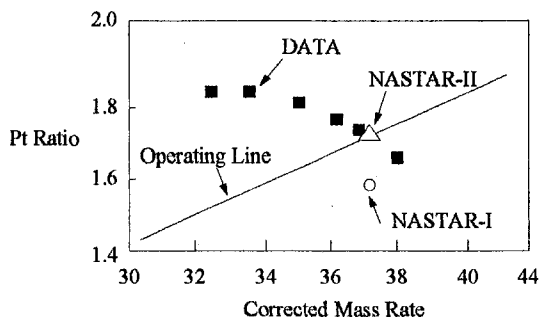


Fig. 17 Global total pressure prediction for Straight HPC

² P&W's 4KMS1 compressor rig.

³ P&W's 4KMS2 compressor rig.

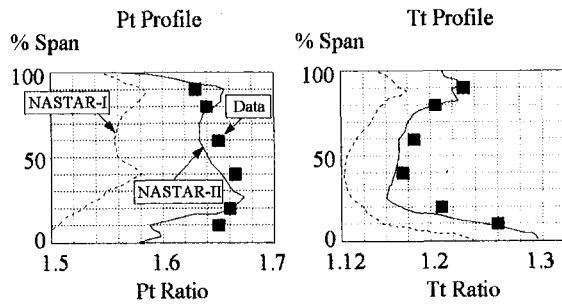


Fig. 18 Pt and Tt profiles at the operating condition for Straight HPC

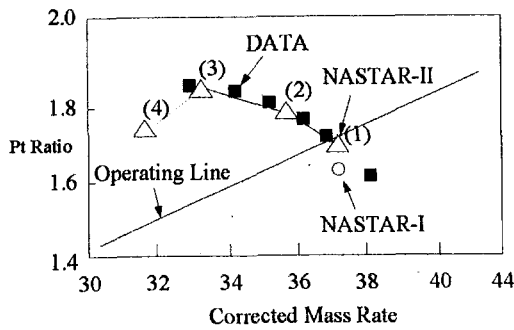


Fig. 19 Global total pressure prediction for Bowed HPC

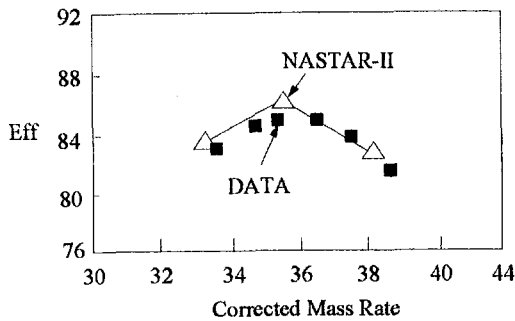


Fig. 20 Efficiency lapse rate prediction for Bowed HPC

tic stresses become important as the flow separation grows as in the case of the Straight HPC or in the Bowed HPC at near-stall conditions. The predicted compressor efficiency lapse rate, plotted in Fig. 20, shows that the maximum efficiency point is well predicted by the NASTAR-II computation. The predicted compressor exit total pressure and total temperature profiles using the NASTAR-II approach at the operating line are in excellent agreement with experimental data as shown in Fig. 21. Figure 22 shows the comparison of blade surface static

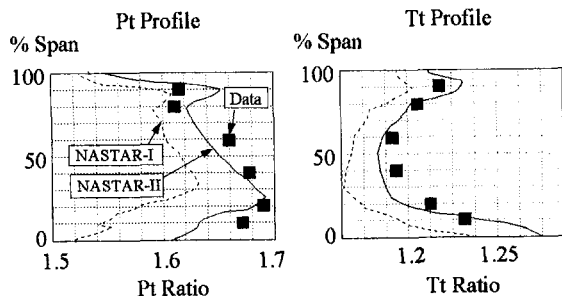


Fig. 21 Pt and Tt profiles at the operating condition for Bowed HPC

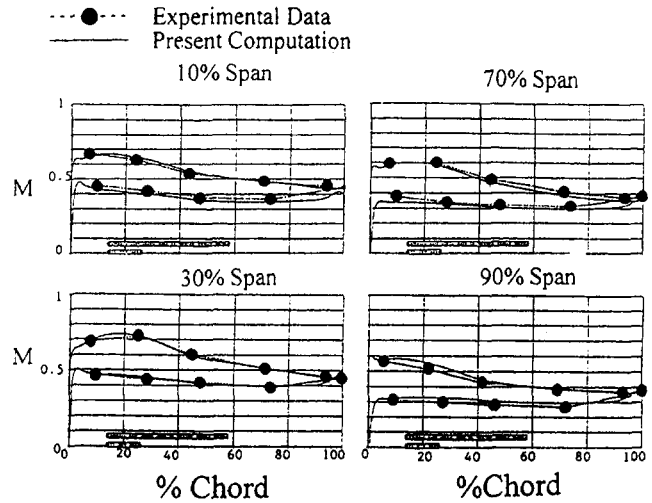


Fig. 22 Surface static pressure comparison at the operating line for third stator (symbol: data/line: present computation)

pressure distribution in terms of isentropic Mach numbers for the third stator at the operating line condition. Excellent surface solution quality is demonstrated.

The Bowed HPC calculation generally shows better accuracy than the previous Straight HPC calculation, because the bowed compressor eliminates large flow separations with the help from advanced computational tools such as the current Navier-Stokes code. Figure 23 shows the predicted radial efficiency profiles at the operating line and near-surge conditions. They show very good comparison with experimental data. The trend of the calculated efficiency profiles provides great physical insight into the understanding of this compressor. At the near-surge condition, the efficiency profile shows serious weakness near the midspan location. This is because the stators develop large flow separations at this radial location. The flow separation is evident in the third stator trailing edge plane total pressure contours shown in Fig. 24. Compressor designers used this information to change the compressor design.

As the calculation is pushed beyond the measured peak pressure point (point (3) in Fig. 19), the calculation also shows loss of pressure rise capability and indicates simulated stall as shown by point (4) in Fig. 19. The accumulated experience from various compressors indicates that the present Navier-Stokes procedure captures stall limit trends very well (e.g., see [21]).

Computing Environment

A typical calculation is for a three-stage (seven blade row) compressor block. The grid used is $120 \times 36 \times 47$ points per blade and approximately 1.5 million grid points for three stages.

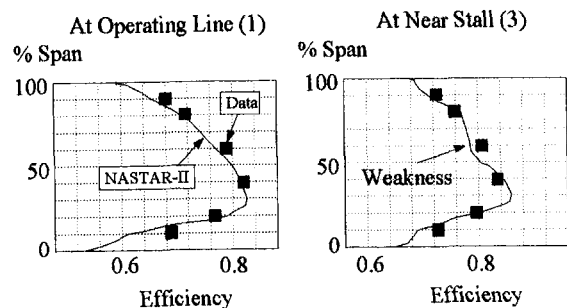


Fig. 23 Efficiency profiles at the operating and near-surge conditions for Bowed HPC

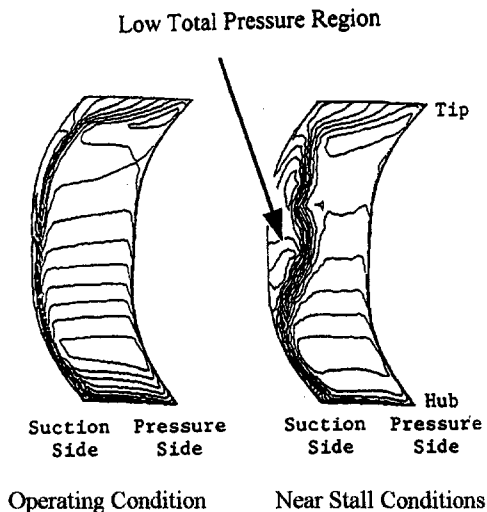


Fig. 24 Total pressure contours at the trailing edge plane for the bowed third stator

The computational platform used is a parallel calculation in an open workstation network [22]. Each blade row is parallelized using a domain decomposition method and the interface boundary conditions are communicated between blade rows at every iteration. The bodyforces and deterministic stresses are communicated at every 10 iterations. It takes about 40 hours for convergence using 21 SUN-SPARC10 workstations.

Application to Current Products

The present Navier–Stokes code was applied during the design and development of the current PW4090 engine high compressor. Relying on the Navier–Stokes code, rather than adhering to conventional design rules, a better compressor was designed. Relative to the previously tested compressor, the new design showed an increase of 1.5 percent in adiabatic efficiency. In addition, the new design resulted in superior stall margin. More details can be found in the companion paper (Part II of this paper, [14]).

Conclusion

This paper described the advanced capability of a Navier–Stokes procedure for multistage compressor analysis. The current continuous interface plane approach based on average passage equations implements bodyforces and major deterministic stresses for multistage simulation. The improved physical modeling terms take into account neighboring blade forces and unsteady flow effects in a rigorous manner. It has been demonstrated through a simple example and controlled numerical experiments that the deterministic stresses represent wake blockage and mixing loss.

A number of comparisons between the experimental data and the computations during the validation phase employing the hundreds of networked workstations demonstrated that the present Navier–Stokes code can accurately capture global performance levels at various operating conditions. A comparison of radial profiles also showed excellent correlations. The success of the validation effort earned substantial credibility for the Navier–Stokes code and pushed the code from the development stage into the compressor design system, where it was used to design an 11-stage high-pressure compressor.

Acknowledgment

The authors would like to thank P&W's management for encouraging us to publish this paper. We would also like to thank numerous people in P&W's compressor group for their help in bringing physical insight into the compressor multistage modeling and their help running the code for validation effort. We would like to thank R. Malecki for bodyforce coding and J. Eley for independent deterministic stress derivation. We would like to thank R. Dring and M. Barnett at UTRC for useful discussions on the multistage modeling, and would like to thank J. Adamczyk and T. Strazisar at the NASA Lewis Research Center for suggesting the bodyforces and deterministic stresses during their visits to P&W.

Reference

- 1 Dawes, W. N., "A Numerical Analysis of the Three-Dimensional Viscous Flow in a Transonic Compressor Rotor and Comparison With Experiment," *ASME JOURNAL OF TURBOMACHINERY*, Vol. 109, 1987, pp. 83–90.
- 2 Von Backstrom, T. W., "Dawes and Denton Codes Applied to a Transonic Compressor Rotor," *ASME Paper No. 90-GT-304*, 1990.
- 3 Adamczyk, J. J., Celestina, M. L., and Greitzer, E. M., "The Role of Tip Clearance in High-Speed Fan Stall," *ASME JOURNAL OF TURBOMACHINERY*, Vol. 115, pp. 28–39.
- 4 Hah, C., and Reid, L., "A Viscous Flow Study of Shock–Boundary Layer Interaction, Radial Transport, and Wake Development in a Transonic Compressor," *ASME JOURNAL OF TURBOMACHINERY*, Vol. 114, 1992, pp. 538–547.
- 5 Chima, R. V., "Viscous Three-Dimensional Calculations of Transonic Fan Performance," *AGARD 77th Symposium on CFD Techniques for Propulsion Applications*, Paper No. 21, NASA TM 103800, May 1991.
- 6 Weber, K. F., and Delaney, R. A., "Viscous Analysis of Three-Dimensional Turbomachinery Flows on Body Conforming Grids Using an Implicit Solver," *ASME Paper No. 91-GT-205*, 1991.
- 7 Jennions, I. K., and Turner, M. G., "Three-Dimensional Navier–Stokes Computations of Transonic Fan Flow Using an Explicit Flow Solver and an Implicit κ – ϵ Solver," *ASME Paper No. 91-GT-309*, 1992.
- 8 Davis, R. L., Hobbs, D. E., and Weingold, H. D., "Prediction of Compressor Cascade Performance Using a Navier–Stokes Technique," *ASME JOURNAL OF TURBOMACHINERY*, Vol. 110, 1988, pp. 520–531.
- 9 Rhie, C. M., Zacharias, R. M., Hobbs, D. E., Sarathy, K. P., Biederman, B. P., Lejambre, C. R., and Spear, D. A., "Advanced Transonic Fan Design Procedure Based on a Navier–Stokes Method," *ASME JOURNAL OF TURBOMACHINERY*, Vol. 116, No. 2, 1994, pp. 179–346.
- 10 Dring, R. P., and Spear, D. A., "The Effects of Wake Mixing on Compressor Aerodynamics," *ASME JOURNAL OF TURBOMACHINERY*, Vol. 113, 1991, pp. 600–607.
- 11 Giles, M. B., "Non-reflecting Boundary Conditions for Euler Equation Calculations," *AIAA Paper No. 89-1942-CP*, 1989.
- 12 Adamczyk, J. J., "Model Equation for Simulating Flows in Multistage Turbomachinery," *ASME Paper No. 85-GT-226*, 1985.
- 13 Mulac, R. A., and Adamczyk, J. J., "The Numerical Simulation of a High-Speed Axial Flow Compressor," *ASME JOURNAL OF TURBOMACHINERY*, Vol. 108, No. 2, 1986.
- 14 Lejambre, C. R., Zacharias, R. M., Biederman, B. P., Gleixner, A. J., and Yetka, C. J., "Development and Application of a Multistage Navier–Stokes Solver: Part II—Application to a High Pressure Compressor Design," *ASME JOURNAL OF TURBOMACHINERY*, Vol. 120, 1998, pp. 215–223.
- 15 Dash, S. M., Beddini, R. A., Wolf, D. E., and Sinha, N., "Viscous/Inviscid Analysis of Curved Sub- or Supersonic Wall Jets," *AIAA J.*, Vol. 23, Jan. 1985, pp. 12–13.
- 16 Rhie, C. M., "Pressure Based Navier–Stokes Solver Using the Multigrid Method," *AIAA J.*, Vol. 27, No. 8, 1989, pp. 1017–1018.
- 17 Rhie, C. M., Stowers, S. T., "Navier–Stokes Analysis for High Speed Flows Using a Pressure Correction Algorithm," *AIAA J. of Propulsion and Power*, 1988, pp. 564–570.
- 18 Evans, R. L., "Turbulence and Unsteadiness Measurements Downstream of a Moving Blade Row," *ASME Paper No. 74-GT-73*, 1973.
- 19 Johnson, R. W., and Adamczyk, J. J., "Kinetic Energy Equations for the Average-Passage Equation System," *AIAA J. Propulsion*, Vol. 5, No. 2, 1989, pp. 252–254.
- 20 Weingold, H. D., Neubert, R. J., Behlke, R. F., and Potter, G. E., "Bowed Stators: An Example of CFD Applied to Improve Multistage Compressor Efficiency," *ASME JOURNAL OF TURBOMACHINERY*, Vol. 119, 1997, pp. 161–168.
- 21 Dring, R. P., Sprout, W. D., and Weingold, H. D., "Navier–Stokes Analysis of the Effect of Tip Clearance on Compressor Stall Margin," *ASME Paper No. 95-GT-190*, 1995.
- 22 Fischberg, C. J., "Use of Hundreds of Workstation for Production Running of Parallelized CFD Application," presented at the Parallel CFD 1995 Conference, Pasadena, CA, June 26–29, 1995.

Development and Application of a Multistage Navier–Stokes Flow Solver: Part II— Application to a High-Pressure Compressor Design

C. R. LeJambre

R. M. Zacharias

B. P. Biederman

A. J. Gleixner

C. J. Yetka

Pratt & Whitney,
E. Hartford, CT

Two versions of a three-dimensional multistage Navier–Stokes code were used to optimize the design of an eleven-stage high-pressure compressor. The first version of the code utilized a “mixing plane” approach to compute the flow through multistage machines. The effects due to tip clearances and flowpath cavities were not modeled. This code was used to minimize the regions of separation on airfoil and endwall surfaces for the compressor. The resulting compressor contained bowed stators and rotor airfoils with contoured endwalls. Experimental data acquired for the HPC showed that it achieved 2 percent higher efficiency than a baseline machine, but it had 14 percent lower stall margin. Increased stall margin of the HPC was achieved by modifying the stator airfoils without compromising the gain in efficiency as demonstrated in subsequent rig and engine tests. The modifications to the stators were defined by using the second version of the multistage Navier–Stokes code, which models the effects of tip clearance and endwall flowpath cavities, as well as the effects of adjacent airfoil rows through the use of “bodyforces” and “deterministic stresses.” The application of the Navier–Stokes code was assessed to yield up to 50 percent reduction in the compressor development time and cost.

Introduction

The design system for compression systems at Pratt & Whitney has evolved since the 1940s. Through the 1950s, the design system was based on one-dimensional fluid dynamics. By the 1960s design technology had advanced to two-dimensional, inviscid, steady flow, when streamline throughflow calculations were used and the two-dimensional blading was based on correlations derived from a cascade test data base. In the 1970s blade-to-blade potential flow solvers were introduced with simple boundary layer model calculations. The potential flow solvers were used to optimize the two-dimensional blading. By the 1980s viscous effects were accounted for through the solution of the two-dimensional Navier–Stokes equations. However, neither the CFD codes nor the computers available to designers were advanced enough to solve three-dimensional problems routinely for design studies. Empirical correlations were applied to account for three-dimensional endwall, tip clearance, and cavity and bleed effects. These correlations were based on the data base developed by commercial engine companies, universities, research laboratories, etc. Final blading was only designed for 20 to 80 percent span; the empirical design rules determined the blading near the endwalls. However, the design rules broke down in the viscous regions of the problem (on the airfoil surface and in the endwalls) when drastic changes were made to the airfoil geometries because these rules did not fundamentally describe the three-dimensional, viscous aerodynamics of compressor flows.

Contributed by the International Gas Turbine Institute and presented at the 40th International Gas Turbine and Aeroengine Congress and Exhibition, Houston, Texas, June 5–8, 1995. Manuscript received by the International Gas Turbine Institute March 15, 1995. Paper No. 95-GT-343. Associate Technical Editor: C. J. Russo.

The development and introduction of novel, three-dimensional blading concepts to optimize the compressor performance were expensive and time consuming. They were limited to small, incremental changes to heavily tested designs because the risk associated with implementing significant changes in airfoil designs was high. A typical high-pressure compressor design proceeded as follows, as depicted in Fig. 1. Overall flow and pressure rise for the compressor were defined. Number of stages and flowpath were chosen, and velocity triangles were created using a meanline program. Preliminary blading was defined using a streamline program with empirical corrections for three-dimensional viscous effects. Two-dimensional airfoil cross sections were defined and stacked to form the three-dimensional airfoil. Simple two-dimensional viscous CFD calculations were made on representative airfoil cross sections to check blade loadings, flow separations, etc. A research rig was then built to test the configuration. The rig usually contained one third of the total number of stages and used variable pitch geometry in order to match the stages properly and refine vane and blade incidences. After the research rig program was completed, a full-size compressor rig test program was undertaken with variable geometry in all stages, again to allow for fine tuning in order to match stages and achieve the design flow capacity and work distributions. Finally, engine hardware was defined and built for a full-scale engine test.

The design was assessed after each step subsequent to the meanline program, and could be changed.

The iterative procedure would typically take up to three years to carry out and cost as much as twenty million dollars. However, the resulting design was not optimum. No detailed understanding of the internal fluid mechanics was gained; it was not yet possible to break from a previous design with any confidence and in a

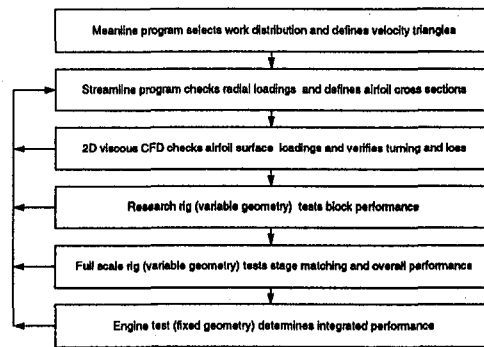


Fig. 1 Empirically based design system

cost-effective manner since the empirically based design system did not extend beyond the data base of tested geometries.

The long development time, high cost, and limited performance gains associated with this design system hastened the development of a new design technology based on the full three-dimensional equations of motion. Design methods based on solving the Navier–Stokes equations became accurate and practical in the 1990s for isolated cascades of airfoils such as fans (Rhie et al., 1994). Early work in developing multistage turbomachinery CFD was done by researchers such as Ni and Bogoiian (1989), Dawes (1992), Denton (1992), Adamczyk et al. (1990), Chima (1991), Hah and Wennerstrom (1991), and Jennions and Turner (1993). As computers became more powerful, it became practical to solve multiple rows of airfoils routinely in order to evaluate new design concepts. This allowed designers to progressively replace the empirical correlations with physics-based models, which resulted in the successful introduction of new three-dimensional blading concepts in the compressor design.

This paper will discuss the application of two versions of a Navier–Stokes based computational fluid dynamics (CFD) design system to high-pressure compressor design. Version I was a multistage code that was a simple extension of the isolated blade row technique, where boundary conditions were applied at midgap locations, and a mixing plane model was used. We will then discuss the application of Version II, where the code was improved by using bodyforces and deterministic stresses to account for the effects of neighboring airfoils more accurately. It will illustrate how designers used CFD as a “numerical rig” in order to conduct “numerical experiments” and interrogate new physical concepts when optimizing new blading concepts. This paper will discuss the application of the new design to a new high compressor design, including the optimization of bowed stators and controlled diffusion rotor endwalls in a multistage environment. The role of CFD in understanding stage matching and the impact of managing radial flow distributions will be discussed. The philosophy of using CFD models to guide the development process from design through test will be stressed (Rubbert, 1994). The resulting reduction in development cost and time, and the increase in compressor performance will be shown.

Navier–Stokes Based Design System

As CFD and computer hardware technology advanced in the late 1980s and early 1990s, it became possible to routinely compute three-dimensional viscous flowfields for compressor cascades. Development of isolated airfoil row CFD models (Rhie et al., 1994) and subsequent development of multistage CFD models, coupled with the implementation of parallel CFD algorithms on networked engineering workstations (Fischberg, 1995; Gundy-Burlet, 1993; Blech et al., 1992) made it possible for compressor designers to conduct extensive development pro-

grams numerically rather than experimentally. These technologies would become the basis of the 1990s design system.

A goal was defined to create a new design system that centered around three-dimensional Navier–Stokes calculations for multistage compressor flows. The three-dimensional CFD would be used to assess the performance of the compressor instead of the research rig tests and full-scale rig tests with variable stator geometry. The objective of the design system was to go to full-scale rig test with engine hardware. The goal was to cut the design cycle costs and time by up to 50 percent, while increasing the performance of the compressor. The new design system is depicted in Fig. 2.

A new design system based on three-dimensional Navier–Stokes analysis was designed as follows. Preliminary flowpath shape and size and preliminary blading are defined using the one-dimensional and two-dimensional meanline and streamline models with empirically derived corrections. However, prior to undertaking any time-consuming and expensive rig or engine testing, the design is extensively tested using a three-dimensional multistage Navier–Stokes CFD code. This code is described in the companion paper (Rhie et al., 1998) and will be briefly reviewed in a later section.

By using the three-dimensional Navier–Stokes procedure to assess the performance of the new design, the designer would be able to “match” stages properly to achieve design pressure rise and flow characteristics more quickly and less expensively than in a rig program. Design rules based on empiricism would be replaced with physics-based models derived from the CFD calculation. The choice to model or grid additional physical features was based on the computational resources required. It was determined that gridding and computing the bleed ports and the stator cavities required the same amount of grid as the airfoil passage (approximately 300,000 grid points). Using a total of 600,000 grid points per blade row would not be possible for a production design system, so it was decided to model the bleed and the cavity through flow extraction/injection techniques. However, it was determined through calibration that the tip clearance region of rotor tips could be accurately gridded and computed by adding 10 percent more grid.

Using the new design system, detailed understanding of the fluid flow would be obtained in three dimensions; the flowfield would be computed to the blade surface and to the endwalls, and sources of blockage and loss such as tip clearance, cavities, bleeds, and airfoil separation would be simulated and understood more accurately than by the empirically based models. In the new Navier–Stokes based design system, three-dimensional blockage/loss effects would be accounted for in the design, and novel three-dimensional blading concepts could be implemented to maximize performance. In addition, the off-design performance of the compressor could be assessed; the effect of flow migration on off-design performance can be simulated and understood, and could therefore be taken into account in the design. With proper validation, the Navier–Stokes-based design

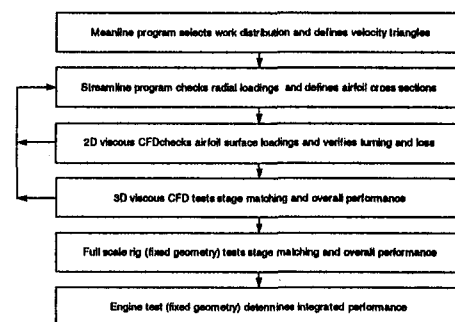


Fig. 2 New design system centers around three-dimensional Navier–Stokes calculations instead of rig testing

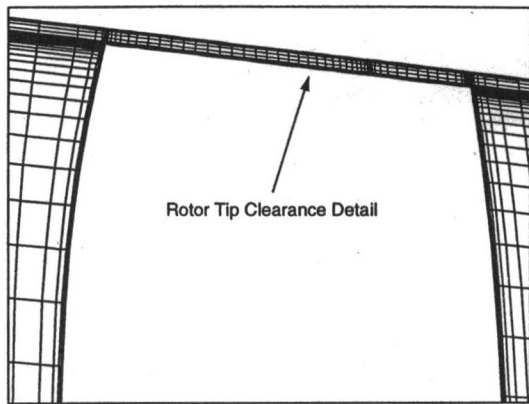


Fig. 3 Detail of grid at rotor tip

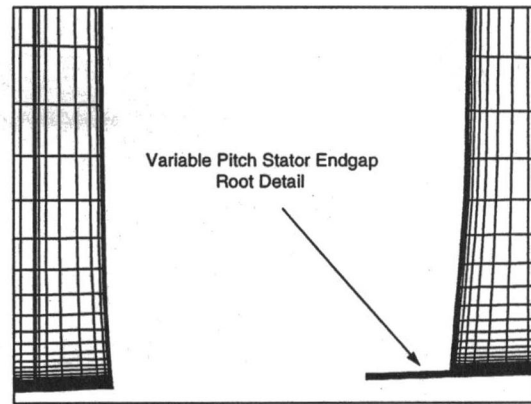


Fig. 4 Grid detail near variable pitch stator root, showing blunt trailing edge at trunnion trailing edge

system would be used to extend designs beyond the current experience envelope. These new three-dimensional designs would be developed and refined in a cost effective manner, which would greatly impact the compressor design cycle cost, time and performance.

Developing and implementing this new design system was an ambitious goal. It was understood by all involved that the system would have to evolve; the degree of accuracy required for design assessment would need to be defined, and the requirement to model real-life features such as rotor tip clearances, variable pitch stator endgaps, stator cavities, and bleeds was unknown. It was therefore decided to develop the system in conjunction with a new eleven stage high compressor design. The data acquired during testing would be used to guide the development of the CFD-based design system.

NASTAR Code

The NASTAR code was the three-dimensional Navier-Stokes solver chosen for use in the new multistage compressor design system, and is described in the companion paper by Rhie et al. (1998) and in Rhie (1988). Important features required for the accurate and economical design computation of compressor flows are described in this section.

The NASTAR code is a finite-volume, implicit, pressure correction Reynolds-averaged Navier-Stokes solver. It uses the standard two-equation $\kappa-\epsilon$ turbulence model integrated to the wall to resolve the viscous boundary layer. The code is parallelized to run on a network of engineering workstations. Each blade row is solved on a computational mesh containing approximately 300,000 points using a standard single block H-mesh.

NASTAR utilizes a grid point "flagging" system, which allows for specific boundary conditions to be applied at a given grid node. A flag is an integer value associated with each grid node that denotes the boundary condition to be applied. Examples include viscous wall, symmetry plan, periodic boundary, mass flow injection or extraction, and flow obstruction (Rhie et al., 1994). The flag system allows for geometric details, such as rotor tip clearances and variable pitch stator endgaps, to be easily incorporated into the computational model.

Figures 3 and 4 show details of the computational mesh for a rotor with tip clearance and a variable pitch stator with endgaps. In these models, mesh points are placed within the airfoil and the flag system is used to describe which points are "solid metal" and which points are "fluid." Careful grid stretchings ensure that boundary layers are properly represented; the first grid point off of a solid surface is typically placed at a $y+$ value of 1.0. A hyperbolic tangent stretching function is used to distribute grid points away from the wall. The stretching function forces the second grid point off of the wall to be placed at a $y+$ value of 2.0.

Other advantages of the flagging system allow for the inclusion of simple stator cavity and endwall bleed models. The cavity and bleed models are simple flow extraction/injection models added to the three-dimensional Navier-Stokes solution, which provide local streamline curvature effects.

Figure 5 shows a schematic of the cavity model. The cavity flow, which is driven by the trailing edge to leading edge pressure gradient, the disk pumping of the drum rotor, and the losses through the knife-edge seals, is modeled as flow extraction at the trailing edge and injection at the leading edge. The driving pressure gradient is extracted from the CFD solution and the pumping and loss through the cavity are driven by a one-dimensional model that accounts for knife edge seal clearance, drum rotor speed, and cavity depth. The model prescribes a cavity flow rate, which is extracted at the stator trailing edge and re-injected at the leading edge. The mass flux is applied uniformly over the extraction and injection slots. The flow solver adjusts the total pressure at the injection location until the prescribed mass flow is achieved. It also prescribes re-injection total temperature boundary at the leading edge. The static pressure at the flow extraction locations near the trailing edge is varied by the solver until the prescribed mass flow rate is achieved. The flow re-injection at the leading edge of the stator creates loss and blockage, which are then accounted for in the three-dimensional solution procedure.

Figure 6 shows a schematic of the bleed model. The bleed flow is extracted from the calculation through an orifice carved out of the computational mesh. This flow extraction is required to compute the flow angles into the next airfoil row properly, because the bleed changes the corrected flow into the next row. As in the cavity model, the mass is extracted uniformly over

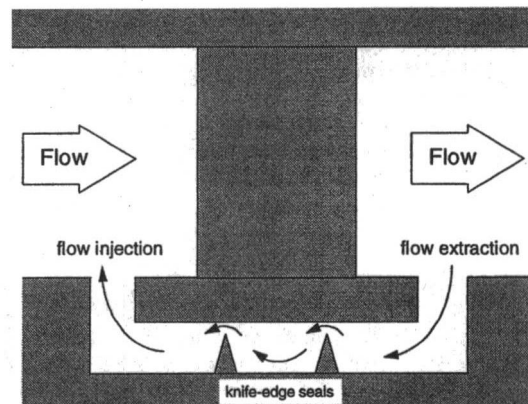


Fig. 5 Schematic of cavity model

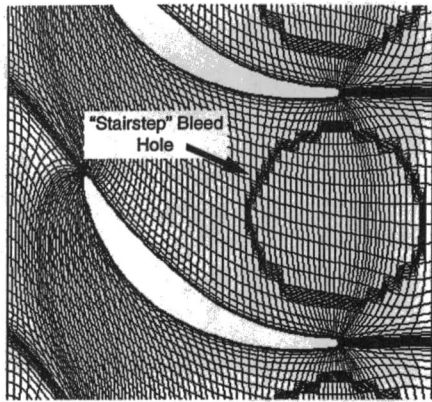


Fig. 6 Grid detail showing model of bleed hole

the orifice. The code treats this zone as an exit boundary condition and varies the local static pressure until the prescribed mass flow extraction is achieved.

The multistage NASTAR code was developed in two versions. In the first, the multistage environment was accounted for by using a "mixing plane" approach. The approach was satisfactory at the design point when flow separations were small. It is shown in the companion paper (Rhie et al., 1998) that the mixing plane model tends to overemphasize the effects of upstream blade row separation on the downstream blade row. The large blockages created upstream are not mixed out properly as they are in the second version, where the multistage environment is accounted for through the use of bodyforce and deterministic stress models (see companion paper by Rhie et al., 1998, and Adamczyk et al., 1986). This approach was developed to allow for analysis off-design, where flow separations become significant and the deterministic stresses tend to mix out the blockage of the upstream blade row.

The first version of the code was a simple extension of the isolated blade row NASTAR code. The total pressure, total temperature, and flow angles are given and held upstream of the first airfoil row. The static pressure is given and held downstream of the last blade row. Intermediate blade rows apply the total pressure, total temperature, and flow angles midway between the trailing edge of the upstream row and the current leading edge. The conditions are convected from upstream through a mixing plane (Dawes, 1992) to account for reference frame changes. The static pressure is applied midway between the current trailing edge and the leading edge of the downstream blade row.

The second version of the code improved the multistage modeling. In this version, multistage effects are modeled through the use of bodyforces and deterministic stresses. As in the first version, far upstream conditions are given and held. Similarly, static pressure is specified far downstream. The difference between the two versions has to do with the way information is passed between intermediate blade rows, and how neighboring blade rows effect an intermediate blade row.

Figure 7 shows a side view (axial-radial projection) of a typical computational mesh for a compressor stage. The top figure is the computational domain for the stator, while the bottom figure is for the downstream rotor. The stator mesh and computation have several features. First, since this is a stage from the front block of the compressor that contains variable pitch stators, the stator endgap clearances are gridded. A side view detail of the stator endgap at the inner diameter was shown in Fig. 3. The stator domain contains an axial extension, which encompasses the down stream rotor. The grid in this region conforms to the geometry of the rotor, and is used to model the back-pressuring effects of the rotor. Pressure forces developed in the rotor computational domain are transferred to the stator

domain and are applied as axisymmetric bodyforce source terms. Deterministic stresses due to circumferentially nonuniform flow in the stator domain are computed and transferred as turbulence-like stresses to the rotor domain.

The rotor mesh and computation has several features. The rotor tip clearance is gridded. A detail of the clearance grid was shown in Fig. 4. Airfoil pressure forces compute on the rotor are axisymmetrically passed to the upstream stator, while deterministic stresses caused by upstream stator flowfield circumferential nonuniformities caused by the rotor (due to leading edge bow shocks, for example) are passed upstream and overlaid on top of the stator as deterministic stresses.

Application to a High-Pressure Compressor Design

The new Navier–Stokes-based design system was developed and used to design and optimize a new high-pressure compressor configuration. The new design was for a growth version of a current high thrust engine, and as such, was required to fit within several pre-established geometric and aerodynamic constraints. It had to match and perform with other engine components such as the low-pressure compressor and the high-pressure turbine. Also, since the growth engine designs are limited by thermal/mechanical design constraints, high compressor efficiency improvements were required to stay within material thermal limits. In this case, the efficiency improvements were less important for fuel burn performance. The goal of the design was to improve high pressure compressor efficiency without sacrificing stall margin.

New technologies were available and were well understood in an isolated environment for improving the high compressor efficiency, such as bowed stators and controlled diffusion rotor root endwalls, but they were not well understood in the multistage environment. The empirically based design system did not account for these fundamental changes in blading in its blockage/loss/turning models. The impact of radical flow redistribution through blading changes introduced a substantial risk in terms of off-design stability performance. The traditional cycle of design/test/redesign would have taken too long, been too expensive, and would have involved too much risk to have a timely impact on growth engine development using these technologies. The Navier–Stokes-based design system was developed to understand and tailor the radial and axial flows, and to optimize the new blading technology to gain efficiency without sacrificing stability.

Design/Off-Design Analysis and Test Program

This section describes the analysis and CFD system development that was performed in support of the new high pressure compressor design.

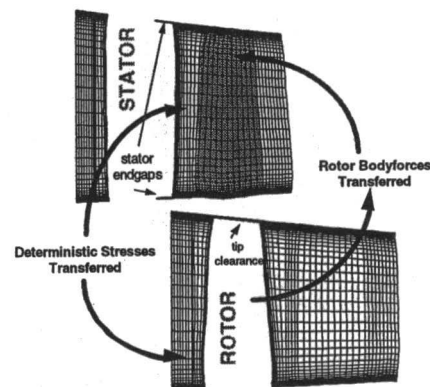


Fig. 7 Multistage modeling in NASTAR includes incorporation of bodyforces through transfer of blade forces

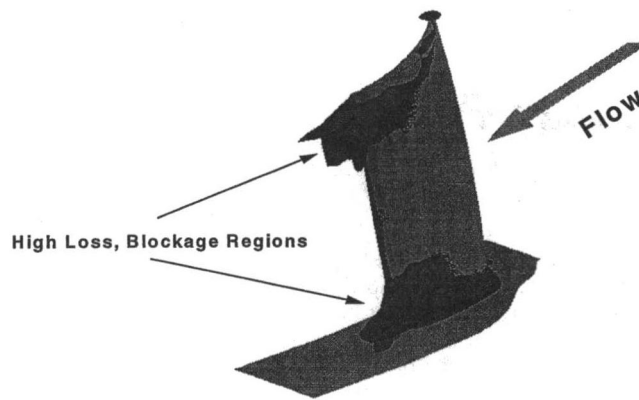


Fig. 8 Isosurface of zero axial flow, showing boundary of three-dimensional separation evident in corners of straight compressor stators

The initial blading design/optimization was carried out with the earliest versions of the multistage NASTAR code. This version used a simplistic interrow mixing plane model to pass the calculated exit conditions of one row to the inlet of the next. This multistage technique was adequate for the designer to optimize three-dimensional blading features (stator bow and rotor root contouring) in order to eliminate/minimize flow separations. It was anticipated that the elimination of flow separation would account for the majority of the required efficiency improvement.

One of the new airfoil contouring technologies employed to eliminate flow separations was bowed stators. An example of how NASTAR was used to understand the physics of bowed stator technology is described. Figure 8 shows a perspective view of a typical middle block straight (two-dimensional) stator. Air flow enters from the right as indicated. The corner separations on the suction surface of the endwall are indicated by the isosurfaces of zero axial flow. The flow within this surface is separated, and is a source of blockage, loss and turning deviation. Figure 9 shows a bowed stator. The effect of the bow is to produce radial forces that drive flow into the corners, and eliminate the corner separations. The isosurfaces of zero axial flow (the envelope of flow separation) are substantially reduced, which reduces the loss and blockage associated with the stator. Additionally, the deviation of flow angle from metal angle has been changed. The aerodynamic impact of stator bowing is well known (Weingold et al., 1995) and was not developed during this design. However, the *interaction* of the bowed stator with its neighboring airfoil rows was not well understood, and was not accounted for in the loss, blockage, and turning empiricisms.

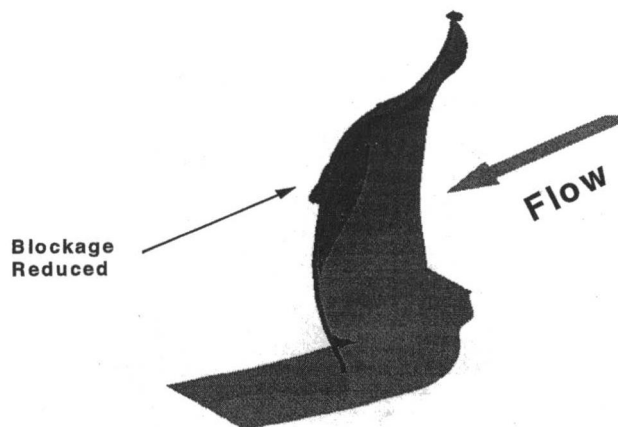


Fig. 9 Isosurface of zero axial flow, showing reduction of three-dimensional separation in bowed compressor stators

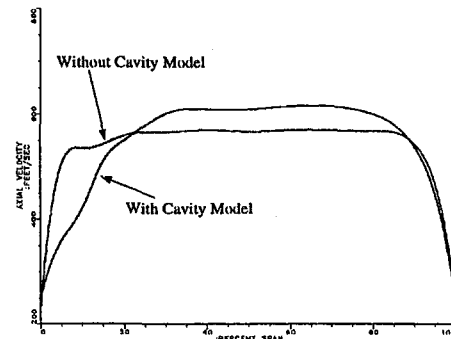


Fig. 10 Straight stators show regions of low axial velocity in the endwalls, and a region of high axial velocity in the midspan, compared to bowed stators

The three-dimensional Navier–Stokes design system allowed designers to *optimize* the bowed stator design in the multistage design-point/off-design environment.

The quantitative effect of bowing the stators is shown in Figs. 10 and 11. Figure 10 is a plot of the circumferentially mass-averaged radial profiles of axial velocity at the stator trailing edge. Both stators were run to the same mass flow rate. The figure shows regions of low axial velocity near the root and the tip for the straight stator. This region of blockage forces flow to the midspan region, where the average axial velocity is higher than the bowed stator.

The effect of stator bowing on average stator exit flow angle is shown in Fig. 11. The circumferentially mass-averaged axial and tangential velocity components were used to compute the average flow angle. Purely axial flow would show a flow angle of 90 deg. The figure shows a severe flow angle falloff in the endwalls of the straight stator, compared to the bowed stator. The large change in stator exit flow angle that occurs when switching from straight to bowed stators forced the designers to alter the rotor leading edge camber angle to properly match the stage. The three-dimensional viscous CFD was used to accomplish this match.

Similar optimization of rotor endwall contouring concepts was achieved using NASTAR. Rotor root contouring, sometimes (mistakenly) referred to as “area-ruling,” was initially employed in the design as a means of increasing the “choke-margin” of high-Mach-number rotors. This was required to improve airfoil durability at higher mechanical speeds. The resulting shape of the ID flowpath wall has additional benefits in that it creates a radial force much the same as stator bow. This radial force redistributes flow and reduces the tendency of the flow to separate at the intersection of the airfoil suction surface and ID flowpath wall. Figure 12 compares the ID wall static pressures of a contoured and noncontoured rotor operating with identical inlet conditions. Figure 13 compares near suction surface and blade-to-blade streaklines of a typical rotor with non-

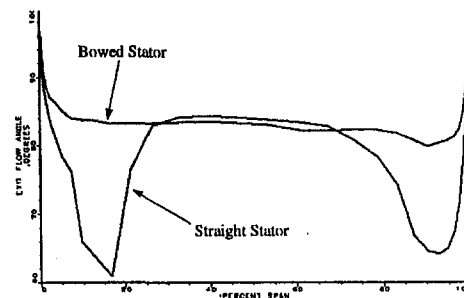


Fig. 11 Effect of stator bow is to change average stator exit flow angle distribution

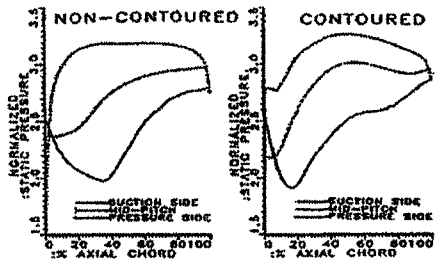


Fig. 12 Comparison of ID wall static pressure for conventional and contoured rotor endwalls

contouring. The remaining separations outboard of the ID wall are due to high two-dimensional airfoil surface loading.

The contoured root not only eliminated separations but has allowed for increased diffusion. The effect, if not accounted for in the design, becomes significant after several compressor stages and can cause the radial total pressure profile to deviate from the design intent. The three-dimensional viscous code was used to optimize the root contour shape and quantify its impact in the multistage environment.

Individual stator/rotor stage pressure ratio/flow capacities were calculated and compared to design intent. Airfoil trailing edge cambers were adjusted based on the initial calculation to achieve the desired flow/pressure ratio levels. Airfoil leading edge angles were also optimized to position each section at the minimum incidence-loss point.

Stator bow angle and radial extent were varied to eliminate endwall corner separations while maintaining unseparated core sections. The depth and chordwise location of the rotor root contouring was also optimized to eliminate separations. Estimates based on these early multistage Navier–Stokes calculations indicated overall compressor efficiency could be improved by as much as 2 percent.

The iterative blade design/Navier–Stokes analysis process was completed within three months of design start, and final blading definition was released for airfoil fabrication. As mentioned earlier in this paper, these airfoils were manufactured with the intent of being directly substituted into development engine compressors. The initial performance, however, was to be demonstrated in a full eleven-stage high-pressure compressor rig. This design using the first version of NASTAR concentrated

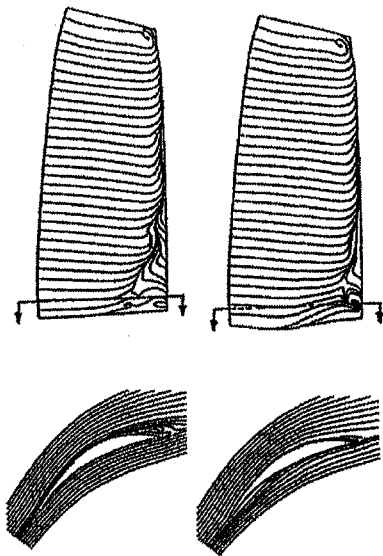


Fig. 13 Streaklines comparing separation near rotor suction surface and near rotor root

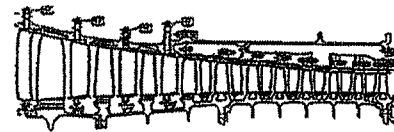


Fig. 14 NASTAR compressor cross section

on increasing performance at the design point. Effects such as tip clearance, stator endgaps, and cavities and bleeds were not modeled. It was not known, however, how the new compressor would perform at off-design conditions, when separations become larger and clearance and cavity flows potentially become more important.

Figure 14 shows a cross section of the NASTAR compressor flowpath and blading. As shown in Table 1, the design point of the NASTAR compressor is identical to the baseline compressor. Besides the solidity increase, the only major features incorporated in the new design were bowed stators and contoured rotor roots.

Rig Build 1. The eleven-stage compressor rig achieved goal performance. Overall pressure rise/flow capacity was within 1 percent of design goal. Efficiency was improved by 2.0 percent over the baseline. The increased efficiency was attributed primarily to bowed stators and contoured rotor roots, which substantially reduced endwall separations. The positive results obtained in this rig test were an important step in the validation of the Navier–Stokes based design system. This rig test is summarized in Fig. 27, which is a plot of compressor efficiency versus stall margin. An assessment of P&W's current state of the art is the shaded line; it shows that compressor efficiency can typically be traded for stall margin. The results of the first rig test can be seen in the upper left portion of the line.

However, the goals of the engine program required that this efficiency be maintained but at a higher level of stall margin. In the interim between release of the final airfoil coordinates and the first testing of the rig, improvements were being made to the NASTAR code. The data suggested that the decrease in the stall margin was due to a decrease in axial flow in the outer half of the compressor, which was causing the rotor tips to become overloaded. Figure 20 shows the measured axial velocity profile at the exit of the compressor at the operating point, and at 11 percent above the operating line. The figure shows the drop in tip axial flow at the higher operating line.

Calculations using the first version of NASTAR, run without bodyforces, deterministic stresses, rotor tip clearances, cavity, or bleed models did not match test data at high operating lines. Version I used the mixing plane model, and tended to overestimate the effect of transferring blockage to the downstream blade row (as discussed in the companion paper, Rhie et al., 1998). Version I also neglected the blockage-producing mechanisms of tip clearance and stator cavities. These effects made Version I unreliable for determining the cause of the surge margin deficit. The addition of more complete physical modeling, which included the above features, provided a better match with the rig data.

Table 1 Baseline versus NASTAR designed compressor design point comparisons

	Baseline HPC	NASTAR HPC
Inlet Corrected Flow	120 lb/sec	120 lb/sec
Pressure Ratio	10:1	10:1
Rotor Solidity	1.095	1.201
Stator Solidity	1.208	1.348
Inlet Axial Mach Number	0.54	0.54
Exit Axial Mach Number	0.23	0.23
Mean Wheel Speed	950 ft/sec	950 ft/sec

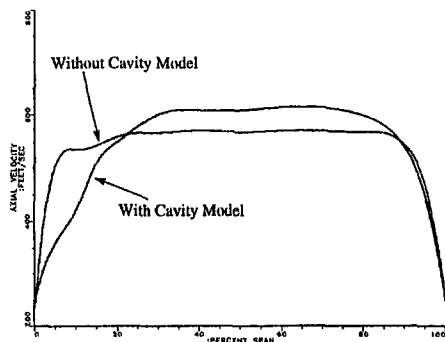


Fig. 15 Cavity model produces blockage at the root of a stator leading edge

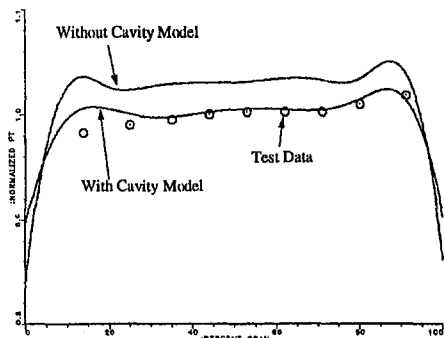


Fig. 16 Cavity model causes pressure rise in downstream rotor to decrease

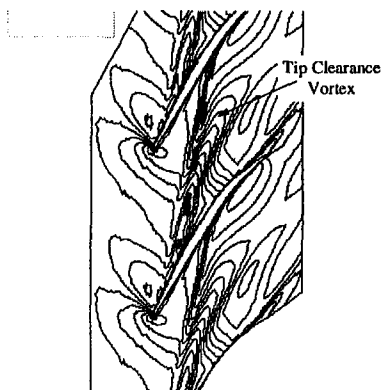


Fig. 17 Rotor tip leakage vortex at onpline condition

An example of how the addition of the cavity model impacted blockage and stage size is shown in Figs. 15 and 16.

Figure 15 is a plot of circumferentially averaged axial velocity versus span at the leading plane of a middle block stator. The re-injection of cavity leakage flow creates a blockage at the root, which causes the axial velocity to increase outboard of 25 percent span.

The radial flow redistribution impacts the downstream rotor. The increase in axial flow delivers a more negative incidence to the rotor, which reduces the work done by the rotor. This effect can be seen in Fig. 16, which shows the normalized, circumferentially averaged total pressure at the downstream rotor trailing edge plotted versus the span. The overall pressure rise for the case with the cavity model is reduced by 3 percent for this single stage.

Similarly, the effect of rotor tip clearance can impact the radial profiles downstream of the rotor. Figure 17 shows a Mach number contour, in a blade-to-blade view, near the tip of a rotor

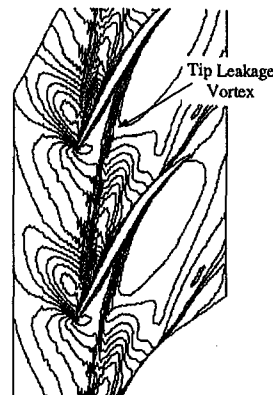


Fig. 18 Tip leakage vortex at high onpline condition, with vortex pushed forward

computed with tip clearance. The effect of the tip leakage vortex on the Mach number is clearly seen. This vortex creates loss, which causes a total pressure falloff in the outer-diameter region of the rotor. As the compressor runs a higher operating lines closer to the stall limit, the leakage vortex responds by getting pushed farther upstream and creating more tip blockage. This effect is shown in Fig. 18, which is the same rotor run at a higher operating line. The clearance vortex is pushed forward for the high onpline case.

Figure 19 shows how the tip clearance blockage increases as the rotor is back-pressured. The figure plots the absolute change in circumferentially average axial velocity as a function of percent span. This figure is for the two cases depicted above. The figure shows that the change in axial velocity is greatest in the tip region, where the blockage due to the clearance vortex increases at the high operating line.

By accounting for clearance flows, the designer also has a mechanism in which to determine the tip clearance sensitivity of the compressor by conducting numerical experiments with various tip clearance gap sizes.

Rig Build 2. Several options were identified to improve the basic compressor stall margin, but these were limited by time and available hardware. A choice was made to re-operate existing blading in the middle stages of the compressor and to return to test. The re-operation of the midblock blading consisted of removing a portion of the stator, or "cutting it back," near the root. A detailed explanation of how the cutbacks impact the radial flow distribution will be given in the following section.

The cutbacks were optimized using the second version of NASTAR. In this redesign, it was critical to predict the flowfield near stall, where separations become large and the mixing plane model breaks down. Here, proper transfer of blockage and the

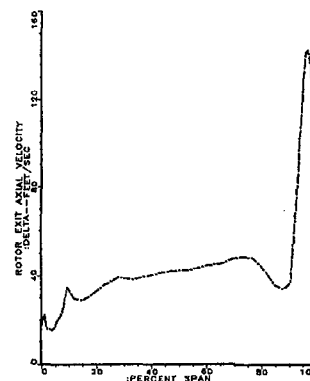


Fig. 19 Rotor tip axial velocity change increases with operating line

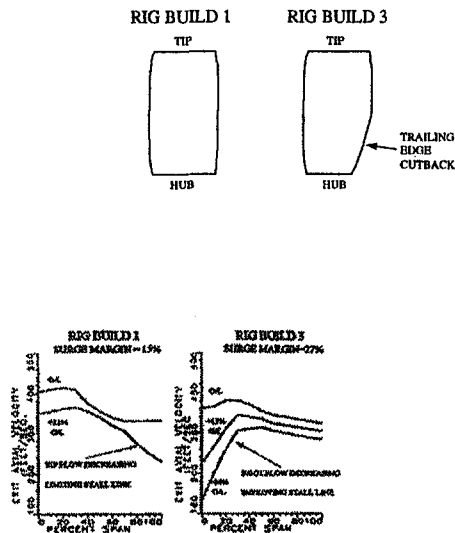


Fig. 20 Stator cutback profiles and effect on radial profiles of axial velocity at compressor exit

potential effects of neighboring blade rows are accounted for by the bodyforces and deterministic stresses. NASTAR was used to tailor the blading changes such that design point performance would not be compromised while improving the compressor's stall margin. The goal of the next rig test would then be to move horizontally to the right on Fig. 27 and truly advance the state-of-the-art design.

The rig teardown, stator modifications, and rig re-build were completed within three months of the previous build's conclusion. Test data indicated that the middle stage stator cutbacks were successful in improving stall margin without sacrificing design point performance. Figure 27 summarizes the second rig build. Stall margin was increased from 15 to 20 percent. The radial flow redistribution suggested by the improved multistage NASTAR analysis was determined to be the source of this stability improvement. In fact, the continuing Navier-Stokes analysis suggested that even more improvements could be realized by extending this radial flow redistribution philosophy further rearward in the compressor. Rear stage stator cutback redesigns were completed and blading modifications were called out.

Rig Build 3. The compressor rig was rebuilt with modified hardware and returned to test. This third and final rig test was successful; stall margin increased an additional 7 percent relative to the previous rig build and a modest gain in efficiency was also demonstrated. Figure 20 shows a typical stator modification used in both the NASTAR rig build 2 and NASTAR rig build 3 compressors. The local trailing edge root cutbacks were easily accomplished by simple reoperations of the existing stator airfoil. The results of the cutbacks are shown in Fig. 20. This figure compares the exit velocity profiles of the build 1 and build 3 compressors. These profiles are based on compressor exit pressure and temperature measurements and streamline throughflow calculations. As seen in the figure, the radial flow redistributions accomplished by the cutbacks changed the off-design behavior of the compressor allowing substantial improvements in stall margin. Maintaining axial velocity near the tip has the desirable effect of offsetting the tip clearance vortex and delaying "tip stall."

Figure 27 summarizes the performance of this build. This rig data also showed that a new state of the art in compressor design was achieved. The next step was to install this compressor directly into a development engine to verify its performance and stability in the engine environment.

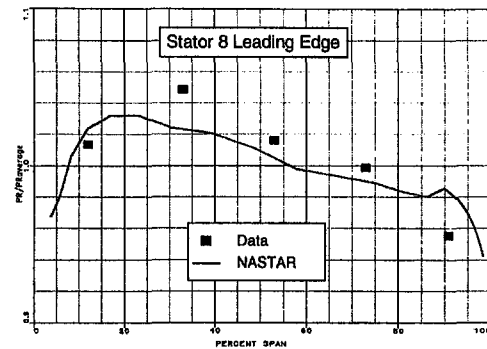


Fig. 21 Total pressure profile at stator 8 leading edge

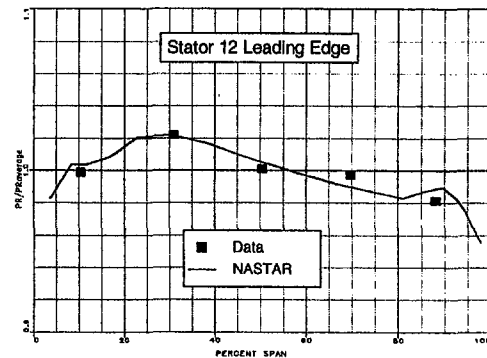


Fig. 22 Total pressure profile at stator 12 leading edge

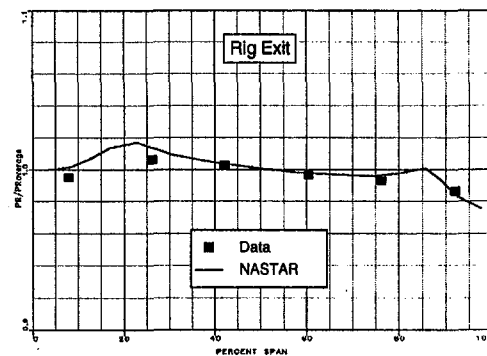


Fig. 23 Total pressure profile at compressor exit

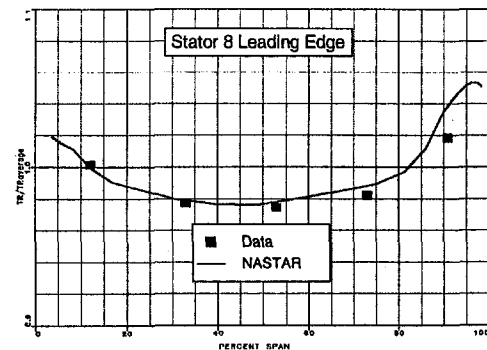


Fig. 24 Total temperature profile at stator 8 leading edge

Figures 21–26 compare the measured rig total pressures and temperatures with NASTAR calculation. The data are taken at the exit of each of the three compressor blocks, and at the

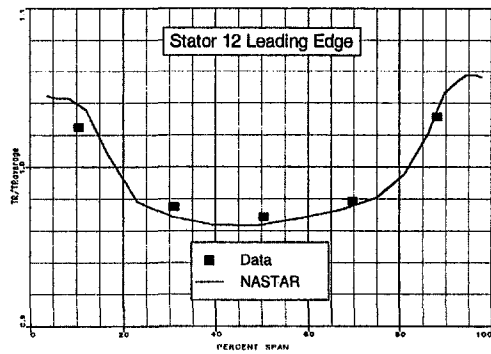


Fig. 25 Total temperature profile at stator 12 leading edge

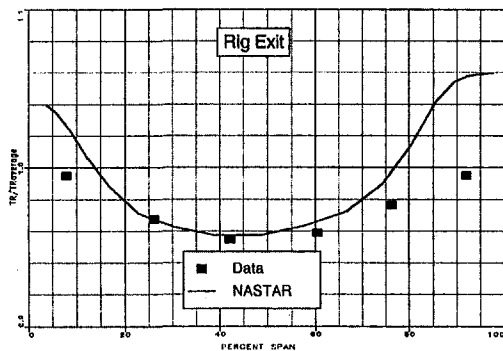


Fig. 26 Total temperature profile at compressor exit

leading edge of stator 8 (front block exit). Although the NASTAR calculation does not match the test data precisely, the calculation predicts the overall stage block pressure and temperature rise within 1 percent, which is within experimental accuracy. The ability of the code to produce solutions of the quality enabled the designers to proceed to the rig test with fixed engine hardware, rather than with variable pitch rig hardware.

Engine Test. Figure 27 summarizes the performance of the compressor in the engine test. The efficiency/stall margin relationship was maintained as measured in the third rig build. The 2.0 percent higher compressor efficiency at no overall stall margin loss has redefined the state-of-the-art performance/stall characteristics for high compressors at Pratt & Whitney. The increase compressor efficiency allows for the greater engine thrust required for the growth engine development program.

Conclusion

A three-dimensional Navier–Stokes-based design system was developed and used to design and optimize a new high-

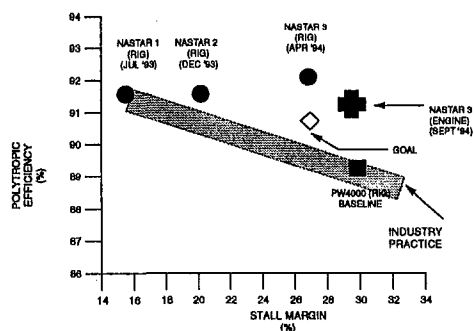


Fig. 27 History of NASTAR based high-pressure compressor performance, including engine test verification.

pressure compressor configuration. Advanced three-dimensional blading concepts, bowed stators, and controlled-diffusion rotor endwalls were included in the design in order to improve compressor performance. An early version of the code used a mixing-plane approach, and was successful in guiding designers in eliminating airfoil separations. The later version of the code used the bodyforce and deterministic stress technology to allow analysis off-design, where flow reparations and the accurate transfer of blockage become important. The three-dimensional CFD design system allowed designers to go directly to test with engine hardware in 25 percent of the time and 50 percent of the cost of a traditional empirically based design system. The new design system avoided research rig tests and full-scale rig test with variable geometry. The CFD system allowed for a state-of-the-art design on the first rig build. The CFD system allowed designers to optimize the stall performance of the HPC prior to subsequent rig builds by carefully controlling the flow distributions at off-design conditions. This was done by defining, numerically testing, and optimizing mid- and rear-block stator modifications in a timely manner. The net result was a compressor design with both high efficiency and high stall margin. As a result of using CFD to numerically test next three-dimensional airfoil concepts, the fundamental understanding of compressor aerodynamics was improved.

Acknowledgments

The authors thank Pratt & Whitney management and colleagues for their support and help in developing and implementing the design system.

References

- Adameczyk, J. J., Celestina, M., Beach, T. A., and Barnett, M., 1990, "Simulation of Viscous Flow Within a Multistage Turbine," *ASME JOURNAL OF TURBOMACHINERY*, Vol. 112.
- Adameczyk, J. J., Mulac, X. X., and Celestina, M. L., 1986, "A Model for Closing the Inviscid Form of the Average-Passage Equation System," *ASME JOURNAL OF TURBOMACHINERY*, Vol. 108, No. 2.
- Bleeh, A. A., Milner, B. B., Quealy, C. C., and Townsend, D. D., 1992, "Turbomachinery CFD on Parallel Computers," *Symposium on High-Performance Computing for Flight Vehicles and NASA TM 105932*.
- Chima, R., 1991, "Viscous Three-Dimensional Calculations of Transonic Fan Performance," *Proc. 77th Symposium of the Propulsion and Energetics Panel Agard*.
- Dawes, W. N., 1992, "Towards Improved Throughflow Capability: The Use of 3D Viscous Flow Solvers in a Multistage Environment," *ASME JOURNAL OF TURBOMACHINERY*, Vol. 114.
- Denton, J. D., 1992, "The Calculation of Three-Dimensional Viscous Flow Through Multistage Turbomachinery," *ASME JOURNAL OF TURBOMACHINERY*, Vol. 114.
- Fischberg, C. J., Rhie, C. M., Zacharias, R. M., Bradley, P. C., and DesSureau, T. M., 1995, "Using Hundreds of Workstations for Production Running of Parallel CFD Applications," *Proc. of Parallel CFD '95*, Pasadena, CA, June.
- Gundy-Burlet, K., 1993, "Computations of Unsteady Multistage Compressor With Swept Blades," *ASME JOURNAL OF TURBOMACHINERY*, Vol. 115, No. 2.
- Hah, C., and Wennerstrom, A. J., 1991, "Three-Dimensional Flowfields Inside a Transonic Compressor With Swept Blades," *ASME JOURNAL OF TURBOMACHINERY*, Vol. 113.
- Jennions, X. X., and Turner, Y. Y., 1993, "Three-Dimensional Navier–Stokes Computations of Transonic Fan Using an Explicit Flow Solver and an Implicit $k-\epsilon$ Solver," *ASME JOURNAL OF TURBOMACHINERY*, Vol. 115, No. 2.
- Ni, R. H., and Bogoian, J. C., 1989, "Prediction of 3D Multistage Turbine Flowfield Using a Multi-Grid Euler Solver," Paper No. AIAA-89-0203.
- Rhie, C. M., 1988, "Pressure Based Navier–Stokes Solver Using the Multigrid Method," *AIAA Journal of Propulsion and Power*, Nov.–Dec., pp. 564–570.
- Rhie, C. M., Zacharias, R. M., Hobbs, D. E., Sarathy, K. P., Biederman, B. P., LeJambre, C. L., and Spear, D. A., 1994, "Advanced Transonic Fan Design Procedure Based on a Navier–Stokes Method," *ASME JOURNAL OF TURBOMACHINERY*, Vol. 116, No. 2, pp. 179–346.
- Rhie, C. M., Gleixner, A. J., Spear, D. A., Fischberg, C. J., and Zacharias, R. M., 1998, "Development and Application of a Multistage Navier–Stokes Solver: Part I—Multistage Modeling Using Bodyforces and Deterministic Stresses," *ASME JOURNAL OF TURBOMACHINERY*, Vol. 120, this issue, pp. 205–214.
- Rubbert, P. E., 1994, "CFD and the Changing World of Airplane Design," AIAA Wright Brothers Lecture, Anaheim, California, Sept. 18–23.
- Weingold, H., Neubert, R., Behlke, R., and Potter, G., 1994, "Reduction of Stator Endwall Losses Through the Use of Bowed Stator," *ASME Paper No. 95-GT-380*.

Stator Performance and Unsteady Loading in Transonic Compressor Stages

M. Durali

Visiting Assistant Professor of Aeronautics
and Astronautics.

J. L. Kerrebrock

R. C. Maclaurin Professor of Aeronautics
and Astronautics.

Massachusetts Institute of Technology,
Cambridge, MA 02139

The structure and behavior of wakes from a transonic compressor rotor and their effect on the loading and performance of the downstream stator have been investigated experimentally. The rotor was 23.25 inches in diameter with a measured tip Mach number of 1.23 and a pressure ratio of 1.66. Time and space-resolved measurements have been completed of the rotor and stator outflow, as well of the pressure distribution on the surface of the stator blades. It was found that the wakes from this rotor have large flow angle and flow Mach number variations from the mean flow, significant pressure fluctuations, and a large degree of variation from hub to tip. There was a significant total pressure defect and practically no static pressure variation associated with the stator wakes. Wakes from the rotor exist nearly undiminished in the exit flow of the stator and decay in the annular duct behind the stator. The pressure at all points along the chord over each of the stator blades' surfaces fluctuated nearly in phase in response to the rotor wakes, that is the unsteady chordwise pressure distribution is determined mainly by the change in angle of incidence to the blade and not by the local velocity fluctuations within the passage. The unsteady forces on the stator blades, induced by the rotor wakes, were as high as 25 percent of the steady forces, and lagged the incidence of the wakes on the leading edge by approximately 180 deg at most radii.

Introduction

Transonic compressors and fans have wide application in aircraft engines. Typical stages of this kind have a rotor that operates with moderate supersonic relative velocities near the tip and high subsonic velocities near the hub. The high overall pressure ratio of such stages requires the outflow from the rotor to have large swirl and high subsonic velocities. The swirl put into the air by the rotor is largely removed by stator blades before the flow enters the next stage. A significant fraction of the overall static pressure rise across the stage comes from the removal of this swirl by the stator. Flow through the stator is very unsteady as a result of the rotor wakes being transported through the stator passages. The rotor wakes subject the stator to large changes in incidence angle, which result in large unsteady forces on the blades and potentially in increased viscous losses.

Time-averaged pressure measurements carried out between the blade rows using stagnation pressure probes show that the stators are responsible for about one-third of the overall stage losses. But a time-averaging measurement of this kind does not yield information about the mechanisms leading to the losses due to unsteadiness in the stator. The aeroelastic response of the stator to excitation by rotor wakes, and fan noise generated as a result of rotor wakes interacting with stators, are other important phenomena connected to rotor wake-stator interaction.

The complex flow field associated with the interaction between the blades in a compressor was studied theoretically as long as four decades ago [20, 23–25], using models that idealized the flow from an upstream blade row to solenoidal wakes and potential disturbances. Although more recent theoretical works have helped in understanding the complex phenomena of blade interactions in turbomachinery they have been limited to two-dimensional, linearized flow analysis [16, 17, 19, 34] or two-dimensional, nonlinear Euler analysis [15, 21], and to some

extent, simplified three-dimensional models [7, 32]. Experimental measurements of pressure on isolated airfoils in unsteady flow have supplied a great deal of information about the unsteady flow over airfoils, for example [5, 18], but comparable data for cascades are scarce. Measurements of unsteady pressure on blading have been done at midspan on stator blades of low-speed high hub-to-tip radius ratio test compressors [3, 4, 10–13, 28, 29], but these results leave open questions concerning the effects of compressibility, hub-to-tip variations, and variations of rotor wakes in highly loaded transonic stages. The rotor wakes in a highly loaded transonic compressor of low hub/tip ratio are significantly different from those modeled by two-dimensional theories or found in low-speed stages, in that they have large radial flows, significant pressure fluctuations, and a high degree of variation from hub to tip [14, 31, 33].

There is therefore a need for experimental documentation of the rotor wake structure and interaction with the stator in transonic stages, to provide a basis for development of more accurate models for the rotor–stator interaction in transonic compressor stages. The objective of this research was to contribute to a data base meeting this need. Although presented by Durali [6] as an MIT Gas Turbine Laboratory Report in 1980, the data have not been more widely disseminated. They are offered here in summary form.

The M.I.T. Transonic Compressor [33] used for this research has a design tip Mach number of 1.2, pressure ratio of 1.6, and conventional multiple-circular arc blade shapes. With high losses compared to highly developed modern stages, it offers a caricature of the rotor stator interactions in such stages. For this study, one stator blade was instrumented with high-frequency miniature pressure transducers to allow time-resolved measurements on both the suction and pressure surfaces. The instrumented blade was made to traverse radially across the annulus to obtain the distributions of static pressure on the blade as a function of time at all radii (though not simultaneously). The steady and unsteady loads on the stator blades were then calculated by integration of the pressure over the blade surfaces.

To establish a basis for determining the response of the stator blades to the structure of the wakes from the rotor, time-resolved

Contributed by the Aeromechanical Interaction Division for publication in the JOURNAL OF TURBOMACHINERY. Manuscript received by the Aeromechanical Interaction Division June 20, 1995; revised manuscript received July 1, 1996. Associate Technical Editor: R. E. Kielb.

radial and circumferential surveys were also carried out of the flow fields behind the rotor and behind the stator, providing information about the structure and the frequency content of the rotor wakes both before and after interaction with the stator. These data were obtained by using the M.I.T. miniature pressure probe (also known as the five-way probe) [8], to survey the flow field behind the rotor and behind the stator. Radial surveys with the probe behind the rotor furnish measurements by which the flow angles, total and static pressure, and flow Mach numbers can be calculated (as a function of time and radial and circumferential positions). A similar time-resolved map of flow properties behind the stator was obtained, by allowing the stator to rotate very slowly during the test time, as will be elaborated below.

Apparatus and Instrumentation

The experiments were performed in the M.I.T. Blowdown Compressor Facility, which is described in detail in [26]. It consists of a compressor test section, which is initially separated from a supply tank by an aluminum diaphragm, and a dump tank into which the compressor discharges.

To prepare for a test, the system is evacuated. The supply tank is then filled with a mixture of argon and freon, and the rotor is brought to speed in vacuum. The test starts by rupture of the diaphragm, which allows the gas in the supply tank to flow through the test section. The rotor's inertia and the supply tank pressure are so matched that the rotational Mach number and axial Mach number are very nearly constant during the test time.

The forward flow time is about 0.2 seconds. The flow through the test section is established in the first 70 milliseconds. The next 40 milliseconds is a quasi-steady period during which the useful data are taken. Measurements are made through several instrumentation ports along the length of the test section.

The MIT Compressor Stage. This compressor stage has a design pressure ratio of 1.6. The stage has a transonic rotor with a design tip tangential Mach number of 1.2 [26]. The rotor has 23 blades, an inlet hub to tip diameter ratio of 0.5, and an outlet hub/tip diameter ratio of 0.64 with a tip diameter of 23.25 inches. The relative Mach number at the tip is 1.3 and the inlet axial Mach number is 0.5. The rotor is followed by a stator with a $\frac{3}{4}$ inch axial gap at the tip. The stator has 48 blades and an outlet hub/tip diameter ratio of 0.68. The blades have a total twist of 11.5 deg from the hub to tip, but otherwise a constant double-circular-arc cross section with a chord length of 1.9 in. and a maximum thickness-to-chord ratio of 0.07.

Rotating Stator. To enable a survey of the flow field behind the stator in the circumferential direction as well as in the radial direction, the stator assembly was supported on bearings to allow slow rotation during the test time. The motion of the stator, at rest before the test, was caused by the torque acting on the stator. The moment of inertia of the stator assembly was chosen large enough that the maximum angular velocity of the stator was only 2 percent of the rotor angular velocity. During the traversing blade experiment, the stator assembly was locked

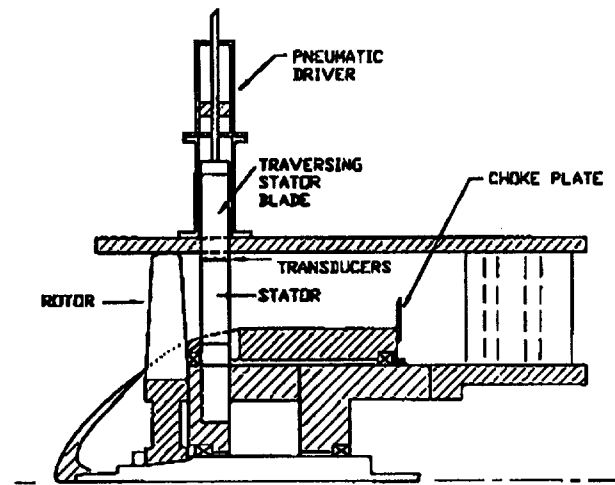


Fig. 1 Section view of the test section

in position to prevent rotation, one of the 48 blades being replaced by the traversing blade.

Traversing Stator Blade Assembly. The traversing blade had the same sectional geometry and twist as the rest of the blades, but it was three times longer. It was instrumented at one spanwise position and five chordwise locations on both the suction and pressure surfaces, the locations of the transducers on the suction and pressure surfaces being displaced about 0.25 in. spanwise from each other. At the hub and the tip, Teflon guides kept the blade at a constant setting angle during the traverse. At the ends of the traverse, the instrumented location of the blade went into cavities beneath the Teflon guides, providing reference pressures at each boundary of the annulus (Fig. 1). A pneumatic driver moved the blade at a nearly constant traverse speed with quick acceleration and deceleration at the two ends. The blade acceleration and deceleration took place while the transducers were out of annulus area, hence the transducers traveled across the annulus at a constant speed. The total traverse time is controllable and can be as short as 25 milliseconds, including the start and stop. The blade radial speed during the traverse for all tests was set at 12 ft/sec. The transducers used on the stator had a silicon circular diaphragm 0.056 in. in diameter and 0.001 in. thick, with a strain gage bridge on the back, installed on Invar rings for stress isolation. The transducers had a natural frequency of 150 kHz, and could withstand pressure differences up to 50 psi. The complete transducer assemblies were flush mounted on the blade surface, being isolated from the blade with soft epoxy (Fig. 2). All the transducers had a vacuum line connected to their back for pressure reference.

The Five-Way Probe. The time-dependent radial and circumferential distribution of Mach numbers and flow angles as well as total and static pressure were determined using a five-diaphragm probe [8]. The probe consisted of a nearly spherical head on which transducers of the type already described were

Nomenclature

F_{aa} = amplitude of unsteady axial force
 F_{at} = amplitude of unsteady tangential force
 F_{ma} = mean value of axial force
 F_{mt} = mean value of tangential force
 f = frequency
 f_b = rotor blade passing frequency
 M = Mach number

M_a = axial Mach number
 M_t = tangential Mach number
 M_{rel} = relative Mach number
 m_a = amplitude of unsteady pitching moment
 m_m = mean value of pitching moment
 P' = unsteady pressure

P_o = upstream total pressure
 R = radius
 R_t = blade tip radius
 t = time
 t_b = rotor blade passing period
 β = tangential flow angle
 ϕ = radial flow angle

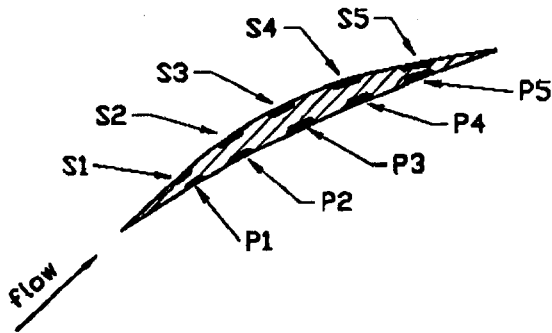


Fig. 2 Instrumented blade section showing transducer locations

mounted. One transducer in the center is surrounded by four others, each at a 45 deg angle to the central one. The probe was traversed across the annulus using a pneumatic driver, the total traverse time being about 25 milliseconds.

Other Time-Dependent Measurements. Flow quantities that have a time constant of variation on the order of one millisecond were referred to as low-speed quantities. Such quantities were wall static pressure at different locations of the test section and the supply and the dump tank stagnation pressures. The high-frequency pressure variations at the casing were measured using high-frequency pressure transducers of a similar type to the one described before. The rotor angular position was also monitored during the test time.

Data Storage and Analysis. The data taken during each test were digitized by analog to digital converters and stored on computer disk. During the test time, the analog signals from high-frequency transducers were sampled at a rate of 100 kHz by the analog to digital converter. For each test over 150,000 data points were recorded. The analysis of the data can be divided into two parts: probe data analysis and the analysis of the data from the traversing blade.

The results of the calibration of a five-way probe model in a two-inch diameter free jet were used to reduce the probe data

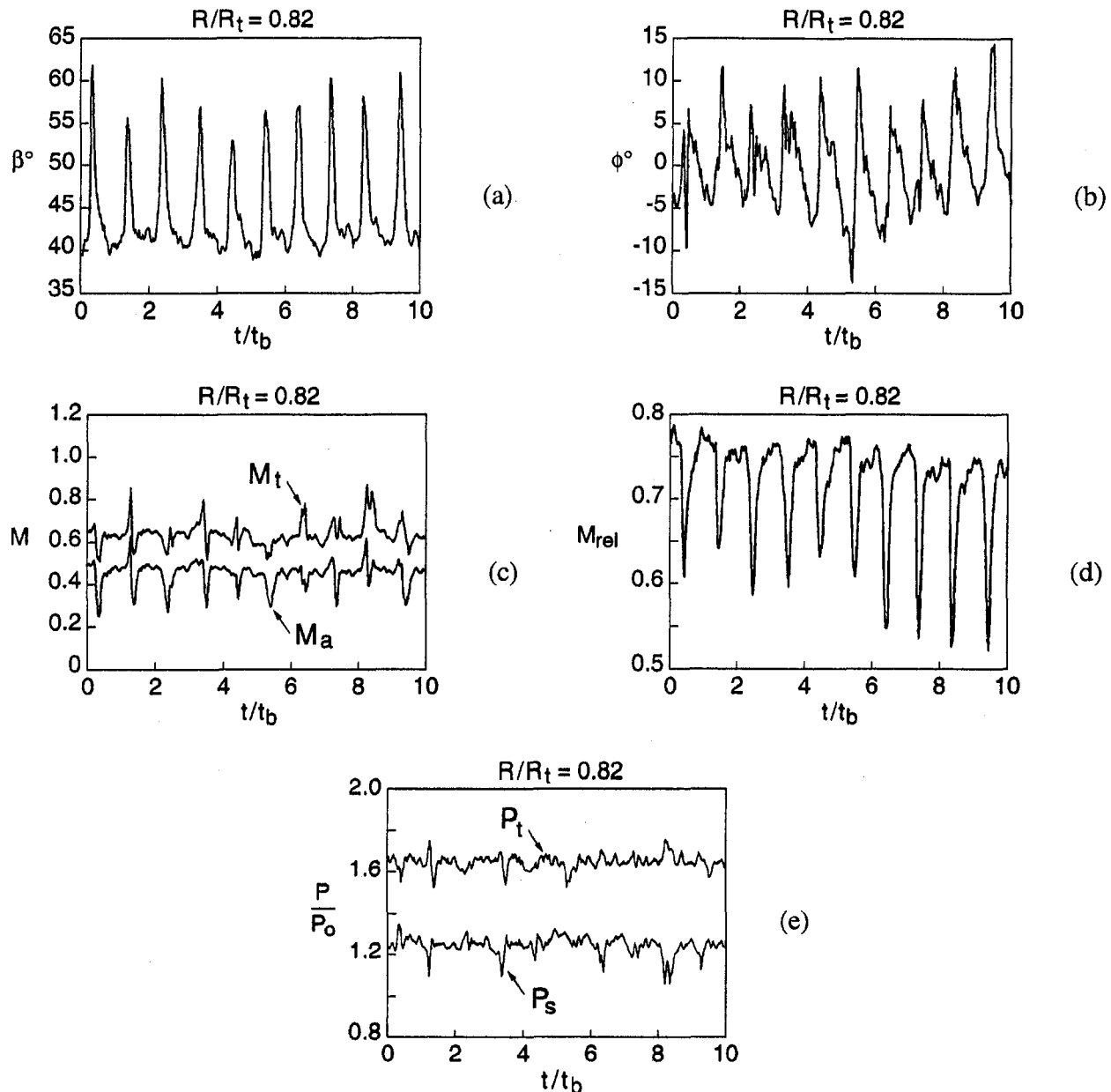


Fig. 3 Flow 0.1 rotor chord length downstream of the rotor at midspan ($R/R_t = 0.82$); (a) tangential flow angle, (b) radial flow angle, (c) Mach numbers, total (M_t), axial (M_a), (d) relative flow Mach number, (e) pressure ratios, total (P_t), static (P_s)

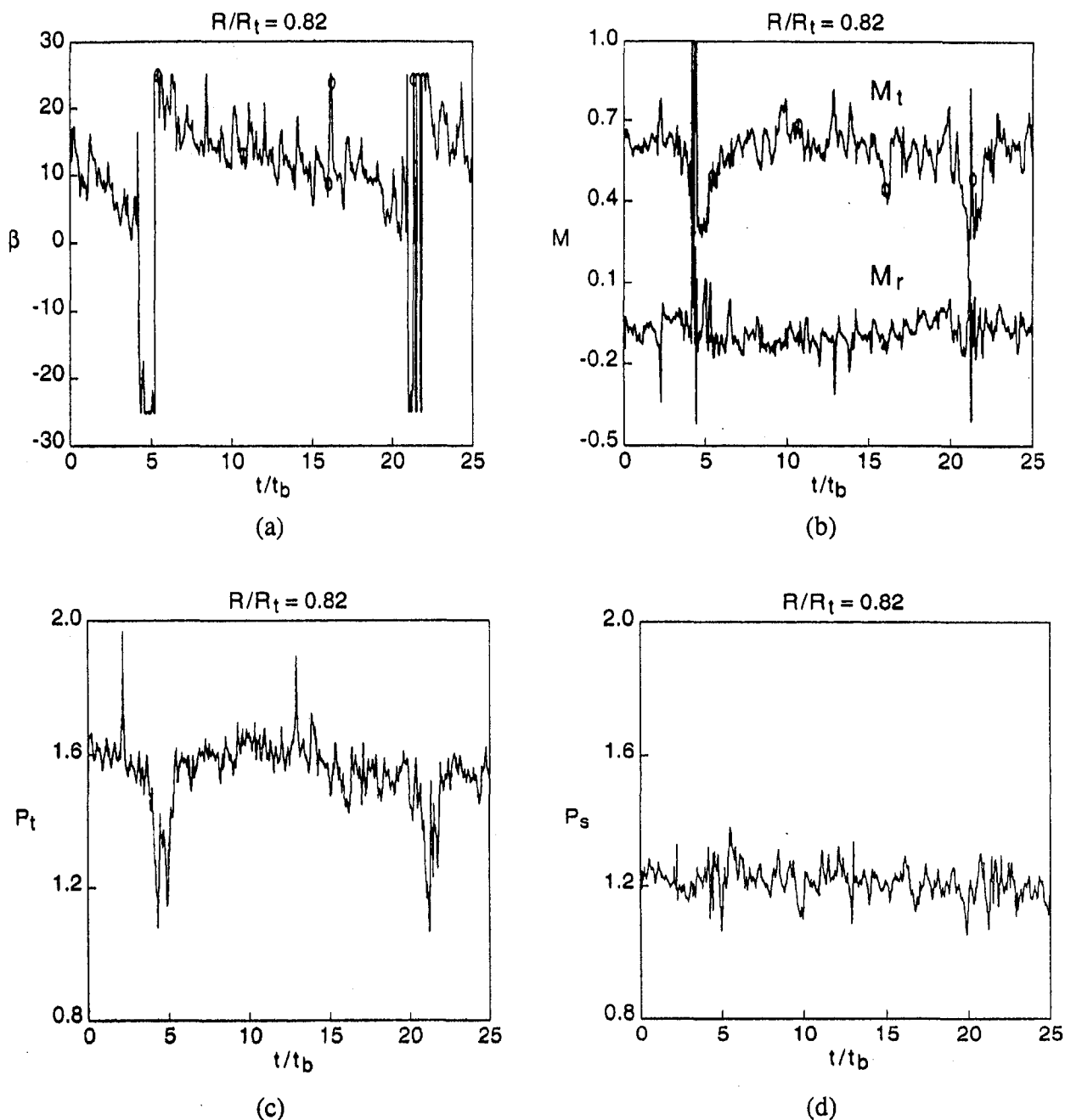


Fig. 4 Flow 0.1 rotor chord downstream of stator: (a) tangential flow angle in degrees, (b) Mach numbers, total (M_t), radial (M_r), (c) total pressure ratio (P_t), (d) static pressure ratio (P_s)

[8]. A computer program was written that numerically solved the calibration equations for each data point.

The blade data were digitally filtered to eliminate all undesirable noise signals due to blade stress, thermal drifts, and mechanical vibrations. To identify the noise introduced to the blade data by blade strain or vibration, several tests without flow as well as in blowdown operation were performed, with the sensing part of the blade transducers both exposed and covered. The noise signals so found, mostly of low frequency, were removed from the useful data using a narrow-band digital filter [6]. The conditioned data from the blade was then processed to retrieve information on unsteady as well as steady pressure distributions and the loading on the blade.

Results

Approximately 10 blowdown experiments were performed to acquire data upstream and downstream of the rotor, and also

downstream of the stator at different axial positions. The test conditions were carefully monitored to assure repeatability and compatibility of the tests results.

(i) **Rotor Overall Performance.** The overall performance of the rotor was calculated from both the probe measurements and wall static measurements. The calculations showed that the rotor had an average total pressure ratio of 1.66, changing from 1.71 at the tip to 1.6 at the hub, and an average total-to-total isentropic efficiency of 0.80, changing from 0.58 at the tip to 0.90 at the hub. The stage had an average total pressure ratio of 1.57 and an average efficiency of 70 percent (radially averaging the circumferentially averaged flow behind the stator). A stage pressure ratio of 1.6 and an efficiency of 73 percent resulted from radially averaging the time averaged total pressure measured downstream of the stator at the middle of the stator passage. This suggested an average 2.5 percent decrement in

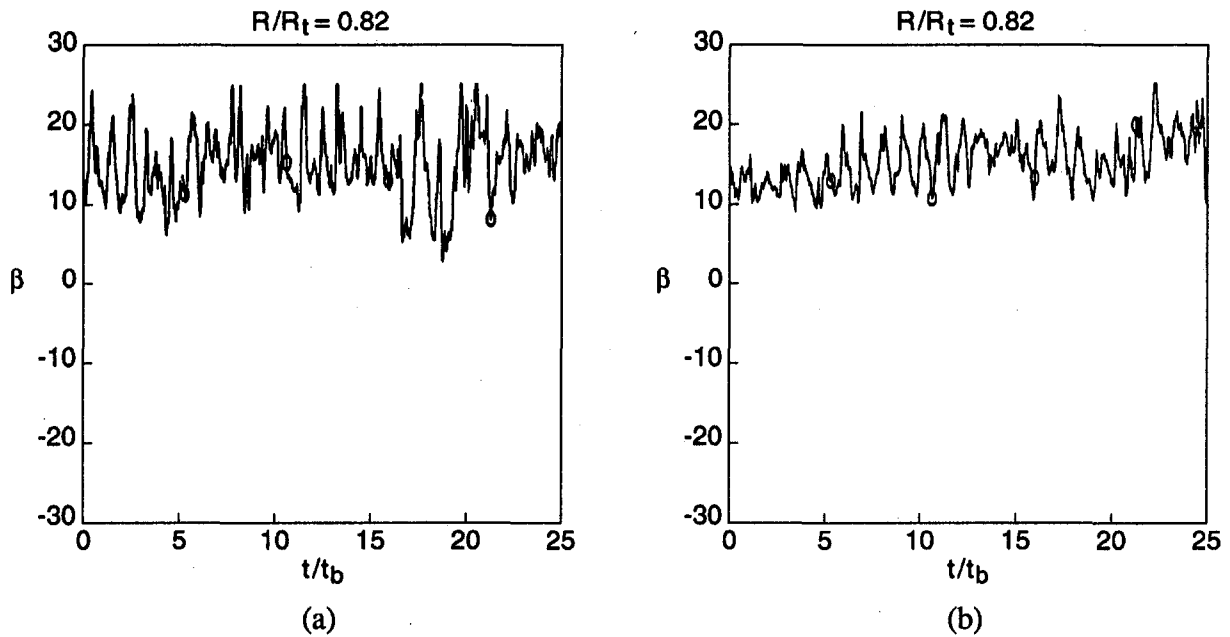


Fig. 5 Tangential flow angle in degrees downstream of stator: (a) 1.0 chord downstream, (b) 2.0 chord downstream

total pressure and 3 percent decrement in efficiency due to stator wakes. Most of these losses come from the stator hub region. The causes of these losses are discussed later.

(ii) **Flow Field Behind the Rotor.** The flow behind the rotor at approximately midspan is shown in Fig. 3. Such data were also acquired at other radii, from near the tip to near the hub, but it is not possible to show the complete data set here. It is available in [6]. Here the data and their analysis will be presented at midspan, and the final results for stator forces and moments will then be given for all radii.

The data of Fig. 3 show large tangential and radial flow angle variations (β , ϕ , respectively) associated with the wakes, sometimes up to 25 deg or more. The radial flow angle is large and positive near the suction side, drops across the passage, and reaches a negative value on the pressure side, indicating a radial shear in the wake, shedding streamwise vorticity downstream. The local efficiency is near 100 percent in the "inviscid" flow between the wakes near the hub and drops in the wakes. Near the tip, the efficiency is low also in the flow between wakes, apparently due to shock pressure losses. Comparison between the different radii shows that near the hub, there is a much larger velocity defect in the wakes, a higher tangential flow angle variation, and a larger axial Mach number defect, than at other radii. Close to the tip, the wakes are not nearly as strong as they are at other radii. This is a result of lower turning by the rotor blades at the tip [6]. The results of the rotor outlet survey show that the flow from the rotor is very unsteady, highly three dimensional, and the wakes from the rotor are very different from the two-dimensional models adopted in theoretical studies.

There are significant total and static pressure fluctuations in the wakes and the flow Mach number changes as much as 30 percent across the wake. The variations in total pressure ratio (in stator coordinates) are readily understood in terms of the wake structure of the rotor. The variations in static pressure are not consistent with the classical model of solenoidal wakes. But they are understandable as the result of shedding of rotor vortex streets, the discrete vortices being mainly radial. Such vortex wake structures have been clearly identified in the outflow of other transonic rotors [7]. The very low static pressures are observed when a vortex core passes over the pressure probe.

Such are not observed at every blade passing because the shedding of the vortices is random in time.

(iii) **Flow Behind the Rotating Stator.** The flow just behind the stator at midspan is shown in Fig. 4. Figure 5 shows the tangential flow angle at locations one and two chords downstream of the stator. In each figure, data are shown from the circumferential survey of the probe over the outlet of a full stator passage plus the wakes of the two bounding stator blades. The data in the midpassage of the stator show the time history of the rotor wakes as they are convected through the stator passage, and the two stator wakes on the sides of the figures show the stator wake structure under the influence of rotor wakes. For some of the flow quantities, such as radial and tangential flow angles and Mach number, the data reduction program is incorrect when the probe is aligned with the stator trailing edge, due to insufficient spatial resolution of the probe in this region. The "spikes" in these regions should therefore be ignored.

The following can be seen in Figs. 4. From the tangential angle plot (Fig. 4(a)), the flow is turned more by the suction side than by the pressure side, also there is a large total pressure deficit in the stator wakes, whereas static pressure is nearly constant in the stator wakes. Not shown are the data for other radii, which shows that the stator wakes are deeper and stronger at the tip than they are at the hub. This is mainly due to the large mean angle of incidence at the inlet to the stator near the tip region.

Comparison of mean flow properties at the stator exit shows that under the influence of rotor wakes the stator performs less turning on the swirling flow than was expected according to calculations based on cascade data. This is mainly due to the fact that the positive angle of attack introduced by the rotor wakes to the stator blades tends to increase the flow deviation at the stator exit. Up to one third of the passage at stator exit is influenced by the wake flow. This indicates a correction must be considered to account for the increased deviation due to unsteady flow from wakes of upstream blades.

One interesting point is that the rotor wakes still exist nearly undiminished in the flow just downstream of the stator. In fact, the radial and tangential flow angles in the stator "inviscid" flow change as much as 20 deg due to the rotor wakes, and

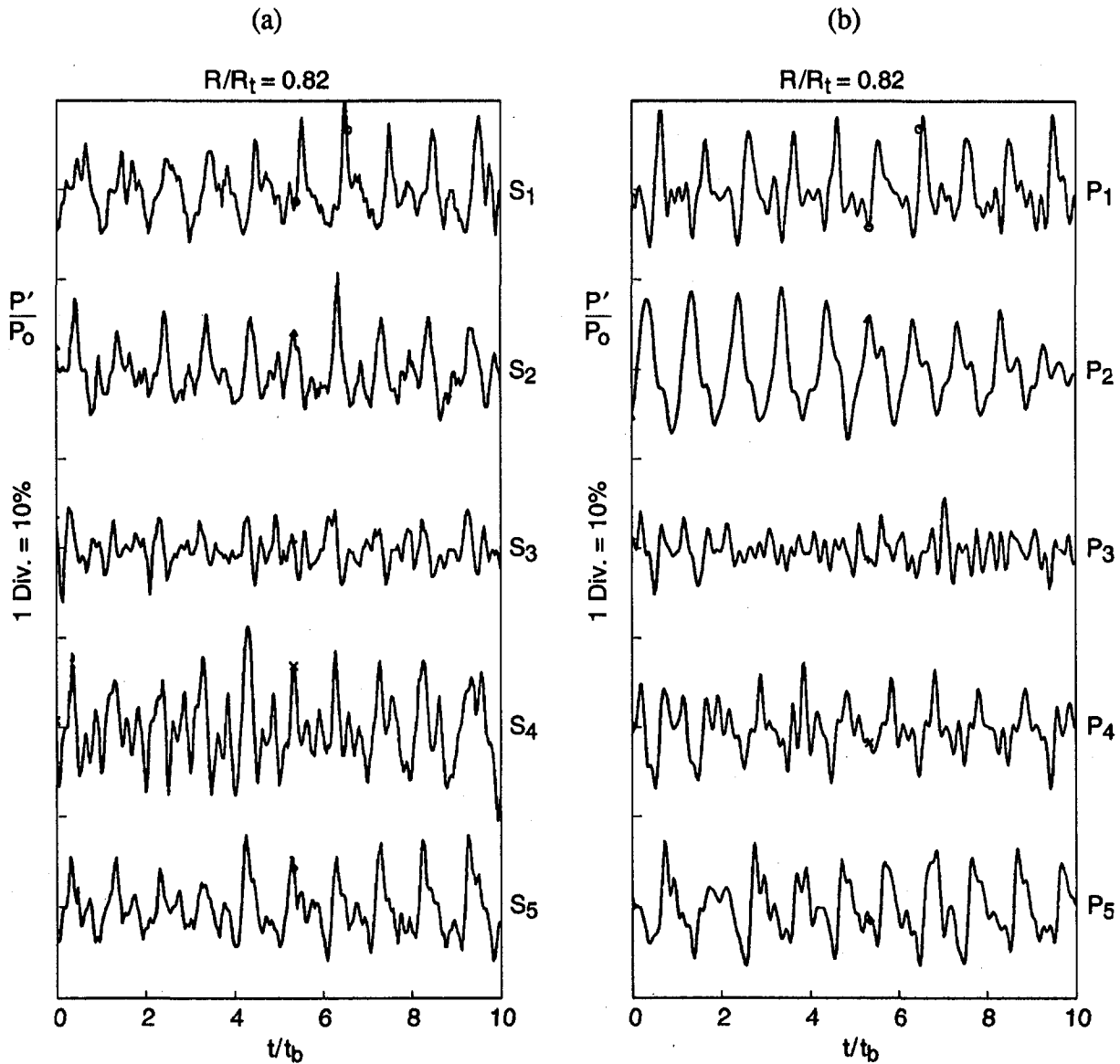


Fig. 6 Pressure fluctuations over the stator blade, $R/R_t = 0.82$; (a) suction side, (b) pressure side

there are significant total and static pressure fluctuations in the flow downstream of the stator as a result of the rotor wakes. At the exit of the stator blades (0.1 rotor chord downstream), the stator wakes exhibit large total pressure deficits, whereas static pressure is nearly constant (Figs. 4(c, d)). This is in contrast to the strong static pressure variations in the rotor wakes. We do not have a complete explanation for this difference, but the stator wakes apparently conform to the classical model of solenoidal wakes, with strong shear but nearly uniform static pressure in the direction normal to the wake plane. Comparison of the results for different radii shows that unsteadiness related to the rotor wakes appears more regularly in the tip region, while close to the hub, some of the wakes seem to have been filled.

Samples of data from measurements at one and two rotor chord lengths behind the stator are shown in Figs. 5(a) and 5(b). Comparison of the data for the three axial positions behind the stator shows that the rotor wakes are nearly undiminished at the exit of the stator relative to the rotor exit, whereas they are seen to decay gradually in the annular duct behind the stator. The stator wakes decay very rapidly so that at a distance of one rotor chord behind the stator they have virtually ceased

to exist. The reason for the difference in decay behavior between the rotor and stator wakes is not fully understood, but may be related to the point made above, that the rotor wakes contain discrete vortex structure, whereas the stator wakes are more nearly of the nature of vortex sheets.

(iv) **Traversing Blade Results.** Figure 6 shows the unsteady pressures (P') acting on the suction and pressure surfaces of the stator blade at midradius. Unsteady pressures are nondimensionalized by dividing by upstream supply tank total pressure (P_0). The probe data shown in Fig. 3 at midradius were so chosen in time as to depict flow properties at the leading edge of the stator for the time at which the unsteady traversing blade data are presented in Fig. 6 (note these two sets of data come from two different tests).

Comparison among the pressure traces on Fig. 6 shows that they are very nearly in phase. By reference to Fig. 3 (which shows the flow properties at the stator leading edge), it can be seen that as the angle of incidence to the blade is changed due to the rotor wakes, the pressure at all the points on the blade changes almost immediately. These observations lead to the conclusion that the chordwise pressure distribution on the stator

blades is largely determined by the change in circulation around the blade as a result of the change in angle of incidence, with the local velocity fluctuations within the stator passage having a lower order effect on the unsteady chordwise pressure distribution.

These results are in qualitative agreement with previous work on isolated airfoils and cascades. Sears' calculation [23, 24] for incompressible flow over an isolated airfoil showed that the pressure at all points over the chord changes in phase in response to the gust. Moreover, the experimental observations of Commerford and Carta [5] showed that for an isolated airfoil in a compressible flow, there is no phase difference between the pressure fluctuations on the pressure surface, and that there is a scattering in the phase for the suction surface. A large scattering in the phase angle of the pressure fluctuations over the chord can also be observed in the experimental results of Fleeter et al. [10]. However, the phase angles for most points over the chord seem to be nearly equal for their 100 percent corrected speed operation data, a point that seems to have been ignored by the authors. Furthermore, the time-marching calculations of Mitchell [30] also showed that the unsteady pressure distribution over a blade in a cascade does not depend on the local fluctuations within the passage, which agrees with what we have found.

The unsteady data from the traversing blade can be presented in forms that are more descriptive as far as the loading on the stator is concerned. The unsteady tangential and axial forces (F_{at} , F_{aa}) and pitching moment (m_a) acting on the stator blades are plotted versus number of rotor blade passing periods in Fig. 7. In each graph loads are nondimensionalized by dividing by the mean value of the load. Comparison of the data presented in Fig. 3 with the unsteady force plots of Fig. 7 shows that the wave form of the tangential force very much follows the shape of the incoming gust, and the dominant frequencies in both cases are the rotor blade passing frequency and its harmonics. Further examination of the data reveals that a positive incidence as a result of wake passage seems to result in a negative tangential force on the stator blade. To find the exact phase relationship between the corresponding frequency components of the force and the gust, they were both decomposed into their Fourier components at blade passing frequency and its harmonics. It turns out that the phase between the components of force and the components of the gust referred to the stator leading edge is a constant at each radius and equal to 90 deg for the hub region and about 180 deg for other radii.

Arnoldi [2] showed that the phase angle between the gust and the induced lift calculated from Sears' function becomes a constant (equal to 45 deg) for reduced frequencies higher than 2, if the gust is referred to the leading edge instead of the midchord of the airfoil.

The reduced frequency based on rotor blade passing frequency " Ω " is equal to 3.58. Although the compressible reduced frequency parameter $K = \Omega M / (1 - M^2)^{1/2}$ for the fundamental harmonic is about 3, which is well above the incompressible limit, it seems that our results are in qualitative agreement with the result for isolated airfoils in incompressible flow. Actually, the effect of interblade phase angle becomes less as the reduced frequency goes above 2 [2], which says for high reduced frequencies the blades in a cascade will behave like isolated airfoils.

The radial variation of the measured phase angle between the force and the gust (90 deg for the hub region and 180 deg for other radii) is most likely due to the variation in the mean angle of incidence to the stator blade. It was shown by Commerford and Carta [5] that as the mean angle of incidence to an isolated airfoil is increased, the phase between the gust and the induced lift differs more from the value predicted by the Sears' function.

In Fig. 8 power spectra of the ratio of the unsteady to mean value of the stator forces and moment are presented for all three radii that were analyzed, as these are the data most directly

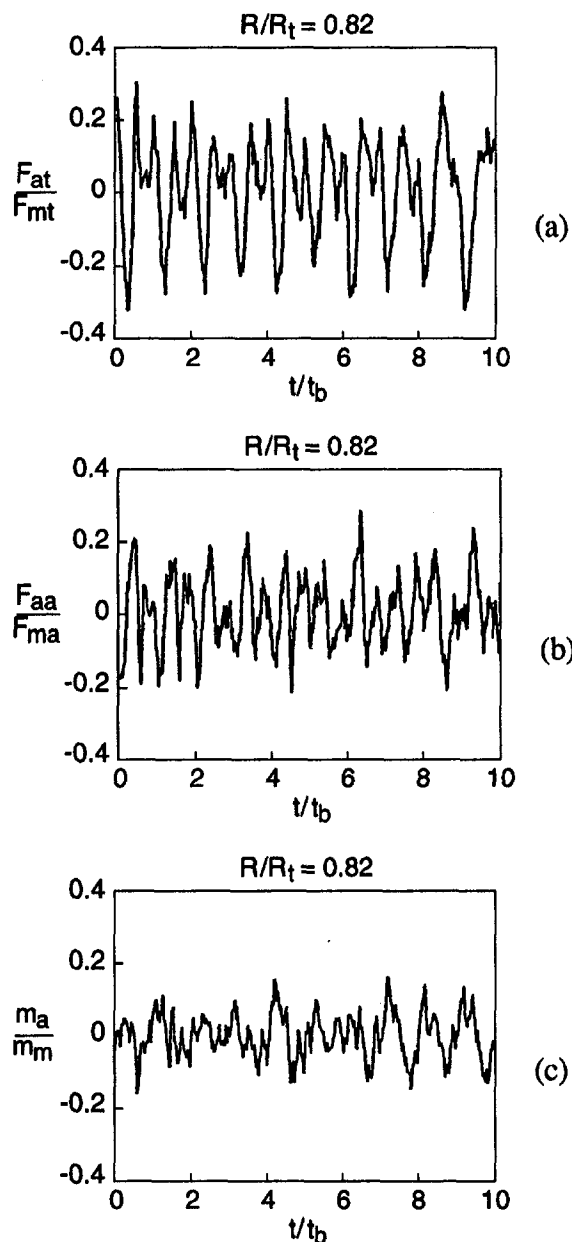


Fig. 7 Unsteady loads on stator blade; $R/R_t = 0.82$

useful for estimating blade excitations and acoustic radiation. The frequency content of the unsteady load on the stator blade is of great importance to the designer too. According to Fig. 8, the axial and tangential forces on the blade oscillate with rotor blade passing frequency (f_b) near the hub and at rotor blade passing frequency and its second harmonic at other radii.

It can also be seen that although at midspan the spectra of the forces have the first and the second harmonic of the blade passing frequency, the second harmonic does not appear in the moment spectrum. This can be understood as a result of the airfoil responding aerodynamically to each component of the incoming gust individually. That is, the position of the airfoil pressure center is different for each component of a complex gust, resulting in the possible cancellation of the moment of the distributed forces due to a particular component.

Conclusions

1 A time and space-resolved survey of the flow downstream of a transonic rotor shows that the rotor wakes have high tangen-

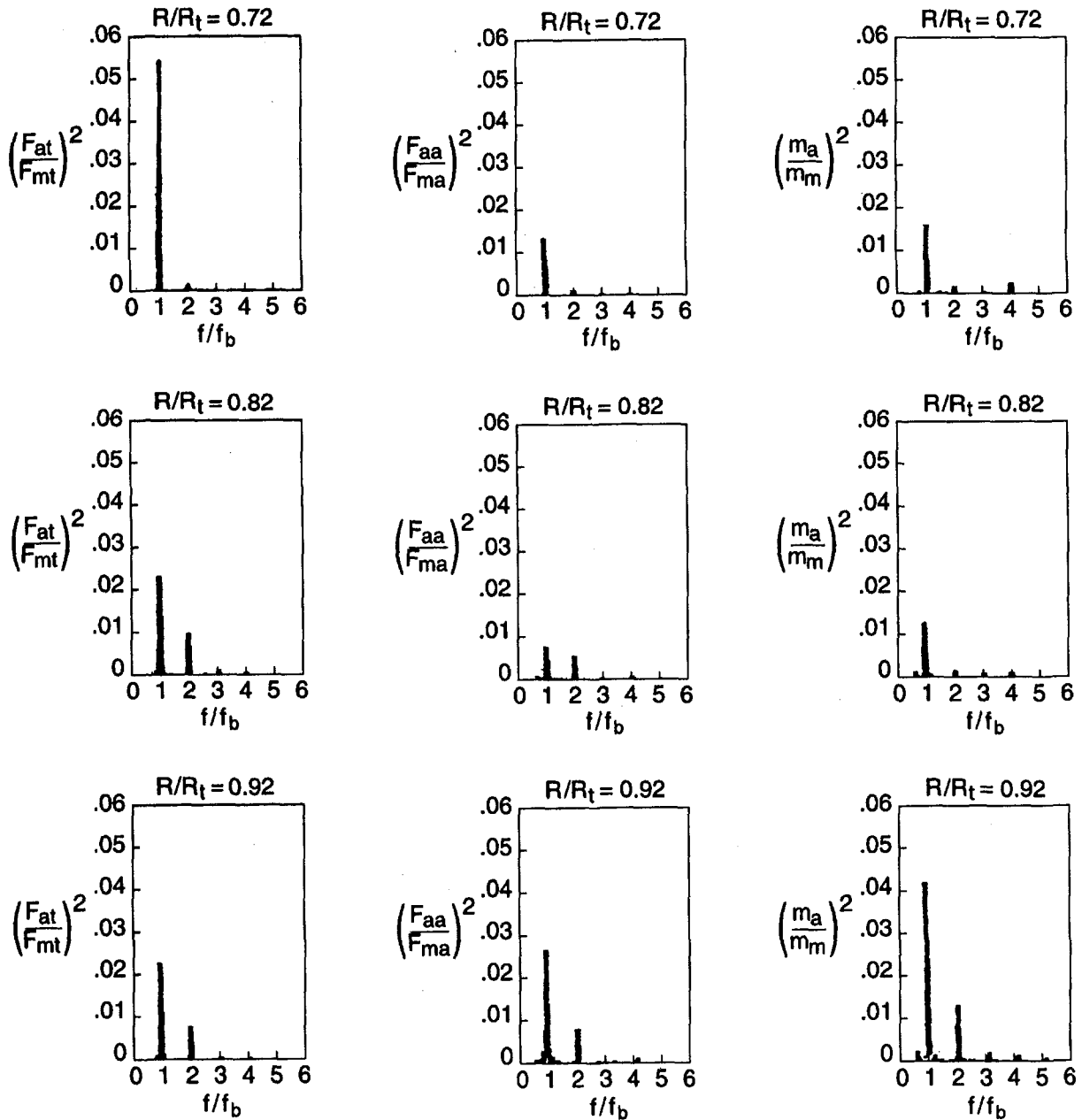


Fig. 8 Power spectra of stator tangential and axial forces and of pitching moment, at three radii: $R/R_t = 0.72, 0.82,$ and 0.92

tial and radial flow angle variations, significant blade-to-blade variation, and a highly three-dimensional structure. Therefore, they are very different from two-dimensional models.

2 Time and space-resolved measurements of flow behind a row of stator blades downstream of the transonic compressor rotor show that:

- (i) Under the influence of the rotor outflow, the wakes from the stator are deeper and stronger near the tip than they are near the hub;
- (ii) there is a significant total pressure defect and practically no static pressure variation associated with stator wakes;
- (iii) the wakes from the rotor exist nearly undiminished in the exit flow from the stator, but they gradually decay in the annular duct behind the stator;
- (iv) unsteadiness related to rotor wakes appears more frequently in the tip region;
- (v) under the influence of high positive fluctuating angle

of incidence due to rotor wakes the outflow from the stator blades has an increased deviation angle.

3 Analysis of time-resolved measurements of the stator blade surface pressure from tip to hub leads to the following conclusions:

- (i) the pressure distribution over the stator blade is nearly periodic with a frequency equal to rotor blade's passing frequency;
- (ii) the pressure fluctuations are nearly in phase at all points along the chord, the chordwise unsteady pressure distributions being determined by the changes in the angle of incidence and not by the local velocity fluctuations within the stator passage;
- (iii) there are large rotor wake induced, unsteady forces on the stator blades, as high as 25 percent of the steady forces for the configuration investigated;
- (iv) the unsteady axial and tangential forces on the stator

blades fluctuate with rotor blade passing frequency in the hub region, and with rotor blade passing frequency and its second harmonic at other radii;

- (v) there seems to be a scattering in phase and magnitude of the forces on the blade relative to those of the rotor wakes, that cannot be predicted by existing two-dimensional models.

References

- 1 Adamczyk, A. A., and Brand, R. S., "Scattering of Sound by an Airfoil of Finite Span in a Compressible Stream," *J. of Sound and Vibration*, Vol. 25, 1972, pp. 139–156.
- 2 Arnoldi, R. A., "Unsteady Airfoil Response," NASA SP-207, pp. 247–256.
- 3 Capece, V. R., and Fleeter, S., "Unsteady Aerodynamics in a Multistage Compressor," ASME paper 87-GT-171, 1987.
- 4 Capece, V. R., Manwaring, S. R., and Fleeter, S., "Unsteady Blade Row Interactions in a Multistage Compressor," presented at AIAA, SAE, ASME, and ASEE 21st Joint Conference, Monterey, CA, 1986.
- 5 Commerford, G. L., and Carta, F. O., "Unsteady Aerodynamic Response of a Two-Dimensional Airfoil at High Reduced Frequency," *AIAA Journal*, Vol. 12, No. 1, Jan. 1974, pp. 43–48.
- 6 Durali, M., "Rotor Wakes Behavior in a Transonic Compressor Stage and Its Effect on the Loading and Performance of the Stator," M.I.T. GTL Report No. 149, 1980.
- 7 Epstein, A. H., Gertz, J. B., Owen, P. R., and Giles, M. B., "Vortex Shedding in Compressor Blade Wakes," *AIAA Journal of Propulsion and Power*, Vol. 4, No. 3, May–June 1988, pp. 236–244.
- 8 Figuerido, W. A., "Spherical Pressure Probe for Retrieving Free Stream Pressure and Directional Data," M.I.T. GTL Report No. 137, Aug. 1977.
- 9 Fleeter, S., "Fluctuating Lift and Moment Coefficient for Cascade Airfoil in a Nonuniform Compressible Flow," *AIAA J. of Aircraft*, Vol. 10, No. 2, Feb. 1973.
- 10 Fleeter, S., Jay, R. L., and Bennet, W. A., "Rotor Generated Unsteady Aerodynamic Response of a Compressor Stator," *ASME Journal of Engineering for Power*, Vol. 100, No. 4 1978.
- 11 Fleeter, S., Stauter, R. C., and Manwaring, S. R., "Three Dimensional Aerodynamics of an Annular Airfoil Cascade Including Loading Effects," *Experiments in Fluids*, Vol. 8, No. 1–2, Oct. 1989.
- 12 Gallus, H. E., "Results of Measurement of the Unsteady Flow in Axial Subsonic and Supersonic Compressor Stages," AGRAD-cp-177.
- 13 Gallus, H. E., Kummel, W., Lambertz, J. F., and Wallmann, T., "Measurement of the Rotor-Stator-Interaction in Subsonic Axial Flow Compressor Stage," R.F.M., Symposium on Aeroelasticity in Turbomachines, Oct. 1976, p. 169.
- 14 Gertz, J. B., and Epstein, A. H., "Unsteady Design-Point Flow Phenomena in Transonic Compressors," Final Report, NASA report No. NAS 1.26:176879, 1986.
- 15 Giles, M. B., "A Numerical Method for Calculation of Unsteady Flow in Turbomachinery," M.I.T. GTL report No. 205, 1991.
- 16 Hall, K. C., and Verdon, J. M., "Gust Response for Cascade Operating in Non-uniform Mean Flows," AGARD-cp-468, 1989.
- 17 Hall, K., and Crawly, E., "Calculation of Unsteady Flows in Turbomachinery Using a Linearized Euler Equation," *Proc. 4th Symposium on Unsteady Aerodynamics and Aeroelasticity of Turbomachines and Propellers*, Aachen, West Germany, 1987.
- 18 Holmes, D. W., "Experimental Pressure Distribution on Airfoils in Transverse and Streamwise Gusts," Cambridge University Publications CUED/A-Turbo/TR 21 (1970).
- 19 Holmes, D. G., and Chuang, H. A., "Two Dimensional Linearized Harmonic Euler Flow Analysis for Flutter and Forced Response," *Proc. 6th Int. Symp. on Unsteady Aerodynamics, Aeroacoustics and Aeroelasticity of Turbomachines and Propellers*, University of Notre Dame, IN, 1991.
- 20 Horlock, J. H., "Fluctuating Lift Forces on Airfoil Moving Through Transverse and Chordwise Gusts," *ASME Journal of Basic Engineering*, Vol. 90, 1968, pp. 494–500.
- 21 Janus, J. M., and Whitfield, D. L., "A Simple Time-Accurate Turbomachinery Algorithm With Numerical Solutions of an Uneven Blade Count Configuration," AIAA Paper No. 89-0206, 1989.
- 22 Kaiser, J. F., and Reed, W. A., "Data Smoothing Using Low-Pass Digital Filters," *Rev. Sci. Instrum.*, Vol. 48, No. 11, Nov. 1977.
- 23 Kemp, N. H., and Sears, W. R., "Aerodynamic Interference Between Moving Blade Rows," *J. of Aeronautical Sci.*, Vol. 20, No. 9, Sept. 1953.
- 24 Kemp, N. H., and Sears, W. R., "The Unsteady Forces Due to Viscous Wakes in Turbomachines," *J. of Aeronautical Sci.*, July 1955, p. 478.
- 25 Kerrebrock, J. L., and Mikolajczak, A. A., "Intra Stator Transport of Rotor Wakes and Its Effect on Compressor Performance," *ASME Journal of Engineering for Power*, 1970, Vol. 92.
- 26 Kerrebrock, J. L., Epstein, A. H., Haines, D. M., and Thompkins, W. T., "The MIT Blowdown Compressor Facility," *ASME Journal of Engineering for Power*, Vol. 96, No. 4, Oct. 1976, pp. 394–405.
- 27 Mani, R., "Compressibility Effects in the Kemp-Sears Problem," NASA SP-304, Part II, 1974, pp. 513–533.
- 28 Manwaring, S. R., and Fleeter, S., "2-E Forcing Function Effect on Turbomachine Gust Unsteady Aerodynamics," *J. of Aerospace Power*, Vol. 6, Jan. 1991.
- 29 Manwaring, S. R., and Wisler, D. C., "Unsteady Aerodynamics and Gust Response in Compressor and Turbines," *ASME JOURNAL OF TURBOMACHINERY*, Vol. 115, 1993, pp. 724–740.
- 30 Mitchell, N. A., "Non-axisymmetric Flow Through Axial Turbomachines," Ph.D. Thesis, St. John's College, Cambridge University, England, 1970.
- 31 Ng, W. F., "A Quasi-Three-Dimensional Model for Intra-Stator Transport of Rotor Wakes," *Proc. Winter Annual Meeting of ASME Conference in Three Dimensional Phenomena in Fluid Machinery*, Miami Beach, FL, 1985.
- 32 Rai, M. M., "Unsteady Three-Dimensional Navier–Stokes Simulation of Turbine Rotor–Stator Interaction," presented at AIAA, SAE, ASME, and ASEE 23rd Joint Conference, San Diego, CA, 1987.
- 33 Tompkins, W. T., Jr., "An Experimental and Computational Study of the Flow in a Transonic Compressor Rotor," M.I.T. GTL, Report No. 129, 1976.
- 34 Verdon, J. M., and Hall, K. C., "Development of a Linearized Unsteady Aerodynamic Analysis for a Cascade Gust Response Predictions," NASA Report NAS3-25425, 1990.

Effects of Inlet Distortion on the Flow Field in a Transonic Compressor Rotor

C. Hah

NASA Lewis Research Center,
Cleveland, OH 44135

D. C. Rabe

Wright-Patterson AFB,
Dayton, OH 45433

T. J. Sullivan

A. R. Wadia

GE Aircraft Engines,
Cincinnati, OH 45215

The effects of circumferential distortions in inlet total pressure on the flow field in a low-aspect-ratio, high-speed, high-pressure-ratio, transonic compressor rotor are investigated in this paper. The flow field was studied experimentally and numerically with and without inlet total pressure distortion. Total pressure distortion was created by screens mounted upstream from the rotor inlet. Circumferential distortions of eight periods per revolution were investigated at two different rotor speeds. The unsteady blade surface pressures were measured with miniature pressure transducers mounted in the blade. The flow fields with and without inlet total pressure distortion were analyzed numerically by solving steady and unsteady forms of the Reynolds-averaged Navier–Stokes equations. Steady three-dimensional viscous flow calculations were performed for the flow without inlet distortion while unsteady three-dimensional viscous flow calculations were used for the flow with inlet distortion. For the time-accurate calculation, circumferential and radial variations of the inlet total pressure were used as a time-dependent inflow boundary condition. A second-order implicit scheme was used for the time integration. The experimental measurements and the numerical analysis are highly complementary for this study because of the extreme complexity of the flow field. The current investigation shows that inlet flow distortions travel through the rotor blade passage and are convected into the following stator. At a high rotor speed where the flow is transonic, the passage shock was found to oscillate by as much as 20 percent of the blade chord, and very strong interactions between the unsteady passage shock and the blade boundary layer were observed. This interaction increases the effective blockage of the passage, resulting in an increased aerodynamic loss and a reduced stall margin. The strong interaction between the passage shock and the blade boundary layer increases the peak aerodynamic loss by about one percent.

Introduction

The design technology of transonic compressors has recently been significantly advanced. The combination of advanced non-intrusive measurement techniques and computational modeling methods has contributed substantially to understanding the detailed flow physics required to further advance transonic compressor design. Knowledge of the compressor response to non-uniform conditions of incoming flow is required for both civilian and military applications. Certain inflow distortions may cause blade vibrations at natural frequencies. Any failure of the vibrating airfoils can lead to catastrophic damage to the entire engine.

Various analytical studies have been reported that study the effects of inlet flow distortion on transonic compressor fields. Horlock (1968) provides some insights into the prediction of the change in aerodynamic loading. Other experimental studies measured aerodynamic performance under the influence of inlet flow distortion. Monsarrat (1969) measured the performance of a highly loaded transonic compressor stage with an inlet total pressure distortion. Bowditch and Coltrin (1983) and Longley (1988) performed experimental investigations on the effects of inlet distortion on compressor stability. Recently Rabe et al. (1995) used miniature high-response pressure transducers mounted on the rotor blade to study blade response to the inlet total pressure distortion in a state-of-the-art transonic compressor. Over the last decade, numerical techniques for the analysis

of turbomachinery flows have progressed significantly (Davis et al., 1988; Dawes, 1986; Denton, 1986; Giles, 1988; Hah, 1984; Moore and Moore, 1981; Rao and Delaney, 1990; etc.). Three-dimensional steady flow calculations based on the Reynolds-averaged Navier–Stokes equations are now relatively well established and routinely used to optimize blading and flow-path contours. At the present time, numerical methods do not always predict the absolute aerodynamic loss exactly because of the inadequate physical models. However, the variations of aerodynamic performance due to design changes are predicted adequately for engineering guidance. As numerical methods for the analysis of isolated blade rows have become mature, more studies have been made to study multistage flow phenomena with steady and unsteady methods (Adamczyk et al., 1986; Copenhaver et al., 1993; Denton and Singh, 1979; Giles, 1988; Gundy-Burlet et al., 1991; Hah et al., 1993; Jorgenson and Chima, 1988; Ni and Bogoian, 1989; Rai, 1985; Rao and Delaney, 1990; etc.). Although various numerical procedures have been developed to study blade row interactions in turbomachinery, very few attempts have been reported to investigate other important unsteady flow phenomena in multistage compressors (Smith, 1966; Mikolajczyk, 1977; Greitzer et al., 1994). For instance, very few numerical studies have been reported in the open literature that address the effects of inlet flow distortion on the time-dependent flow field in a transonic compressor. Hall et al. (1996) conducted a numerical study on the effects of inlet distortions on endwall treated fan rotors.

The present paper describes a study to advance our current understanding of the flow structure in a low-aspect-ratio, high-speed, high-pressure-ratio, transonic compressor rotor with inlet flow distortions. The experimental technique and the numerical

Contributed by the International Gas Turbine Institute and presented at the 41st International Gas Turbine and Aeroengine Congress and Exhibition, Birmingham, United Kingdom, June 10–13, 1996. Manuscript received at ASME Headquarters February 1996. Paper No. 96-GT-547. Associate Technical Editor: J. N. Shimm.

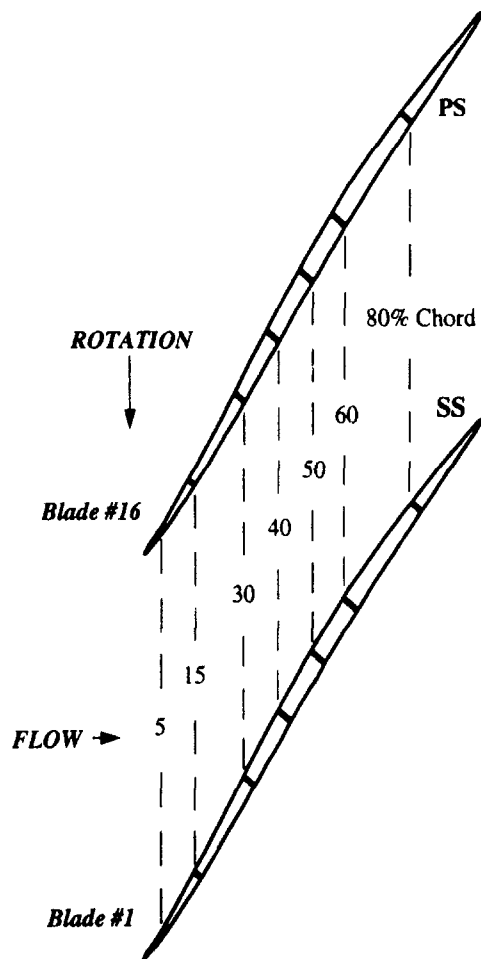


Fig. 2 Blade-mounted transducer configuration

ture. This temperature was considered to be constant and uniform from that measurement station to the compressor inlet in all test conditions.

Rotor exit total pressure and temperature measurements were made using steady-state probes located on the leading edge of the first stage stator (S1) in Fig. 1. Three of the 41 stators, approximately equally spaced circumferentially, were instrumented at seven radial locations. These measurements were area-averaged to obtain the overall rotor exit total pressure and temperature. With these measurements at the rotor inlet and exit, overall performance could be calculated.

With a distorted inlet test condition, the exit total temperature profile and inlet and exit total pressure profiles were enhanced by rotating the distortion screen to 10 different positions within one period of the distortion pattern. At each screen position, the inlet and exit total pressure and temperature measurements were acquired. This resulted in 400 inlet total pressure measurements and 210 exit total pressure and exit total temperature measurements. These measurements were area-averaged to quantify the rotor inlet total pressure and the rotor exit total pressure and temperature with distortion. Overall mass flow was measured by a venturi located approximately 30 m downstream from the compressor.

Additional measurements of the unsteady rotor blade surface pressure and end-wall pressure provided detailed measurements for comparison with computational results. The blade surface pressure measurements were obtained using two sets of seven pressure transducers that were embedded in two adjacent blades of the first-stage rotor, as shown in Fig. 2. These transducers were located along a line representing a stream line used in the

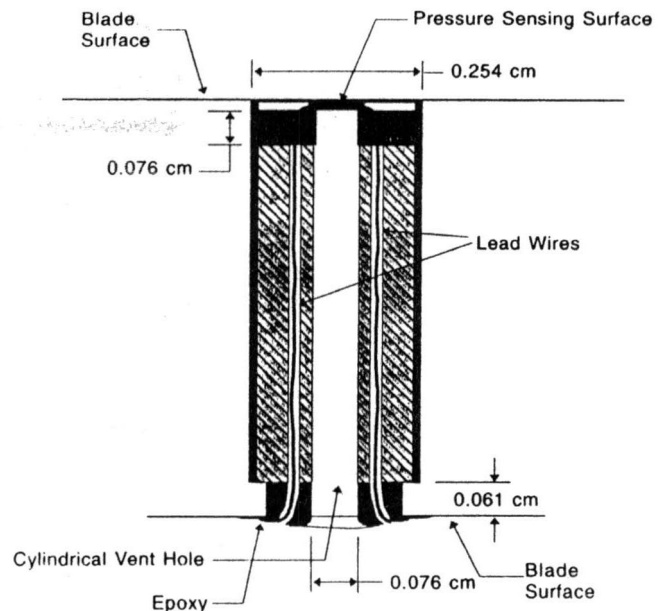


Fig. 3 Blade-mounted transducer installation

initial rotor design. This resulted in the transducers being at an angle of one degree to the rotor centerline as shown in Fig. 1. The mounting of the transducers is shown schematically in Fig. 3. As seen in this figure, one surface of the pressure transducer is essentially flush with the blade surface while the reference side of the pressure transducer is at the end of a reference hole. For all of the transducer mounting configurations, the length of this hole permitted a natural frequency of 20 kHz or higher. These transducers were installed in the blade such that the sensing surface was essentially flush on the surface of the blade facing the accompanying instrumented blade. The axial positions of these transducers are shown in Fig. 2. This configuration resulted in redundancy of the unsteady differential surface pressure measurement at each chord location that provided data

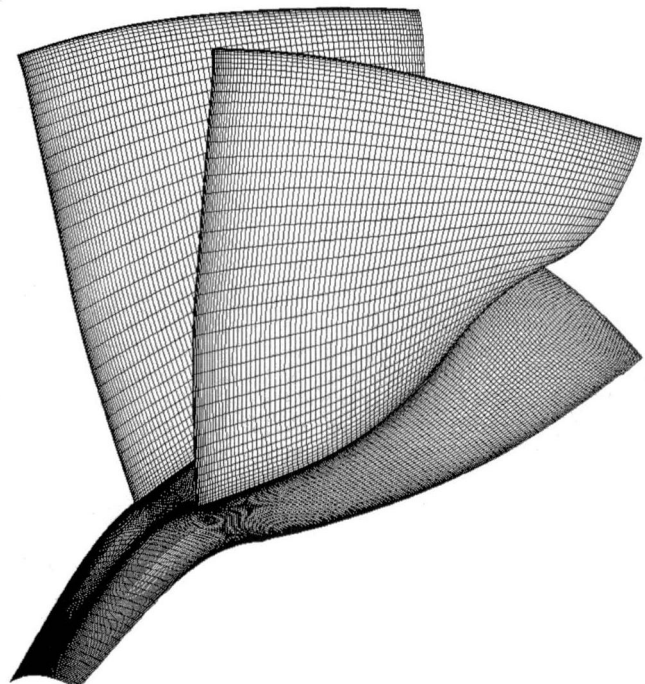


Fig. 4 Computational grid

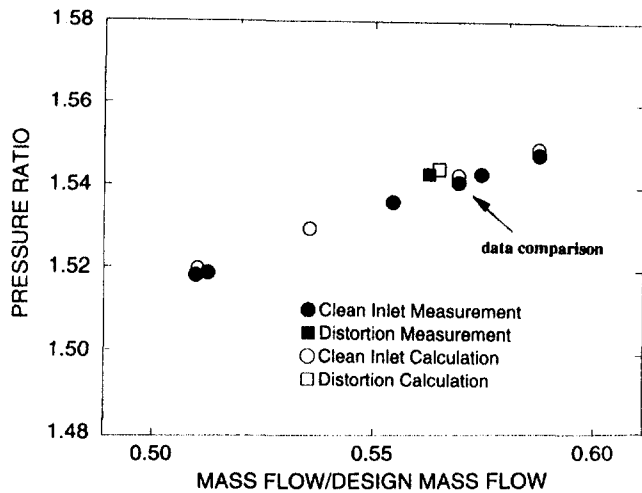


Fig. 5(a) Rotor speed line at 68 percent speed

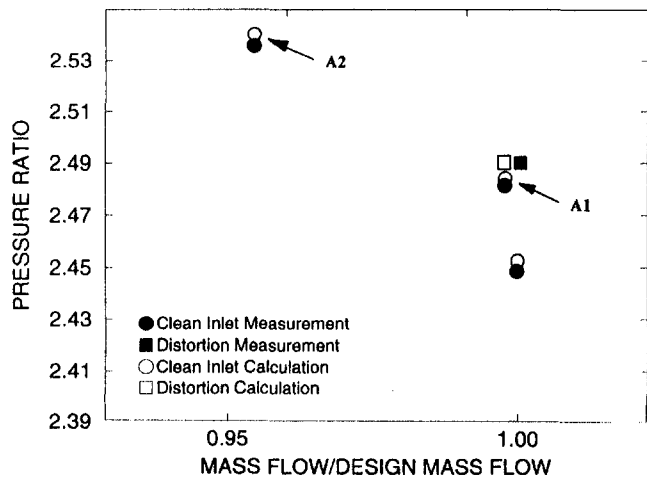


Fig. 5(b) Rotor speed line at 98 percent speed

validation and became beneficial with transducer attrition during the test. During data acquisition of the blade surface pressure measurements, the eight inlet rakes located at the distortion plane in Fig. 1 were removed so the only distortion present in the flow resulted from the distortion screen. These measurements were then compared to the unsteady results of the computational analysis.

The case-mounted high response pressure transducers also provided detailed flow measurements that could be used for validation of the numerical analysis. Sixteen of these transducers were located over the first-stage rotor blade. The data obtained from these measurements were processed as described by Russler (1995). These measurements were only acquired with a clean inlet condition. These measurements were then used to provide a detailed representation of the blade passage flow field that was compared to the computational results.

Accuracy of the measurements was maintained such that the temperatures were accurate to $\pm 0.17^\circ\text{C}$, the inlet steady-state pressure measurements were accurate to ± 0.002 atm, and the stator 1 pressure measurements were accurate to ± 0.007 atm. This resulted in an uncertainty of 0.8 percent in pressure ratio and 0.1 percent in temperature ratio. This accuracy does not consider the uncertainty due to averaging discrete pressures to determine the measurement plane average. The mass flow accuracy was considered to be ± 0.5 percent at design flow. The unsteady differential pressure measurements on the blade were considered accurate to ± 0.031 atm, which is approximately equal to the maximum pressure recorded by these pressure transducers. The high response pressure measurements on the case

endwall were considered accurate to ± 0.031 atm or 2.3 percent of the maximum exit static pressure measured during the test. All of these measurements were averaged to reduce the effect of noise or scatter on the measurement. The steady-state pressure and temperature values consisted of an average of 30 individual measurements. The case pressures were ensemble-averaged over at least 100 revolutions of a specific blade passage. The blade pressure measurements were ensemble-averaged from at least 1200 periods of distortion.

Numerical Method

Two types of numerical analysis were performed for the current study. A steady three-dimensional Navier–Stokes analysis was applied to the rotor flow field with the clean inflow condition. The detailed numerical procedures for the steady flow analysis were previously reported (Hah, 1987; Hah and Wenerstrom, 1990). With a circumferentially nonuniform distribution of inlet flow conditions, the compressor flow field becomes time dependent. To capture proper physics inside the blade passage, an unsteady, three-dimensional, viscous flow analysis was used for the flow with inlet distortions. For a time-periodic inflow condition, any instantaneous flow variable can be split

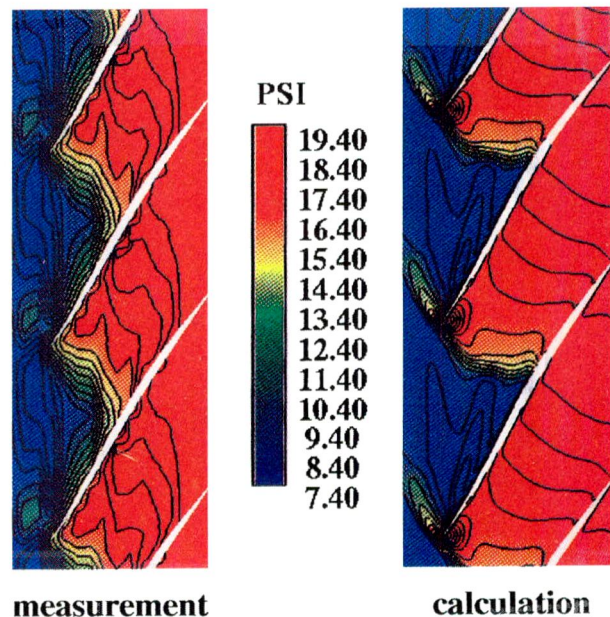


Fig. 6(a) Shroud static pressure distribution near peak efficiency

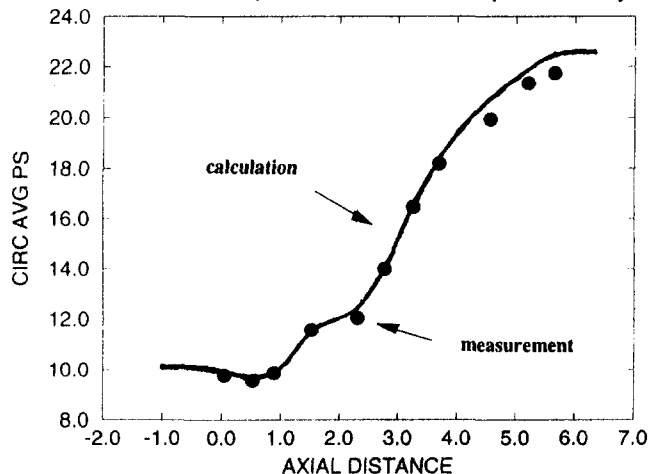


Fig. 6(b) Comparison of static pressure rise on the endwall

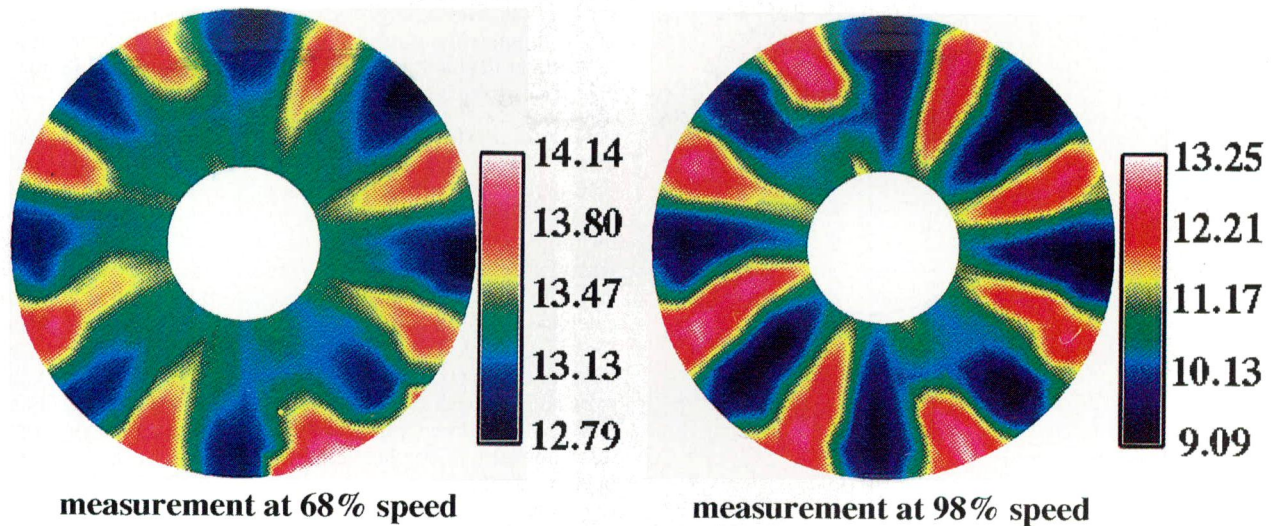


Fig. 7 Total pressure distributions at inlet

into three components: the time-averaged component, the periodic fluctuation due to the inlet flow distortion, and the turbulent fluctuation. The sum of the first two parts is the phase-averaged value, which is a function of time and space. The present study aims to solve numerically for this ensemble-averaged flow field. The effects of the turbulent fluctuations are included through the turbulence model. The turbulence is represented by the ensemble-averaged turbulence kinetic energy and the turbulence dissipation rate. These two turbulence variables are obtained by solving unsteady semi-empirical transport equations.

A three-dimensional steady Navier–Stokes code, which has been successfully tested for a wide range of turbomachinery flows (Hah, 1984, 1987), was extended to execute the time-accurate calculations. Previous studies (Cho et al., 1993; Hah et al., 1993) have shown that high-order discretization schemes are necessary in both space and time to avoid excessive numerical dissipation. For the time-dependent terms, an implicit second-order scheme is used. For unsteady flow calculations, the size of the time step is primarily determined by the requirement for physical accuracy. However, the time step is also restricted

by the numerical stability. For the current implicit time integration approach, a subiteration is performed at each time step. The computational grid is shown in Fig. 4. The grid consists of 100 nodes in the blade-to-blade direction, 46 nodes in the spanwise direction, and 152 nodes in the streamwise direction. Six nodes in the spanwise direction are used to describe the tip clearance region. With eight inlet distortion cells per revolution, two rotor blade passages encompass one period of the inlet distortion. Therefore, flows in two rotor blade passages shown in Fig. 4 were solved numerically. The numerical solution is advanced in time such that the two blade passages traverse one distortion pattern in 100 time steps. This corresponds to an actual time step of 0.0000057 s. Between 10 and 20 subiterations are necessary at each time step to reduce the residual below an acceptable value.

At each time step, the governing equations are solved with an implicit relaxation method using a fully conservative control volume approach. A third-order accurate interpolation scheme is used for the discretization of the convection terms and central differencing is used for the diffusion terms. The method is of

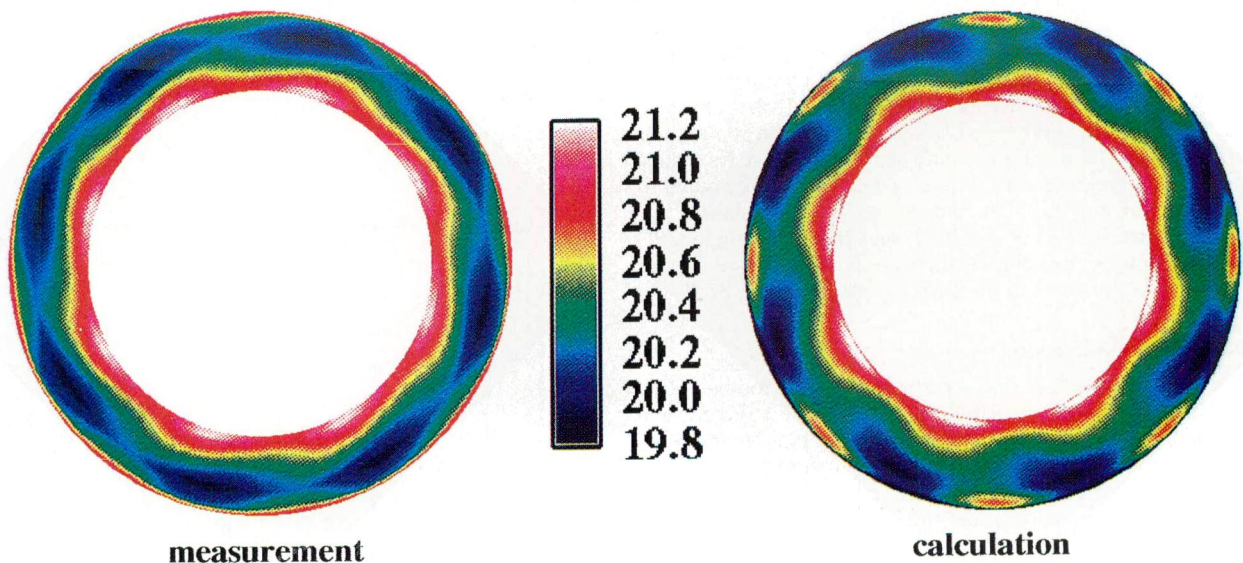


Fig. 8 Comparison of total pressure distributions at exit for 68 percent rotor speed

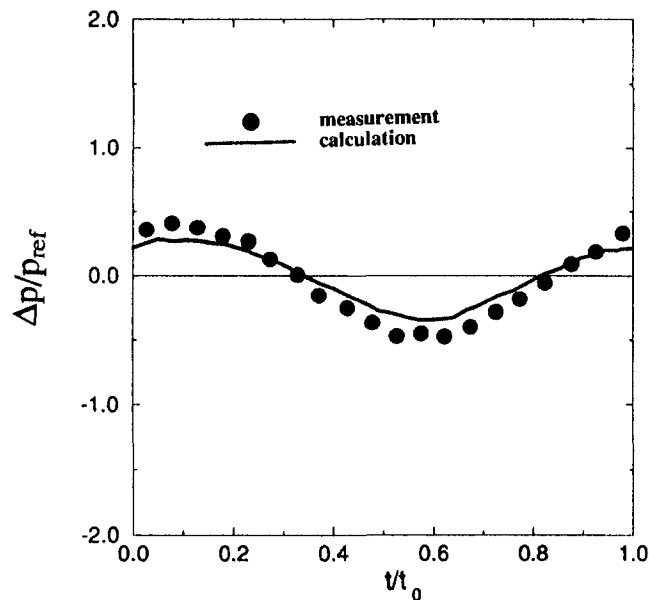


Fig. 9 Transient static pressure difference at 80 percent chord for 68 percent rotor speed

second-order accuracy with smoothly varying grids. At the inlet of the computational domain, instantaneous values of the total pressure that correspond to the distortion pattern are specified along with the total temperature. Also, two velocity components are specified at the inlet. No unsteady measurements of static pressure or other flow variables are available downstream of the rotor. Therefore, static pressure was prescribed at one circumferential location on the shroud at the outlet of the computational domain. Nonreflective procedures are used at the exit to minimize the influence of upstream effects. Residuals of each finite difference equation are integrated over the entire flow domain at each subiteration. When the integrated residuals of all the equations are reduced by four orders of magnitude from their initial values during the subiteration, the solution is advanced to the next time step. Further details of the computational procedures for the unsteady flow analysis are given by Hah et al. (1993) and Gallus et al. (1995). A steady solution is first obtained, and the converged steady solution is used as a starting condition for the unsteady calculations. Variations of mass flow rate and rotor efficiency were monitored to determine the convergence. When these quantities became periodic, the solution was assumed to be converged. A relatively large number of computational cycles is required to reach a periodic unsteady solution because of vortex shedding inside the rotor passage. For the lower rotor speed, about twelve distortion periods were calculated to reach a periodic state. About twenty distortion periods were necessary to obtain a converged periodic unsteady solution for the high rotor speed. The calculation was executed on a CRAY C-90 computer and about one single-CPU hour was required to advance the time-accurate solution over one distortion period with the current computational grid.

Results and Discussion

The primary objective of the current study was to investigate the effects of inlet flow distortion on the flow structure and the aerodynamic performance of a low-aspect-ratio, high-speed, transonic axial flow compressor. The computational results were compared to experimental data when appropriate to gain confidence in the computational and the experimental results. This comparison was first performed with the clean inlet flow condition to obtain the overall performance of rotor 1 and the detailed flow structure near the casing. Then, comparisons were made

for the flow with inlet distortion. After establishing confidence in the computational results, the numerical results were used to understand detailed flow structures that are responsible for the changes in aerodynamic performance of the rotor.

Overall Performance and Shock Structure With Clean Inlet. The design pressure ratio and mass flow occurred at 98.6 percent of the intended design speed of 13,288 rpm. The tip speed of the rotor at 98.6 percent speed was 483.5 m/s resulting in a blade tip Mach number of 1.7. The compressor was also tested at 98 and 68 percent rotor design speed with and without an inlet total pressure distortion. The measured and calculated pressure rise characteristics of the rotor are given in Fig. 5. The calculated performance of the rotor with the inlet distortion was obtained by area-averaging instantaneous values over one periodic cycle similar to the experimental technique.

When a blade encounters a low total pressure region of the distortion pattern, the blade loading increases because the blade operates with the same exit static pressure. Therefore, the effective blockage inside the rotor passage increases and the rotor operates closer to the stall condition. To study the effects of the inflow distortion on the blade efficiency, the flow with the inlet distortion at 98 percent speed is compared with a clean inlet flow, which has a distribution of blade loading similar to that of the distortion case, and to the clean inlet flow with the initial blade loading. Altogether, measured flow fields at four operating conditions and calculated flow fields at five conditions are investigated in detail. The four measured and five calculated flow conditions are marked in Fig. 5. The total pressure ratios in Fig. 5 were obtained by area-averaging for both the measurement and the calculation. The results in Fig. 5 indicate that the numerical solution calculates a slightly higher pressure rise than the measured value, both with a clean inlet and with an inlet distortion. However, the overall trend is very well represented by the calculation.

In Fig. 6, measured and calculated endwall shock structures and the static pressure rise across the rotor near peak efficiency with clean inlet at 98 percent rotor speed are compared. The numerical results show a stronger interaction between the tip clearance vortex and the passage shock than the measurements near the entrance of the rotor passage. Similar flow interactions inside the tip clearance region were previously observed in a high-speed compressor rotor (Copenhaver et al., 1993; Hah and

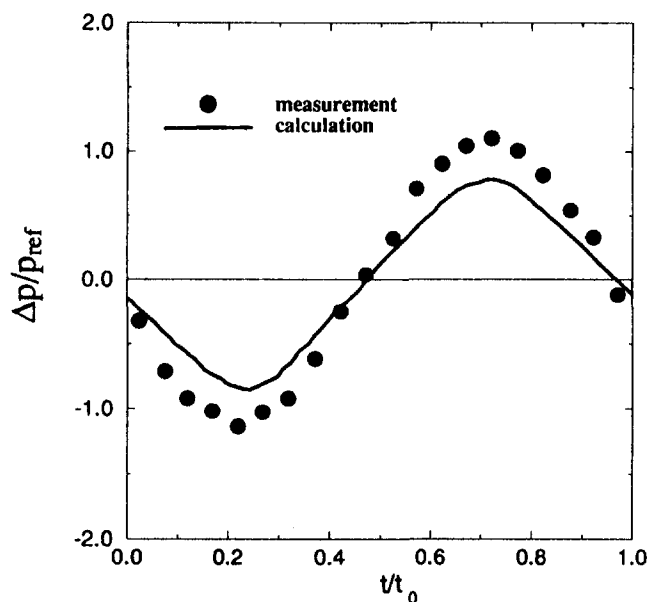


Fig. 10 Transient static pressure difference at 80 percent chord for 98 percent rotor speed

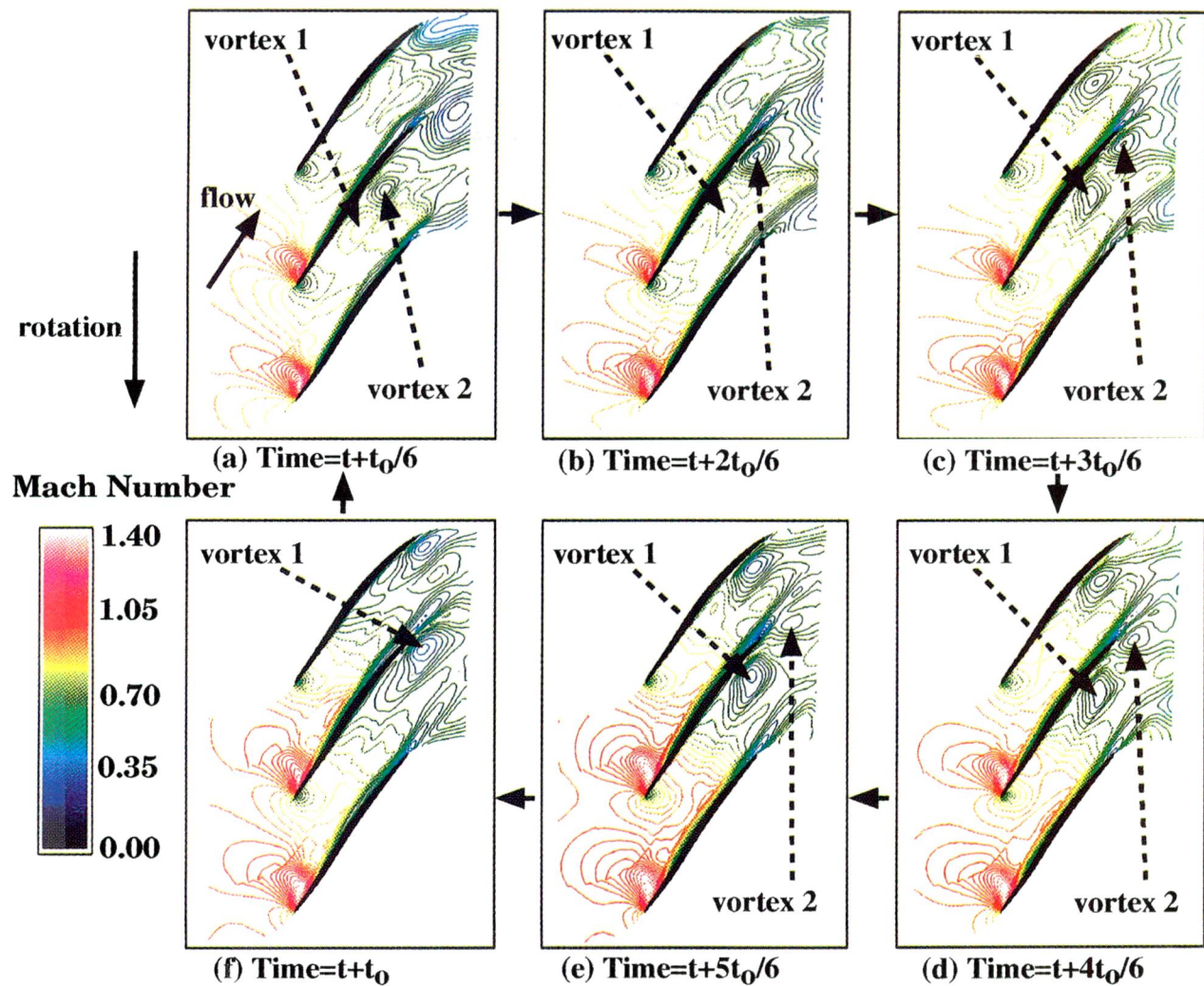


Fig. 11 Instantaneous Mach number contours at 85 percent span for 68 percent rotor speed

Wennerstrom, 1990). The limited number of pressure transducers mounted on the endwall limits the resolution of the flow field. Reasonably good agreements between the measurements and the calculation shown in Figs. 5 and 6 indicate that overall flow structures in the present high-pressure ratio compressor rotor are properly modeled by the current numerical procedure.

Flow Fields With Inlet Total Pressure Distortion. Inlet total pressure distortion patterns were created with an eight per revolution screen in the experimental study (Russler, 1994). The test conditions were selected to provide forcing functions to evaluate the rotor at resonance conditions. For the present work, effects of inlet distortion on the rotor flow field are studied in detail at two rotor speeds. In the following sections, the changes in distortion pattern through the rotor and transient static pressure at 85 percent span are first compared between the measurement and the calculation. Then, detailed flow characteristics in the rotor passage with the inlet distortion are examined with the numerical solution.

Distortion Pattern and Transient Blade Static Pressure. The measured distributions of inlet total pressure are shown in Fig. 7 at two test conditions. As shown in Fig. 7, each distribution has eight nearly sinusoidal profiles per revolution. The average maximum and minimum values of the total pressure for the eight periods are 12.86 psi and 9.27 psi for the high rotor speed. Corresponding values for the low rotor speed are

13.96 psi and 12.93 psi. The change in total pressure across the distortion is more than three times larger at high rotor speed than that at low speed. However, the relative magnitude of the total pressure change to the inlet dynamic head is about the same for the two speeds. For numerical analyses, the eight profiles at each rotor speed are averaged and eight identical distortion patterns per revolution are assumed. These averaged profiles, which are slightly asymmetric, are used as the inflow boundary conditions for the unsteady flow calculations.

In Fig. 8, total pressure distributions at the exit of the rotor are compared between the measurement and the calculation at 68 percent rotor design speed. The total pressure distributions shown in Fig. 8 are in the stationary frame, and the distributions are due to the nonuniform distribution upstream of the rotor. These total pressure profiles are convected to the following stator. The measurements show that the inlet distortion patterns are not mixed out completely by the rotor. The numerical results agree well with the measurements. The numerical values in Fig. 8 were obtained by averaging 100 instantaneous values through one distortion cycle after the periodic unsteady solution was obtained. A region with high total pressure near the hub and a region with low total pressure near 60–70 percent of the span are both observed from the measurement as well as from the calculation. Near the shroud, both high total pressure and low total pressure regions are shown. The distribution of total pressure near the shroud may be due to the interaction of the incom-

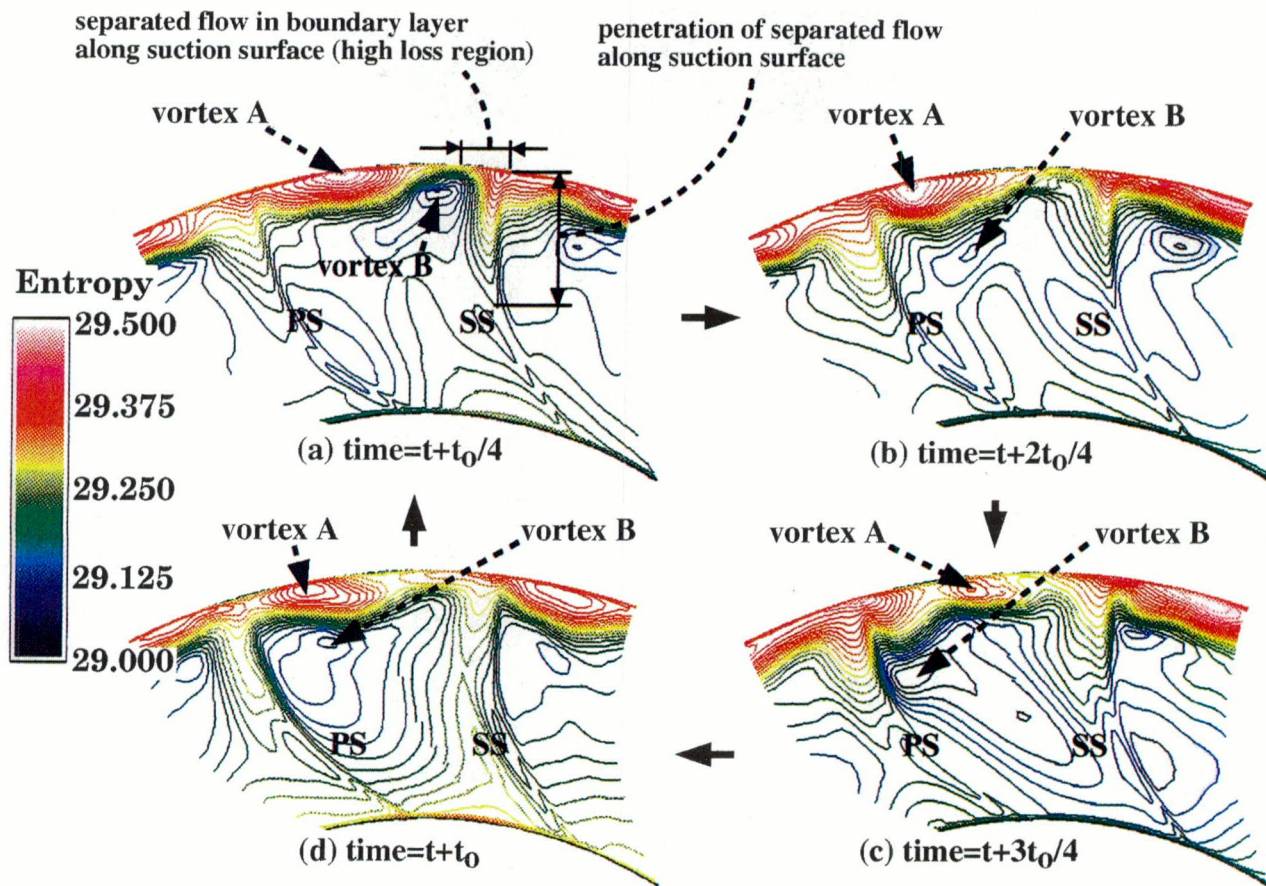


Fig. 12 Instantaneous entropy contours at 5 percent chord downstream of trailing edge for 68 percent rotor speed

ing distortion pattern with the tip clearance vortex. The results in Figs. 7 and 8 show that the total pressure distortion pattern travels through the rotor passage. The distortion pattern changes its shape substantially. However, eight distinctive distortion cells are present at the exit of the rotor.

Transient static pressure profiles at 80 percent blade chord and at 85 percent span are compared between the measurements and the calculation in Figs. 9 and 10. The values in Figs. 9 and 10 are the transient difference between the static pressures on the suction and the pressure sides of the blade for one period of distortion. The numerical profiles agree fairly well with the measured values. However, the calculated peak-to-peak variation is smaller than that measured at both rotor speeds. For the current numerical analysis, it is assumed that the geometric deflection of rotor blades does not change during rotation. The change of the blade deflection during the rotation may change the peak-to-peak variation of the transient static pressure field. Comparisons in Figs. 9 and 10 show that the pressure wave due to the inlet total pressure distortion travels through the rotor passage. The amplitude and the resulting unsteady aerodynamic loading at high rotor speed are roughly twice those at the low rotor speed.

Effects of Inlet Distortion on Flow Structure. Instantaneous Mach number contours at 85 percent span are plotted to study the unsteady flow fields inside the rotor with inlet distortion. In Fig. 11, instantaneous relative Mach number contours at six equally spaced times during a distortion period are shown. Since the rotor has 16 blades and there are eight distortion patterns per revolution, two blade passages make a nominal periodic cycle.

At this low rotor speed, a passage shock is not expected at 85 percent span. Thus, upstream flow disturbances are not

blocked by shock wave and the inflow distortion affects the entire flow passage almost simultaneously. For both blade passages, a vortex with low Mach number is formed near the pressure side of the blade. The vortex cores (marked as vortices 1 and 2 in Fig. 11) are convected downstream as shown in Figs. 11(a-e). Vortex 2 is convected completely downstream of the blade passage in Fig. 11(f) and a new vortex core is formed. This vortex is convected downstream as the blade moves through the distortion profile. As shown in Fig. 7, the variation of the total pressure across the distortion profile is relatively small at the 68 percent rotor speed. When this distortion pattern reaches the rotor leading edge, a small change in incidence angle is expected. Detailed contours near the leading edge in Fig. 11 show relatively small changes in the flow near the leading edge during the distortion period. Contour lines near the suction surface of the blade show that the boundary layer is almost completely attached during the cycle, although the boundary layer itself is clearly unsteady. The vortex near the pressure surface of the blade is convected downstream, but the thickness of the boundary layer does not increase. The boundary layer on the pressure side of the blade seems to be energized by the unsteady vortex system. Also, flow downstream of the rotor shows more disturbances than the incoming distortion due to the shed vortex. Previous studies of multistage axial compressor aerodynamics have shown that the stage efficiency increases when the axial gap is decreased in some subsonic operating conditions (Smith, 1970; Mikolajczyk, 1977). Smith (1966) suggested a possible explanation of this fascinating phenomenon using the mixing mechanism of an incoming stator wake through the following rotor blade passage. The results in Fig. 11 suggest that there may be other possible mechanisms in reducing aerodynamic losses with narrower gaps between

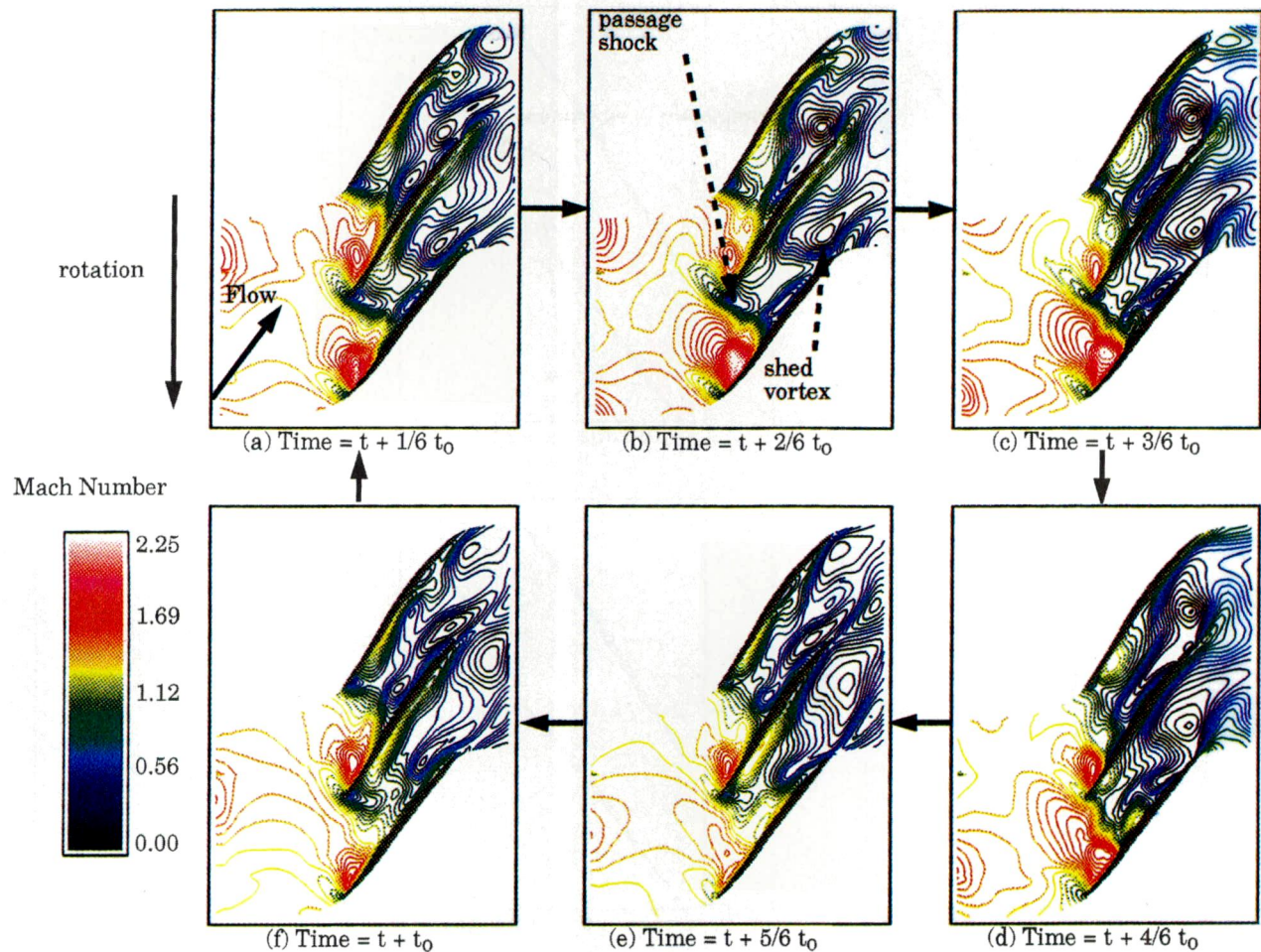


Fig. 13 Instantaneous Mach number contours at 85 percent span for 98 percent rotor speed

blade rows. The detailed flow structures in Fig. 11 suggest that a favorable interaction between the vortex and the blade boundary layer might be one such mechanism.

The instantaneous entropy contours at 5 percent blade chord downstream of the rotor are given in Fig. 12. Regions with high entropy contours represent areas with high aerodynamic losses. A highly fluctuating vortex system (vortex B) is observed in Fig. 12. Entropy generation is confined near the casing and no significant loss is observed in the area of the fluctuating vortex. Further interpretation of the vortex structure in Fig. 12 will be given later in this section with the results at 98 percent rotor speed. The effect of this fluctuating vortex on the rotor performance will be further examined in the next section.

In Fig. 13, instantaneous relative Mach number contours are shown for the 98 percent rotor speed. As shown in Fig. 7, the variation of the total pressure across the distortion pattern is more than 30 percent of the mean value. Therefore, the effects of inlet total pressure distortion on the rotor flow field are expected to be more substantial than at the low rotor speed. At this high rotor speed, a strong passage shock develops near the leading edge of the rotor. The instantaneous Mach number contours in Fig. 13 indicate that the passage shock system oscillates substantially when the rotor blade traverses through the distortion pattern. A strong interaction between the moving shock and the blade boundary layers is observed in Fig. 13. As a result of this strong interaction, large vortices are generated and convected downstream. The formation and convection of a vortex in the blade passage are illustrated in Fig. 14 using constant Mach number contours. During the distortion cycle,

the vortex grows as it is convected downstream within the blade passage. The flow field inside the rotor blade passage is dominated by these vortices. Also, the blade boundary layers grow significantly due to this oscillating shock system. In Fig. 15, the movement of the passage shock during one distortion period is illustrated by the instantaneous sonic line during the cycle. The passage shock moves approximately 20 percent of the chord during the cycle. Ng and Epstein (1985) found for a similar transonic compressor that a very small shock oscillation (about 1 percent of tip chord) can cause an increase of compressor aerodynamic loss of 0.15 percent. A quantitative estimation of the increased loss due to the shock movement in the current rotor will be given in the next section. From the results in Figs. 13, 14, and 15, it is clear that the interaction between the oscillating passage shock and the blade boundary layer, and the resulting vortex shedding shown in Fig. 14, are the dominating flow structures when the transonic compressor encounters a strong circumferentially nonuniform flow distortion.

The instantaneous entropy contours at 5 percent chord downstream of the rotor for 98 percent rotor speed are given in Fig. 16. The time-dependent entropy contours downstream of the rotor at 68 and 98 percent rotor speeds, which are shown in Figs. 12 and 16, respectively, show a complex three-dimensional flow interaction open to several interpretations. Our views on the flow phenomenon calculated by the analysis are summarized as follows.

Two distinct vortex cores labeled vortices A and B are observed at both 68 and 98 percent rotor speeds as illustrated in Figs. 12 and 16. Vortex A represents the flow field associated

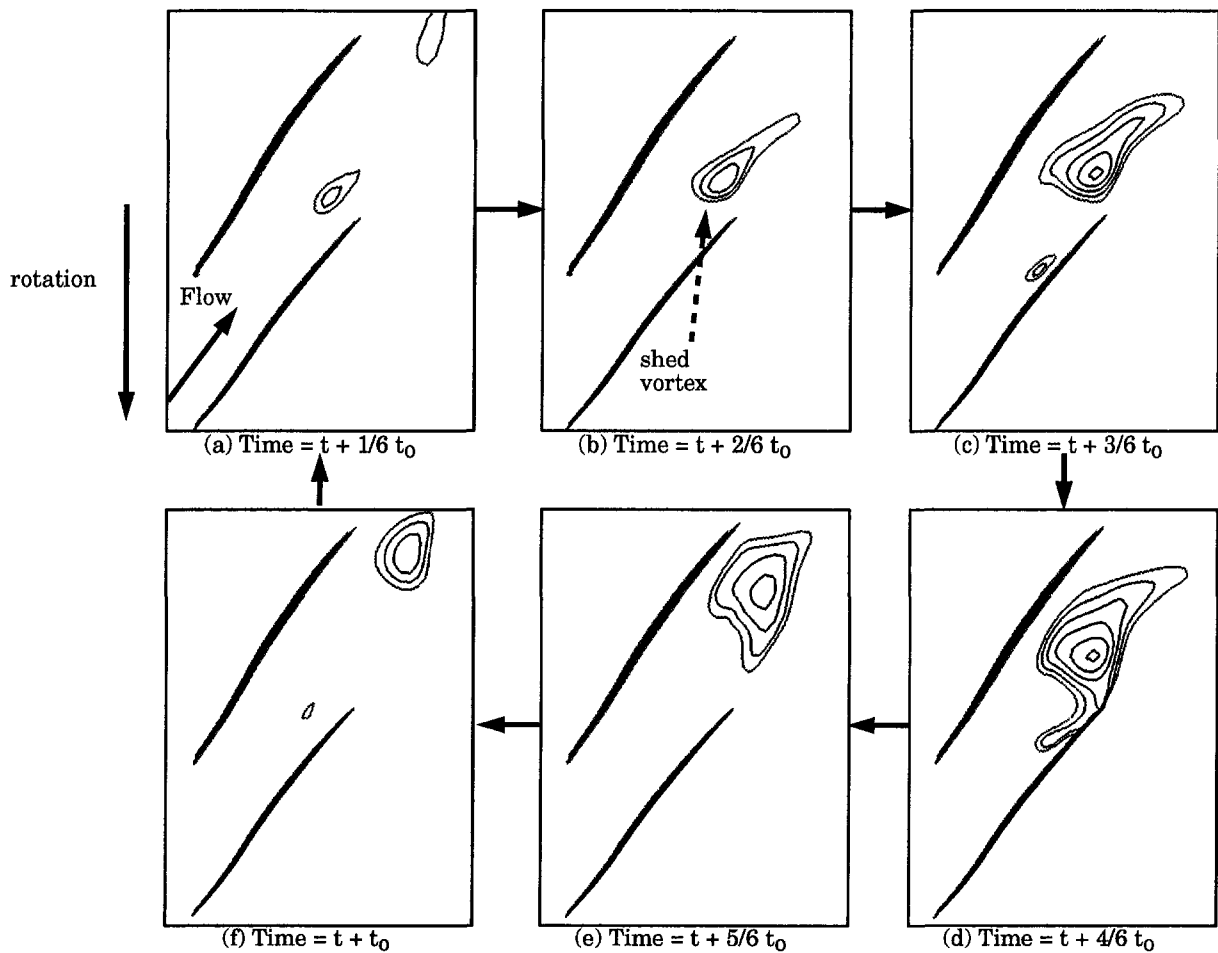


Fig. 14 Formation and convection of a vortex at 85 percent span for 98 percent rotor speed

with the tip shock and the clearance flow and vortex B is related to the secondary flow being centrifuged radially outward along the suction surface of the airfoil.

The core of vortex A, shown in Fig. 12, is circumferentially located approximately 40 percent of the distance from the airfoil pressure surface to the adjacent suction surface, and extends about 20 percent span inward from the casing wall. At higher relative velocities (98 percent speed), the interaction between the tip clearance vortex and the relatively stronger leading edge shock is larger and vortex A extends deeper to about 40 percent span inward from the casing endwall as shown in Fig. 16. The unsteady motion of the vortex A, attributed in part to the shock oscillation (typically illustrated in Fig. 15), is shown at selected time steps in Figs. 12(a-d) for 68 percent speed and Figs. 16(a-d) for 98 percent speed. At both speeds, the core of vortex A relocates from midpassage ($t + t_0/4$) to the pressure side of the airfoil ($t + 2t_0/4$). The core moves back to midpassage as the solution progresses to the next time step ($t + 3t_0/4$ in Figs. 12 and 16). As stated above, the motion of vortex A is supported by the shock oscillation reported in Fig. 15.

The secondary flow vortex (vortex B) forms a vortex core near the casing at $t + t_0/4$ as shown in Figs. 12 and 16 and migrates from the suction side toward the pressure side of the airfoil as the numerical calculations progress in time from $t + t_0/4$ and $t + 3t_0/4$ to $t + t_0$ as shown in Figs. 12(b-d). Little interaction between the secondary flow and the clearance vortex occurs at 68 percent speed; vortices A and B maintain their identities as they migrate with time. However, at 98 percent speed, the effect of the secondary flow vortex is considerably

masked by the stronger and more dominant tip clearance vortex flow, as shown in Figs. 16(a-d).

Effects of Inlet Distortion on Compressor Performance.

To compare the overall effects of inlet total pressure distortion on the performance of the rotor, spanwise distributions of blade section efficiency are compared between the clean inlet flow and the flow with the distortion. In Fig. 17, comparisons at 68 percent of the rotor design speed are presented. The measured distributions and the calculated distributions are compared. The calculated profiles are obtained by averaging instantaneous profiles over the distortion period. According to the measured distributions, the blade section efficiency improves above 70 percent of the blade span for the presently investigated distortion compared to the clean inlet case. The calculation shows the same changes as the measurements. Because of the increased blade section efficiency near the shroud, the overall blade efficiency increases by 0.4 percent with distortion. At this flow condition, the distortion does not change the blade section efficiency near the hub as shown in Fig. 17. To examine the flow behavior further, the instantaneous entropy contours at 85 percent span are averaged and compared with the steady results for the clean inlet condition in Fig. 18. This comparison indicates that the time-averaged unsteady flow field with the distortion shows no noticeable increase in boundary layer growth compared to the clean inlet case. The results shown in Fig. 17 indicate that the vortex generated inside the passage (as shown in Fig. 11) does not contribute to added overall loss. The smaller generation of entropy in Fig. 18 for the flow with inlet distortion suggests

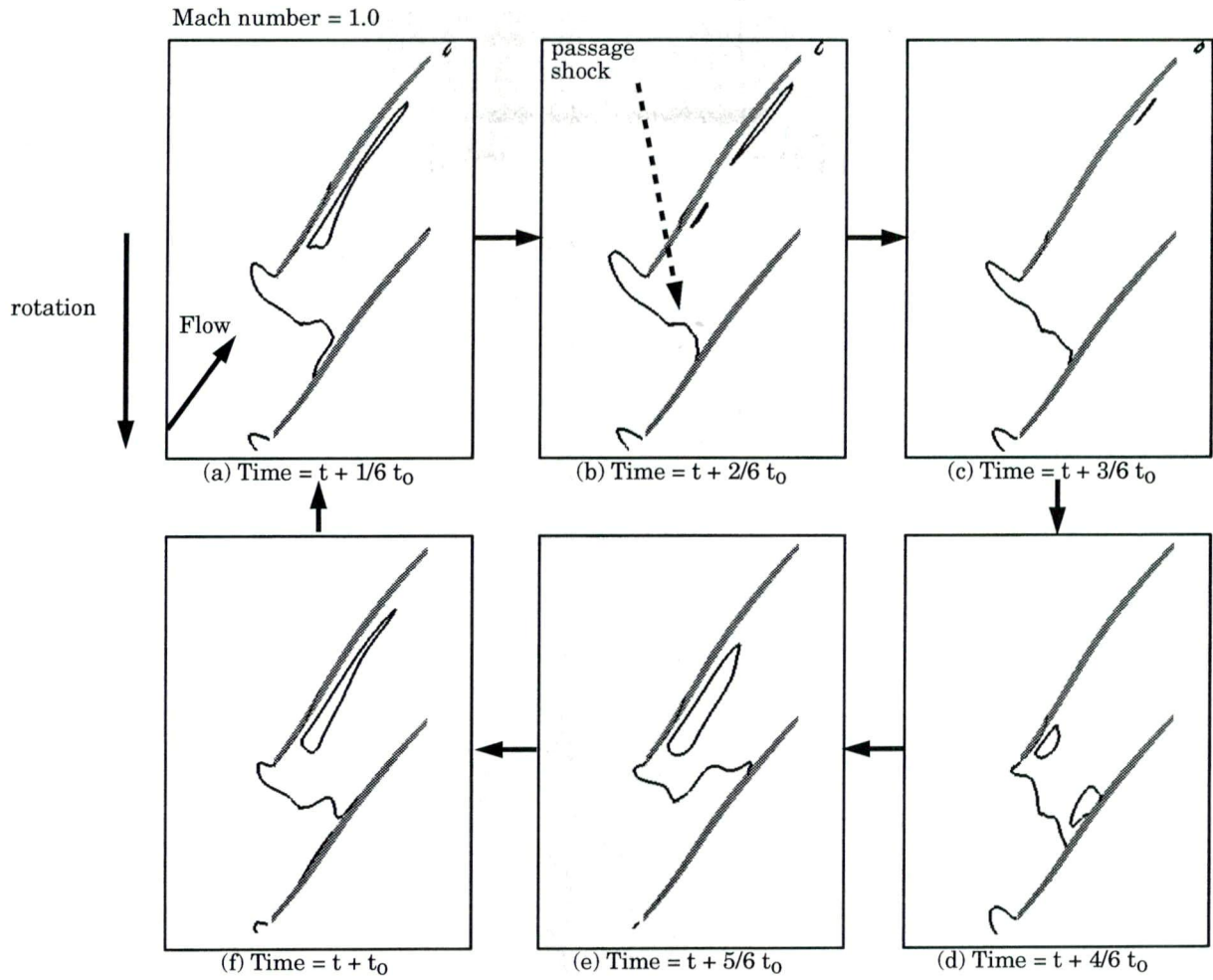


Fig. 15 Movement of passage shock over one distortion period at 85 percent span for 98 percent rotor speed

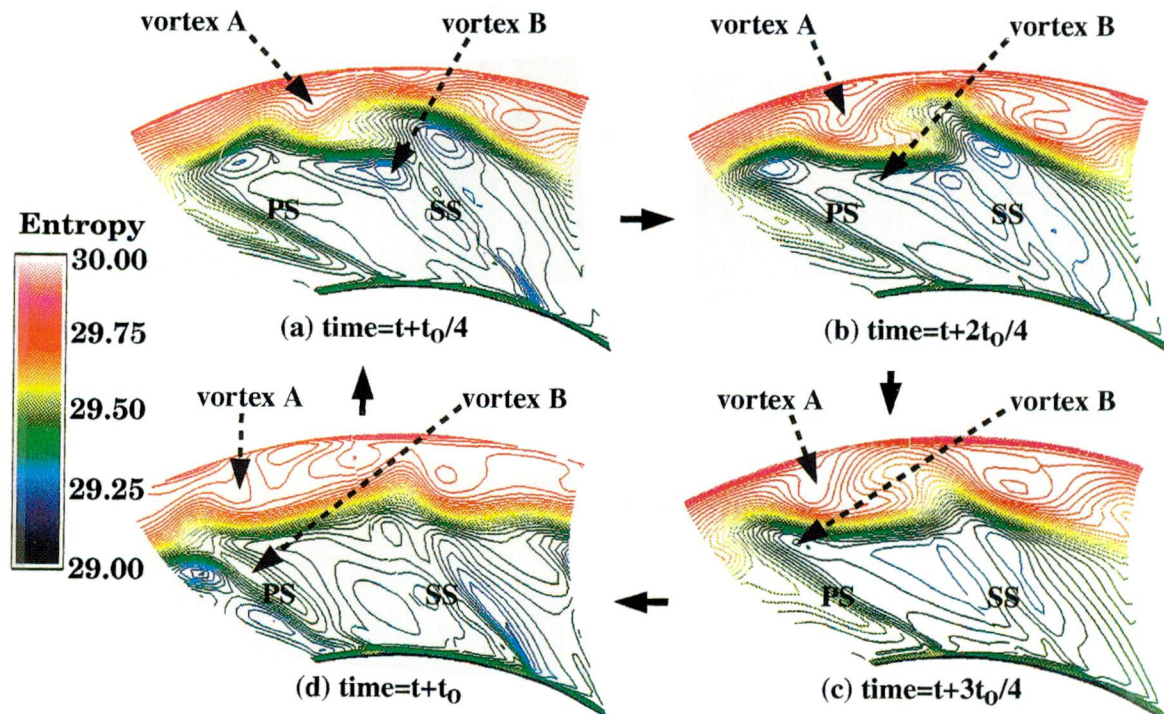


Fig. 16 Instantaneous entropy contours at 5 percent chord downstream of trailing edge for 98 percent rotor speed

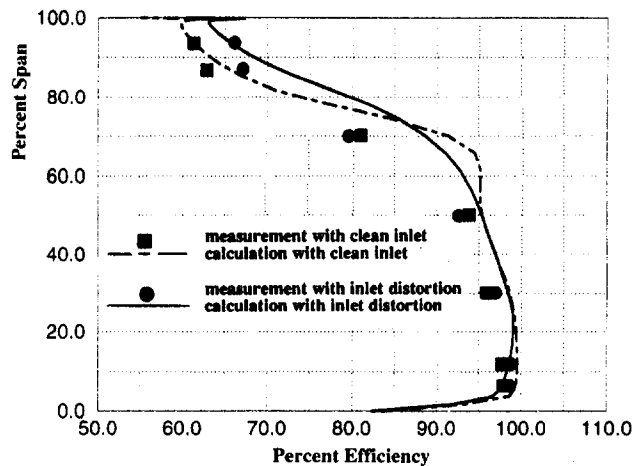


Fig. 17 Comparison of blade section efficiency at 68 percent rotor speed

that the flow near the blade surface is energized by the shed vortex.

As shown in Fig. 13, the effective blockage inside the blade passage increases with the inlet distortion, resulting in an increased blade loading. To obtain a more realistic assessment of the effects of distortion, an additional rotor flow field without distortion at a high pressure ratio is also compared. This operating condition is marked in Fig. 5. The shock structures at two operating conditions are compared with the time-averaged unsteady solution with the inlet distortion in Fig. 19. The blade section efficiencies are compared in Fig. 20 for the 98 percent rotor design speed. At this high speed, the spanwise distribution of loss is quite different from that at low speed. The measurements show that the blade section efficiency is higher with the inlet distortion below 60 percent of the span while the efficiency is somewhat lower above 60 percent of the span when compared to the efficiency with clean inlet. The numerical results show the same trend for the effects of inlet distortion on blade section efficiency as the measurements. As shown in Fig. 19, the rotor operates at a higher loading with the inlet distortion. Therefore, the blade section efficiency with the inlet flow distortion should be compared with the clean inlet flow, which has a similar loading distribution. As shown in Fig. 20, the blade section efficiency with the distortion is lower than that of the flow with the clean inlet and a similar shock structure near the end wall. This decrease in the blade section efficiency is due to the strong interaction between the oscillating passage shock and the blade boundary layer that is shown in Fig. 13. Because the mass flow rate is higher near the shroud, the overall rotor efficiency decreases with the inlet distortion. The calculated decrease is 1 percent with the inlet total pressure distortion. Time-averaged instantaneous entropy contours at 85 percent span are compared with the steady results in Fig. 21. This comparison indicates that the large entropy generation is concentrated near the suction side of the blade for the flow with the distortion. This again indicates that unsteady interaction between the passage shock and the suction surface boundary layer is the major contributor to the aerodynamic loss when a transonic rotor flow field is subjected to a strong inlet total pressure distortion.

Concluding Remarks

The effects of inlet total pressure distortion on the flow field in a low-aspect-ratio, high-speed, transonic compressor rotor have been investigated. Both experimental and numerical techniques are applied in a complementary way to ad-

vance our present understanding of this very complex flow field. The following is a summary of the current study:

1 The inlet flow distortion travels through the rotor passage and is convected into the following stator. The highly transient flow field is observed at both low and high rotor speeds with the inlet flow distortion.

2 At 68 percent rotor design speed, both the measurement and the calculation show that the blade section efficiency with the inlet distortion is higher than that with clean inlet flow above 70 percent of the span. The numerical results indicate that the increased blade section efficiency in the outer region of the rotor blade might be the result of favorable effects of the interaction between the passage vortices and the blade boundary layer.

3 At 98.6 percent rotor design speed, a strong interaction between the oscillating passage shock and the blade suction surface boundary layer increases the effective blockage and forces the rotor to operate closer to the stall condition. When compared to a clean inlet flow field with a similar loading, inlet total pressure distortion decreases the blade section efficiency above 60 percent of the blade span. However, improvements in blade section efficiency are observed near the hub when com-

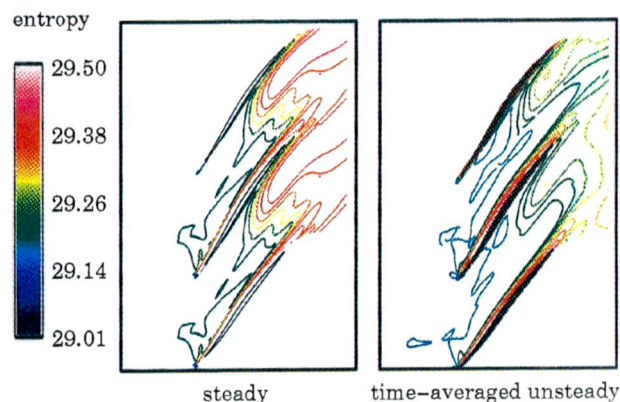


Fig. 18(a) Comparison of entropy contours at 85 percent span for 68 percent rotor speed

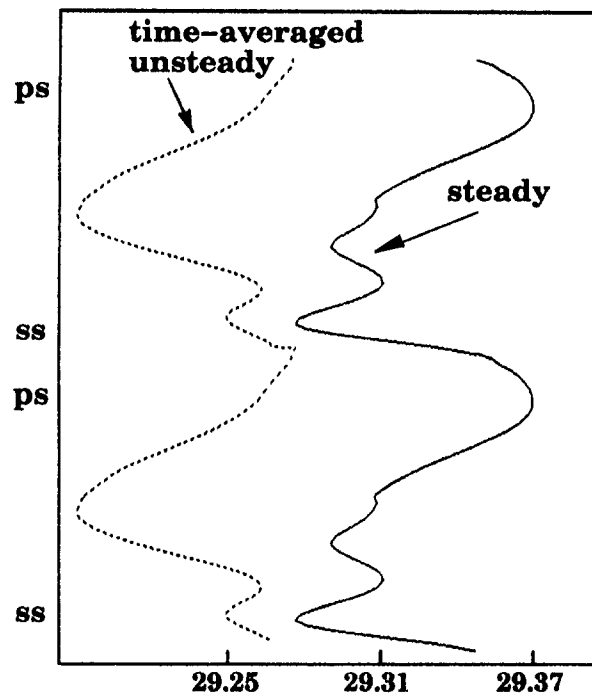


Fig. 18(b) Comparison of entropy distribution at 20 percent chord downstream and 85 percent span for 68 percent rotor speed

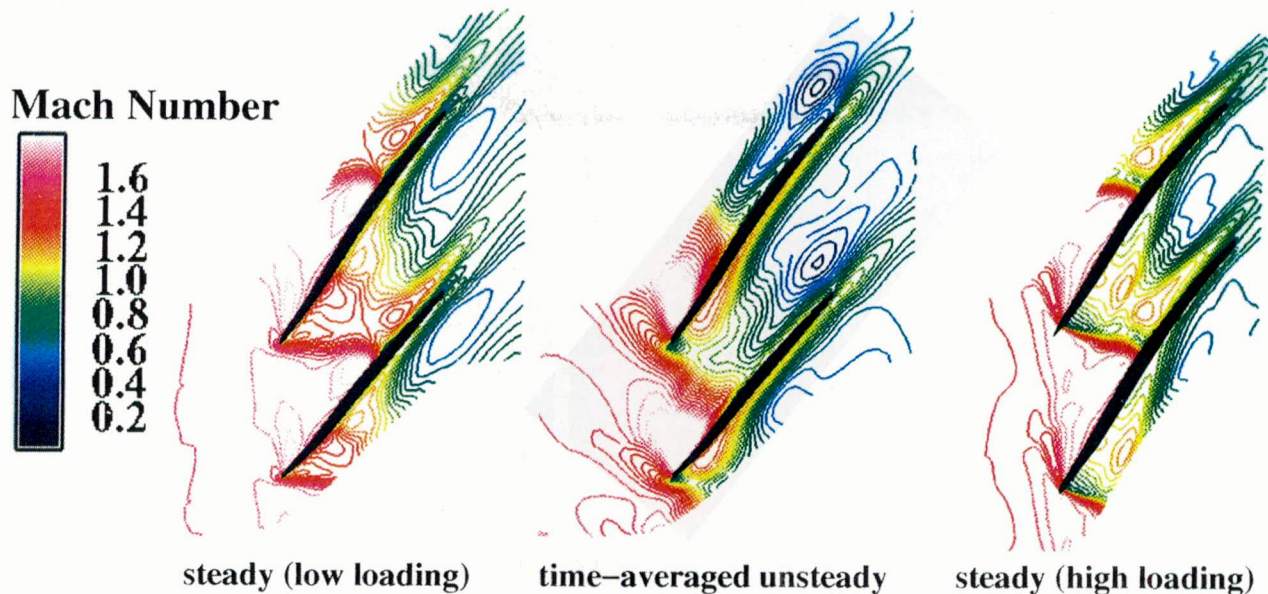


Fig. 19 Comparison of relative Mach number contours at 85 percent span for 98 percent rotor speed

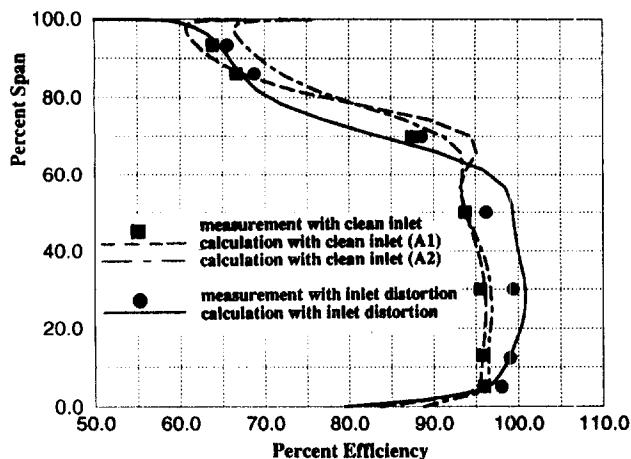


Fig. 20 Comparison of blade section efficiency at 98 percent rotor speed

pared to the clean rotor flow field. The numerical results show that the increased loss in the outer part of the blade is due to the strong interaction between the oscillating passage shock and the blade boundary layer. A vortex shedding occurs due to this interaction. The passage shock moves by as much as 20 percent of the chord during the distortion period. The blade boundary layer thickens substantially due to the unsteady interaction with the passage shock.

4 The current study indicates that the inlet total pressure distortion increases aerodynamic losses when a strong unsteady interaction between the passage shock and the blade boundary layer develops. However, a subsonic flow range exists in which the inlet total pressure distortion can actually improve the rotor performance.

Acknowledgments

The authors would like to acknowledge the contribution of J. Loellbach and F. Tsung of ICOMP at NASA Lewis Research Center in preparing the illustrations. Also, we would like to thank G. E. Aircraft Engine Company, Wright Laboratory, and NASA for allowing us to present this work.

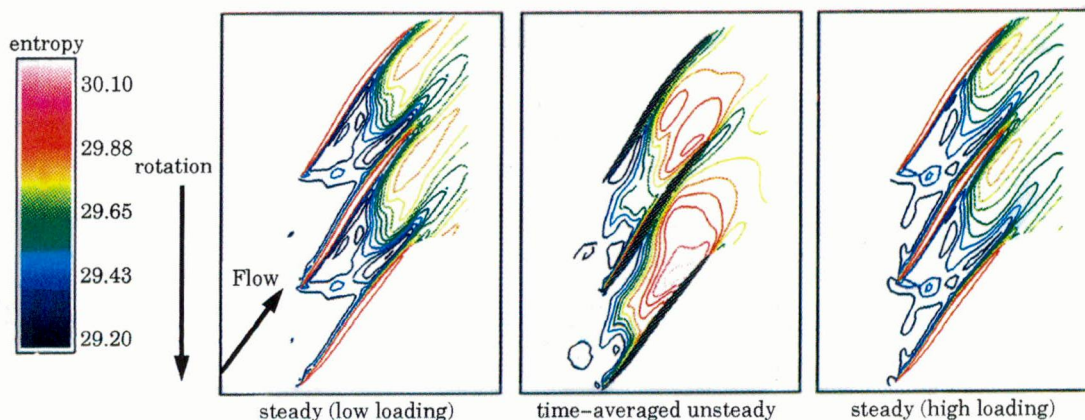


Fig. 21 Comparison of entropy contours at 85 percent span for 98 percent rotor speed

References

- Adamczyk, J. J., Mulac, R. A., and Celestina, M. L., 1986, "A Model for Closing the Inviscid Form of the Average Passage Equations," *ASME JOURNAL OF TURBOMACHINERY*, Vol. 108, pp. 180–186.
- Bowditch, D. N., and Coltrin, R. E., 1983, "A Survey of Engine Inlet Distortion Capability," NASA TM-83421.
- Cho, N.-H., Liu, X., Rodi, W., and Schonung, B., 1993, "Calculation of Wake-Induced Unsteady Flow in a Turbine Cascade," *ASME JOURNAL OF TURBOMACHINERY*, Vol. 115, pp. 675–686.
- Copenhaver, W. W., Hah, C., and Puterbaugh, S. L., 1993, "Three-Dimensional Flow Phenomena in a Transonic, High-Through-Flow Compressor Stage," *ASME JOURNAL OF TURBOMACHINERY*, Vol. 115, pp. 240–248.
- Davis, R. L., Hobbs, D. E., and Weingold, H. D., 1988, "Prediction of Compressor Cascade Performance Using a Navier–Stokes Technique," *ASME JOURNAL OF TURBOMACHINERY*, Vol. 110, pp. 520–531.
- Dawes, W. N., 1986, "Development of a 3D Navier–Stokes Solver for Application to All Types of Turbomachinery," ASME Paper No. 86-GT-70.
- Denton, J. D., and Singh, U. K., 1979, "Time Marching Methods for Turbomachinery Flow Calculation," VKI Lecture Series, 1979–7.
- Denton, J. D., 1986, "The Use of a Distributed Body Force to Simulate Viscous Flow in 3D Flow Calculations," ASME Paper No. 86-GT-144.
- Gallus, H. E., Zeschky, J., and Hah, C., 1995, "Endwall and Unsteady Flow Phenomena in an Axial Turbine Stage," *ASME JOURNAL OF TURBOMACHINERY*, Vol. 117, pp. 562–570.
- Giles, M. B., 1988, "Stator/Rotor Interaction in a Transonic Turbine," AIAA Paper No. 88-3093.
- Greitzer, E. M., Tan, C. S., Wisler, D. C., Adamczyk, J. A., and Strazisar, A. J., 1994, "Unsteady Flow in Turbomachines: Where's the Beef?" ASME AD-Vol. 40, Ng, W., Fant, D. and Povinelli, L., eds.
- Gundy-Burlet, K. L., Rai, M. M., Stauter, R. C., and Dring, R. P., 1991, "Temporally and Spatially Resolved Flow in a Two-Stage Axial Compressor: Part 2—Computational Assessment," *ASME JOURNAL OF TURBOMACHINERY*, Vol. 113, pp. 227–232.
- Hah, C., 1984, "A Navier–Stokes Analysis of Three-Dimensional Turbine Flows Inside Turbine Blade Rows at Design and Off-Design Conditions," *ASME Journal of Engineering for Gas Turbines and Power*, Vol. 106, pp. 421–429.
- Hah, C., 1987, "Calculation of Three-Dimensional Viscous Flows in Turbomachinery With an Implicit Relaxation Method," *AIAA Journal of Propulsion and Power*, Vol. 3, No. 5, pp. 415–422.
- Hah, C., and Wennerstrom, A. J., 1990, "Three-Dimensional Flowfields Inside a Transonic Compressor With Swept Blades," *ASME JOURNAL OF TURBOMACHINERY*, Vol. 113, pp. 241–251.
- Hah, C., Puterbaugh, S. L., and Copenhaver, W. W., 1993, "Unsteady Aerodynamic Flow Phenomena in a Transonic Compressor Stage," AIAA Paper No. 93-1868; to be printed in the *AIAA Journal of Propulsion and Power*.
- Hall, E. J., Heidegger, N. J., and Delaney, R. A., 1996, "Performance Prediction of Endwall Treated Fan Rotors With Inlet Distortion," AIAA Paper No. 96-0244.
- Horlock, J. H., 1968, "Fluctuating Lift Forces on Airfoils Moving Through Transverse and Chordwise Gusts," *ASME Journal of Basic Engineering*, Vol. 90, Paper No. 68-FE-28.
- Jorgenson, P. C. E., and Chima, R. V., 1988, "An Explicit Runge-Kutta Method for Unsteady Rotor/Stator Interaction," AIAA Paper No. 88-0049.
- Longley, J. P., 1988, "Inlet Distortion and Compressor Stability," Ph.D. Dissertation, Cambridge University.
- Mikolajczak, A. A., 1977, "The Practical Importance of Unsteady Flow," AGARD CP-177, *Unsteady Phenomena in Turbomachinery*.
- Monsarrat, N. T., 1969, "Design Report: Single-Stage Evaluation of Highly-Loaded High-Mach-Number Compressor Stages," NASA CR 72562.
- Moore, J., and Moore, J. E., 1981, "Calculations of Three-Dimensional Viscous Flow and Wake Development in a Centrifugal Impeller," *ASME Journal of Engineering for Power*, Vol. 103, pp. 367–372.
- Ng, W. F., and Epstein, A. H., 1985, "Unsteady Losses in Transonic Compressors," *ASME Journal of Engineering for Gas Turbines and Power*, Vol. 107, pp. 345–353.
- Ni, R. H., and Bogoian, J. C., 1989, "Prediction of 3D Multi Stage Turbine Flow Field Using a Multiple Grid Euler Solver," AIAA Paper No. 89-0203.
- Rabe, D., Bolcs, A., and Russler, P., 1995, "Influence of Inlet Distortion on Transonic Compressor Blade Loading," AIAA Paper No. 95-2461.
- Rai, M. M., 1985, "Navier-Stokes Simulations of Rotor–Stator Interaction Using Patched and Overlaid Grids," AIAA Paper No. 85-1519.
- Rao, K., and Delaney, R., 1990, "Investigation of Unsteady Flow Through Transonic Turbine Stage," AIAA Paper No. 90-2408.
- Russler, P. M., 1994, "Acquisition and Reduction of Blade-Mounted Pressure Transducer Data From a Low Aspect Ratio Fan," WR-TR-94-2021.
- Russler, P. M., 1995, "Acquisition and Reduction of Rotor Tip Static Pressure Transducer Data From a Low Aspect Ratio Transonic Fan," WR-TR-95-2022.
- Smith, L. H., 1966, "Wake Dispersion in Turbomachines," *ASME Journal of Basic Engineering*, Vol. 88, pp. 688–690.
- Smith, L. H., 1970, "Casing Boundary Layers in Multistage Axial Flow Compressors," in: *Flow Research on Blading*, L. S. Dzung, ed., Elsevier Publishing Company, Amsterdam, No. 3, pp. 688–690.
- Wennerstrom, A. J., 1984, "Experimental Study of a High-Through-Flow Transonic Axial Compressor Stage," *ASME Journal of Engineering for Gas Turbines and Power*, Vol. 106, pp. 552–560.

Three-Dimensional Inverse Method for Turbomachinery Blading Design

A. Demeulenaere

R. Van den Braembussche

von Karman Institute for Fluid Dynamics,
Rhode-Saint-Genese, Belgium

An iterative procedure for three-dimensional blade design is presented, in which the three-dimensional blade shape is modified using a physical algorithm, based on the transpiration model. The transpiration flux is computed by means of a modified Euler solver, in which the target pressure distribution is imposed along the blade surfaces. Only a small number of modifications is needed to obtain the final geometry. The method is based on a high-resolution three-dimensional Euler solver. An upwind biased evaluation of the advective fluxes allows for a very low numerical entropy generation, and sharp shock capturing. Non-reflecting boundary conditions are applied along the inlet/outlet boundaries. The capabilities of the method are illustrated by redesigning a transonic compressor rotor blade, to achieve, for the same mass flow and outlet flow angle, a shock-free deceleration along the suction side. The second example concerns the design of a low aspect ratio turbine blade, with a positive compound lean to reduce the intensity of the passage vortices. The final blade is designed for an optimized pressure distribution, taking into account the forces resulting from the blade lean angle.

Introduction

In many cases blade design is still done in an empirical way by successive modifications of the blade geometry and verifications by wind tunnel testing or flow calculations. Such a process can be very time consuming, depending on the designers' experience, and may result in high design costs and delays. It does not necessarily lead to the best possible blade required for improved efficiency of compressors and turbines. This can be overcome by means of inverse methods, allowing the direct generation of geometries achieving prescribed performance.

A first generation of potential methods solve the inverse problem analytically, or iteratively. They are limited to shock-free irrotational flows, and/or are difficult to extend to three dimensions (Lighthill, 1945; Sanz, 1988; Schmidt, 1980; Murugesan and Raily, 1969; Bauer et al., 1972; Dulikravitch and Sobieczky, 1982; Chen Naixing et al., 1986; Wang Zhengming, 1985; Liu and Yan, 1991).

The three-dimensional method proposed by Hawthorne et al. (1984) designs blades from a prescribed average mean swirl (radius times tangential velocity) distribution throughout the meridional section of the machine. The method has been extended to transonic flows in radial and mixed flow machines, and some viscous effects, such as boundary layer blockage, have been introduced (Borges, 1990; Zangeneh, 1994; Dang and Isgro, 1995). The main drawback is that the streamwise velocity distribution results from the calculation, and hence the diffusion along the blades is not really controlled.

The method presented in this paper allows a pressure distribution to be imposed on the blade surfaces. Solving the Euler equations, the method can handle rotational flows including shocks. The equations are solved in a numerical domain, of which some boundaries, i.e., the blade walls, are the solution of the problem. The method is therefore iterative, and a first guess of the geometry is necessary to initialize the calculation.

The modification of the geometry can be performed by a purely mathematical algorithm, minimizing an error function

that expresses the difference between the desired and actual pressure distributions. These methods have the disadvantage of being very expensive in terms of CPU time, because many flow analyses are usually required (Van der Plaats, 1979; Eyi and Lee, 1995).

The method presented here uses a physical model to calculate the geometric changes required for achieving the prescribed performance, and has been shown to be very efficient (Léonard, 1992).

The proposed solution consists of calculating the flow obtained when the required pressure distribution is imposed on the blade walls of the actual geometry. If this distribution is different from the one resulting from a direct calculation around the same geometry, the velocity will not be tangent to the walls. The streamlines of the flow give a quantitative "indication" of the required change of geometry.

As the flow calculation is performed with a time-marching procedure, there is a possibility to modify the blade walls at each time step, such that they remain parallel to the flow (Zanetti, 1987; Meauzé, 1982). The walls on which the required pressure is prescribed are then considered as flexible and impermeable. Starting from some initial configuration, the computation follows the transient, which occurs while the flexible walls move until they reach a steady shape. Such a method requires a grid generation at each iteration, which increases the CPU time.

The number of geometry modifications can be strongly reduced by using permeable wall boundary conditions on the walls where the pressure is specified (Léonard, 1992). The permeable boundaries, through which the flow can enter or leave the numerical domain, are modified only after full convergence of the time marching computation, by means of a transpiration model.

The design procedure then continues with the analysis of the flow around the new geometry, by means of a direct solver with solid wall boundary conditions along the blade surfaces. The new geometry shows a pressure distribution closer to the target one, provided that this target corresponds to a realistic geometry. This sequence of "inverse" Euler calculations, modification of the geometry and "direct" analysis, schematically shown in Fig. 1, is repeated until the calculated pressure distribution equals the required one.

Contributed by the International Gas Turbine Institute and presented at the 41st International Gas Turbine and Aeroengine Congress and Exhibition, Birmingham, United Kingdom, June 10–13, 1996. Manuscript received at ASME Headquarters February 1996. Paper No. 96-GT-39. Associate Technical Editor: J. N. Shinn.

Boundary Conditions

The only difference between the direct and inverse Euler solvers lies in the way boundary conditions are applied along the blade walls.

The hyperbolic character of the Euler equations is imposed to account for the direction of propagation of information when treating the problem of the boundary conditions. The solution of the equations can be written as the superposition of five wave-like solutions, associated with the eigenvalues and eigenvectors of the jacobian matrix.

The equations can be reformulated as differential relations written along the wave fronts. These five compatibility relations, associated with each wave, are obtained by multiplying the five equations by the corresponding eigenvector, and allow the definition of the following unknowns at the time step $n + 1$:

Eigenvalue	Compatibility relation
W_n	$\rho^{n+1} = \rho^* + \frac{p^{n+1} - p^*}{a^2}$
W_n	$W_t^{n+1} = W_t^*$
W_n	$W_s^{n+1} = W_s^*$
$W_n + a$	$W_n^{n+1} = W_n^* - \frac{p^{n+1} - p^*}{\rho a}$
$W_n - a$	$W_n^{n+1} = W_n^* + \frac{p^{n+1} - p^*}{\rho a}$

where the state * is a first approximation of the variables, obtained from the numerical scheme.

If the information propagated by one wave front reaches a boundary, coming from the inside of the calculation domain, the value of the corresponding unknown must be calculated from this information, and not from a boundary condition. The information can be obtained from the corresponding compatibility relation. On the contrary, if the information enters the numerical domain through the boundary, the value of the unknown must be imposed by a boundary condition.

The propagation velocities of the waves in the direction normal to the boundary are the eigenvalues W_n , W_n , W_n , $W_n + a$, and $W_n - a$. The normal velocity W_n is considered as positive if directed toward the outside of the domain; hence, the number of boundary conditions to be imposed is the number of negative eigenvalues.

At the inflow boundary (and if a subsonic axial velocity is considered), only $W_n + a$ is positive, and therefore four boundary conditions are imposed, usually the total pressure and temperature, and two flow angles. Along the outflow boundary, only $W_n - a$ is negative, and the static pressure can be imposed.

Only one eigenvalue is negative on a solid wall ($W_n - a$), and the slip condition ($W_n = 0$) can be imposed. The first four compatibility relations can be used to update the other variables.

Permeable Wall. Imposing the required static pressure along the blade wall, the velocity component normal to the wall is not necessarily zero, and the slip condition can no longer be imposed in the "inverse" calculation.

Nomenclature

a = speed of sound
 c_p = specific heat at constant pressure
 M = Mach number
 p = static pressure
 T = static temperature
 T_{0r} = relative total temperature
 U = vector of conservative variables
 W = relative velocity

γ = specific heat ratio
 ρ = density
 Ω = speed of rotation

Subscripts

n = normal component
 r = radial component
 s = binormal component

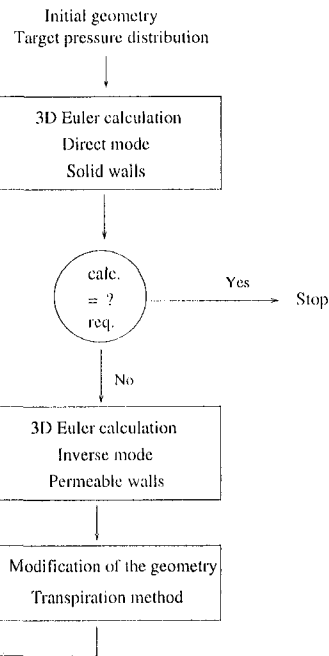


Fig. 1 Iterative inverse method

The number of boundary conditions or compatibility relations to be used depends on the sign of the normal velocity, which is not known *a priori*. The modifications of the geometry are assumed sufficiently small, such that the normal velocity is subsonic, and the fourth and fifth eigenvalues are respectively positive and negative. One boundary condition can always be imposed ($p^{n+1} = p^{req}$), and the fourth compatibility relation can then be used to calculate W_n :

$$W_n^{n+1} = W_n^* - \frac{p^{req} - p^*}{\rho a}$$

Depending on the sign of W_n^{n+1} , 0 or 3 additional boundary conditions must be imposed. If W_n is positive, the first three compatibility relations allow for the computation of the other variables.

On the contrary, three additional boundary conditions are required if W_n is negative. The first two consist of imposing the relative total temperature and pressure. Due to the radius change (in case of rotating blade rows), eventual shock losses and discretization errors, the local total conditions can be different from the inlet ones. They are therefore imposed at their local values at the previous iteration. The relative total conditions being defined, the static temperature and the magnitude of the total tangential velocity can be obtained from the isentropic relations:

$$T^{n+1} = T^n \left(\frac{p^{n+1}}{p^n} \right)^{(\gamma-1)/\gamma}$$

$$W^2 = 2c_p(T_{0r}^n - T^{n+1})$$

$$W_t^2 + W_s^2 = W^2 - W_n^2$$

The last boundary condition that will be imposed is the ratio of the two components of the tangential velocity, which is also imposed at its value at the previous iteration:

$$\left(\frac{W_t}{W_s}\right)^{n+1} = \left(\frac{W_t}{W_s}\right)^n$$

If the normal velocity remains negative during the whole calculation, the total conditions, as well as the direction of the tangential velocity, remain unchanged, and are equal to the values resulting from the previous direct analysis. The inverse calculation is anyway followed by an analysis, which only imposes a zero normal velocity, and recalculates the streamlines and total conditions on the final blade surface.

Non-reflecting Inlet/Outlet Boundary Conditions. Inlet/outlet boundary conditions based on the compatibility relations cause the reflection of the incident waves, which perturbs the convergence, and even deteriorates the solution in case of transonic flow conditions. Non-reflecting boundary conditions are therefore imposed along the inlet and outlet boundaries. Contrary to classical reflecting boundary conditions, only the average changes of the incoming characteristic variables are imposed, to respect the physical boundary conditions.

A distribution of local changes is calculated, as a function of the outgoing characteristic variables, to prevent reflection of the incident waves. The computation of this distribution is based on a linearization of the Euler equations along the inlet/outlet boundaries (jacobian matrices assumed constant), and a resolution of the equations by means of Fourier decomposition (Giles, 1989).

Such boundary conditions improve the convergence rate, by reducing the generation of spurious nonphysical reflections at the inlet/outlet boundaries, and allow calculations to be performed on truncated domains.

Modification of the Geometry

After convergence of the inverse Euler calculation, the resulting flow field is used to define the new blade shape. A three-dimensional transpiration model calculates the position of the new streamsurfaces in the flow. It makes use of the calculated normal and tangential velocity field along the initial blade suction and pressure sides.

Keeping the stagnation line unchanged, the method progresses from the stagnation point to the trailing edge, separately along the pressure and suction surfaces.

The grid points are located on a series of axisymmetric surfaces, distributed between the hub and tip endwalls, which are not modified by the method. The grid points are therefore displaced along the projection of the local normal to the blade surface on their corresponding grid surface.

At each step of the procedure, all the grid points defined along the blade height are displaced. The amplitude of the displacement is obtained by applying the mass equilibrium in the cell defined between the old and new blade walls (Fig. 2).

The flux through the elementary surface ($\Delta s \Delta t$) of the old blade wall is calculated by:

$$F_n^k = (\rho W_n \Delta s \Delta t)^k$$

where Δs and Δt are the dimensions of the face in the binormal and tangential directions.

The new blade wall is assumed to be a streamsurface. The tangential fluxes are defined by:

$$F_{in}^k = (\rho W_t \Delta s)^k \xi_{in}^k$$

$$F_{out}^k = (\rho W_t \Delta s)^k \xi_{out}^k$$

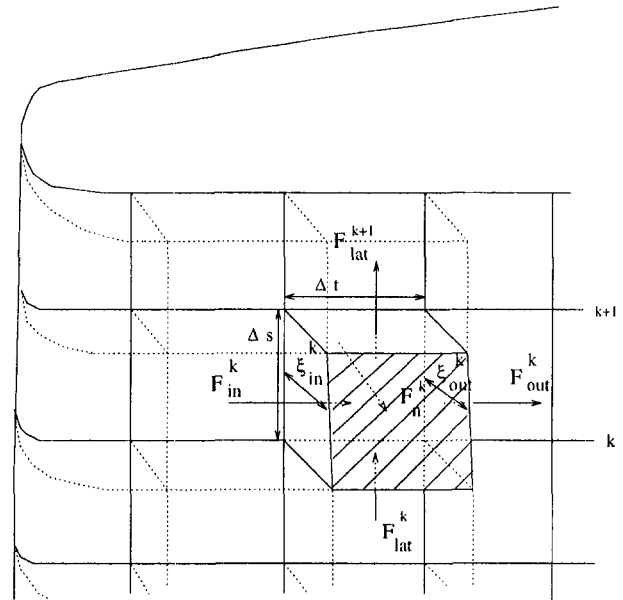


Fig. 2 Three-dimensional transpiration

The hub and tip walls are impermeable, and no mass flux can enter or leave the two extreme cells through them. The lateral mass fluxes F_{lat} through the interior surfaces cause an interaction between the neighboring cells:

$$F_{lat}^k = (\rho W_s \Delta t)^k \frac{\xi_{in}^k + \xi_{out}^k + \xi_{in}^{k-1} + \xi_{out}^{k-1}}{4}$$

The density and velocity components are obtained by interpolation, from the values at the calculation nodes. If the three-dimensional grid contains KM surfaces from hub to tip, the following tridiagonal system of $KM - 1$ equations is obtained, and solved for the unknowns ξ_{out}^k :

- equilibrium of the hub cell ($F_{lat}^1 = 0$):

$$F_{in}^1 + F_n^1 = F_{lat}^2 + F_{out}^1$$

- equilibrium of the interior cells ($k = 2$ to $KM - 2$):

$$F_{in}^k + F_n^k + F_{lat}^k = F_{lat}^{k+1} + F_{out}^k$$

- equilibrium of the tip cell ($F_{lat}^{KM} = 0$):

$$F_{in}^{KM-1} + F_n^{KM-1} + F_{lat}^{KM-1} = F_{out}^{KM-1}$$

The displacements of the KM grid points are then deduced from the displacements ξ_{out}^k , by interpolation for the interior points, and by extrapolation at the hub and tip points.

After completion of the transpiration procedure, all blade sections are eventually modified, to respect geometric constraints:

- the suction and pressure sides are rotated around the leading edge, to obtain a trailing edge thickness prescribed from mechanical considerations. Even if no solution that corresponds to the prescribed target pressure distribution exists, the method provides the user with a "realistic" geometry having a pressure distribution that is as close as possible to the required one.
- it has been mentioned that the stagnation line is kept unchanged. Any other blade point, e.g., the trailing edge or the center of gravity, can be used to stack the blade sections along any arbitrary stacking line.

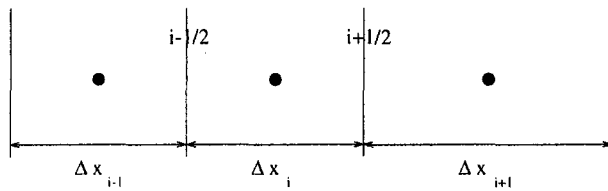


Fig. 3 M.U.S.C.L. reconstruction

Euler Solver

The inverse method could be based on any Euler solver. However, the validity of the results clearly depends on the accuracy of the flow calculation. A high-resolution three-dimensional solver has been developed for this purpose, and is described hereafter, with emphasis on some features introduced to enhance the accuracy.

The computation of the advective terms is based on the Finite Volume approach. Structured grids are used to discretize the numerical domain, and the nodes are located at the centers of the cells, which are then identical to the control volumes. The three-dimensional grid is composed of two-dimensional ones, defined on a series of axisymmetric surfaces, distributed between the hub and tip endwalls.

The unsteady three-dimensional Euler equations are integrated in time in an explicit way, with a four-step Runge-Kutta algorithm, until the steady solution is reached.

Advective Flux Computation. The Flux Vector Splitting approach (van Leer, 1982) is adopted. This "upwind" method respects the physics of supersonic flows, does not need any additional dissipation to ensure the convergence of the procedure, and guarantees the capturing of the grid-aligned shock waves in two or three discretization points.

The flux is decomposed into two separate contributions of a left and a right state, defined on both sides of the face:

$$H = H^+(U^L) + H^-(U^R)$$

In case of supersonic flow in the direction normal to the face ($|W_n| > a$), only one contribution is present:

$$H^+(U^L) = H(U^L) \quad \text{and} \quad H^-(U^R) = 0 \quad \text{if} \quad M_n > 1$$

$$H^+(U^L) = 0 \quad \text{and} \quad H^-(U^R) = H(U^R) \quad \text{if} \quad M_n < -1$$

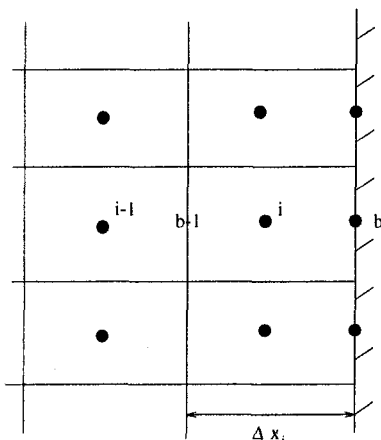


Fig. 4 Boundary points

$$\text{with } H(U) = \begin{pmatrix} \rho W_n \\ \rho W_x W_n + p n_x \\ \rho W_\theta W_n + p n_\theta \\ \rho W_r W_n + p n_r \\ \rho W_n \left(c_p T + \frac{W^2 - (\Omega r)^2}{2} \right) \end{pmatrix}$$

If the flow is subsonic, the left and right fluxes are calculated by:

$$H^\pm = \pm \frac{\rho a}{4} (1 \pm M_n)^2$$

$$\times \begin{pmatrix} 1 \\ W_x \pm (2 \mp M_n) a n^x / \gamma \\ W_\theta \pm (2 \mp M_n) a n^\theta / \gamma \\ W_r \pm (2 \mp M_n) a n^r / \gamma \\ \frac{2a^2}{\gamma^2 - 1} \pm \frac{M_n a^2 (2 \mp M_n)}{\gamma + 1} + \frac{W^2 - (\Omega r)^2}{2} \end{pmatrix}$$

As the relative motion is considered, the energy flux has been adapted, by adding the rotational speed term needed to transform total enthalpy into rothalpy.

M.U.S.C.L. Reconstruction. Taking the left and right states U^L and U^R at the nodes located on both sides of the face leads to a first-order-accurate solution. Higher-order-accurate results are obtained by means of one-dimensional reconstructions along the grid directions of the solution at the center of the face. This procedure is generally referred to as the M.U.S.C.L. approach (van Leer, 1979). Third-order Taylor expansions are constructed from the values at three successive nodes (Fig. 3): for the left (right) state computation, the central point is the one located on the left (right) side of the face.

The classical M.U.S.C.L. formulation assumes equidistant mesh points, and is therefore not accurate for "stretched" grids. A more general approach is presented hereafter, that accounts for the difference of distance between the two successive pairs of nodes.

The Taylor expansion of the unknown u around u_i is:

$$u(x) = u_i + \frac{\partial u}{\partial x} \Big|_i (x - x_i) + \frac{\partial^2 u}{\partial x^2} \Big|_i \frac{(x - x_i)^2}{2} + \theta(\Delta x^3)$$

The solution calculated by the finite volume approach at the point i must be seen as an average over the cell:

$$\bar{u}_i = \frac{1}{\Delta x_i} \int_{x_i - (\Delta x_i/2)}^{x_i + (\Delta x_i/2)} u(x) dx$$

The Taylor expansion then becomes:

$$u(x) = \bar{u}_i + \frac{\partial u}{\partial x} \Big|_i (x - x_i) + \frac{\partial^2 u}{\partial x^2} \Big|_i \left[\frac{(x - x_i)^2}{2} - \frac{\Delta x_i^2}{24} \right] + \theta(\Delta x^3)$$

In order to obtain third-order accuracy, the first derivative must be evaluated with second-order accuracy, while the second-order derivative requires first-order accuracy.

The left state at the face $i + \frac{1}{2}$ is defined by:

$$u_{i+1/2}^L = \bar{u}_i + \frac{\partial u}{\partial x} \Big|_i \frac{\Delta x_i}{2} + \eta \frac{\partial^2 u}{\partial x^2} \Big|_i \frac{\Delta x_i^2}{4}$$

Third-order accuracy is achieved by a value of $\eta = \frac{1}{3}$. By applying the Taylor expansion at the points $i + 1$ and $i - 1$,

the expression of the derivatives is obtained. The expression of $u_{i+1/2}^L$ then becomes:

$$u_{i+1/2}^L = \bar{u}_i + \frac{\Delta x_i}{4\Delta x} \left[(u_i - u_{i-1}) \left(\frac{1 + \epsilon/2 - \eta \frac{\Delta x_i}{\Delta x}}{1 - \epsilon/2} \right) + (u_{i+1} - u_i) \left(\frac{1 - \epsilon/2 + \eta \frac{\Delta x_i}{\Delta x}}{1 + \epsilon/2} \right) \right]$$

where

$$\bar{\Delta x} = \frac{\Delta x_{i-1} + 2\Delta x_i + \Delta x_{i+1}}{4}$$

$$\epsilon = \frac{\Delta x_{i+1} - \Delta x_{i-1}}{\Delta x}$$

An identical procedure leads to:

$$u_{i-1/2}^R = \bar{u}_i - \frac{\Delta x_i}{4\Delta x} \left[(u_i - u_{i-1}) \left(\frac{1 + \epsilon/2 + \eta \frac{\Delta x_i}{\Delta x}}{1 - \epsilon/2} \right) + (u_{i+1} - u_i) \left(\frac{1 - \epsilon/2 - \eta \frac{\Delta x_i}{\Delta x}}{1 + \epsilon/2} \right) \right]$$

In case of a uniform mesh ($\epsilon = 0$), these equations reduce to the classical M.U.S.C.L. formulae.

Due to the "cell-centered" organization of the code, a special problem appears at the boundaries, along which additional nodes are defined (Fig. 4). They are located at a distance $\Delta x_i/2$ from the last interior node. This difference of distance between (u_{i-1}, u_i) and (u_i, u_b) has to be taken into account in the calculation of the right state u_{b-1}^R of the last interior face. The above formula is applied, with $\Delta x_{i+1} = 0$. In case of a uniform mesh, the state u_{b-1}^R is given by:

$$u_{b-1}^R = u_i - \frac{1}{6}[4(1 - \eta)(u_b - u_i) + (1 + 2\eta)(u_i - u_{i-1})]$$

Limiters. High-order schemes are liable to produce spurious oscillations in the vicinity of discontinuities, like shock waves. T.V.D. schemes (Total Variation Diminishing) are obtained by decreasing the order of accuracy in the regions where the flow is unsmooth. In the M.U.S.C.L. approach this is

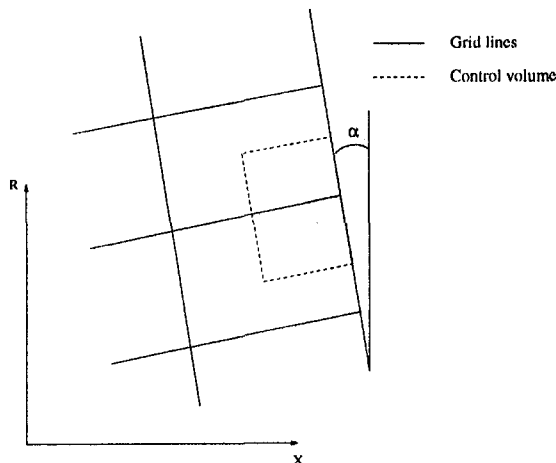


Fig. 5 Control volume in meridional plane

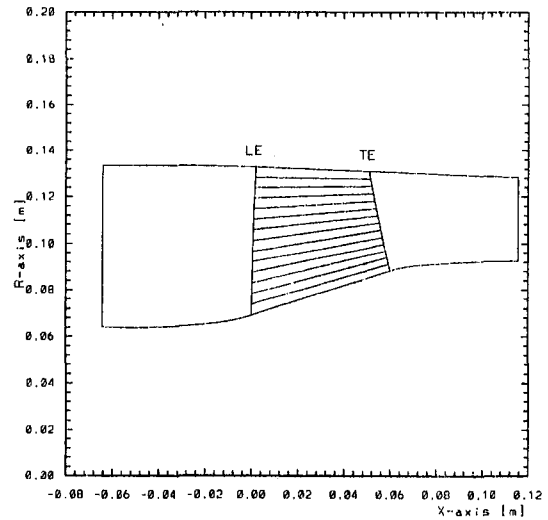


Fig. 6 Meridional view and axisymmetric grid surfaces

achieved by constraining the gradients $(u_{i+1} - u_i)$ and $(u_i - u_{i-1})$ within some bounds, via nonlinear functions, called limiters (Yee, 1989).

The classical minmod or Van Albada limiters are used, only for transonic and supersonic flow computations.

Outlet Pressure Distribution. At each radial position of the outlet boundary, the static pressure is imposed. The distribution of the pressure from the hub to the tip must be compatible with the equations. The static pressure is specified by the user at a certain position, and calculated at the other stations, to respect the momentum equations in the radial and axial directions.

Experience has shown that the accuracy of this calculation has an important influence on the stability of the calculation, especially for transonic flow computations in compressors, close to the limits of stability.

A finite volume formulation is adopted: Control volumes are defined in the meridional plane, along the outlet boundary (Fig. 5). The equation used is a combination of the axial and radial momentum equilibriums, weighted as a function of the angle α between the outlet boundary and the radial direction:

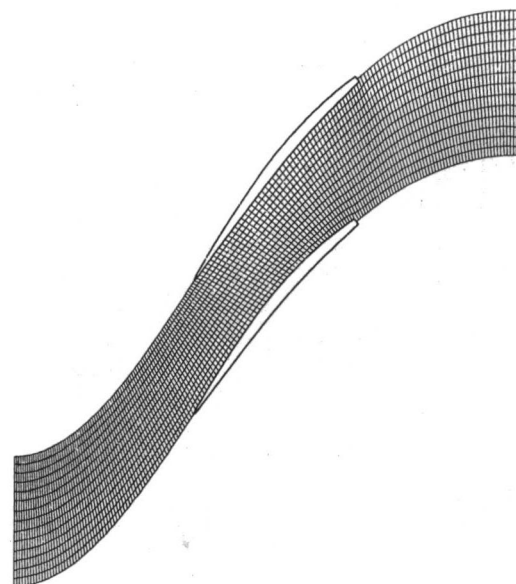


Fig. 7 Nonperiodic H-grid discretization at the mean section

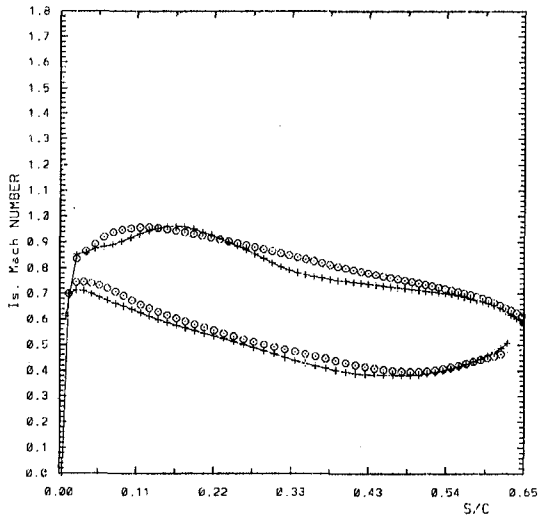


Fig. 8 Initial (+) and imposed (O) isentropic Mach number distributions at the hub section

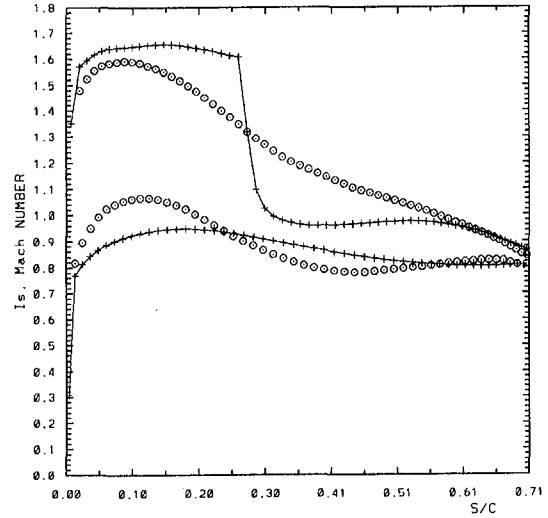


Fig. 10 Initial (+) and imposed (O) isentropic Mach number distributions at the tip section

$$\sum_{\text{faces}} [(\rho V_r^2 + p)n_r + (\rho V_r V_x)n_x] \Delta S \cos \alpha - \sum_{\text{faces}} [(\rho V_r V_x)n_r + (\rho V_x^2 + p)n_x] \Delta S \sin \alpha + \Delta p_{\text{corr}} = \left(\frac{\rho V_\theta^2 + p}{r} \right) \Delta V \cos \alpha$$

The fluxes through the faces, as well as the source term, are evaluated from their values at the four corners of the control volumes, which are obtained by averaging along the circumferential direction.

If the equilibrium is not respected, the pressure at the two outlet corners is modified, such that the equilibrium is satisfied. One of the two pressure changes has previously been obtained from the equilibrium of the upper (lower) control volume. The method progresses from the point where the pressure is specified, to the hub and tip endwalls. The term Δp_{corr} is zero at convergence, when the equilibrium is satisfied, and the pressure distribution is no longer modified.

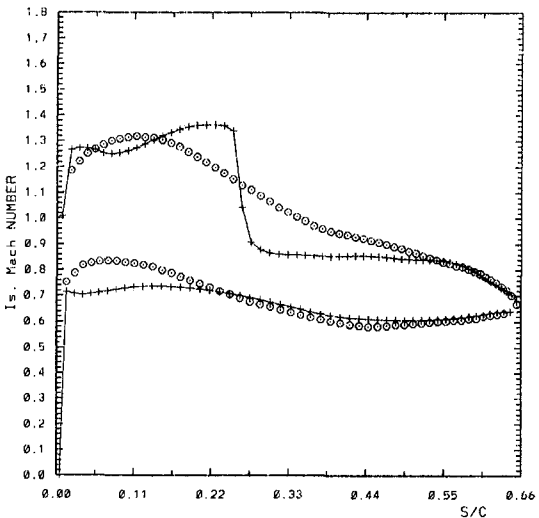


Fig. 9 Initial (+) and imposed (O) isentropic Mach number distributions at the mean section

Numerical Results

Redesign of a Transonic Compressor Rotor Blade. The first example concerns the design of a shock-free transonic axial compressor rotor, with 14 highly twisted blades, rotating at 31264 rpm. The hub/tip diameter ratio is 0.5 at the inlet, and the meridional view shows a nonnegligible contraction of the passage (Fig. 6). The numerical domain is discretized with 15 nonperiodic H-grids (Fig. 7), defined on axisymmetric surfaces, uniformly distributed between the hub and tip endwalls.

The three-dimensional flow field around the initial impeller has been calculated for an outlet isentropic Mach number of

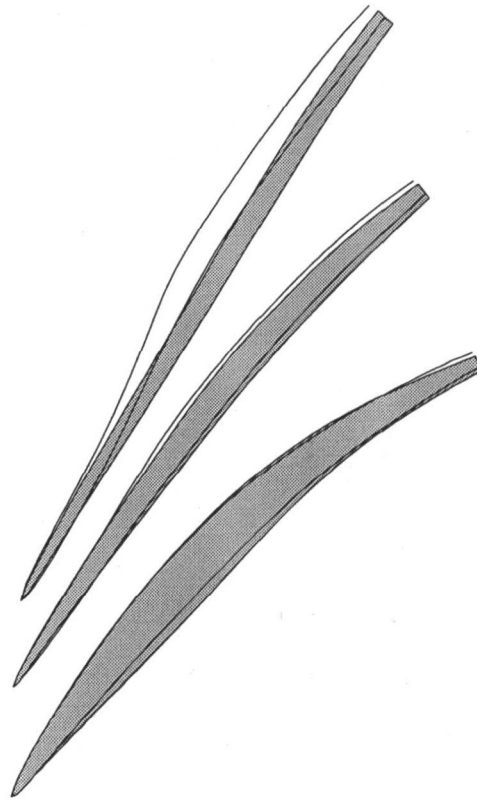


Fig. 11 Initial (grey) and final geometries at the hub, mean, and tip sections

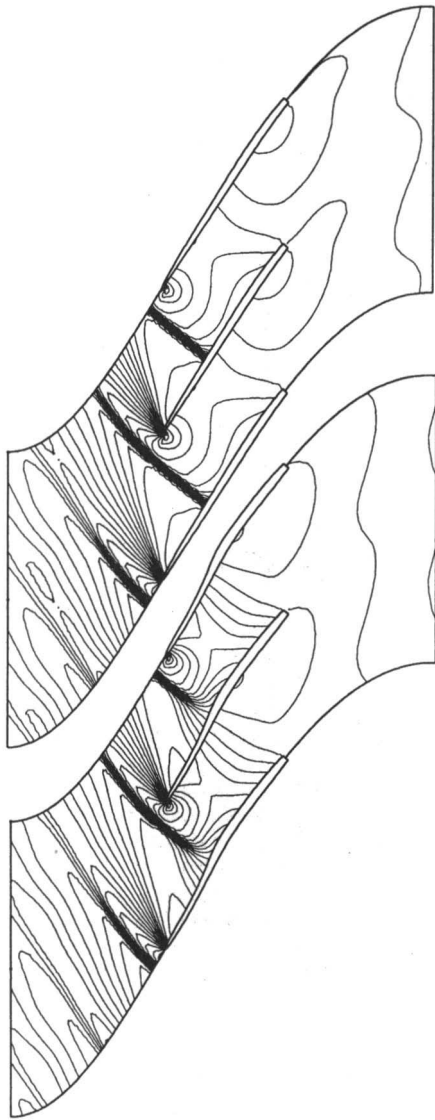


Fig. 12 Iso-density lines at the tip section for the initial (upper) and final (lower) blades

0.76 at the mean radius. The corresponding inlet relative Mach number varies from 0.74 at the hub section, up to 1.35 at the tip. Calculated isentropic Mach number distributions along the hub, mean, and tip sections of the blades are indicated by crosses in Figs. 8 to 10. The iso-density field shown in Fig. 12 illustrates the effect of the non reflecting boundary conditions, which permit the bow shock to cross the inlet boundary, without being influenced.

The blade has been modified, to achieve the shock-free isentropic Mach number distribution, represented by circles in Figs. 8 to 10. The corresponding target pressure distribution has been prescribed at five equidistant sections between the hub and tip endwalls, and calculated at all intermediate grid points by interpolation between these sections.

Special attention has been paid to conserve the outlet angle distribution, as well as the blade thickness. This is not imposed in the solver, but obtained by defining an appropriate target pressure distribution. In transonic flow conditions with shocks, this task is more difficult than in potential flows, where the outlet angle is controlled by the circulation, and the blade thickness by the mean velocity level.

The first target pressure distributions used in the present example were different from the initial ones on the suction side

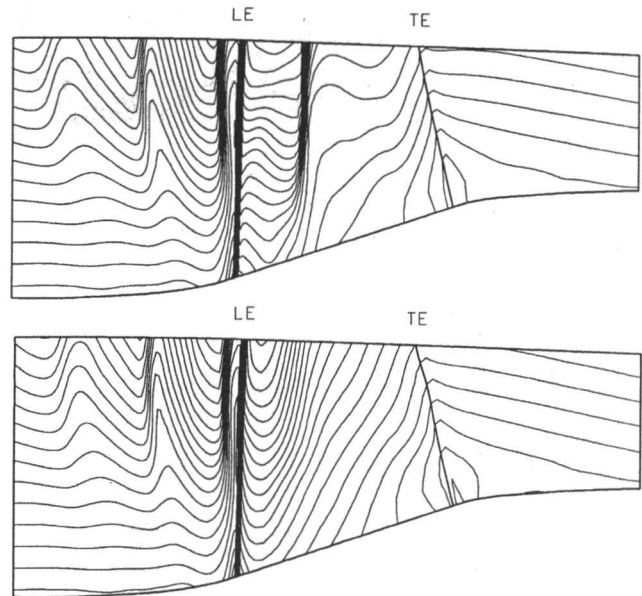


Fig. 13 Meridional view of the iso-pressure lines on the first grid surface (containing the suction side) for the initial (upper) and final (lower) blades

only. The redesigned blade showed a nearly shock-free deceleration on the suction side after six modifications, but with a higher turning and a thinner blade at the hub, and a much thicker blade at the tip. The target has then been modified also on the pressure surface, to recover the initial outlet angle and thickness distributions.

Three additional iterations have been required, to obtain a perfect agreement between the calculated and imposed pressure distributions. The hub, mean, and tip cross sections of the initial and final blades are compared in Fig. 11. The final iso-density lines at the tip section are compared to the initial ones in Fig. 12. The final blade is S-shaped near the shroud, generating compression waves, converging into the bow shock, which no longer interacts with the suction surface. The meridional projections of the initial and final iso-pressure lines on the first grid surface (containing the suction side) are compared in Fig. 13, and show that the bow shock is still present in the final flow



Fig. 14 Subtraction of the boundary layer: mean section

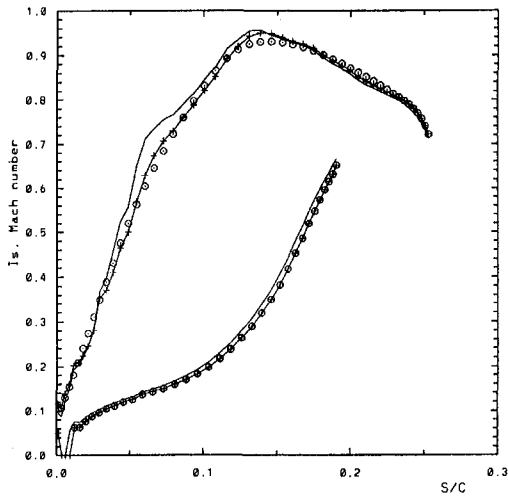


Fig. 15 Initial blade with radial stacking: (—) initial blade with positive compound lean; (+) final blade; (○) hub section

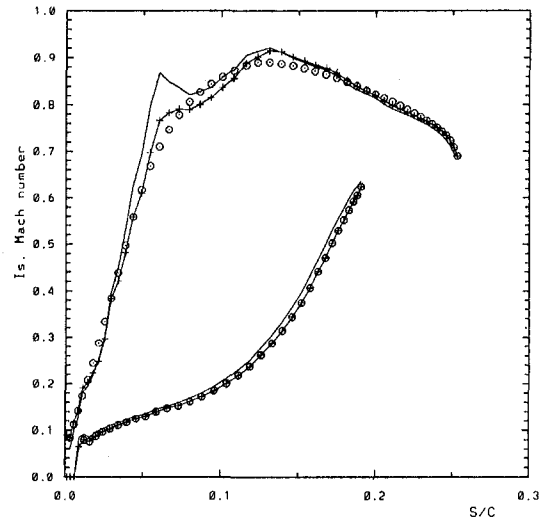


Fig. 17 Initial blade with radial stacking: (—) initial blade with positive compound lean; (+) final blade; (○) tip section

field, but that the suction side compression extends continuously over a wider surface.

Euler solvers do not account for viscous effects, and the boundary layer displacement thickness has to be subtracted from the designed blade to obtain the “real” blade. The boundary layer displacement thickness can be calculated from the required Mach number distribution, before the blade geometry is known, so that the sum of the geometric and boundary layer displacement thicknesses at the trailing edge can be imposed as a constraint on the designed geometry. After completing the inverse design of the blade, the boundary layer displacement thickness is subtracted, to obtain the metal blade shape (Fig. 14). The trailing edge thickness of the metallic blade is still nonzero, and equals the diameter of the initial blade trailing edge round-off circle, which is cut off in order to avoid nonphysical accelerations (especially for transonic turbine blades) in our inviscid calculations.

Redesign of a Low Aspect Ratio Turbine Nozzle. The second example illustrates the redesign of an axial turbine nozzle blade row. The number of blades is 35, the aspect ratio is 0.3, and the pitch-to-chord ratio is 0.9 at the mean section. The initial geometry has a constant VKI-LS89 profile from hub to tip.

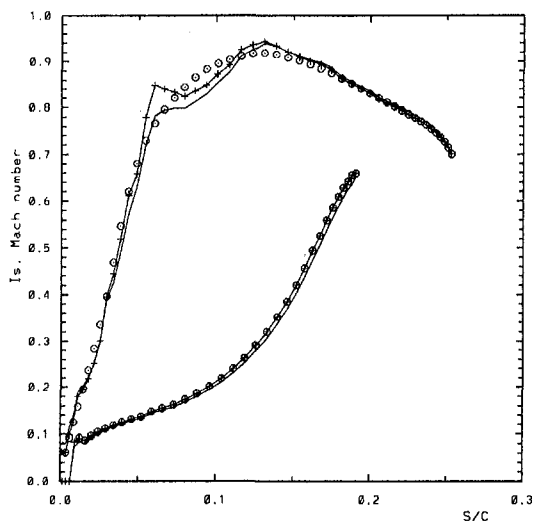


Fig. 16 Initial blade with radial stacking: (—) initial blade with positive compound lean; (+) final blade; (○) mean section

The flow through such a low-aspect-ratio blade is dominated by secondary flows. The passage vortices extend over a large portion of the blade height at the outlet of the channel, and may even meet at the center, generating high secondary losses (Mansour et al., 1985).

It is shown in the literature that the intensity of the secondary flows can be decreased by means of a positive compound lean, reducing the blade loading near the endwalls, but increasing it at the midsection (Han et al., 1994).

Isentropic Mach number distributions corresponding to the radially stacked and leaned blades are compared at the hub, mean, and tip sections (Figs. 15 to 17). The loading is clearly

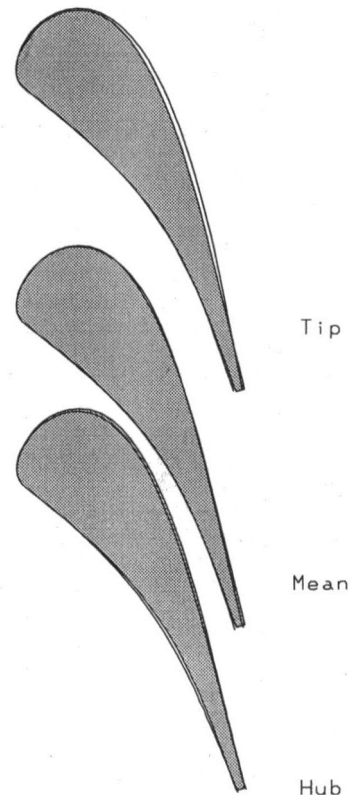


Fig. 18 Initial (gray) and final blades: hub, mean, and tip section

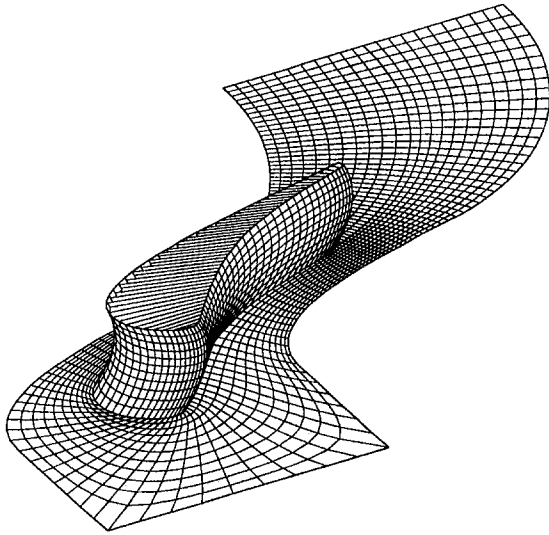


Fig. 19 Final blade: three-dimensional view

reduced near the endwalls, and increased at the mean section. The Mach number distribution is improved at the tip under the influence of the lean, but is definitely not optimal at the mean section.

The leaned blade has been redesigned with the inverse solver, to achieve the smooth acceleration along the suction side shown in Figs. 15 to 17, taking into account the effect of lean. The target pressure distribution is obtained after only four modifications of the geometry. The initial and final blade hub, mean, and tip sections are compared in Fig. 18. A three-dimensional view of the final blade is also shown in Fig. 19.

Conclusions

A three-dimensional analysis code was successfully transformed into a design code, by changing the boundary conditions on the blade walls, and by means of a geometry modification algorithm.

The method shows a rapid convergence to the blade geometry corresponding to the target pressure distribution, for subsonic and transonic design. Shock-free pressure distributions can be achieved on the blade surfaces.

The solver is able to treat highly three-dimensional flows and geometries, and the effects of a blade lean are taken into account, which is an advantage, when compared to two-dimensional design methods.

An important advantage of the method is the possibility of using the same code for the design and analysis of a blade.

Acknowledgments

The financial support of F.R.I.A. (Fonds pour la Formation à la Recherche dans l'Industrie et l'Agriculture) is gratefully acknowledged.

References

- Bauer, F., Garabedian, P., and Korn, D., 1972, *Supercritical Wing Sections*, Vol. I, Springer-Verlag, New York.
- Borges, J. E., 1990, "A Three-Dimensional Inverse Method for Turbomachinery: Part 1," *ASME JOURNAL OF TURBOMACHINERY*, Vol. 112, pp. 346–354.
- Chen Naixing, Zhang Fengxian, and Li Weihong, 1986, "An Inverse (Design) Problem Solution Method for the Blade Cascade Flow on Streamsurface of Revolution," *ASME JOURNAL OF TURBOMACHINERY*, Vol. 108, pp. 194–199.
- Dang, T., and Isgro, V., 1995, "Euler-Based Inverse Method for Turbomachine Blades, Part I: Two-Dimensional Cascades," *AIAA Journal*, Vol. 33, No. 12, pp. 2309–2315.
- Dulikravitch, D. S., and Sobieczky, H., 1982, "A Computational Design Method for Transonic Turbomachinery Cascades," *ASME Paper No. 82-GT-117*.
- Eyi, S., and Lee, D., 1995, "High-Lift Design Optimization Using the Navier–Stokes Equations," *Paper No. AIAA 95-0477*.
- Giles, M., 1989, "Non Reflecting Boundary Conditions for Euler Equations Calculations," *AIAA Journal*, Vol. 108, No. 12, pp. 2050–2058.
- Han, W., Tan, C., Shi, H., Zhou, M., and Wang, Z., 1994, "Effects of Leaning and Curving of Blades With High Turning Angles on the Aerodynamic Characteristics of Turbine Rectangular Cascades," *ASME JOURNAL OF TURBOMACHINERY*, Vol. 116, pp. 417–424.
- Hawthorne, W. R., Tan, C. S., Wang, C., and McCune, J. E., 1984, "Theory of Blade Design for Large Deflections: Part I—Two-Dimensional Cascades," *ASME Journal of Engineering for Gas Turbines and Power*, Vol. 106, pp. 346–353.
- Léonard, O., 1992, "Conception et Développement d'une Méthode Inverse de Type Euler et Application à la Génération de Grilles d'Aubes Transsoniques," PhD Thesis, von Karman Institute and Faculté Polytechnique de Mons.
- Léonard, O., and Van den Braembussche, R., 1992, "Design Method for Subsonic and Transonic Cascade With Prescribed Mach Number Distribution," *ASME JOURNAL OF TURBOMACHINERY*, Vol. 114, pp. 553–560.
- Léonard, O., and Van den Braembussche, R., 1992, "Inverse Design of Compressor and Turbine Blades at Transonic Flow Conditions," *ASME Paper No. 92-GT-430*.
- Lighthill, J. M., 1945, "A New Method of Two-Dimensional Aerodynamic Design," *ARC R&M 2112*.
- Liu, G., and Yan, S., 1991, "A Unified Variable-Domain Variational Approach to Hybrid Problems of Compressible Blade-to-Blade Flow," *ASME Paper No. 91-GT-169*.
- Mansour, M. L., Hamed, A., and Mobarak, A., 1985, "Influence of Low Aspect Ratio on the Energy Loss in a Turbine Cascade," *ASME FED-Vol. 32, Three-Dimensional Flow Phenomena in Fluid Machinery*, pp. 55–62.
- Meauzé, G., 1982, "An Inverse Time Marching Method for the Definition of Cascade Geometry," *ASME Journal of Engineering for Power*, Vol. 104, pp. 650–656.
- Murugesan, K., and Raily, J. W., 1969, "Pure Design Method for Airfoils in Cascades," *Journal Mechanical Engineering Science*, Vol. 11, No. 5, pp. 454–465.
- Sanz, J. M., 1988, "Automated Design of Controlled Diffusion Blades," *ASME JOURNAL OF TURBOMACHINERY*, Vol. 110, pp. 540–544.
- Schmidt, E., 1980, "Computation of Supercritical Compressor and Turbine Cascades with a Design Method for Transonic Flows," *ASME Journal of Engineering for Gas Turbines and Power*, Vol. 102, pp. 68–74.
- Vanderplaats, G. N., 1979, "Approximation Concepts for Numerical Airfoils Optimization," *NASA TP-1370*.
- van Leer, B., 1979, "Towards the Ultimate Conservative Difference Scheme, V: A Second Order Sequel to Godunov's Method," *Journal of Computational Physics*, Vol. 32, pp. 101–136.
- van Leer, B., 1982, "Flux Vector Splitting for the Euler Equations," *ICASE, Report No. 82-30*.
- Wang Zhengming, 1985, "Inverse Design Calculations for Transonic Cascades," *ASME Paper No. 85-GT-6*.
- Yee, H. C., 1989, "A Class of High-Resolution Explicit and Implicit Shock-Capturing Methods," *NASA Ames Research Center, Moffett Field, CA*.
- Zangeneh, M., 1994, "Inviscid–Viscous Interaction Method for 3D Inverse Design of Centrifugal Impellers," *ASME JOURNAL OF TURBOMACHINERY*, Vol. 116, pp. 280–290.
- Zannetti, L., 1987, "Time Dependent Computation of the Euler Equations for Designing Fully 3D Turbomachinery Blade Rows," *Paper No. AIAA-87-0007*.

A. P. Tarabrin

Polzunov Boiler and Turbine
Research Institute,
NPO CKTI,
St. Petersburg, Russia

V. A. Schurovsky

Gas Research Institute,
VNIIGAS,
Moscow, Russia

A. I. Bodrov

Engineer,
Institute of Machine Building,
PIMACH, St. Petersburg, Russia

J.-P. Stalder

Turbotect Ltd.,
Baden, Switzerland

An Analysis of Axial Compressor Fouling and a Blade Cleaning Method

The paper describes the phenomenon of axial compressor fouling due to aerosols contained in the air. Key parameters having effect on the level of fouling are determined. A mathematical model of a progressive compressor fouling using the stage-by-stage calculation method is developed. Calculation results on the influence of fouling on the compressor performance are presented. A new index of sensitivity of axial compressors to fouling is suggested. The paper gives information about Turbo-TECT's deposit cleaning method of compressor blading and the results of its application on an operating industrial gas turbine. Regular on-line and off-line washings of the compressor flow path make it possible to maintain a high level of engine efficiency and output.

Introduction

The air used for the operation of gas turbines always contains a certain amount of aerosols: airborne solid and liquid particles. Their quantity greatly increases under unfavorable conditions: dust and sand storms, dirty industrial environments, etc. To reduce the adverse effect of fouling on the compressor blading and its performance, an effective filtration system can be installed in the compressor inlet. Theoretically, complete inlet air purification can be obtained, but there is no purpose to this in view of great expense and additional losses in output and efficiency. Therefore the main function of inlet filters is to protect the blading from erosion, and compressor fouling cannot be completely eliminated. It is noted (Diakunchak, 1992) that compressor blading fouling is caused mainly by dust particles of about $2\ \mu\text{m}$ and less in diameter and their mass constitutes up to 80–90 percent of the total dust mass behind the filter.

The sources of fouling of the compressor inlet air are described in Diakunchak (1992), Mikhaylov et al. (1978), Schurovsky and Levikin (1986), and Olhovsky (1985). Fouling of the compressor blades is caused by the "soft" aerosols contained in the air: dirt, dust, pollen, insects, oil and water vapor, sea water salt, sticky industrial chemicals, unburned hydrocarbons, soot particles, etc. Some of these contaminants are products of the operating process of the engine main components and auxiliaries: oil leaks from compressor seals and bearings, salt and mechanical impurities from the water-evaporative cooling system, etc. Some of these particles falling on the blade surface adhere to it, stick to each other, and produce a deposit. This leads to changes in aerodynamic form, profile roughness, and angle of attack. According to Olhovsky (1985), the deposits do not considerably change the throat of a compressor profile cascade. The compressor fouling causes a decrease in its mass flow, efficiency, pressure ratio, and surge margin. For example, as was noted (Diakunchak, 1992) compressor fouling resulted in a drop of about 5 percent in the mass flow, 2.5 percent in the efficiency, and 10 percent in the output. Further, and to enhance this, General Electric found (Hoefl, 1993) that an air-

flow reduced by 5 percent will reduce output by 13 percent and increase heat rate by 5.5 percent.

In connection with the development of gas turbine diagnostics, it is necessary to develop reliable methods for predicting the behavior of engine performance in the course of fouling.

Some mathematical simulations of fouling in multistage compressors have recently appeared (Aker and Saravanamuttoo, 1989; Seddigh and Saravanamuttoo, 1991). Using the field operating data, it was found that the first stages of a compressor are the most fouled ones and the number of fouled stages constitutes 40–50 percent of the total. Besides that, the degree of fouling diminishes from stage to stage. Based on these physical considerations, Aker and Saravanamuttoo (1989) suggested the linear progression of fouling in compressor stages ($k_1:k_2$), where k_1 is a percentage of the flow coefficient reduction from $n \times k_1$ for the first stage to k_1 for the n th stage; in the same way k_2 factor is applied to stage efficiency. The stage-stacking technique (Howell and Calvert, 1978) was used in this mathematical model to calculate a compressor map through the performance of every stage. Attempts were made to lay down an index of fouling (Seddigh and Saravanamuttoo, 1991) in order to determine axial compressors sensitivity to fouling. In the authors' opinion the parameter $N_e/(Gc_p\Delta T_{stg})$ is the most suitable index for comparing different engines in order to determine the sensitivity of their compressor to fouling. It can be seen that sometimes this index is the same for engines with small and large output, that is, for the engines of small and large sizes. At the same time there is evidence (Seddigh and Saravanamuttoo, 1991) that the performance of a smaller engine shows more deterioration by fouling than that of a larger one.

In this connection it seems to be reasonable to consider principles of the motion of particles in the flow path of the compressor and the mechanism of the deposit's formation, and to work out on this basis a new generalized criterion (index) for the compressor sensitivity to fouling.

Mechanism of Fouling

The mechanism of entrainment of particles by a surface of a body situated in the stream of the air-aerosol mixture was described in Fuks (1955). The deposition of particles on the surface of a blade takes place under the action of inertia forces acting on the particles and forcing them to move across the curved streamlines (the particle trajectory deviates from the

Contributed by the International Gas Turbine Institute and presented at the 41st International Gas Turbine and Aeroengine Congress and Exhibition, Birmingham, United Kingdom, June 10–13, 1996. Manuscript received at ASME Headquarters February 1996. Paper No. 96-GT-363. Associate Technical Editor: J. N. Shinn.

stream lines). Particles of dirt (dust) colliding with the blade can stick to the blade surface. On the other hand, when the particles move in the flow path of compressor the centrifugal inertia forces make them move to the periphery of the compressor passage.

The coefficient of entrainment or the separation factor E according to Fuks (1955) is determined as a ratio:

$$E = \frac{\text{number of particles colliding with the surface of the body}}{\text{number of particles that could fall on the body surface if the streamlines were not deviated by the body}}$$

In this case it is assumed that all the particles stick to the body when they collide with it. On Fig. 1 one can see the trajectories of the particles and the streamlines of the flow around the cylindrical body. If the particles are uniformly distributed in the air at a certain distance from the body, and the radius of the particle is negligible if compared with the radius of the cylinder, then

$$E = h/L \quad (1)$$

The limit trajectory is a trajectory of the particles that are still seized by the cylinder.

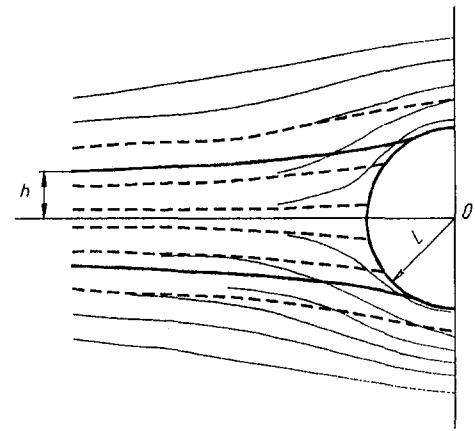
In the general case, E can be presented as a function (Green and Lane, 1964):

$$E = f(St_k, d_p/2L, Re_f) \quad (2)$$

where

$$St_k = \rho_p d_p^2 C_0 / (18\mu 2L); Re_f = \rho 2L C_0 / \mu$$

In case of a cascade, Fig. 2,



— stream line
- - - limit trajectory
..... trajectory of a particle

Fig. 1 Inertial deposition of particles on cylinder surface

$$L = b \sin(\beta_b - \beta_1) \quad (3)$$

can be taken for the characteristic size (Olhovskiy, 1985).

The coefficient of entrainment for the cylinder with $L = b \sin(\beta_b - \beta_1)$ within the unbounded stream will be the following:

Nomenclature

A_f = cascade throat, m	N_e = output, kW	x_f = position of maximum profile concavity, m
b = chord, m	N_{e0} = nominal output, kW	z = number of compressor stages
b/t = solidity	N_{e10}^* = operational output corrected to design conditions, kW	z_f = number of fouled compressor stages
C_0 = stream velocity at the distance upstream, m/s	n = rotation speed, rpm	β_b = stagger angle with the axis u , deg
C_z = axial component of absolute velocity, m/s	n_0 = nominal rotation speed, rpm	β_1 = flow angle with the axis u , deg
C_{1u} = circumferential component of absolute velocity in the inlet, m/s	P_{in}^* = total pressure in the inlet of the compressor, Pa	β_2 = flow outlet angle, deg
C_{2u} = circumferential component of absolute velocity in the outlet, m/s	P_{ex}^* = total pressure in the exit of the compressor, Pa	β_1' = blade inlet angle, deg
c_p = specific heat, J/(kg K)	Re_f = Reynolds number of flow	β_2' = blade outlet angle, deg
c_{max} = maximum thickness of profile, m	r_1 = mean radius in the inlet of the wheel, m	ϵ = blade camber, deg
D_c = tip diameter, m	r_2 = mean radius in the outlet of the wheel, m	ξ_{in} = loss coefficient of inlet duct
D_h = hub diameter, m	\bar{r}_n = hub/tip ratio of the first stage	ξ_{ex} = loss coefficient of exhaust duct
d_p = particle diameter, m	St_k = Stokes number	ρ = air density, kg/m ³
E = entrainment coefficient	T_{in}^* = total temperature in the inlet of the compressor, K	ρ_p = particle density, kg/m ³
E_c = cascade entrainment coefficient	T_1^* = total temperature in the inlet of the stage, K	ρ_{stg} = degree of reaction,
G = mass flow, kg/s	T_2^* = total temperature in the outlet of the stage, K	π = pressure ratio
G_0 = nominal mass flow, kg/s	T_3^* = total temperature in the inlet of the gas turbine, K	η_{ad} = adiabatic efficiency
H = real head, J/kg	ΔT_{stg}^* = average total temperature rise per stage, K	η_c = compressor efficiency
H_{th} = theoretical head, J/kg	t = pitch of a cascade, m	η_t = turbine efficiency
h = distance between the stream centerline and the limit trajectory at the upstream infinity, m	u = circumferential velocity, m/s	δ = deviation, deg
i = incidence angle, deg	w_1 = flow velocity in the inlet of the blade, m/s	χ_1 = angle between the chord and the tangent to the profile centerline in the inlet of the blade, deg
k = adiabatic coefficient	w_2 = flow velocity in the outlet of the blade, m/s	χ_2 = angle between the chord and the tangent to the profile centerline in the outlet of the blade, deg
k_f = factor of fouling	x_{cmax} = position of maximum profile thickness, m	μ = coefficient of viscosity, Pa s
k_{Hf} = work done factor including fouling effect		Δk_{Hf} = coefficient of theoretical head loss because of fouling
k_{Ne} = output coefficient of the technical condition		$\Delta \bar{p}_{\Sigma}^*$ = coefficient of the total pressure loss
L = characteristic size of the body, m		$\Delta \bar{p}_{\Sigma}^*$ = coefficient of the total pressure loss including fouling effect
		ω = wheel angular velocity, rad/s

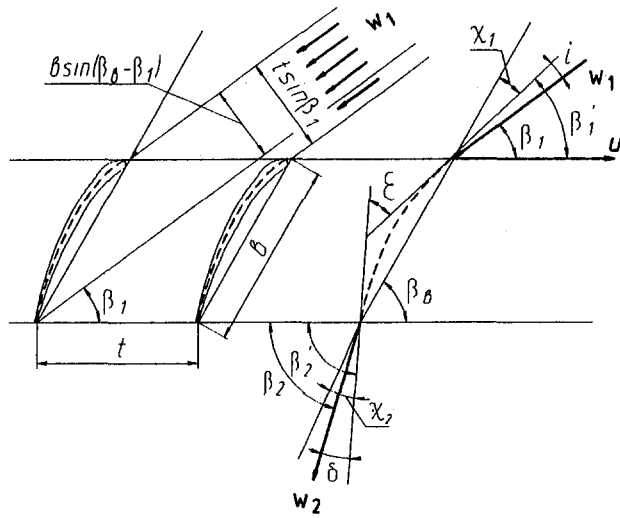


Fig. 2 Cascade of profiles of axial compressor

$$E = h/(b \sin(\beta_b - \beta_1)) \quad (4)$$

Considering that in the cascade the flow path is bounded by two adjacent profiles with pitch t , one can take for the cascade entrainment coefficient:

$$E_c = \frac{\text{number of particles sticking to surface}}{\text{number of particles in the flow for one pitch of the cascade}} \quad (5)$$

Then

$$E_c = h/(t \sin \beta_1) = h/(b \sin(\beta_b - \beta_1))(b/t) \times (\sin(\beta_b - \beta_1)/\sin \beta_1) \quad (6)$$

or

$$E_c = E (b/t)(\sin(\beta_b - \beta_1)/\sin \beta_1) \quad (7)$$

It can be seen from Fig. 2 that

$$\beta_1 = \beta_1' - i = \beta_b - \chi_1 - i \quad (8)$$

$$\beta_2 = \beta_2' - \delta = \beta_b + \chi_2 - \delta \quad (9)$$

From Eqs. (8) and (9) for a profile with a mean (skeleton) line of circular arc

$$\frac{1}{2}(\beta_1 + \beta_2) = \beta_b - \frac{1}{2}(\delta + i) \quad (10)$$

Taking into account that for the cascade situated in the mean radius of a compressor stage and for the optimal regime of work $i \approx 0^\circ$ and $\delta \approx 8^\circ - 10^\circ$, we will roughly obtain

$$\beta_b \approx \frac{1}{2}(\beta_1 + \beta_2) \quad (11)$$

and

$$\beta_b - \beta_1 = \frac{\beta_2 - \beta_1}{2} = \frac{\Delta\beta}{2} \quad (12)$$

The entrainment coefficient E for the endless cylinder at large Reynolds numbers can be defined theoretically by calculating its potential flow. Based on the data obtained from the calculation of the potential flow around the cylinder by T. Langmuir, K. Bladget, and H. Landahl (Fuks, 1955) within the full range of the Stokes numbers, characteristic for axial compressors, the dependence Eq. (2) at large Reynolds numbers can be approximated by the formula:

$$E = (1 + 0.77/St_k)^{-1} \quad (13)$$

For the cascade the Stokes number equals:

$$St_k = \frac{\rho_p d_p^2 w_1}{18 \mu b \sin(\beta_b - \beta_1)} \quad (14)$$

Considering Eqs. (12) and (13), Eq. (7) can be written in the form:

$$E_c = (1 + 0.77/St_k)^{-1} \frac{b \sin(\Delta\beta/2)}{t \sin \beta_1} \quad (15)$$

As the head (work in a stage) of the compressor stage increases, the flow turning angle ($\Delta\beta$) and the solidity (b/t) of the cascade also increase. Therefore, the high-head stages are more sensitive to fouling than the low-head ones.

If we compare geometrically similar compressors, b/t is constant, then it follows from Eqs. (14) and (15), when the size of the chord decreases, the Stokes number and the entrainment coefficient increase, that is, a model compressor is more sensitive to fouling than a full-scale one. Besides that, when the velocity w_1 increases, the value of E_c also increases.

It is evident that Eq. (15) defines the inertial deposition of the particles on the windward side of the blade facing the flow. The deposition of the particles is also present on the leeward side of the blade profile as a result of the whirls and turbulence. The results of the investigation of the deposit formation on the gas turbine compressors blading performed by Olhovskiy (1985) have shown that the fouling affects the first 5–6 compressor stages. The blades fouling becomes less as the air passes from stage to stage. The blade fouling is present on both the concave and the convex sides.

As Fig. 2 and Eq. (15) display, the separation coefficient E_c increases with the increase of angle of attack. This also leads to the increasing number of the tear-off whirls on the convex side of the blade and, consequently, the deposition of the particles becomes more intensive on both sides of the blade.

In the process of deriving Eqs. (1)–(15) it has been assumed that all particles stick to the surface of the body if they collide with it. However, it should be observed that not all the small particles that have reached the blade stick to it. A number of them rebound from the blade surface and are taken away by the flow. Significant factors that influence the adhesion of the particles are the humidity of the air, the presence of oily evaporation, etc. In case of the rotation, the value of E will be influenced by the centrifugal and the Coriolis forces. However, as is evident, these effects are not taken into consideration in Eq. (15).

After this, one can make some conclusions upon the sensitivity of the cascades and stages of axial compressors to fouling:

- on condition of keeping the aerodynamic and geometrical similarity, the compressor of a smaller size (a model) is more sensitive to fouling than a full-scale one;
- sensitivity to fouling of the axial compressor stage increases when the stage head grows;
- the degree of the particles deposition on the blades increases when the angle of attack grows.

Having determined the main factors influencing the sensitivity of the axial compressor to fouling, in the next section of the present paper we have made an attempt to find a generalized criterion for the sensitivity and to develop a mathematical model for evaluation of the change in the compressor performance in the course of fouling.

Fouling Effect on the Performance of Axial Compressor

As was mentioned in the introduction, the methods of estimation of the fouling effect on the compressor performance were

developed recently. In these methods mathematical models are used for the calculation of the behavior of the compressor under fouling. The application of these methods allows one to get a clear idea about the dynamics of the change in the performance of a compressor and a gas turbine unit, as well as to establish a correlation between the change in such parameters as pressure at the exit of compressor, inlet turbine temperature, rotation speed of a gas generator, compressor mass flow, and the decrease in output and efficiency caused by fouling. Some authors try to find a criterion for sensitivity of a compressor to fouling.

Further, and as was noted in the introduction, Aker and Saravanamuttoo (1989) and Seddigh and Saravanamuttoo (1991) developed mathematical models for calculating the performance of the axial compressor with fouled blades. Based on the operational data, the authors stated that the number of fouled stages constitutes $\bar{z}_f = z_f/z = 40\text{--}50$ percent of the total number of the compressor stages. In axial compressors of heavy-duty gas turbines, the number of compressor stages is generally from 8 to 20. In this case, if the percentage ratio is the same (e.g., 50 percent), the number of the fouled stages will range from 4 to 10, i.e., it will depend directly on the total number of stages. In this connection, if we use the mathematical model proposed by these authors, the results of the calculation of the compressor main parameters will also depend on the number of fouled stages, considering that \bar{z}_f is the same. Besides that, it can be shown that the index of sensitivity of the compressor to fouling proposed by Seddigh and Saravanamuttoo (1991) is directly connected with the number of the compressor stages. In fact,

$$\frac{N_e}{Gc_p \Delta T_{\text{stg}}^*} \cong \left(\frac{T_3^* \eta_c \eta_t}{T_{\text{in}}^* \pi^{(k-1)k}} - 1 \right) z \quad (16)$$

If we compare the engines with equal π , T_{in}^* , T_3^* we can see that the value $N_e/(Gc_p \Delta T_{\text{stg}}^*)$ mainly depends only on z . It is evident that in this case the changes occurred due to fouling in N_e , P_{ex}^* , and other parameters, will also be determined mainly by a number of compressor stages with $\bar{z}_f = \text{const}$.

Following Seddigh and Saravanamuttoo (1991), we have developed the linear progressive model of compressor fouling. However, in contrast to Seddigh and Saravanamuttoo (1991), in the present paper it is assumed that in a multistage compressor the number of the fouled stages equals 5 to 6, that is, the first five or six stages retain almost all dirt entering the compressor. This conclusion is based on the experimental data and the field observations of fouling of compressors with number of stages from 6 to 22. In the linear progressive model of fouling it is assumed that the process of fouling goes by intervals; each of them increases the number of fouled stages by one. The first interval corresponds to the fouling of the first stage when the decrease in its head and efficiency equals ΔH and $\Delta \eta_{\text{ad}}$, the second interval causes further decrease in the head and efficiency of the first stage equal to $2 \Delta H$ and $2 \Delta \eta_{\text{ad}}$, accordingly, and the decrease in the second stage characteristics by ΔH and $\Delta \eta_{\text{ad}}$, and so on to the sixth stage.

The method based on the cascade test results is used in the present paper for the stage-by-stage calculation of the compressor performance using the computer program. For calculating on the mean radius of each rotor and stator vane, the following values are given: b , β_1' , β_2' , $\bar{x}_{\text{cmax}} = x_{\text{cmax}}/b$, $\bar{x}_f = x_f/b$, $\bar{c}_{\text{max}} = c_{\text{max}}/b$, b/t , $\bar{A}_1 = A_1/t$, D_c , D_h , ξ_{in} , ξ_{ex} , n , P_{in}^* , T_{in}^* . The mass flow is defined in the process of solving the equation from the maximum one to the surge limit. In the process of calculation the coefficient of mass flow, the parameters of the flow before and after the vane are determined for each stage.

The real head of the stage is determined as:

$$H = c_p(T_2^* - T_1^*) = k_{Hf} \omega (C_{2u} r_2 - C_{1u} r_1) \quad (17)$$

where $k_{Hf} = k_H - \Delta k_{Hf}$.

The summary coefficient of total pressure loss including fouling effect for the cascade is written in the form:

$$\Delta \bar{p}_{fz}^* = k_f \Delta \bar{p}_z^* \quad (18)$$

where $\Delta \bar{p}_z^* = 2(p_{1w}^* - p_{2w}^*)/(\rho_1 w_1^2)$; p_{1w}^* , p_{2w}^* = total pressure in the relative motion in the inlet and the outlet of the rotor blade, ρ_1 = air density in the inlet of the rotor blade.

Equation (15) can be written in the form:

$$E_c = \left(1 + \frac{27.72 \mu (b/D_c) D_c \sin(\Delta\beta/2) \sin\beta_1}{\rho_p d_p^2 C_z} \right)^{-1} \times \frac{b \sin(\Delta\beta/2)}{t \sin\beta_1} \quad (19)$$

For the nominal regimes of the cascade flow there exists an empirical formula (Howell):

$$\frac{b}{t} = \frac{1.5 H_{th}/(C_z u)}{1.55 - H_{th}/(C_z u)} \quad (20)$$

where $H_{th} = C_z u (\text{ctg}\beta_1 - \text{ctg}\beta_2)$.

At the same time, it can be shown that

$$\frac{H_{th}}{C_z u} = f\left(\frac{\rho_{\text{stg}}}{\bar{C}_z}, \frac{b}{t}\right) \quad (21)$$

where $\bar{C}_z = C_z/u$, $\rho_{\text{stg}} = 1 - (C_{1u} + C_{2u})/2u$.

The axial speed component is defined from the equation of mass flow:

$$C_z = \frac{G}{\rho(\pi/4)D_c^2(1 - \bar{r}_h^2)} \quad (22)$$

As follows from the foregoing statements, the sensitivity of the compressor stage to fouling depends mainly on the following parameters:

$$\text{Sensitivity to fouling} = f\left(\frac{b}{D_c}, C_z, u, H_{th}, D_c, \rho_{\text{stg}}\right) \quad (23)$$

Considering Eqs. (15), (19), (20), and (22) and the conclusions made at the end of the first paragraph, we propose that the index of compressor sensitivity to fouling (ISF) be presented as:

$$\text{ISF} = \frac{Gc_p \Delta T_{\text{stg}}^*}{(1 - \bar{r}_h^2) D_c^3} 10^{-6} \quad (24)$$

It is obvious that $\text{ISF} \neq E$, but ISF presents a complex of parameters that are arguments of E and that determine the sensitivity to fouling. We suppose that this value will reflect qualitatively the sensitivity of the axial compressor to fouling under similar environmental conditions. The values of ISF for different compressors are given in Table 1.

As one can see from this table, the Centaur compressor has the largest value of ISF in comparison with the other units shown in Table 1. Assuming the same operation mode and time, the same air quality and its degree of filtration, the Centaur compressor will have a greater reduction in inlet mass flow, pressure ratio, and efficiency than the LM 2500 compressor or the LMZ GTE-150 model compressor. Therefore, the regimes of washing of these compressors must be quite different.

An account of the influence of fouling on the compressor performance is carried out using the factors Δk_{Hf} and k_f . From the physical point of view it is evident that these coefficients must depend on ISF and also on a concentration and fractional composition of aerosols. Comparing the sensitivity to fouling of different compressors operating in the same environment, we suppose that Δk_{Hf} and k_f values are linear functions of argument ISF:

Table 1 Index of sensitivity to fouling (ISF) for different compressors

Parameters	engine compressors				
	Centaur Solar	LM 2500 General Electric	GTE-150 LMZ model $i=1.4, 14$	GTE-150 LMZ full scale	V 94.2 Siemens
engine output, kW	2850	20134	-	150000	150000
air mass flow, kg/s	17.2	65.80	35.47	630.00	500.0
pressure ratio	9:1	17.2:1	12.5:1	12.9:1	10.6:1
number of stages	11	16	14	15	16
hub/tip ratio of the first stage	-0.6	0.480	0.422	0.422	0.520
ΔT_{stg} per a stage, K	28.20	25.90	24.60	23.34	19.25
tip diameter of the first stage, m	0.4400	0.7356	0.5712	2.3650	2.1730
nominal rotation speed of a gas generator, rpm	15015	9160	12420	3000	3000
ISF	8.94	5.59	5.72	1.36	1.29

$$\Delta k_{Hf} = m \text{ ISF} \quad (25)$$

$$k_f = 1 + n \text{ ISF} \quad (26)$$

where m and n are constants.

It is obvious that when $\text{ISF} = 0$ (when there is no fouling) then $\Delta k_{Hf} = 0$ and $k_f = 1$. We suppose that values $\Delta k_{Hf} = 0.01$, $k_f = 1.1$ with $\text{ISF} = 12.5$; then $m = 8 \times 10^{-4}$, $n = 8 \times 10^{-3}$.

Equations (25) and (26) and the chosen values of m and n are approximate, but they reflect qualitatively the data obtained by GASPROM of Russia concerning the changes in the performance of the gas turbines of different output operating at the same station, due to fouling. No special experiments on this problem have been carried out up to now. These coefficients will be defined more precisely in the process of accumulation of experimental data.

The developed mathematical model of the progressive fouling has been adapted to the calculation of performance of the model axial compressor GTE-150 LMZ.

The design parameters of the compressor under the initial conditions $P_{in}^* = 101.340 \text{ kPa}$, $T_{in}^* = 288 \text{ K}$ are $G = 35.47 \text{ kg/s}$, $n_0 = 12,420 \text{ rpm}$, $\pi = 12.5$, $\eta_{ad} = 0.86$, $D_c = 0.5712 \text{ m}$, $\bar{r}_h = 0.422$, $\text{ISF} = 5.72$.

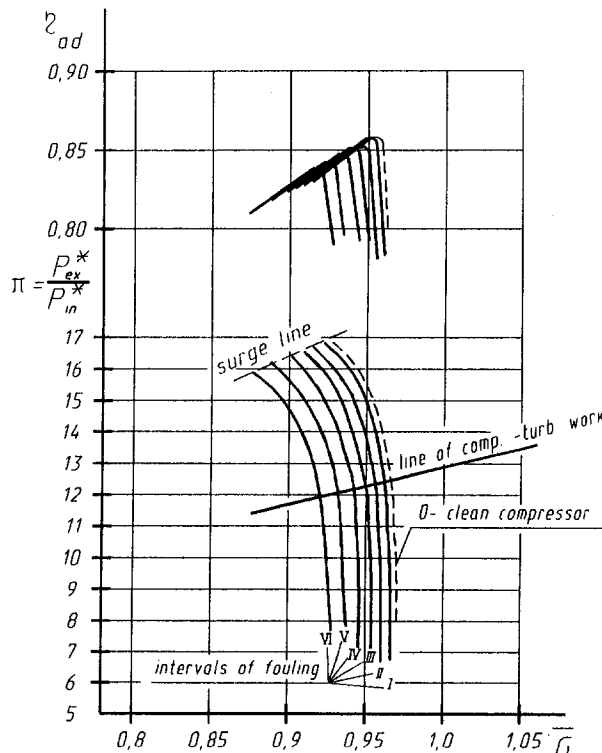


Fig. 3 Performance of the model compressor GTE-150 LMZ under fouling conditions ($\bar{n} = 1.0$)

As can be seen in this case, $\Delta k_{Hf} = 0.5$ percent and $k_f = 1.05$. Calculation results of the compressor performance are shown in Fig. 3, where $\bar{\pi} = \pi/n_0$, $\bar{G} = G/G_0$.

In accordance with the assumed number of fouled stages ($z_f = 6$), the calculation included six intervals; during the last interval the characteristic of the first stage was calculated with $\Delta k_{Hf}^{VI} = 6 \times 0.005 = 0.03$, $k_f^{VI} = 1.05^6 = 1.340$, but the sixth-stage characteristic was calculated with $\Delta k_{Hf}^I = 0.005$, $k_f^I = 1.05$. As one can see from Fig. 3 when the first six stages are fouled (after the sixth interval of progressive fouling), this results in a 4.5 percent reduction in inlet mass flow, 4 percent reduction in pressure ratio and 2 percent reduction in compressor efficiency.

In connection with the development of axial compressor and turbine diagnostics, the method of estimation of engine performance deterioration under fouling gains more ground. The above-described method can be used for this purpose. It allows one to determine not only a tendency but also a character and a degree of a change of the main parameters of a compressor and a gas turbine as a whole under fouling conditions; it helps the operators to take a decision about the cleaning (washing) of the compressor. There are also some recommendations concerning the regularity of cleaning, based on the operational experience.

It was shown in Schurovsky and Levikin (1986) that the behavior of compressor fouling is similar to the exponential law: After 1000–2000 operational hours the engine performance stabilization was noted because there took place the stabilization of a thickness and a form of deposits. An empirical formula was proposed to estimate the relative output change under fouling:

$$\Delta k_{Ne} = a(1 - e^{-b\tau}) \quad (27)$$

where $a = 0.07$, $b = 0.005 \text{ h}^{-1}$, $k_{Ne} = N_{e0}^T/N_{e0}$, τ = operational time of an engine before cleaning in hours.

Equation (27) has been obtained on the basis of the measurements of the actual output of the following gas turbines: GT-700-4, GT-700-5, GT-6-750, GTK-10, GPA-C-6.3, GTK-10I (MS 3000 GE) that have operated for 100 to 1000 hours without cleaning at the compressor stations. After the cleaning the output has been restored to the level of $k_{Ne} = 0.965\text{--}0.985$ in dependence of the time period between cleanings of 300 or 100 hours. The cleaning (washing) of compressor allows one to restore the lost output to some extent; in some cases the initial output can be restored almost completely. The degree of restoration depends on the period of cleaning: long intervals between cleanings are not effective. Based on the field data, a formula was worked out in Schurovsky and Levikin (1986) to calculate the mean integrated coefficient k_{Ne} when cleanings (washings) took place:

$$k_{Ne} = 1 - a [1 - (1 - e^{-bT_0})/(bT_0)] \quad (28)$$

where T_0 is a time period between cleanings in hours; a and b are the same as in Eq. (27).

It was at the time recommended to do cleaning every 200–300 hours to maintain high values of the output coefficient of technical condition ($k_{Ne} = 0.97$ when $T_0 = 250$ h).

Regular washings (cleanings) of compressor blading are the most effective way to resist fouling. They allow one to maintain output and efficiency at a high level during operation. Wet cleaning is the most effective means when it is carried out using the optimized regime of on-line and off-line compressor washing. The important practical results in applying compressor cleaning technique have been demonstrated by Turbotect; see Nicholson (1990), Stalder and Oosten (1994). This technique was tested on a large gas turbine at Utrecht, the Netherlands. A washing solution of 20 percent T-927, an organic solvent-based cleaner, and demineralized water was used. It does not cause pollution, it is safe in service for the operational personnel and it does not cause corrosion of engine elements (compressor, gas turbine, combustion chamber, and regenerator). A compressor wet cleaning system comprises 30 on-line and 7 off-line injection nozzles. During experimental work the optimal arrangement of the nozzles in the intake of a compressor was found. The nozzles are arranged so as to inject a fine atomized spray into the air stream, which will mix and will be carried uniformly into the compressor bellmouth. The period of on-line and off-line washing was determined with minimum consumption of the washing solution, electric power, and labor input.

Summary

1 This paper describes the main factors producing an effect on the sensitivity of an axial compressor to fouling:

- given aerodynamic and geometric similarity, a compressor of a smaller size (a model) is more sensitive to fouling than a full-scale one;
- sensitivity to fouling of the axial compressor stage increases when the stage head grows;
- the degree of the particle deposition on the blades increases when the angle of attack grows.

2 The mathematical model of progressive fouling of the compressor flow path has been developed using the stage-by-stage calculation method based on the test results of cascades in a wind tunnel. Calculation of the model compressor GTE-150 LMZ performance under fouling conditions has been carried out. Fouling up to the sixth stage of the compressor causes reduction in the mass flow by 4.5 percent, pressure ratio by 4 percent, and efficiency by 2 percent.

The index of compressor sensitivity to fouling is proposed in the form:

$$ISF = \frac{Gc_p \Delta T_{stg}^*}{(1 - F_h^2) D_c^3} 10^{-6}$$

When two compressors with different geometric dimensions and different performance are compared, a greater ISF corresponds to a greater sensitivity of a compressor to fouling.

3 For a new installation, it is recommended to select the most appropriate and effective air inlet filtration system for the best cleaning efficiency at the lowest additional losses of output and heat rate. Climatic conditions and plant environment are to be considered.

4 Regular washings (cleanings) of compressor blading are the most effective way to resist fouling. They allow one to maintain output and efficiency at a high level during operation. Wet cleaning is the most effective means when it is carried out using the optimized regime of on-line and off-line compressor washing.

References

- Aker, G. F., and Saravanamuttoo, H. I. H., 1989, "Predicting Gas Turbine Performance Deterioration Due to Compressor Fouling Using Computer Simulation Techniques," *ASME Journal of Engineering for Gas Turbines and Power*, Vol. 111, pp. 343–350.
- Diakunchak, I. S., 1992, "Performance Deterioration in Industrial Gas Turbines," *ASME Journal of Engineering for Gas Turbines and Power*, Vol. 114, pp. 161–168.
- Fuks, N. A., 1955, *The Mechanism of Aerosols*, Moscow, USSR Academy of Science.
- Green, H., and Lane, W., 1964, *Particulate Clouds: Dust, Smokes and Mist*, 2nd ed., London.
- Hoelt, R. F., 1993, "Heavy Duty Gas Turbine Operating and Maintenance Considerations," GER-3620B, GE I&PS.
- Howell, A. R., and Calvert, W. J., 1978, "A New Stage Stacking Technique for Axial-Flow Compressors Performance Prediction," *ASME Journal of Engineering for Gas Turbines and Power*, Vol. 100, pp. 698–703.
- Mikhaylov, E. I., et al., 1978, *The Complex Aerocleaning Devices of the Energetical Gas Turbine Installation*, Leningrad, Mashinostroenie.
- Nicholson, G., 1990, "Gas Turbine Cleaning at the Utrecht Site of Dutch Utility Company," *Turbomachinery International*, May/June.
- Olhovskiy, G. G., 1985, *Power Gas Turbine Units*, Moscow, Energoatomizdat.
- Schurovsky, V. A., and Levikin, A. P., 1986, "Fouling and Cleaning of Gas Turbine Axial Compressor Flow Path," Moscow, series "Transport and Gas Conservation," Vol. 11.
- Seddigh, F., and Saravanamuttoo, H. I. H., 1991, "A Proposed Method for Assessing the Susceptibility of Axial Compressors to Fouling," *ASME Journal of Engineering for Gas Turbines and Power*, Vol. 113, pp. 595–601.
- Stalder, J. P., and Oosten, P., 1994, "Compressor Washing Maintains Plant Performance and Reduced Cost of Energy Production," *ASME Paper No. 94-GT-436*.

Unsteady Flow in Oscillating Turbine Cascades: Part 1 — Linear Cascade Experiment

L. He

School of Engineering,
University of Durham,
Durham, DH1 3LE, United Kingdom

An experimental and computational study has been carried out on a linear cascade of low-pressure turbine blades with the middle blade oscillating in a torsion mode. The main objectives of the present work were to enhance understanding of the behavior of bubble-type flow separation and to examine the predictive ability of a computational method. In addition, an attempt was made to address a general modeling issue: Was the linear assumption adequately valid for such kind of flow? In Part I of this paper, the experimental work is described. Unsteady pressure was measured along blade surfaces using off-board mounted pressure transducers at realistic reduced frequency conditions. A short separation bubble on the suction surface near the trailing edge and a long leading-edge separation bubble on the pressure surface were identified. It was found that in the regions of separation bubbles, unsteady pressure was largely influenced by the movement of reattachment point, featured by an abrupt phase shift and an amplitude trough in the first harmonic distribution. The short bubble on the suction surface seemed to follow closely a laminar bubble transition model in a quasi-steady manner, and had a localized effect. The leading-edge long bubble on the pressure surface, on the other hand, was featured by a large movement of the reattachment point, which affected the surface unsteady pressure distribution substantially. As far as the aerodynamic damping was concerned, there was a destabilizing effect in the separated flow region, which was, however, largely balanced by the stabilizing effect downstream of the reattachment point due to the abrupt phase change.

Introduction

The trend of modern gas turbine/aero-engine design with higher aerodynamic loading and smaller physical size/lighter weight has attracted much attention to the aeroelastic behavior of blades, not only in compressors/fans, but also in turbines. Considerable theoretical, computational, and experimental efforts have been made to understand relevant physical mechanisms and to enhance prediction capability for turbomachinery blade flutter. One very important aspect of research work is unsteady aerodynamics around oscillating blades. Unsteady viscous flow effect on blade flutter is of great interest.

Under a typical Reynolds number, bubble-type boundary layer separation often occurs on turbine blade surfaces. On suction surfaces, laminar separation in the region downstream of the suction peak is normally unavoidable at design and off-design conditions. The suction surface separation will be followed by a transition to turbulent in the separated shear layer, which is then followed by an immediate turbulent reattachment. On pressure surfaces, the boundary layer may separate near leading edge, at a negative incidence. The pressure surface leading edge separation tends to be more persistent even with a transition to turbulent, and as a result a long separation bubble will be formed. From an aeroelastic point of view, little has been known about the behavior of the bubble-type separation and its effect on turbine blade flutter, which is of great practical importance.

Detailed and reliable experimental data are needed to provide first-hand evidence to enhance our physical understanding of complex blade flutter problems. They are also essential for validation of developed numerical methods. It is strongly felt that

understanding of the flow phenomena to be modeled is very useful for directing further development of computational models and methods. Experimental rigs with externally driven oscillating blades (linear or annulus cascade) have been widely used (e.g., Carta, 1983; Bölscs and Fransson, 1986). Typically, turbomachinery blade flutter can be described by the so-called "tuned cascade model," i.e., all blades in a cascade would oscillate in an identical frequency and a constant blade-to-blade phase angle (interblade phase angle). Hence there would be a circumferentially phase-shifted periodicity. For an annular cascade rig, an aerodynamic phase-shifted periodicity depends, to a large extent, only upon the phase-shifted periodicity of the externally driven blade vibration motions. While for a typical linear cascade, even the phase-shifted periodicity for blade vibration could be maintained, it would be much more difficult to obtain an aerodynamic phase-shifted periodicity due to the wind tunnel wall effects (e.g., Buffum and Fleeter, 1993). This difficulty may be avoided by using the influence coefficient method (Hanamura et al., 1980), in which only a reference (middle) blade in a linear cascade is oscillating and measurements are made on this reference blade and its several neighboring blades. By assuming a linearity, the resultant unsteady parameters on a tuned cascade with the phase-shifted periodicity can be obtained by superposition. Use of the influence coefficient method provides an opportunity of having a much simplified experimental setup. However, one has to ensure that the linear assumption would be valid for the situations concerned.

The issue of linearity is relevant not only to experimental modeling of blade flutter using the Influence Coefficient method, but also (and probably in a more general sense) relevant to development to computational methods for blade flutter predictions. There are two distinctively different approaches under current development. The time-marching methods integrate the nonlinear flow equations in the time domain, with either the inviscid Euler model (e.g., Fransson and Pandolfi,

Contributed by the International Gas Turbine Institute and presented at the 41st International Gas Turbine and Aeroengine Congress and Exhibition, Birmingham, United Kingdom, June 10–13, 1996. Manuscript received at ASME Headquarters February 1996. Paper No. 96-GT-374. Associate Technical Editor: J. N. Shinn.

1986; Gerolymos, 1988, 1992; He, 1989), or the Navier–Stokes model (e.g., Huff, 1987; Giles and Haimes, 1993; He, 1993). On the other hand, the flow equations can be linearized and solved in the frequency domain, such as those with the potential flow models by Verdon and Caspar (1982) and Whitehead (1982) and with the Euler models by Hall and Clark (1993). It is well recognized that time-marching approaches are much more computationally expensive than the time-linearized approaches. The question is: When and where can one adopt the time linearization for practical flutter predictions? One area of focus is in the transonic flow regime with shock oscillations, as analyzed by Lindquist and Giles (1994) and Hall et al. (1994) based on the Euler equations. Unsteady flow separation is another area of interest.

The objectives of the present work were twofold, first to produce a set of detailed experimental data to identify the behavior of unsteady flow separations on oscillating turbine blades and to validate a developed time-marching Navier–Stokes solver, and second to address the issue of linearity/nonlinearity for flows with separations. The experimental facility, method, results, and discussions are presented as follows.

Experimental Facilities and Techniques

Test Rig and Cascade. The low-speed duplex wind tunnel in the Whittle Laboratory, Cambridge University, was used for the present experimental work. The tunnel was powered by an electrical fan and exhausted to the atmospheric condition. The test section was made of a wooden frame and perspex plates. The flow velocity was controlled by throttling, giving an exit flow up to about 50 m/s for the test section used in the present work.

A linear cascade consisting of seven blades of a low-pressure turbine blade profile with chord length of 148 mm and aspect ratio of 1.5 was used in the experiment. The cascade configuration is shown in Fig. 1. The middle blade (Blade 0) oscillated in a torsion mode, driven by a DC motor with a rotation-translation conversion mechanism. The torsion axis was located at the midchord in the axial direction and at the middle point between the blade upper and lower surfaces in the tangential direction. The middle (oscillating) blade and one stationary blade were tapped at the middle span section with 24 tappings on the suction surface and 16 tappings on the pressure surface. The tapped stationary blade could be interchanged with one of other stationary blades so that unsteady surface pressure distributions for all the blades could be measured.

Unsteady Pressure Measurement. As demonstrated in the previous work (He and Denton, 1991), for a low-speed wind tunnel experiment, unsteady pressure measurement could be carried out very cost effectively. Under a low flow velocity, we can achieve a reasonably high reduced frequency condition of practical interest with a low oscillation frequency. Because of

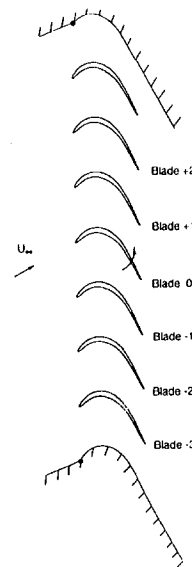


Fig. 1 Linear cascade test section configuration

the low oscillation frequency, we can connect a surface pressure tapping with a pressure transducer, which is mounted outside of the wind tunnel side wall, through plastic tubing. This “off-board” pressure transducer connection would greatly save experimental costs.

The schematic layout of the unsteady pressure measurement system is shown in Fig. 2. Five SENSYSM transducers of the type 142SC01D with pressure range: 0–1 psi; sensitivity: 5 V/psi, were “off-board” mounted (8 measurements were therefore needed for each blade of 40 tapping points). The same transducers were used in the previous experiment (He and Denton, 1991), and the effect of the tubing length on the unsteady pressure results was shown to be negligible for similar flow conditions and oscillation frequencies to those in the present experiment.

A MICROLINK interface system was used as a contact between the output voltage of the pressure transducers and an APRICOT-XEN computer. A multichannel PGA16 analog module was used to digitalize the output voltage and to transfer it to the computer. The data acquisition was started by an electromagnetic trigger referencing a fixed phase of the middle blade oscillation movement.

Unsteady pressure data (output voltages of transducers) were ensemble-averaged. The PGA16 module was controlled to collect the output voltage in N_{enb} periods and the ensemble-averaged value was

$$\overline{\text{Volt}}(n) = \frac{1}{N_{\text{enb}}} \sum_{N=1}^{N_{\text{enb}}} \text{Volt}(n, N) \quad (n = 1, 2, \dots, n_p)$$

Nomenclature

Am_{p1} = amplitude of first harmonic pressure
 Am_t = amplitude of blade torsion vibration
 C = blade chord length
 Cax = blade axial chord length
 CM = first harmonic aerodynamic moment coefficient
 CP = steady pressure coefficient = $(P_0 - P)/(P_0 - P_2)$
 $|CP_1|$ = amplitude of first harmonic pressure coefficient $(Am_{p1})/(P_0 - P_1)Am_t$

K = reduce frequency (based on true chord and exit flow velocity)
 P_0 = inlet stagnation pressure
 $P.S.$ = parameters on pressure surface
 $S.S.$ = parameters on suction surface
 α = blade torsion displacement, positive in anti-clockwise direction
 β_1 = steady inlet flow angle
 ϕ = phase angle of first harmonic pressure

Subscripts

0 = steady time-averaged parameter
 1 = first harmonics; inlet parameter
 2 = second harmonics; outlet parameter
 e = inviscid parameters
 i = imaginary part of complex number
 R = parameters at reattachment point
 S = parameters at separation point
 T = parameters at transition point

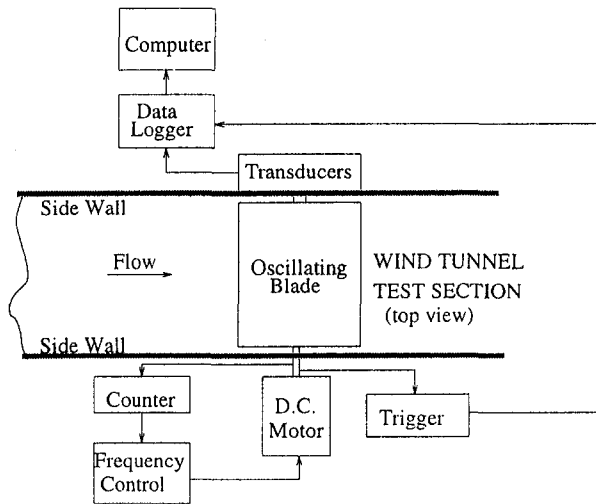


Fig. 2 Schematic layout of measurement system

where n_p was the number of sample points in one period of oscillation for each transducer, which was usually taken to be 50. It was found that 20 period ensemble-averaged signals (i.e., $N_{\text{enb}} = 20$) were sufficient to give well-defined periodic data.

Experimental Results and Discussion

Steady Flow Results. The steady flow conditions for the present experiment were:

- Outlet flow velocity: 24 m/s
- Reynolds number (based on exit velocity): 2.2×10^5
- Inlet flow angles β_1 : 20 deg, 30 deg, 40 deg

Figure 3 shows the steady pressure coefficient distributions at inlet flow angles 20, 30, and 40 deg. Dye paint was also used to visualize blade surface flow patterns. Photos of the visualizations were taken for the suction surface. A typical example of the suction surface flow visualization pictures is shown in Fig. 4, which was taken at a position downstream of the trailing edge ("T.E." marks the blade trailing edge). A small suction surface separation bubble at around 75 percent axial chord was clearly indicated by a strip of dye deposition. It was found that the suction surface separation bubble existed for all the three inlet flow angle conditions, and its chordwise position remained roughly unchanged. The flow visualization also indicated a large leading edge separation bubble on the pressure surface. The size of the pressure surface separation bubble changed considerably with inlet flow angle conditions. At the inlet flow angle of 20 deg, it covered more than 60 percent of the pressure surface measured from the leading-edge in the axial

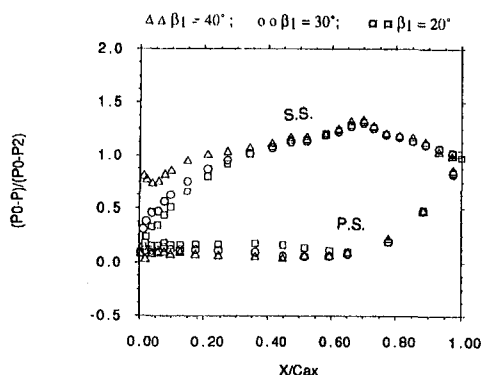


Fig. 3 Experimental steady pressure coefficient along axial chord

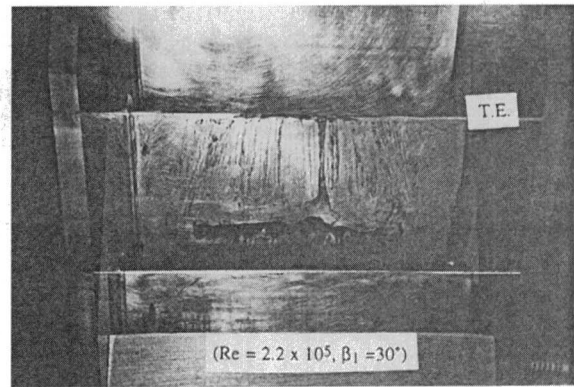


Fig. 4 Suction surface flow visualization

direction. At the inlet flow angle of 40 deg, the size of the bubble decreased to about 15 percent of the axial chord. From the steady surface pressure distributions (Fig. 3), these separation bubbles could not be easily identified. The existence of these bubbles is confirmed by the unsteady pressure results presented later.

Unsteady Pressure Results. Detailed unsteady surface pressure measurements were carried out for six blades, Blade -3, Blade -2, Blade -1, Blade 0, Blade +1 and Blade +2, as shown in Fig. 1. Some preliminary measurement was also conducted on the blade adjacent to the tunnel upper wall (Blade +3) and the result showed almost no unsteady pressure response. Therefore, no further unsteady pressure data were taken on this blade.

All the unsteady pressure measurements presented here were carried out with the middle blade (Blade 0) being oscillated in a torsion mode with:

- Oscillation frequency: 20 Hz
- Reduced frequency (based on the exit velocity): 0.7
- Torsion amplitude Am_t : 1 deg

The torsion movement of the middle blade was in the form of:

$$\alpha = Am_t \sin \omega t \quad (1)$$

The ensemble-averaged unsteady pressure results were processed using the Fourier transform. For a sinusoidal blade motion, only the first harmonic components will contribute to the aerodynamic damping (i.e., the net work input to the blade vibration). The higher harmonics would however be an indication of nonlinearity. Figure 5 shows the first harmonic pressure coefficient along axial chord on Blade -2 - Blade +1 for $\beta_1 = 30$ deg. Apparently the unsteady aerodynamic responses converged quite quickly away from the middle oscillating blade, which would be required if the influence coefficient method was to be used. The main unsteady aerodynamic response came from the suction and pressure surfaces of the oscillating blade (Blade 0) and the suction surface of its lower adjacent blade (Blade -1). In the rest of paper, discussions will be mainly concentrated on the unsteady pressure results on these two blades. The amplitude and phase of the first harmonic unsteady pressure coefficients on the middle blade are shown in Fig. 6. The results for Blade -1 are given in Fig. 7.

It can be seen from the results that the unsteady pressure due to oscillation of the middle blade is only of significant magnitude on the suction and pressure surfaces of the middle oscillating blade (Blade 0) and on the suction surface of its lower adjacent blade (Blade -1). The unsteady pressure magnitude on the pressure surface of the upper adjacent blade (Blade +1) is considerably lower. This feature can be explained by looking at the change of blade passage throat area due to the middle blade oscillation. When the middle blade was oscillating in the

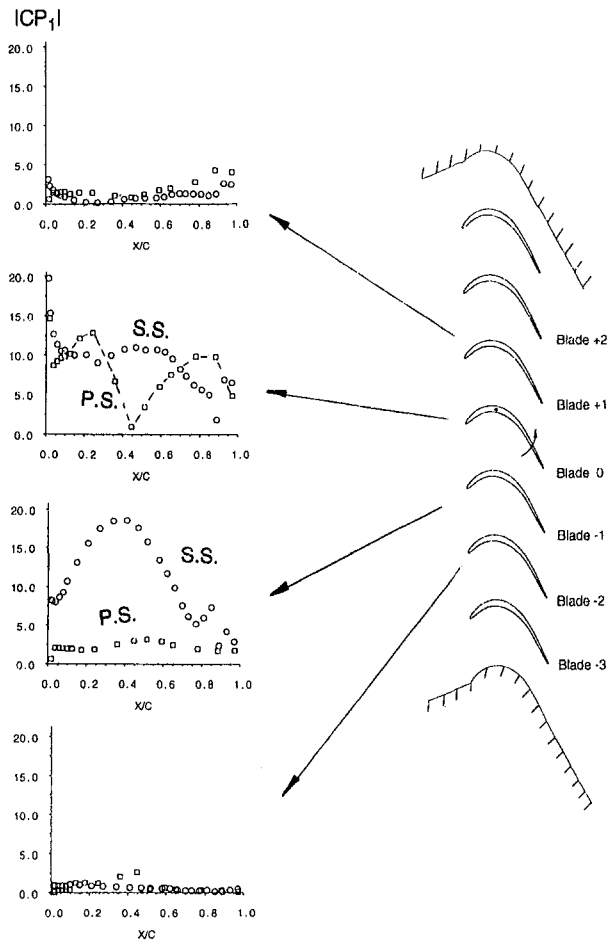


Fig. 5 Unsteady pressure due to oscillation of blade 0 ($\beta_1 = 30$ deg)

torsion mode around its middle chord position, the throat area of the lower blade passage between Blade 0 and Blade -1 would experience more change than that of the upper blade passage between Blade 0 and Blade +1. In addition, the higher velocity on the suction surface is more sensitive to change of passage area (Blockage). As a result, there would be a large unsteady pressure response on the suction surface of Blade -1. It is also noted that the region with a large unsteady pressure magnitude covers a large proportion of the suction surface of Blade -1 (with a peak around around 40 percent axial chord). This feature may also suggest that the unsteady pressure on the suction surfaces be significantly driven by the passage area change instead of a local incidence effect around the leading edge.

By contrast to the steady pressure distributions (Fig. 3), the existence of the separation bubbles on both the suction surface and the pressure surface can be easily identified from the unsteady pressure results (Figs. 5-7). Typically the first harmonic unsteady pressure distribution around a separation bubble would feature an abrupt change in amplitude and phase. The effect of separation bubbles on unsteady pressure distributions can be clearly seen from the three-dimensional space-time (S-T) plots of the ensemble-averaged instantaneous unsteady pressure on the suction and pressure surfaces for the middle blade at the 20 deg inlet flow angle, as shown in Fig. 8.

Suction Surface Short Separation Bubble. From the steady flow surface dye visualization, the suction surface separation bubble starts at around 75 percent axial chord with a bubble length of about 10-15 percent of axial chord. The unsteady pressure results (Figs. 6 and 7) showed that marked variations

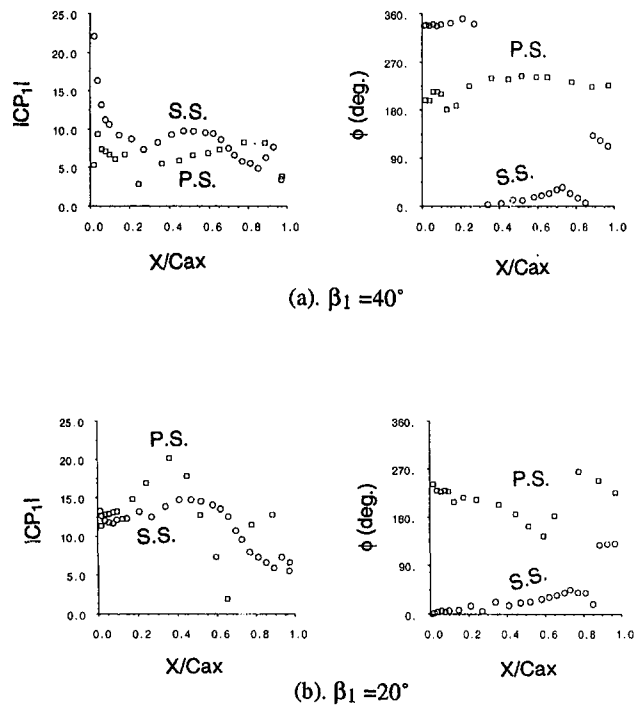


Fig. 6 Unsteady pressure on middle blade (Blade 0)

in terms of amplitude and phase of unsteady pressure occurred in the region of the separation bubble (70-95 percent axial chord).

To help understand the unsteady pressure distributions around a short separation bubble, it was attempted to use a quasi-steady separation bubble model. For steady flows, Horton (1969) proposed a laminar separation bubble model with a typical surface velocity distribution as shown in Fig. 9(a) (where "S" indicates the separation point, "T" the transition point, and "R" the reattachment point). In Horton's model, a pressure (or an equivalent inviscid flow flow velocity) would remain constant

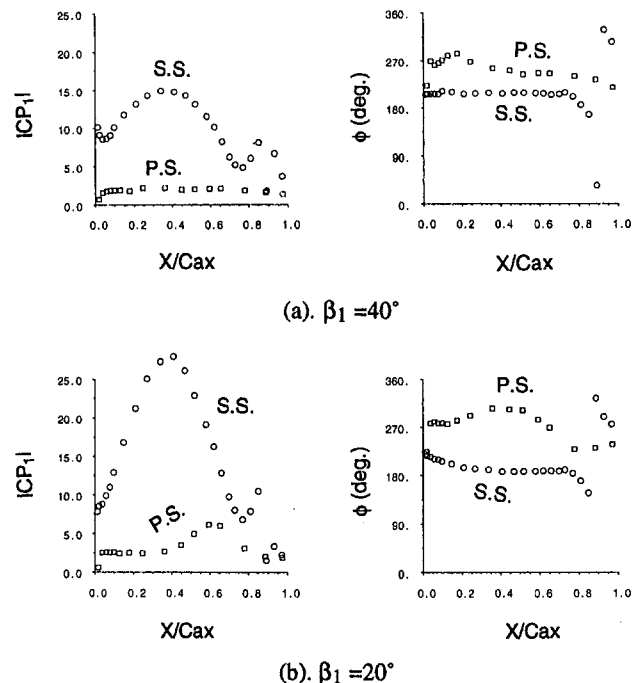


Fig. 7 Unsteady pressure on the lower adjacent blade (Blade -1)

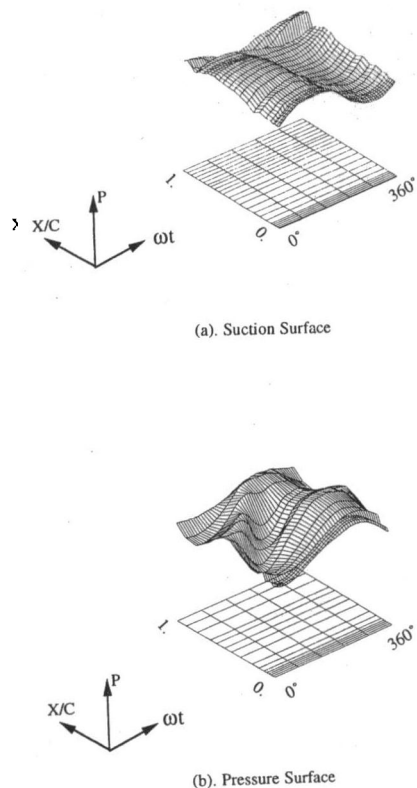


Fig. 8 S-T plot of ensemble-averaged unsteady pressure ($\beta_1 = 20$ deg)

over the laminar part of the separation bubble, which would be followed by a laminar-turbulent transition and an immediate turbulent reattachment. The length of laminar part of the bubble can be estimated according to Horton's model by:

$$L_s = 4 \times 10^4 \frac{\mu}{(\rho_e \mu_e)_s} \quad (2)$$

where the subscript "e" indicates the parameters at boundary layer edge; "s" indicates the parameters at the position of the boundary layer separation.

Assuming Horton's model to be valid for an unsteady flow case in a quasi-steady manner, we can then examine the corresponding pressure variation around the bubble due to the blade oscillation. From the Horton's model (Eq. (2)), neglecting changes of μ and ρ_e , we would have a shorter laminar bubble length (a higher u_e) with a more upstream separation point if the adverse pressure gradient is increased. Conversely, we would have a longer laminar bubble length if the separation point is moved downstream under a smaller adverse pressure gradient. The quasi-steady model suggests that the instantaneous surface pressure distribution would, in one period of oscillation, vary between two extreme distributions ($S_1 - T_1 - R_1$ and $S_2 - T_2 - R_2$) corresponding to the maximum and the minimum pressure gradients, as shown in Fig. 9(a). For simplicity, the change of pressure at the reattachment point was not considered.

Tracing the instantaneous pressure variation using this quasi-steady separation bubble model, following features can be noticed:

(a) Around the "time-mean" separation point, the schematic temporal variation would look like that shown in Fig. 9(b). The phase of the unsteady pressure would be similar to those upstream of the separation, whilst the amplitude would depend largely on the amplitude of the separation point movement.

(b) In the region where the reattachment point moved, the unsteady pressure would be largely influenced by a step function, as shown in Fig. 9(c). The pressure variation due to the step function had a phase shift of 180 deg compared to the pressure around the separation point. It was also featured by high magnitudes of the first and second harmonic amplitudes.

The first harmonic pressure results around the suction surface separation bubble seemed to be qualitatively in agreement with the simple quasi-steady argument. The abrupt phase shift was clearly observed at all conditions, although the experimental data normally showed a phase increase of about 100 deg, instead of 180 deg. It was also observed that there was a relatively high second harmonic amplitude around the reattachment point, as expected from the above quasi-steady bubble model.

The effect of the suction bubble on the aerodynamic damping was illustrated by the distribution of aerodynamic work input in terms of the imaginary part of the local first aerodynamic moment coefficient per unit surface length, as shown in Fig. 10. Apparently, as far as the middle blade was concerned, the suction surface bubble had a stabilizing effect for both the low and high inflow angle conditions. Although the unsteady pressure variation in the separated flow region around 75-85 percent axial chord showed a tendency toward a negative damping, it was soon dominated by the stabilizing effect due to the abrupt phase increase and the high amplitude around the reattachment point.

Pressure Surface Long Separation Bubble. First it is recognized that the behavior of a leading-edge long separation bubble would be different from that of a short bubble even for steady flows. For a short bubble, the transition point (and there-

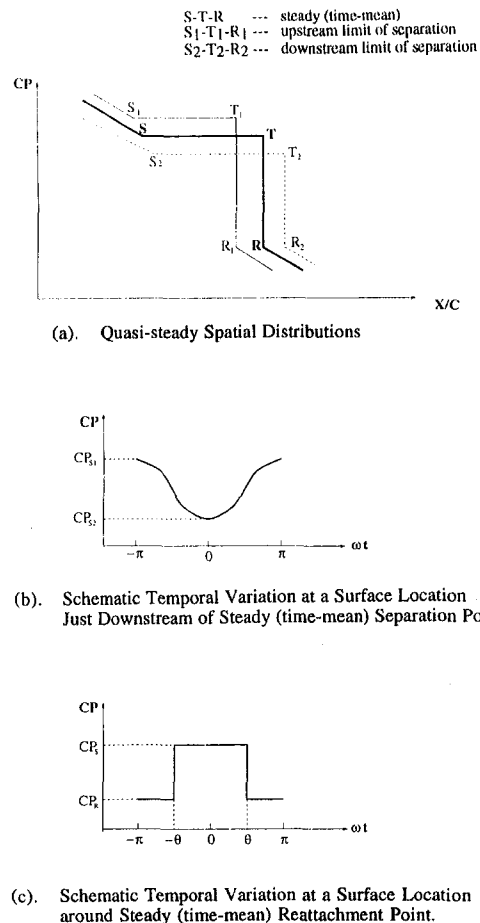


Fig. 9 Pressure distributions over a laminar separation bubble

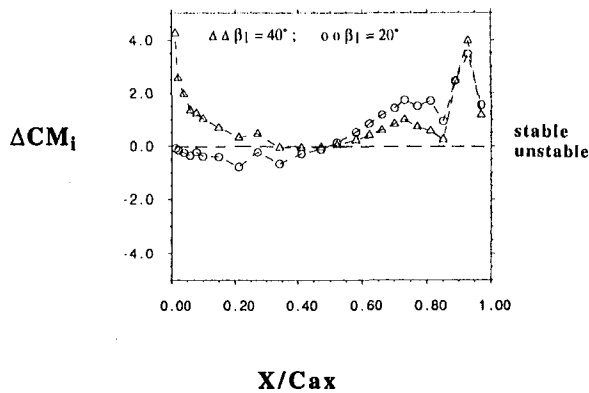


Fig. 10 Chordwise specific damping coefficient (CMi per unit surface-length) on suction surface (Blade 0)

fore the reattachment point) could be adequately determined by correlations (e.g., Horton's model) and the effect of the short bubble on the flow field is very localized. Effectively the bubble length is determined by what happens at the separation point (Eq. (2)). As long as the separation point is moving quasi-steadily, the transition point (the reattachment point) would be moving in quasi-steady way.

However, for the leading-edge long separation bubble, the reattachment may not be determined by the transition. For instance, the surface hot-film measurement in the previous work (He and Denton, 1991) had indicated that a leading-edge long bubble could have a considerable length of turbulent part before a reattachment. Also, a strong interaction between the long bubble and the flow field is expected. The bubble size (the reattachment point) would be strongly influenced by the amount of viscous diffusion in the separated shear-layer and by the local pressure gradient.

From the first harmonic pressure on the pressure surface of the middle blade (Blade 0) at the two flow angle conditions (Fig. 6(a, b)), we can see that unsteady pressure around the separation point (adjacent to the leading edge) did not seem to have a distinctive feature. But farther downstream (20–70 percent axial chord), the unsteady pressure changed drastically, especially at the low inflow angle (Fig. 6(b)). Around the "time-mean" reattachment point, there were a trough in the magnitude and a shift in the phase in the first harmonic pressure distributions.

The unsteady behavior of the pressure surface separation bubble could be illustrated from the ensemble-averaged S–T plot of the surface pressure for the middle oscillating blade (Fig. 8(b)). At $\omega t = 0$ deg, the blade was at its "time-mean" position and the incidence was being reduced by the anti-clockwise torsion movement. A peak of high pressure corresponding to the instantaneous reattachment point appeared around 50 percent axial chord. As the incidence was reduced ($\omega t = 0-90$ deg), the separation bubble was enlarged, indicated by the S–T trace of the downstream movement of the pressure peak associated with the reattachment point. When the incidence started to increase after $\omega t = 90$ deg, the downstream movement of the reattachment point was not immediately reversed, as one would expect in a quasi-steady sense. Nevertheless, the further downstream movement of the reattachment point after $\omega t = 90$ deg had a less marked pressure peak. Another pressure peak at around 40 percent axial chord started to form after the instant with maximum incidence ($\omega t = 270$ deg) was passed. The resultant surface unsteady pressure variation had the following features:

(a) The movement of the reattachment point covered a large surface distance (probably about 40–50 percent axial chord). This movement resulted in a phase shift of about 100 deg.

(b) The region between 30–60 percent axial chord experienced two pressure peaks in one period. The first one corresponded to the "local" downstream movement of the reattachment point, which could be regarded as being of a step-function type, similar to that observed for the suction surface short separation bubble. The second pressure peak corresponded to the "global" pressure variation in response to the blade passage area variation due to the blade oscillation. It should be noted that the "global" pressure variation around the long separation bubble was considerably enhanced by the interaction between the bubble and the main flow field through a blockage variation due to the bubble. For the present case, both peaks were of the same magnitudes and they appeared in one period about 180 deg phase apart. This phase relationship could also be expected considering that the enlargement of the separation bubble would be accompanied by a high pressure gradient (a lower local pressure) in a quasi-steady sense. As a result of this phase relationship, the first harmonic pressure components due to the two events tended to cancel each other and the second harmonic pressure became relatively high in this region. This may explain why there was a trough in the magnitude of the first harmonics around the "time-averaged" reattachment point.

The unsteady pressure in the separated flow region showed a phase lag to the blade oscillating (Fig. 6(b)). Thus the contribution to the aerodynamic damping for the torsion vibration around the midchord showed a destabilizing effect, as shown in Fig. 11 (note that the anti-clockwise was defined as the positive direction for the torsion movement). This negative damping effect was apparently enhanced with the enlarged separation at the low inflow angle condition. However, due to the phase change around the time-mean reattachment point, the pressure in the region downstream the reattachment showed a stabilizing effect (Fig. 11), which, to a large extent, balanced the negative damping contributed in the separated flow region. As a result, there appeared to be no apparent net effect on the aerodynamic damping of the blade.

Concluding Remarks

Detailed surface unsteady pressure has been measured for a linear turbine cascade with its middle blade oscillating in a torsion mode, with the intention to use the influence coefficient method to obtain unsteady pressure for a tuned cascade. The results showed some marked effects of bubble types of separation on the unsteady pressure, which mainly resulted from the movements of reattachment points.

The behavior of the short bubble on the suction surface seemed to follow closely a simple quasi-steady separation bubble model. Around the reattachment point, unsteady pressure was characterized by a region of high first harmonic amplitudes

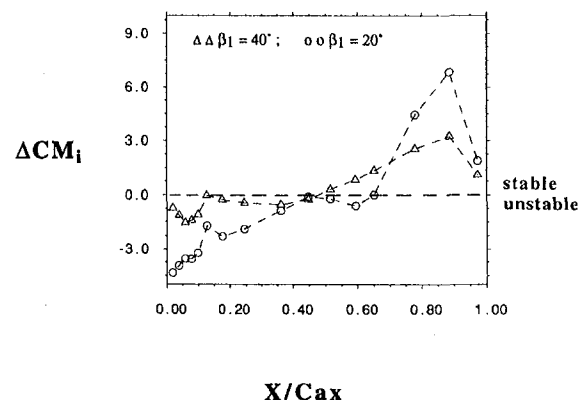


Fig. 11 Chordwise specific damping coefficient (CMi per unit surface-length) on pressure surface (Blade 0)

and an abrupt phase increase of about 100 deg, which contributed to the blade aerodynamic damping with a stabilizing effect.

The leading-edge long bubble on the pressure-surface did not seem to behave in a quasi-steady manner. It affected unsteady loading substantially at a low inflow angle condition. The unsteady pressure distribution around the reattachment point was largely driven by the local pressure peak due to the movement of reattachment point, coupled with a global pressure variation in response to the blade oscillation. This resulted in a trough in the distribution of the first harmonic pressure amplitude and a rapid phase increase around the reattachment point. In the separated flow region, the unsteady pressure had a destabilizing effect. This destabilizing effect was, however, largely balanced by the stabilizing effect in the region downstream the reattachment, due to the rapid phase change.

Considering the behavior of the unsteady viscous flow observed in the present experiment, there arose a question about the validity of the linear assumption, which was not only fundamentally required for the influence coefficient method, but also of more general interest.

The use of the present test data for validation of a computational method and the issue concerning the linearity of the unsteady flow response will be discussed in Part 2.

Acknowledgments

The experimental work was carried out at the Whittle Laboratory, Cambridge University while the author worked as a Rolls-Royce Senior Research Fellow at Girton College. Financial sponsorship from Rolls-Royce plc is gratefully acknowledged. The author wishes to thank Professor John Denton (Cambridge) and Dr. Peter Stow (Rolls-Royce) for their help during the course of this work.

References

Böls, A., and Fransson, T. H., 1986, "Aeroelasticity in Turbomachines—Comparison of Theoretical and Experimental Cascade Results," *Communication*

du Laboratoire de Thermique Appliquée et de Turbomachines, No. 13, Lausanne, EPFL.

Buffum, D. H., and Fleeter, S., 1993, "Wind Tunnel Wall Effects in a Linear Oscillating Cascade," *ASME JOURNAL OF TURBOMACHINERY*, Vol. 115, pp. 147–156.

Carta, F. O., 1983, "Unsteady Aerodynamics and Gapwise Periodicity of Oscillating Airfoils," *Journal of Engineering for Power*, Vol. 105, No. 3.

Fransson, T. H., and Pandolfi, M., 1986, "Numerical Investigation of Unsteady Subsonic Compressible Flows Through Oscillating Cascade," *ASME Paper No. 86-GT-304*.

Gerolymos, G. A., 1988, "Numerical Integration of the 3D Unsteady Euler Equations for Flutter Analysis of Axial Flow Compressors," *ASME Paper No. 88-GT-255*.

Gerolymos, G. A., 1992, "Advances in the Numerical Integration of the 3-D Euler Equations in Vibrating Cascades," *ASME Paper No. 92-GT-170*; *ASME JOURNAL OF TURBOMACHINERY*, Vol. 115, No. 3, 1993.

Giles, M. B., and Haines, R., 1993, "Validation of a Numerical Method for Unsteady Flow Calculations," *ASME JOURNAL OF TURBOMACHINERY*, Vol. 115, No. 1.

Hall, K. C., and Clark, W. S., 1993, "Linearized Euler Predictions of Unsteady Aerodynamic Loads in Cascades," *AIAA Journal*, Vol. 31, No. 3.

Hall, K. C., Clark, W. S., and Lorence, C. B., 1994, "A Linearized Euler Analysis of Unsteady Transonic Flows in Turbomachinery," *ASME JOURNAL OF TURBOMACHINERY*, Vol. 116, No. 3.

Hanamura, Y., Tanaka, H., and Yamaguchi, Y., 1980, "A Simplified Method to Measure Unsteady Forces Acting on the Vibrating Blades in Cascade," *Bulletin of JSME*, Vol. 23, No. 18.

He, L., and Denton, J. D., 1991, "An Experiment on Unsteady Flow Over an Oscillating Airfoil," *ASME Paper No. 91-GT-181*.

He, L., 1989, "An Euler Solution for Unsteady Flows Around Oscillating Blades," *ASME JOURNAL OF TURBOMACHINERY*, Vol. 112, No. 4, pp. 714–722.

He, L., 1993, "A New Two-Grid Acceleration Method for Unsteady Navier–Stokes Calculations," *AIAA Journal of Power and Propulsion*, Vol. 9, No. 2.

He, L., 1998, "Unsteady Flow in Oscillating Turbine Cascade: Part 2—Computational Study," *ASME JOURNAL OF TURBOMACHINERY*, Vol. 120, this issue, pp. 269–275.

Horton, H. P., 1969, "A Semi-Empirical Theory for the Growth and Bursting of Laminar Separation Bubble," A.R.C. CP-1073.

Huff, D. L., 1987, "Numerical Simulation of Unsteady, Viscous, Transonic Flow Over Isolated and Cascade Airfoils Using Deformed Grid," *AIAA Paper No. 87-1316*.

Lindquist, D. R., and Giles, M. B., 1994, "Validity of Linearized Unsteady Euler Equations With Shock Capturing," *AIAA Journal*, Vol. 32, No. 1.

Verdon, J. M., and Caspar, J. R., 1982, "Development of a Linear Unsteady Aerodynamics for Finite-Deflection Cascades," *AIAA Journal*, Vol. 20, No. 9.

Whitehead, D. S., 1982, "The Calculations of Steady and Unsteady Transonic Flow in Cascade," Cambridge University Engineering Department Report, CUED/A-Turbo/TR118.

Unsteady Flow in Oscillating Turbine Cascades: Part 2—Computational Study

L. He

School of Engineering,
University of Durham,
Durham, DH1 3LE, United Kingdom

Unsteady flow around a linear oscillating turbine cascade has been experimentally and computationally studied, aimed at understanding the bubble type of flow separation and examining the predictive ability of a computational method. It was also intended to check the validity of the linear assumption under an unsteady viscous flow condition. Part 2 of the paper presents a computational study of the experimental turbine cascade that was discussed in Part 1. Numerical calculations were carried out for this case using an unsteady Navier–Stokes solver. The Baldwin–Lomax mixing length model was adopted for turbulence closure. The boundary layers on blade surfaces were either assumed to be fully turbulent or transitional with the unsteady transition subject to a quasi-steady laminar separation bubble model. The comparison between the computations and the experiment was generally quite satisfactory, except in the regions with the flow separation. It was shown that the behavior of the short bubble on the suction surface could be reasonably accounted for by using the quasi-steady bubble transition model. The calculation also showed that there was a more apparent mesh dependence of the results in the regions of flow separation. Two different kinds of numerical test were carried out to check the linearity of the unsteady flow and therefore the validity of the influence coefficient method. First, calculations using the same configurations as in the experiment were performed with different oscillating amplitudes. Second, calculations were performed with a tuned cascade model and the results were compared with those using the influence coefficient method. The present work showed that the nonlinear effect was quite small, even though for the most severe case in which the separated flow region covered about 60 percent of blade pressure surface with a large movement of the reattachment point. It seemed to suggest that the linear assumption about the unsteady flow behavior should be adequately acceptable for situations with bubble-type flow separation similar to the present case.

Introduction

As described in Part 1 of this paper (He, 1998), the behavior of bubble-type separation on aeroelastic performance of oscillating low-pressure turbine blades had been experimentally investigated using a linear cascade with the middle blade being oscillated. The experimental data had revealed some distinctive features in amplitude and phase variations of the first harmonic unsteady pressure in the regions of bubble-type separation, in particular around the reattachment point. In the mean time, a set of detailed data had been obtained, which could be used for validations of unsteady viscous flow solvers under current development.

For blade flutter calculations, computational methods would normally be developed for flow around a so-called “tuned cascade,” in which all blades would be oscillating at the same amplitude and frequency and a constant interblade phase angle. The influence coefficient method would be necessarily required to convert the present experimental data to those for a tuned cascade. However, the preliminary analysis of the experimental data left some question on the use of the influence coefficient method. In order to avoid any confusion that might be caused by the validity of the linear assumption, it was decided that as the first step of validating the computational method, a computational code dealing with exactly the same configuration as in the experiment should be developed so that a direct comparison

between the experiment and computation could be made. As described later, this development turned out to be also very useful in assessing the validity of the influence coefficient method.

Numerical Model and Boundary Condition

Unsteady flow Model and Basic Discretization. The unsteady flow field was assumed to be governed by the two-dimensional unsteady Navier–Stokes equations written in the conservative form over a moving grid. The basic discretization followed. The cell-vertex finite volume scheme (Ni, 1981; Denton, 1983) was used to discretize the equations in space. The explicit four-stage Runge–Kutta scheme was used to temporally integrate the discretized equations with the second and fourth-order adaptive smoothing to suppress numerical oscillations (Jameson et al., 1981). A temporal acceleration of the time-marching solution was achieved by using a time-consistent two-grid method. More detailed descriptions of the basic numerical model can be found in other publications (He, 1990, 1993).

Turbulence Model and Treatment of Laminar Separation Bubble. The basic flow solver could be used for either fully laminar flow, or a fully turbulent flow, in which a laminar-to-turbulent transition was assumed to occur at the blade leading edge. For the latter case, the turbulence stress terms are closed by using the conventional Baldwin–Lomax mixing-length model.

It is clear from the experimental observation that for the suction surface short bubble, the unsteady movement of the

Contributed by the International Gas Turbine Institute and presented at the 41st International Gas Turbine and Aeroengine Congress and Exhibition, Birmingham, United Kingdom, June 10–13, 1996. Manuscript received at ASME Headquarters February 1996. Paper No. 96-GT-375. Associate Technical Editor: J. N. Shinn.

transition from laminar to turbulent, which effectively determined the reattachment point, must be modeled if we want to predict the effect of the bubble separation. In the present work, the following simple unsteady transition model was proposed to be used in conjunction with the Navier–Stokes solver.

As described in Part 1 (He, 1998), in Horton's laminar separation bubble model for steady flow (Horton, 1969), the length of the laminar part (i.e., the streamwise distance between the separation point and the transition point) was correlated with the equivalent inviscid flow parameters at the separation point by

$$L_s = 4 \times 10^4 \frac{\mu}{(\rho_e u_e)_s} \quad (1)$$

It was assumed in the present work that this correlation was applicable to an unsteady flow situation in a quasi-steady manner, i.e., it could be applied at each time step. Then as long as the instantaneous laminar separation point was known, the transition point would be known. This effectively would give the turbulent reattachment point, if the immediate turbulent reattachment happened, as expected. Three steps were taken in implementing this quasi-steady model at each time step:

(a) starting the laminar Navier–Stokes solution from the blade leading edge;

(b) detecting the surface laminar separation point and evaluate the length of the laminar part of the bubble (Eq. (1)). The equivalent “inviscid” velocity u_e at the separation point was evaluated using the local static pressure and an equivalent inviscid stagnation pressure P_0 , which was obtained by assuming an isentropic flow process from the inlet stagnation condition;

(c) introducing the turbulent eddy viscosity from the Baldwin–Lomax model after the transition point. In practice, an intermittent region of 2 percent surface length was introduced to avoid a sudden change from a pure laminar solution to a fully turbulent solution.

Multiple-Passage Domain Arrangement and Boundary Condition. Two different multiple blade passage domain arrangements were adopted in the computations. The first one was for direct simulations of the experiment rig configuration; the second one was for a tuned oscillating cascade with a given interblade phase angle.

For a direct comparison with the experiment, a computational domain was chosen to contain eight blade passages. The middle blade was oscillated as in the experiment. A typical mesh arrangement is shown in Fig. 1. At the inlet the one-dimensional nonreflecting condition (Giles, 1990) was used while at exit a fixed back pressure was specified, since in the experiment, the flow at exit was exhausted to an atmospheric condition. On all the blade surfaces, the nonslip velocity condition was applied. At the lower and upper boundaries (A–D and E–H in Fig. 1),

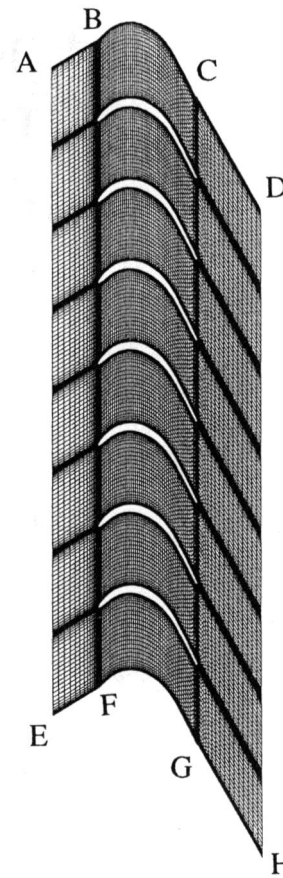


Fig. 1 Multipassage computational domain

the solid wall condition was applied to simulate the effect of top and bottom walls of the wind tunnel. To avoid the ambiguity of the blockage effect due to inlet top and bottom wall boundary layers, the inviscid slip wall condition (zero normal velocity) was applied from the inlet to the leading edge station (A–B and E–F), while the nonslip wall condition was applied from the leading edge to the exit (B–D and F–H), at the lower and upper boundaries.

For a tuned cascade, all blades were oscillated with the same frequency, mode shape, and interblade phase angle. The only different boundary condition was that the direct repeating (periodic) condition, instead of the solid wall condition as mentioned above, was applied at the top and bottom boundaries upstream and downstream of the blade passage, i.e., the flow variables and mesh grid motion would be periodic between A–B and E–

Nomenclature

Am_{p1} = amplitude of first harmonic pressure
 Am_t = amplitude of blade torsion vibration
 C = blade chord length
 Cax = blade axial chord length
 CP = steady pressure coefficient = $(P_0 - P)/(P_0 - P_2)$
 $|CP_1|$ = amplitude of unsteady pressure coefficient ($Am_{p1}/(P_0 - P_1)Am_t$) for linear cascade with single blade oscillating

$|CP_1|$ = amplitude of unsteady pressure coefficient for tuned oscillating cascade
 K = reduced frequency (based on true chord and exit flow velocity)
 P_0 = inlet stagnation pressure
 $P.S.$ = pressure surface
 $S.S.$ = suction surface
 α = blade torsion displacement, positive in anti-clockwise direction
 β_1 = steady inlet flow angle

ϕ = phase angle of first harmonic pressure (single blade oscillating)
 ϕ' = phase angle of first harmonic pressure (tuned oscillating cascade)
 σ = interblade phase angle

Subscripts

0 = steady time-averaged parameter
 1 = first harmonics; inlet parameter
 2 = second harmonics; outlet parameter
 e = inviscid flow parameters
 s = parameters at separation point

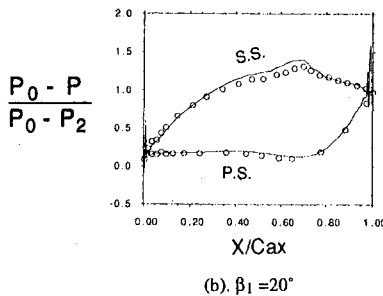
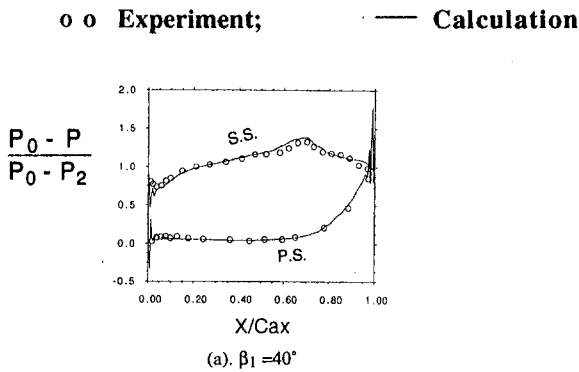


Fig. 2 Steady pressure distribution

F (and between C-D and G-H). In this case the number of blade passages in the computational domain would be chosen according to the interblade phase angle (e.g., two passages for an interblade phase angle of 180 deg).

Computations With Experimental Cascade Configuration

In order to avoid the uncertainty of the linear assumption in the influence coefficient method, it was decided that the experimental rig configuration should be directly simulated first. The computational mesh as shown in Fig. 1 was of 101 mesh points in the streamwise direction and 61 mesh points in the pitchwise direction for each passage. Different mesh densities were also used to examine mesh dependence of the computational results.

It is well known that the convergence of time-marching methods would become very poor at very low Mach number conditions such as in the present experiment (the inlet Mach number was about 0.04). Hence all the calculations were carried out at a higher Mach number condition ($M_1 = 0.15$) with the effect of compressibility still being negligible. The Reynolds number of 2.2×10^5 was used, which was the same as in the experiment for both steady and unsteady cases. For unsteady flow calculations, the reduced frequency was kept the same as in the experiment.

Steady Flow Results. First steady flow calculations were carried out. It was found that a steady solution was very difficult to obtain if the whole flow field was assumed to be laminar. This might be expected because the suction surface separation would become an open-type, which was very unstable. With the bubble transition model, some difficulty in convergence was also encountered in the region of the long leading edge separation bubble on the pressure surface. It should be pointed out that Horton's original bubble model had been based on empirical relations verified mainly against midchord short bubbles and its validity for the long separation bubble near the leading edge was not clear even for steady flows. Also the evaluation of the equivalent inviscid parameters on the separation point would be subject to a large numerical error in the leading-edge region

with high velocity (pressure) gradients. Hence the present calculations were conducted only at either of the following two modes:

- fully turbulent on both suction surface and pressure surface;
- laminar with the bubble transition model on the suction surface and fully turbulent on the pressure surface.

Figure 2 shows the steady surface pressure distributions compared with the experimental data, for the inlet flow angles of 20 and 40 deg. The comparison with the experiment showed good agreement. The calculated velocity vector fields are shown in Fig. 3 for the high inflow angle ($\beta_1 = 40$ deg) and the low inflow angle ($\beta_1 = 20$ deg) conditions. At the inflow angle of 20 deg the boundary layer on the pressure surface separated right from the leading edge and became reattached around 60 percent axial chord (Fig. 3(b)). At the high inflow condition ($\beta_1 = 40$ deg), the existence of the pressure surface separation bubble was also predicted, which started from about 10 percent axial chord and reattached around 25–30 percent of axial chord (Fig. 3(a)). On the other hand, the separation bubble on the suction surface was very small and could not be clearly shown from the velocity vector plots. The calculated surface shear stress distributions (Fig. 4) show a laminar separation bubble starting around 85 percent axial chord and ending around 95 percent axial chord. This can be compared with the experimental observation that the separation bubble started around 75 percent axial chord and ended at 85–90 percent axial chord. The discrepancy in the predicted separation point in comparison with the experiment might be due to the numerical dissipation inherent in the computational scheme. This explanation was supported by the fact that the prediction of the separation point had some apparent mesh dependence. The computational results with a coarser mesh density 100×41 predicted a separation point 5 percent chord length further downstream, compared to that with the mesh density of 101×61 .

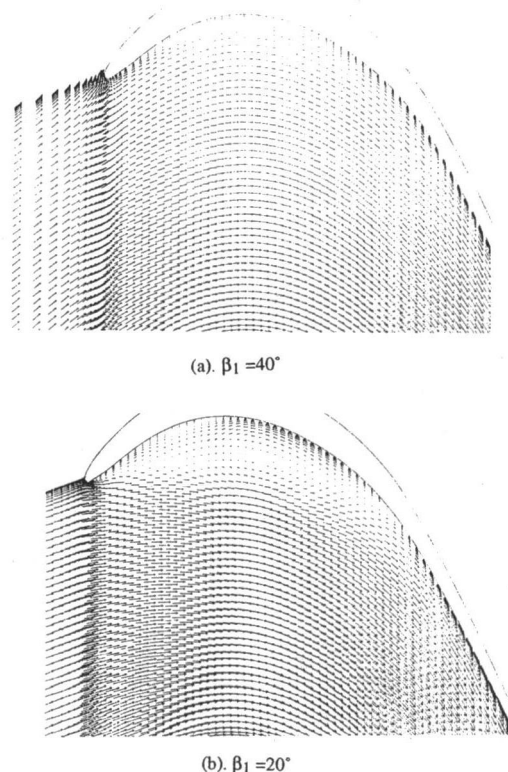


Fig. 3 Calculated velocity vector field

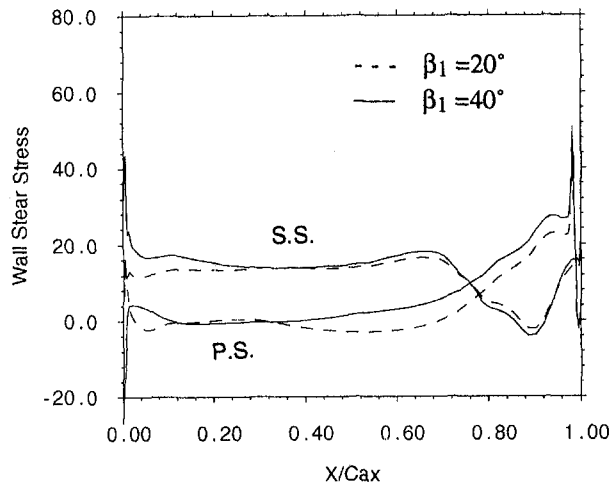
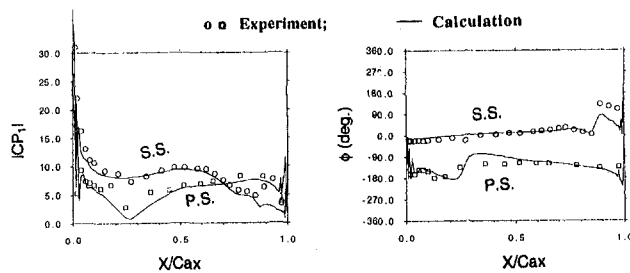


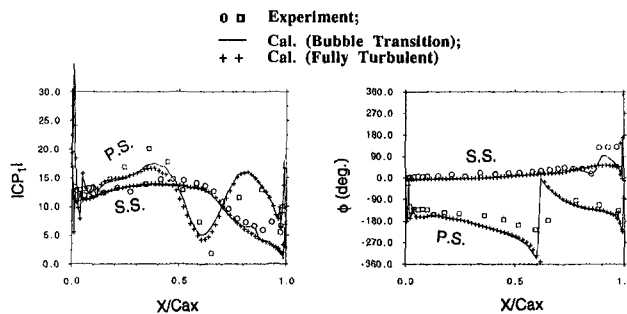
Fig. 4 Calculated surface shear stress

Unsteady Flow Results. The unsteady calculations were carried out with the middle blade being oscillated with the same amplitude ($Am_t = 1$ deg) and reduced frequency ($k = 0.7$) as in the experiment. It should be pointed out that the use of the bubble transition model on the suction was important in obtaining a convergence to a periodic state with the blade vibration frequency, otherwise the laminar separation would become open at the trailing edge, which was unstable due to a purely self-excited instability and did not seem to be locked in to the blade vibration. In all the calculations to be presented and discussed, the convergence to the periodicity defined by the blade vibration was obtained.

The calculated first harmonic pressure coefficient distributions on the middle blade (Blade 0) at the high and low inflow angles are shown in Fig. 5. The corresponding calculated results

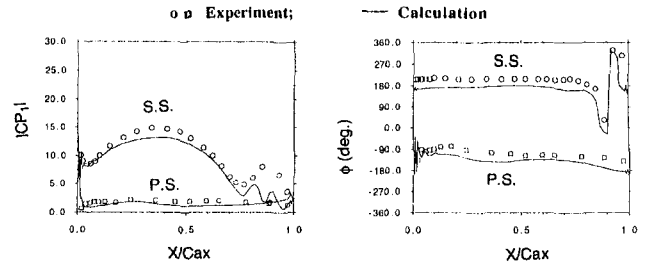


(a). $\beta_1 = 40^\circ$

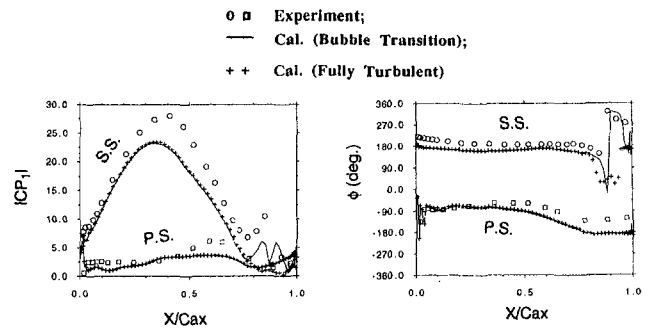


(b). $\beta_1 = 20^\circ$

Fig. 5 Unsteady pressure on middle blade (Blade 0)



(a). $\beta_1 = 40^\circ$



(b). $\beta_1 = 20^\circ$

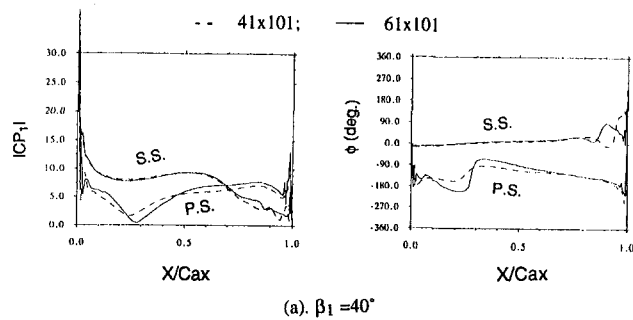
Fig. 6 Unsteady pressure on lower adjacent blade (Blade -1)

on the lower adjacent blade (Blade -1) are shown in Fig. 6. The overall agreement with the experimental data was quite satisfactory.

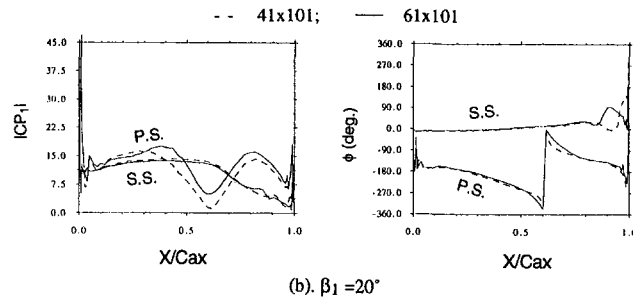
The behaviors of the separation on both the pressure surface and the suction surface were reasonably well predicted. At the low inflow angle ($\beta_1 = 20$ deg) condition, the unsteady pressure amplitude in the region of separated flow was underpredicted. This might be partially due to the lack of resolution of the present structured H mesh in the region of separated shear layer, and partially due to the inadequacy of the present transition/turbulent model. The discrepancy in predicting the pressure surface leading edge long bubble of the middle blade might be responsible for the peak amplitude being underpredicted on the suction surface of the lower blade (Blade -1) as shown in Fig. 6(b).

As far as the suction surface short bubble is concerned, the adoption of the quasi-steady bubble transition seemed to be able to pick up the abrupt phase change around the reattachment point quite well, although the amplitudes in this region were underpredicted. Calculations assuming a fully turbulent flow were also conducted and the comparison of the results (Figs. 5(b) and 6(b)) clearly indicated the influence of the bubble transition as predicted by the quasi-steady model, which was completely missed by the fully turbulent calculations.

The mesh dependence of the results was examined by comparing the results with the density of 101×61 and that of 101×41 , as shown in Fig. 7. The results showed that the mesh dependence was apparent in the regions with flow separation, and more pronounced as the separation became more extensive, which also had a marked effect on the region downstream the reattachment point (Fig. 7(b)). It was found that the calculated unsteady pressure in the separated flow region would be significantly affected if the pitchwise mesh points were less than 30. Considering that the mesh densities used in the present calculations are typical for current unsteady flow calculations with multiple blade passages, caution must be taken when evaluating different turbulence/transition models. This feature of



(a). $\beta_1 = 40^\circ$



(b). $\beta_1 = 20^\circ$

Fig. 7 Calculated first harmonic pressure with different mesh densities

mesh dependence and its implication would need to be further investigated in the future.

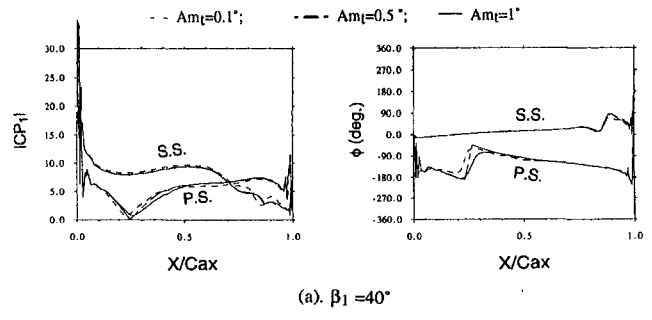
The direct comparison between the computational results and the experimental data has formed a basis for further analysis and discussion in the following section.

Examination of Linearity

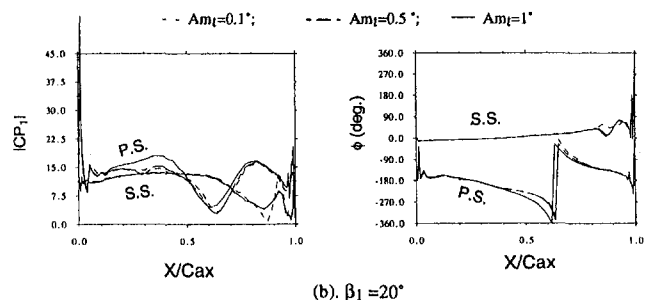
As described in the introduction to this paper, one question of general interest was about the linear assumption of the unsteady flow in response to the blade vibration, which was also fundamental for validity of the influence coefficient method. In particular for the present case there was a massive separation region with a considerable movement of reattachment on the pressure surface at the low inflow angle, which was expected to be very sensitive to small disturbances. Therefore the linearity issue needs to be addressed. Having had the direct comparison of the computational results with the experiment, we have a reasonable confidence in the nonlinear time-marching solver and it appeared that some numerical tests would be very useful. Two different types of calculation were carried out.

Calculations With Different Amplitudes. A simple examination of the linearity would be to obtain unsteady aerodynamic response at different blade vibration amplitudes by nonlinear computations to check if the variation would be linear. Having performed the calculations described above, it was decided that further computations should be carried out for the experimental configuration, but with different amplitudes of the middle blade oscillation.

Since turbomachinery blades were relatively stiff and their vibrations were characterized by small amplitudes, it would probably be more significant to look at amplitudes smaller than 1 deg. Apart from the calculations with the experimental amplitude 1 deg, calculations were also carried out with amplitudes 0.5 and 0.1 deg. The calculated first harmonic unsteady pressure coefficients (normalized by the blade vibration amplitudes) were shown in Fig. 8 for the middle blade at the three amplitudes. It was noted that for the high inflow angle case (Fig.



(a). $\beta_1 = 40^\circ$



(b). $\beta_1 = 20^\circ$

Fig. 8 Calculated first harmonic pressure with different torsion amplitudes

8(a)), the difference in the unsteady pressure distribution between 1 and 0.1 deg amplitudes was quite small, even in the separated flow region on the pressure surface.

The integrated unsteady aerodynamic moments with different amplitudes at the two inflow angle conditions were shown in Fig. 9, in which linear variations based on the values at the amplitude 0.1 deg were also shown for comparison purposes. At $\beta_1 = 40$ deg the moments showed a very linear variation. In this case the maximum deviation at the amplitude 1 deg from the linear variation was around 3 percent. At the low inflow condition, the unsteady pressure distributions on the pressure surface showed some apparent differences for different amplitudes (Fig. 8(b)), indicating nonlinearity. Nevertheless, the effect of this nonlinearity did not seem to be as significant as previously suspected. Although the local maximum difference in the unsteady pressure coefficient distribution were in the magnitude of about 15 percent, the integrated aerodynamic mo-

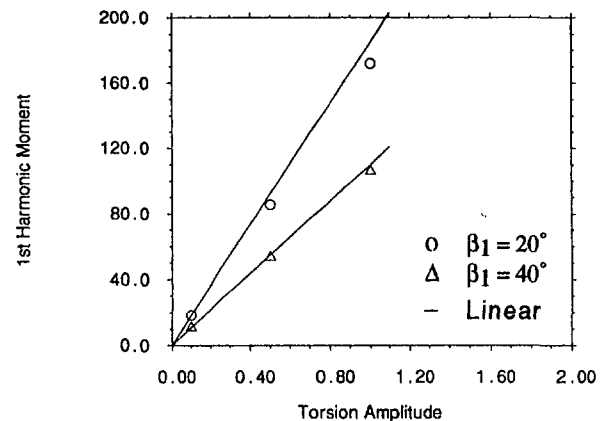


Fig. 9 Unsteady aerodynamic moment with different torsion amplitudes

ment followed closely the linear variation with the maximum deviation from the linear variation being about 5 percent at the amplitude of 1 deg (Fig. 9).

It was also interesting to note that the amplitude dependence of the results (Fig. 8) seemed to be smaller than the mesh dependence (Fig. 7), considering that both the amplitudes and computational mesh used were in the ranges of practical interest and current computational modeling.

Calculations Using Tuned Cascade Model and Using Influence Coefficient Method. As an alternative and further examination on the linearity, the results obtained by using the influence coefficient method could be compared with other results obtained without the linear assumption. Under the linear assumption, the unsteady pressure on a blade in a tuned cascade (i.e., all blade oscillating in the same frequency, the same amplitude and a constant interblade phase angle) could be obtained by a linear superposition of unsteady pressure on all the blades in a cascade in which only one blade was oscillated. For the present cascade configuration with seven blades, we had

$$CP'_1 = \sum_{n=-3}^3 CP_1(n)e^{-in\sigma} \quad (2)$$

where CP'_1 was the unsteady pressure coefficient for a tuned cascade with an interblade phase angle σ ; $CP_1(n)$ was that on the n th blade from the cascade with the middle blade oscillating.

The unsteady pressure for the tuned cascade could be calculated directly using a multiple passages domain and repeating (periodic) boundary condition. Because no assumption concerning the linearity was made, so that the results obtained from the direct multiple-passage tuned cascade calculations could be used as a basis for comparison with those obtained from the influence coefficient method (Eq. (2)). Here for a tuned cascade, two passages were used in the computational domain. Therefore the interblade phase angle was 180 deg.

Figure 10 showed the results of the two different computations at $\beta_1 = 40$ and $\beta_1 = 20$ deg for the interblade phase angle of 180 deg. Overall, these results were very consistent with the numerical tests with different amplitudes as discussed earlier. At the high inflow angle ($\beta_1 = 40$ deg), there was very little indication of nonlinearity, though at this condition there was still considerable flow separation on the pressure surface. It should be mentioned that the apparent phase difference around 25–30 percent axial chord (Fig. 10(a)) was not significant because of the very small local amplitude. Therefore the linear assumption could be regarded as very adequate for this kind of situation. At the low inflow angle ($\beta_1 = 20$ deg) with massive separation (Fig. 10(b)), it appeared there was some indication of nonlinearity in the region on the pressure surface with the massive separated zone. Nevertheless, the difference between these two computations in the worst case was in the range of 10 percent and would not be regarded as big enough to invalidate the linear assumption. From a modeling point of view, all the comparisons seemed to suggest that for the turbine blades with a bubble (closed) type of separation, time-linearized computational methods should be applicable, provided that the viscous effect are properly included.

The superposed unsteady pressures for the tuned cascade were also obtained from the experimental data by using the influence coefficient technique and the results were presented in Fig. 10. The comparison between the experimental and computational results showed some discrepancies. It was quite clear that these discrepancies were mainly due to errors in computational modeling and/or the experimental measurements rather than the linear assumption used in the influence coefficient method. Some of the discrepancies due to the computational modeling were discussed earlier in the direct comparisons with the experimental data, which would give more clear and direct indications for improving computational modeling in the future.

□ Experiment (Influence Coefficient)
 — Calculation (Influence Coefficient)
 - - Calculation (Tuned Cascade)

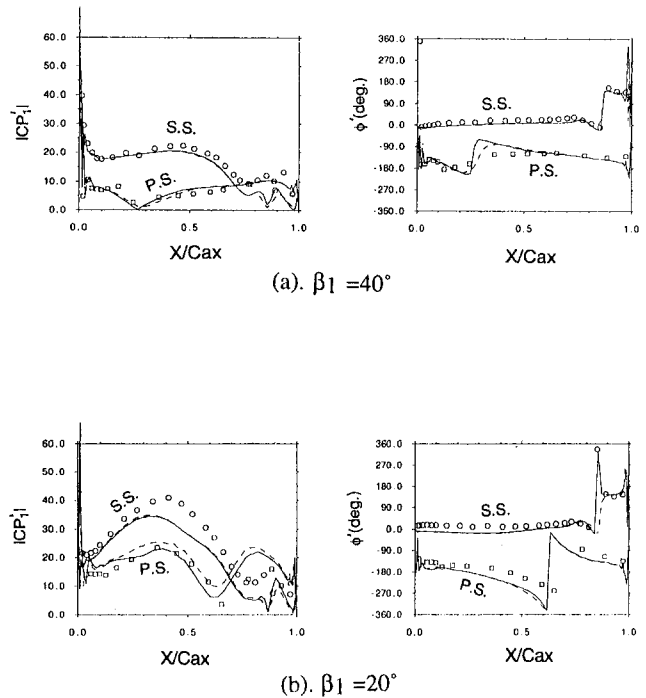


Fig. 10 Unsteady pressure coefficient along axial chord for tuned cascade ($\sigma = 180$ deg)

Concluding Remarks

A computational study of the case has been carried out on a linear turbine cascade for which detailed unsteady pressure data were available as discussed in Part 1 of this paper. A nonlinear time-marching Navier–Stokes solver with a mixing-length turbulence model was used.

The solver was first verified against the experimental data for the original test rig configuration. The comparison between the experiment and computation was reasonably satisfactory, and discrepancies were mainly in the regions of flow separation.

A quasi-steady bubble-transition model was proposed and it was shown that the model could produce a reasonable account of the behavior around the reattachment point, which would be otherwise completely lost in a fully turbulent solution.

The computational results in the region with separation flow revealed markedly more apparent mesh dependence compared to other parts of flow field.

In order to clarify the validity of the linear assumption, two different kinds of numerical test were carried out. All the results from the present calculations consistently showed that nonlinearity was generally small. For the most severe case in which 60 percent pressure surface was covered by a long separation bubble, the maximum error in unsteady pressure associated with the linear assumption was on the order of 10 percent, with the error in integrated parameters being much smaller. Thus the influence coefficient method should be applicable to the present case. The present results seemed to suggest that for bubble-type separation, time-linearized approaches with viscous flow modeling should be able to produce adequately accurate predictions.

Acknowledgments

The experimental work presented in Part 1 was carried out at the Whittle Laboratory, Cambridge University, while the author

worked as a Rolls-Royce Senior Research Fellow at Girton College. The support from Rolls-Royce plc is gratefully acknowledged. The author wishes to thank Professor John Denton (Cambridge) and Dr. Peter Stow (Rolls-Royce) for their help during the course of this study.

References

Denton, J. D., 1983, "An Improved Time Marching Method for Turbomachinery Flow Calculations," *ASME Journal of Engineering for Power*, Vol. 105, pp. 514-524.

Giles, M. B., 1990, "Non-reflecting Boundary Conditions for Euler Equation Calculations," *AIAA Journal*, Vol. 28, No. 12.

He, L., 1990, "An Euler Solution for Unsteady Flows Around Oscillating Blades," *ASME JOURNAL OF TURBOMACHINERY*, Vol. 112, No. 4, pp. 714-722.

He, L., 1993, "A New Two-Grid Acceleration Method for Unsteady Navier-Stokes Calculations," *AIAA Journal of Power and Propulsion*, Vol. 9, No. 2.

He, L., 1998, "Unsteady Flow in Oscillating Turbine Cascade: Part 1—Linear Cascade Experiment," *ASME JOURNAL OF TURBOMACHINERY*, Vol. 120, this issue, pp. 262-268.

Horton, H. P., 1969, "A Semi-Empirical Theory for the Growth and Bursting of Laminar Separation Bubble," A.R.C. CP-1073.

Jameson, A., Schmidt, W., and Turkel, E., 1981, "Numerical Solutions of the Euler Equation by Finite Volume Method Using Runge-Kutta Time-Stepping Scheme," AIAA Paper No. 81-1259.

Ni, R. H., 1981, "A Multiple Grid Scheme for Solving the Euler Equation," *AIAA Journal*, Vol. 20, No. 11, pp. 1565-1571.

On the Interpretation of Measured Profile Losses in Unsteady Wake–Turbine Blade Interaction Studies

H. P. Hodson

W. N. Dawes

Whittle Laboratory,
Cambridge University
Engineering Department,
Madingley Road,
Cambridge CB3 0DY, United Kingdom

The interaction of wakes shed by a moving blade row with a downstream blade row causes unsteady flow. The meaning of the free-stream stagnation pressure and stagnation enthalpy in these circumstances has been examined using simple analyses, measurements, and CFD. The unsteady flow in question arises from the behavior of the wakes as so-called negative jets. The interactions of the negative jets with the downstream blades lead to fluctuations in static pressure, which in turn generate fluctuations in the stagnation pressure and stagnation enthalpy. It is shown that the fluctuations of the stagnation quantities created by unsteady effects within the blade row are far greater than those within the incoming wake. The time-mean exit profiles of the stagnation pressure and stagnation enthalpy are affected by these large fluctuations. This phenomenon of energy separation is much more significant than the distortion of the time-mean exit profiles that is caused directly by the cross-passage transport associated with the negative jet, as described by Kerrebrock and Mikolajczak. Finally, it is shown that if only time-averaged values of loss are required across a blade row, it is nevertheless sufficient to determine the time-mean exit stagnation pressure.

Introduction

This paper considers the effects of unsteady inflow on the stagnation quantities at exit from a turbomachine blade row. The unsteady flow in question arises because of the interactions of the flow fields associated with the stator and rotor blade rows.

One of the first studies of the effects of rotor–stator interactions upon the aerodynamic efficiency of a turbomachine was conducted by Lopatitskii et al. (1970) using a single-stage axial flow turbine. They reported that, depending upon the blade geometry and Reynolds number, the rotor profile loss was between two and four times that of the same cascade operating with steady inflow. It is as a result of investigations such as these that the subject of rotor–stator interactions has received much attention during the past decade or so. The effect of upstream wakes on blade row performance has been of particular interest at the Whittle Laboratory. This is known to be an important contributor to the differences noted between the performance of a given profile in cascade and turbomachine environments (Hodson, 1989).

The effect of unsteady flow on the loss (entropy creation) of a blade row is not the main subject of this paper. However, the loss is usually determined from measurements of the stagnation pressure and stagnation temperature. Unfortunately, the unsteadiness arising from rotor–stator interactions also modifies the stagnation pressure and stagnation temperature fields, irrespective of any change in blade row efficiency. This problem and its consequences in the context of rotor–stator wake interactions are considered here.

One of the first studies of the interaction of rotor wakes with a stationary blade was conducted by Meyer (1958). Figure 1 is a schematic interpretation of his model of the interaction in

the context of a turbine rotor. Each wake is initially represented as a perturbation (the so-called “negative jet”) of a uniform flow. The wakes are transported with the main flow and are chopped into segments by the downstream blade row. Within the passage, the wake segments continue to behave as negative jets. The velocity induced by the negative jet causes a build-up of wake fluid on the suction and a removal of fluid from the pressure surface.

Kerrebrock and Mikolajczak (1970) observed that the circumferentially nonuniform stagnation temperature profile at the exit of a high Mach number compressor stator could be explained by assuming that the stagnation temperature is a convected scalar in unsteady flow. This is interpreted in the present context in Fig. 1. Since the wake represents a defect in rotor-relative stagnation temperature, an increase in the same quantity is to be expected on the suction side of the passage with a commensurate decrease on the pressure side. Actual evidence of the kinematic behavior of wakes in compressors can be found in the experimental data of Adachi and Murakami (1979) and Weyer and Dunker (1983) who, in independent studies, measured the velocity field within the passages of compressor stators.

Smith (1966) noted that as a result of the blade circulation, the wake segments are sheared and stretched as they progress through the blade passage. These phenomena are particularly evident in axial turbines. In one of the first studies of wake-transport in axial turbines, Hodson (1985a, b) traversed the flow within the rotor passage of an axial-flow turbine using hot-wire anemometers. To obtain a picture of the unsteady flow, the time-mean velocity data was subtracted from the phase-locked ensemble averages at each measurement location within the rotor passage. These experimental results and the subsequent numerical predictions of Hodson (1985a, b), Giles (1987), Rai (1987), Korakianitis (1993), and Dawes (1993) confirm that simple kinematic theory can be used to explain the movement of wakes through downstream blade rows, whether in turbines or compressors.

Curtis et al. (1997) have reported an experimental study of profile losses in low-pressure turbine cascades that were sub-

Contributed by the International Gas Turbine Institute and presented at the 41st International Gas Turbine and Aeroengine Congress and Exhibition, Birmingham, United Kingdom, June 10–13, 1996. Manuscript received at ASME Headquarters February 1996. Paper No. 96-GT-494. Associate Technical Editor: J. N. Shinn.

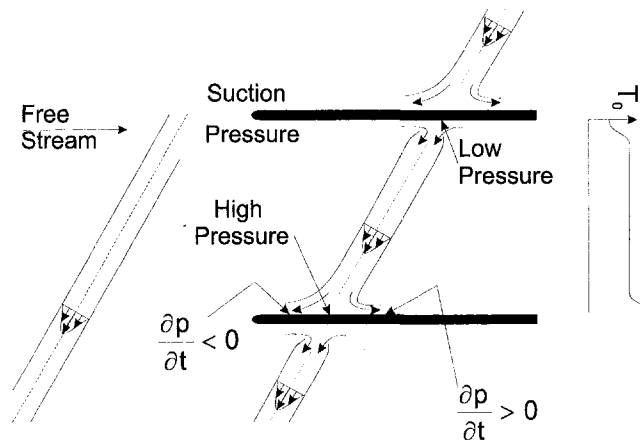


Fig. 1 Representation of a wake as a negative jet and resulting distortion of the relative stagnation temperature profile at exit from a turbine rotor

jected to incoming wakes. Figure 2 shows an example of the data that were acquired one quarter axial chord downstream of a representative cascade using a conventional pressure probe. The results are typical of a large number of measurements. Apart from the blade wakes, the measured exit flow is characterized by nonuniform stagnation pressures in the "free stream." An apparent loss of stagnation pressure appears as a lump toward the pressure side of the passage. An apparent gain (on the face of it violating the second law of thermodynamics) appears on the suction side. The incoming wakes represented a defect in cascade-relative stagnation pressure. Cross-passage transport in the negative jet would be expected to create free-stream nonuniformities of the opposite sign. Therefore, the free-stream nonuniformities in Fig. 2 cannot be explained using the Kerrebrock and Mikolajczak model (1970). Nor is it caused by unsteady effects on the probe used for the measurements. He (1994) presented a preliminary discussion of this problem. The primary purpose of this paper is to describe in detail the true mechanism.

Much of the work on blade-wake interactions at the Whittle Laboratory has been carried out using large-scale facilities. Since Reynolds numbers must be representative in such experiments, the use of large-scale facilities usually means that the experiments are conducted at Mach 0.1 or less. At typical ambient stagnation conditions and at Mach 0.1, the static temperature is only 0.6 K lower than the stagnation temperature and the static pressure is about 700 Pa lower than the stagnation pressure. Systems capable of measuring pressure differences of this order, and much less, are readily available whereas equivalent temperature measurement systems are not. In practice, therefore, only stagnation pressure measurements are available with which to evaluate the entropy creation. Since it will be shown that unsteadiness affects the stagnation pressure and stagnation temperature fields, a secondary purpose of this paper is to discover whether the measurement of stagnation pressure alone is sufficient for the evaluation of thermodynamic loss.

Nomenclature

h = enthalpy
 \dot{m} = mass flow rate
 P = pressure
 \dot{Q} = rate of heat transfer inward
 ρ = density
 R = gas constant
 s = entropy

τ = periodic time
 T = thermodynamic temperature
 t = time
 u = velocity
 ω = vorticity
 \dot{W}_s = power output

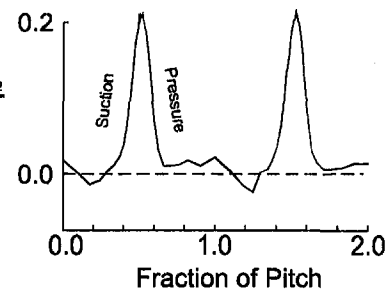


Fig. 2 Time-mean absolute stagnation pressure at one quarter axial chord downstream of blades—measured (see Curtis et al., 1997)

Methodology

Numerical Simulation Using CFD. The numerical simulations that form the basis of this paper were performed with the unsteady Navier–Stokes solver presented by Dawes (1993). This code solves the three-dimensional Reynolds-averaged Navier–Stokes equations on an unstructured, solution-adaptive mesh. The equations of motion are discretized to second-order space accuracy on a cloud of tetrahedrons and integrated forward in time using a standard four-step Runge–Kutta algorithm. A standard blend of second and fourth-order artificial smoothing is applied, by way of a pressure switch.

The turbulence is represented by a low-Reynolds; number form of the $k-\epsilon$ model. It is not known what capabilities this turbulence model might possess in the prediction of wake-blade interactions. In the context of steady flow, studies of wake development behind lobed mixers showed good agreement with accepted wake decay rates (O'Sullivan et al., 1994). Nevertheless, the present study is very much about following the kinematics of the wake away from the blade boundary layers, rather than the details of the wake-boundary layer interaction itself, and so the approach is believed to be adequate. Applications of the calculation method to cylinder vortex shedding and to the wake-rotor interaction case of Hodson (1985a, b) were reported in Dawes (1993), to an axial compressor stage interaction in Dawes (1994) and to a centrifugal compressor stage interaction in Dawes (1995).

In the present study, for reasons of economy and simplicity, a thin spanwise slice of a two-dimensional cascade was simulated and a 1:1 ratio was assumed between upstream wakes and blade count. Table 1 gives further details of the calculated flow.

Experimental Details: Low-Speed Moving-Bar Cascade. The cascade wind tunnel is normally used to study the effects of wakes on the performance of turbine cascades. The wakes are shed from a moving bar system ahead of the blades. The facility is described by Curtis et al. (1997). The very low Mach numbers (typically <0.05) encountered in this facility mean that it is impossible to make useful measurements of the change in stagnation temperature across the cascade. Therefore, only stagnation pressure measurements are available with which to evaluate the entropy creation. The present investigation was undertaken to explain the measurements of stagnation pressure in this facility.

Table 1 Operating conditions and wake details for turbine calculation

Exit Mach number (M_2)	0.6
Exit flow angle (steady flow)	-62.8°
Average loss of incoming wakes	0.035 ($\overline{P_{01}} - P_2$)
Inlet flow angle (relative)	+62.8°
Inlet flow angle (absolute, free stream)	+30.4°
Inlet flow angle (abs., wake centre-line)	+16.6°
Wake width (= $2b$)	0.3 x pitch
Max. stagnation pressure defect (rel)	0.05 $\overline{P_{01rel}}$
Max. stagnation pressure defect (abs)	0.019 $\overline{P_{01}}$
Maximum stagnation temp. defect (rel)	0.0 $\overline{T_{01rel}}$
Maximum stagnation temp. defect (abs)	0.0059 $\overline{T_{01}}$
Mesh Size (nodes) per 2-D plane	5000

A Pitot probe placed downstream of the moving bars was intended to provide the reference cascade inlet stagnation pressure. However, by traversing the Pitot in the axial direction in the absence of the cascade, it was found that the effects of unsteadiness on the readings from this Pitot probe were significant at the selected measurement location for some of the data presented here. For this reason, the stagnation pressure loss and therefore the drag of the stationary bars was determined and this was then used to calculate the change in stagnation pressure across the moving bars. A comparison of the results of the calculation with experimental data (see Schulte and Hodson, 1998) shows that the calculation yields faithful values for the mixed-out stagnation pressure downstream of the moving bars.

Normally, a conventional pneumatic probe system (e.g., a Neptune tube connected by about a metre of small bore tubing to a Scanivalve system) is used to perform pitchwise traverses at midspan to measure the profile loss of the cascade. Here, a Kulite XCS062 (1.5 mm dia) fast response pressure transducer was fitted to the inlet of a Pitot tube and was used to traverse the exit flow alongside the conventional pneumatic probe. The relatively low bar-passing frequency ensures a faithful measurement by the Kulite probe of the instantaneous fluctuations in stagnation pressure. The unsteady data are added to the data provided by the conventional probe to produce the "instantaneous" exit stagnation pressure profiles. Only ensemble-average and time-mean data are reported in this paper. The traverses were performed at a distance 0.5 axial chords downstream of the trailing edge plane of the cascade.

The cascade contains airfoils that are typical of modern thin low pressure turbine blades operating at a typical cruise Reynolds number and flow coefficient. Whereas the cascade geometry and the inlet velocity triangle of the cascade were identical to that used by Curtis et al. (1997), the diameter and spacing of the moving bars were doubled so that the wake was greater in intensity and the relative pitch of the bars and cascade was approximately unity. Under these conditions, the cascade simulates a stator blade subjected to incoming rotor wakes rather than the opposite situation investigated by Curtis et al. Table 2 provides details of the wakes shed by the moving bars.

Results and Discussion

Theory. The question of the relevance of stagnation pressure measurements to assess entropy creation in the unsteady environment of turbomachines has received little attention in

the literature. Only the work of Epstein et al. (1989) is known to the authors. They examined the effect of potential interactions between compressor rotor and stator blades on the measurement of rotor efficiency. Their study shows how the difference between the actual and the perceived adiabatic efficiency of the rotor varies as the positions of a stagnation pressure probe and a stagnation temperature probe vary in the circumferential direction when placed between the rotor and stator blades. The present paper complements the study of Epstein et al.

As the wake segments convect through a blade passage, they create fluctuations in the velocity and static pressure. These are especially pronounced near to the surface. Greitzer (1984) points out that kinematic model of Kerrebrock and Mikolajczak (1970) does not consider the effects of fluctuating static pressures on the time-mean stagnation quantities. Yet, it is well known that the stagnation enthalpy of a particle changes as it traverses an inviscid flow where the static pressure fluctuates. This may be written

$$\frac{Dh_0}{Dt} = \frac{1}{\rho} \frac{\partial p}{\partial t} \tag{1}$$

Dean (1959) showed that this form of the First Law of Thermodynamics is consistent with the fact that in the case of a turbine rotor, where the stagnation enthalpy falls, a stationary observer would see, at a fixed viewpoint, a decreasing pressure with time (i.e., $\partial p / \partial t < 0$) as first the pressure side and then the suction side of the passage passes the observer's viewpoint.

The Second Law of Thermodynamics relates changes in stagnation pressure and stagnation enthalpy by

$$T_0 ds = dh_0 - \frac{1}{\rho_0} dp_0 \tag{2}$$

where s is the entropy. Equations (1) and (2) together reveal that whenever the flow is *unsteady*, the stagnation enthalpy (or stagnation temperature) and the stagnation pressure of a given particle may *not* in general remain constant, even if the flow is isentropic. In particular, changes in stagnation temperature may generate commensurate changes in stagnation pressure without affecting the thermodynamic loss. The phenomenon of energy separation, as this effect is sometimes called, is often found in von Karman vortex streets.

Unsteady Flow Field. For convenience, the computational domain is taken to represent the absolute frame of reference and the wake, the relative frame of reference in the discussion that follows.

Considerable insight into the flowfield was obtained from the numerical simulations. Figure 3 shows a composite view of the unsteady velocity vectors (instantaneous minus the time-mean) and the entropy field at a certain instant in time. Plots such as these have been used by many authors to describe wake-blade interactions. The entropy contours are plotted as the quantity

Table 2 Wake details for turbine cascade

Average loss of incoming wakes (Curtis et al)	0.032 ($\overline{P_{01}} - P_2$)
Average loss of incoming wakes	0.032 ($\overline{P_{01}} - P_2$)
Pitch of bars/Cascade Pitch (Curtis et al)	0.57
Pitch of bars/Cascade Pitch	1.15
Inlet flow angle (relative)	+62.8°
Inlet flow angle (absolute - free stream)	+30.4°

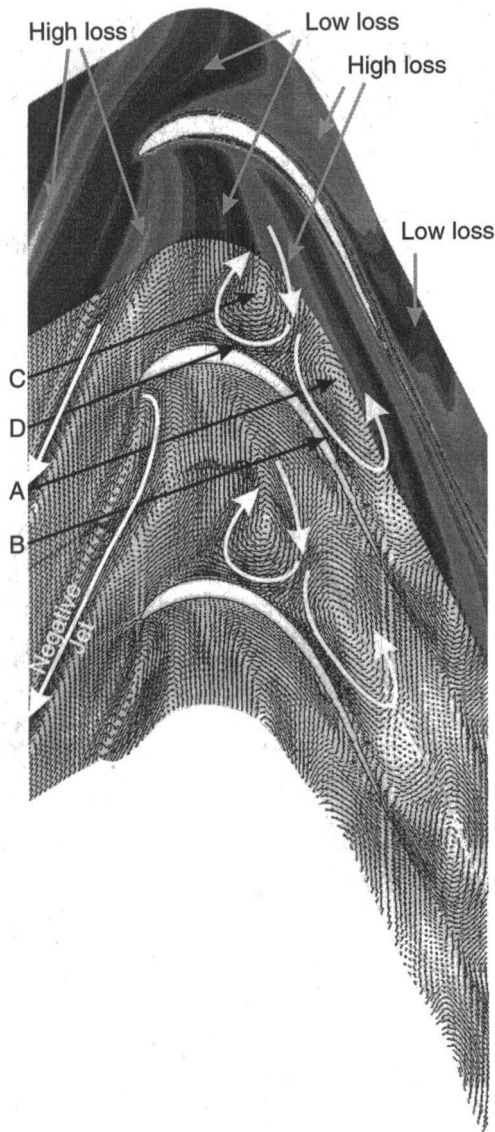


Fig. 3 Predicted contours of entropy and unsteady velocity vectors at one instant in time (contours increase cyclically through black, grey, white)

$$P_{01} \exp\left(-\frac{s-s_1}{R}\right) \quad (3)$$

where P_{01} and s_1 are the time-mean values at inlet. This quantity represents the entropy within the flow as an equivalent (stagnation) pressure. Since entropy is convected by the flow, the incoming wakes may be identified by lower values of the above quantity. The entropy contours of Fig. 3 show that as a wake shed from a moving source passes through the computational domain, it experiences the bowing, chopping, stretching, and shearing, which may be explained using kinematic principles. Owing to the relatively high loading of this blade row, the distortion of the wake segments is very pronounced.

In the case of a compressor, Kerrebrock and Mikolajczak argued that variations in the time-mean stagnation temperature field at exit from a stator downstream of a rotor may be accounted for by examining the redistribution of flow that takes place due to the unsteady velocity field (see Fig. 1). In the present study the maximum perturbation in absolute velocity at inlet amounts to 13.5 percent of the mean exit velocity (25.5 percent of the mean inlet velocity). The unsteady velocity vec-

tors of Fig. 3 reveal the existence of the so-called "negative jet" at inlet to the blade row. It also shows that this phenomenon persists as the wakes progress through the blade row. As expected, a recirculating velocity field is established on each side of the wake as the wake enters the blade row. The cross-passage transport tends to move fluid and therefore entropy from the pressure toward the suction side of the blade passage. This was shown schematically in Fig. 1.

The maximum unsteady velocity in Fig. 3 is 17 percent of the mean exit velocity (similar to that at the inlet) and is to be found near the centerline of the wakes between the regions labeled A and C. This magnitude is a measure of the strength of the cross-passage transport. From Fig. 3, it can be seen that approximately one wake passing cycle is required to convect the bulk of the wake-segment through the blade passage. In this time, a particle at the centerline of the wake will have moved a maximum distance equivalent only to approximately one quarter pitch relative to the adjacent free stream. The movement is toward the suction side of the passage. It causes an increase in the time-averaged entropy (loss) on the suction side of the passage, and a decrease on the pressure side as free-stream fluid replaces the wake fluid.

Figure 4 presents the predicted pitchwise distribution of the entropy at one half axial chord downstream of the cascade. The entropy is plotted as a loss coefficient based on the quantity defined in Eq. (3). The time-mean, maximum, and minimum values are shown across two blade pitches. Figure 4 shows that relative to the mean, wake fluid (i.e., loss) has on average accumulated toward the suction side of the passage (higher loss) while free-stream fluid has accumulated toward the pressure side (lower loss). Between the wakes, the predicted mean value rises approximately from $-0.014(\bar{P}_{01} - P_2)$ to $0.024(\bar{P}_{01} - P_2)$. If the lower half (i.e., suction side) of each passage were to contain all of the incoming wake fluid, the mean value of loss (neglecting any entropy creation) would be approximately $0.035(\bar{P}_{01} - P_2)$ in this half of the passage, with an equally negative value of $-0.035(\bar{P}_{01} - P_2)$ in the other half. The predicted free-stream variation in time-mean entropy (loss) is consistent with the magnitude of the cross-passage transport velocities noted above.

The effect of the cross-passage transport can also be seen in the amplitude of the entropy fluctuations as indicated by the

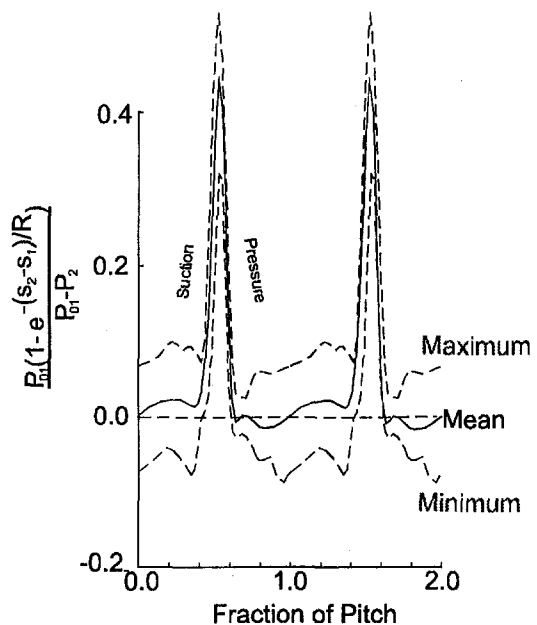


Fig. 4 Time-mean, maximum and minimum entropy at one half axial chord downstream of blades—predicted

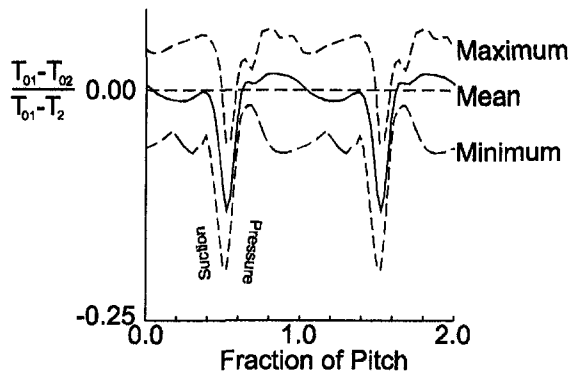


Fig. 5 Time-mean, maximum, and minimum absolute stagnation temperature at one half axial chord downstream of blade—predicted

difference between the maximum and minimum values. In the free stream, near the pressure side of the wake, this difference has diminished. Elsewhere in the free stream, the amplitude is almost constant. The reduction near the pressure side suggests that the each wake has moved approximately one quarter pitch relative to the adjacent free stream by the time it reaches the location corresponding to Fig. 4.

Table 1 shows that in the wake-relative frame of reference, the wake appears as a reduction in stagnation pressure ($0.05\bar{P}_{01rel}$) with constant stagnation temperature. In the absolute frame of reference, the wake appears to the cascade as a region of low stagnation pressure ($\Delta P_{0max} = 0.019P_{01}$) and a region of low stagnation temperature ($\Delta T_{0max} = 0.0059T_{01}$), so that the fluctuations in stagnation pressure and stagnation temperature contribute equally to the fluctuations in entropy. If the cross-passage transport model of Kerrebrock and Mikolajczak were to be applied to the convection of the stagnation temperature (enthalpy) and stagnation pressure within the wakes, then in the absence of any other effects, free-stream time-mean exit distributions similar to that of the entropy (see Fig. 4) would be expected as the incoming wake has a deficit of these stagnation quantities.

Figures 5 and 6 present the predicted distributions of absolute stagnation temperature and absolute stagnation pressure at one half axial chord downstream of the cascade. Time-mean, maximum, and minimum variations and rms fluctuations are shown as coefficients. A comparison of the two figures shows that in general, the distributions of the time-mean values are very similar in the free stream. The highest values are to be found nearer the pressure side while the lowest occur toward the suction side. These variations do not in general mimic the loss (entropy) variations in the free stream shown in Fig. 4. Therefore, a mechanism must exist that not only causes an effect that is opposite in sign to that of the negative jet but also is of greater significance. An examination of the unsteady entropy field, which is the approach favored by many authors, cannot reveal this mechanism.

Comparing the maximum amplitudes of the stagnation quantities in Figs. 5 and 6 with the inlet deficits given in Table 1 shows that the maximum amplitudes of the stagnation pressure and stagnation temperature fluctuations are predicted to be about twice those that arise in the inlet flow. Furthermore, the pitchwise variations of the amplitude of the stagnation pressure and stagnation temperature (enthalpy) within the free stream also show a degree of similarity. These observations suggest that the mechanism that is sought must lie in the unsteady physics associated with the stagnation enthalpy transport equation (Eq. (1)).

At this point, it is useful to compare the measured unsteady exit flow data with that predicted to demonstrate some confidence in the numerical simulations and any interpretations that arise from them. Time-mean, maximum, minimum, and rms

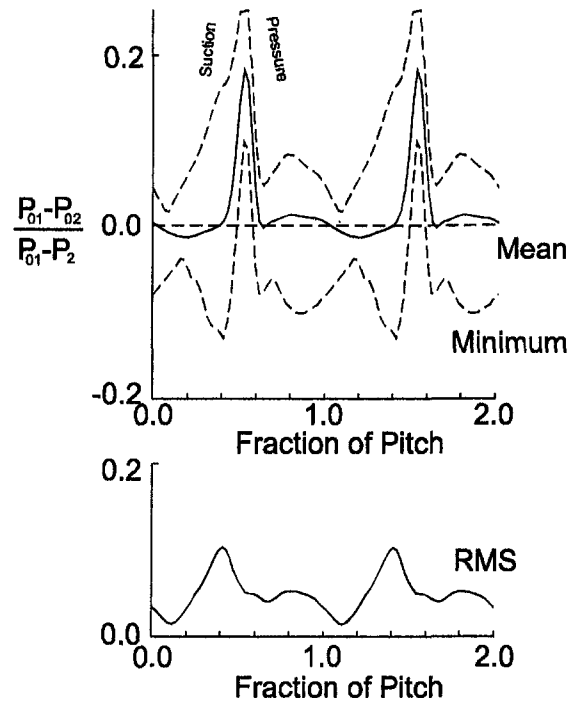


Fig. 6 Time-mean, maximum, minimum, and rms absolute stagnation pressure one half axial chord downstream of blades—predicted

fluctuations of the measured exit ensemble-average stagnation pressures are shown in Fig. 7. A comparison of the predictions in Fig. 6 with the measurements of Fig. 7 is encouraging. In the free stream, the pitchwise variation of the time-mean is well predicted and the rms fluctuations are in good quantitative

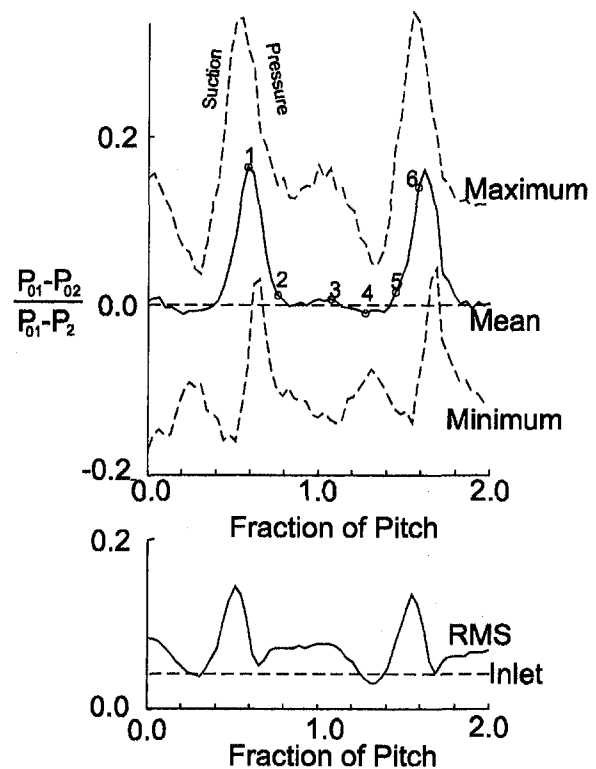


Fig. 7 Time-mean, maximum, minimum, and rms of phase-locked average stagnation pressure one half axial chord downstream of blades—measured

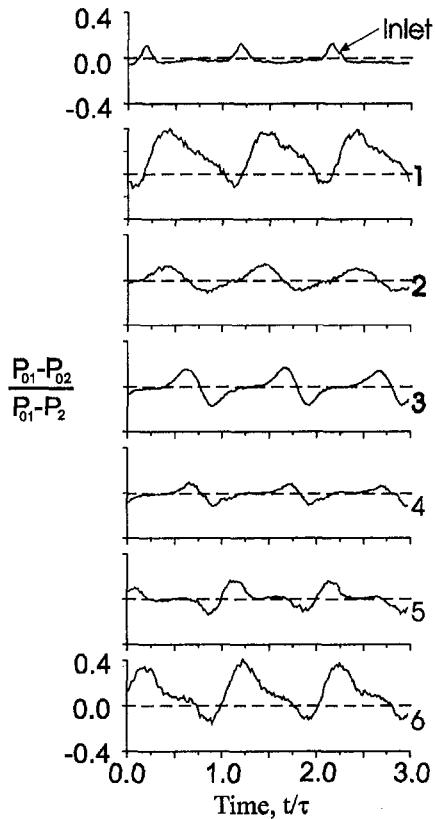


Fig. 8 Phase-locked average stagnation pressure one half axial chord downstream of blades—measured (for locations, see Fig. 7)

agreement. The very large unsteady envelope is well represented. The rms distributions shown in Figs. 6 and 7 show that the fluctuations in stagnation pressure are greater almost everywhere at exit than at inlet to the cascade. Indeed, the maximum–minimum variation is rather larger than the depth of the cascade wakes.

Figure 8 shows the time-histories of the measured ensemble-averaged stagnation pressures at inlet (top trace) and at various pitchwise locations across the exit traverse plane (lower traces). The exit locations are numbered 1 to 6 and are shown in Fig. 7. Three wake-passing cycles are shown in each trace. It can be clearly seen that the fluctuations in the traces at exit are much larger than those at inlet. Within the free stream (locations 2–5), the increased magnitude of the fluctuations must have their origin within the unsteady fluid dynamics of the flow field.

The key to understanding the unsteady phenomenon lies in an exploration of the predicted unsteady (instantaneous minus time-mean) static pressure field and its variation with time. The time-mean static pressure field is of much less consequence. Contours of the unsteady static pressure for the same instant as in Fig. 3 are plotted in the lower part of Fig. 9. The pressure perturbations within the passage arise largely as a result of the recirculating unsteady velocity field that is established within the blade passage. The center of rotation on the downstream side of the wake (region A) is associated with a region of low unsteady static pressure. At the instant shown, this region of low unsteady pressure extends across passage with the region of lowest unsteady pressure (region B) adjacent to the suction surface. A further, more localized and less pronounced region of low unsteady pressure is associated with the center of the recirculating flow on the upstream side of the wake (region C) at this instant in time. Below region C is the region of highest unsteady static pressure. It is not a coincidence that this region (region D) is located near to

where the centerline of the negative jet impinges on the blade surface. The unsteady pressure decreases along the suction surface just upstream of region D.

An examination of the movement of regions A–D during a wake-passing cycle would reveal that these features arise as the wake enters the blade passage, or soon after, and that although their associated magnitudes change, they tend to convect with the main flow. Indeed, an examination of the unsteady blade-surface static pressures would show that the perturbations on the pressure side propagate at the same speed as the flow in the center of the passage. On the suction side, a more complicated picture arises though again, a convective characteristic is discernible. While recognizing the pressure field is subject to more than just convective influences, the simple kinetic model does seem to explain some of the features of the unsteady static pressure field.

Equations (1) and (2) show that the stagnation pressure and temperature of a particle will change as the particle traverses an unsteady static pressure field (i.e., a nonzero $\partial p/\partial t$ field). Figure 9 contains, in the upper passage, a contour plot of the quantity $\partial p/\partial t$ at the same instant as Fig. 3. In general, the largest values of $|\partial p/\partial t|$ arise near to the leading edge as the wake arrives in that vicinity. However, Figs. 3 and 9 do not correspond to that moment. For these figures, a time was chosen

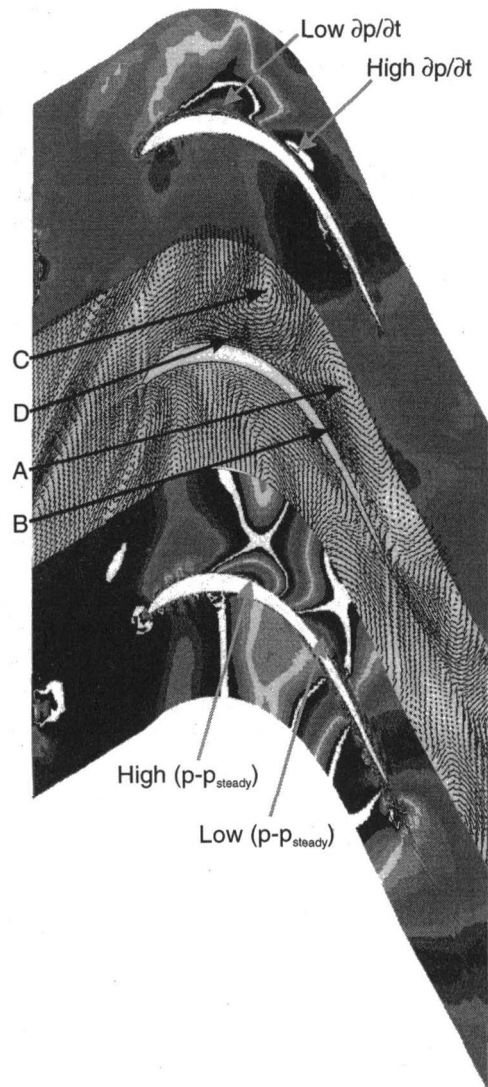


Fig. 9 Contours of $\partial p/\partial t$ (upper) and unsteady static pressure (lower) at same instant as in Fig. 3 (contours increase cyclically through black, grey, white)

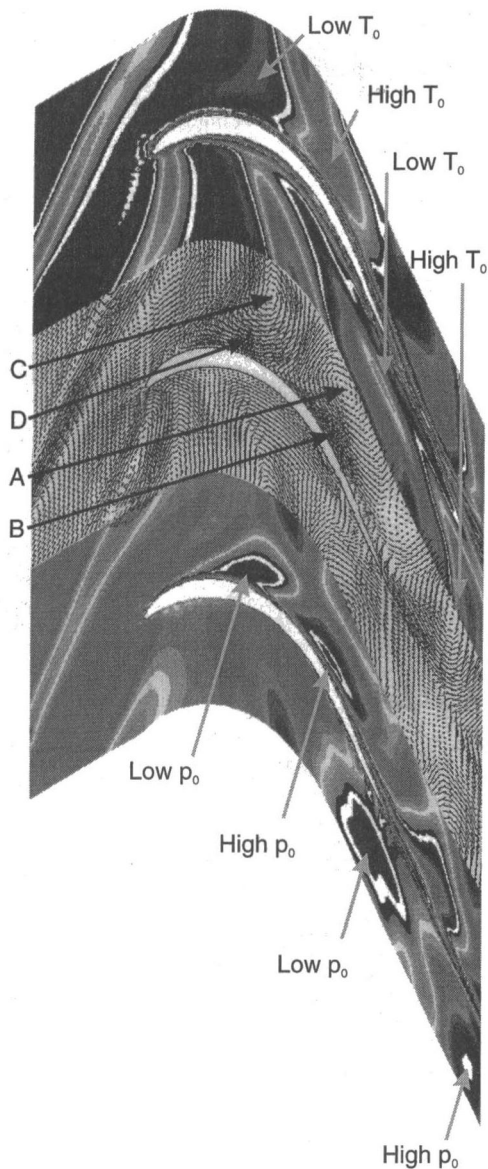


Fig. 10 Contours of absolute stagnation temperature (upper) and absolute stagnation pressure (lower) at same instant as in Fig. 3 (contours increase cyclically through black, grey, white)

when the distortion of the wake-segment within the blade passage is well established. At this instant, Fig. 9 shows that the region of most negative $\partial p/\partial t$ lies near to the suction surface, just upstream of region D, the region of highest unsteady static pressure. The region of most positive $\partial p/\partial t$ can be found between the local pressure maximum (region D) and minimum (region B). These regions of positive and negative $\partial p/\partial t$ arise because $\partial p/\partial t$ represents the rate of change of static pressure at a fixed point and the unsteady pressure maximum (region D) and minimum (region B) tend to convect with the main flow.

Contours of the stagnation temperature and stagnation pressure at the same instant as in Fig. 3 are presented in the upper and lower passages of Fig. 10 respectively. The intervals of the contours of the stagnation quantities represent the same changes of entropy as do the contours in Fig. 3. The incoming wakes may be identified using either of the stagnation quantities in Fig. 10. Moreover, it requires only a cursory examination of the figure to see that there are much larger variations within the flow than those associated directly with the entropy defect within the upstream wakes. For example, the difference between

the maximum and minimum values of the "free-stream" stagnation pressure in Fig. 10 is approximately five times that of the initial wake defect. The growth in the magnitude of the stagnation pressure fluctuations could also be seen in the measurements presented in Fig. 8. As the wakes do not mix out, changes commensurate with the stagnation pressure changes arise in the stagnation temperature field.

The largest perturbations of the stagnation quantities arise near the suction surface. A comparison of the contour map of $\partial p/\partial t$ in Fig. 9 with those of Fig. 10, together with Eqs. (1) and (2) explains why this is so. There is a correspondence between the locations of the additional peaks and troughs in the stagnation quantities and the regions of high and low $\partial p/\partial t$. Once created, the peaks and troughs in the stagnation quantities essentially convect with the flow. However, the unsteady static pressure field is partially convective and so is the $\partial p/\partial t$ field. Thus, some particles tend to be convected within a region of mostly positive $\partial p/\partial t$ and so their stagnation pressure and enthalpy tend to increase. Others tend to always be in a region of negative $\partial p/\partial t$ and so the above stagnation quantities will decrease. In this way, the peaks and troughs tend to be reinforced and large amplitude fluctuations of the stagnation quantities begin to appear.

It has been explained that the unsteady static pressure field (strictly, $\partial p/\partial t$) gives rise to variations in time and space of the stagnation pressure and stagnation temperature. It has also been shown the pitchwise variations of the same time-mean stagnation quantities cannot be explained using the negative jet model of Kerrebrock and Mikolajczak. Though this effect undoubtedly exists, it does not dominate. The cause lies in the nature of the unsteady flow field. On average, more particles on the suction side of the passage experience a more positive $\partial p/\partial t$ for longer than a negative value. This is believed to be associated with the skewed nature of the wake and the unsteady recirculation of the flow that creates a more intense region of low unsteady static pressure on the downstream side of the wake (regions A and B). In a compressor, the distortion effects are much less pronounced and the negative-jet model of Kerrebrock and Mikolajczak may well dominate.

Determination of Loss. We now turn to the question of how to assess thermodynamic loss.

It has been shown that the stagnation pressure and stagnation enthalpy fluctuations that arise due to the unsteady static pressure field are significant in the present context. Fast response pressure-transducer-based probes allow us to measure the instantaneous stagnation pressure with relative ease. The measurement of the instantaneous stagnation temperature is much more difficult, though possible in specific circumstances. Without the instantaneous stagnation temperature, it will not be possible to distinguish between those changes in stagnation pressure due to unsteadiness and those due to viscous phenomena and so the instantaneous loss cannot be determined.

The time-mean entropy generation is now considered. Applying the First Law of Thermodynamics to a control volume containing the flow through a whole blade passage at a given instant leads to the result that

$$(\dot{Q} - \dot{W}_x) = \left(\int_{\text{pitch}} h_{02} d\dot{m}_2 - \int_{\text{pitch}} h_{01} d\dot{m}_1 \right) + \frac{dE_{CV}}{dt} \quad (4)$$

where dE_{CV}/dt represents the rate of change of energy (internal plus kinetic) of the control volume. Although there are unsteady forces acting upon the control volume, the point of application of these forces (i.e., the blade surfaces) does not move. Consequently, there is no work transfer. Given that the flow is also adiabatic, the left-hand side of Eq. (4) is equal to zero. Integrating this equation over one wake-passing cycle leads to the result that

$$\int_{\text{pitch}} \overline{h_{02} dm_2} = \int_{\text{pitch}} \overline{h_{01} dm_1} \quad (5)$$

where the overbars denote the time-mean. Since the time-mean mass flow rate is the same at inlet and at exit, there is no change in the time-mean stagnation enthalpy across the cascade. Equation (5) is true, whether or not the flow is uniform at inlet to or exit from the control volume since no work is transferred.

Here we consider the case of incompressible flow as found in the experiments. For small changes, Eqs. (2) and (5) together lead to the result that the time-mean, pitchwise-averaged entropy change is given by

$$\dot{m}(\bar{s}_2 - \bar{s}_1) \approx \frac{R}{P_{01}} \left(\int_{\text{pitch}} \overline{p_{01} dm_1} - \int_{\text{pitch}} \overline{p_{02} dm_2} \right) \quad (6)$$

Equation (6) shows that in the case of the experiments described in this paper, it is sufficient to measure the instantaneous change in stagnation pressure (and the mass flows) across the stationary cascade in order to evaluate its stagnation pressure loss coefficient. Alternatively, the exit conditions may be determined using conventional pneumatic probes once the unsteady flow has dissipated and become steady.

Unfortunately, the exit flow is rarely steady at the location where exit traverses are made. An assessment of the importance of this aspect can be obtained from a simple calculation that represents the "worse-case" scenario. A mixing calculation may be performed in which two parallel streams of identical entropy, mass flow and static pressure but different stagnation temperature and stagnation pressure are mixed adiabatically and in the absence of work to form a single stream occupying the same total flow area. The mean stagnation pressure must fall as entropy is created in the mixing process. If the difference in stagnation temperature between the two streams is equal to the maximum amplitude predicted at exit from the cascade ($0.13 (\bar{T}_{01} - T_2)$) by the CFD code, then the mixing process generates an entropy increase equivalent to 0.5 percent of the isentropic exit dynamic pressure (i.e., $0.005 (\bar{P}_{01} - P_2)$).

In practice, the actual mixing loss associated with the unsteady flow will be less than that calculated above. To investigate this aspect further, an inviscid (Euler) calculation was used to predict the unsteady flow through the cascade. The exit Mach number was again 0.6 in the calculation. The levels of energy separation predicted by this approach were only slightly greater than those predicted by the viscous (Navier–Stokes) method. Mixing out the unsteady flow at the exit of the inviscid flow field generated an increase in entropy equivalent to only 0.25 percent of the exit dynamic pressure. This relatively small rise in entropy indicates that the so-called energy separation that arises in the unsteady flow and which here manifests itself as commensurate changes in stagnation pressure and temperature produces little loss, even at the realistic Mach numbers encountered in the predictions. For comparison, mixing out the incoming wakes at inlet amounts to a loss equal to 0.13 percent of the isentropic exit dynamic pressure (i.e., $0.0013 (\bar{P}_{01} - P_2)$). It would seem that for low-speed applications at least, and quite probably for higher Mach number cases, it is sufficient to measure the stagnation pressure change across the cascade to determine the entropy creation.

Conclusions

Measurements of stagnation pressure at exit from a turbine cascade that is subjected to incoming wakes have been presented. The measured exit flow is characterized by the presence of large pitchwise variations in stagnation pressure in the "free stream," some of which appears as an apparent loss of stagna-

tion pressure toward the pressure side of the passage and some as an apparent gain near the suction side.

The cross-passage transport that is embodied in the negative jet model of Kerrebrock and Mikolajczak is shown to exist but cannot be used to explain the observed nonuniformity in stagnation pressure at the exit from the cascade because it is in the wrong direction.

Predictions and measurements of the unsteady flow field reveal fluctuations in stagnation pressure and stagnation temperature that are greater than the defects that occur in the wake at inlet to the blade row in question. The large stagnation temperature fluctuations are caused by large variations in $\partial p/\partial t$, which are mostly associated with the suction side flow and are driven by the wake interaction. The flowfield predictions of entropy show little evidence of nonuniformity outside the blade wakes, which suggests that many of the stagnation pressure fluctuations are isentropic in origin and therefore related to variations in stagnation temperature. The observed time-mean nonuniformity in stagnation pressure at cascade exit is a direct consequence of these unsteady processes.

Although the fluctuations are relatively large, the time-mean change in stagnation pressure across the cascade is shown to be representative of the entropy generation within the blade row. The mixing loss associated with the unsteady flow field increases by a factor of two as the wakes pass through the blade row, but even at exit, this only amounts to about 0.25 percent of the exit dynamic pressure.

Acknowledgments

The authors wish to thank R. J. Howell and E. M. Curtis of the Whittle Laboratory for providing some of the experimental data presented in this paper. They also wish to thank N. A. Cumpsty for his helpful comments.

References

- Adachi, T., and Murakami, Y., 1979, "Three Dimensional Velocity Distribution Between Stator Blades and Unsteady Force Due to Passing Wakes," *JSME*, Vol. 22, No. 170, Aug., pp. 1074–1082.
- Curtis, E. M., Hodson, H. P., Banieghbal, M. R., Howell, R. J., and Harvey, N. W., 1997, "Development of Blade Profiles for Low-Pressure Turbine Applications," *ASME JOURNAL OF TURBOMACHINERY*, Vol. 119, pp. 531–538.
- Dawes, W. N., 1993, "Simulating Unsteady Turbomachinery Flows on Unstructured Meshes Which Adapt Both in Time and Space," *ASME Paper No. 93-GT-104*.
- Dawes, W. N., 1994, "A Numerical Study of the Interaction of a Transonic Compressor Rotor Overtip Leakage Vortex With the Following Stator Blade Row," *ASME Paper No. 94-GT-156*.
- Dawes, W. N., 1995, "A Simulation of the Unsteady Interaction of a Centrifugal Impeller With Its Vaned Diffuser: Flow Analysis," *ASME JOURNAL OF TURBOMACHINERY*, Vol. 117, pp. 213–222.
- Dean, R. C., 1959, "On the Necessity of Unsteady Flow in Fluid Machines," *ASME Journal of Basic Engineering*, Vol. 81, pp. 24–28.
- Epstein, A. H., Giles, M. B., Shang, T., and Sehra, A. K., 1989, "Blade Row Interaction Effects on Compressor Measurements," *Proc. AGARD Conf PEP 74a on Unsteady Flows in Turbomachines*, AGARD CP 468.
- Giles, M. B., 1987, "Calculation of Unsteady Wake/Rotor Interactions," *AIAA Paper No. 87-0006*.
- Greitzer, E. M., 1984, "An Introduction to the Unsteady Flow in Turbomachines," in *Thermodynamics and Fluid Mechanics of Turbomachinery*, AGARD Special Course, Ucer, A. S., and Stow, P., eds.
- He, L., 1994, "Unsteady Flows and Flutter," *Advanced Programme for Industry*, Cambridge Univ.
- Hodson, H. P., 1989, "Modelling Unsteady Transition and Its Effects on Profile Loss," *Proc. AGARD Conf PEP 74a on Unsteady Flows in Turbomachines*, AGARD CP 468.
- Hodson, H. P., 1985a, "An Inviscid Blade-to-Blade Prediction of a Wake-Generated Unsteady Flow," *ASME Journal of Engineering for Gas Turbines and Power*, Vol. 107, pp. 337–344.
- Hodson, H. P., 1985b, "Measurements of Wake-Generated Unsteadiness in the Rotor Passages of Axial Flow Turbines," *ASME Journal of Engineering for Gas Turbines and Power*, Vol. 107, pp. 467–476.
- Kerrebrock, J. L., and Mikolajczak, A. A., 1970, "Intra-stator Transport of Rotor Wakes and Its Effect on Compressor Performance," *ASME Journal of Engineering for Power*, Vol. 92, pp. 359–368.
- Korakiantis, T., 1993, "On the Propagation of Viscous Wakes and Potential Flow in Axial-Turbine Cascades," *ASME JOURNAL OF TURBOMACHINERY*, Vol. 115, pp. 118–127.

Lopatitskii, A. O., et al., 1970, "Energy Losses in the Transient State of an Incident Flow on the Moving Blades of Turbine Stages," *Teploenergetika*, Vol. 17, No. 10, pp. 21–23.

Meyer, R. X., 1958, "The Effect of Wakes on the Transient Pressure and Velocity Distributions in Turbomachines," *ASME Journal of Basic Engineering*, Vol. 80, pp. 1544–1552.

O'Sullivan, M. N., Waitz, I. A., Greitzer, E. M., Tan, C. S., and Dawes, W. N., 1994, "A Computational Study of Viscous Effects on Lobed Mixer Flow Features and Performance," presented at the 30th AIAA/ASME/SAE/ASEE Joint Propulsion Conference, 27–29 June, Indianapolis, IN.

Rai, M. M., 1987, "Navier–Stokes Simulations of Rotor–Stator Interactions Using Patched and Overlaid Grids," *J. Prop. Power*, Vol. 3, No. 5, pp. 387–396.

Schulte, V. S., and Hodson, H. P., 1998, "Unsteady Wake Induced Boundary Layer Transition in Highly Loaded LP Turbines," *ASME JOURNAL OF TURBOMACHINERY*, Vol. 120, No. 1.

Smith, L. H., 1966, "Wake Dissipation in Turbomachines," *ASME Journal of Basic Engineering*, Vol. 88D, Sept, pp. 688–690.

Weyer, H., and Dunker, R., 1983, "Flow-Measurements in Stator Rows Behind a Transonic Axial Compressor," AGARD CP-351, *Viscous Effects in Turbomachines*, Copenhagen.

Simulation and Validation of Mach Number Effects on Secondary Flow in a Transonic Turbine Cascade Using a Multigrid, $k-\epsilon$ Solver

M. Koiro

B. Lakshminarayana

Center for Gas Turbines and Power,
The Pennsylvania State University,
University Park, PA 16802

An existing three-dimensional Navier–Stokes flow solver with an explicit Runge–Kutta algorithm and a low-Reynolds-number $k-\epsilon$ turbulence model has been modified in order to simulate turbomachinery flows in a more efficient manner. The solver has been made to converge more rapidly through use of the multigrid technique. Stability problems associated with the use of multigrid in conjunction with two-equation turbulence models are addressed and techniques to alleviate instability are investigated. Validation for the new code was performed with a transonic turbine cascade tested by Perdichizzi. In the fully three-dimensional turbulent cascade, real convergence (i.e., CPU time) was improved nearly two times the original code. Robustness was enhanced with the full multigrid initialization procedure. The same test case was then used to perform a series of simulations that investigated the effect of different exit Mach numbers on secondary flow features. This permitted an in-depth study into the mechanisms of secondary flow formation and secondary losses at high Mach numbers. In this cascade, it was found that secondary losses and secondary flow deviation, which are fairly constant in incompressible flows with similar geometries, underwent a large reduction in the compressible flow range. The structure of the trailing edge shock system and the reduced endwall boundary layer at supersonic exit conditions were shown to be very significant in reducing the amount of secondary flow and losses.

Introduction

Computational Fluid Dynamics (CFD) has become an effective tool in both analyzing complex flow physics and in guiding engineers toward final designs. The proper description of the complex flow inside a turbine is one of the most difficult problems in fluid mechanics and a powerful test of the capabilities of a CFD code. A CFD simulation has the obvious benefit over experimental investigations that a wide variety of exit Mach numbers can be investigated. Additionally, CFD allows regions inside the passage that could not be measured and certain quantities that are nearly impossible to measure to be investigated. Most of the simulations of turbine endwall and secondary flow carried out hitherto (e.g., Ho and Lakshminarayana, 1996), with the exception of Bassi and Savini (1992) are in the area of low-speed simulation and validation of data from low-speed cascades. The thrust of this paper is on the effects of Mach number on secondary flow development in compressible regimes.

A substantial amount of research has been done over the past two decades to improve the efficiency of flow solvers while attempting to maintain a high level of accuracy. The multigrid technique has proven to be a powerful means of accelerating complex turbulent flows to the steady state, particularly for explicit algorithms. Many researchers (e.g., Arnone et al., 1993; Hall et al., 1994) have shown a fourfold increase in the speed of their explicit flow solvers. Although multigrid has proven its worth in accelerating flow problems with a large number of

grid nodes while using algebraic turbulence models, work with higher order turbulence models has been limited. In order to achieve the level of accuracy required to resolve secondary flow features, at least a two-equation turbulence model is required (Lakshminarayana, 1986). However, the stiffness associated with explicit evaluation of the turbulent kinetic energy and dissipation rate equations can create stability problems that impede convergence to a steady-state solution. One could just incorporate the multigrid algorithm into the mean flow equations and integrate the k and ϵ equations only on the fine grid in order to calculate a turbulent viscosity, as is done for many algebraic turbulence models. For greater stability, a point implicit treatment of turbulence source terms like Mavriplis and Martinelli (1991) or fully implicit treatment of the k and ϵ equations as was done by Turner and Jennions (1993) could be used. However, if the stability problems of incorporating the multigrid technique can be handled without changing from a fully explicit treatment of the turbulence transport equations, then incorporating multigrid becomes much easier than the two previously mentioned implicit techniques. This method (henceforth referred to as the fully explicit method) and the point implicit method are the two procedures that were investigated in this paper. It was found (Koiro, 1996) that the fully explicit procedure was sufficiently stable for turbomachinery calculations when implemented in the current two and three-dimensional flow solvers.

The objectives of the paper are to develop an efficient and accurate algorithm and simulate the Mach number effects in turbines. A further objective is to gain a detailed understanding of the flow mechanisms and losses associated with secondary flow in high-speed cascades and provide guidelines to the designer in assessing the Mach number effect on secondary flow in blading design.

Contributed by the International Gas Turbine Institute and presented at the 41st International Gas Turbine and Aeroengine Congress and Exhibition, Birmingham, United Kingdom, June 10–13, 1996. Manuscript received at ASME Headquarters February 1996. Paper No. 96-GT-544. Associate Technical Editor: J. N. Shinn.

A transonic/supersonic turbine cascade experimentally investigated extensively by Perdichizzi et al. (1989) was used to validate the code and show improved convergence realized by incorporation of the multigrid technique. The results of simulation at several exit Mach numbers were used to analyze the interaction of shock waves with the secondary loss structure. The authors performed an in-depth examination of the secondary flow structure in order to isolate and possibly quantify some of the features responsible for higher or lower losses in the compressible flow range. The presence of shock waves and their subsequent interaction with the secondary flow vortex structures in the flow field adds an additional factor not present in incompressible flow discussions. The effect of Mach number on wake decay in the free-stream and endwall regions was also examined as part of this study because of the importance of wake deficits and their interaction with downstream blade rows in real machines.

Mathematical Model and Numerical Solution

The governing equations are the Favre mass-averaged Navier–Stokes equations of mass, momentum, and energy. A low-Reynolds-number turbulence model devised by Chien (1982) is used for the turbulence closure. Further details on the formulation and implementation of this model and a discussion of the artificial dissipation technique used can be found from Kunz and Lakshminarayana (1992a, b).

The base numerical algorithm incorporates a standard four-stage Runge–Kutta scheme. A finite central difference discretization is used to evaluate the fluxes and the turbulent transport and mean flow equations are integrated at the same time level, or coupled, as discussed by Kunz and Lakshminarayana (1992a, b). Eigenvalue scaling and near-wall velocity scaling are used to minimize the amount of artificial dissipation required in the algorithm. Modifications to the existing code described in this paper include incorporation of multigrid in both the mean and turbulence transport equations.

For all the cases computed, the flow is subsonic at the inlet and either subsonic or supersonic at the exit. For turbulent calculations, the free-stream length scale is set to 0.01 times the blade pitch. For the midspan boundary required in the half-height cascade, a symmetry condition is applied and periodicity of the solution is enforced at periodic boundaries.

To accelerate the solution to the steady-state, local timestepping, Full Approximation Storage (FAS) multigrid, and full multigrid are used. Local timestepping is used to compute the maximum allowable time step based on a linear stability analysis of the discretized Navier–Stokes equations performed by Kunz and Lakshminarayana (1992a, b). The FAS multigrid is based on the method originally developed for the Euler equa-

tions by Jameson and Baker (1983). As in Jameson and Baker's development, the coefficients in the four-stage Runge–Kutta scheme have been modified in order to improve high wave damping and the convergence to the steady-state scheme. In this development, a standard sawtooth method is adopted with as many as three coarse grid levels. A full multigrid procedure, which uses successive grid refinement in conjunction with FAS multigrid, is used effectively to initialize the flow. The full multigrid technique, sometimes referred to as coarse grid initialization or grid refinement, is used effectively to initialize the flowfield before proceeding to FAS multigrid. On the coarse grids, boundary conditions and inviscid and viscous fluxes are evaluated in precisely the same manner as on the fine grid. The computation of the viscous fluxes on all of the grids, as adopted by Arnone et al. (1993) in their turbulent flow simulations, was found to be a consistent method and it is the one chosen in this work. For the coarse grids, artificial dissipation is calculated by using a fixed coefficient second difference. This has the advantage of less computational overhead than the fine grid dissipation scheme and improves convergence on the coarse grids. The fine-to-coarse solution transfer is by straight injection while the coarse grid forcing function uses an unweighted average of the neighboring fine grid residuals. The coarse grid corrections and solution are transferred back to the fine grid via trilinear interpolation. On highly stretched or skewed meshes, the interpolation procedure can create high-frequency error in the fine grid solution that can hamper convergence. This error is reduced by smoothing the coarse grid corrections through a second-order implicit filter before interpolating them to the finer grid.

On both the fine and coarse grids, the inviscid fluxes are evaluated every time step while boundary conditions, viscous fluxes, turbulent source terms and artificial dissipation are evaluated prior to the first stage of the Runge–Kutta cycle and held constant during the remaining stages.

Multigrid Technique Applied to the $k-\epsilon$ Transport Equations. As mentioned previously, researchers have cited stability problems due to the source terms in the turbulence transport equations as the prime hindrance to straightforward implementation of the multigrid procedure into a $k-\epsilon$ solver. This instability is caused by the fact that time step constraints associated with spatial operators such as the convective and diffusive fluxes are reduced on coarser grids while time step constraints on source terms, which are strictly local in nature, are not. In other words, the increased grid spacing on the 2h mesh (where $h = \Delta x = \Delta y$) allows a time step roughly twice that of the fine grid. Since source terms are evaluated only at a single grid node, however, their time step constraints are the same on all grid levels. So, if the source terms are the limiting constraint on the overall time step,

Nomenclature

b = axial chord length
 C = chord length
 C_f = friction coefficient = $2\tau_w/(\rho V^2)$
 C_L = lift coefficient = $2L/(\rho V^2)$
 CFL = Courant–Fredericks–Lewy number
 H = blade height
 i = leading edge incidence angle
 k = turbulent kinetic energy
 M = Mach number
 P_0 = total pressure, N/m^2
 p = static pressure, N/m^2
 S = blade spacing (one pitch distance)
 u^+ = friction velocity

V = total velocity
 V_d = wake velocity deficit = $V_{\max} - V_{\min}$ at the wake centerline
 V_{sec} = secondary velocity = $V - V_{MS}$
 y^+ = near-wall turbulence inner variable = yu^+/ν
 X = distance from leading edge
 Y = distance from suction surface
 Z = distance from endwall
 α_1, α_2 = inlet and exit flow angle measured from the axial direction
 $\Delta\alpha_s$ = secondary flow deviation angle = $\alpha_2 - \alpha_{2\text{design}}$
 μ_t = turbulent viscosity
 θ = momentum thickness
 ζ = loss coefficient (Eqs. (1), (2), and (3))

Superscripts

$\bar{\quad}$ = pitch-averaged
 $\overline{\quad}$ = passage-averaged
 $'$ = blade metal angle

Subscripts

1, 2 = inlet and exit of the cascade
 te = trailing edge
 is = isentropic quantity
 MS = midspan value
 ref = reference values
 s = secondary
 c = correlation

it will not be possible to use larger time steps on the coarse grid and thus the multigrid technique will not be as effective. This is the reasoning for a point implicit or fully implicit treatment of the k and ϵ transport equation source terms. However, if the primary time step constraint is due to the spacial operators, source terms may be treated explicitly without the penalty of reduced convergence or stability. In their discussion on the ramifications of stability and order of magnitude analysis on maximum allowable time step, Kunz and Lakshminarayana (1992a, b) conclude that it is hyperbolic and parabolic constraints due to grid clustering, *not* stiffness due to turbulent source terms, that hamper convergence in turbulent flow solutions. Since the present code is based on their work, it was judged that a fully explicit method could be used. To test this hypothesis, both the point implicit and fully explicit treatments were investigated in two dimensions and it was found that the fully explicit method was just as stable as and much simpler to implement than the point implicit method. This conclusion was made on both simple cases such as a turbulent flat plate and in a complex case such as a transonic turbine cascade. Hence, the fully explicit method is used in the present investigation.

For the fully explicit turbulent source term treatment, the coarse-to-fine grid interpolation scheme was modified to increase the effectiveness of the multigrid technique. The turbulent viscosity, μ_t , is calculated only on the fine grid and is injected and held constant on all successively coarse grids. Straight injection in a manner analogous to the mean flow quantities is used to transfer μ_t to the coarser grids. Physically, k and ϵ represent quantities that must remain positive. During the course of an iteration cycle, these quantities can approach zero or negative values in the far field (i.e., in primarily inviscid regions). When using the multigrid technique, corrections to the fine grid turbulent solution can be created that, when interpolated, would also make the solution nonpositive. To ensure positivity, these corrections, wherever they would create a negative k or ϵ value, are simply omitted. Another possible solution to the problem of negative corrections would be simply not to interpolate any values. This is similar to the early methods of implementing multigrid into the k - ϵ model in that the turbulence quantities are determined only by the fine grid. It has been found, however, that convergence is significantly improved for both k and ϵ transport equations when interpolation is performed (Koiro, 1996). The improvement in convergence rate for the meanflow and turbulence transport equations in a full three-dimensional cascade over the original, single grid code are covered in the next section.

Computation of Three-Dimensional Turbine Cascade Flows

The test case chosen for this study is a cascade experimentally investigated extensively by Perdichizzi et al (1989). The details of the blade geometry, based on a steam turbine rotor, are $C = 47.7$ mm, $S/C = 0.63$, $H/C = 1.05$, $\alpha'_1 = -2.6$ deg, $\alpha'_2 = 66.0$ deg, stagger angle = 44.8 deg, $b = 33.8$, $i = 20.0$ deg, number of blades = 12. The test facility is a blowdown-type facility where exit back pressure is atmospheric and inlet flow conditions are controlled by varying total pressure in a large upstream storage tank. Experimental data were provided by Perdichizzi for isentropic exit Mach numbers of $M_{2is} = 0.5, 1.02, \text{ and } 1.4$. Complete traverses were carried out at axial stations $x/b = -0.8, 1.1, 1.5, \text{ and } 1.9$. The traverse in the upstream plane at $x/b = -0.8$ was performed with a flattened probe so that a complete description of the endwall inlet boundary layer could be obtained. The other three locations, $x/b = 1.1, 1.5, \text{ and } 1.9$, were traversed using a miniature five-hole probe at 20 pitchwise and 10 spanwise locations on a measuring plane that extended half of the blade span and approximately 1.5 times the pitch. Hot-wire measurements published by Perdichizzi et al. (1989)

give an inlet turbulence intensity of 2.5 percent. Further details of the test facility can be found from Perdichizzi (1990).

The computational grid composed of $121 \times 53 \times 53$ streamwise, pitchwise, and spanwise nodes respectively is generated by stacking a two-dimensional H -grid in the spanwise direction. In order to reduce the amount of grid points used in the computations, only half of the cascade was actually modeled by enforcing a no-slip condition on the upper wall and a symmetric boundary condition on the midspan region. This is valid approximation because measured quantities show that even at the lowest exit isentropic number tested, spanwise velocities are negligible near the midspan region. Near-wall stretching was performed to insure that y^+ value of 2 or less could be maintained on all solid surfaces.

Computational Results: Multigrid Convergence Acceleration. Before any comparison with experimental data is made, it is instructive to look at the enhanced convergence resulting from the use of the multigrid solution technique for turbulent flow shown in Figure 1. The multigrid yields a converged solution 3.5 times faster than the single grid solution for a 3.5 order drop in the RMS density residual. The per-iteration computational overhead on a Cray YMP is 1.8, so the multigrid-to-single grid CPU rate is 1.94 to 1. Figure 1 also highlights another important difficulty during the first five hundred to one thousand iterations for turbulent flows using the single grid k - ϵ model. Both mean flow and turbulent residuals are erratic for a significant number of iterations before the more monotonic convergence of an established flow field can be seen. It can also be seen that for a stable solution, the code had to be run in laminar mode in order to establish the mass flow and wall boundary layers. However, when using the full multigrid technique, the problem of early instability of turbulent solutions is resolved because boundary layers and global flow features are fairly well established when the solution is interpolated to the finest grid level.

Computational Results: Comparison With Experimental Data. Before a simulation of the effects of Mach number is made, it is necessary to validate the code against data acquired in a transonic cascade at the exit Mach numbers, 0.5, 1.02, and 1.4. Computed and experimental results are compared in terms of local loss coefficient, secondary flow velocity vectors, pitch-averaged secondary loss and deviation angle, and total passage-averaged secondary loss. The local loss coefficient can be pre-

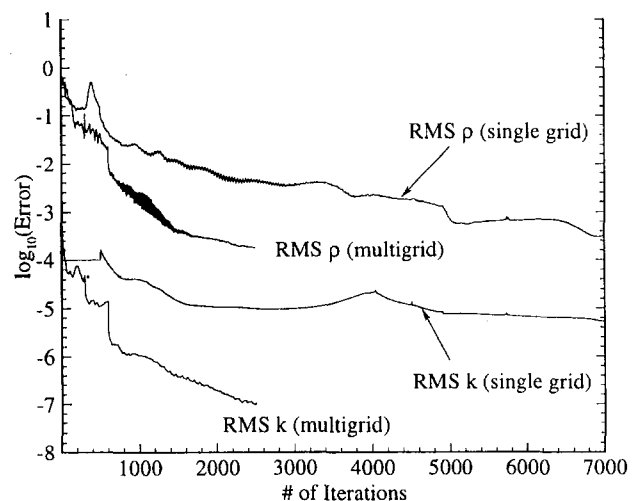


Fig. 1 Comparison of rms density and rms turbulent kinetic energy convergence with and without multigrid for the turbine cascade at $M_{2is} = 1.02$

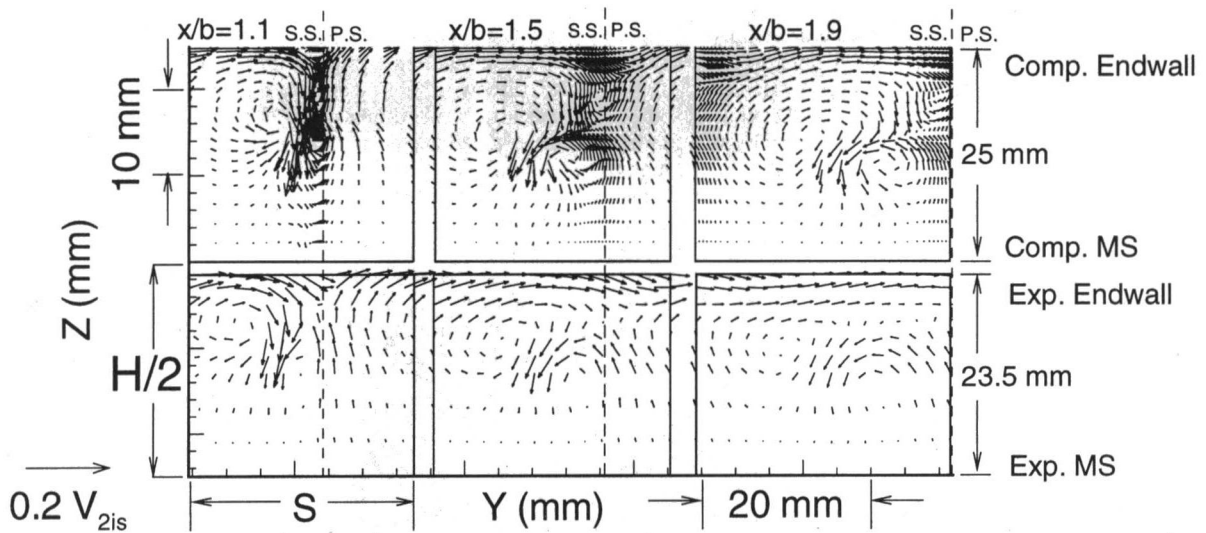


Fig. 2 Comparison between experimental (bottom row) and computed (top) secondary velocity vectors (V_{sec}) for $M_{2is} = 0.5$. V_{sec} has been normalized by V_{2is} .

sented in two forms. The first loss coefficient, ζ_1 , is a kinetic energy formulation given by Perdichizzi (1990) as:

$$\zeta_1 = \frac{V_{2is}^2 - V_2^2}{V_{2isMS}^2} = \frac{[p_2/P_{02}]^{(\gamma-1)/\gamma} - [p_2/P_{01}]^{(\gamma-1)/\gamma}}{1 - [\bar{p}_{2MS}/P_{01}]^{(\gamma-1)/\gamma}} \quad (1)$$

The second loss coefficient ζ_2 , which is a more standard approach, is a total pressure loss formulation given by:

$$\zeta_2 = \frac{P_{01} - P_{02}}{\frac{1}{2} \rho V_{2is}^2} \quad (2)$$

For consistency with Perdichizzi's data, the first loss coefficient is used in the validation of the code. In the next section on Mach number simulation, the second formulation was necessary to compare with existing secondary loss correlations. The secondary velocity, as presented by Perdichizzi (1990), is defined as the projection of the total velocity vector on a plane normal to the velocity vector at the midspan for a given tangential position. Hence, the velocity vector at midspan defines the primary flow direction and any deviation from it is considered secondary flow. When comparing secondary velocity vectors, both the raw experimental data and the computed results were processed using the same technique. Whenever predicted loss contour traverse planes are shown, the experimental traverse planes are shown as lower half mirror images for ease of com-

parison even though measurements were actually taken in the upper half of the cascade. Note that for the computed secondary flow velocity vectors, the entire computational domain (25 mm high) is shown in order to visualize the corner vortices. Since the experimental domain is only 23.5 mm, any distance comparison between the two must be made from the midspan reference line, not the endwall.

Results at $M_{2is} = 0.5$. The measured secondary velocity vectors and loss contours at all three measuring stations are compared with predictions in Figs. 2 and 3, respectively. Note that these plots and all subsequent loss and secondary flow plots are shown from a view inside the passage looking downstream to be consistent with the data provided by Perdichizzi. The secondary velocity vectors are normalized by the pitch-averaged streamwise velocity. It is clear that the predicted results are in good agreement with the measured values.

In Figs. 2 and 3, there are four main loss features: (1) the secondary flow loss core, which is usually located 15–20 percent of span away from the endwall, (2) the endwall/corner vortex structure located 3–5 percent span away from the wall, (3) the distinct wake region, which is clearly visible and extends from the loss core to midspan, and (4) a wake–secondary flow interaction vortex structure near the blade trailing edge that is opposite in direction to the passage vortex and near the wake

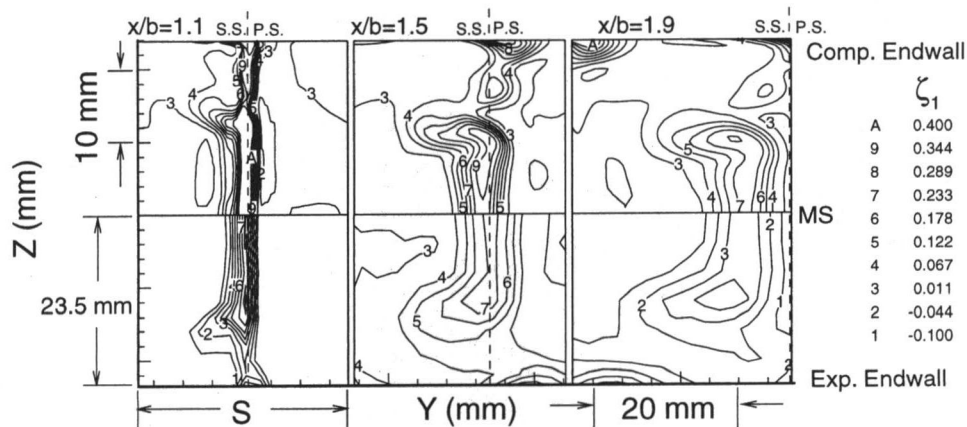


Fig. 3 Comparison between experimental and computed loss contours for $M_{2is} = 0.5$ (the numbers in the contours and legend refer to values of the loss coefficient, ζ_1)

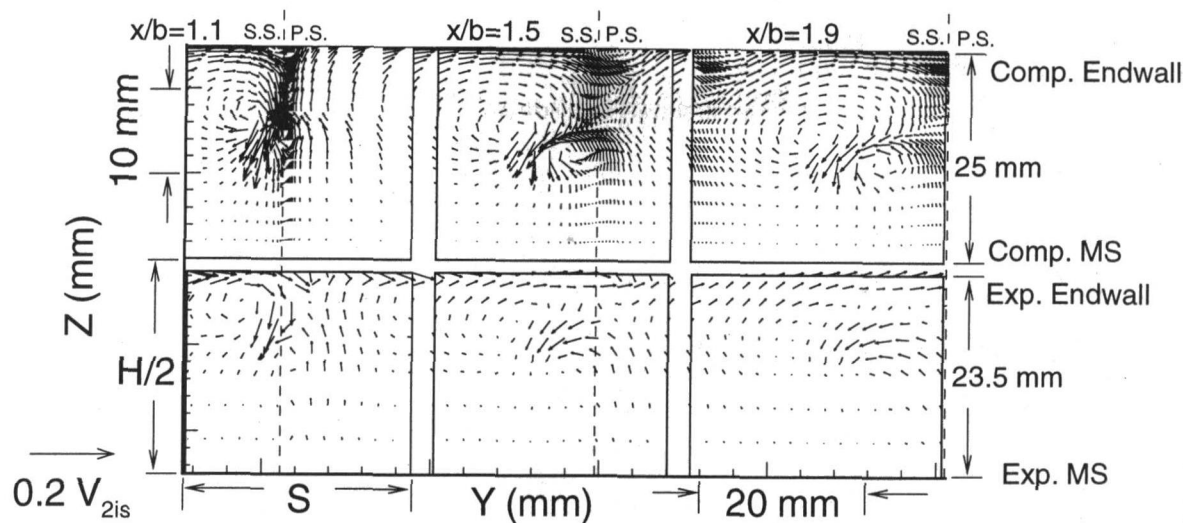


Fig. 4 Comparison between experimental (bottom row) and computed (top) secondary velocity vectors for $M_{2is} = 1.02$

at about 25 percent of the span from the wall. The $M_{2is} = 0.5$ flow case is characterized by a very strong loss core and a large migration of the corner vortex loss region as the flow proceeds downstream. The strong loss core seems to be created by the interaction of the passage and the wake-secondary flow interaction vortex systems. If one examines each axial station in Fig. 2, it can be seen that as these two structures merge, they create a large sweeping motion, which draws the low-momentum fluid out of the wake and into the secondary flow region, causing the large 'bulge' visible in Fig. 3. So, it can be recognized that there is a combination of effects, not just the action of the passage vortex, that creates the downstream expansion of the loss core. Here one can see a real benefit from computing the flow because it is difficult to draw this conclusion from the coarse experimental measuring. As shown in both Figs. 2 and 3, both the migration of the corner vortex across the pitch (very important later when considering the effects of Mach number) and the broad expansion of this loss zone are captured.

Results at $M_{2is} = 1.02$. The secondary flow velocity vectors and loss contours at $M_{2is} = 1.02$ shown in Figs. 4 and 5, respectively, reveal that the loss core is closer to the endwall than at $M_{2is} = 0.5$ for all three measuring planes. As in the subsonic Mach number case, the agreement between measured and computed data is good except for the presence of a smaller loss region between the secondary loss core and the corner vortex. Examination of secondary flow vectors is inconclusive as to

whether this is computational anomaly or a detail that was lost due to the coarseness of the experimental measuring grid. The secondary flow plots in Fig. 4 also show that the wake-secondary flow interaction vortex structure is closer to the endwall and it occupies a much smaller pitchwise area than the subsonic case. The end result is a less vigorous interaction of the passage and wake-secondary flow interaction vortices than at $M_{2is} = 0.5$. The corner loss structure has a slightly smaller pitchwise migration away from the wake centerline than at $M_{2is} = 0.5$. This fact becomes very useful in understanding how the overturning contributes to losses when examining the pitch averaged quantities below.

Since the $M_{2is} = 1.02$ case represents the middle range of the exit isentropic Mach numbers tested, it is instructive to examine the development of the secondary flow through the cascade closely. Figure 6 shows the secondary flow vectors at $x/b = 0.02, 0.25, 0.57,$ and 0.93 . At the inlet of the cascade ($x/b = 0.02$), it is clear that there is already a significant amount of crossflow developing. The reason for this becomes clear when examining velocity vectors one grid point (about 0.15 mm) to the endwall in Fig. 7. The saddle point can clearly be seen and the evolution of the pressure side separation line created by the action of the pressure side horseshoe vortex, defined as S_{p1} by Sieverding (1985), is also visible. Looking again at Fig. 6 at the $x/b = 0.25$ location, the suction side horseshoe vortex can still be seen, but it seems to be affected by the

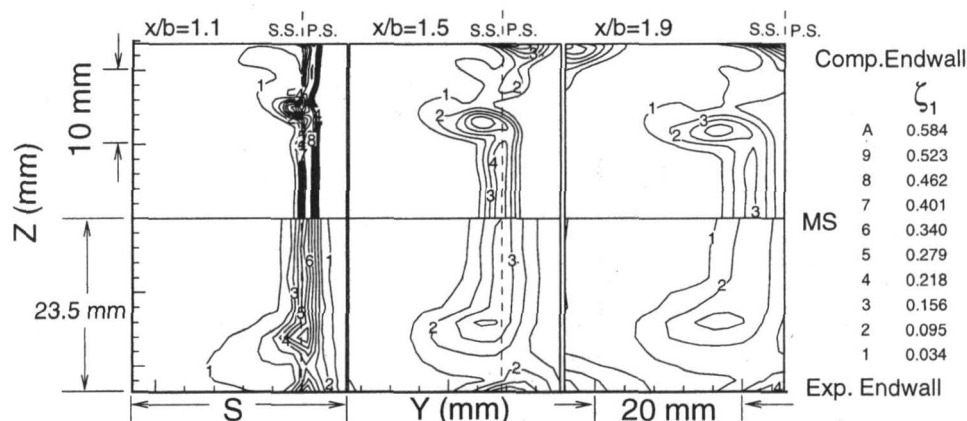


Fig. 5 Comparison between experimental and computed loss coefficient (ζ_1) contours for $M_{2is} = 1.02$

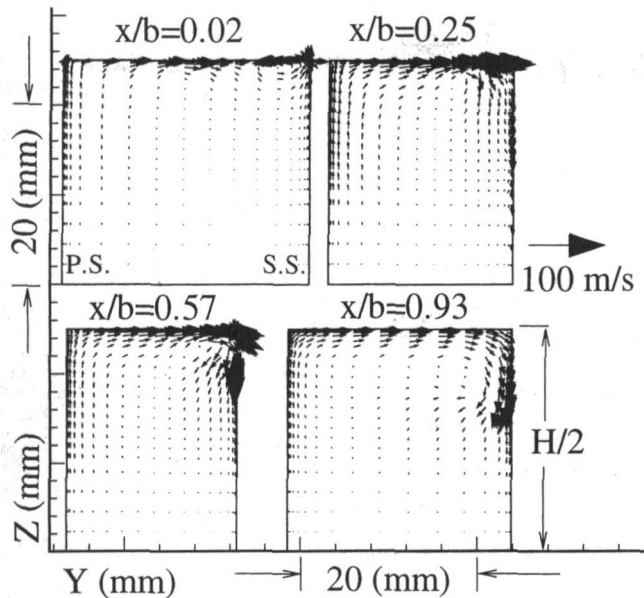


Fig. 6 Secondary flow velocity vectors in the blade passage at $x/b = 0.02, 0.25, 0.57,$ and 0.93 for $M_{2is} = 1.02$

inception of the passage vortex. In Fig. 6 at $x/b = 0.57$, the pressure side horseshoe vortex has impinged on the suction side (also visible in Fig. 7) and essentially wiped out the suction side horseshoe vortex. It seems that the strong pressure side vortex completely dominates the flow, causing the dissipation of the suction side vortex throughout the remainder of the blade row. The final station, $x/b = 0.93$, confirms that, except for an insignificant corner vortex, the passage vortex dominates the entire passage. The sweeping motion of the passage vortex and the interference from the pressure side horseshoe vortex have a direct effect on the suction side boundary layer growth. As described by Sieverding (1985) the endwall boundary layer swept into the suction side forms the S_4 stagnation line, which is visible through C_f contours in Fig. 8. This line roughly delineates the maximum extent of the endwall boundary layer and the maximum distance away from the endwall where secondary flow effects are significant in the passage. If the spanwise location of the S_4 line at the trailing edge is compared with Fig. 4, it can be deduced that the S_4 line feeds into the wake-secondary flow interaction vortex (also described by Sieverding). Although no data were taken in the passage, all of the flow features described here are in good agreement with the Sieverding's (1985) descriptions of secondary flow development in a turbine passage.

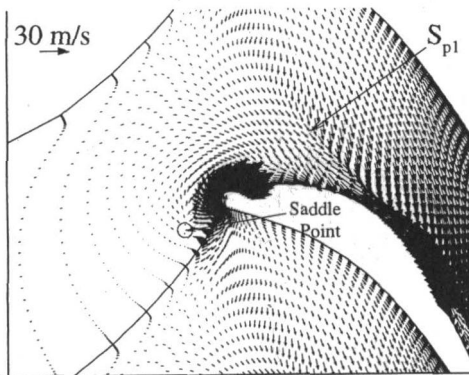


Fig. 7 Total velocity vectors at the first grid point away from the endwall at the leading edge for $M_{2is} = 1.02$

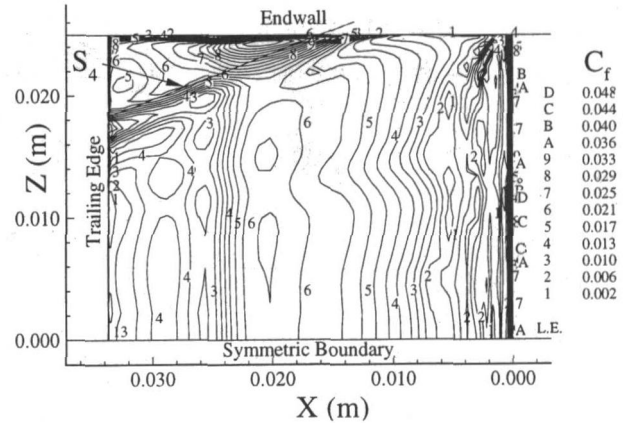


Fig. 8 Contours of skin friction C_f and the S_4 stagnation line on the suction side of the blade at $M_{2is} = 1.02$

Results at $M_{2is} = 1.4$. The secondary flow velocity vectors and loss contours plotted in Figs. 9 and 10, respectively, show that the passage vortex and loss core stay closer to the endwall as compared to $M_{2is} = 0.5$ and 1.02 . Additionally, there is a significant motion of the core away from the blade suction sideline. This is due mainly to reduced turning of the flow in the midspan region at the higher exit Mach number. If it were a migration of the core away from the wake centerline as in $M_{2is} = 0.5$, a much stronger secondary flow pattern and a more vigorous interplay between the passage and wake-secondary flow interaction vortices would be visible in Fig. 9. At this exit Mach number, it is instructive to use midspan static pressure contours to examine the shock structure. Figure 11 clearly shows a double oblique shock pattern off of the blade trailing edge. The trailing suction side shock wave is very distinct before crossing the wake after which it smears out considerably.

A key feature that was well captured at all three exit Mach numbers was the location of the corner and passage vortices. The accuracy of this prediction will become important later when the role of over- and underturning and its effect on shock wave/secondary flow interaction is studied in depth in the next section.

Pitch and Area-Averaged Quantities. Pitch-averaged quantities are obtained by mass averaging the quantities across the pitch and subtracting off the midspan-averaged value at each spanwise location. For loss coefficient and outlet angle, the pitch-averaged values are defined by:

$$\zeta_p = \zeta - \zeta_{MS} \quad \Delta\alpha_p = \alpha - \alpha_{MS} \quad (3)$$

The pitch-averaged secondary loss coefficient is shown in Fig. 12 for the three exit Mach numbers. It is clear that the location and magnitude of the loss core are predicted reasonably well and the near-wall losses (endwall boundary layer) are predicted very well. Additionally, the loss bucket due both to the migration of the loss core away from the endwall and the change from flow overturning to underturning is captured at all three exit Mach numbers. The pitch-averaged exit angle shown in Fig. 13 also shows that the change from overturning near the endwall to underturning in the core region has been predicted fairly accurately. However, there is an extra "hump" in the computed data not visible in the measured quantities. This hump, which is responsible for the extra loss region in Figs. 3 and 5, is visible in other secondary flow data (Gregory-Smith et al., 1992), so the presence of such a flow feature is plausible. As mentioned above, it was very difficult to speculate about the role of the wake-secondary flow interaction vortex (which seems to be mainly responsible for this loss region) in the experimental results because of the coarse measuring grid. This anomaly in the deviation angle could have been obscured due

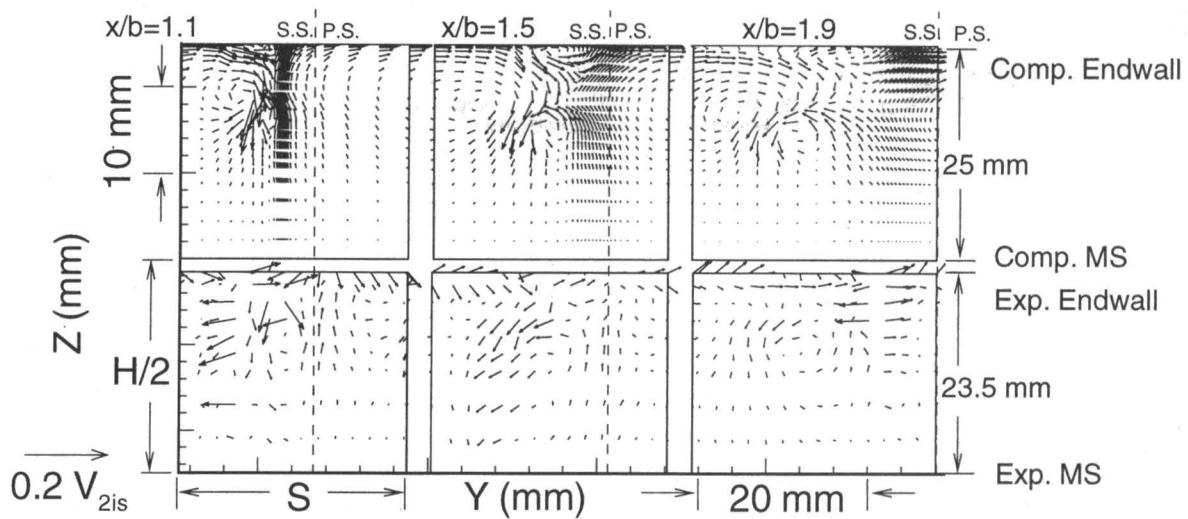


Fig. 9 Comparison between experimental (bottom row) and computed (top) secondary velocity vectors for $M_{2is} = 1.4$

to this coarseness. Lack of grid resolution (in the computation) in this high flow gradient region could also be a plausible explanation.

Simulation of Mach Number Effects

After achieving confidence in the code through validation, the test case was used to carry out a systematic numerical simulation of the effects of Mach number on secondary flow by varying the exit Mach number. This study was carried out in order to understand the effects of compressibility, shocks, and other high-speed-flow features on the secondary losses. This investigation has the advantage over experiment that very detailed information on the flow can be displayed with either mean flow or turbulent quantities (which were not measured in the compressible flow range) at any axial station. Also, the accuracy of five-hole probe measurements at transonic and supersonic velocities, even with corrections, is still a research topic. In the following discussion, three more simulations were run with exit isentropic Mach numbers of 0.7, 1.2, and 1.6.

In most of this section on simulation, instead of examining each simulation individually, an integrated approach is used where the data at various Mach numbers are viewed collectively. For brevity and clarity, only the predictions at $x/b = 1.5$ are presented. This one is chosen because, of the three measuring locations, it is the most representative of the blade row spacing in practical machines.

Mach Number Effects on Secondary Flow. Figures 14 and 15 show the secondary flow velocity vectors and loss contours, respectively, for $M_{2is} = 0.5, 0.7, 1.02, 1.2, 1.4,$ and 1.6 at $x/b = 1.5$. As the Mach number increases, both of the figures show that the secondary loss core stays closer to the endwall but moves farther away from the suction surface. The secondary flow vectors, plotted in Fig. 14, show that the magnitude of the secondary velocity decreases with increasing exit Mach number. Note that for each different exit Mach number, secondary velocities are normalized by their respective V_{2is} values. Even though dividing by the larger exit velocity may diminish the apparent secondary flow velocity magnitude in Fig. 14, Fig. 15 clearly shows that the losses drop off rapidly in the transonic and supersonic regimes. This decrease becomes more apparent when one examines the pitch-averaged secondary loss in Fig. 16. The magnitude of the loss peak is reduced and the spanwise movement of the core toward the endwall with increasing Mach number discussed above is clearly visible in Fig. 16. In Fig. 17, the amount of both overturning and underturning are significantly reduced with increasing Mach number. Also visible in Figs. 14 and 15 is pitchwise migration (to the right) of the corner vortex loss system away from the secondary loss core with decreasing exit Mach number. It is clear from Figs. 14 and 15 for $M_{2is} = 0.5, 0.7,$ and 1.02 , that the corner loss system location is far to the right of the pitchwise location of the secondary loss core. From the pressure surface,

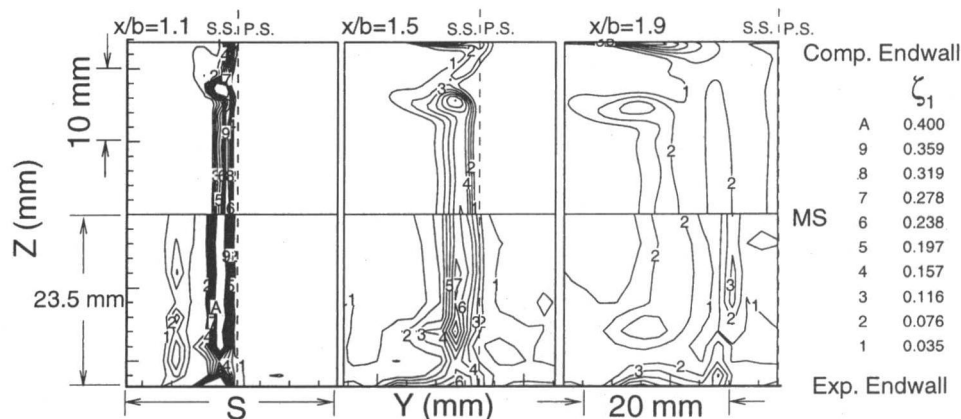


Fig. 10 Comparison between experimental and computed loss coefficient (ζ_1) contours for $M_{2is} = 1.4$

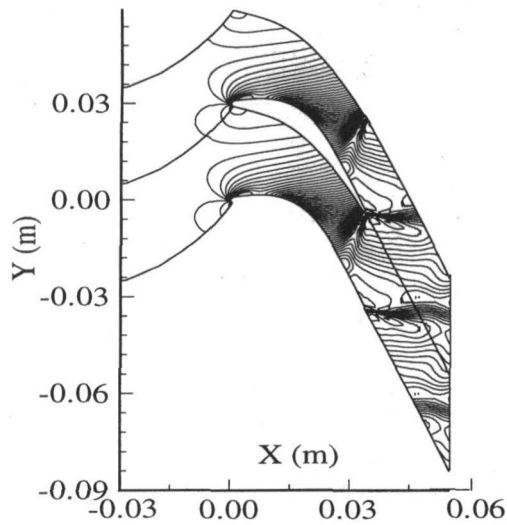


Fig. 11 Trailing edge shock pattern visualized by static pressure contours at midspan for $M_{2is} = 1.4$

the corner vortex seems to feed directly into the passage vortex and near the suction surface, part of the passage vortex then feeds right back into the corner vortex, creating a significant pitchwise flow migration (which is the underturning). This situation changes, however, as Mach number increases and more of the passage vortex flow is diverted to the secondary loss core region so that less of an endwall crossflow (and subsequent lower overturning) develops. Also at the higher Mach numbers beginning significantly at $M_{2is} = 1.2$, the corner vortex is no longer easily pushed to the right by the passage vortex because the underturning near the wall is becoming stronger. This trend reaches a maximum at $M_{2is} = 1.6$ where the near-wall underturning is so large that it almost changes the entire endwall flow to underturning, which can be seen by the very small left-running secondary flow velocity vectors at the top of the $M_{2is} = 1.6$ plot in Fig. 14. The end result of the passage vortex and corner loss system interaction at the subsonic exit Mach numbers is higher pitch-averaged overturning and secondary losses visible in Figs. 16 and 17. Likewise, the presence of a weaker passage vortex and a more resilient corner loss structure at the supersonic exit Mach numbers creates lower pitch-averaged turning and losses. Finally, the area-averaged secondary losses, plotted in Fig. 18 for the six exit Mach numbers tested, show the loss dropping off rapidly in the transonic range and then staying fairly constant in the supersonic range. Also included in this plot is the subsonic correlation, which is discussed in the final section of this paper. All of these trends are in agreement with those presented by Perdichizzi (1990).

The first and perhaps most obvious explanation for the reduced secondary flow is that the higher flow acceleration reduces the endwall boundary layer thickness, thus preventing large near-wall crossflows. To investigate this assumption, the endwall momentum thickness was plotted in Fig. 19 for the six exit isentropic Mach numbers. The boundary layer thickness is diminished at the higher speeds, but this effect alone may be only partially responsible for the rapid drop in secondary losses. Another reason for the drop in losses might be the reduced lift coefficient due to the decrease in overall turning ($C_L \propto (\alpha_1 - \alpha_2)$) at the supersonic Mach numbers. To examine this idea, the passage-averaged secondary losses were normalized by C_L^2 . The magnitude of ζ_s/C_L^2 at the supersonic exit Mach numbers, however, was still considerably lower than the subsonic values.

It is clear from Fig. 18 that not only do the secondary losses drop off with Mach number, but the downstream growth of secondary losses is also reduced. The quantitative effects of the

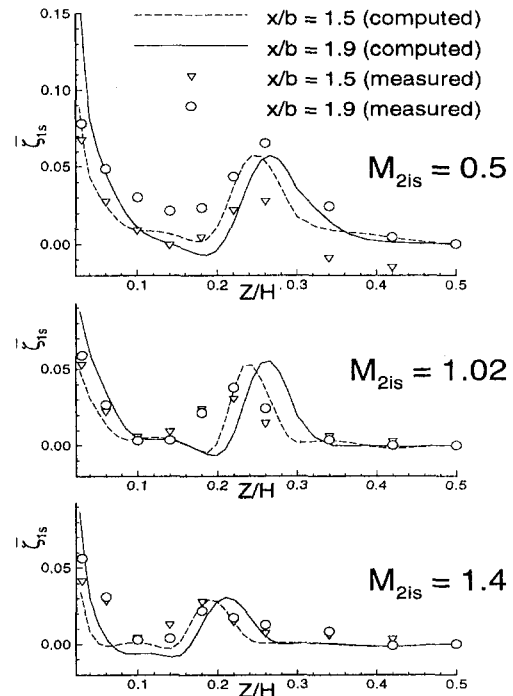


Fig. 12 Comparison of measured and predicted pitch-averaged secondary loss at $M_{2is} = 0.5, 1.02, \text{ and } 1.4$

lower lift coefficient have been addressed, but a more qualitative and perhaps more useful method of examining the real fluid effects in the cascade is to examine particle traces. As was shown previously, a portion of the higher secondary losses can be attributed to the spanwise migration of the corner vortex (Fig. 14) and larger overturning (Fig. 17) present at the lower exit Mach numbers. Usually, in incompressible or mildly compressible regimes, secondary flow is created when the endwall

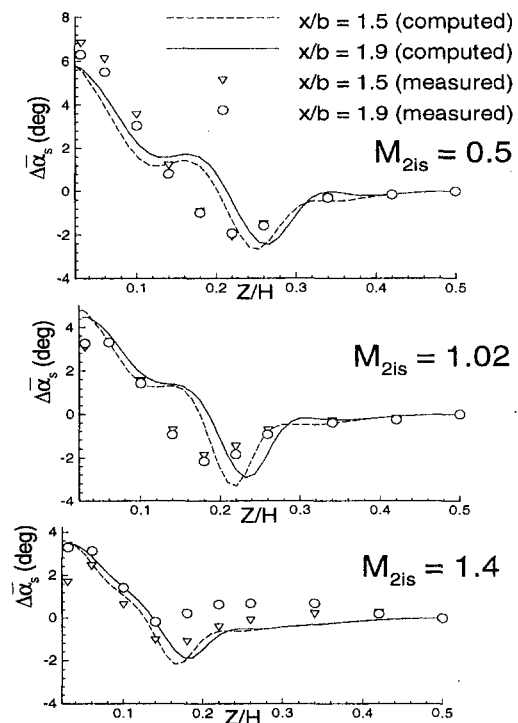


Fig. 13 Comparison of measured and predicted pitch-averaged deviation angle ($\Delta\alpha_s$) at $M_{2is} = 0.5, 1.02, \text{ and } 1.4$

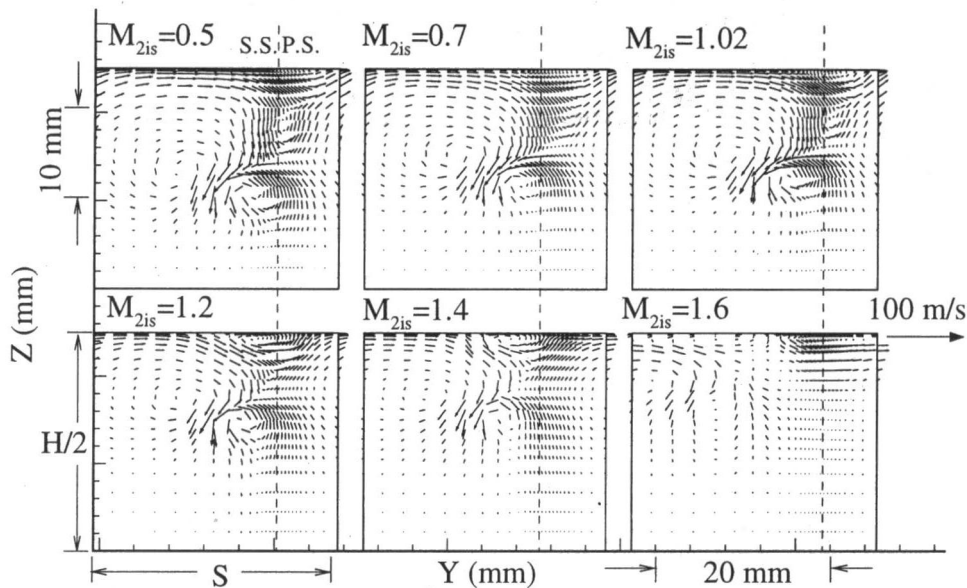


Fig. 14 Predicted secondary flow velocity vectors at $x/b = 1.5$ for $M_{2is} = 0.5, 0.7, 1.02, 1.2, 1.4,$ and 1.6

boundary layer that is being turned in the passage sets up a crossflow near the endwall. This crossflow causes the overturning shown in Figs. 2, 14, and 17 and it is responsible, along with the corner vortex, for the endwall loss zone visible in Figs. 3, 15, and 16. The low-pressure region created by the overturning flow transporting fluid away from the endwall draws in air from the core region of the passage. This is one of the main effects that keeps the secondary flow and the passage vortex energized even after the turning action of the blade is no longer being applied. However, as the Mach number increases, the presence of the trailing edge oblique shocks acts as an underturning mechanism on the flow along the entire span. The result is that the corner secondary vortex, no longer driven by the overturning, cannot effectively transport momentum in the pitchwise or subsequent spanwise directions.

This phenomenon can be studied more effectively if one examines colored stream traces released at the same spanwise locations for different exit Mach numbers. Figure 20(a) shows a schematic of exactly where the stream traces were released into the flowfield and provides the viewing angle for Figs. 20(b-d). Three horizontal traces sets consisting of 8-10 release points, each with the same pitchwise extent and varying spanwise location, were used. The traces (Trace Set 1) were

released at the bottom of the "box" seen in Fig. 20(a). Trace Set 2 was released along the dotted line 3.13 mm from the endwall. Trace Set 3 was released closest to the wall at a distance of 1.37 mm. The axial location of the release point, $x/b = 0.73$, was chosen to best illustrate the shock effects on the secondary flow development. The three Mach numbers compared are (1) $M_{2is} = 0.5$ to illustrate the standard stream trace path in a nearly incompressible and shock free regime, (2) $M_{2is} = 1.02$ to show the onset of shock waves, and (3) $M_{2is} = 1.6$ to examine the effect of strong shock patterns.

For $M_{2is} = 0.5$ in Fig. 20(b), the typical pattern for secondary flow in a turbine can be visualized by using the stream traces. For Trace Set 1, points near the suction side are turned away from the endwall, while points released near the pressure side turned toward the endwall, indicating that this spanwise release location is aligned roughly with passage vortex. Note that the complimentary secondary velocity pattern in Fig. 2 is from a view looking from the blade passage toward the exit, while Fig. 20(b) is looking from the exit of the computational domain toward the passage. For Trace Set 2, the pattern is similar to Set 1 except that the flow turning is so much more severe that the turning rolls up into a vortex. Finally, for Set 3, the traces are swept nearly parallel to the endwall, transported away from

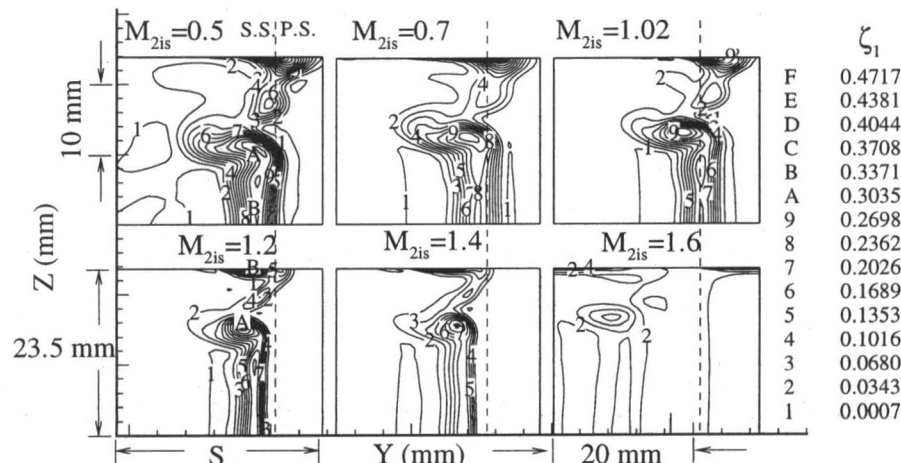


Fig. 15 Predicted loss coefficient (ζ_1) contours at $x/b = 1.5$ for $M_{2is} = 0.5, 0.7, 1.02, 1.2, 1.4,$ and 1.6

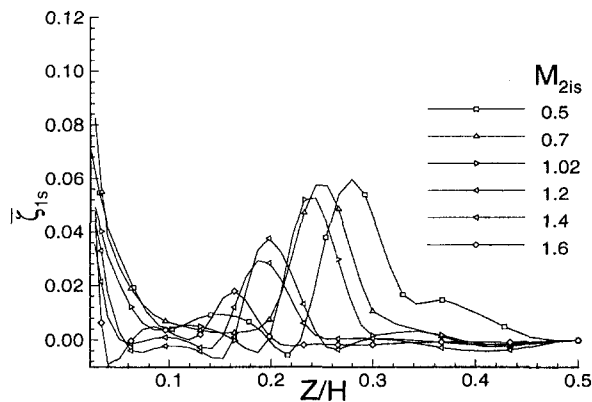


Fig. 16 Predicted pitch-averaged secondary loss at $x/b = 1.5$ for $M_{2is} = 0.5, 0.7, 1.02, 1.2, 1.4,$ and 1.6

the endwall by the actions of the wake-secondary flow interaction and passage vortex structures, and then rolled up into a large vortex structure before exiting the computational domain.

In Fig. 20(c), the exit sonic Mach number produces only a weak shock and the particle traces show a vortex pattern due to secondary flow very similar to $M_{2is} = 0.5$. However, the amount that Trace Sets 1 and 2 are turned by the passage vortex is noticeably smaller than in Fig. 20(b). In Set 2, the passage vortex is not even sufficiently strong to roll up the streamlines like Set 2 at $M_{2is} = 0.5$. Stream Set 3 seems to be swept in the pitchwise direction as much as in Fig. 20(b), but the spanwise migration of the rolled traces at the computational domain exit is much smaller. This, of course, matches the observations from Figs. 14 and 15 that the loss core and secondary flow regions at $M_{2is} = 1.02$ are closer to the endwall than at $M_{2is} = 0.5$. Although some of the reduction of turning and secondary losses can be attributed to the inception of a small oblique shock at the sonic exit condition, a much more prevalent and qualitatively useful shock effect exists at $M_{2is} = 1.6$.

For $M_{2is} = 1.6$, shown in Fig. 20(d), the stream trace pattern is radically different than at $M_{2is} = 0.5$ and 1.02 . In Stream Set 1, instead of roughly following the blade trailing edge angle, the flow is strongly underturned. This is not a secondary flow effect, but a core and midspan flow turning due to the trailing edge oblique shock. Trace Set 2 exhibits a wavy behavior due to the interaction with the strong trailing edge oblique shock pattern. Following the traces from their release point, they begin to turn with the blade contour until they are forcibly underturned by the oblique shock. Because the flow is not allowed to overturn like Set 2 at $M_{2is} = 0.5$ and 1.02 , there is no subsequent spanwise transport of low-momentum fluid away from the end-

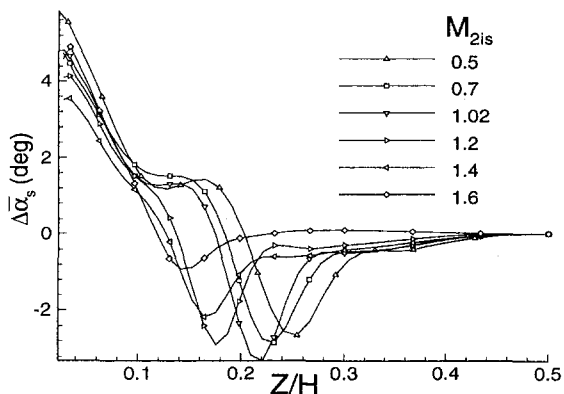


Fig. 17 Predicted pitch-averaged secondary deviation angle at $x/b = 1.5$ for $M_{2is} = 0.5, 0.7, 1.02, 1.2, 1.4,$ and 1.6

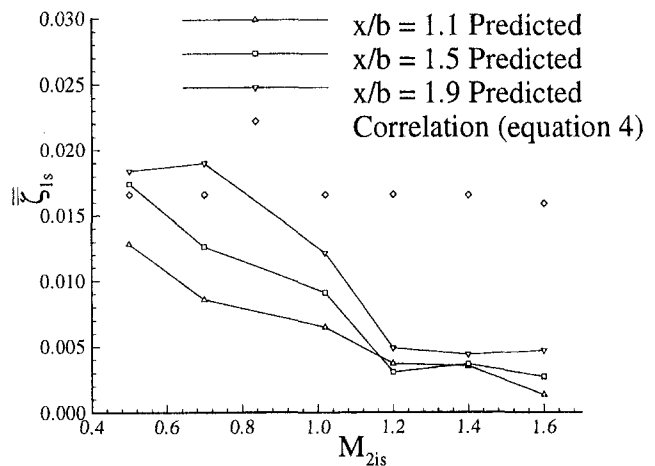


Fig. 18 Area-averaged secondary loss for the entire passage at $x/b = 1.5$ and a secondary loss correlation for $M_{2is} = 0.5, 0.7, 1.02, 1.2, 1.4,$ and 1.6

wall. This phenomenon becomes even more pronounced for Trace Set 3 where the traces near the suction side, which are actually beginning to both overturn and move away from the endwall, are forced to underturn and roll up into a vortex, which is much tighter and closer to the endwall than at $M_{2is} = 0.5$ and 1.02 . Again, by using Figs. 14 and 15, the flow pattern suggested by the particle traces can be confirmed. Although there are surely other complicating factors present in this flowfield, it is primarily the underturning action of the oblique shock wave that prevents pitchwise and spanwise momentum transport and subsequent spanwise growth of the secondary loss core at the supersonic exit Mach numbers.

These observations about the underturning effects were instrumental in developing physical insight into the Mach number effects. Although Figs. 20(a-d) can be used to see some of the shock wave interaction with the secondary flow, this phenomenon and the static methods used to view it here are rather crude. By releasing short bursts of particles instead of a continuous stream, the motion of individual fluid elements, as in a Lagrangian viewpoint, can be observed. By using this technique, the underturning of the flow and the radical change in the secondary flow pattern as the particles pass through the shock wave becomes much clearer. This effect has been recorded in

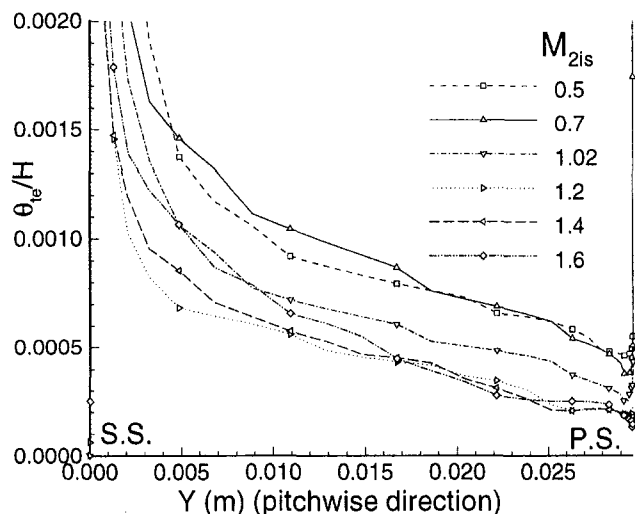


Fig. 19 Endwall momentum thickness at the trailing edge for $M_{2is} = 0.5, 0.7, 1.02, 1.4,$ and 1.6

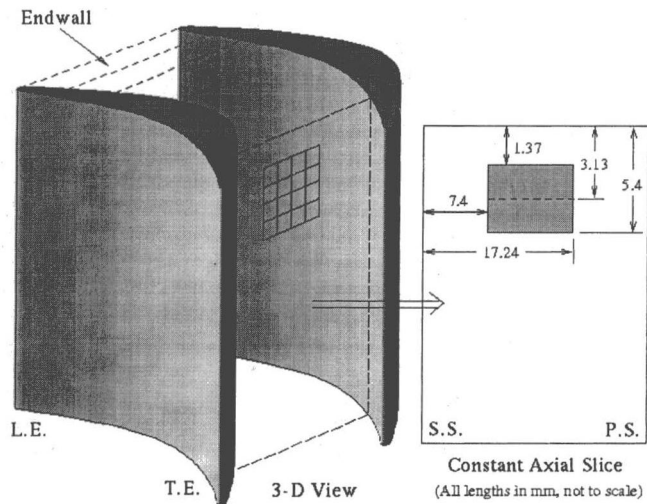


Fig. 20(a) Schematic of trace set release points and viewing orientation for Figs. 20(b), 20(c), and 20(d)

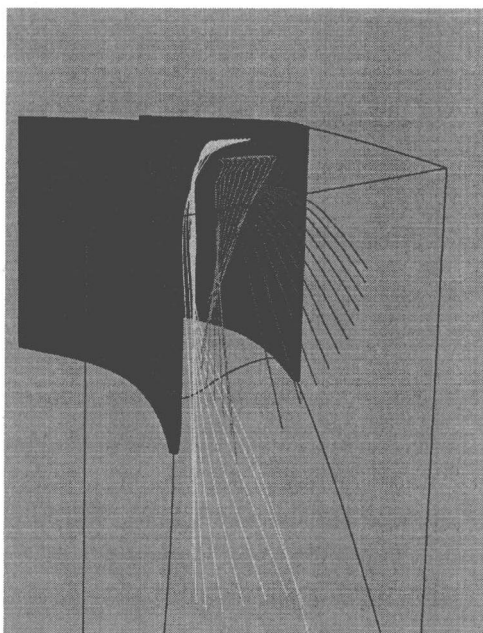


Fig. 20(b) Trace Sets 1, 2, and 3 for $M_{2is} = 0.5$

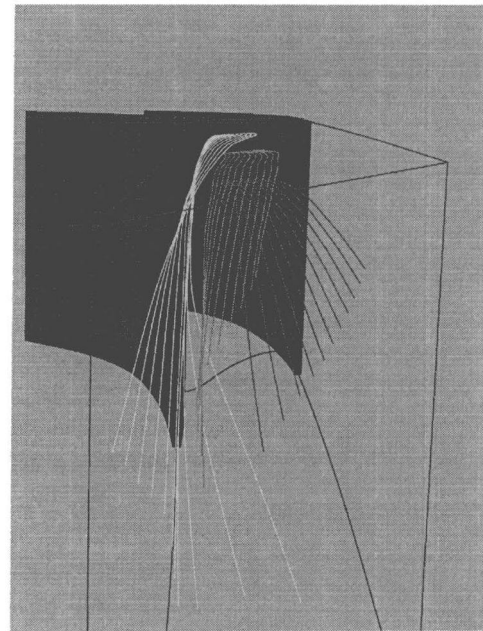


Fig. 20(c) Trace Sets 1, 2, and 3 for $M_{2is} = 1.02$

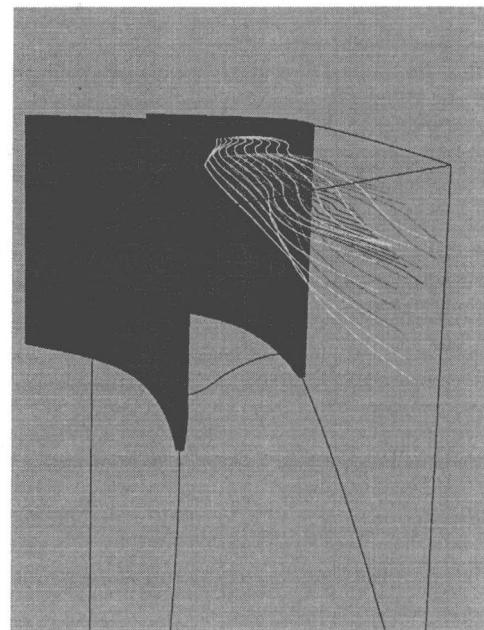


Fig. 20(d) Trace Sets 1, 2, and 3 for $M_{2is} = 1.6$

a standard digital movie format, which can be downloaded by the reader via the Internet using directions in the appendix.

Mach Number Effects on Wake Decay. Another very useful parameter in turbomachinery design is the decay of the wake downstream of the blade trailing edge. The wake decay parameter is defined as V_d/V_{max} at a given axial station, where $V_d = V_{max} - V_{min}$ is the velocity defect at the center of the wake. Previous work (Prato and Lakshminarayana, 1993) in compressors has shown that in the secondary flow and endwall regions, the rate of decay in the wake is reduced. As the $M_{2is} = 0.5$ cases in Figs. 21 and 22 show, the same conclusion can be made about this turbine case. Unlike Prato and Lakshminarayana's incompressible case, however, the effects of compressibility and shocks can be examined. Figures 21 and 22 also show the wake decay at both midspan and secondary flow regions for the six exit isentropic Mach numbers tested. It can be seen here that all of the exit Mach numbers are fairly well correlated in the near-wake region ($x/b = 1.0$ to 1.2) at midspan. Shock wave effects in the far wake area, however, prevent a general conclusion on the behavior of the wake in this region.

In Fig. 22, the effect of shock waves on the endwall velocity deficit is very clear. When checked against static pressure contours, each jump in the velocity deficit corresponded to the shock impingement location on the wake.

Loss Correlations: Mach Number Effects. In preliminary designs, loss correlations are often a quick and convenient way to estimate efficiencies in a turbine. However, many of the correlations are based on incompressible or only mildly compressible cases. For low-speed turbines, both correlations and actual data (Sieverding, 1985; Perdichizzi, 1990) show that the amount of secondary flow does not vary appreciably with Mach number. However, as can be seen above and in Perdichizzi (1990), any correlation used above $M_{2is} = 0.5$ should be modified for compressibility effects. The correlation examined here, first proposed by Dunham (1970), is given by:

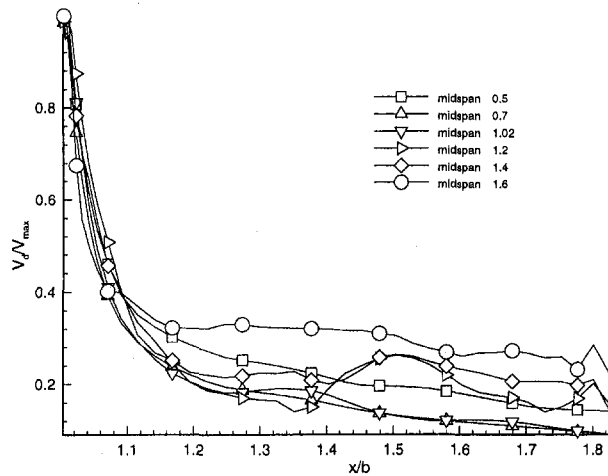


Fig. 21 Midspan wake decay at $x/b = 1.5$ for $M_{2le} = 0.5, 0.7, 1.02, 1.2, 1.4,$ and 1.6

$$\zeta_{SC} = [0.0055 + 0.078 \sqrt{\delta/C}] \times C_L^2 \frac{\cos^3 \alpha_2}{\cos^3 \alpha_m} \frac{C}{H} \left(\frac{C}{S}\right)^2 \frac{1}{\cos \alpha_1} \quad (4)$$

where $\alpha_m = (\alpha_1 + \alpha_2)/2$ and δ is the inlet boundary layer thickness. This loss correlation was plotted previously along with the computed secondary losses at $x/b = 1.5$ in Fig. 18. Even though the computed loss in the compressible flow range can be seen to drop off quite markedly, the incompressible correlation cannot capture this. We should expect this result because of some of the reasoning given in the previous sections, which is summarized below. In each reason discussed, a possible means of using these observations to modify the correlation for use in the compressible flow range is mentioned.

1 The reduced endwall boundary layer momentum thickness growth inside the passage at the higher Mach numbers significantly reduces the amount of secondary flow and the transport of low-momentum fluid toward the suction surface. This thinning of the boundary layer, shown in Fig. 19, is due to larger accelerations in the passage at the supersonic exit Mach numbers. Even a two-dimensional relation for an accelerating flat plate could be a useful qualitative factor to simulate this phenomenon.

2 The reduced endwall boundary layer results in a wake-secondary flow interaction vortex that is closer to the endwall. As was discussed previously, a closer wake-secondary flow interaction region prevents both the larger overturning crossflow near the endwall and the stronger passage vortex/wake interaction vortex interplay (which form the secondary loss core) seen at the lower Mach numbers. One would have to use three-dimensional boundary layer properties along with a relation from (1) to estimate the strength of the vortex and spanwise distance that the S_4 stagnation line migrates away from the endwall to quantify this effect.

3 The particle trace study revealed that the presence of the shocks at the trailing edge works as a strong overturning mechanism, which limits the tendency of the flow to overturn at the endwall as exit Mach number is increased. This observation is the most visible and most useful because fairly accurate shock and subsequent flow angles can be calculated using a two-dimensional Euler code.

Although an appropriate Mach number correction to Dunham's incompressible correlation could be achieved by simply fitting a quadratic to the ζ_{SC} values in order to match the computed quantities, any practical modification proposed should be

based more on flow physics available from the simulation and rigorous fluid dynamics relations. An attempt was made to develop a modified correlation by using compressible flow theory and some of the factors discussed above (Koiro, 1996), but the authors felt that without a wider range parametric study and a more sizable cross section of geometries, any modification proposed would lack sufficient generality and scientific basis.

Conclusions

Comparison between the original, single grid, three-dimensional explicit Navier-Stokes, $k-\epsilon$ solver and the version with multigrid indicates that a much more efficient and sufficiently robust code could be developed. When validated against experimental data for a three-dimensional turbine cascade, the modified code proved that it could capture most of the complex flow physics. Additionally, the improved resolution in the computation allowed for a much more thorough inspection of secondary flow features both at locations that were experimentally investigated (downstream of the blade row) and in the passage where the flow could not be measured. Some of the key features that were revealed in the validation process were:

- Four primary loss/vortex structures downstream of the passage were identified: (1) secondary flow passage vortex, (2) corner loss structure, (3) wake loss region, and (4) wake-secondary flow interaction vortex.
- Evolution of the pressure side horseshoe vortex into the passage vortex and the dissipation of the suction side horseshoe vortex was clearly visible.
- Growth of the endwall boundary layer on the blade suction side was characterized by the S_4 stagnation line. Near the passage exit, this line marks the location of, and feeds into the wake-interaction vortex.

The improved efficiency of the multigrid code allowed for an in-depth examination of the secondary flow structure in order to isolate and possibly quantify some of the features responsible for higher or lower losses in the compressible flow range. For the range of exit Mach numbers tested, it was found that:

- The spanwise extent and overall magnitude of both secondary losses and appreciable secondary flow velocities is reduced at higher exit Mach numbers.
- The momentum thickness of the endwall boundary layer is reduced at the higher Mach number due to the higher flow acceleration in the passage. The thinner endwall boundary layer helps to prevent the formation of signifi-

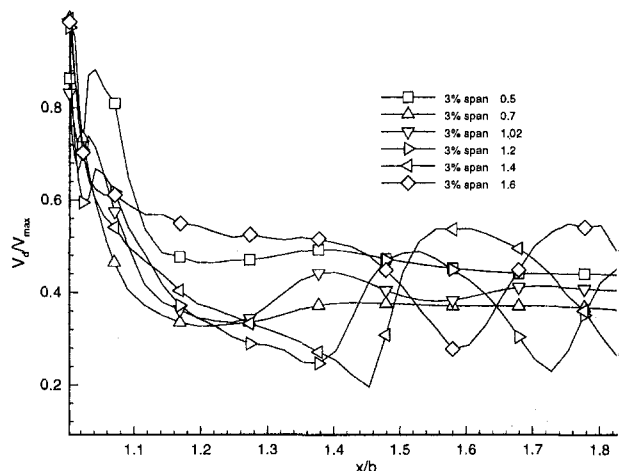


Fig. 22 Secondary flow region wake decay at $x/b = 1.5$, for $M_{2le} = 0.5, 0.7, 1.02, 1.2, 1.4,$ and 1.6

cant crossflows that eventually create secondary flow downstream of the blade passage.

- The amount of over- or underturning at the wall is directly related to the presence and strength of the trailing edge oblique shock system. A strong shock at the high exit Mach numbers substantially underturns the flow and prevents the formation of the pitchwise and spanwise velocities associated with subsonic secondary flow generation.
- The wake decay both at midspan and near the endwall is correlated fairly well with increasing Mach number. However, the presence of shocks and their drastic influence on the velocity deficit make any general conclusions difficult.

Passage-averaged secondary losses indicate that at supersonic Mach numbers, standard incompressible secondary flow loss correlations are not adequate. It is speculated that quantities from the endwall momentum thickness and Euler solver exit flow angles would be useful in modifying this correlation for use in a compressible flow regime.

Acknowledgments

This work was supported by NASA Contract NAS 8-38867, monitored by Lisa Griffin at the NASA Marshall Space Flight Center. The first author was supported by the Penn State Propulsion Research Center through a NASA Traineeship. The authors wish to acknowledge NASA for providing the supercomputer resources at the National Aerodynamic Simulation Facility at NASA Ames Research Center and at the NASA Marshall Space Flight Center. In addition, the authors wish to thank A. Perdichizzi for providing the experimental data used for the code validation and A. Arnone for his assistance with some key aspects of the multigrid technique.

References

- Arnone, A., Liou, M. S., and Povinelli, L. A., 1993, "Multigrid Calculation of Three-Dimensional Viscous Cascade Flows," *Journal of Propulsion and Power*, Vol. 9, No. 4, pp. 605-614.
- Bassi, F., and Savini, M., 1992, "Secondary Flow in a Transonic Cascade: Validation of a 3-D Navier-Stokes Code," ASME Paper No. 92-GT-62.
- Chien, K., 1982, "Prediction of Channel and Boundary Layer Flows With a Low Reynolds Number Turbulence Model," *AIAA Journal*, Vol. 20, No. 1, p. 33.
- Dunham, J., 1970, "A Review of Cascade Data on Secondary Losses in Turbines," *J. Mechanical Eng. Science*, Vol. 12, pp. 48-59.

Gregory-Smith, D. G., and Cleak, J. G. E., 1992, "Secondary Flow Measurements in a Turbine Cascade With High Inlet Turbulence," *ASME JOURNAL OF TURBOMACHINERY*, Vol. 114, pp. 173-183.

Hall, E. J., Topp, D. A., and Delaney, R., 1994, "Aerodynamic and Heat Transfer Analysis of Discrete Site Film Cooled Turbine Airfoils," AIAA Paper No. 94-3070.

Ho, Y.-H., and Lakshminarayana, B., 1996, "Computational Modeling of Three-Dimensional Endwall Flow Through a Turbine Rotor Cascade With Strong Secondary Flows," *ASME JOURNAL OF TURBOMACHINERY*, Vol. 118, pp. 250-261.

Jameson, A., and Baker, T. J., 1983, "Multigrid Solutions of Euler Equations Aircraft Configurations," AIAA Paper No. 84-0093.

Koiro, M., 1996, "Simulation of Mach Number Effects in a Transonic Turbine Using a Multigrid, $k-\epsilon$ Solver," M.S. Thesis, Penn State University.

Kunz, R., and Lakshminarayana, B., 1992a, "Stability of an Explicit 3-D Navier-Stokes Procedure Using a $k-\epsilon$ and $k-\epsilon/\text{Algebraic Reynolds Stress Model}$," *Journal of Computational Physics*, Vol. 103, p. 141.

Kunz, R., and Lakshminarayana, B., 1992b, "Three-Dimensional Navier-Stokes Computation of Turbomachinery Flows Using an Explicit Numerical Procedure and a Coupled $k-\epsilon$ Turbulence Model," *ASME JOURNAL OF TURBOMACHINERY*, Vol. 116, pp. 625-642.

Lakshminarayana, B., 1986, "Turbulence Modeling for Complex Flows," *AIAA Journal*, Vol. 24, No. 12, pp. 1900-1917.

Lakshminarayana, B., 1996, *Fluid Dynamics and Heat Transfer of Turbomachinery*, Ch. 6, Wiley, New York.

Mavriplis, D. J., and Martinelli, L., 1991, "Multigrid Solution of Compressible Turbulent Flow on Unstructured Meshes Using a Two-Equation Model," AIAA Paper No. 91-0237.

Perdichizzi, A., Ubaldi, M., and Zunino, P., 1989, "Secondary Flows and Reynolds Stress Distributions Downstream of a Turbine Cascade at Different Expansion Ratios," AGARD CP-469, Reference 6.

Perdichizzi, A., 1990, "Mach Number Effects on Secondary Flow Development Downstream of a Turbine Cascade," *ASME JOURNAL OF TURBOMACHINERY*, Vol. 112, pp. 643-651.

Prato, J., and Lakshminarayana, B., 1993, "Experimental Investigation of Rotor Wake Structure at Peak Pressure Rise Coefficient and Effects of Loading," *ASME JOURNAL OF TURBOMACHINERY*, Vol. 115, pp. 487-500.

Sieverding, C. H., 1985, "Recent Progress in the Understanding of the Basic Aspects of Secondary Flows in Turbine Blade Passages," *ASME Journal of Engineering for Gas Turbines and Power*, Vol. 107, pp. 248-257.

Turner, M. G., and Jennions, I. K., 1993, "An Investigation of Turbulence Modeling in Transonic Fans Including a Novel Implementation of an Implicit $k-\epsilon$ Turbulence Model," *ASME JOURNAL OF TURBOMACHINERY*, Vol. 115, pp. 249-260.

APPENDIX

To download an MPEG movie file from the Penn State Turbomachinery Web Site, open a URL to <http://turbo5.aero.psu.edu/> and transfer to Mike Koiro's homepage. There, one can find MPEG movie files for particle traces at $M_{2is} = 0.5, 1.02$ and 1.6 , a short explanation about each file, and directions for downloading and viewing. These movies give the steady flow an almost unsteady feel that substantially enhances understanding of the flow development.

Flow Development Through Interturbine Diffusers

R. G. Dominy

D. A. Kirkham

University of Durham,
School of Engineering,
Durham, United Kingdom

A. D. Smith

Rolls-Royce plc
Derby, United Kingdom

Interturbine diffusers offer the potential advantage of reducing the flow coefficient in the following stages, leading to increased efficiency. The flows associated with these ducts differ from those in simple annular diffusers both as a consequence of their high-curvature S-shaped geometry and of the presence of wakes created by the upstream turbine. Experimental data and numerical simulations clearly reveal the generation of significant secondary flows as the flow develops through the diffuser in the presence of cross-passage pressure gradients. The further influence of inlet swirl is also demonstrated. Data from experimental measurements with and without an upstream turbine are discussed and computational simulations are shown not only to give a good prediction of the flow development within the diffuser but also to demonstrate the importance of modeling the fully three-dimensional nature of the flow.

Introduction

Interturbine diffusers are increasingly used in the context of gas turbine design to diffuse the flow between the H.P. or I.P. turbine and the L.P. turbine while maintaining surface continuity. Diffusing the flow upstream of the L.P. turbine and increasing the mean passage radius allows higher turbine stage efficiency to be achieved as a consequence of reducing both the flow coefficient and the stage loading coefficient. To avoid unacceptable weight penalties, the diffuser must be achieved in the shortest possible length while preventing boundary layer separation and instability in the rapidly diffusing flow.

Diffuser Flows. Simple diffusers and their associated flows have been well documented (e.g., ESDU, 1976) and the factors influencing their efficiency are predominantly the area ratio of the diffuser and the length of the flow path over which the diffusion occurs. The modification of the local pressure gradients as a result of wall curvature and the consequent influence upon turbulent boundary layer behavior may substantially change the performance of the diffuser, as may turbulence within the wakes from upstream blade rows or other sources. Published data on S-shaped, annular ducts relate mostly to inter-compressor passages of reducing radius with local, curvature-induced pressure gradients but little or no overall diffusion. Britchford et al. (1993) showed that the addition of an upstream rotor led to a reduction in the hub boundary layer shape factor in the diffusing zone around the first bend, which they attributed to increased turbulent mixing. Although radial flow migration within the low-energy wakes under the influence of the cross-passage pressure gradient was very weak, the authors concluded that this was responsible for the re-energizing of the hub boundary layer, which consequently reduced its tendency to separate.

Pfeil and Going (1987) observed that the development of the turbulent boundary layers in a straight-cored annular diffuser behind a single compressor stage is greatly influenced by wake propagation. Although their measurements showed a contrast between the essentially two-dimensional boundary layers at midpitch and the strongly three-dimensional nature of the flow in the wake region, the extent of the wake influence remains unknown. A thorough review of the published literature is provided by Dominy and Kirkham (1996).

Only Dominy and Kirkham (1995, 1996), have published comparable data for ducts with both significant diffusion and curvature. Their data confirmed that the flow is strongly influenced by wake propagation and that cross-passage pressure gradients induce radial flows within the wakes, leading to clearly defined secondary flows with their consequent redistribution of loss and significant local yaw and pitch over much of the passage.

Swirling Flows. The local effect of swirl in an annular diffuser is to produce a radial pressure gradient to balance the centrifugal force which increases the static pressure along the casing wall and decreases it at the hub. For a diffusing, swirling flow the pressure coefficient at some axial location x is given by the expression (Lohmann et al., 1979):

$$Cp_x = \left(1 - \frac{\rho_i A_i^2}{\rho_x A_x^2} \right) + \tan^2 \alpha_i \left(1 - \frac{\rho_i r_{im}^2}{\rho_x r_{xm}^2} \right) \quad (1)$$

The first diffusion term is due to geometric area change and the second results from the conservation of angular momentum in a flow of changing mean radius. If the inlet swirl angle is nonzero, a change of mean radius leads to a static pressure rise even for a constant area duct. The static pressure rise through the diffuser is strongly dependent upon both the inlet swirl angle and the cant angle. Coladipietro et al. (1975) and Kumar and Kumar (1980) both reported that for unstalled, straight-walled annular diffusers the static pressure rise coefficient increased with increasing swirl. Kumar and Kumar (1980) also reported that as the inlet swirl angle was increased, the pressure rise reached a peak and then decayed with further swirl increase. This was attributed to the increased path length, giving rise to increased rotational kinetic energy losses through skin friction. McDonald and Fox (1971) found that the performance of stalled, conical diffusers with an axial inlet flow could be improved by the introduction of swirl, but unlike Kumar and Kumar (1980), he found little benefit from swirl for unstalled flows. Bradshaw (1973) demonstrated that centrifugal and Coriolis body forces alter the turbulent structure of the flow. For swirling flow in an annular passage, the production of turbulent energy is suppressed in the vicinity of the hub wall, where the radial pressure gradient is positive and enhanced near the casing where the gradient relative to the boundary layer is reversed with an implied variation in the rate of growth of the surface boundary layers. The difference in turbulent energy production would suggest that in an annular diffuser inlet swirl would stabilize the casing and destabilize the hub boundary layers.

Contributed by the International Gas Turbine Institute and presented at the 41st International Gas Turbine and Aeroengine Congress and Exhibition, Birmingham, United Kingdom, June 10–13, 1996. Manuscript received at ASME Headquarters February 1996. Paper No. 96-GT-139. Associate Technical Editor: J. N. Shinn.

Table 1 Geometric and operating parameters of the Durham S-shaped diffuser rig

Inlet hub diameter	0.286m
inlet casing diameter	0.412m
exit hub diameter	0.551m
exit casing diameter	0.660m
Area Ratio exit / inlet	1.5
Inlet Reynolds Number (based on inlet passage height)	3.9×10^5
Inlet Dynamic Head (nominal)	4.5 kPa
Number of Inlet Swirl Vanes	34
Inlet Free Stream Turbulence	2.5%

This has been confirmed experimentally by Lohmann et al. (1979) who reported premature separation on the hub and Kumar and Kumar (1980) who reported that inlet swirl reduced the likelihood of separation occurring on the casing of stalled diffusers. Hoadley and Hughes (1969) have also shown that separation in a parallel-cored, annular diffuser may be completely suppressed or moved from the normal outer wall location to the inner core depending upon the degree of inlet swirl. For turbines designed to operate with axial exit flow, the evidence suggests that off-design operation with its associated introduction of a small degree of swirl is likely to have a stabilizing effect upon the critical casing flow and is not therefore of major concern during the design process.

In this study the quasi-steady influence of a nonuniform inlet flow arising from wake propagation has been investigated through measurements in the Durham University annular diffuser rig and computations made using the Moore Elliptic Flow Program (MEFP). Inlet swirl angles of 0 and 15 deg were chosen to simulate realistic design and off-design operating conditions, but work is currently in progress to investigate the effect of more extreme degrees of swirl. The additional effects of blade-generated secondary flows and rotation are addressed through measurements made by Rolls-Royce plc in a model turbine test rig.

Experimental Facility

The Durham University Diffuser Rig. The Durham University S-Shaped Duct Facility has been described in detail by Dominy and Kirkham (1995, 1996) and the important geometric and operational parameters are described in Table 1.

The initial duct curvature begins 2.5 inlet passage heights downstream from a row of 34 swirl vanes and the flow is turned radially through a nominal angle of 36 deg. Traversing within the diffuser may be performed at 12 alternative axial positions. Data from four of those traverse planes are presented here and their locations are shown in Fig. 1(a). Static pressure tappings are located at each traverse plane on both the hub and the casing and additional tappings are positioned at the points of greatest change of surface pressure gradient. Area traverses were performed using 2-mm-dia, five-hole pressure probes for the bulk of the flow and 0.8-mm-thick, three-hole cobra-type probes close to the walls. The confines of the duct preclude the adoption of probe nulling so a calibration method was adopted allowing flow angles of up to ± 40 deg in yaw and pitch to be measured.

Nomenclature

A = local cross-sectional area
 C_p = pressure rise coefficient
 L = duct axial length
 h = inlet passage height
 p = static pressure
 P_o = stagnation pressure
 q = dynamic head

r = radius
 Re = Reynolds number
 x = axial distance
 α = swirl angle
 δ^* = boundary layer displacement thickness
 ρ = density

Subscripts

e = exit plane
 i = inlet plane
 m = mean
 n = number of traverse plane
 x = local axial position

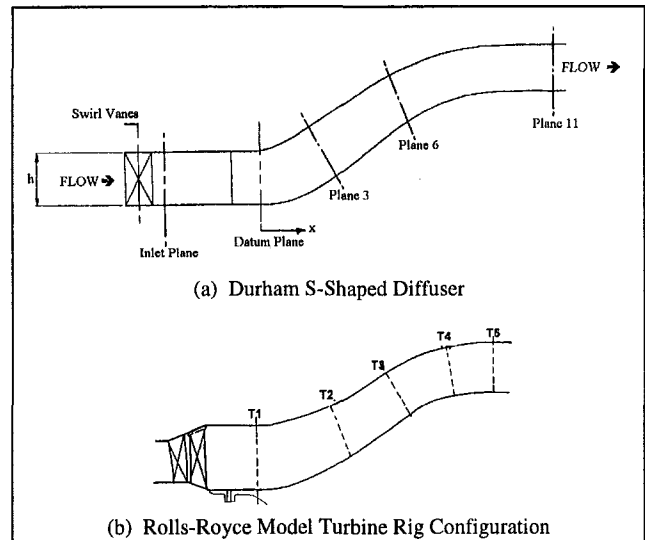


Fig. 1 Traverse plane locations and general geometry of (a) the Durham rig and (b) the model turbine rig

The probes were calibrated at the operating Reynolds number to minimize potential calibration errors (Dominy and Hodson, 1993) and typical, estimated measurement uncertainties were $0.01q_i$ for stagnation pressure and ± 0.8 deg for radial and circumferential flow angle.

The Model Turbine Rig. Measurements in a scaled duct were performed downstream of a single-stage LP turbine in the Rolls-Royce No. 4 Turbine Test Facility (Fig. 4). Measurements were made at a Reynolds number of 3.2×10^5 and at a fixed axial Mach number of 0.23 at the diffuser inlet with a typical, uniform inlet temperature of 370 K. Area traversing was possible at the inlet and exit planes of the diffuser and radial traversing was performed at three intermediate planes. Static pressures were measured along the duct at three alternative circumferential positions to assess circumferential variation. All of the pressure measurements were made using fixed probes and tappings and represent time averages.

CFD

The numerical analysis of the flow was performed using the Moore Elliptic Flow Program, which has been thoroughly described in the published literature (e.g., Moore and Moore, 1985; Moore, 1985). The code solves the Reynolds-averaged Navier–Stokes equations in three dimensions and the elliptic nature of the equations allows reversed flows and hence separations to be indicated. Further details of the application of the code to the particular flows assessed here are provided in the relevant sections of the text.

Results and Discussion

Axial Inlet Flow. Area traverses were performed in the model turbine rig at the inlet and exit planes (planes T1 and

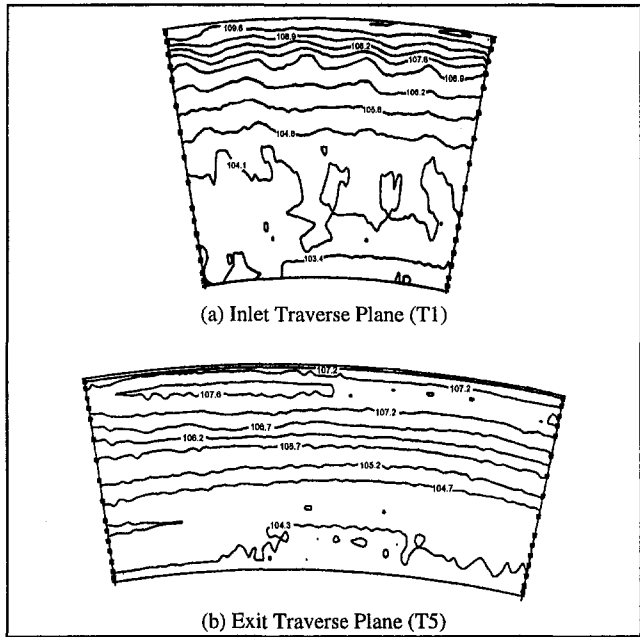


Fig. 2 Turbine rig total pressure contours (kPa) at the inlet and exit planes

T5, Fig. 1(b)) at a Reynolds number of 3.2×10^5 and the corresponding contours of total pressure are shown in Fig. 2. The time-averaged, inlet total pressure traces display reasonable circumferential uniformity although small perturbations are observed. These may be due solely to measurement uncertainty but they may also be associated with asymmetric flow from the upstream NGV's and rotor. No additional data were available to investigate this observation further. The development of the time-averaged hub and casing boundary layers is shown in Fig. 3 together with a numerical calculation based upon a circumferentially uniform inlet flow, which was matched to the measured data. The calculations were performed using 76 axial planes and 41 radial planes using both the Baldwin-Lomax model (presented here) and an alternative one-equation model. In this

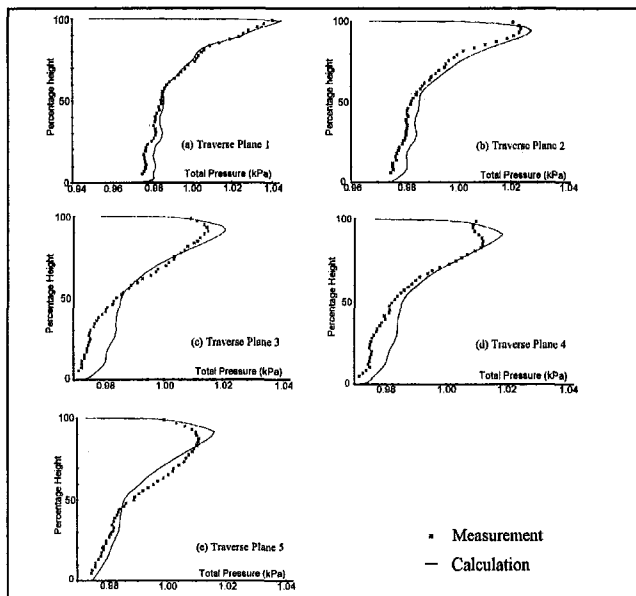


Fig. 3 Total pressure profile development through the turbine rig with an upstream stage

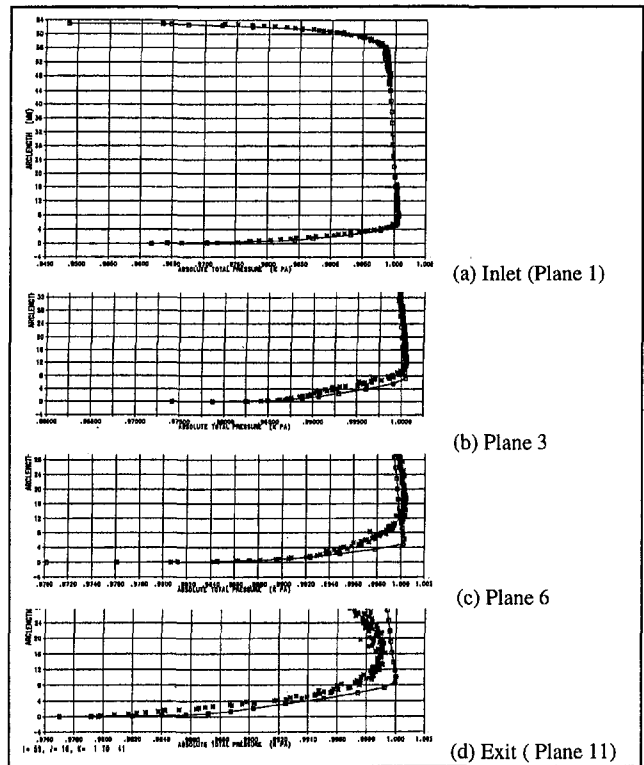


Fig. 4 Durham rig (no swirl vanes): total pressure [**measurement; -□- prediction]

diffuser the boundary layers are always fully turbulent and no differences were apparent between calculations using the two turbulence models.

At the exit traverse plane the simulation displays a good likeness to the measured data but the development of the flow upstream from the exit shows errors particularly near the hub where the calculation overpredicts the total pressure. With the same computational grid and turbulence model, predictions of the near-hub flow in the Durham rig more closely match the experimental data (Fig. 4) suggesting underlying differences in the flows through the two rigs. The Durham rig provides a much simplified inlet flow (Fig. 4(a)), which helps to clarify the development of the flow through the diffuser.

The slight total pressure gradient that is observed is due to a small velocity gradient at the plane of the inlet turbulence grid and the increasing scatter in the data through the duct arises from slight unsteadiness created in the inlet contraction which is exaggerated in the diffusing flow.

In the turbine rig the inlet flow angle is nominally zero, but it may be seen from Fig. 5 that locally the swirl may deviate from the mean by almost 20 deg. However, there are more

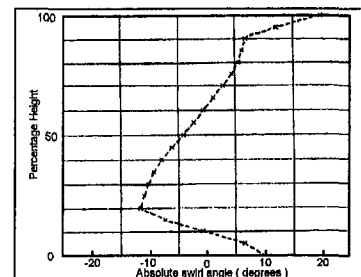


Fig. 5 Turbine rig: radial variation of circumferentially averaged swirl angle (measurement)

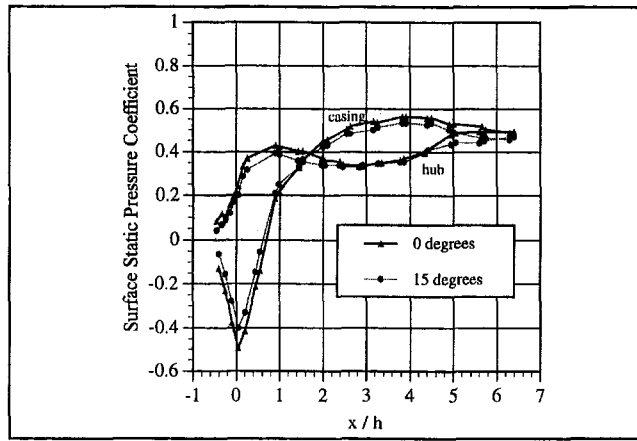


Fig. 6 Axial surface static pressure distribution with and without swirl (measurement, Durham rig)

fundamental differences in the inlet flows of the two rigs. These relate to the flows generated by and through the upstream stage, i.e., the effects of blade wakes from the stator and rotor, secondary flow vortices and periodic, rotating wake-wall interactions. Predictions of the rotor wake influence upon the flow through the turbine test rig suggest that for this application, the wake pressure and velocity deficit have largely dissipated by the plane of entry of the diffusing duct but there are no equivalent unsteady measurements for validation. To allow the first step in a parametric study of these flows, the Durham rig has been tested with representative wakes passing along the duct. The wakes were generated by a fixed row of guide vanes situated 0.85 passage heights upstream of the geometric entry to the diffuser. The term geometric entry is used to emphasize that the presence of the diffuser has an influence upon the local static pressure profile that extends upstream from this point. The development of the inlet flow in the absence of inlet swirl and the development of that flow through the duct has been fully described by Dominy and Kirkham (1994) and is briefly summarized below.

The pressure distribution through the duct (Fig. 6) clearly demonstrates zones of strong diffusion and cross-passage pressure gradients and the most rapid diffusion occurs where the influences of the wall curvature and the rapidly increasing duct area are additive. Dominy and Kirkham (1996) have shown that in the absence of wake propagation, this pressure distribution provides a severe but well-behaved test case in which the boundary layers remain attached at the design flow condition.

The inlet wake structure shows only very minor interaction between the wake and the wall boundary layers (Fig. 7). As the flow passes around the first bend the pressure gradient between the hub and the casing leads to a radially outward flow component within the low-energy wake. By traverse plane 3

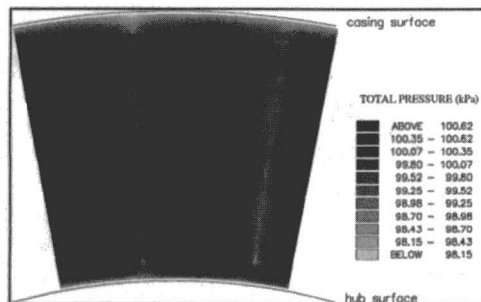


Fig. 7 Measured inlet total pressure contours (Durham rig, inlet guide vanes fitted, zero swirl)

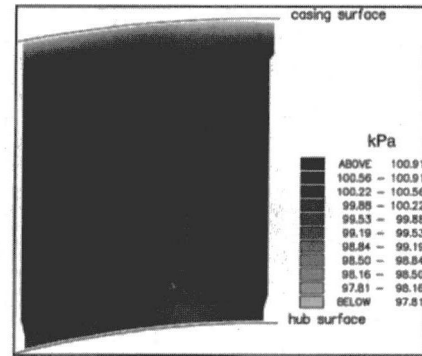


Fig. 8 Measured total pressure contours (plane 3, $x/h = 1.17$, zero swirl)

(nominal $x/h = 1.169$) the cross-passage driving pressure gradient has fallen from a peak of almost 65 percent of the inlet dynamic head to about 20 percent. Total pressure contours (Fig. 8) show a slight broadening and weakening of the wake relative to the inlet flow and also a thickening of the casing boundary layer. By plane 6 (nominal $x/h = 2.62$) the strong adverse pressure gradient on the casing downstream from the first curvature has resulted in further boundary layer growth, which is exaggerated by the radially outward flow of low energy fluid that has occurred within the wakes (Fig. 9).

As the flow is turned back toward the axial direction, the sign of the radial pressure gradient reverses, reaching a peak cross-passage pressure difference corresponding to 20 percent of the inlet dynamic head. Plane 11 ($x/h = 5.57$) lies in the parallel section of the duct downstream from the second bend where the cross-passage pressure difference has decayed almost to zero. The cumulative influence of the zone of reversed pressure gradient does not significantly influence the three-dimensional character of the flow that has developed (Fig. 10(a)) and the remaining wake is very weak. Vortices are observed either side of the wake at both the hub and the casing (Fig. 10(b)) but the casing vortices are both larger and stronger. One influence of the secondary vortices is to accumulate loss close to the wall but away from the wake axis. The asymmetry of the flow suggests that there must have been some inlet asymmetry or swirl, which has been exaggerated as the diffusing flow developed. Despite the growth of the wake-induced secondary flows, their influence upon the overall performance of the diffuser is remarkably slight in terms of both pressure recovery and loss generation with the changes lying close to the limits of experimental accuracy. No change in the surface static pressure distribution is observed relative to the wake-free case, which implies that the three-dimensional flows result primarily in a redistribution of the inlet loss and not a creation of additional loss. In view of these wake-induced secondary flows, it is not surprising to find that CFD analysis of the flow in the turbine rig based upon a circumferentially averaged inlet flow results

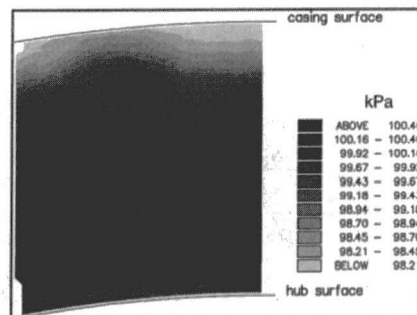


Fig. 9 Measured total pressure contours (plane 6, $x/h = 2.62$, zero swirl)

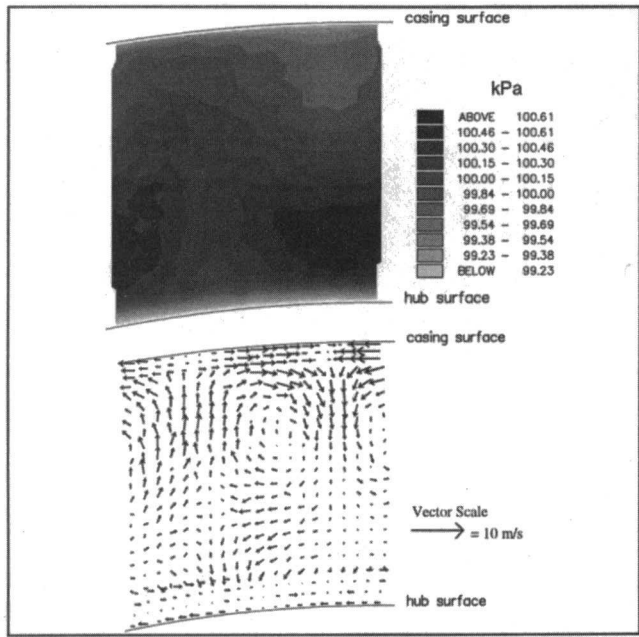


Fig. 10 Total pressure contours and secondary velocity vectors (measurement plane 11, $x/h = 5.57$, zero swirl)

in a maldistribution of the pressures and losses. The diffuser flow within the Durham rig has therefore been analyzed to investigate the simulation of the wake-induced flows arising from the fixed inlet guide vanes. The computational mesh comprised 76 axial grid points and 41 radial points (matching the two-dimensional calculations) and 31 circumferential grid points over one guide vane pitch. The inlet flow conditions were matched exactly to the measured data. Figure 11 shows the development of the total pressure profile at different circumferential locations at each of the four sample traverse planes and the circumferential nonuniformity of the flow is clearly evident. The predictions are compared with the radial profiles measured midway between the inlet guide vanes wake axes and here the measured data indicate a more mixed-out flow than the prediction. However, it has been discovered that the plane where the inlet traverse was measured was farther upstream of the

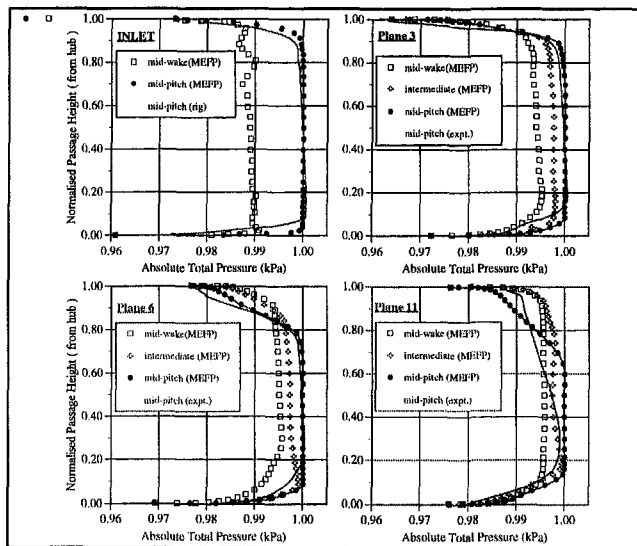


Fig. 11 Predicted radial distribution of total pressure at different circumferential positions with measured, midpitch data

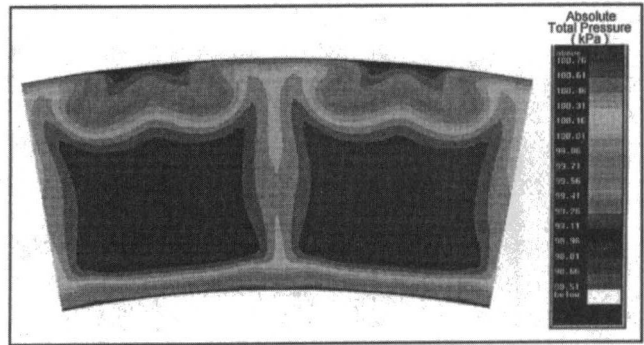


Fig. 12 Predicted exit total pressure contours (plane 11, swirl vanes set for zero swirl)

calculation grid inlet than was believed at the time of the calculations so some additional mixing will be evident in the measured data. Comparing the measured exit flow (Fig. 10) with the MEFP prediction (Fig. 12), similar trends are observed. The prediction shows stronger secondary flow vortices and less inward migration of the casing boundary layer, indicating less mixing. This will be influenced by the mismatched inlet lengths described above but may also be a function of the chosen turbulence model. The latter influence requires further investigation.

15 deg Inlet Swirl. Predictions of the flow development through the duct with inlet swirl show similar trends when compared to experimental data. Figure 13 demonstrates the loss generation and redistribution as the flow progresses through the diffuser. With the introduction of inlet swirl, the wake breadth increases due to stalling of the guide vanes and a relative thinning of the wake near the walls is observed arising from secondary flow creation at the vane tips. The untwisted inlet guide vanes generate an almost uniform inlet yaw angle across the passage in the bulk flow but the wake axes are no longer truly radial.

A full discussion of the inlet flow and its development is provided by Dominy and Kirkham (1995), but the important observations are summarized here. On turning through the initial, radially outward bend the skew of the wakes is exaggerated and by plane 3 ($x/h = 1.17$) the wakes remain clearly defined but strongly skewed, as shown by both the numerical prediction and by measured total pressure data (Fig. 14). By plane 6 ($x/h = 2.62$) the radial pressure gradient has reversed but remains relatively weak. Here the wakes are observed to have skewed further and the high-loss fluid that is associated with those wakes has almost entirely accumulated at the casing. The vortical motion that continued to drive the flow against the cross passage pressure gradient in the axial case (Dominy and Kirkham, 1996) is much reduced in the absence of any significant

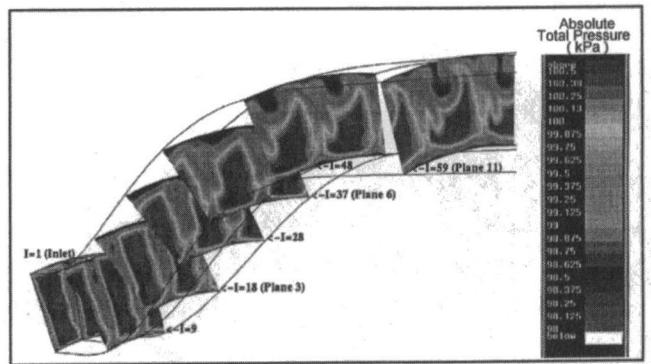


Fig. 13 Predicted development of the total pressure distribution through the diffuser (15 deg inlet swirl)

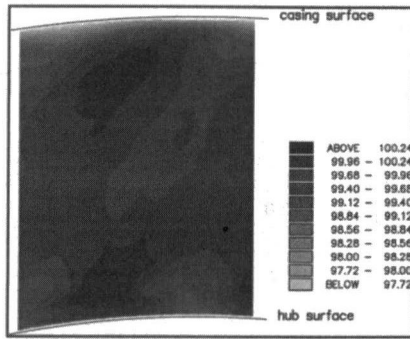


Fig. 14 Measured total pressure contours (traverse plane 3, $x/h = 1.17$, 15 deg swirl)

radial flow component in the wake. As a consequence the form of the casing "boundary layer" is as much due to the merging of the natural boundary layer and the wake as to the classical growth of the wall boundary layer.

Figure 15 shows a pronounced vortex associated with the loss core at plane 11, but its character differs significantly from the zero swirl case where the velocity vectors provide clear evidence of four vortices with a stronger, counterrotating pair lying symmetrically either side of the wake near the casing and a much weaker pair in the hub side of the passage. In the swirling flow, the skew of the wakes and the relative circumferential shift of the casing vortex pair relative to the hub pair appears to result in the merging of the hub and casing vortices of the same sign albeit with the casing side vortex clearly the dominant partner.

Despite the observed differences in the detail of the flow structures within the duct under the influence of swirl, their influences upon the overall performance of the diffuser are surprisingly small with little difference observed in the exit static pressures (Fig. 6). As a result of the effective reduction of wall curvature that is experienced by the swirling flow, the magnitude of the static pressure coefficient at the point of maximum velocity is reduced by 20 percent and a similar reduction is observed in the hub diffusion around the first bend. The loss generation through the duct also remains little changed by the presence of swirl. Figure 16 shows the normalized increase of stagnation pressure loss through the duct for both the zero swirl and 15 deg swirl cases. Each data point shows the loss generated within the duct (downstream from the inlet traverse plane) based on inlet dynamic head normalized against the mixed out exit loss value for the zero swirl case, i.e.,

$$\text{normalized loss} = \left[\frac{P_{0,x} - P_{0,i}}{(P_0 - p)_i} \right] \div \left[\frac{P_{0,e} - P_{0,i}}{(P_0 - p)_i} \right]_{\text{zero swirl}} \quad (2)$$

The loss grows most rapidly between the bends and the overall loss increases with swirl as a consequence of the increased

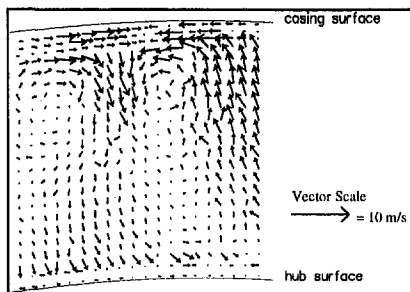


Fig. 15 Measured secondary velocity vectors (traverse plane 11, $x/h = 5.57$, 15 deg swirl)

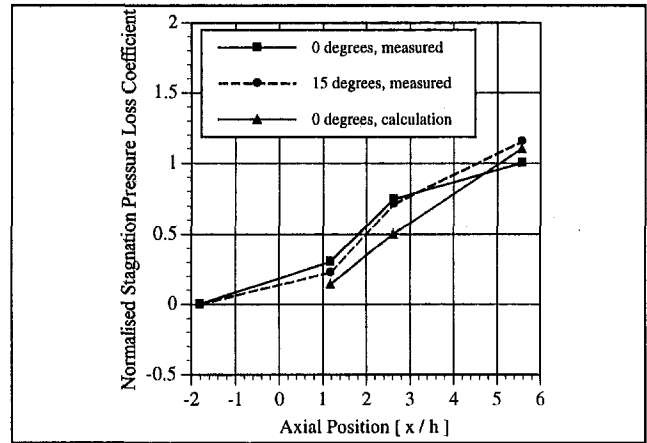


Fig. 16 Loss development with and without swirl

path length. The measured distribution of the loss indicates that the initial loss is reduced with swirl, which is probably a consequence of the initial radial pressure gradient being more favorable and thus mixing is reduced. Up to the second bend and beyond, the pressure gradients increase with swirl, promoting more mixing and hence loss. The overall predicted loss compares well with the measured loss, although ahead of the second bend the measured loss is higher than that predicted. This may be due to the discrepancies between the calculation and measurement at the inlet plane and also to the accuracy of the turbulence model. Overall MEFP gives a good prediction of the duct flow with wakes. The effect of the shorter calculation inlet length is probably only secondary, since it will be the diffusion and curvature in the duct that will have the greatest effect upon the loss generation.

Conclusions

The influence of wakes and swirl upon the flow through a diffusing, S-shaped duct is shown to have a significant effect upon the detailed structure of the flow. Secondary flows resulting from the influence of cross-passage pressure gradients upon the low-energy wake and boundary layer flows are clearly evident with their associated redistribution of loss and local variations in yaw and pitch. Swirl is shown to influence the character of the flow particularly through the skewing of the wakes as they pass through the diffuser. This is observed to change the distribution of loss within the duct, although the evidence suggests that this is mostly a redistribution of the loss generated near the wall and of the loss already present in the inlet flow. Computational simulations generally give a good prediction of the flow development within the diffuser and of the loss generation when the truly three-dimensional nature of the flow is represented. Calculations based upon a circumferentially averaged inlet flow show clear limitations.

Acknowledgments

The work described was supported by the Defence Research Agency and Rolls-Royce plc. The assistance of their representatives and their permission to publish the work described in this paper is gratefully acknowledged.

References

- Bradshaw, P., 1973, "Effects of Streamline Curvature on Turbulent Flow," AGARD AG-169.
- Britchford, K. M., Manners, A. P., McQuirk, J. J., and Stevens, S. J., 1993, "Measurement and Prediction of Flow in Annular S-Shaped Ducts," *Proc. 2nd International Symposium on Engineering Turbulence Modelling and Measurements*, Florence, Italy, pp. 785-794.

- Coladipietro, R., Schneider, J. H., and Sridhar, K., 1975, "Effects of Inlet Flow Conditions on the Performance of Equiangular Diffusers," *Trans. CSME*, Vol. 3, No. 2, pp. 75–82.
- Dominy, R. G., and Hodson, H. P., 1993, "An Investigation of Factors Influencing the Calibration of Five-Hole Probes for Three-Dimensional Flow Measurements," *ASME JOURNAL OF TURBOMACHINERY*, Vol. 115, pp. 513–519.
- Dominy, R. G., and Kirkham, D. A., 1995, "The Influence of Swirl on the Performance of Inter-Turbine Diffusers," VDI Berichte No. 1186.
- Dominy, R. G., and Kirkham, D. A., 1996, "The Influence of Blade Wakes on the Performance of Inter-Turbine Diffuser," *ASME JOURNAL OF TURBOMACHINERY*, Vol. 118, pp. 347–392.
- ESDU, 1976 (amended 1990), "Introduction to Design and Performance Data for Diffusers," Engineering Science Data Unit data item 66027, ISBN 0 85679 164 4.
- Hoadley, D., and Hughes, D. W., 1969, "Swirling Flow in an Annular Diffuser," Report CUED/A-Turbo/TR5, Department of Energy, University of Cambridge, United Kingdom.
- Kumar, D. S., and Kumar, K. L., 1980, "Effect of Swirl on Pressure Recovery in Annular Diffusers," *Journal of Mechanical Engineering Science*, Vol. 22, No. 6, pp. 305–313.
- Lohmann, R. P., Markowski, S. J., and Brookman, E. T., 1979, "Swirling Flow Through Annular Diffusers With Conical Walls," *ASME Journal of Fluids Engineering*, Vol. 101, No. 2, pp. 224–229.
- McDonald, A. T., and Fox, R. W., 1971, "Effects of Swirling Flows on Pressure Recovery in Conical Diffusers," *AIAA Journal*, Vol. 9, No. 10, pp. 2014–2018.
- Moore, J. G., 1985, "An Elliptic Calculation Procedure for Three-Dimensional Viscous Flow," AGARD-LS-140 4.1–4.16.
- Moore, J., and Moore, J. G., 1985, "Performance Evaluation of Linear Turbine Cascades Using Three-Dimensional Viscous Flow Calculations," *ASME Journal of Engineering for Gas Turbines and Power*, Vol. 107, No. 4, pp. 969–975.
- Pfeil, H., and Going, M., 1987, "Measurements of the Turbulent Boundary Layer in the Diffuser Behind an Axial Compressor," *ASME JOURNAL OF TURBOMACHINERY*, Vol. 109, pp. 405–412.
-

P. W. Giel

NYMA, Inc.,
Engineering Services Division,
Brook Park, OH 44142

D. R. Thurman

U.S. Army Research Laboratory,
NASA Lewis Research Center,
Cleveland, OH 44135

G. J. Van Fossen

S. A. Hippensteele

R. J. Boyle

Internal Fluid Mechanics Division,
NASA Lewis Research Center,
Cleveland, OH 44135

Endwall Heat Transfer Measurements in a Transonic Turbine Cascade

Turbine blade endwall heat transfer measurements are presented for a range of Reynolds and Mach numbers. Data were obtained for Reynolds numbers based on inlet conditions of 0.5 and 1.0×10^6 , for isentropic exit Mach numbers of 1.0 and 1.3, and for free-stream turbulence intensities of 0.25 and 7.0 percent. Tests were conducted in a linear cascade at the NASA Lewis Transonic Turbine Blade Cascade Facility. The test article was a turbine rotor with 136 deg of turning and an axial chord of 12.7 cm. The large scale allowed for very detailed measurements of both flow field and surface phenomena. The intent of the work is to provide benchmark quality data for CFD code and model verification. The flow field in the cascade is highly three dimensional as a result of thick boundary layers at the test section inlet. Endwall heat transfer data were obtained using a steady-state liquid crystal technique.

Introduction

As the dependence on computational analyses for aerodynamics and heat transfer increases in the design of turbomachinery, so does the need for detailed, benchmark quality experimental data. These data are required for validation of existing turbomachinery CFD analyses, and to provide data for improved modeling of flow field characteristics. Because the life of high-pressure turbine components is sensitive to metal temperature, validation of the procedures used to predict these temperatures is essential. Current design trends aimed at reducing NO_x emissions tend to flatten combustor exit temperature profiles. The decrease in peak temperatures near midspan is accompanied by an increase in near-endwall temperatures, resulting in increased importance of accurate endwall heat transfer predictions. CFD validations should be done at conditions that approach engine operating conditions as closely as possible.

Several experiments have obtained detailed data for turbine rotor geometries. Langston et al. (1977), Gregory-Smith and Graves (1983), Marchal and Sieverding (1977), Yamamoto (1987a, b), and Gregory-Smith et al. (1988) presented detailed results of aerodynamic measurements for rotor blades tested in linear cascades at relatively low Mach numbers. Mee et al. (1992a, b) presented measurements for a rotor linear cascade tested at transonic conditions obtained in a short duration blow-down facility. Heat transfer measurements for turbine rotor geometries were obtained by Graziani et al. (1980) and Goldstein and Spores (1988) in linear cascades, and by Blair (1994) in a rotating cascade. All of the heat transfer experiments were done in large-scale test facilities, but at low Mach numbers. To increase confidence in the ability of computational analyses to predict turbine rotor heat transfer under actual engine conditions, there exists a need to obtain both aerodynamic and heat transfer data at high Mach numbers.

A Transonic Turbine Blade Cascade Facility was built at the NASA-Lewis Research Center to provide detailed aerodynamic and heat transfer measurements at Reynolds and Mach numbers relevant to high pressure turbine applications. The facility is a

linear cascade. It was recognized that a linear cascade cannot simulate rotation effects or tip clearance effects. Nonetheless, a linear cascade was chosen over an annular cascade for a number of reasons. The primary reason was the objective of obtaining detailed measurements at transonic flow conditions. One design constraint was the mass flow of air that could be moved at transonic speeds. An annular cascade of engine typical aspect ratios would require several times more mass flow than a linear cascade for blades of the same chord length. Also, a linear cascade provides easier access for instrumentation. Computationally, a linear geometry minimizes the effects of the three-dimensional mesh on the CFD solution, thus giving a clearer analysis of the actual flow solver.

Some noteworthy features of the facility are: its ability to achieve transonic Mach numbers, its high blade count to ensure good periodicity, and its large scale. The large-scale facilitates highly detailed flow and heat transfer measurements. Because of the large scale ($C_x = 12.7$ cm), and transonic flow conditions, inlet Reynolds numbers up to one million can be achieved with an inlet pressure near one atmosphere.

The rotor tested in the cascade is of constant cross section, so that the geometry of the cascade is two dimensional. It was desired to provide verification data for three-dimensional CFD analyses. A highly three-dimensional flow field was obtained in the blade passages by allowing boundary layers to develop in the long inlet section upstream of the cascade. Giel et al. (1996a) show that with thick inlet boundary layers, the spanwise variation of surface pressure was of the same order as the spanwise variation experienced in an actual engine.

Endwall heat transfer data were obtained using a steady-state liquid crystal technique, primarily because of its good spatial resolution. Several versions of the technique have been used for gas turbine related measurements. A transient technique was used by Martinez-Botas et al. (1995) while a steady-state technique was used by Hippensteele and Russell (1988).

The objective of the current paper is to present the results of endwall heat transfer measurements that were made in the Transonic Turbine Blade Cascade. Eight different flow conditions were run to examine the effects of varying Reynolds number, exit Mach number, and the inlet turbulence grid. Measurements were made at inlet Reynolds numbers of 0.5 and 1.0×10^6 , at pressure ratios corresponding to exit isentropic Mach

Contributed by the International Gas Turbine Institute and presented at the 41st International Gas Turbine and Aeroengine Congress and Exhibition, Birmingham, United Kingdom, June 10–13, 1996. Manuscript received at ASME Headquarters February 1996. Paper No. 96-GT-180. Associate Technical Editor: J. N. Shinn.

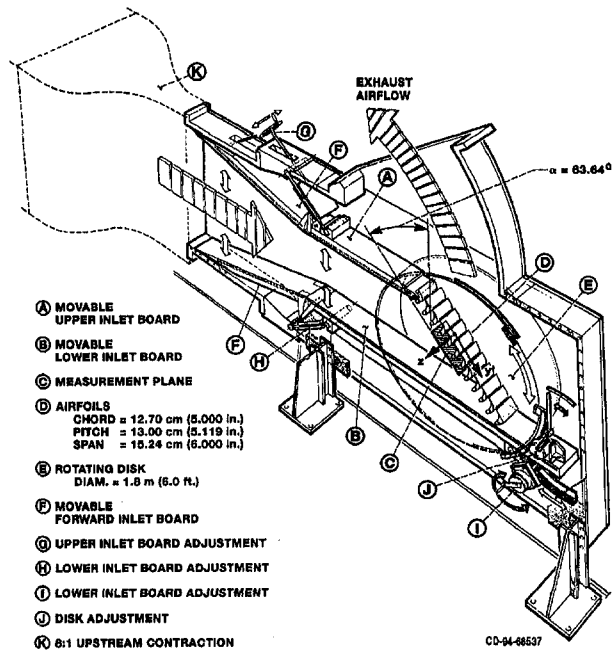


Fig. 1 Overall view of transonic turbine blade cascade test section

numbers of 1.0 and 1.3, and at high and low inlet turbulence levels.

Description of Facility

An initial description of the facility was given by Verhoff et al. (1992). Subsequently, the cascade inlet section was analyzed and redesigned (Giel et al., 1996b) to improve the inlet flow uniformity. The facility is shown in Fig. 1 with the new inlet boards in place.

High-pressure air at ambient temperature is throttled to an inlet total pressure of approximately one atmosphere. Low-Reynolds-number tests were run at half this pressure. The air discharged into a 15.9 kPa (2.3 psia) exhaust header. A valve between the test section and exhaust header was used to throttle the flow to the desired exit Mach number. As seen in Fig. 1, the test section is mounted on a large disk that can be rotated to give a range of incidences. All of the results described were obtained at the design inlet flow angle of 63.6 deg, resulting in

Table 1 Blade and cascade parameters and dimensions

Geometric parameter	Value
axial chord	12.70 cm (5.000 inches)
pitch	13.00 cm (5.119 inches)
span	15.24 cm (6.000 inches)
true chord	18.42 cm (7.250 inches)
stagger angle	41.54°
throat diameter	3.358 cm (1.393 inches)
leading edge diameter	2.657 cm (1.046 inches)
trailing edge diameter	0.518 cm (0.204 inches)
turbulence grid	2.54 cm square bar
Flow parameter	Value
Inlet Re_{C_x}	1.0×10^6 or 0.5×10^6
Exit Re_{C_x}	1.8×10^6 or 0.9×10^6
Inlet M_{IS}	0.38
Exit M_{IS}	1.32 or 0.97
$\dot{m} - Re_{C_x} = 1.0 \times 10^6$	12.9 kg/s (28.5 lb/s)
$\dot{m} - Re_{C_x} = 0.5 \times 10^6$	6.5 kg/s (14.2 lb/s)
Inlet δ - no grid	3.2 cm (1.2 inch)
- with grid	2.0 cm (0.8 inch)
Inlet flow angle	63.6°
Design flow turning	136°

a flow turning of about 136 deg. To prevent shock reflections in the downstream section, no exit tailboards were used.

The blade shape used in these tests, while generic in nature, was designed to simulate the flow characteristics of a high specific work rotor. Details of the blade and of the cascade are given in Table 1. The test section is shown in Fig. 2. The figure shows the positions of the five 0.025 mm (0.001 in.) thick Inconel sheets on the heated endwall. Passage 5 is the primary measurement passage. The heated section begins upstream of the blade leading edge plane at $-0.3 C_x$ and extends downstream to $2.1 C_x$. The heaters are two blade pitches wide. The figure also shows the outline of the 6.35 cm (2.50 in.) thick plexiglas window that was used for optical access. The window formed the endwall opposite the instrumented endwall. Three 35 mm still cameras were used to photograph the liquid crystals. Their fields of view are also shown in the figure. Cameras 1 and 2 had 135 mm lenses while Camera 3 had an 85 mm lens. Camera

Nomenclature

A = heater area, cm^2
 C_p = specific heat $\text{J/kg} \cdot \text{K}$
 C_x = blade axial chord, cm
 Ec = Eckert number = $U^2 / (C_p \Delta T)$
 h = heat transfer coefficient, $\text{W/m}^2 \cdot \text{K}$
 k = thermal conductivity, $\text{W/m} \cdot \text{K}$
 I = electrical current, A
 L = heater length in y direction, cm
 L_x = longitudinal integral turbulence length scale, cm
 \dot{m} = cascade mass flow rate, kg/s
 M = Mach number
 p = blade pitch, cm
 P = pressure, Pa
 Pr = Prandtl number = $\mu C_p / k$
 q = heat transfer rate, W
 r = recovery factor = $Pr^{1/3}$

\mathcal{R} = heater resistance, Ω
 R = gas constant, $\text{J/kg} \cdot \text{K}$
 Re_{C_x} = Reynolds number = $\rho U_{in} C_x / \mu$
 s = blade span, cm
 St = Stanton number
 t = thickness, cm
 T = temperature, K
 Tu = turbulence intensity
 U = total velocity, m/s
 V = electrical voltage, V
 x = chordwise (axial) direction
 y = pitchwise (tangential) direction
 z = spanwise (radial) direction
 α = pitch angle (x - y plane), deg
 γ = specific heat ratio = 1.4
 δ = 99 percent boundary layer thickness, cm

ϵ = emissivity
 μ = dynamic viscosity, $\text{kg/s} \cdot \text{m}$
 ρ = density, kg/m^3
 σ = Stefan-Boltzmann constant

Subscripts

aw = adiabatic wall temperature
 lc = liquid crystal
 ex = exit free-stream value
 in = inlet free-stream value
 IS = isentropic value
 htr = heater
 ref = evaluated at Eckert's reference temperature
 s = surface

Superscripts

' = total conditions

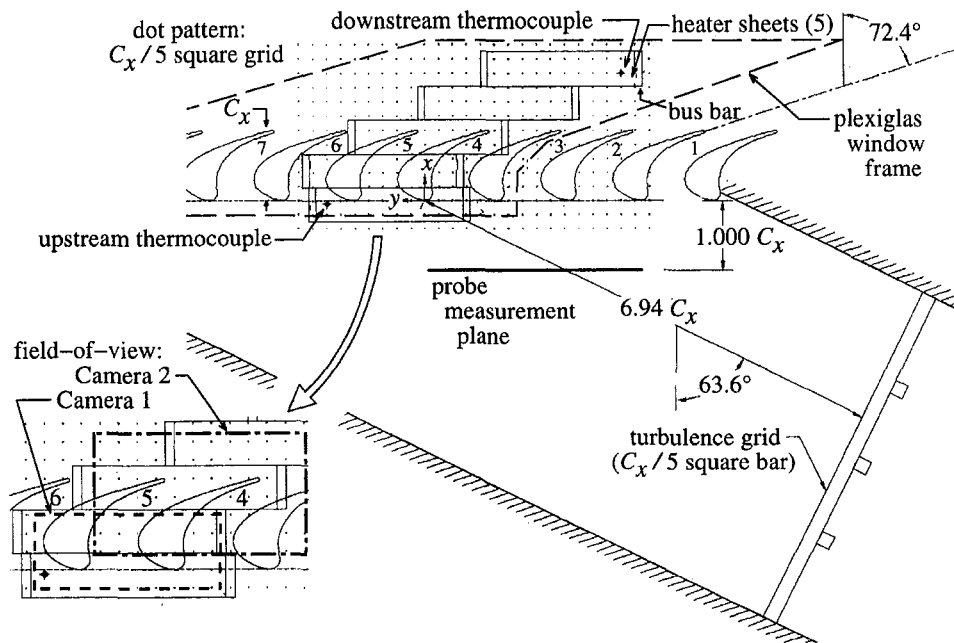


Fig. 2 Geometry of endwall test section

3's lens allowed it to photograph the far-down-stream region, as well as the upstream region near the heater leading edge where Camera 1's view was shadowed by the plexiglas window frame. All of the cameras were positioned 2.0 m from the instrumented endwall.

The outer wall of the instrumented test section was 3.8 cm (1.5 in.) thick stainless steel to withstand a pressure difference of one atmosphere. There was 2.3 cm (0.90 in.) of low thermal conductivity ($k_{\text{foam}} = 0.029 \text{ W/mK}$), high-temperature, closed-cell foam between the outer wall and the heaters. The foam was coated with 0.3 cm (0.10 in.) of gelcoat epoxy to provide a smooth surface. T-shaped electrical bus bars were positioned flush with the endwall and passed through the outer wall. The inner ends of the bus bars are evident in Fig. 2 at both ends of each heater. The foil was tack welded to the bus bars along these ends. The bus bars were thermally as well as electrically conductive, and were therefore placed outside the test passage. The foil was stretched tightly and bonded to the gelcoat surface with double-sided adhesive tape. The heaters were connected in series outside the test section.

The foil heaters were first painted with flat black lacquer paint and then a uniform grid of white dots was painted on with a template. The dots were used in the data reduction process to determine spatial location. The locations of the dots are shown in Fig. 2.

Because the blades were made of stainless steel, those in contact with the heaters needed to have electrically insulated ends. RTV silicone was used to coat the ends of the blades. A thickness of 0.4 mm ($\frac{1}{64}$ in.) was determined from a heat conduction analysis to best balance the insulating effect of the blade, which would tend to allow overheating, and the fin cooling effect of the blade, which would tend to overcool the endwall region near the blade.

The optional 74 percent open area square bar turbulence grid is also shown in Fig. 2. The grid consisted of one square 25 mm \times 25 mm (1 in. \times 1 in.) pitchwise bar that extended between the inlet boards at midspan and three square spanwise bars located on 150 mm centers.

Measurement Techniques

Inlet Flow Measurements. As shown in Fig. 2, aerodynamic measurements were made on a plane one axial chord

upstream of the blade leading edges. The measurements covered three blade pitches and extended from near the endwall, $z/s = 8.3 \times 10^{-4}$, to just above midspan, $z/s = 0.54$. Details of the measurements are given by Giel et al. (1996a). Time mean flow measurements were made with a three-hole boundary-layer probe near the endwall and a five-hole pitch-yaw probe away from the endwall. Turbulence measurements were made with a constant-temperature hot-wire anemometer.

Endwall Static Pressure Measurements. The local isentropic surface Mach number is needed to calculate Stanton numbers. Surface static pressures were measured with a separate endwall, instrumented only with pressure taps. The test passage and two adjacent passages were instrumented with 87 pressure taps per passage. The taps extended axially from $x = -0.4C_x$ to $x = 2.1C_x$. Fewer taps were located in passages away from the test passages. More details of the endwall static pressure measurement techniques are given by Giel et al. (1996a).

Heat Transfer Measurements. The steady-state liquid crystal technique was chosen for the present study for several reasons. Primarily, the method is relatively insensitive to substrate nonhomogeneity (e.g., air bubbles, thickness variations, etc.). Furthermore, the isotherms can be photographed with higher quality still cameras rather than with video cameras that have poorer spatial and color resolution.

Two micro-encapsulated chiral nematic liquid crystals with yellow-band temperatures of $T_{ic,1} = 37.9 \pm 2^\circ\text{C}$ ($100.2 \pm 3.6^\circ\text{F}$) and $T_{ic,2} = 64.5 \pm 3^\circ\text{C}$ ($148.1 \pm 5.4^\circ\text{F}$) were mixed and sprayed onto the surface. The crystal temperatures were calibrated using the surface-mounted thermocouples shown in Fig. 2. As described by Moffat (1990), micro-encapsulated crystals tend to be less sensitive to illuminating and viewing angles than non-encapsulated crystals. While the optical axes of all three cameras were orthogonal to the planar endwall, photographic strobes were mounted at various angles. Each camera had two strobes, which together completely illuminated the surface. Near-simultaneous photographs were taken using each strobe in turn. No differences in isotherm location were ever detected between the photographs. The short duration of the strobes prevented radiative heating of the crystals.

The voltage drop, V , across each of the five heaters was measured independently. The current, I , through the entire cir-

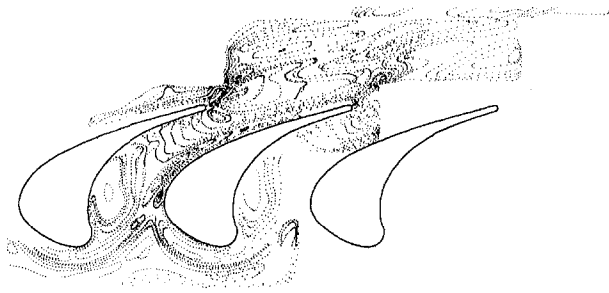


Fig. 3 Sample digitized data point distribution

cuit was measured with three redundant 0.1 percent accuracy shunts. From these measurements, the power, $q_{\text{hr}} = VI$, and the resistance, $R = V/I$, were calculated, displayed, and recorded.

The steady-state liquid crystal technique requires relatively long run times because thermal equilibration needs to be achieved. After changing the heater power level, steady-state conditions were verified by monitoring the isotherm position. Inconel was chosen as the heater material because of its low coefficient of thermal resistivity. Even though the measured resistance varied by less than 0.5 percent over the entire range of heater power settings, variations in resistance with temperature could be monitored because the voltage and current measurements had high signal-to-noise ratios. Stability of the resistance was therefore also used as an indicator of steady-state conditions.

When steady-state conditions were attained, 35 mm color slide photographs were taken of the heated surface. Pressures, temperatures, voltages, etc., were recorded simultaneously. The resulting slides were then projected onto paper marked with the dot pattern shown in Fig. 2. The dot patterns were aligned and composite sketches of the yellow line positions were made on the paper with each camera and crystal temperature on a separate drawing. Flow condition data, crystal temperature, and power level were associated with each line. These lines were then digitized. Typically, about 5000 digitized points were stored for each flow condition. A sample digitized point distribution is shown in Fig. 3. The full range of Stanton numbers was typically obtained from 25 power settings ranging from 200 to 1200 W in increments of 15 to 100 W. The particular power settings used depended on the inlet ambient temperature.

The coordinates and the associated data of each digitized point were read into a data reduction program. The purpose of the program was to calculate the Stanton number at each digitized point, but this calculation required knowledge of the local adiabatic wall temperature. Interpolation from a CFD calculation of endwall surface static pressure was used to obtain M_{IS} and then T_{aw} at each point. The calculated values provided significantly better spatial resolution than the experimental pressure distribution and agreed well with measurements. The Stanton and Mach numbers were then interpolated onto a uniform, rectangular grid for contour plotting. A 176×41 grid was used on each heater. Three-point linear interpolation was used, and care was taken never to interpolate across the blade boundaries. Because the Mach numbers originated as calculated values, they had extremely fine spatial resolution. The interpolation procedure was validated by comparing contour plots of the original, input CFD Mach number distribution with contour plots generated after the Mach numbers had been interpolated onto each digitized point and then interpolated onto the rectangular grid. The contour plots disagreed only in regions of insufficient data in which no St contours should be shown. This situation arose only near the edges of the measurement area.

The range of electric power supplied to the heaters was limited so that they became neither too hot nor too cool. The heaters were assembled in a highly stretched condition at room temperature. If cooled, the thin heaters could stretch beyond

their elastic limit, and then wrinkle when warmed. This situation could arise at low power levels, especially in the downstream region, because of the low adiabatic wall temperatures associated with high Mach numbers. At high power levels, and thus at high surface temperatures, the adhesion of the double-faced tape is reduced and the heaters could unbond from the surface. The choice of crystal temperatures was made with consideration to these high and low power limits.

Definition of the Heat Transfer Coefficient. The surface thermocouples were used to determine the most appropriate Stanton number definition, i.e., the definition that results in values that are independent of the surface heat flux. Because of the low temperature differences and the high Mach numbers, local Eckert numbers were very high. Consequently, the choice of temperature difference used as the driving potential and the choice of a reference temperature for thermophysical properties significantly affected the heat transfer coefficient. The heat transfer coefficient, h , and the Stanton number, St, were defined as follows:

$$\text{St} = \frac{h}{\rho U_{\text{in}} C_p} = \frac{q/A}{\rho U_{\text{in}} C_p (T_s - T_{\text{aw}})}$$

where q represents the net surface heat transfer rate. U_{in} was chosen as the reference velocity and C_p was assumed to be constant. The local adiabatic wall temperature, T_{aw} , is defined as:

$$\frac{T_{\text{aw}}}{T'_{\text{in}}} = r + \frac{1 - r}{1 + 0.5(\gamma - 1)M^2}$$

The isentropic surface Mach number, M , was determined from endwall static pressures. The reference temperature, T_{ref} , given by Eckert (1955) was used to evaluate μ and k in Pr for the recovery factor, $r = \text{Pr}^{1/3}$:

$$T_{\text{ref}} = T + 0.5(T_s - T) + 0.22(T_{\text{aw}} - T)$$

This definition unfortunately requires iteration because of the interdependency between T_{aw} and T_{ref} . The density, ρ , used in the Stanton number definition, unlike the value used for the Reynolds number, is not the actual physical density. It was defined as $\rho = P'_{\text{in}}/(RT_{\text{ref}})$. The thermocouple data showed a repeatability in St of about 5 percent.

The primary reason for the high sensitivity of the Stanton number to the choice of temperatures is that local Eckert numbers are high. At the blade row exit, and at a temperature corresponding to the lower temperature liquid crystal, the local Eckert number was approximately 8. At these relatively high Eckert numbers, heat transfer rates are a function of both Reynolds number and Mach number. The careful definition of Stanton number properly accounts for the Mach number dependency through the use of the adiabatic wall temperature and Eckert's reference temperature. The reference temperature also accounts for thermophysical property variations. More details of the Stanton number definition are given in Giel et al. (1996c).

The net surface heat transfer rate, q , used to calculate the Stanton number, is the heater power corrected for conductive and radiative heat losses:

$$q = q_{\text{hr}} - k_{\text{foam}} A (T_s - T_{\text{foam}}) / t_{\text{foam}} - \epsilon \sigma A (T_s^4 - T_{\text{aw}}^4)$$

where $q_{\text{hr}} = VI$ and A is the total heater area (824.2 cm^2). The second term in this equation represents the back-face heat conduction loss, and was less than 0.6 percent of q_{hr} . The third term represents the radiative losses, and was less than 4.5 percent of q_{hr} . T_s was the liquid crystal temperature, T_{foam} was measured on the back face of the insulating foam, k_{foam} and t_{foam} were given above, and $\epsilon = 0.98$.

An uncertainty analysis was performed following the method of Kline and McClintock (1953). The ΔT term in the calcula-

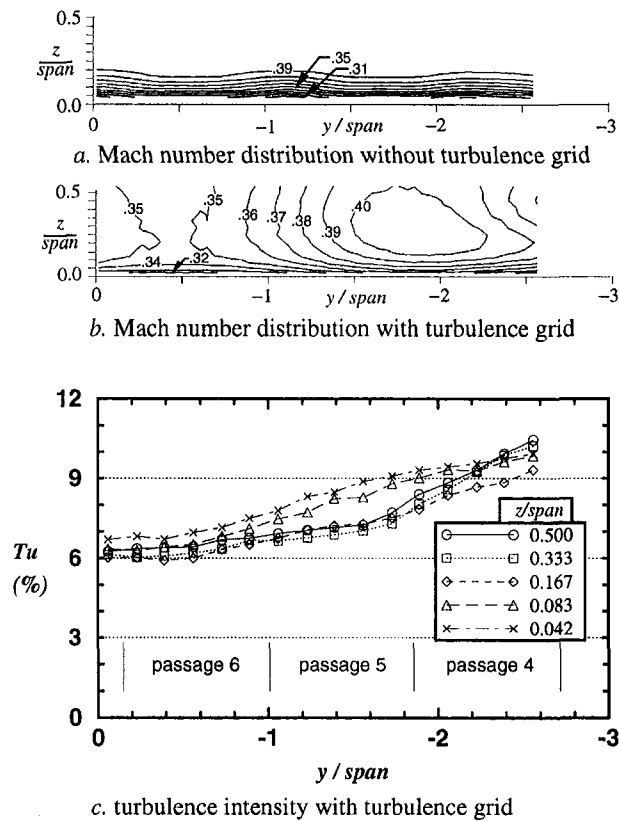


Fig. 4 Aerodynamic inlet conditions

tion of Stanton number was the primary source of uncertainty. Based on the following uncertainties: $T_{ic,1} = \pm 0.5^\circ\text{C}$ ($\pm 0.9^\circ\text{F}$), $T_{ic,2} = \pm 0.8^\circ\text{C}$ ($\pm 1.4^\circ\text{F}$), and $T_{aw} = \pm 0.6^\circ\text{C}$ ($\pm 1.0^\circ\text{F}$), the overall uncertainty in St ranged from 6 to 11 percent. The liquid crystal uncertainties were estimated by powering the heaters and monitoring the surface thermocouples. The crystals were viewed using the same photographic techniques that were used during actual data acquisition. During this calibration, heat transfer through the thin paint layer was minimized by reducing the test section pressure to near vacuum. During the actual data acquisition, high-temperature liquid crystal data were used if the temperature difference, ΔT , using the low temperature liquid crystal was too low to maintain the desired maximum Stanton number uncertainty.

Measurement Results

Inlet Flow Measurements. Well-documented inlet boundary conditions are needed for CFD calculations. Figure 4 shows the results of aerodynamic inlet measurements on a plane one axial chord upstream of the blade leading edge plane. Figures 4(a) and 4(b) show local Mach number contours with and without the turbulence grid installed. Both figures present data obtained at $Re_{c_x} = 1.0 \times 10^6$. Based on flat plate boundary layer correlations, the $Re_{c_x} = 0.5 \times 10^6$ cases can approximately be expected to have a 10 percent thicker inlet boundary layer. Pitchwise averaged values of δ_{in} at $Re_{c_x} = 1.0 \times 10^6$ are listed in Table 1. The exit Mach number for the endwall heat transfer cases was either 1.0 or 1.3 leaving the flow choked at the throat and thus leaving the inlet flow independent of M_{ex} .

Figure 4 shows that without the turbulence grid there is a thick and pitchwise periodic inlet boundary layer. Because of the large leading edge diameter, the effects of the blades are evident even one axial chord upstream. Comparing Figs. 4(a) and 4(b) shows that the presence of the grid adversely affects

the flow uniformity. The primary measurement passage, Passage 5, has a midrange level of turbulence intensity, but a higher than average velocity. In terms of Reynolds number, Re_{c_x} in Passage 6 was reduced about 8 percent while Re_{c_x} in Passage 4 remained about the same. Without a grid, the inlet Tu was uniform at about 0.25 percent for $Re_{c_x} = 1.0 \times 10^6$ and 0.50 percent at $Re_{c_x} = 0.5 \times 10^6$. Figure 4(c) shows the turbulence intensity distribution with the grid installed. The turbulence intensity, Tu , has been normalized by the spanwise and pitchwise averaged inlet velocity. The roughly linear dependence of Tu on pitchwise distance resulted from the grid being installed normal to the mean flow, making it skewed with respect to the measurement and blade leading edge planes. Gregory-Smith and Cleak (1992) showed that a 42.75 deg skewed grid produced a mean flow deflection of more than 1.0 deg. Skewing the grid in the present study may have resulted in a more uniform Tu distribution, but it probably would have detrimentally affected the mean velocity. The spanwise and pitchwise averaged inlet velocity was used to calculate Re_{c_x} and St .

Turbulence length scales can have a significant influence on heat transfer rates. A longitudinal, integral turbulence length scale for the present case was estimated by extrapolating data given by Van Fossen et al. (1994) to higher speeds. Their measurements were made in a low-speed wind tunnel (45 m/s) of the same width (15.24 cm) and with the same grid configuration as the present test. As shown by Roach (1987) and Van Fossen et al. (1994), the length scale generated by grids is independent of Reynolds number, making extrapolation to higher speeds reasonable. The length scale, L_{τ} , thus estimated was $0.38 C_x$ at the leading edge of Passage 5.

Endwall Static Pressure Measurements. Endwall static pressure distributions were needed along with the surface temperatures to evaluate Stanton numbers. Figure 5 shows measurements of P/P'_{in} for an exit Mach number of 1.3. Also shown are predictions made using the three-dimensional Navier-Stokes code, RVC3D (Chima and Yokota, 1990). The analysis was done for flow around an isolated blade in an infinite cascade. Excellent agreement is seen with the only substantial difference being with the 0.3 contours downstream of the trailing edge. The minimum P/P'_{in} values for the data and for the calculations were 0.3055 and 0.2796, respectively. These values correspond to only a 0.6°C (1°F) difference in T_{aw} . Even with 87 taps per passage, the experimental data may not have enough resolution to define these low-pressure islands adequately. For this reason, the isentropic Mach number used to calculate the Stanton number was obtained from the CFD calculations. The Mach number distribution was not affected by Reynolds number, so only two exit Mach number calculations were needed to process the data. Other endwall static pressure data are available from Giel et al. (1996a).

Figure 5 also shows the strong three-dimensionality of the flow. This is particularly evidenced by the distortion of the $P/P'_{in} = 0.8$ contour line, resulting from the horseshoe vortex. Downstream aerodynamic probe data and pressure measurements on the blade surface (Giel et al., 1996a) also verified strong three dimensionality. Near midchord there was nearly a 30 percent decrease in the rotor pressure differential at 5 percent of span as compared to the midspan value.

Heat Transfer Measurements. Table 2 lists test conditions for the full factorial experiment of three variables at two levels each, i.e., eight cases. Note that one of the low Reynolds number cases, Case 5, showed a greater variability in exit conditions during the run. However, even this variability was small.

Endwall Stanton number data for the eight cases are presented in Figs. 6–13. Each of these figures will be first discussed separately, then compared to each other in order to summarize

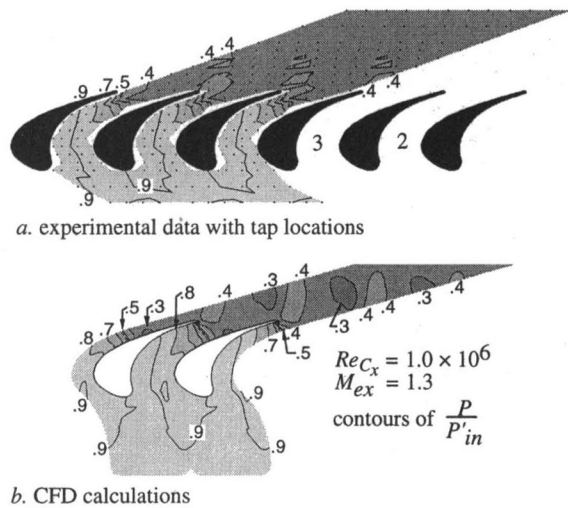


Fig. 5 Endwall static pressure distributions

the effects of each flow parameter. The figures are arranged such that the effects of Re_{C_x} can be observed by comparing any two figures that are horizontally opposite each other, e.g., Fig. 6 and Fig. 10. The effects of M_{ex} can be observed by comparing sequentially numbered figures, e.g., Fig. 6 and Fig. 7. Finally, turbulence grid effects can be observed by comparing every other figure, e.g., Fig. 6 and Fig. 8. Because all of the data were interpolated onto the same grid, it was possible to subtract the local values from any two cases to determine percentage changes in St brought about by changes in one or more flow parameters. While the authors used this procedure to help interpret the results, the large number of figures that it generates prevents their inclusion here. Simply subtracting St values at the same (x, y) location from any two figures leads to the same conclusions.

Figure 6 shows the endwall Stanton number distribution for a case with $Re_{C_x} = 1.0 \times 10^6$, $M_{ex} = 1.3$, and without the turbulence grid—Case 1. Heating begins $0.3 C_x$ upstream of the blade leading edge plane so high Stanton numbers are expected because of unheated starting length effects. Even though the Stanton number is theoretically infinite at the heater leading edge, a flat plate correlation (Kays and Crawford, 1980) shows that it is reduced to 2.4×10^{-3} at a distance $0.1 C_x$ from the start of heating. This low value results from the thick inlet boundary layer, which corresponds to a Reynolds number, Re_x , of 14.6×10^6 .

The presence of the blades quickly distorts the Stanton number distribution from the flat plate correlation results. Near the leading edge, Stanton numbers are significantly influenced by the horseshoe vortex. As the flow approaches the leading edge, there is a general increase in heat transfer. High Stanton numbers are seen very close to the blade, near its stagnation point, in agreement with the effects observed by Goldstein and Spores (1988) of a leading edge corner vortex. As the flow accelerates around the suction surface, there is a region of very high heat transfer, $St \times 1000 > 4.5$. This establishes a region of high pitchwise gradients, since there is a relatively low heat transfer near midpassage.

A comparison of the data in the primary measurement passage with the data in the adjacent passage indicates good periodicity. Minimum heat transfer regions are seen at midchord near each of the pressure surfaces. This is as expected, since as Fig. 5 shows, this is a low-velocity region. Stanton numbers gradually increase downstream from here. Near the suction surface, levels decrease in the streamwise direction from the peak levels downstream of the stagnation region. The effects of the pressure-side leg of the horseshoe vortex are seen clearly further

along the suction surface. The pressure-side leg of the horseshoe vortex no longer scours the endwall after it lifts off. A localized peak in St of 4.5×10^{-3} is observed near the presumed lift-off point. From this point, the passage vortex causes an accumulation of secondary-flow fluid near the suction surface. The temperature of this fluid increased as it passed over the heated endwall, resulting in lower heat transfer rates near the suction surface. In fact, the lowest Stanton numbers on the endwall are seen on the downstream of the throat along the uncovered portion of the suction surface. Note that the minimum Stanton number in this region is somewhat lower in Passage 5 than in Passage 6. This is caused by the fact that heaters cover the entire secondary flow path in Passage 5, but only a portion of Passage 6 is heated. This allows the secondary flow to become warmer in Passage 5, thus decreasing heat transfer rates near the suction surface.

Highly localized heat transfer peaks occur in the wake region, 0.20 to $0.25 C_x$ (5 to 6 trailing edge diameters) downstream of the trailing edge. Goldstein and Spores (1988) saw a similar peak, but located much closer to the blade, only 0.06 to $0.07 C_x$ downstream of the trailing edge. Farther downstream, several distinct low heat transfer regions are seen. These regions are defined by the shock structure evident in Fig. 5. Stanton numbers generally decrease in the streamwise direction as the thermal boundary layer grows on the endwall. Overall, Fig. 6 shows good periodicity and strong evidence of highly three-dimensional flow.

Endwall Stanton number contours for Case 2 are shown in Fig. 7. The flow conditions were the same as for Case 1 except that M_{ex} was reduced to slightly less than 1.0 to eliminate shocks. Because the flow remained nearly choked at the throat, heat transfer rates upstream of the throat were expected to be the same as for Case 1. Comparing Figs. 6 and 7 shows that this is generally true within the experimental uncertainty. The figure does not quite show the same peak St of 4.5×10^{-3} near the blade stagnation point as was seen in Case 1. This was probably due to insufficient resolution of q_{hr} settings for Case 2. Along the pressure surface, St increases gradually in streamwise direction with contour lines approximately being normal to the pressure surface. This was also true for Case 1.

The low heat transfer region along the uncovered portion of the suction surface is still present but with higher St levels and with a smaller area. The peak heat transfer $St > 5.5 \times 10^{-3}$ downstream of the trailing edge remains the same, but its location is slightly closer to the trailing edge, 3 to 5 trailing edge diameters downstream. Downstream of the blade row Stanton numbers are 40 to 60 percent higher than for Case 1. With no shocks present to disturb the endwall boundary layers, Stanton number contours from midchord to the exit generally follow the paths of inviscid streamlines and do not appear in distinct regions as they did in Case 1.

Figure 8 shows the endwall Stanton number distribution for the same Re_{C_x} and M_{ex} as Fig. 6 but with the turbulence grid installed. Surprisingly, the primary effect of the turbulence grid

Table 2 Description of endwall heat transfer cases

Case	Re_{C_x}	M_{ex}	Tu grid
1	$0.937 \pm 0.007 \times 10^6$	1.321 ± 0.002	no
2	$0.938 \pm 0.009 \times 10^6$	0.962 ± 0.001	no
3	$0.973 \pm 0.016 \times 10^6$	1.328 ± 0.001	yes
4	$0.952 \pm 0.017 \times 10^6$	0.992 ± 0.001	yes
5	$0.473 \pm 0.004 \times 10^6$	1.272 ± 0.036	no
6	$0.475 \pm 0.003 \times 10^6$	0.961 ± 0.004	no
7	$0.493 \pm 0.003 \times 10^6$	1.313 ± 0.006	yes
8	$0.493 \pm 0.004 \times 10^6$	0.982 ± 0.002	yes

(all repeatabilities based on 95% confidence limits)

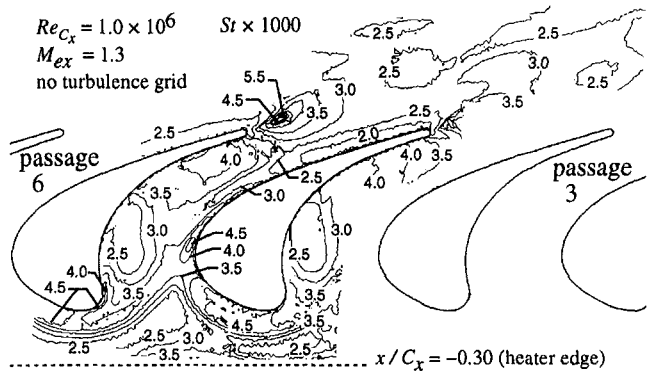


Fig. 6 Endwall St distribution—Case 1

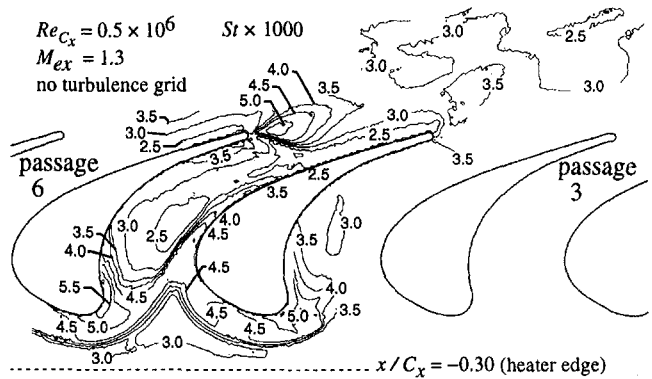


Fig. 10 Endwall St distribution—Case 5

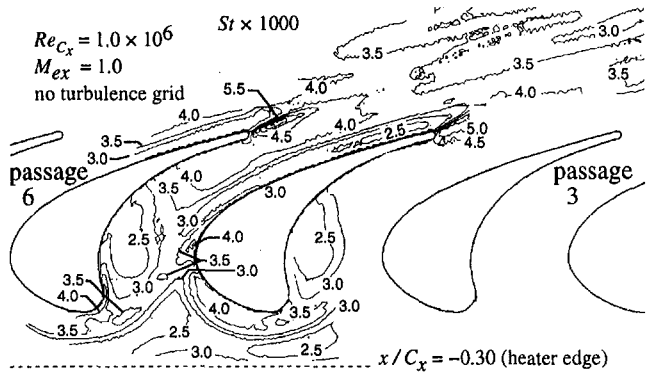


Fig. 7 Endwall St distribution—Case 2

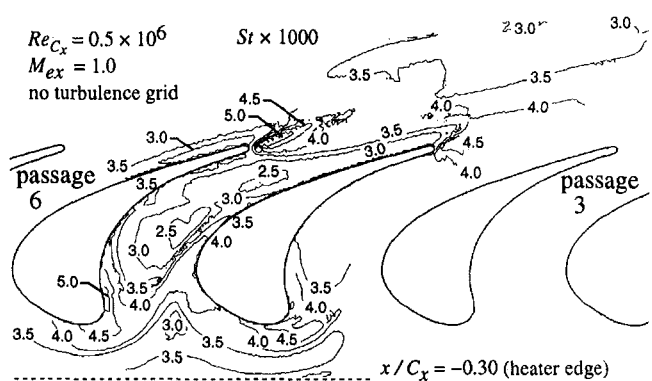


Fig. 11 Endwall St distribution—Case 6

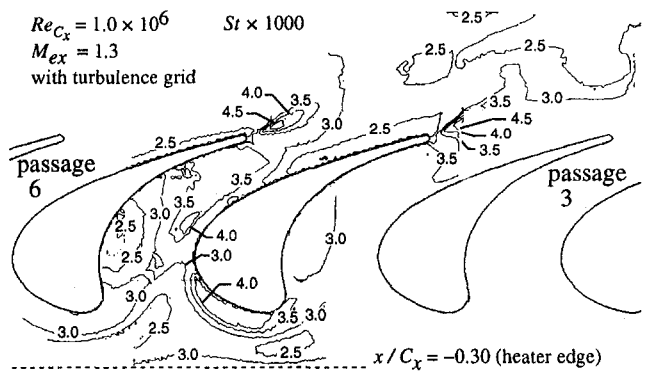


Fig. 8 Endwall St distribution—Case 3

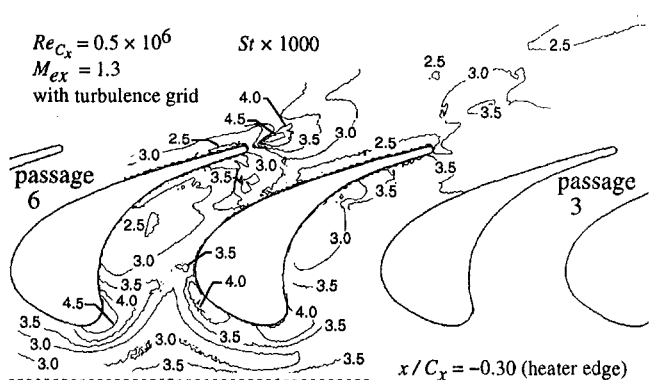


Fig. 12 Endwall St distribution—Case 7

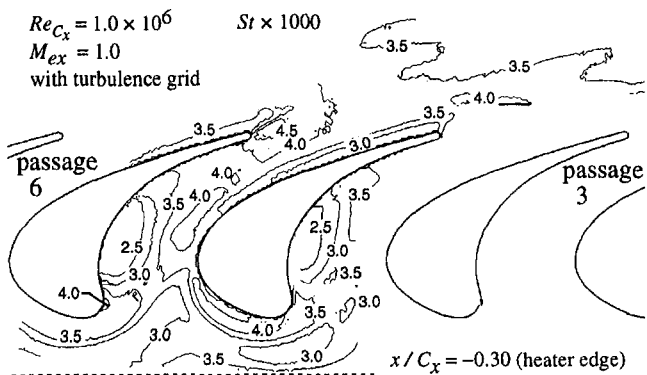


Fig. 9 Endwall St distribution—Case 4

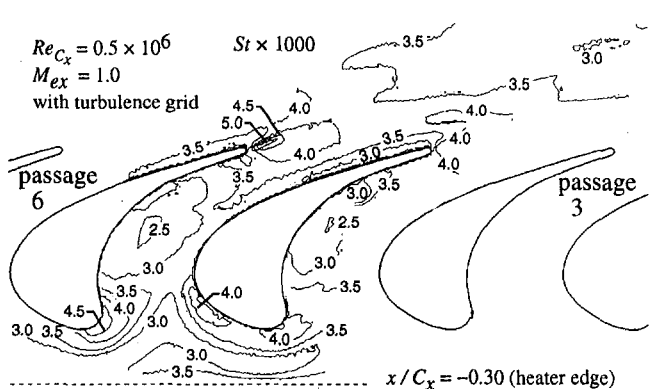


Fig. 13 Endwall St distribution—Case 8

appears to be lower peak heat transfer levels. The most significant differences are in front of the blades in the horseshoe vortex path. The low upstream $St = 2.5 \times 10^{-3}$ regions are still seen, but the steep St gradients near midpitch seen in Fig. 6 are missing. Recall that the turbulence grid significantly reduced δ_m . Blair (1983) showed that, when corrected for the length scale L_x , a free-stream Tu of 7 percent can result in less than a 10 percent increase in St . The reduction in St caused by reduced secondary flows resulting from the thinner inlet boundary layer thus may overshadow the increase caused by increased turbulence. The peak St area seen in Fig. 6 near the presumed vortex lift-off point has moved away from the suction surface, followed by 10 to 20 percent higher Stanton numbers. This also indicates that the secondary flow structure has changed. Figure 8 shows that the region downstream of the blades is similar to Case 1. This is because for both cases, vortices scour the endwall, increasing the free-stream turbulence levels and eliminating the thick endwall boundary layers.

Figure 9 shows the final high Reynolds number case, Case 4. The trends for this case are generally the same as for the cases discussed above. In comparing Fig. 9 with Fig. 7, it is evident that the increased St levels near the suction surface are more pronounced for this case. Downstream of the blade row, however, the Stanton number levels are again very similar.

Figure 10 shows the endwall Stanton number distribution for Case 5. Contrasting this figure with Fig. 6 shows the effects of reducing Re_{c_x} for a supersonic exit case with no turbulence grid. These effects are significant in the upstream and leading edge regions. Increases in St exceed the 15 to 20 percent increase that would be expected from assuming that $St \propto Re^{-0.2}$ based on a turbulent flow analogy. The peak stagnation region Stanton number increases from about 4.5×10^{-3} for Case 1 to about 5.5×10^{-3} for Case 5. Farther upstream, the heat transfer remains about the same, resulting in higher gradients of St near midpitch. The blade passage, particularly near the pressure surface, shows the most significant Reynolds number effects. Stanton numbers at quarter-chord near the pressure surface increase by more than 50 percent. The minimum St region has moved significantly closer to the suction surface and slightly downstream. Heat transfer near the suction surface also increases by 10 to 30 percent. However, levels near midpassage, from 0.5 to 0.75 C_x , decrease by 30 percent or more. This all has the effect of producing very large St gradients near midchord. These large effects are almost certainly due to the thicker inlet boundary layer and the changes in the horseshoe vortex that it brings about. The entire region downstream of the throat shows levels that are generally higher than for the $Re_{c_x} = 1.0 \times 10^6$ case. The localized peaks downstream of the trailing edge are again nearly the same, but the area of higher heat transfer surrounding this peak is significantly larger.

Figure 11 shows the St distribution for Case 6. The area upstream of the throat agrees reasonably well with the data of Case 5. The area downstream of the throat generally shows increased St levels, the same M_{ex} effect that was seen for other cases. In comparing Fig. 11 with Fig. 7, it is seen that the Reynolds number effects are also consistent with those discussed above.

The Stanton number distribution for Case 7 is shown in Fig. 12. This is a 0.5×10^6 Reynolds number case with the inlet turbulence grid installed. The lower Reynolds number would normally produce a thicker inlet boundary layer, but it is reduced by the turbulence grid. The net result is that the pressure surface low St region characteristic of the higher Reynolds number cases has still moved downstream and closer to the suction surface, but not as much as for the no-grid cases (5 and 6). Gradients of St near the suction surface at midchord are therefore not as large as for the no-grid cases. Decreasing Re_{c_x} with the turbulence grid installed produces trends similar to the no-grid cases, but the magnitude of the differences is reduced.

The final endwall Stanton number distribution, Case 8, is seen in Fig. 13. Comparing it to Fig. 9 shows the same Reynolds number trends that have been shown throughout. Comparing it to Fig. 11 shows consistent turbulence-grid effects. When compared to Fig. 12, the consistent downstream Mach number trend of 40 to 60 percent higher St levels associated with the lower M_{ex} levels is again seen. Also, the agreement with Case 7 in the region upstream of the throat is excellent.

Summary and Conclusions

In general, lowering Re_{c_x} by a factor of two affects endwall heat transfer in excess of the 15–20 percent increases expected from flat plate correlations. Stanton numbers near the pressure surface increase by more than 50 percent, while those near the suction surface increase by nearly 30 percent. Lower Reynolds numbers also move the minimum passage Stanton number slightly downstream and towards the suction surface, decreasing levels at midpassage by 30 percent or more. These effects result in large St gradients near the suction surface at about midchord. The Reynolds number effects were most evident in Cases 5 and 6 with no grid, but were also seen for Cases 7 and 8 with the turbulence grid.

The shocks in the supersonic M_{ex} cases break up the smooth St distributions seen in the sonic M_{ex} cases. Stanton numbers are 40 to 60 percent higher for the lower exit Mach number cases. In all cases, downstream Stanton number levels decrease in the streamwise direction as the endwall thermal boundary layer grows.

The data show the somewhat surprising result that the primary effect of the turbulence grid is to lower peak heat transfer levels. This result is thought to be due to the secondary flow change brought about by the reduced inlet boundary layer thickness. Downstream of the blade row the turbulence grid had essentially no effect on endwall heat transfer.

The results show the significant differences in the heat transfer that resulted from variations in flow parameters. In every case, however, a peak heat transfer region occurred in a small downstream region, between 3 to 6 diameters downstream of the trailing edge.

Overall, the steady-state liquid crystal technique proved to be quite valuable for obtaining CFD code validation endwall heat transfer data. The good spatial resolution offered by the large scale of the cascade and by the liquid crystal technique allowed the effects of the secondary flows in the blade passages to be clearly quantified. The analysis of thermocouple data showed the importance of a careful Stanton number definition.

Well-defined inlet flow measurements were presented, important for specifying boundary conditions to CFD codes. The endwall heat transfer data presented here, along with the aerodynamic data presented by Giel et al. (1996a) comprise a complete set of data suitable for CFD code and model validation. Also, as required by most CFD analyses, the endwall heat transfer measurements show good periodicity. Electronic tabulations of all data presented in this paper are available upon request. Comparing CFD calculations to all eight cases would give greater confidence in the ability of CFD to predict endwall heat transfer.

Acknowledgments

This work was supported by the NASA Lewis Research Center under contract NAS3-27186 with NYMA, Inc., with Mr. Robert J. Boyle as monitor. The support of Ms. Susan Zeleznik in digitizing the data is also gratefully acknowledged.

References

- Blair, M. F., 1983, "Influence of Free-Stream Turbulence on Turbulent Boundary Layer Heat Transfer and Mean Profile Development: Part II—Analysis of Results," *ASME Journal of Heat Transfer*, Vol. 105, pp. 41–47.

- Blair, M. F., 1994, "An Experimental Study of Heat Transfer in a Large-Scale Turbine Rotor Passage," *ASME JOURNAL OF TURBOMACHINERY*, Vol. 116, pp. 1–13.
- Chima, R. V., and Yokota, J. W., 1990, "Numerical Analysis of Three-Dimensional Viscous Internal Flows," *AIAA Journal*, Vol. 28, No. 5, pp. 798–806.
- Eckert, E. R. G., 1955, *J. Aero. Sci.*, pp. 585–587.
- Giel, P. W., Thurman, D. R., Lopez, I., Boyle, R. J., VanFossen, G. J., Jett, T. J., Camperchioli, W. P., and La, H., 1996a, "Three-Dimensional Flow Field Measurements in a Transonic Turbine Cascade," *ASME Paper No. 96-GT-113*.
- Giel, P. W., Sirbaugh, J. R., Lopez, I., and VanFossen, G. J., 1996b, "Three-Dimensional Navier–Stokes Analysis and Redesign of an Imbedded Bellmouth Nozzle in a Turbine Cascade Inlet Section," *ASME JOURNAL OF TURBOMACHINERY*, Vol. 118, pp. 529–535.
- Giel, P. W., Thurman, D. R., VanFossen, G. J., Hippensteele, S. A., and Boyle, R. J., 1996c, "Endwall Heat Transfer Measurements in a Transonic Turbine Cascade," *ASME Paper No. 96-GT-180*; NASA TM-107387.
- Goldstein, R. J., and Spores, R. A., 1988, "Turbulent Transport on the Endwall in the Region Between Adjacent Turbine Blades," *ASME Journal of Heat Transfer*, Vol. 110, pp. 862–869.
- Graziani, R. A., Blair, M. F., Taylor, R. J., and Mayle, R. E., 1980, "An Experimental Study of Endwall and Airfoil Surface Heat Transfer in a Large Scale Turbine Blade Cascade," *ASME Journal of Engineering for Power*, Vol. 102, pp. 1–11.
- Gregory-Smith, D. G., and Graves, C. P., 1983, "Secondary Flows and Losses in a Turbine Cascade," in: *Viscous Effects in Turbomachines*, AGARD-CP-351.
- Gregory-Smith, D. G., Graves, C. P., and Walsh, J. A., 1988, "Growth of Secondary Losses and Vorticity in an Axial Turbine Cascade," *ASME JOURNAL OF TURBOMACHINERY*, Vol. 110, pp. 1–8.
- Gregory-Smith, D. G., and Cleak, J. G. E., 1992, "Secondary Flow Measurements in a Turbine Cascade With High Inlet Turbulence," *ASME JOURNAL OF TURBOMACHINERY*, Vol. 114, No. 1, pp. 173–183.
- Hippensteele, S. A., and Russell, L. M., 1988, "High-Resolution Liquid Crystal Heat-Transfer Measurements on the End Wall of a Turbine Passage With Variations in Reynolds Number," presented at the 25th ASME Heat Transfer Conf., Houston, Texas, July 24–27; also NASA TM-100827.
- Kays, W. M., and Crawford, M. E., 1980, *Convective Heat and Mass Transfer*, 2nd ed., McGraw-Hill, New York.
- Kline, S. J., and McClintock, F. A., 1953, "Describing Uncertainty in Single-Sample Experiments," *Mechanical Engineering*, Vol. 75, Jan., pp. 3–8.
- Langston, L. S., Nice, M. L., and Hooper, R. M., 1977, "Three Dimensional Flow Within a Turbine Cascade Passage," *ASME Journal of Engineering for Power*, Vol. 99, pp. 21–28.
- Marchal, P., and Sieverding, C. H., 1977, "Secondary Flows Within Turbomachinery Bladings," in: *Secondary Flows Within Turbomachines*, AGARD-CP-214.
- Martinez-Botas, R. F., Lock, G. D., and Jones, T. V., 1995, "Heat Transfer Measurements in an Annular Cascade of Transonic Gas Turbine Blades Using the Transient Liquid Crystal Technique," *ASME JOURNAL OF TURBOMACHINERY*, Vol. 117, pp. 425–431.
- Mee, D. J., Baines, N. C., Oldfield, M. L. G., and Dickens, T. E., 1992a, "An Examination of the Contributions to Loss on a Transonic Turbine Blade in Cascade," *ASME JOURNAL OF TURBOMACHINERY*, Vol. 114, pp. 155–162.
- Mee, D. J., Baines, N. C., and Oldfield, M. L. G., 1992b, "Detailed Boundary Layer Measurements on a Transonic Turbine Cascade," *ASME JOURNAL OF TURBOMACHINERY*, Vol. 114, No. 1, pp. 163–172.
- Moffat, R. J., 1990, "Experimental Heat Transfer," *Proc. of the Ninth Int'l Heat Transfer Conf.*, Jerusalem, Israel, Vol. 1, pp. 187–205.
- Roach, P. E., 1987, "The Generation of Nearly Isotropic Turbulence by Means of Grids," *Int. J. Heat Fluid Flow*, Vol. 8, pp. 82–92.
- Van Fossen, G. J., Simoneau, R. J., and Ching, C. Y., 1994, "Influence of Turbulence Parameters, Reynolds Number, and Body Shape on Stagnation-Region Heat Transfer," NASA TP-3487.
- Verhoff, V. G., Camperchioli, W. P., and Lopez, I., 1992, "Transonic Turbine Blade Cascade Testing Facility," AIAA Paper No. 92-4034; NASA TM-105646.
- Yamamoto, A., 1987a, "Prediction and Development of Secondary Flows and Losses in Two Types of Straight Turbine Cascades: Part 1—A Stator Case," *ASME JOURNAL OF TURBOMACHINERY*, Vol. 109, pp. 186–193.
- Yamamoto, A., 1987b, "Prediction and Development of Secondary Flows and Losses in Two Types of Straight Turbine Cascades: Part 2—A Rotor Case," *ASME JOURNAL OF TURBOMACHINERY*, Vol. 109, pp. 194–200.

Discharge Coefficient of Turbine Cooling Holes: A Review

N. Hay

D. Lampard

Department of Mechanical Engineering,
University of Nottingham,
Nottingham, United Kingdom

Published information on the discharge coefficient of film cooling holes is classified in terms of the hole geometry, the external flow conditions at inlet and outlet, and the method of evaluation. This may be either theoretical or experimental. The information is reviewed primarily in the context of its use for evaluating discharge coefficients for conditions not directly covered by published data. It is shown that potential flow analyses can give acceptable accuracy for simple geometries with crossflows, while more complex cases require the use of correlated data, which may be incorporated in a range of predictive schemes. Deficiencies and inconsistencies in the published information are highlighted, and future developments are discussed.

Introduction

Gas turbine engines incorporate a multiplicity of internal passages, which serve to channel air bled from the compressors to various components that require cooling (Fig. 1). A large proportion of the cooling air is ultimately used for internal and film cooling of the blades.

The advantages of blade cooling are well known. It allows an increase in turbine entry temperature reflecting in higher power output and efficiency. The penalty is a loss of output as the coolant, which could be 5 percent or more of the total flow, is not heated in the combustion chamber, bypasses one to two turbine stages, and so does less work. It is thus obvious that the cooling air must be kept to the minimum that will achieve the required cooling performance. Control of the flow to a cooling film is effected by choosing the size and number of holes, so the designer needs to know the discharge coefficient, C_d , for the wide range of geometries and flow conditions that can arise. This need is critical as coolant underfeed or overfeed can both result in the formation of hot spots on the surface, and consequently reduced component life.

The objective of this paper is to review published information on the discharge coefficient of cooling holes. Its usefulness and limitations, and the methods of prediction proposed will be examined. Also, areas where further data are required will be identified. The review has the need of the designer as the primary consideration.

Geometrical and Flow Conditions

The range of variables that enter in determining the value of C_d is large and includes geometric as well as flow parameters. Referring to Fig. 2, the geometric parameters include:

- 1 The length-to-diameter ratio of the hole (L/d).
- 2 The angle of inclination of the hole (θ).
- 3 The angle of orientation of the hole (α).
- 4 RADIUSING of the hole at inlet and/or outlet and the degree of radiusing (r/d).
- 5 Chamfering of the hole (w/d).
- 6 Flaring of the hole and the resultant geometry.

and the flow parameters include:

- 7 The pressure ratio across the hole.
- 8 The Reynolds number of the flow inside the hole.
- 9 The presence of crossflow at inlet.

- 10 The thickness of the boundary layer near the hole entry.
- 11 The presence of crossflow at outlet.
- 12 The thickness of the boundary layer near the hole outlet.
- 13 The presence of swirl within the hole
- 14 Rotation of the hole.

These parameters can exist singly or in a variety of combinations leading to a multiplicity of situations for which data on C_d are required.

Classification of C_d Publications

The publications found in the literature for both holes and slots are classified in Table 1, firstly in relation to the geometric and flow parameters listed above and their various combinations in order of complexity, and second according to whether the work is experimental, analytical, or numerical and whether an empirical correlation for C_d is given in the paper.

Approaches to Obtaining C_d From Published Data

From Table 1 it is apparent that the majority of the work reported is experimental. Analytical predictions are limited to slots and even then cover only limited cases. The correlations that exist for holes cover the simpler range of geometric parameters. For the more complex chamfered, flared, and fanned holes only a few sets of experimental data exist.

Unless his exact conditions are in the published literature, the designer has three courses of action open to him:

(a) Examine the flows in the immediate vicinity of the hole inlet and outlet separately, using empirical correlations, potential flow, or CFD solutions as appropriate to get pressure loss coefficients for the hole inlet and outlet.

The complete hole C_d can then be obtained by using a simple loss coefficient based analysis, including mixing within the hole.

(b) Modify a basic hole C_d using empirical correlations or other means to determine the changes that arise from the presence of crossflows, and geometric variations such as inlet radiusing.

(c) Measure or calculate C_d for the complete hole geometry under the specified flow conditions.

Examples of each of these approaches will be presented in the following sections.

Separate Treatment of Inlet and Outlet Flows

The accuracy and economy of this "building block" approach depends on the lack of strong mutual interactions between successive elements. Its success in simple cases is exem-

Contributed by the International Gas Turbine Institute and presented at the 41st International Gas Turbine and Aeroengine Congress and Exhibition, Birmingham, United Kingdom, June 10–13, 1996. Manuscript received at ASME Headquarters February 1996. Paper No. 96-GT-492. Associate Technical Editor: J. N. Shinn.

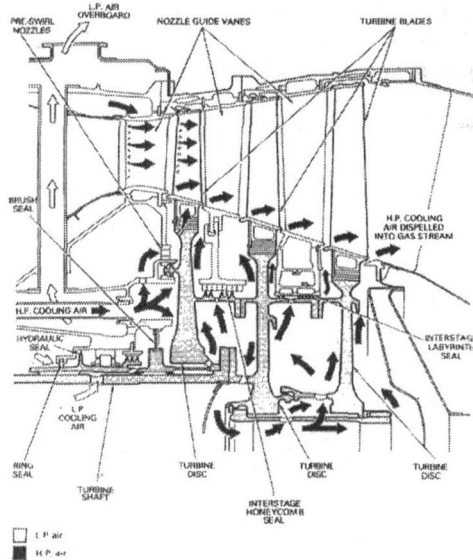


Fig. 1 Internal air cooling in an aero-engine

plified by the analysis of Andrews and Mkpadi (1983) of a normal cooling hole fed from a plenum.

For sharp-edged holes and slots, C_d is limited primarily by the separation at the inlet edges, especially when the length is not sufficient for the flow to reattach fully. Most combustor liner cooling holes fall into this category, having $L/d < 1$. For turbine blades and vanes, $2 < L/d < 8$ usually, so reattachment occurs within the hole, but wall friction losses are negligible compared with the irreversible mixing losses downstream of the separated zone. Modeling of the separation zone, at least as far as the vena contracta, and determination of the associated losses, are thus clearly important in any prediction scheme. It is also clear that crossflows must be included as they modify the separation.

While CFD can be used to model the inlet flow, the separation point must then be predicted within the calculation procedure. Potential flow techniques lend themselves better to the prediction of simple flows with separation points fixed by sharp edges. Conformal mapping techniques readily yield the contraction coefficient for a slit in an infinite wall as 0.611, which, it should be noted, is less than 3 percent higher than that for a circular orifice.

These techniques can also accommodate the presence of inlet crossflow (McNown and Hsu, 1959; Morland, 1988; Dewynne et al., 1989).

Although limited in scope to slits and normal slots in plane walls, such analyses give an idea of the sensitivity of the contraction coefficient C_c , and hence of C_d , to the flow and geometric parameters, and an insight into the underlying flow mechanisms. C_d is seen to be strongly influenced by the crossflow, as is the angle at which the flow emerges from the slot. The duct height becomes an important parameter if it is of the same order as the slot width.

The correlating parameter that emerges for C_c is the ratio of the crossflow velocity to the velocity along the separation streamline—essentially the “ideal” velocity at the vena contracta. This can be expressed also in terms of the stagnation to static pressure drops for the two streams, usually referred to as the “velocity head ratio.”

It is this parameter that is embodied in Fig. 3 where predictions derived from the analysis of McNown and Hsu (1959) for a slit (labeled “potential flow analysis”) are seen to compare satisfactorily with the data of Adkins and Geroui (1986) for a model combustor with short circular cooling holes.

Long cooling holes can be treated with a modified analysis for C_c incorporating a lip on the downstream edge of the slit, and a simple “sudden enlargement” calculation to account for the post-reattachment pressure recovery. Agreement is satisfactory for velocity head ratios over 5, Fig. 4. It might have been improved if the analysis of Dewynne et al. (1989) had been used as this allows for the proper location of the stagnation point, rather than assuming it to be fixed on the downstream lip.

An appreciation of the way the stagnation point moves as the slot flow increases relative to the duct flow is crucial to a proper understanding of the variation of the discharge coefficient with crossflow. For high slot flows, the stagnation point is on the duct wall downstream of the slot, and this means that there will be a reverse flow into the downstream slot, and a separation from the downstream edge.

Byerley (1989) pointed out that this separation will be more severe for an inclined slot than a normal one, leading to a smaller discharge coefficient. As the crossflow increases, the stagnation point moves upwind to the slot edge, and then into the slot so that the separation bubble associated with the reversed flow is suppressed. The separation from the upwind edge of inclined slot is smaller than for a normal one and consequently its discharge coefficient is higher for large crossflow velocities.

The “velocity head ratio” $p_c^+ - p_\infty / p_c^+ - p_c$ used to correlate the data in Figs. 3 and 4 has been shown to work over a wide range of inlet cross flow Mach numbers for orifices with $L/d > 2$ (Rhode et al., 1969), and so is applicable for the film cooling holes of blades and vanes.

The modeling of outlet flows using potential flow techniques has been less successful. Again, only normal slots have been investigated (Fitt et al., 1985). Problems arise at very low blowing rates when the momentum deficit of the approaching boundary layer has a significant effect on the interaction of the jet with the cross flow. The simple theory of Rogers and Hersh (1975) in which the dividing streamline is treated as a lid over the hole can accommodate boundary layer effects. However, while it works adequately for slots with low blowing rates, it is highly empirical, particularly when circular holes are treated, and was developed for short, normal holes.

The results of the analysis imply that data should correlate with the ratio of the hole and crossflow velocities, although the model implies that it is the momentum flux ratio that controls the discharge coefficient. This is supported by the work of Forth (1985), who shows that both the momentum flux ratio and the discharge coefficient correlate with the pressure ratio over a range of coolant and crossflow temperatures.

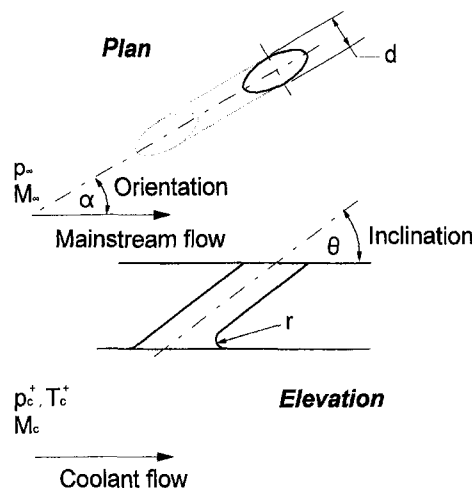


Fig. 2 Geometries and flow parameters for turbine cooling

Table 1 Publications in the literature (numbers in the table correspond to those given in the references section)

	Experimental Work	Analytical Work	Numerical Work	Empirical Correlation
90° Slot				
C_{d0}	29	29		
+ external crossflow	11	11		11
+ internal crossflow	29	29, 27, 10		
30° Slot				
C_{d0}	12			
+ external crossflow	12,30	30		
Other angled slots			6	
90° Hole				
Sharp edged long	23, 2, 26, 9, 1, 25, 5		21	23, 2, 26, 9
+ L/D + radiusing	26, 21, 31, 22		21	26, 31
+ internal crossflow	26, 32, 28, 33, 19, 35, 20, 5		21	26, 32, 33, 35
+ external crossflow	33, 19, 35, 9, 20, 5		21	33, 35, 9, 20
+ internal and external crossflow	19, 35, 36, 20, 5			35, 36, 20
+ chamfering	15			
+ angle to flow direction	5, 36			
+ flare	17			
+ flare + internal crossflow	17			
+ flare + external crossflow	17			
+ rotation	37		37	
30° Hole				
Sharp edged long	19, 20, 12, 5			
+ radiusing	9, 18			
+ internal crossflow	19, 35, 36, 20, 7, 18, 5			
+ external crossflow	19, 9, 20, 12, 24, 18, 5			35, 20, 18
+ internal and external crossflow	19, 35, 36, 20, 18, 5			9, 20, 18
+ angled to flow direction, sharp	16, 36, 7, 5			35, 36, 20, 18
+ angled to flow direction, radiused	16			
+ flare	17			
+ flare + internal crossflow	17			
+ flare + external crossflow	17, 8			
+ flare + angled + internal crossflow	17			
+ flare + angled + external crossflow	17			
Other Angled Holes				
45°	32, 35, 36, 13			
50°	3, 4			32, 35
60°	19			

Modification of a Baseline C_d

The prediction scheme for normal holes devised by McGreehan and Schotsch (1988) is a good example of this approach. Taking the flow through a sharp-edged orifice at the appropriate Reynolds number as the starting point, successive corrections are applied. First, the hole L/d is accounted for, next entry edge radiusing, and finally inlet crossflow.

Individual effects are well-modeled. For example, Fig. 5 compares predictions of inlet radiusing effects with recent data from Hay and Spencer (1992) not used in the construction of the correlations.

The method has been further developed by Parker and Kercher (1991) to reduce the amount of iteration needed.

An alternative approach that is not restricted to normal holes and that permits also outlet crossflows to be accounted for is that developed by Tillman and Jen (1984) and Tillman et al. (1984).

The distortions of the hole inlet or outlet flows arising from the imposition of cross flows are taken to give rise to "additional losses." These are determined experimentally by measuring the pressure drop required to drive a fixed mass flow rate

through the hole both with and without a cross flow. The difference between these pressure drops is the additional loss due to the crossflow.

Nondimensionalization using the dynamic pressure within the hole gives the additional loss coefficients, which are correlated with the ratio of the hole momentum flux and the crossflow momentum flux, as in Fig. 6. The inlet and outlet pressure losses are added to the loss for the basic "no crossflow" condition to calculate the discharge coefficient. This is an iterative process.

The success of the method when crossflows are present at both ends of the hole depends on the hole being sufficiently long for the distortion of the inlet flow caused by the crossflow to have decayed before the outlet is reached. From the evidence of Khaldi (1987), $L/d = 6$ is certainly sufficient.

Measured data are available for both normal and inclined holes, at two hole orientations, and also with inlet and outlet radiusing (Tillman and Jen, 1994; Tillman et al., 1984; Hay et al., 1987; 1994).

Khaldi (1987) used CFD to predict the additional loss coefficients. The PHOENICS code was used for this. Both inlet and outlet additive loss coefficients were overpredicted, with the

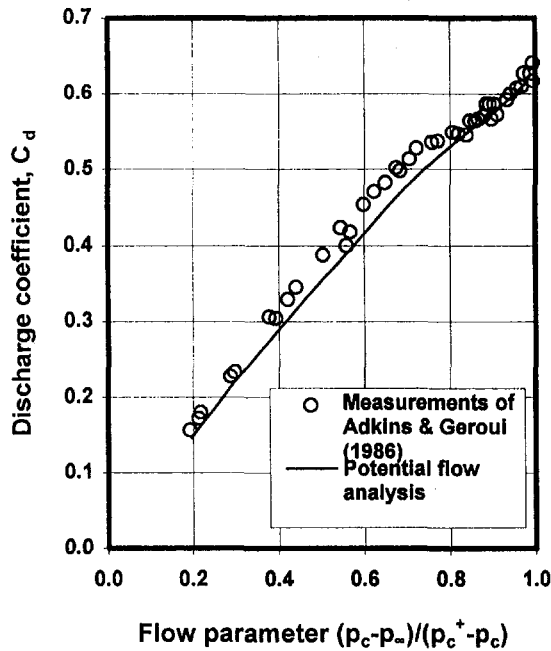


Fig. 3 Discharge coefficient of combustor cooling holes (from Adkins and Geroui, 1986)

result that the discharge coefficient was underpredicted by about 10 percent, see Fig. 7. Note, however, that the form of the variation with pressure ratio is correct, and that the change in discharge coefficient resulting from rounding the inlet edge is well-predicted.

Although the “additional loss” approach can be applied to any geometry, essentially it is just a means of correlating crossflow effects. New data are required for each geometry considered.

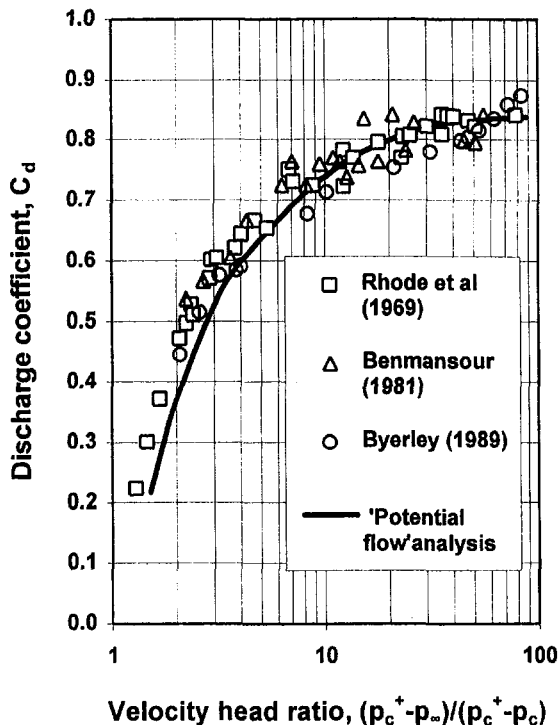


Fig. 4 Normal cooling holes with an inlet crossflow (from Benmansour, 1983)

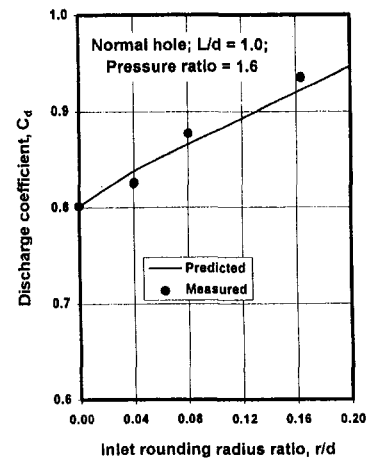


Fig. 5 Normal holes with inlet edge radius (from Hay and Spencer, 1992)

Measurement or Computation of the Complete Hole C_d

In the course of generating data for many of the correlations referred to earlier, C_d for complete holes has been measured. Many of these data are confined to sharp-edged normal holes with only the hole pressure ratio and the inlet crossflow being varied. Inclined hole data is relatively plentiful for a 30 deg angle, but Table 1 shows that it is much sparser for other inclinations. Very little is available for hole orientations with the axis other than parallel to the crossflow, or with significant mutually perpendicular crossflows such as occur in turbine blades.

Both inclination and orientation are sensitive parameters. C_d may change by 30 percent or more over the range of angles encountered in blade design (Hay et al., 1983; 1994; Byerley, 1989), see Fig. 8.

Some of the published data, notably those originating from the von Karman Institute, have been obtained on blade or vane models. Often, the primary aim has been the acquisition of heat transfer data, with C_d being determined as a check on the performance of the injection system.

Some data, e.g., Ligrani and Camci (1985), show good agreement with that of other investigators. However, there are some apparent inconsistencies between, for example, low free-stream Mach number data for a double row of cylindrical 50 deg inclined holes determined on the pressure surface (Arts and Bourignon, 1990) and on the suction surface of a vane (Arts and Lapidus, 1993). The apparent discrepancies may arise from the effect of external or internal geometries, or the difficulties of determining flow conditions near the hole within such models.

There has been a trend toward the use of holes with flared exits in recent years, driven by the need to keep film injection velocities small to maintain attached films at high coolant flow rates. Here, there are very few data in the open literature to help the designer. Recent data of Hay and Lampard (1995) indicate that an increased C_d may be expected and that sensitivity to crossflow is reduced. The data of Camci and Arts (1990) for conically flared holes show surprisingly low C_d values. These latter data were obtained on a model vane.

CFD holds the long-term prospect of resolving many of the problems associated with the assessment of individual data sets.

Good progress has recently been reported by Wittig et al. (1996) with the difficult problem of modeling a short hole in a rotating disk. The predictions lie about 15 percent below experimental data, but the trend of C_d with the ratio of the local disk speed to the flow velocity in the hole is properly forecast. Improvements in the speed and capacity of the hardware coupled with better turbulence modeling will permit both accuracy gains and the modeling of more complex geometries.

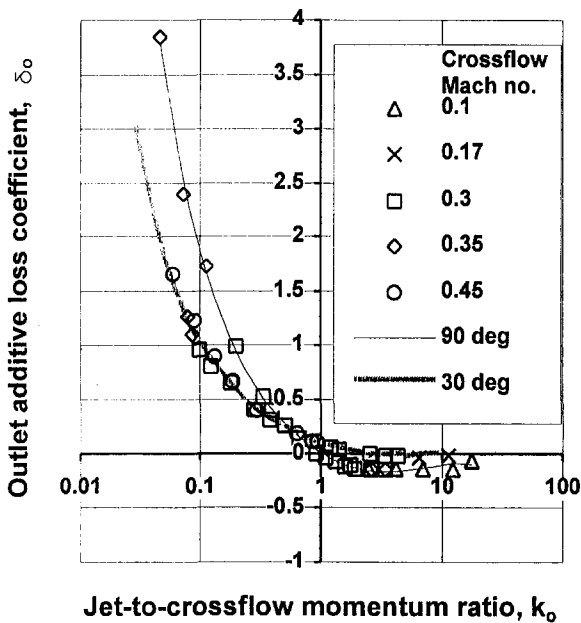
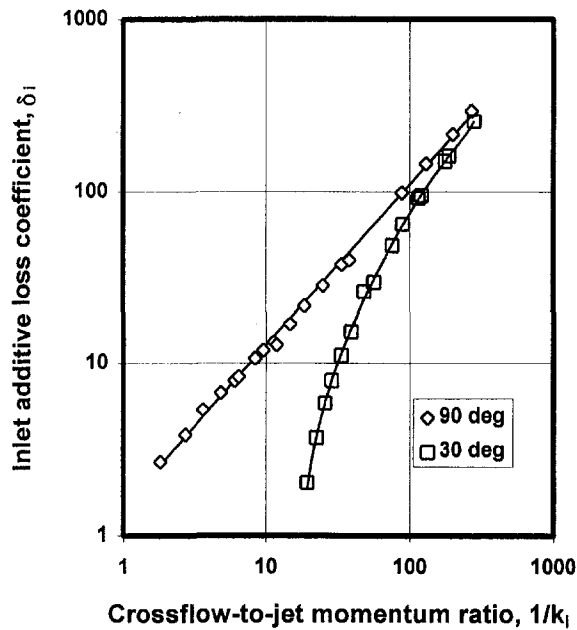


Fig. 6 Additional loss coefficients for sharp-edged normal and inclined holes (from Khaldi, 1987)

It is clear from Table 1 that there are still a lot of areas that need documentation. Some areas lack even the most basic experimental data. The correlations that exist are restricted to comparatively simple cases. The more complex hole shapes now made possible with spark and laser drilling have not as yet had adequate coverage experimentally or predictively. Analytical solutions do not hold a lot of promise as the geometric and flow situations are too complex.

Conclusion

The way ahead appears to be:

Immediate

- 1 Further experimental work to supplement existing data and to document new designs of hole shapes.

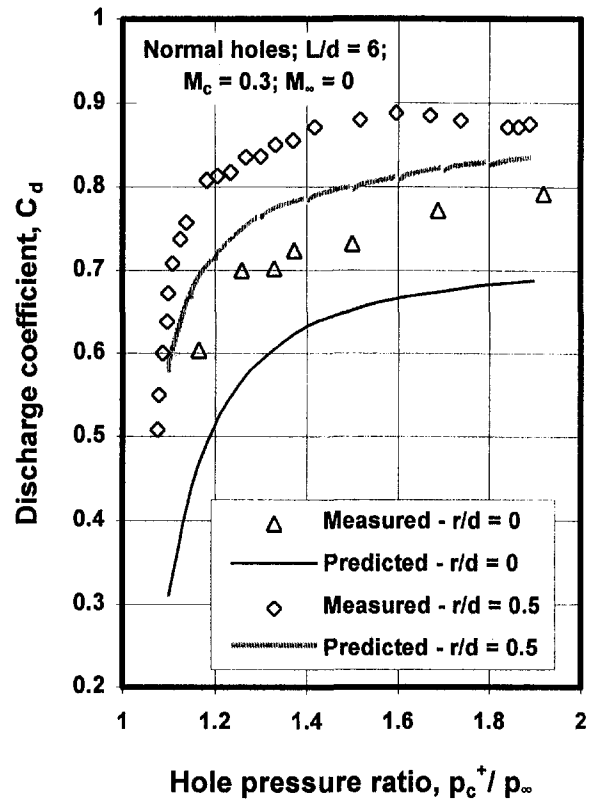


Fig. 7 Discharge coefficients calculated using CFD predictions of additional loss coefficients (from Khaldi, 1987)

- 2 Tune up and establish CFD codes against carefully gathered experimental results to give reliable output, then use the codes to conduct "numerical experiments."

Midterm

- 3 Correlations (for example for loss coefficients) could then be derived either from the experimental results or

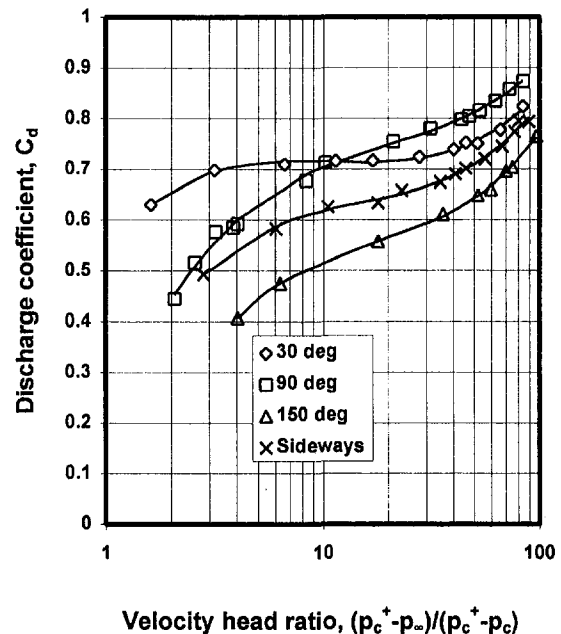


Fig. 8 Effect of hole inclination and orientation on the discharge coefficient (Byerley, 1989)

from the "numerical experiments," probably from both, for use in design.

Long Term

- 4 Ultimately numerical codes will provide a full solution for the flow at exit from the hole, taking into consideration all internal and external geometric and flow conditions. A discharge coefficient will then be unnecessary.

References

[Note: Reference numbers refer to Table 1.]

- 1 Adkins, R. C., and Gueroui, D., 1986, "An Improved Method for Accurate Prediction of Mass Flow Through Combustion Liner Holes," *ASME Journal of Engineering for Gas Turbines and Power*, Vol. 108, pp. 491-497.
- 2 Andrews, G. E., and Mkpadi, M. C., 1984, "Full Coverage Discrete Hole Wall Cooling: Discharge Coefficients," *ASME Journal of Engineering for Gas Turbines and Power*, Vol. 106, pp. 183-192.
- 3 Arts, T., and Lapidus, I., 1993, "Thermal Effects of a Coolant Film Along the Suction Side of a High Pressure Turbine Nozzle Guide Vane," AGARD Conference Proceedings 572, pp. 3-1 to 3-8.
- 4 Arts, T., and Bourignon A. E., 1990, "Behaviour of a Coolant Film With Two Rows of Holes Along the Pressure Side of a High-Pressure Nozzle Guide Vane," *ASME JOURNAL OF TURBOMACHINERY*, Vol. 112, pp. 513-521.
- 5 Benmansour, S., 1983, "Discharge Coefficient of Film Cooling Holes," MPhil Thesis, University of Nottingham, United Kingdom.
- 6 Benz, E., and Wittig, S., 1992, "Prediction of the Interaction of Coolant Ejection With the Main Stream at the Leading Edge of a Turbine Blade: Attached Grid Application," International Symposium, Heat Transfer in Turbomachines, Greece.
- 7 Byerley, A. R., 1989, "Heat Transfer Near to a Film Cooling Hole in a Gas Turbine Blade," DPhil Thesis, University of Oxford, United Kingdom.
- 8 Camci, C., and Arts, T., 1990, "An Experimental Convective Heat Transfer Investigation Around a Film-Cooled Gas Turbine Blade," *ASME JOURNAL OF TURBOMACHINERY*, Vol. 112, pp. 497-503.
- 9 Chu, T., Brown, A., and Garrett, S., 1985, "Discharge Coefficients of Impingement and Film Cooling Holes," ASME Paper No 85-GT-81.
- 10 Dewynne, J. N., Howison, S. D., Ockendon, J. R., Moorland, L. C., and Watson, E. J., 1989, "Slot Suction From Inviscid Channel Flow," *Journal of Fluid Mechanics*, Vol. 200, pp. 265-282.
- 11 Fitt, A. D., Ockendon, J. R., and Jones, T. V., 1985, "Aerodynamics of Slot-Film Cooling: Theory and Experiment," *Journal of Fluid Mechanics*, Vol. 160, pp. 15-27.
- 12 Forth, C. J. P., 1985, "An Investigation of Scaling Parameters Governing Film-Cooling," DPhil Thesis, Oxford University, United Kingdom.
- 13 Foucault, E., Demiboire, P., Bousgarbies, J. L., Vullieme, J. J., and Dorignac, E., 1993, "Etude Experimentale du Transfert de Chaleur pres d'une Paroi Plane Chauffee en Presence d'Injections Multiples (Ecoulement Subsonique)," AGARD Conference Proceedings 572, pp. 4-1 to 4-10.
- 14 Haas, W., Rodi, W., and Schönung, B., 1992, "The Influence of Density Difference Between Hot and Coolant Gas on Film Cooling by a Row of Holes: Predictions and Experiments," *ASME JOURNAL OF TURBOMACHINERY*, Vol. 114, pp. 747-755.
- 15 Hay, N., and Spencer, A., 1992, "Discharge Coefficients of Cooling Holes With Radiused and Chamfered Inlets," *ASME JOURNAL OF TURBOMACHINERY*, Vol. 114, No. 4, pp. 701-706.
- 16 Hay, N., Henshall, S. E., and Manning, A., 1994, "Discharge Coefficients of Holes Angled to the Flow Direction," *ASME JOURNAL OF TURBOMACHINERY*, Vol. 116, No. 1, pp. 92-96.
- 17 Hay, N., and Lampard, D., 1995, "The Discharge Coefficient of Flared Film Cooling Holes," ASME Paper No 95-GT-15.
- 18 Hay, N., Lampard, D., and Khaldi, A., 1994, "The Coefficient of Discharge of 30° Inclined Film Cooling Holes with Rounded Entries or Exits," ASME Paper No. 94-GT-180.
- 19 Hay, N., Lampard, D., and Benmansour, S., 1983, "Effect of Crossflows on the Discharge Coefficient of Film Cooling Holes," *ASME Journal of Engineering for Power*, Vol. 105, No. 2, pp. 243-248.
- 20 Hay, N., Khaldi, A., and Lampard, D., 1987, "Effect of Crossflows on the Coefficient of Discharge of Film Cooling Holes With Rounded Entries or Exits," 2nd ASME/JSME Thermal Engineering Conference, HI.
- 21 Khaldi, A., 1987, "Discharge Coefficient of Film Cooling Holes With Rounded Entries or Exits," PhD Thesis, University of Nottingham, United Kingdom.
- 22 Kutz, K. J., and Speer, T. M., 1994, "Simulation of the Secondary Air System of Aero Engines," *ASME JOURNAL OF TURBOMACHINERY*, Vol. 116, pp. 306-315.
- 23 Lichtarowicz, A., Duggins, R. K., and Markland, E., 1965, "Discharge Coefficients for Incompressible Non-cavitating Flow Through Long Orifices," *Journal of Mechanical Engineering Science*, Vol. 7, No. 2, pp. 210-219.
- 24 Ligrani, P. M., and Camci, C., 1985, "Adiabatic Film Cooling Effectiveness From Heat Transfer Measurements in Compressible Variable-Property Flow," *ASME Journal of Heat Transfer*, Vol. 107, pp. 313-220.
- 25 Lloyd, S., and Brown, A., 1985, "Fluid Flow and Heat Transfer Characteristics in the Entrance Region of Circular Pipes," ASME Paper no 85-GT-121.
- 26 McGreehan, W. F., and Schotsch, M. J., 1988, "Flow Characteristics of Long Orifices With Rotation and Corner Radiusing," *ASME JOURNAL OF TURBOMACHINERY*, Vol. 110, pp. 213-217.
- 27 McNown, J. S., and Hsu, E. T., 1959, "Application of Conformal Mapping to Divided Flow," Paper No 6, First Mid-Western Conf. on Fluid Mechanics.
- 28 Meyfarth, P. F., and Shine, A. J., 1965, "Experimental Study of Flow Through Moving Orifices," *ASME Journal of Basic Engineering*, pp. 1082-1083.
- 29 Morland, L. C., 1988, "Mathematical Models for a Fluid Flow Arising in Turbine Blade Cooling Passages," DPhil Thesis, University of Oxford, United Kingdom.
- 30 O'Malley, K., 1988, "An Experimental and Theoretical Investigation of Slot Injection and Flow Separation," DPhil thesis, University of Oxford, United Kingdom.
- 31 Parker, D. M., and Kercher, D. M., 1991, "An Enhanced Method to Compute the Compressible Discharge Coefficient of Thin and Long Orifices With Inlet Corner Radiusing," ASME HTD-Vol 188.
- 32 Rhode, J., Richard, R., and Metger, G. W., 1969, "Discharge Coefficients for Thick Plate Orifices With Approach Flow Perpendicular and Inclined to Orifice Axis," NASA TND-5467.
- 33 Rogers, T., and Hersh, A. S., 1975, "The Effect of Grazing Flow on the Steady State Resistance of Square-Edged Orifices," AIAA 2nd Aero-Acoustics Conference, Paper No. 75-493.
- 34 Sasaki, M., Takahara, K., Sakata, K., and Kumagai, T., 1969, "Discharge Coefficients for Thick Plate Orifices With Approach Flow Perpendicular and Inclined to Orifice Axis," NASA TND-5467.
- 35 Tillman, E. S., and Jen, H. F., 1984, "Cooling Airfoil Studies at the Leading Edge of a Film Cooled Airfoil," *ASME Journal of Engineering for Gas Turbines and Power*, Vol. 106, pp. 106-221.
- 36 Tillman, E. S., Hartel, E. O., and Jen, J. F., 1985, "The Prediction of Flow Through Leading Edge Holes in a Film Cooled Airfoil With and Without Inserts," *ASME Journal of Engineering for Gas Turbines and Power*, Vol. 107, pp. 92-98.
- 37 Wittig, S., Kim, S., Jakoby, R., and Weissert, I., 1996, "Experimental and Numerical Study of Orifice Discharge Coefficients in High-Speed Rotating Disks," *ASME JOURNAL OF TURBOMACHINERY*, Vol. 118, pp. 400-407.

An Experimental Investigation of the Velocity and Temperature Fields of Cold Jets Injected Into a Hot Crossflow

H. A. Rydholm

Volvo Aero Corp.,
Trollättan, Sweden;
Chalmers University of Technology,
Dept of Thermo and Fluid Dynamics,
Göteborg, Sweden

It is shown here by dimensional analysis that the near-wall flow field of an effusion-cooled combustor can be scaled if the Reynolds, Mach, and Prandtl numbers and the temperature and velocity ratios are kept constant. It is also demonstrated that a practical model experiment can be designed, which fulfills all the scaling laws. A test rig meeting these requirements has been designed, built and tested. The experimental conditions have been chosen to correspond to the conditions usually met in a real effusion-cooled combustion chamber. One geometric configuration has been investigated. This consists of one transverse row of holes drilled with a 30 deg angle to the wall through which the cooling air enters a cross-flowing mainstream. The mean values of all three velocity components and the three normal fluctuating Reynolds stresses as well as the mean temperature have been measured in a large number of points surrounding the central injection hole. Experiments were carried out for jet-to-mainstream density ratios of 1.2 and 1.8. The results indicate that realistic density ratios are necessary to provide data directly applicable to effusion-cooling design.

Introduction

Film cooling by discrete holes (effusion cooling) is used as a method to give the walls of combustors necessary thermal protection. To improve the efficiency, the air injection configuration must be designed such that the cooling effect is obtained with the least amount of cooling air. Numerical simulations are used in the analysis of effusion cooling, and more extensive experimental validation is required to improve these calculations. The purpose of this project is therefore to provide a portion of this validation.

Literature Review

Studies of effusion cooling have focused mainly on the variables that control heat transfer. The majority of film-cooling research is focused on the adiabatic wall temperature and its dependence on the geometry and flow parameters. Such work has basically generated data for use in design activities, presented most commonly in the form of adiabatic film-cooling effectiveness, η .

In modern engines the coolant-to-main flow density ratios are well above one. Cost considerations, however, have resulted in many investigations being carried out at density ratios near unity. In a series of studies by Goldstein et al. (1970, 1974), measurements of the adiabatic wall temperature (T_{aw}) were performed for the injection of a slightly heated jet, both for a single jet and for a row of jets. Eriksen and Goldstein (1974) continued this work with measurements of heat transfer coefficient distributions for the same geometry.

Some of the work has attempted to map the complex three-dimensional flow field around a jet in a crossflow, in order to increase the understanding of the flow field and to provide validation data for numerical calculations. Most of these measurements have been done at unity density ratio. For example

Bergeles et al. (1976, 1977) made velocity field measurements with $DR = 0.85$ both for a normal and a 30 deg inclined jet. Andreopoulos and Rodi (1984) performed a detailed study of a flow field around a normal jet in a crossflow. Others have performed film-cooling studies with density ratio effects. These studies have mainly been limited to adiabatic wall effectiveness data derived by injecting foreign gases and measuring their concentration at an impermeable wall, using a mass transfer-temperature analog. Pedersen et al. (1977) presented a study that indicated a significant dependency of the density ratio on effusion cooling. Foster and Lampard (1975, 1980) focused on a DR of 2.0 using mass transfer studies to acquire effectiveness data at different injection angles. Velocity field measurements have recently been made with realistic density ratio created by a large temperature difference between the jet and main flow. Pietrzyk et al. (1989, 1990) made detailed velocity measurements in a flow field downstream of a row of holes for density ratios 1.0 and at 2.0. This work was followed by Sinha et al. (1991), who made surface temperature measurements on the same test rig for a density ratio range from 1.2 to 2.0.

Dimensional Analysis

Starting with the three basic laws of conservation:

Conservation of A: mass, B: momentum, and C: energy:

$$A: \partial \rho / \partial t + \partial (\rho u_j) / \partial x_j = 0$$

$$B: \rho \partial u_i / \partial t + \rho u_j \partial u_i / \partial x_j = -(\partial p / \partial x_i) + \rho g_i + \partial / \partial x_j (\tau'_{ij})$$

$$C: \rho (\partial h / \partial t + u_j \partial h / \partial x_j) - (\partial p / \partial t + u_j \partial p / \partial x_j) = \tau'_{ij} \partial u_i / \partial x_j + \partial / \partial x_k (k \partial t / \partial x_k)$$

These equations involve only the assumptions that the fluid forms a continuum and is in thermodynamic equilibrium. The only effective body force is gravity. The heat conduction follows Fourier's law and there are no internal heat sources. We also assume that:

- 1 The gas ideal: $dh = c_p dT$ ($c_p = c_{p0} = \text{constant}$) and $\rho = p/RT$.
- 2 The mechanical pressure is equal to the thermodynamic pressure: $\partial u_j / \partial x_j - \frac{2}{3} \partial u_k / \partial x_k \delta_{ij} = 0$.

Contributed by the International Gas Turbine Institute and presented at the 41st International Gas Turbine and Aeroengine Congress and Exhibition, Birmingham, United Kingdom, June 10–13, 1996. Manuscript received at ASME Headquarters February 1996. Paper No. 96-GT-491. Associate Technical Editor: J. N. Shinn.

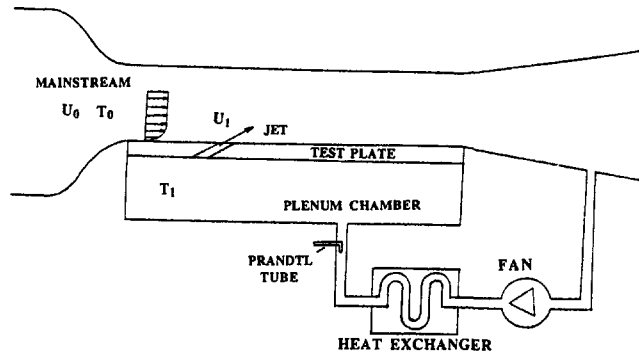


Fig. 1 A schematic illustration of the experimental setup

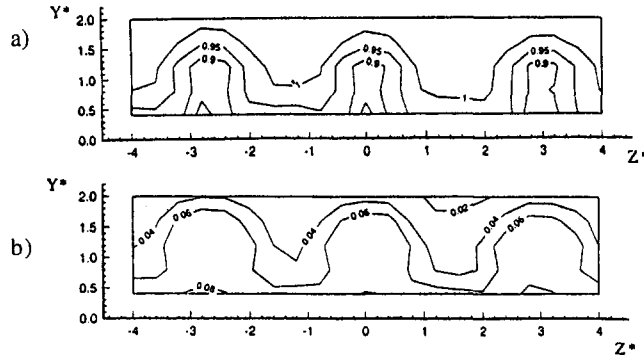


Fig. 2 (a) U^* and (b) the u_{rms}^* at $x^* = x/D = 12$ (Series 2: $MR = 1.35$ and $DR = 1.17$)

- The fluid is Newtonian with the viscous stresses: $\tau'_{ij} = \mu(\partial u_i/\partial x_j + \partial u_j/\partial x_i - \frac{2}{3}\partial u_k/\partial x_k\delta_{ij})$.
- In the momentum equation we assume: $g = 0$. In the energy equation we assume that the pressure fluctuations: $(\partial p/\partial t + u_j\partial p/\partial x_j) = 0$, and the dissipation: $\phi = \tau'_{ij}\partial u_i/\partial x_j = 0$.
- The viscosity $\mu = \mu_0(T/T_0)^n$ and the thermal conductivity $k = k_0(T/T_0)^m$ (n and m are constants).

With these assumption we are now able to simplify A, B, and C:

$$A: \partial(p/T)/\partial t + \partial(\rho u_j/T)/\partial x_j = 0$$

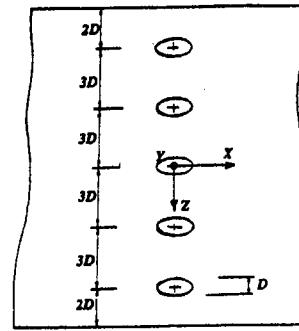


Fig. 3 The geometry and coordinate system used

$$B: p/RT(\partial u_i/\partial t + u_j\partial u_i/\partial x_j) = -(\partial p/\partial x_j) + \mu_0(T/T_0)^n(\partial^2 u_i/\partial x_j^2)$$

$$C: \rho c_{p0}/RT(\partial T/\partial t + u_j\partial T/\partial x_j) = k_0(T/T_0)^m(\partial^2 T/\partial x_k^2)$$

The next step is to nondimensionalize the three equations with the variables: $u_j^* = u_j/u_0$, $x_j^* = x_j/D$, $t^* = tu_0/D$, $T^* = T/T_0$ and $p^* = p/\rho_0 u_0^2 = pRT_0/\rho_0 \mu_0^2$.

With some simplifications we can obtain:

$$A: \partial T^*/\partial t^* + \partial(u_j^* p^*/T^*)/\partial x_j^* = 0$$

$$B: p^*/T^*(\partial u_i^*/\partial t^* + u_j^*\partial u_i^*/\partial x_j^*) = 1/\gamma M^2 \cdot \{-\partial p^*/\partial x_j^*\} + 1/\gamma M^2 \cdot 1/Re \cdot \{T^{*n}(\partial u_i^*/\partial x_j^*)^2\}$$

$$C: p^*/T^*(\partial T^*/\partial t^* + u_j^*\partial T^*/\partial x_j^*) = 1/\gamma M^2 \cdot 1/Re \cdot 1/Pr \cdot \{T^{*m}\partial^2 T^*/\partial x_j^2\}$$

where the three nondimension parameters are,

$$\text{Reynolds number: } Re = \rho_0 \cdot u_0 D / \mu_0 = \rho_0 / RT_0 \cdot Du_0 / \mu_0$$

$$\text{Mach number: } M = u_0 / a_0 = u_0 / (\gamma RT_0)^{1/2}$$

$$\text{Prandtl number: } Pr = \mu_0 c_{p0} / k_0$$

All should have the same value in our scaled wind tunnel as they have in a real combustor (the Prandtl number is assumed to be constant). Furthermore the boundary conditions should

Nomenclature

D = injection hole diameter
 DR = density ratio = ρ_1/ρ_0
 MR = momentum ratio = $\rho_1 U_1 / \rho_0 U_0$
 M = Mach number
 Pr = Prandtl number
 p = pressure
 R = gas constant
 Re = Reynolds number
 T = temperature
 TR = temperature ratio = T_1/T_0
 U, V, W = mean velocity components
 VR = velocity ratio = U_1/U_0
 a = speed of sound; time constant
 c_p = specific heat at constant pressure
 g = gravitational acceleration

h = enthalpy
 k = thermal conductivity
 t = time
 u, v, w = instantaneous velocity components
 $u_{rms}, v_{rms}, w_{rms}$ = rms values of the velocity fluctuations
 x, y, z = Cartesian coordinates
 γ = specific heat ratio
 δ_{ij} = Kronecker delta
 μ = dynamic viscosity
 ρ = density
 τ_{ij} = stress tensor
 η = adiabatic film-cooling effectiveness = $(T_{aw} - T_1)/(T_0 - T_1)$

ϕ = dissipation
 ΔT^* = dimensionless temperature difference = $(T - T_1)/(T_0 - T_1)$

Subscripts

0 = free-stream condition far from the wall
 1 = coolant-jet condition
 aw = conditions for adiabatic wall
 f = full size
 m = model
 rms = root mean square

Superscripts

* = dimensionless value
 $^\circ$ = degree

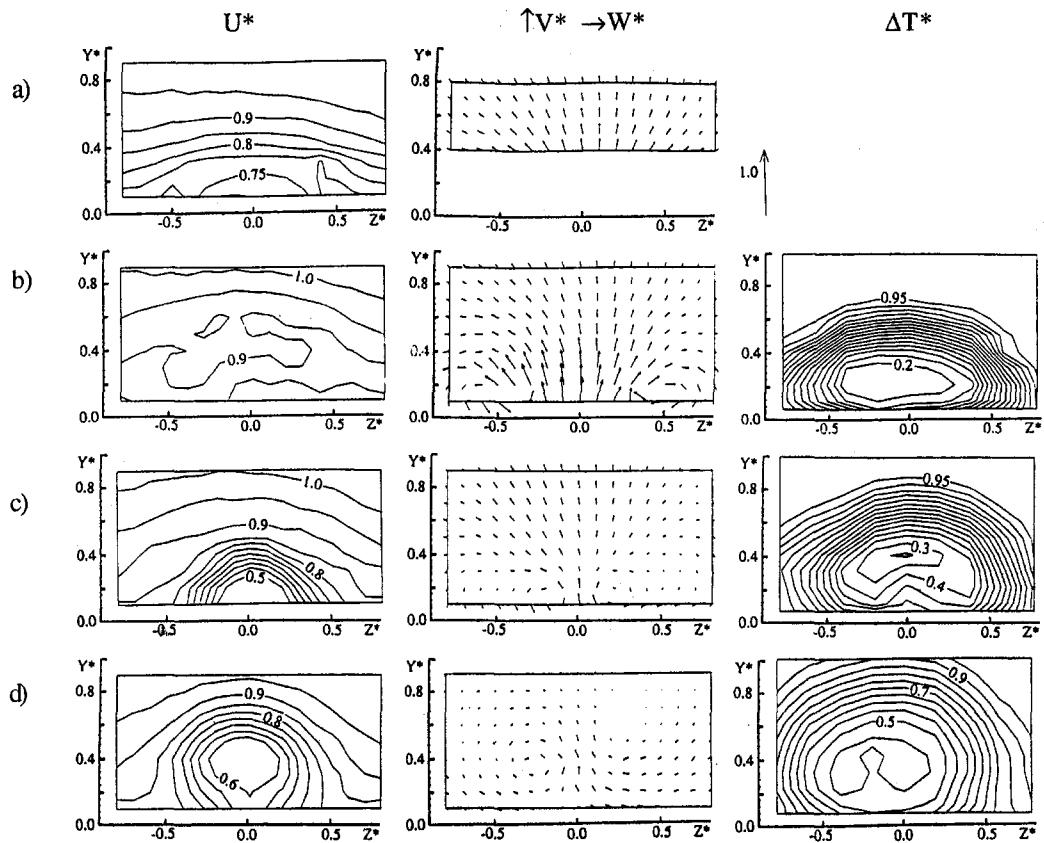


Fig. 4 Series 1 ($MR = U_1 \rho_1 / U_0 \rho_0 = 1.01$ and $DR = \rho_1 / \rho_0 = 1.17$): the streamwise velocity $U^* = U/U_0$ (left), the vertical and lateral velocities $V^* = V/V_0$ and $W^* = W/W_0$ (middle), and the temperature $\Delta T^* = (T - T_1)/(T_0 - T_1)$ (right). For (a) $x^* = x/D = 0$, (b) $x^* = 1$, (c) $x^* = 2$, and (d) $x^* = 4$.

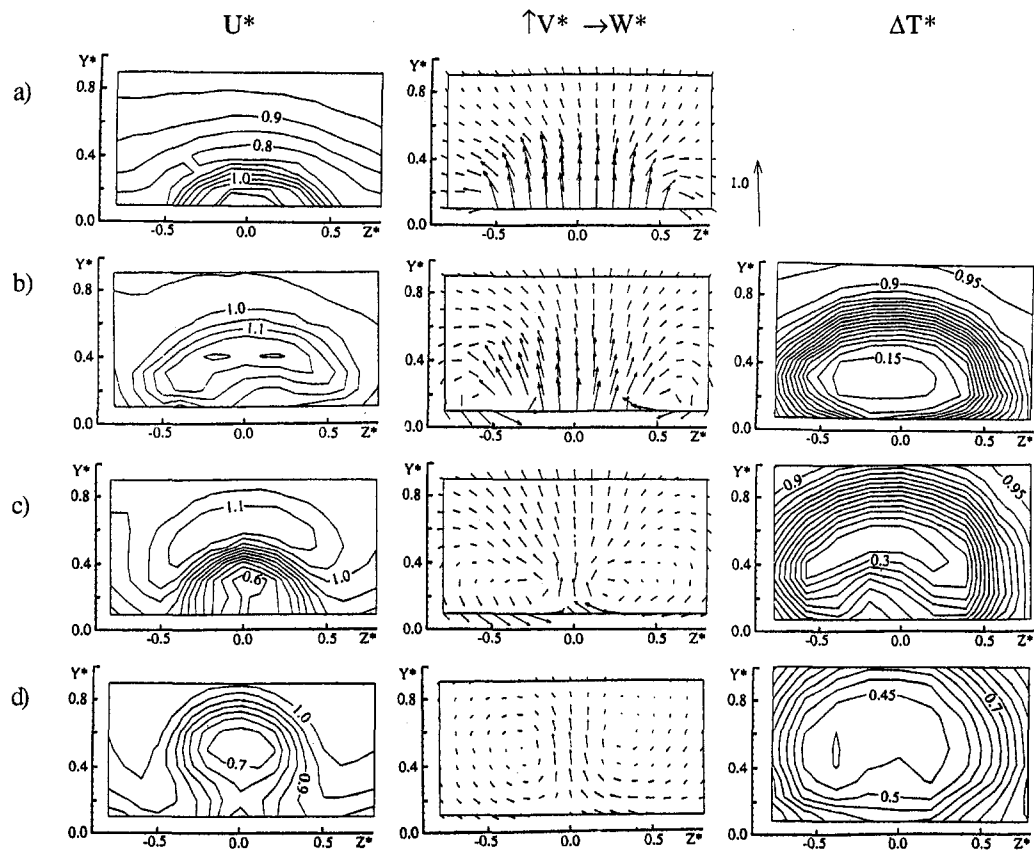


Fig. 5 Series 2 ($MR = U_1 \rho_1 / U_0 \rho_0 = 1.35$ and $DR = \rho_1 / \rho_0 = 1.17$): the streamwise velocity $U^* = U/U_0$ (left), the vertical and lateral velocities $V^* = V/V_0$ and $W^* = W/W_0$ (middle), and the temperature $\Delta T^* = (T - T_1)/(T_0 - T_1)$ (right). For (a) $x^* = x/D = 0$, (b) $x^* = 1$, (c) $x^* = 2$, and (d) $x^* = 4$.

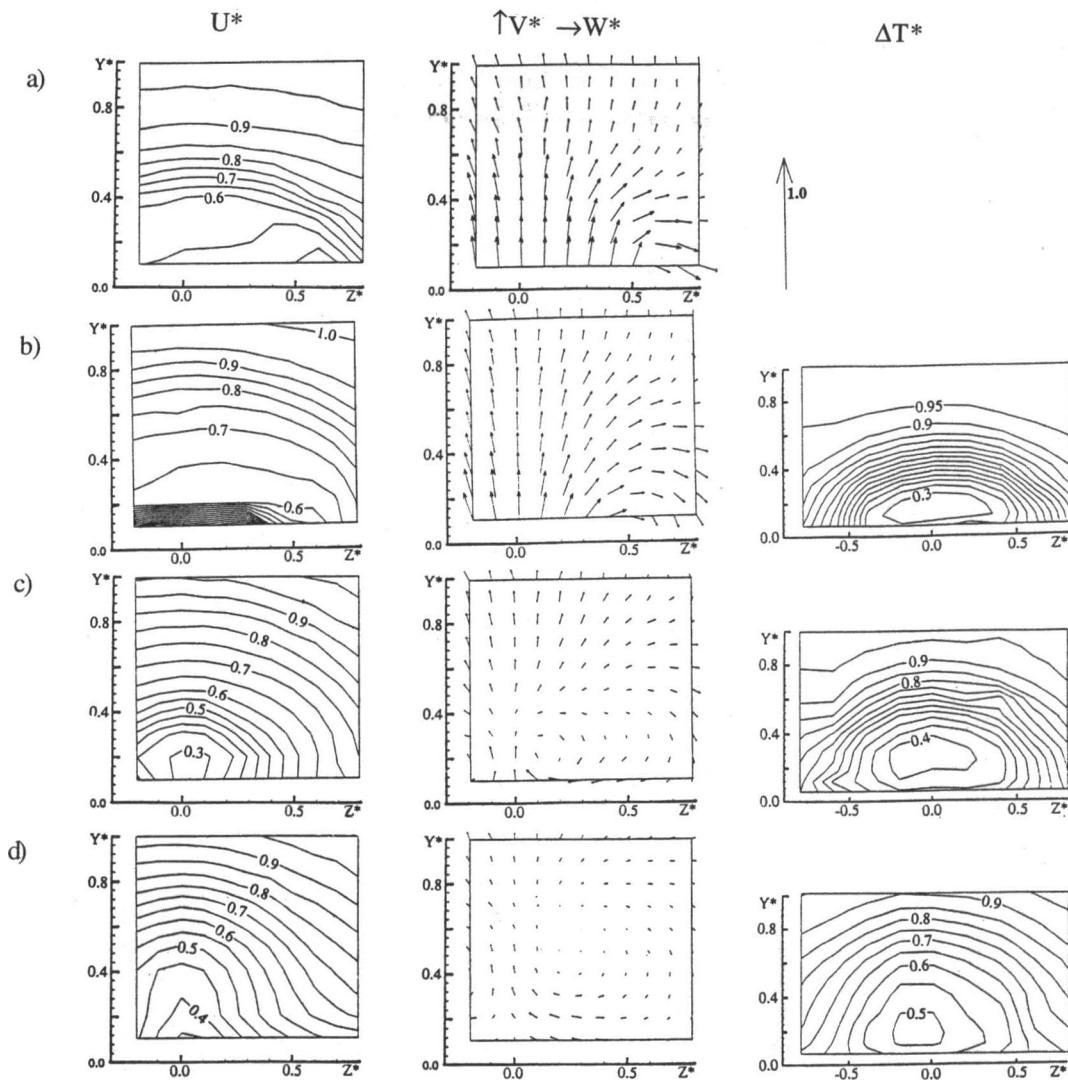


Fig. 6 Series 3 ($MR = U_1 \rho_1 / U_0 \rho_0 = 0.94$ and $DR = \rho_1 / \rho_0 = 1.74$): the streamwise velocity $U^* = U/U_0$ (left), the vertical and lateral velocities $V^* = V/V_0$ and $W^* = W/W_0$ (middle), and the temperature $\Delta T^* = (T - T_1)/(T_0 - T_1)$ (right). For (a) $x^* = x/D = 0$, (b) $x^* = 1$, (c) $x^* = 2$, and (d) $x^* = 4$.

be unchanged, which gives the following two relations: $(u_1/u_0)_f = (u_1/u_0)_m$ and $(T_1/T_0)_f = (T_1/T_0)_m$. Assuming typical values in a real combustor: $p_0 = 2.0$ MPa, $T_0 = 1480$ K, $T_1 = 770$ K, $u_0 = 80$ m/s and $D = 0.7$ mm. It would simplify our experiments if we could use a nonpressurized (atmospheric) wind tunnel and use cooling air at room temperature, which gives the following values in our scaled experiments: $p_0 = 0.1$ MPa, $T_0 = 580$ K, $T_1 = 300$ K, $u_0 = 50$ m/s and $D = 5$ mm. Note that only the mean values are scaled, and the main flow values of turbulent energy and size of the turbulent eddies are not included in the scaling.

Facility and Instrumentation

The experiments were conducted in a closed-loop, recirculating, wind tunnel, specially designed to resist temperatures up to 300°C. The test section, with the dimensions $80 \times 80 \times 800$ mm, was preceded by a 5:1 contraction; see Fig. 1.

The free-stream turbulence intensity in the test section was about 1 percent and the velocity boundary layer thickness 3.5 mm (three diameters upstream from the jet exit hole center) at a main flow temperature of 75°C and velocity U_0 of 47.4 m/s, and 5.0 mm at $T_0 = 300^\circ\text{C}$ and $U_0 = 46.7$ m/s. Air was injected

into the mainstream through a row of five holes, 5 mm in diameter, drilled in a detachable flat steel plate. All five jets issued from a common plenum chamber located below the plate. Air to the jets is supplied by a secondary flow loop driven by a radial fan. Different blowing ratios were obtained by varying the flow rate through the secondary flow loop while maintaining a constant mainstream velocity. The flow rate was measured by a Prandtl tube, placed in the plenum chamber entrance. The jet velocity U_1 was calculated by dividing the secondary flow by the cross-sectional area of the five holes (and checked by LDA measurements at the jet exits). A heat exchanger was installed to cool the secondary flow in order to maintain the jet-to-mainstream density ratio. The fact that all five jets have the same U_1 was checked by LDA measurements at jet exit (both in the case with and without a mainstream velocity). Measurements of U^* and u_{rms}^* demonstrate good symmetry between the three central jets at 12 D downstream the row of holes; see Fig. 2. In the bottom plate of the test section five holes inclined 30 deg, were drilled with a lateral spacing of 3 diameters; see Fig. 3. They were located 18 diameters downstream of the start of the test section, and the length of the holes was eight times the diameter.

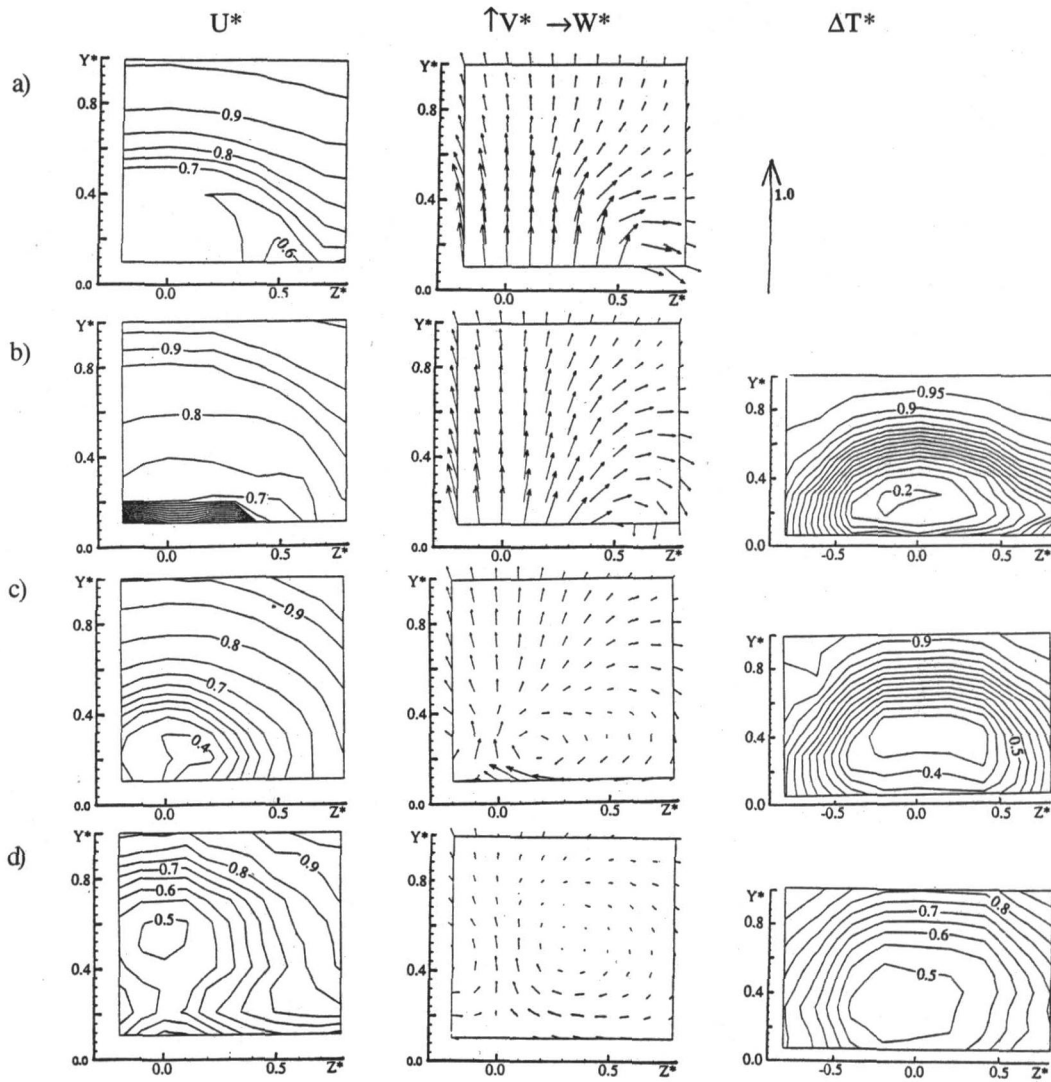


Fig. 7 Series 4 ($MR = U_1 \rho_1 / U_0 \rho_0 = 1.28$ and $DR = \rho_1 / \rho_0 = 1.77$): the streamwise velocity $U^* = U/U_0$ (left), the vertical and lateral velocities $V^* = V/V_0$ and $W^* = W/W_0$ (middle), and the temperature $\Delta T^* = (T - T_1)/(T_0 - T_1)$ (right). For (a) $x^* = x/D = 0$, (b) $x^* = 1$, (c) $x^* = 2$, and (d) $x^* = 4$.

Velocity Measurements

Velocity measurements were made with a Laser-Doppler Anemometer (LDA), which require optical access, and thus glass is used for the roof and one wall of the test section. To allow measurements near the wall, it was necessary to tilt the entire probe 8 deg downward to prevent the lower beam from intersecting the floor of the wind tunnel. The presented lateral mean velocities, V , have been calculated from the measured V and W components (the velocity fluctuations could not be compensated in this way).

The LDA system was equipped with frequency shifting in order to distinguish between forward and reverse flow and to avoid fringe bias errors in measurements. The LDA probes were precisely positioned by a computer-controlled traverse system, and the positional errors are estimated to less than ± 0.3 mm ($\pm 0.06 D$). A atomizer was used to seed the flow with $1.5 \mu\text{m}$ silicon carbide particles, which we believe followed the flow sufficiently well for correct measurement of the mean and fluctuating velocities. The seeding unit was arranged to give equal concentrations in the main- and jet-flow in order to avoid particle density bias. The LDA measurements were conducted using side scattering, which reduced the probe volume diameter to

less than 0.1 mm. The probability of obtaining a sample is proportional to the speed of the flow; therefore statistical particle bias corrections were applied to the LDA data by weighting each individual sample based on the residence time of a particle in the probe volume. Total measurement time at one point varied from about 20 s to 140 s. At each point, the measurements of U and V were obtained from 3000 samples and W from 500 samples.

Uncertainties in the mean velocity measurements can be estimated for U and V to ± 0.5 m/s (or ± 1 percent of U_0) and for W to ± 1 m/s (or ± 2 percent of U_0). Uncertainties in the turbulence measurements can be estimated to ± 5 percent for u_{rms} and v_{rms} , and to ± 10 percent for w_{rms} .

Temperature Measurements

The temperature was measured by an iron/constantan thermocouple with one end at the edge of a holder while the other end was kept at a constant temperature of 0°C . The electromagnetic force between the two ends was measured with a voltmeter and transformed to temperature using a calibrated chart provided by the manufacturer.

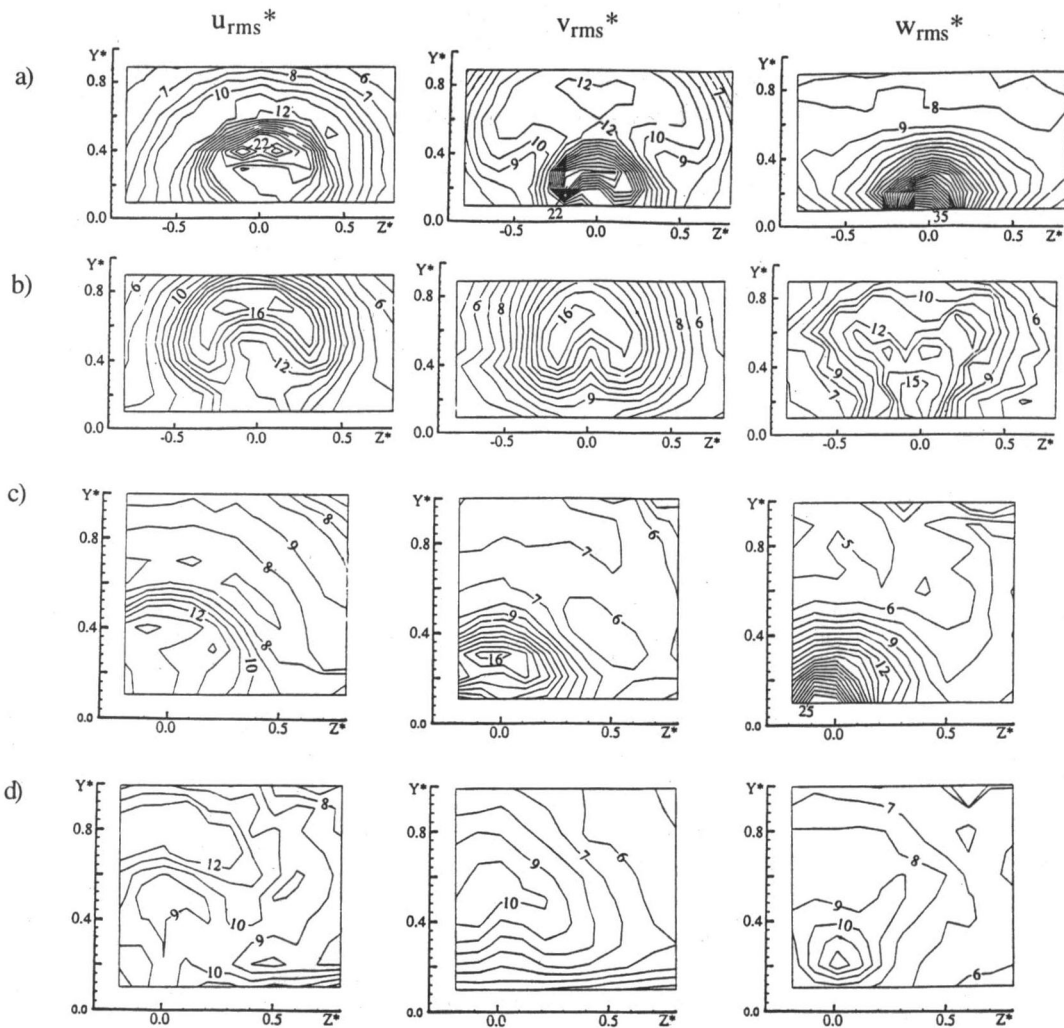


Fig. 8 The rms values in percent of the velocities $u_{rms}^* = u_{rms}/U_0$ (left), v_{rms}^* (middle), and w_{rms}^* (right) for Series 2 ($MR = U_1\rho_1/U_0\rho_0 = 1.35$ and $DR = \rho_1/\rho_0 = 1.17$) (a) $x^* = x/D = 1$, (b) $x^* = 4$, and for Series 4 ($MR = U_1\rho_1/U_0\rho_0 = 1.28$ and $DR = \rho_1/\rho_0 = 1.77$) (c) $x^* = x/D = 2$, (d) $x^* = 4$.

In these measurements, the glass used as roof in the test section was replaced with a steel plate with a slit in the middle, allowing the traversal of the thermocouple holder in all three directions. The same computer-controlled traverse system was used as in the LDA measurements, and the positional errors are estimated to less than ± 0.5 mm (± 0.1 D). The measuring control volume had an estimated diameter of about 0.7 mm. The mean temperature values were read manually from a digital voltmeter, with an accuracy estimated at $\pm 0.5^\circ\text{C}$.

The total temperature, not the static temperature, was measured, which is about 1°C lower, and the thermocouple was heated by radiation from the walls of the test section, which results in a maximum calculated error of 1°C .

Experimental Plan

The velocity and temperature fields were measured at different conditions for series 1 to 4 according to Table 1. Velocity

Table 1 The conditions for measurement series 1 to 4

Series	T_0 ($^\circ\text{C}$)	U_0 (m/s)	T_1 ($^\circ\text{C}$)	U_1 ($^\circ\text{C}$)	MR	DR
1	75.0	47.4	25.5	41.1	1.01	1.17
2	75.0	47.4	25.5	55.0	1.35	1.17
3	300.5	46.7	57.8	25.3	0.94	1.74
4	300.5	46.7	51.2	33.8	1.28	1.77

and temperature data were taken throughout the vertical–lateral plane (y – z plane) normal to the main flow at different streamwise positions $x^* = x/D$. The different locations at which data were collected are shown in Table 2.

Discussion

The different measurements were conducted by varying the momentum ratio (MR) and the density ratio (DR). The variation in MR was achieved by increasing the jet velocity while keeping the mainstream velocity constant, and the variation in DR was achieved by increasing the main flow temperature while keeping the jet temperature constant.

Not surprisingly, the velocity profiles measured at different MR and DR differ. The high DR measurements (series 3 and 4) were conducted at a main flow temperature (T_0) of 300°C with a viscosity about twice as high as in the low DR cases (series 1 and 2), resulting in higher velocity diffusion and weaker velocity gradients. The distance between the wake and the wall does not change with different DR (but with different MR). The high main flow temperature, at high DR , not only results in a high velocity diffusion but also in a high temperature diffusion. That is why the high DR cases have a higher relative core temperatures (ΔT^*) and weaker temperature gradients, compared to the low DR cases with $T_0 = 75^\circ\text{C}$.

At $x^* = 1$, the high density ratio jets demonstrate velocities close to zero in the near wall region ($z^* < 0.2$), which probably

Table 2 Locations of measurements

	x^*	y^*	Step	z^*	Step
Velocity (series 1 & 2):	0, 1, 2, 4	0.1/0.9	0.1	-0.8/0.8	0.1
Velocity (series 3 & 4):	0, 1, 2, 4	0.1/1.0	0.1	-0.2/0.8	0.1
Temperature:	1, 2, 4	0.05/1.0	0.05	-0.8/0.8	0.1

indicates a recirculation zone just downstream of the jet exit. A very strong velocity gradient just above this recirculation zone results in extremely high and nonisotropic turbulence. No recirculation of this kind was detected in the low DR measurements (there may be a recirculation bubble in the low DR flows, but it must be within 0.1 D distance from the wall, where no measurements were taken).

The vector plot of the secondary velocities (V and W) shows differences between the two jets with different density ratios. The low DR jets have a stronger vortices, with a center farther away from the wall, resulting in a strong in-bound lateral velocity, which is not detected at high DR .

By comparing the mean and fluctuating streamwise velocities 4 diameters downstream from the jet exit center ($x^* = 4$), we see that the higher velocity diffusion due to the higher mainstream temperature at high DR results in weaker velocity gradients and lower maximum turbulence levels, compared to the low DR case. The streamwise velocity contours at high and low DR now show similarities of shape, although the initial development, farther upstream, was quite different.

From a comparison of the U^* and u_{rms}^* measurements, of series 2 and 4, it is obvious that a strong connection exists between the velocity gradient and the turbulence level. A comparison between the velocity and temperature fields gives a less clear picture. When the jets proceed downstream from $x^* = 2$ to 4, an increase in the distance between the wake and the wall is seen in the mean velocity measurements, but not in the temperature measurements where the cool core of the jet stays at almost the same distance from the wall. This result could not be explained by any measurement error.

The turbulence fields are highly nonisotropic where the different turbulence components clearly show different patterns. An increase in the momentum ratio does not change this, but only results in higher turbulence levels.

Conclusions

The main purpose of this work has been to provide validation data for numerical computations, and the results give a detailed picture of the mean and fluctuating velocity components in all three directions as well as the mean temperature field, in the vicinity of an injection hole.

The flow field in the vicinity of the jet exit is strongly three dimensional with two counterrotating vortices, on both sides of the jet, creating a downwash of fast-speed fluid down to the wall and a transport of slow-speed fluid from the wall into the mainstream, which creates a velocity deficit wake surrounded

by a highly turbulent shear layer. An increase of the momentum ratio will increase both the strength of these vortices and the distance between the wake and the wall. An increase of the density ratio will, on the contrary, result in weaker velocity gradients and thus, in lower turbulence levels. This is probably due to the rise in viscosity and thermal conductivity at the higher (mainstream) temperatures.

The measurements show that the turbulence near the hole exit is highly nonisotropic. Higher MR does not change this turbulence pattern, it only increases its intensity. When the jet proceeds downstream, an increase in the distance between the velocity deficit wake and the wall is seen in the velocity measurements. But according to the temperature measurement, the cool core of the jet is at almost the same distance from the wall at different downstream locations. A recirculating flow was present only at high DR , just behind the jet exit, and the near wall lateral velocity (W^*) was stronger at low DR .

References

- Andreopoulos, J., and Rodi, W., 1984, "Experimental investigation of jets in a crossflow," *J. Fluid Mech.*, Vol. 138, pp. 93-127.
- Bergeles, G., 1976, "Three dimensional discrete-hole cooling processes—an experimental and theoretical study," Ph.D thesis, Univ. of London, London, England.
- Bergeles, G., Gosman, D., and Launder, B. E., 1977, "Near-field character of a jet discharged through a wall at 30° to mainstream," *AIAA Journal*, Vol. 15, No. 4, pp. 499-504.
- Eriksen, V. L., and Goldstein, R. J., 1974, "Heat transfer and film-cooling following injection through inclined circular tubes," *ASME Journal of Heat Transfer*, Vol. 96, pp. 239-245.
- Foster, N. W., and Lampard, D., 1975, "Effects of density and velocity on discrete hole film cooling," *AIAA Journal*, Vol. 13, No. 8, pp. 1112-1114.
- Foster and Lampard, D., 1980, "The flow and film cooling effectiveness following injection through a row of holes," *ASME Journal of Engineering for Power*, Vol. 102, pp. 584-588.
- Goldstein, R. J., Eckert, E. R. G., Eriksen, V. L., and Ramsey, J. W., 1970, "Film-cooling following injection through clined circular tubes," *Israel J. of Tech.*, Vol. 8, pp. 145-154.
- Goldstein, R., Eckert, E. R. G., and Burggraf, F., 1974, "Effects of hole geometry and density on three-dimensional film-cooling," *Int. J. Heat Mass Transfer*, Vol. 17, pp. 595-607.
- Pedersen, D. R., Eckert, E. R. G., and Goldstein, R. J., 1977, "Film cooling with large density differences between the mainstream and the secondary fluid measured by the heat mass transfer analogy," *ASME Journal of Heat Transfer*, Vol. 99, pp. 620-627.
- Pietrzyk, J. R., Bogard, D. R., and Crawford, M. E., 1989, "Hydrodynamic measurements of jets in crossflow for gas turbine film cooling applications," *ASME JOURNAL OF TURBOMACHINERY*, Vol. 112, pp. 437-443.
- Pietrzyk, J. R., Bogard, D. R., and Crawford, M. E., 1990, "Effects of density ratio on the hydrodynamics of film-cooling," *ASME JOURNAL OF TURBOMACHINERY*, Vol. 111, pp. 139-145.
- Sinha, A. K., Bogard, D. R., and Crawford, M. E., 1991, "Film cooling effectiveness downstream of a single row of holes," *ASME JOURNAL OF TURBOMACHINERY*, Vol. 113, pp. 442-449.

Flowfield Measurements for Film-Cooling Holes With Expanded Exits

K. Thole¹

M. Gritsch

A. Schulz

S. Wittig

Institut für Thermische
Strömungsmaschinen,
Universität Karlsruhe,
Karlsruhe, Federal Republic of Germany

One viable option to improve cooling methods used for gas turbine blades is to optimize the geometry of the film-cooling hole. To optimize that geometry, effects of the hole geometry on the complex jet-in-crossflow interaction need to be understood. This paper presents a comparison of detailed flowfield measurements for three different single, scaled-up hole geometries, all at a blowing ratio and density ratio of unity. The hole geometries include a round hole, a hole with a laterally expanded exit, and a hole with a forward-laterally expanded exit. In addition to the flowfield measurements for expanded cooling hole geometries being unique to the literature, the testing facility used for these measurements was also unique in that both the external mainstream Mach number ($Ma_\infty = 0.25$) and internal coolant supply Mach number ($Ma_c = 0.3$) were nearly matched. Results show that by expanding the exit of the cooling holes, both the penetration of the cooling jet and the intense shear regions are significantly reduced relative to a round hole. Although the peak turbulence level for all three hole geometries was nominally the same, the source of that turbulence was different. The peak turbulence level for both expanded holes was located at the exit of the cooling hole resulting from the expansion angle being too large. The peak turbulence level for the round hole was located downstream of the hole exit where the velocity gradients were very large.

Introduction

New challenges in better turbine blade cooling are ever present with the aim of increasing turbine inlet temperatures to improve gas turbine efficiencies. The attempts in meeting those challenges have focused on improving inner blade convective heat transfer and improving external blade film-cooling. Blade film-cooling is attained by injecting the inner blade convective coolant fluid through the blade surface into the external blade boundary layer.

From a flowfield perspective, ideal film-cooling would occur when a film-cooling jet has minimal penetration into the mainstream such that the jet remains attached to the cooling surface, yet the jet should have a high enough mass flow rate to cover a large area of the blade. Also, the cooling jet should have relatively low turbulent mixing to avoid dilution of the jet by the hot mainstream fluid. In many past studies the focus has been to optimize film-cooling fluid mechanical parameters, such as jet-to-mainstream blowing ratio and momentum flux ratio, for round film-cooling holes that are inclined at nominally 30 deg. Further optimization is still needed. In particular, one viable alternative is to optimize the cooling hole geometry. By gaining a better understanding of the complex flowfield that results from cooling holes that have been laterally and forward-laterally expanded, improvements can be made to the hole geometry to ultimately provide better cooling characteristics of the film.

This paper presents detailed flowfield measurements for three different single, scaled-up, cooling hole geometries for a blowing ratio (M), momentum flux ratio (I), and density ratio (DR) of unity. The three hole shapes include a baseline round hole, a hole with a laterally expanded exit, and a hole with a forward-

laterally expanded exit. Thus far, there are no reported detailed flowfield measurements for these hole geometries. This study is also unique because in addition to the mainstream flow, representing the external blade flowfield, there is a parallel flowing coolant supply channel, representing the inner blade convective passage between the midspan and trailing edge of a nozzle guide vane. Thus far, there are no reported detailed flowfield measurements for holes that have both primary and coolant flow passages.

Expanded Cooling Hole Studies

Although it has been over 20 years since Goldstein et al. (1974) first reported their adiabatic effectiveness measurements for laterally expanded cooling holes, there have been relatively few studies reported in the open literature since that time discussing contoured film-cooling holes. Goldstein et al. (1974) showed that by laterally expanding the hole 10 deg, improved adiabatic effectiveness values were measured for a large range of blowing ratios. Specifically, Goldstein et al. showed that for a blowing ratio range between $0.8 < M < 2.2$, the centerline adiabatic effectiveness remained constant at seven hole diameters downstream for the laterally expanded hole. In contrast, they showed for a blowing ratio above $M > 0.3$, the effectiveness dropped significantly for a round hole because of jet detachment. They attributed the improved performance for the laterally expanded hole to the reduced momentum of the exiting jet. A reduction in the exiting jet momentum can be achieved for the same jet mass flow rate by expanding the cooling hole exit area.

In a later study, Makki and Jakubowski (1986) measured higher adiabatic effectiveness values for a forward-laterally expanded hole in comparison to a round hole. Sen et al. (1996) showed that improved cooling performance at a high momentum flux ratio ($I = 3.9$) could also be obtained for a 60 deg compound angle hole when the hole had a forward expansion. Compound angle holes refer to holes that inject the coolant laterally with respect to the mainstream. Without the forward

¹ Present address: Department of Mechanical Engineering, University of Wisconsin, Madison, WI 53706-1572.

Contributed by the International Gas Turbine Institute and presented at the 41st International Gas Turbine and Aeroengine Congress and Exhibition, Birmingham, United Kingdom, June 10–13, 1996. Manuscript received at ASME Headquarters February 1996. Paper No. 96-GT-174. Associate Technical Editor: J. N. Shinn.

expansion, Sen et al. (1996) showed that the film-cooling was completely ineffective.

Flowfield Structures of Film-Cooling Jets

Past flowfield investigations have given some physical insight as to the primary flow structures dictating the interaction between the cooling jet and the mainstream crossflow for a round hole geometry. These flowfield investigations include those of Yoshida and Goldstein (1984), Jubran and Brown (1985), Pietrzyk et al. (1989), Subramanian et al. (1992), Benz et al. (1993), Leylek and Zerkle (1993), Lee et al. (1994) and Garg and Gaugler (1995). At high blowing ratios, $M \geq 1$, the dominating flow structures for a round hole film-cooling jet include a separation region which forms at the inlet of the cooling hole, intense shear regions as the mainstream interacts with the jet, and longitudinal vortices that form at the lateral edges of the jet.

The formation of a separation region was first identified by Pietrzyk et al. (1989) to occur at the hole entrance on the leeward side of the hole. In the Pietrzyk et al. (1989) study, the coolant was supplied by a plenum and as a result the flow encountered a large turning angle on the leeward side of the hole, which caused a separation region. This separation region skewed the exiting jet toward the windward side of the hole. Benz et al. (1993), Leylek and Zerkle (1993), and Garg and Gaugler (1995) also discuss the importance of numerically simulating the jet flow inside the cooling hole to achieve realistic exiting conditions. In addition to skewing the jet, the separation region causes high turbulence levels in the exiting jet, which promotes turbulent mixing and jet dilution.

Upstream of the obstructing jet, the external boundary layer encounters a large blockage effect decelerating the boundary layer. At the upstream hole edge, the jet velocity is faster relative to the mainstream boundary layer, which then produces an intense shear region.

Based on detailed flowfield measurements, Andreopoulos and Rodi (1984) first identified counterrotating vortices in their study of a normal jet issuing into a mainstream. Similarly for an inclined film-cooling jet, measurements presented by Pietrzyk (1989) and Subramanian et al. (1992) showed a pair of counterrotating vortices that entrain "hot" mainstream fluid and transport that fluid toward the blade surface.

Based on these flowfield characteristics, it was the intent of this investigation to determine the effect of the hole geometry on this complex flowfield in order to improve upon the overall heat transfer characteristics of a film-cooling jet. In particular, the primary improvements to the film cooling process can be made by insuring the jet remains attached to the surface, by eliminating the counterrotating vortices, and by minimizing the velocity gradients. The remainder of this paper discusses the experimental facility and instrumentation used for this investi-

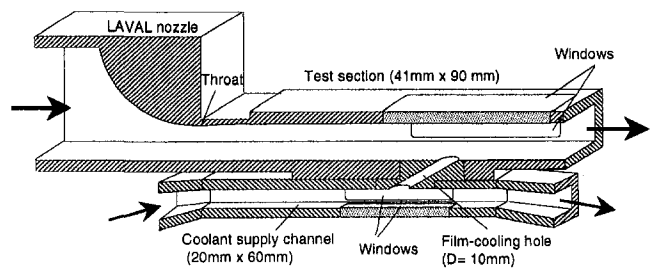


Fig. 1 Schematic of the film-cooling test section

gation and the flowfield mappings for three different geometric cooling holes.

Experimental Facility and Instrumentation

The experiments discussed in this paper were conducted in a new test facility at the Institut für Thermische Strömungsmaschinen, Universität Karlsruhe, which is described in detail by Wittig et al. (1996). A sketch of the test section is shown in Fig. 1. Mainstream and coolant flow channels, which can be independently controlled, were included in the test facility to simulate the flowfields associated with external and internal blade cooling. The flow conditions in the primary and coolant channels are given in Table 1. The blowing ratio for each of the three holes tested was $M = 1$ at a density ratio of $DR = 1$.

The air for both flow channels was supplied by a large compressor that has a capacity of producing 1 kg/s at a pressure of 11 bar. Flow for the coolant channel was also provided by the compressor, but driven through the secondary flow loop by a sealed external blower.

Table 1 Flow conditions for primary and coolant channels

	Primary Channel	Coolant Channel
Mach Number	0.25	0.30
Mean Freestream Velocity (m/s)	85.0	102.7
Freestream Turbulence Intensity (%)	1.5	1.0
Stagnation Pressure (Bars)	1.05	1.05-1.09
Total Temperature at Injection (K)	300	300
Re_D	5.2×10^4	6.6×10^4
δ_{99}/D at $x/D = -2$	0.8	
δ_{99}/D at $x/D = -7$		0.2
Re_θ at $x/D = -2$	3800	

Nomenclature

D = cooling hole diameter at hole inlet
 DR = jet-to-mainstream density ratio
 I = jet-to-mainstream momentum flux ratio = $\rho_j V_j^2 / \rho_\infty V_\infty^2$
 L = cooling hole length along centerline axis
 M = jet-to-mainstream blowing or mass flux ratio = $\rho_j V_j / \rho_\infty V_\infty$
 Ma = Mach number
 Re_D = hole diameter Reynolds number
 Re_θ = momentum thickness Reynolds number
 Tu = turbulence intensity = $100 \cdot \sqrt{0.5(u'^2 + v'^2)} / U_\infty$

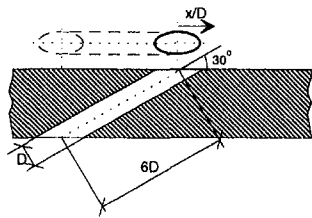
Tu_j = turbulence intensity inside hole = $100 \cdot \sqrt{u'^2} / V_j$
 u', v', w' = streamwise, vertical, and lateral rms velocities
 U, V, W = streamwise, vertical, and lateral mean velocities
 $\overline{\rho u' v'}$ = turbulent shear stress components
 $\overline{\rho u'^2}, \overline{\rho v'^2}$ = turbulent normal stress components
 V_j = total jet velocity using hole inlet and mass flux
 x = streamwise distance based on hole centerline

y = vertical distance based on exit of hole
 z = spanwise distance based on hole centerline
 δ_{99} = boundary layer thickness, 99 percent point
 θ = momentum thickness
 ρ = density

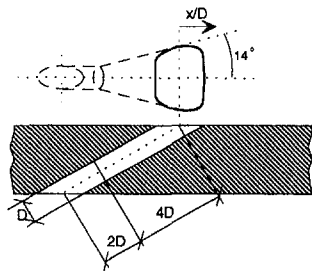
Subscripts and Superscripts

ex = exit conditions
 j = jet conditions
 ∞ = mainstream conditions

Round Hole



Lateral Expanded Hole



Forward-Lateral Expanded Hole

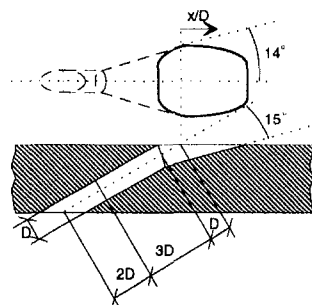


Fig. 2 Film-cooling hole geometries

The flow rate in the coolant channel was 0.12 kg/s and, at a blowing ratio of unity, the flow rate through the cooling hole was 7.5e-03 kg/s. As a result of the large disparity between the two flow rates, high uncertainties would occur if the flow rates upstream and downstream of the cooling hole were measured using the continuity equation to determine the blowing ratio. To reduce the uncertainty, the blowing ratio of the cooling hole was set by measuring the coolant mass flow entering the coolant channel. Leak tests were conducted on the coolant supply channel to insure that all of the mass flow rate entering the coolant channel was exhausted only through the cooling hole. The coolant channel flow was considered to be a boundary layer flow with a thickness of $\delta_{99} = 2$ mm as compared to a channel half-height of 10 mm at a location of seven hole diameters upstream of the hole inlet.

The three single, scaled-up hole shapes that were investigated are shown in Fig. 2. These hole geometries were obtained in cooperation with several European gas turbine companies. The diameter of all three holes at the inlet was 10 mm. These holes were machined into flat aluminum test plates 30 mm thick. All three holes were inclined at 30 deg, giving a length-to-hole diameter ratio of $L/D = 6$, where L is measured along the hole centerline axis at the hole inlet. The lateral expansion angle, which started two hole diameters after the hole inlet for the two contoured holes, was 14 deg. The forward expansion angle for the forward-laterally expanded hole was 15 deg relative to the hole centerline axis and started five hole diameters after the hole inlet. The streamwise distance, x , also shown in Fig. 2, had the origin at the hole centerline axis just at the exit of the hole. The length of the round and lateral expanded holes, as viewed from above the hole exit, extended two hole diameters

in the streamwise direction. The length of the forward-lateral expanded hole extended four hole diameters.

A two-component, coincident, fiber optic laser-Doppler velocimeter (LDV) was used to measure velocity fields for the three shaped holes. The commercial LDV system was an 85 mm fiber optic probe from Dantec. The processors used were Dantec's Enhanced Burst Spectrum Analyzers. The probe volume size was reduced, using a beam expander, to a diameter of 74 μm and a length of 0.6 mm. The LDV was rotated at 45 deg and tilted at nominally 4.5 deg to allow near-wall measurements. As a result of the tilt, the vertical velocity, v , reported in this paper contains a small lateral velocity component. The tilt does not affect the streamwise velocity component. The data were post-processed using a 2 μs coincident window and bias corrected using residence time weighting. Both the primary and coolant channel flows were seeded with oil (DES) particles having a mean diameter of 0.5 μm . Because the coolant channel and primary flow were at different pressures, valves were used downstream of the seeder such that the seeding injection was independently controlled to avoid velocity biases.

Vertical velocity profiles were taken at 14 streamwise locations at the streamwise centerline of the cooling holes. Vertical velocity profiles were taken at seven spanwise positions on one side of the cooling hole at $x/D = 4$ to compare the lateral spreading of the jet.

Uncertainty Estimates

Based on a 95 percent confidence interval, both bias and precision uncertainties were quantified. The data presented in this paper were typically averaged over 10,000 points or more depending on the data rate. The bias uncertainty for the mean velocities was 0.4 percent, whereas the precision uncertainties were 1 percent in the free stream and 3.4 percent near the wall. The precision uncertainty for the rms velocity measurements was 1.4 percent in the free stream and 5.8 percent near the wall. The precision uncertainty in the turbulent shear stress was 5.6 percent. Positioning uncertainty of the LDV probe volume with respect to the hole was $\Delta x = \pm 0.05$ mm, $\Delta y = \pm 0.05$ mm, and $\Delta z = \pm 0.05$ mm. The uncertainty in setting the coolant mass flow rate was 2 percent.

Results

Although flowfield measurements have previously been reported for round holes, as mentioned in the introduction, there have not been any reported flowfield studies in the open literature that have used a round hole geometry with a flowing coolant supply channel at the hole inlet. Prior to presenting the results with a flowing coolant supply, a benchmark comparison was made by turning off the blower that drives the coolant supply channel. By turning off the blower, the coolant channel was operated as a plenum supplying the cooling hole. Comparisons could then be made to data presented by Pietrzyk et al. (1989), who used a plenum. As can be seen in Fig. 3, the centerline velocity profiles at $x/D = 3$ agree fairly well. The differences between the data can be attributed to the present study having a larger hole length-to-diameter ratio of $L/D = 6$ relative to that of Pietrzyk et al. (1989) who used an $L/D = 3.5$, and the angle for the Pietrzyk et al. data was slightly steeper at 35 deg.

The following sections present the mean flowfield results and turbulent flowfield results for all three hole geometries at a blowing ratio of $M = 1$. Velocity contours inside the cooling hole plane will be presented. This discussion will be followed by a discussion on the flowfield between $-2 < x/D < 10$ in a vertical streamwise plane at the hole centerline and in a vertical-lateral plane at a streamwise location of $x/D = 4$.

Film-Cooling Hole Flowfield

By mounting the LDV fiber optic probe above the test section, it was possible to measure the streamwise velocity components

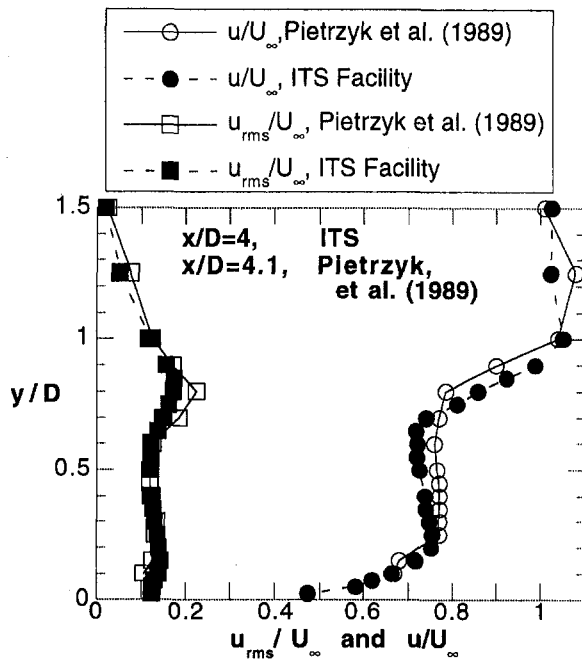


Fig. 3 Comparison of mean and rms velocity data with those presented in the literature at $M = 1$ and $DR = 1$

inside the film-cooling hole. These measurements were made in a vertical spanwise plane at $x/D = -0.75$, which corresponds to just $0.25D$ downstream of the windward start of the cooling hole. Note that this location is much downstream of the start of the lateral expansion in both of the expanded holes, but is still upstream of the start of the forward expansion for the forward-laterally expanded hole.

Figure 4 compares streamwise velocity contours inside the cooling hole for the three different hole geometries. For the round hole, the highest velocities are found in the center of the cooling hole. The differences between these measurements and those numerical predictions presented by Leylek and Zerkle (1993), in which the highest speed fluid was predicted to occur on the top of cooling hole (windward side of the cooling hole), can be attributed to the differences between the jet coolant supply. In the study of Leylek et al., the coolant was supplied by a stagnant plenum, whereas in the present configuration, the jet fluid was supplied by a crossflow at the entrance. As described by Thole et al. (1997), the presence of the crossflow at a round hole entrance can have a major influence on the coolant jet.

The streamwise velocity contours for the cooling holes with the expanded exits, also shown in Fig. 4, indicate the highest velocities occurring near the bottom and in the spanwise center of the cooling holes. There is little or no jet fluid occurring at the top of both the holes. The laterally-expanded hole does show slightly less variation in the spanwise direction, or rather the coolant does expand to fill the hole slightly better than the forward-lateral hole.

Figure 5 shows the turbulence level contours for the three hole geometries at $x/D = -0.75$ inside the coolant hole. The turbulence levels are based on the rms of the streamwise velocity fluctuations and the total jet velocity as calculated from the blowing ratio ($Tu_j = u'/V_j$). These results indicate much higher turbulence levels occurring inside the coolant hole for the two expanded cooling holes, 12 percent $< Tu_j < 20$ percent, than for the round hole, 6 percent $< Tu_j < 12$ percent.

Mean Flowfield Results

Normalized mean velocity vectors in the near-hole region for the round, laterally expanded, and forward-laterally expanded hole geometries are shown in Fig. 6. The upstream and downstream edges of the holes are indicated by the lines placed below the x axis.

At the leading edge of the cooling hole ($x/D = -1$), the round hole geometry shows a larger deceleration in the near-wall region as compared to both the expanded holes, indicating a more severe blockage effect. In the case of the round hole, just downstream of the leading edge of the hole at an $x/D = -0.5$, an upward penetration can already be detected. Farther downstream but still over the hole exit, the velocity vectors for the round hole show a stronger penetration relative to either of the expanded holes. In the case of the laterally expanded hole, it is not until the hole centerline ($x/D = 0$) that the streamlines indicate an upward motion. In the case of the forward-laterally expanded hole, the vertical deflection is even less, as indicated by the only slightly positive vertical velocity vectors starting at the hole centerline ($x/D = 0$). Because the jet-to-free stream momentum at the hole exit is the highest for the round hole relative to the expanded holes, there is a stronger penetration of the jet into the boundary layer. The jet-to-mainstream momentum flux ratio at the hole exit is $I_{ex} = 1$ for the round hole, whereas at the exit of the two expanded holes, the momentum flux ratio is $I_{ex} = 0.25$ (based on the area perpendicular to the hole centerline axis measured where the upstream edge of the hole hits the top of the test plate). Although the momentum flux ratio is nominally the same for both the lateral and forward-lateral holes at the hole exits, the forward expansion reduces the jet penetration relative to the laterally expanded hole.

Upstream of the hole centerline between $-1 < x/D < -0.5$ for the forward-laterally expanded hole, the measured vertical

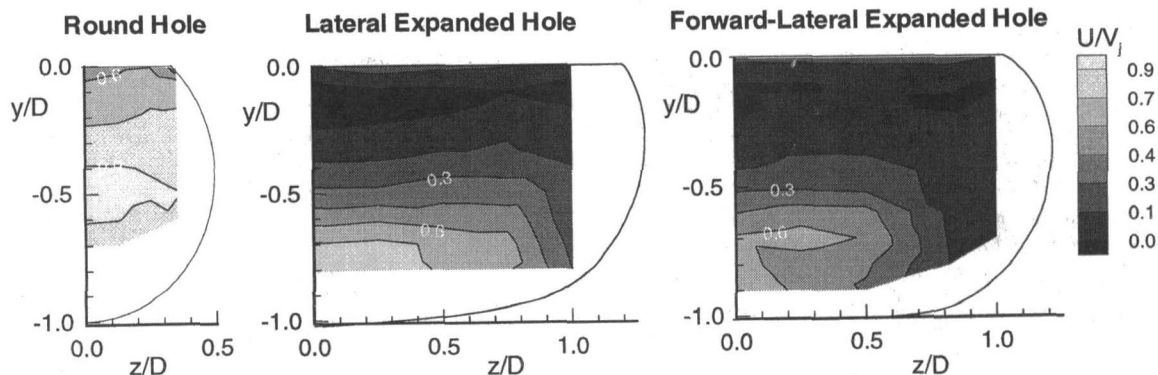


Fig. 4 Streamwise velocity contours inside the coolant hole at $x/D = -0.75$ for the (a) round, (b) laterally expanded, and (c) forward-laterally expanded holes

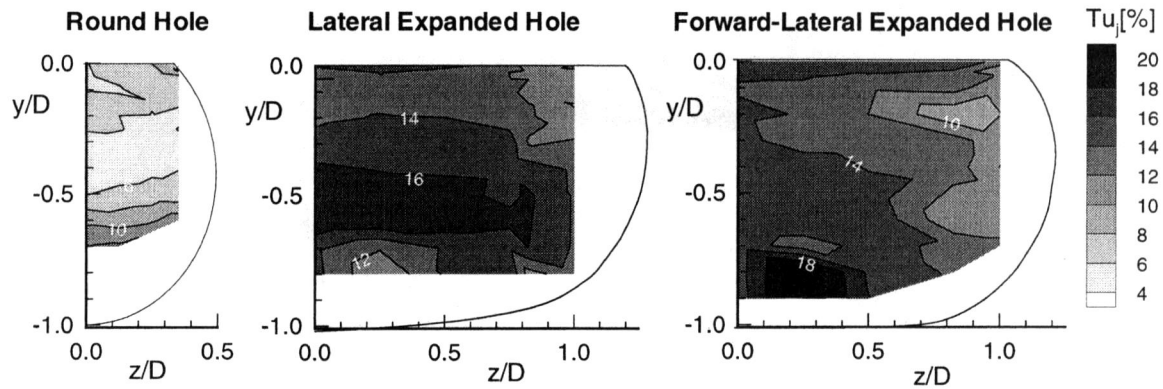


Fig. 5 Jet turbulence level contours inside the coolant hole at $x/D = -0.75$ for the (a) round, (b) laterally expanded, and (c) forward-laterally expanded holes

velocities, although quite low in magnitude, were negative in sign, indicating that some of the mainstream fluid is being ingested into the leading edge of the hole. From the standpoint of cooling, ingestion of the hot mainstream into the coolant hole would produce an overall lower possible cooling effectiveness. Measurements of the vertical velocity component for both the round hole and the laterally expanded hole were positive along the entire jet exit centerline.

Figures 7 and 8 compare the mean streamwise and vertical velocity components for all three holes geometries at three streamwise positions, $x/D = 0, 2,$ and 10 . As a point of reference, also shown in Fig. 7 is the one-seventh power law for turbulent boundary layer with no injection. At the hole centerline ($x/D = 0$) of the round hole, the formation of a shear layer

is indicated by a negative velocity gradient near the hole exit. The negative velocity gradient indicates a jet velocity that is slightly higher than the mainstream at the exit of the cooling hole. The velocity profile for the laterally expanded hole indicates essentially a zero velocity gradient near the hole exit and no formation of a negative velocity gradient shear layer. For the forward-laterally expanded hole, the jet exits primarily from the downstream portion of the hole and, thus, at the hole centerline only a slight deceleration with respect to a turbulent boundary layer is detected. As expected, a higher vertical mean velocity component, shown in Fig. 8, occurs for the round hole relative to the expanded holes at the hole centerline.

The intense shear layers for a round film cooling hole geometry are quite evident at an $x/D = 2$, as shown in Fig. 7(b).

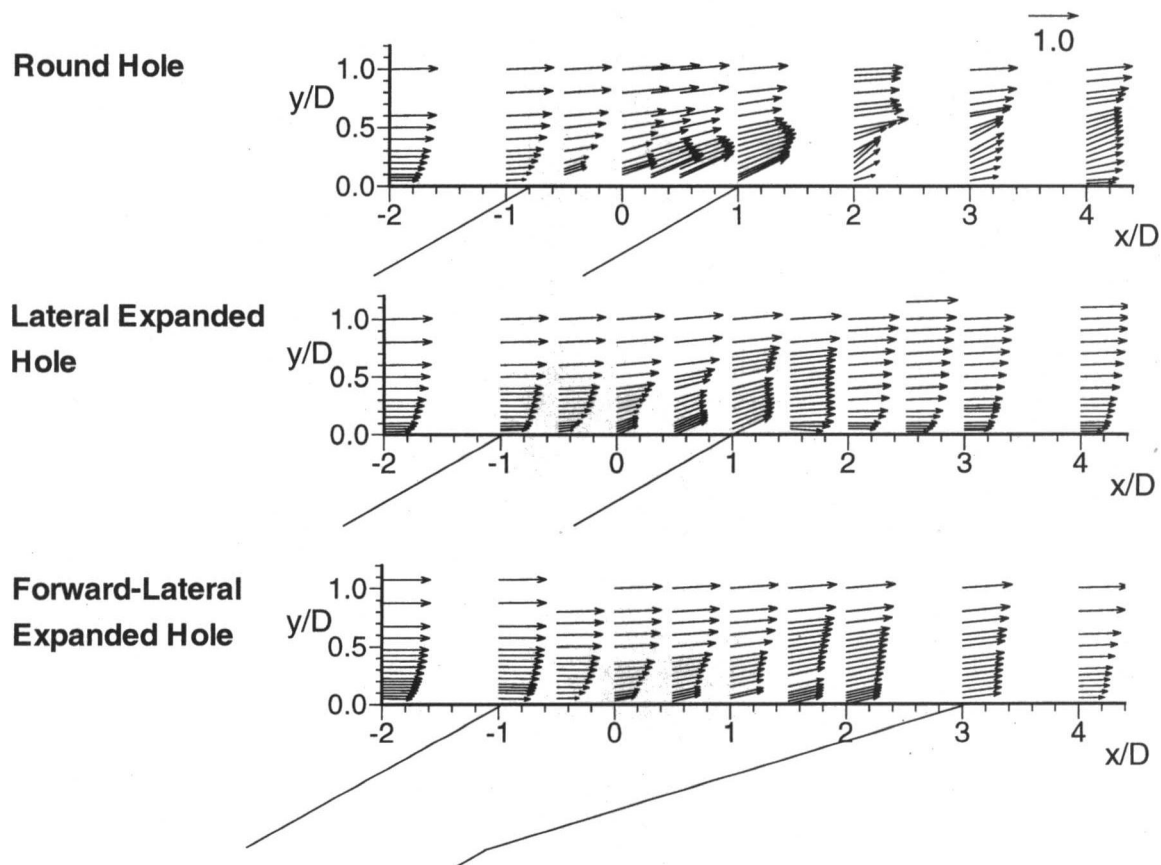


Fig. 6 Mean velocity vectors for the (a) round, (b) laterally expanded, and (c) forward-laterally expanded cooling holes

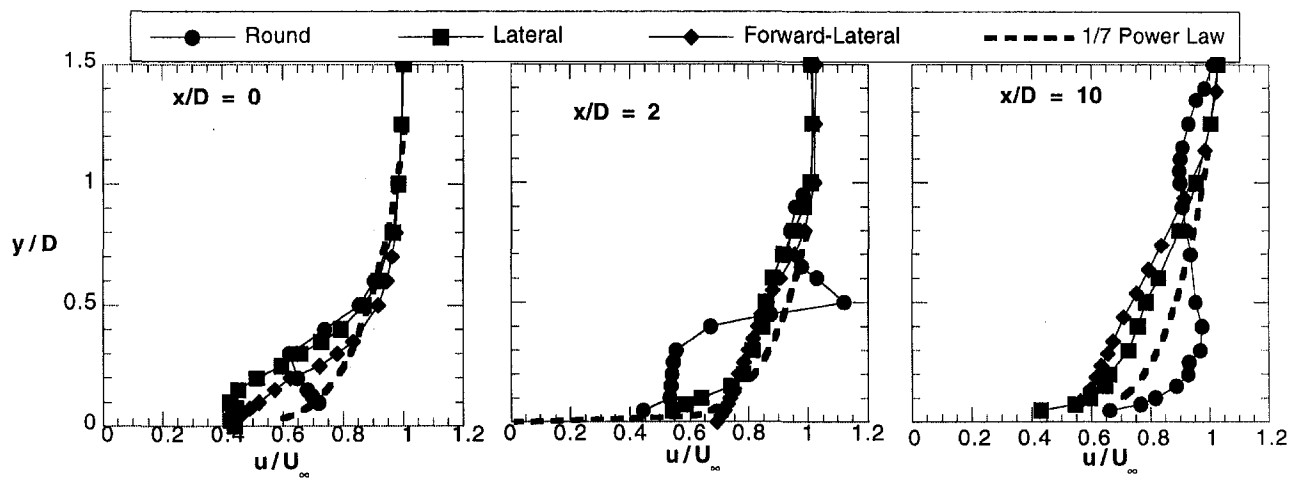


Fig. 7 Mean streamwise velocity profiles for all three hole geometries at (a) $x/D = 0$, (b) $x/D = 2$, and (c) $x/D = 10$

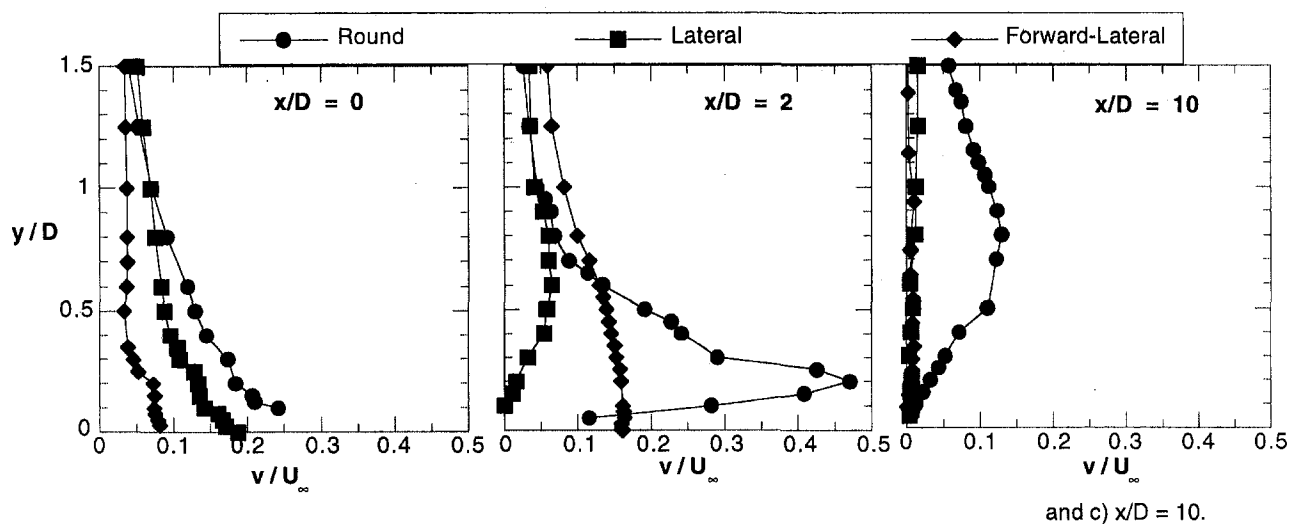


Fig. 8 Mean vertical velocity profiles for all three hole geometries at (a) $x/D = 0$, (b) $x/D = 2$, and (c) $x/D = 10$

Note that the peak mean streamwise velocity is $u/U_\infty = 1.2$ and greater than unity as a result of the skewed exiting jet profile. This is similar to those results already presented in the literature in Fig. 3. This streamwise location is one hole diameter beyond the downstream hole edge for both the round and laterally expanded cooling holes and is still over the hole exit for the forward-laterally expanded cooling hole. The shear layer forming at the windward side of the cooling hole, as discussed above, is clearly evident for the round hole at a $y/D = 0.5$. In the case of both expanded holes, there is no indication of the formation of a strong shear layer. In particular, the velocity profile for the forward-laterally expanded hole is relatively flat all the way down to the hole exit. The vertical velocity component of the round jet is much higher than that of the expanded holes as seen in Fig. 8(b). Because the jet primarily exits from the downstream portion of the forward-laterally expanded hole, a larger vertical velocity component was measured relative to the laterally expanded hole at an $x/D = 2$.

Remnants of the upstream shear layer, as indicated in Fig. 7(c), are still evident at an $x/D = 10$ for the round hole. The streamwise velocity profile for the round hole indicates a larger velocity in the near-wall region, between $0 < y/D < 1$, than for the expanded holes. These higher velocities also represent a larger overall massflow in the near-wall region. One plausible

explanation for the higher massflow is due to the mainstream entrainment by the longitudinal vortices. Since only two components of velocity were measured, longitudinal vortices could not be quantified in this study. However, comparisons of the vertical velocity components measured in a lateral-vertical plane at $x/D = 4$ are consistent with the presence of longitudinal vortices for the round hole geometry. At an $x/D = 4$ for the round hole geometry, positive vertical velocities were measured at the hole centerline and negative vertical velocities were measured at the outer edges of the jet. In comparison, the vertical velocity component for both the laterally expanded and forward-laterally expanded holes indicated only a slightly positive vertical velocity at the jet centerline and no negative velocities at the jet edges. These results indicate that strong counterrotating vortices do not exist at an $x/D = 4$ for either of the expanded holes. Figure 8(c) shows the continued presence of a higher vertical velocity component for the round hole relative to the expanded holes at an $x/D = 10$.

The spreading of the jet can be seen from the streamwise velocity contours presented in Fig. 9, which were measured in a vertical-lateral plane at an $x/D = 4$. Whereas the laterally and forward-laterally expanded holes show relatively uniform spanwise velocity contours, the round hole still has characteristics of a round jet.

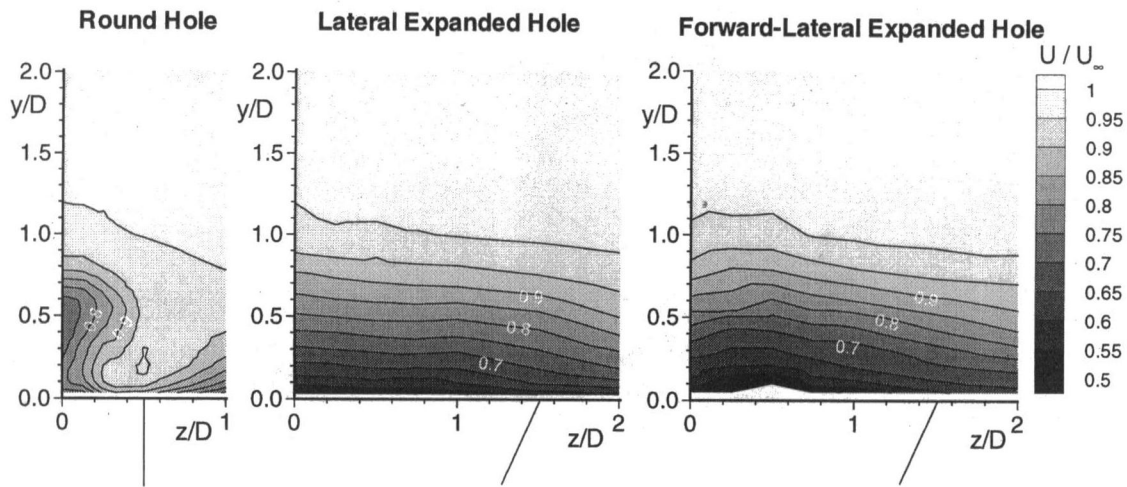


Fig. 9 Comparison of the mean streamwise velocity contours at an $x/D = 4$ for the (a) round, (b) laterally expanded, and (c) forward-laterally expanded holes

Turbulent Flowfield Results

Before comparing the turbulent fields for these three geometries, it is important to recognize differences between a round hole with a flowing supply channel and a round hole with a plenum supply. As indicated in the introduction, past studies have identified the formation of a separation region on the leeward side of the cooling hole inlet, causing the exiting jet to be skewed toward the upstream edge of the hole at high blowing ratios ($M = 1$). The formation of this separation region was consistent with the high turbulence levels exiting the hole. A separation region occurs for a plenum condition because a large turning angle is required on the leeward side of the hole entrance. In the present configuration where the mainstream flow and coolant supply flow are both flowing in the same direction, it is expected that if there is a separation region, it would most likely occur on the upstream edge of the round hole entrance. However, based on the low turbulence intensities measured inside the round hole and at the exit plane of the hole for these flow conditions, a separation region was not apparent.

Previous experiments completed by Pietrzyk et al. (1989) discuss the relationship between mean velocity gradients and both the normal and shear stress production. As already discussed, the streamwise mean velocity gradients for the round hole geometry are much larger than for the expanded cooling holes.

Turbulence level contours in the near-hole region for all three hole geometries are shown in Fig. 10. The peak turbulence levels for the round, laterally expanded, and forward-laterally expanded cooling holes are $Tu = 19.5$, 18, and 17 percent, respectively. Although the peak turbulence levels for all three holes are comparable, the location of the peak turbulence level is quite different for the round hole as compared to the expanded holes. In the case of the round hole, the peak turbulence level is downstream of the hole exit at $x/D = 2$ as shown in Fig. 10(a). In the case of the expanded holes, the peak turbulence level and turbulent shear stress occurs over the hole exit as shown in Figs. 10(b) and 10(c). Since the inlet geometry and flow conditions for all three holes are the same and since the turbulence levels exiting the round hole are quite low, thereby indicating no separation region inside the round hole, it can be expected that the expanded holes also have no separation region at the hole inlets. However, high turbulence levels do occur at the exits of the expanded holes. These high turbulence levels are a result of having a lateral expansion angle too large thereby allowing the jet to separate from the side walls. Recall, the lateral expansion half angle is 14 deg.

Not only do the high turbulence levels begin at a location farther downstream for the round hole relative to the expanded

holes, the extent of the high turbulence region is over a much larger surface area. Turbulence levels as high as 18 percent are shown between $1.5 < x/D < 3.5$ for the round hole, whereas for the laterally expanded hole the high-turbulence regions extend only over half of the hole exit. Because of the absence of strong shear layers for the expanded holes, there is no sustenance for the turbulence production over a region beyond the exit of the hole.

The turbulence level contours in Fig. 11 are for the vertical-lateral plane at an $x/D = 4$. At this location the turbulence levels for both the expanded holes are much less than the round hole and, again, the jet characteristics are still evident for the round hole. The turbulence levels are slightly higher for the forward-laterally expanded jet because this location is only one hole diameter downstream of the hole edge.

Figure 12 shows the turbulent shear stress contours in the near-hole region for the three hole geometries. The peak magnitudes of the turbulent shear stress for the round, laterally expanded, and forward-laterally expanded holes are $u'v'/U_\infty^2 = -0.014$, -0.016 , and -0.015 , respectively. There is a relatively good correspondence between the location of peak turbulence level (normal stress) and peak turbulent shear stress for all three hole geometries. Again, the peak shear stress levels are similar in magnitude and sign for the three holes but the locations are much different.

These measurements indicate a good correspondence between mean gradients and the peak stress locations. In the case of the round hole, the peak location is at $x/D = 2$, as shown in Fig. 12(a), which corresponds to a location of a large positive streamwise velocity gradient ($\partial U/\partial y$) and a large negative vertical velocity gradient ($\partial V/\partial y$) both of which contribute to a negative $u'v'$ production. Positive normal stress production (u'^2) occurs when the streamwise velocity gradient ($\partial U/\partial y$) and turbulent shear stress ($u'v'$) are opposite in sign, which coincides with the peak shear stress location. Similarly, in this region the vertical velocity gradient ($\partial V/\partial y$) is negative giving a positive normal stress production of v'^2 .

Results reported by Pietrzyk et al. (1989) showed relatively high positive $u'v'$ values exiting the windward side of the round cooling hole similar to those shown in Fig. 12(a). However, unlike Pietrzyk et al., who showed $u'v'$ values equal in magnitude but opposite in sign exiting on the downstream portion of the hole, these measurements show relatively low negative $u'v'$ values exiting the downstream portion of the hole. This difference can be attributed to the separation region inside the coolant hole.

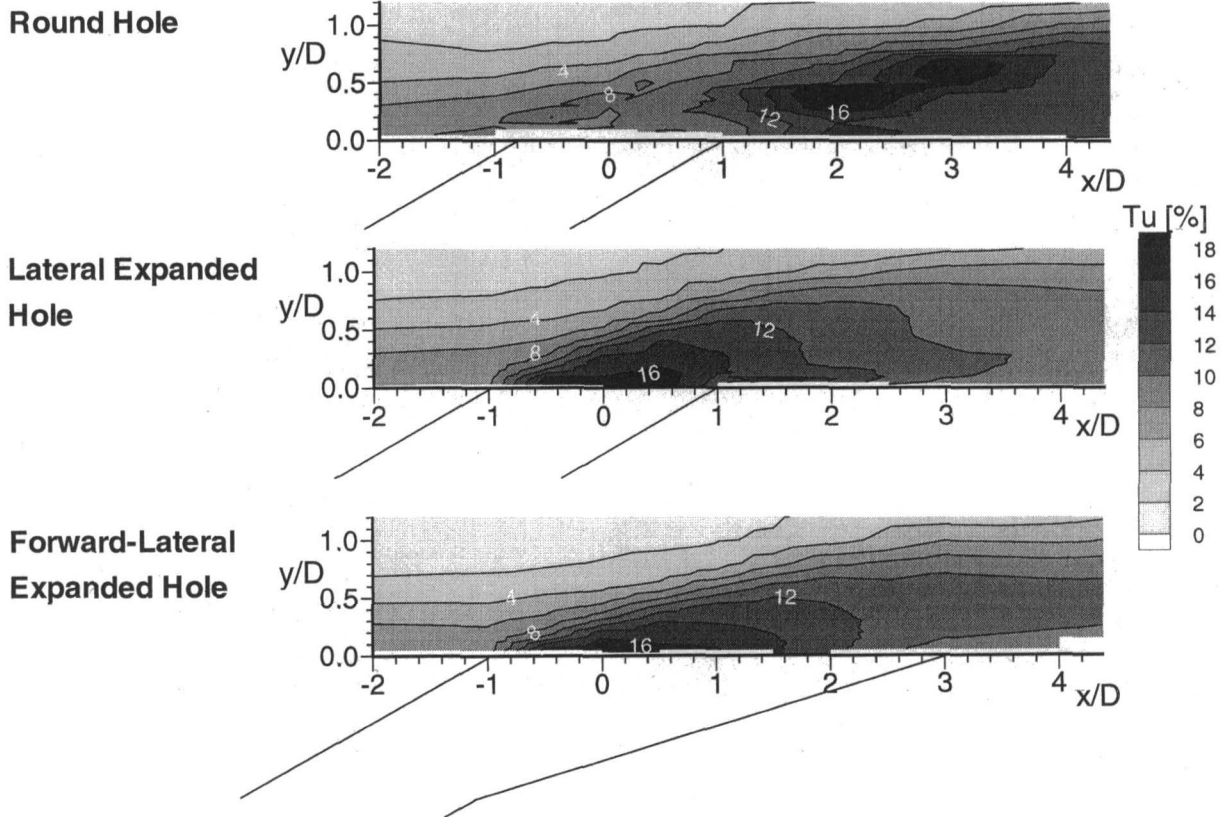


Fig. 10 Turbulence level contours for the (a) round, (b) laterally expanded, and (c) forward-laterally expanded cooling holes

For both expanded holes, high negative $\overline{u'v'}$ values occur at the upstream portion of the cooling hole and relatively high positive $\overline{u'v'}$ values occur in the downstream portion of the cooling hole as shown in Figs. 12(b) and 12(c). In both the upstream and downstream regions of the expanded cooling holes, there is a relatively small vertical velocity gradient ($\partial V/\partial y$) and large positive streamwise velocity gradients ($\partial U/\partial y$) with the latter dictating the shear stress production. The positive $\overline{u'v'}$ values exiting the lee of the jet are lower in magnitude because of the reduced velocity gradients inside the expanded holes.

Conclusions

Flowfields for three different film-cooling hole geometries have been measured and compared at a blowing ratio of $M = 1$. Past heat transfer studies have indicated that by laterally expanding the exit of the hole, higher effectiveness values could be obtained over a wide range of blowing ratios (Goldstein et al., 1974). From a cooling standpoint, expanding the hole exit as much as possible also allows for greater blade surface coverage.

In comparing both the expanded hole flowfields with the round hole flowfield, the jet penetration as well as the velocity

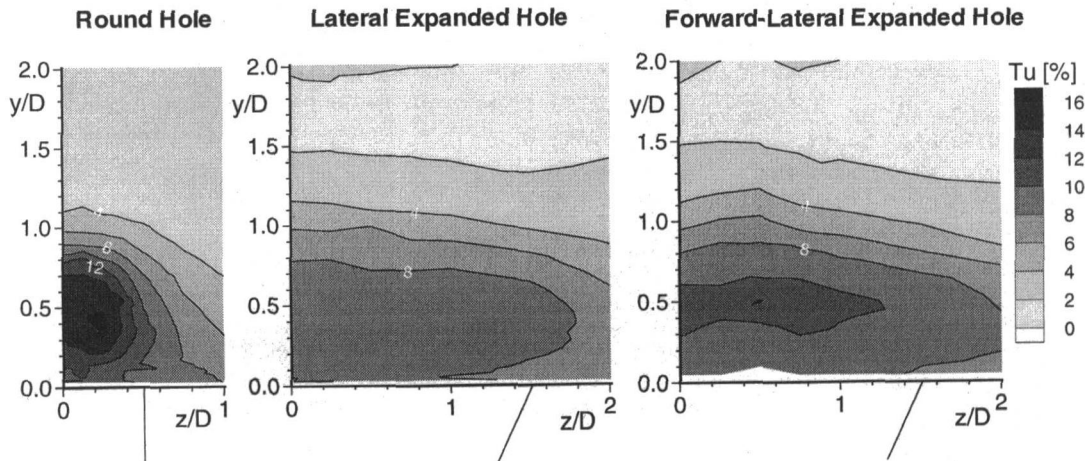
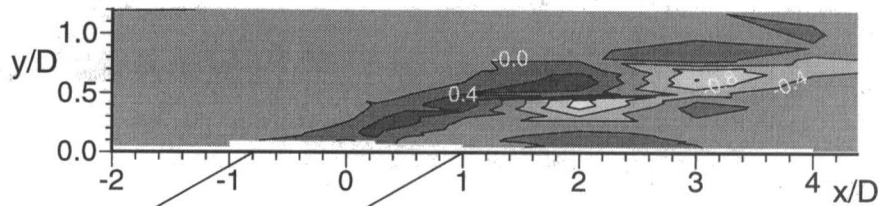
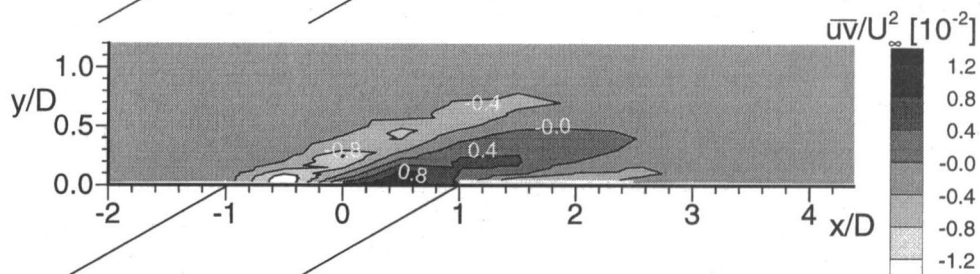


Fig. 11 Turbulence level contours at an $x/D = 4$ for the (a) round, (b) laterally expanded, and (c) forward-laterally expanded cooling holes

Round Hole



Lateral Expanded Hole



Forward-Lateral Expanded Hole

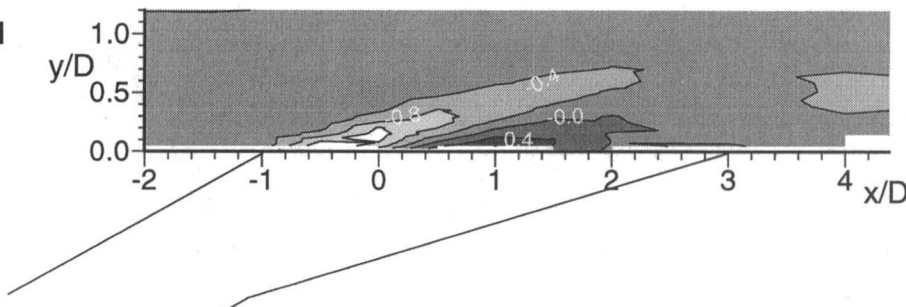


Fig. 12 Turbulent shear stress contours for the (a) round, (b) laterally expanded, and (c) forward-laterally expanded holes

gradients were significantly reduced for the laterally and forward-laterally expanded holes. Because the velocity gradients were reduced by expanding the cooling holes, the turbulence production downstream of the expanded holes was quite low relative to the round hole. The peak turbulence levels for both the expanded holes occurred over the hole exit, whereas the peak level for the round hole occurred downstream of the hole exit where the velocity gradients were very large. The high levels of turbulence exiting the expanded cooling holes resulted from having large expansion angles. Improved cooling performance for the expanded holes can be expected because of reduced jet penetration and because there was no indication of a strong vortical motion occurring at $x/D = 4$. Based on the flowfield measurements, the primary improvement to the expanded holes is to reduce the expansion angle with the trade-off being a reduced lateral coverage.

Both the laterally expanded and forward-laterally expanded flowfields were quite similar in terms of velocity gradients. The primary disadvantage, however, for the forward-laterally expanded hole is that even though the blowing ratio was quite high, the jet exits primarily from the leeward side of the cooling hole, thereby allowing ingestion of the mainstream fluid into the windward side of the cooling hole. This ingestion would reduce the performance of the film-cooling jet.

In comparing the performance of each of the three hole geometries, this study has reaffirmed the importance of understanding how the jet forms inside the film-cooling hole for all hole geometries. The location and duration of the peak turbulence levels, which dictate the dilution of the cooling jet, depend upon what happens inside the cooling hole. As shown by previous investigators, the peak turbulence level at high blowing ratios for a round hole geometry occurs at the exit of the cooling hole. These turbulence levels result from a large separation region inside the hole that occurs due to the coolant fluid being supplied by a stagnant plenum. Lower turbulence levels over the cooling

hole exit (relative to previous studies) were presented in this paper for a round cooling hole that was supplied by a channel flowing parallel to the mainstream. These low turbulence levels indicate the lack of a (or only a small) separation region.

Acknowledgments

This study was partly funded by the European Union through a grant by the Brite Euram program "Investigation of the Aerodynamics and Cooling of Advanced Engine Turbine Components" under Contract No. AER2-CT92-0044. The authors wish to express their gratitude to the partners involved in the program for the permission to publish this paper and to R. Clifford from Rolls-Royce, who coordinated the program.

References

- Andreopoulos, J., and Rodi, W., 1984, "Experimental Investigation of Jets in a Crossflow," *Journal of Fluid Mechanics*, Vol. 138, pp. 93–127.
- Benz, E., Wittig, S., Beeck, A., and Fottner, L., 1993, "Analysis of Cooling Jets Near the Leading Edge of Turbine Blades," 72nd Fluid Dynamics Panel Meeting and Symposium on "Computational and Experimental Assessment of Jets in Cross Flow," Winchester, UK, Paper No. 37.
- Garg, V., and Gaugler, R., 1995, "Effect of Velocity and Temperature Distribution at the Hole Exit on Film Cooling of Turbine Blades," ASME Paper No. 95-GT-275.
- Goldstein, R. J., Eckert, E. R. G., and Burggraf, F., 1974, "Effects of Hole Geometry and Density on Three-Dimensional Film Cooling," *International Journal of Heat and Mass Transfer*, Vol. 17, pp. 595–607.
- Jubran, B., and Brown, A., 1985, "Film Cooling From Two Rows of Holes Inclined in the Streamwise and Spanwise Directions," *ASME Journal of Engineering for Gas Turbines and Power*, Vol. 107, pp. 84–91.
- Lee, S. W., Lee, J. S., and Ro, S. T., 1994, "Experimental Study on the Flow Characteristics of Streamwise Inclined Jets in Crossflow on Flat Plate," *ASME JOURNAL OF TURBOMACHINERY*, Vol. 116, pp. 97–105.
- Leylek, J. H., and Zerkle, R. D., 1993, "Discrete-Jet Film Cooling: A Comparison of Computational Results With Experiments," *ASME JOURNAL OF TURBOMACHINERY*, Vol. 116, pp. 358–368.
- Makki, Z. H., and Jakubowski, G. S., 1986, "An Experimental Study of Film Cooling From Diffused Trapezoidal Shaped Holes," AIAA Paper No. 86-1326.

- Pietrzyk, J. R., 1989, "Experimental Study of the Interaction of Dense Jets With a Crossflow for Gas Turbine Applications," Ph.D. Dissertation, University of Texas at Austin.
- Pietrzyk, J. R., Bogard, D. G., and Crawford, M. E., 1989, "Hydrodynamic Measurements of Jets in Crossflow for Gas Turbine Film Cooling Application," *ASME JOURNAL OF TURBOMACHINERY*, Vol. 111, pp. 1139–145.
- Schlichting, H., 1979, *Boundary Layer Theory*, McGraw-Hill, New York.
- Sen, B., Schmidt, D. L., and Bogard, D. G., 1996, "Film Cooling With Compound Angle Holes: Heat Transfer," *ASME JOURNAL OF TURBOMACHINERY*, Vol. 118, pp. 800–806.
- Subramanian, C. S., Ligrani, P. M., Green, J. G., Doner, W. D., and Kaisuwan, P., 1992, "Development and Structure of a Film-Cooling Jet in a Turbulent Boundary Layer With Heat Transfer," *Rotating Machinery Transport Phenomena, Proc. Third International Symposium on Transport Phenomena and Dynamics of Rotating Machinery (ISROMAC-3)*, pp. 53–68.
- Thole, K., Gritsch, M., Schulz, A., and Wittig, S., 1997, "Effect of Inlet Conditions for Jets-in-Crossflow as Applied to Film-Cooling," *ASME Journal of Fluids Engineering*, Vol. 119, pp. 533–540.
- Wittig, S., Schultz, A., Gritsch, M., and Thole, K., 1996, "Transonic Film Cooling Investigations: Effects of Hole Shapes and Orientations," *ASME Paper No. 96-GT-222*.
- Yoshida, T., and Goldstein, R. J., 1984, "On the Nature of Jets Issuing From a Row of Holes into a Low Reynolds Number Mainstream Flow," *ASME Journal of Engineering for Gas Turbines and Power*, Vol. 106, pp. 612–618.
-

Characterization and Laboratory Simulation of Turbine Airfoil Surface Roughness and Associated Heat Transfer

D. G. Bogard

D. L. Schmidt

The University of Texas at Austin,
Austin, TX 78712

M. Tabbita

Pratt & Whitney,
West Palm Beach, FL 33410

The physical characteristics of surface roughness observed on first-stage high-pressure turbine vanes that had been in service for a long period were investigated in this study. Profilometry measurements were utilized to provide details of the surface roughness formed by deposits of foreign materials on different parts of the turbine vane. Typical measures of surface roughness such as centerline average roughness values were shown to be inadequate for characterizing roughness effects. Using a roughness shape parameter originally derived from regular roughness arrays, the turbine airfoil roughness was characterized in terms of equivalent sand-grain roughness in order to develop an appropriate simulation of the surface for laboratory experiments. Two rough surface test plates were designed and fabricated. These test plates were evaluated experimentally to quantify the heat transfer rate for flow conditions similar to that which occurs on the turbine airfoil. Although the roughness levels on the two test plates were different by a factor of two, both surfaces caused similar 50 percent increases in heat transfer rates relative to a smooth surface. The effects of high free-stream turbulence, with turbulence levels from 10 to 17 percent, were also investigated. Combined free-stream turbulence and surface roughness effects were found to be additive, resulting in as much as a 100 percent increase in heat transfer rate.

Introduction

In this study we have analyzed the surface roughness characteristics of turbine vanes that have undergone a significant number of hours of operation. Surface roughness on turbine airfoils can increase drastically due to oxidation, corrosion, or deposition of foreign materials on the surface during operation of the engine. Prediction of the heat transfer characteristics, including effects on film cooling, requires quantification of these roughness characteristics for operational turbine blades and vanes. Besides this quantification, we have designed and tested surfaces that simulated the roughness characteristics of the turbine vanes.

There have been several studies detailing the effects on operation efficiency when there is significant surface roughness on the turbine blades and vanes. Bammert and Sanstede (1972, 1976) showed that surface roughness ranging from $k_s/l = 10^{-3}$ to 10^{-2} decreased efficiency from 5 to 10 percent compared to smooth surfaces. Using roughened turbine blades in a steam turbine, Forster (1967) found that roughness of $k_s = 0.25$ mm ($k_s/l = 2.8 \times 10^{-3}$) caused 6 percent decrease in efficiency. Besides these direct measurements of the decrease in turbine efficiency due to roughness, there will also be a turbine blade cooling penalty since the increased surface roughness can as much as double the surface heat transfer rates (Hosni et al., 1991) resulting in higher blade temperatures.

In the studies cited above, surface roughness was obtained by gluing emery paper to the surfaces, or by gluing emery grit to the surface. In all cases the equivalent sandgrain roughness, k_s , for the surfaces was based on an earlier study by Speidel (1954) in which the skin friction drag for various emery paper

surfaces was measured. Although these studies have provided valuable information about the effects of surface roughness, the question of what type and magnitude of roughness is representative of operational turbine blades was not addressed.

In more recent studies, Taylor (1990) measured average roughness values ranging from $R_a = 2$ μ m to 11 μ m on in-service turbine blades from two aero-engines, while Tarada and Suzuki (1993) quote a survey of aero-engine, industrial, and marine engine blades in which roughness varied from $R_a = 25$ μ m to 150 μ m. Although these studies give an appreciation of the magnitude of surface roughness for turbine airfoils, in this paper we show that commonly used statistical quantifications of surface roughness, such as R_a , are not sufficient. As noted by Acharya et al. (1986), most calculation procedures for rough wall boundary layers rely on a knowledge of equivalent sand grain roughness, k_s . In this work, profilometer measurements have been used to characterize the roughness for typical in-service turbine vanes, and the appropriate equivalent sand grain roughness has been determined. Furthermore, we designed and built simulated rough surfaces, which were equivalent to that on typical turbine vanes, and tested the heat transfer characteristics of these surfaces.

Airfoil Roughness Measurement and Characterization

Representative samples of first-stage high-pressure turbine vanes were taken from two military aero-engines, which had been operated in excess of 500 hours. The turbine vanes were installed in similar engines, which were on aircraft operated in two different locations. These turbine vanes used film cooling so the effect of foreign material deposition to the surface around and within film cooling holes was evident. These vanes were chosen because the surface deposition is typical of that seen in the turbine section of a military engine. Roughening of the surfaces was due to surface oxidation and deposition foreign

Contributed by the International Gas Turbine Institute and presented at the 41st International Gas Turbine and Aeroengine Congress and Exhibition, Birmingham, United Kingdom, June 10–13, 1996. Manuscript received at ASME Headquarters February 1996. Paper No. 96-GT-386. Associate Technical Editor: J. N. Shinn.

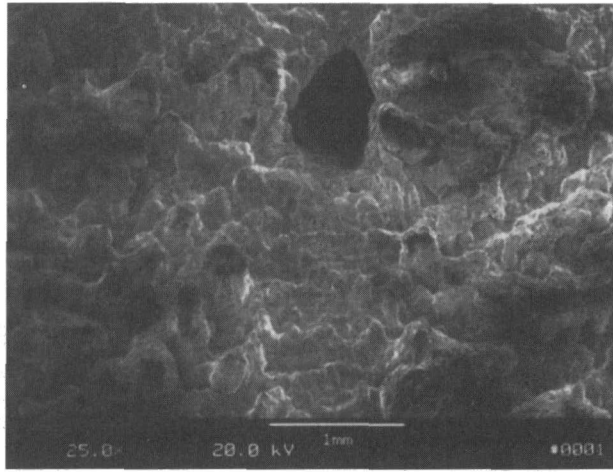


Fig. 1 Vane surface roughness including area around a film cooling hole. Flow direction is top to bottom.

materials such as airborne particles of sand, dirt, ash, and compressor abrasible.

Deposition occurs primarily on the pressure side of the airfoil, probably due to centrifugal forces on the heavy particles driving them towards the pressure side. A photograph of the surface (one of a stereo pair taken using a scanning electron microscope) around a film cooling hole is shown in Fig. 1. This photograph shows that the general surface character of the roughness is better described as scales rather than an accumulation of grit as used in previously cited studies. One of the vanes was cut, sectioned, ground, and polished to allow for microscopic examination of the surface deposition profile. Figure 2 shows a cross section made in the axial direction including a film cooling hole. Particularly evident in Fig. 2 is the accumulation of foreign material deposition in the film cooling hole, which would significantly affect the cooling flow.

Quantitative measurements of the roughness were made using a Rodenstock model RM 600 laser stylus profilometer with a spatial resolution of 2–4 μm . Roughness profiles were measured on the pressure surface along axially directed lines at three different positions along the span of the airfoil, and along radially directed lines at nine different positions along the length of the airfoil. Representative profiles measured along axial and radial lines are presented in Figs. 3(a) and 3(b), respectively. Note that the surface distance scale has been compressed by more than a factor of 10 relative to the vertical scale, which causes the roughness to appear more jagged than it actually is. The magnitude of the roughness is quantified using two measures, the centerline average, R_a , and the roughness depth, R_z .

For R_a the mean height of the surface is defined as the centerline, and the R_a value is defined as the integral average of the absolute value of deviations from this center line along a specified integration length. The R_z value is defined as the average of five samples of the maximum excursions from positive to negative peaks. R_z was representative of the average height of discrete roughness elements.

Results from the profilometer measurements at different positions along the airfoils are presented in Table 1. For vane #1 the roughness values ranged from $R_a = 8$ to $22 \mu\text{m}$, and for vane #2 they ranged from $R_a = 21$ to $46 \mu\text{m}$. These values are in contrast to a new vane, which typically has a roughness level of $R_a = 1.5 \mu\text{m}$. Clearly there is a distinct difference in the magnitude of the roughness for vanes #1 and #2 indicating the importance of the operational environment to the amount of foreign particulate that is deposited on the vane surface. For both vanes there was a tendency for the roughness magnitude to increase toward the trailing edge of the airfoil, with the magnitude more than doubling for vane #1.

Predicting the skin friction drag or heat transfer rates for a rough surface requires determination of the equivalent sand grain roughness height, k_s , for the surface. Strictly speaking, k_s is defined as the roughness height that would yield the same skin friction for a sand grain surface (as quantified in the series of experiments by Nikuradse, 1933) as for the surface in question. Note that k_s may not be similar to the actual roughness height k . For example, when the roughness elements are widely spaced the resulting skin friction is not greatly increased, which yields a k_s value much smaller than the actual roughness height. Also, if the roughness elements are closely packed so that the flow passes above the roughness elements, the k_s value can be somewhat smaller than k . Furthermore, the shape of the roughness element will affect the k_s value with rounded roughness elements flush to the surface having significantly smaller k_s values. Neither is the R_a value simply related to k_s , with widely different k_s values for surfaces with the same R_a value.

A number of studies have proposed conversions from R_a to k_s for different rough surfaces. Forster (1967) found that machine-ground surfaces typically have a ratio of $k/R_a \approx 5$, and using a ratio of $k_s/k \approx 0.4$ for this type of surface, estimated that $k_s/R_a \approx 2$. For emery papers with a range of grit sizes Forster (1967) found $k/R_a \approx 5$, and using a value of $k_s/k \approx 1.5$ from Speidel (1954), obtained a value of $k_s/R_a \approx 7$. Similarly Koch and Smith (1976) estimated a value of $k_s/R_a \approx 6$ for emery paper, and Bammert and Sanstede (1976) present an equation that yields a value of $k_s/R_a \approx 2$ for typical milled surfaces. These studies have established the conversion from the measured R_a value to the k_s roughness parameter for two specific surface types, machined and emery paper. Note, because of the wide variety of machining techniques, these results should not

Nomenclature

A_f = roughness element frontal area
 A_s = roughness element windward wetted area
 C_f = coefficient of friction
 d = base diameter of simulated roughness elements
 h = heat transfer coefficient
 k = height of simulated roughness elements
 k_s = equivalent sand grain roughness height
 l = chord length
 Pr = Prandtl number
 Pr_t = turbulent Prandtl number

R_a = centerline average roughness height
 R_z = roughness depth
 Re_θ = momentum thickness Reynolds number
 Re_{ks} = roughness Reynolds number = u^*k_s/ν
 S = surface area without roughness
 S_f = total frontal surface area of roughness elements
 St = Stanton number
 St_{ks} = roughness Stanton number
 St_0 = smooth surface, low- Tu Stanton number

s = spacing of simulated roughness elements
 Tu = turbulence level = u_{rms}/U_∞
 U_∞ = free-stream velocity
 u^* = friction velocity
 u_{rms} = rms of fluctuating streamwise velocity
 x = streamwise coordinate
 ΔT = surface temperature; free-stream temperature
 θ = momentum thickness
 Λ_s = roughness shape/density parameter
 ν = fluid kinematic viscosity



Fig. 2 Micrograph showing roughness caused by deposits of foreign materials along the surface and in a film cooling hole

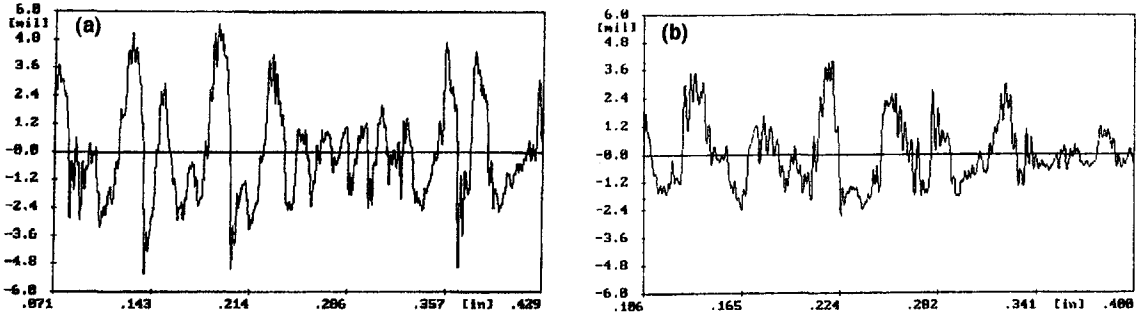


Fig. 3 Representative profilometer measurements of the vane surface roughness: (a) profile along an axial line, (b) profile along a radial line

Table 1 Roughness R_a values for various positions on the surfaces of vane #1 and #2

Section	Position and direction of profile	R_a (μm)	
		Vane 1	Vane 2
1A	AXIAL, ID, FROM TE FORWARD	14.7	31.8
1B	AXIAL, ID, FROM MIDCHORD FORWARD	8.3	35.8
2A	AXIAL, MIDSPAN, FROM TE FORWARD	18.9	42.9
2B	AXIAL, MIDSPAN, FROM MIDCHORD FORWARD	8.6	30.7
3A	AXIAL, OD, FROM TE FORWARD	11.5	42.2
3B	AXIAL, ID, FROM MIDCHORD FORWARD	11.2	30.5
4	RADIAL, FORWARD BETWEEN ROWS 1&2, ID TO OD	10.0	23.3
5	RADIAL, CENTER BETWEEN ROWS 1&2, ID TO OD	10.7	20.7
6	RADIAL, AFT BETWEEN ROWS 1&2, ID TO OD	8.9	23.3
7	RADIAL, FORWARD BETWEEN ROWS 3&4, ID TO OD	8.8	27.2
8	RADIAL, CENTER BETWEEN ROWS 3&4, ID TO OD	9.9	35.3
9	RADIAL, AFT BETWEEN ROWS 3&4, ID TO OD	9.6	31.8
10	RADIAL, FORWARD BETWEEN ROWS 6&7, ID TO OD	21.5	28.4
11	RADIAL, CENTER BETWEEN ROWS 6&7, ID TO OD	21.6	36.1
12	RADIAL, AFT BETWEEN ROWS 6&7, ID TO OD	22.0	46.2

Note: film cooling hole rows 1 through 7 are roughly equally spaced from 0.15 to 0.77 of the chord.

be considered as generally representative of machined surfaces. Also, the studies show that surfaces can have the same k/R_a ratio but very different k_s/R_a ratios. However, these results do not provide a general method for determining the k_s parameter for an arbitrary roughness geometry.

The sensitivity of k_s to both the spacing of roughness elements and the shape of the elements led Sigal and Danberg (1990) to develop a roughness shape/density parameter Λ_s , which can be used to predict k_s for arbitrary roughness geometries. This parameter is defined as follows:

$$\Lambda_s = (S/S_f)(A_s/A_f)^{1.6} \quad (1)$$

where S/S_f is the ratio of the (planform) surface area without roughness to the total frontal area of the roughness elements, A_f is the frontal area of an element, and A_s is the windward wetted surface area of an element. The ratio S/S_f is a roughness density parameter, although it is also a function of the element geometry; and the ratio A_f/A_s is a shape factor to allow for arbitrary roughness geometries. The variation of k_s/k with Λ_s is shown in Fig. 4 where it is evident that the Λ_s parameter provides a good correlation for the experimental data. This figure shows that the maximum k_s/k ratio occurs at a value of $\Lambda_s \approx 20$. Values of $\Lambda_s < 20$ represent surface roughness for which the roughness elements are closely packed together resulting in decreased skin friction. Roughness elements that are blunt and

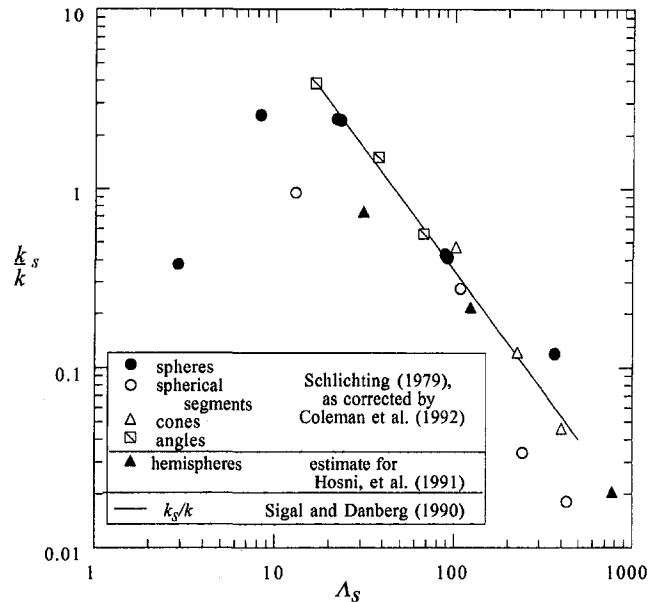


Fig. 4 The effect of roughness geometry on the equivalent sand grain roughness

sharply projecting from the surface will have a smaller A_s/A_f ratio and assume a smaller value for Λ_s , closer to the peak value of k_s/k .

The Λ_s parameter developed by Sigal and Danberg (1990) was developed for predicting k_s for surface roughness with a systematic geometric arrangement. However, for this study we estimated Λ_s for the random surface roughness of the turbine vane by estimating the size, shape, and number density of roughness elements from three-dimensional profilometer traces. Examination of these profilometer traces showed that in general the shape of the roughness elements could be modeled as a truncated cone with an average height equal to R_z . The number density (number per unit area) was found from a count of elements over a representative area of the vane. The diameters of these roughness elements were also found from the profilometer contour plots of the surface roughness. Based on these

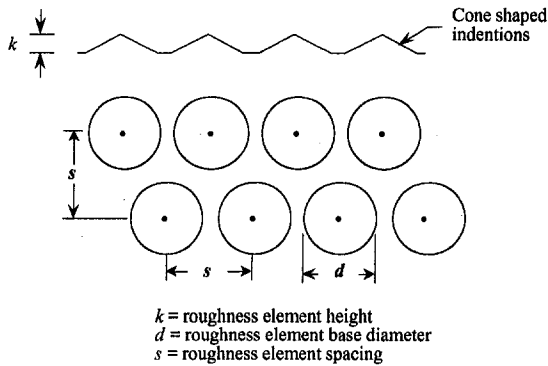


Fig. 5 Schematic of the simulated rough surface

data, values for S/S_f and A_s/A_f were estimated, and the value for Λ_s was determined using Eq. (1). The vane surface roughness was found to have a shape/density parameter value of $\Lambda_s = 60 \pm 30$ (note the large uncertainty was due to the imprecision of estimating Λ_s for the highly contorted surface profile). Figure 4 was used to determine the corresponding range for equivalent sand grain roughness of $k_s/k = 0.8 \pm 0.4$. As mentioned previously, the average roughness height was found to be approximately R_z , i.e., $k = R_z$. Profilometer measurements of the vane roughness indicated $k/R_a \approx 5$, so that $k_s/R_a \approx 4$ for the vane surface roughness.

Design and Testing of Simulated Vane Surface Roughness

For the wind tunnel testing of the rough surface, flat test plates were used, and the flow over a specified region of the airfoil was simulated. Since these test plates were ultimately to be used to investigate the effects of rough surfaces on film cooling, the section of the airfoil to be simulated was selected to follow a row of film cooling holes near the leading edge of the airfoil. At this position on the airfoil, computational prediction of the boundary layer flow indicated that the momentum thickness Reynolds number was $Re_\theta = 320$. The wind tunnel simulation required matching Re_θ and the roughness Reynolds number Re_{ks} . Based on a wind tunnel free-stream velocity of $U_\infty = 10$ m/s, matching these Reynolds numbers required that geometric length scales, such as the roughness height, be 25 times larger than that for the turbine vanes.

The rough surfaces were modeled using uniform cone sizes and distributions. Note that for an array of randomly sized roughness elements, the R_a and k_s values are dictated by the larger roughness elements. This suggests that a reasonable simulation of the roughness can be obtained by using uniformly sized roughness elements scaled to the largest elements on the rough surface to be simulated. The negligible influence of the smaller roughness elements is also indicated by the results of Colebrook and White (1937) and Blair (1994). Colebrook and White (1937) modified surfaces having uniform sand grain roughness by adding a small number of much larger roughness elements. They showed that the start of transitionally rough flow was controlled by the large elements. Blair (1994) simulated a very rough surface by using a uniform distribution of particles with the particle size scaled to match the max-to-min roughness height (a measure of the largest roughness element size) measured on the airfoil to be simulated. He noted that using this max-to-min value in the Van Driest damping function for turbulent flow, modified for a rough wall, resulted in good predictions for the STAN-5 boundary layer code.

Three rough surface designs were evaluated. All three designs used a staggered array of elements, as shown in Fig. 5. Dimensions for cone height (k), cone base diameter (d), and

Table 2 Rough surface roughness element dimensions

Description	k , mm	d , mm	s , mm	k/d	k/s
Surface #1	2.5	9.5	11.4	0.26	0.22
Surface #2a	5.1	9.5	11.4	0.54	0.45
Surface #2b	5.1	19.1	22.9	0.27	0.22

Table 3 Rough surface roughness element parameters

Surface	$\frac{k}{\theta}$	$\frac{R_a}{\theta}$	Λ_s	$\frac{k_s}{k}$	$\frac{k_s}{\theta}$	Re_{ks}
vane 1	2.8	0.6	60	0.8	2.2	50
vane 2	5.6	1.4	60	0.8	4.5	110
Surface #1	4.4	0.9	74	0.5	2.2	60
Surface #2a	8.9	1.8	18	3.2	28.9	1000
Surface #2b	8.9	1.8	74	0.5	4.4	120

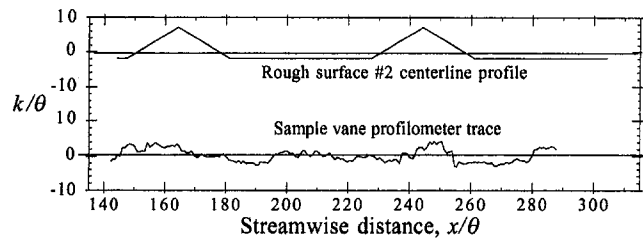


Fig. 6 Comparison of sample vane and modeled rough surface #2

spacing (s) for each design are listed in Table 2. Surface #1 simulated the surface for Vane 1. For Vane 2, the surface roughness R_a was 2–3 times larger than that for Vane 1, and designs surface #2a and surface #2b were different approaches for doubling the simulated roughness. Designs #2a and #2b had the same roughness height k , but design #2a had a larger number of elements and the elements had steeper cone angles. Roughness parameters for the vanes and the three roughness designs are presented in Table 3. Note that, due to the uniform element spacing, calculation of R_a values for the designed surfaces required an area integration rather than the line integration normally used. The roughness parameters presented in Table 3 are nondimensionalized using the appropriate boundary layer momentum thickness so that parameters for the vanes and the wind tunnel test surfaces are directly comparable. The values for R_a/θ and k/θ for the three design test surfaces were slightly higher but essentially the same range as those values for the turbine vanes. Equivalent sand grain roughness, k_s , values were determined by calculating Λ_s for each design geometry and obtaining k_s/k from Fig. 4. Table 3 shows that k_s/θ and Re_{ks} for vane 1 and vane 2 were matched by design surfaces #1 and #2b, respectively. Figure 6 shows the similarity between a cross section of surface #2b and a representative profile from vane 2.

Design surfaces #2a and #2b illustrate the importance of the roughness shape and density. Both these surfaces had the same R_a and k values, but substantially different Λ_s values, and consequently different k_s values. Clearly, with Re_{ks} eight times larger than for the vane, design surface #2a would not have been representative of the vane roughness although the k and R_a values essentially matched that of the vanes.

Based on the analysis of the design surfaces, two rough surface test plates were constructed with geometries of designs #1 and #2b listed in Table 2. One smooth surface was also constructed. All three plates were 1.2 m long and were designed to be used interchangeably as adiabatic plates or constant heat flux plates. Roughness elements were formed in a 0.05-mm-

thick 304 annealed stainless steel foil by confining the foil, then pressing an array of conical protrusions into the foil. Four sections of stainless steel foil were constructed, each 60 cm wide and 30 cm long, and these sections were bonded to a 1.3-cm-thick polystyrene sheet. These sections were connected in series through copper bus bars at the sides. A dc power supply provided power to the heater, and total electrical power input was measured. The polystyrene foam on which the stainless steel foils were mounted was bonded to 1.9 cm thick plywood for structural rigidity. Below the plywood were 15 cm of Corning fiberglass and 2.5 cm of polystyrene insulation.

The test plates were installed in two closed-loop, subsonic wind tunnels. One wind tunnel, with a $0.6 \times 0.6 \times 2.4$ m test section, was used to obtain low free-stream turbulence data (details of this tunnel are given by Pietrzyk et al., 1990). The second wind tunnel had a $0.15 \times 0.6 \times 1.8$ m test section and was equipped with a special jets-in-crossflow turbulence generator, which enabled operation with free-stream turbulence levels as high as $Tu = 17$ percent (details about this wind tunnel, the high free-stream turbulence generator, and the streamwise distribution and length scales for the free-stream turbulence are presented by Thole et al., 1994). Experiments conducted with the test plates were designed to simulate the boundary layer flow on the turbine airfoil. As mentioned previously, this simulated flow was accomplished by matching the Re_θ for the wind tunnel tests with that predicted for the turbine airfoil flow. An elliptical leading edge, with a suction slot immediately preceding this leading edge to remove the upstream boundary layer, was used to establish a new laminar boundary layer upstream of the rough surface test plate. With this configuration there was 27-cm-long unheated section from the leading edge to the start of the test plate. A 0.8 mm diameter wire, which tripped transition to a turbulent boundary layer, was placed on the surface of the unheated section at varying positions from 10 cm to 14 cm downstream of the leading edge. The position of this boundary layer trip was adjusted to obtain the required Re_θ value at the start of the rough surface. The momentum thickness was determined from an integration of mean velocity profiles measured using a single component hot-wire.

The total convective heat transfer rate from the test plate was determined by subtracting the radiative heat transfer rate from the total generated heat rate. Backside conduction losses were determined to be negligible. The convective heat flux was determined using the planform area of the test plate rather than the total surface area for the rough surfaces so that increases in heat flux would be proportional to increases in total heat transfer rate. For both rough surfaces the ratio of the total surface area to the planform area was 1.07. Surface temperatures were measured using an infrared camera (Inframetrics Model 600L) calibrated using thin ribbon thermocouples attached to the surface. Free-stream temperatures were measured with thermocouples positioned at the test section midheight upstream and downstream of the test plate. For the rough surfaces there was a significant variation of the surface temperature across the roughness element, and in the valleys between roughness elements, because of the variation of the local heat transfer rate. The variations of local heat transfer rates (surface temperatures) were as much as 20 percent of the average for rough surface #1, and as much as 50 percent for rough surface #2b. Heat transfer coefficients were calculated using a temperature spatially averaged across the roughness element and the surrounding valley area. Bias and precision uncertainties were estimated as follows. Bias uncertainties were primarily due to uncertainties in the thermocouples used for free-stream and surface temperature measurements, accuracy of the infrared camera calibration and drift of the infrared camera, and the accuracy of the averaging procedure for the surface temperature. Combined this resulted in a bias uncertainty for the differential temperature ΔT of $\pm 0.5^\circ\text{C}$. Uncertainties in the surface heat flux and the radiation correction were negligible. The resulting bias uncer-

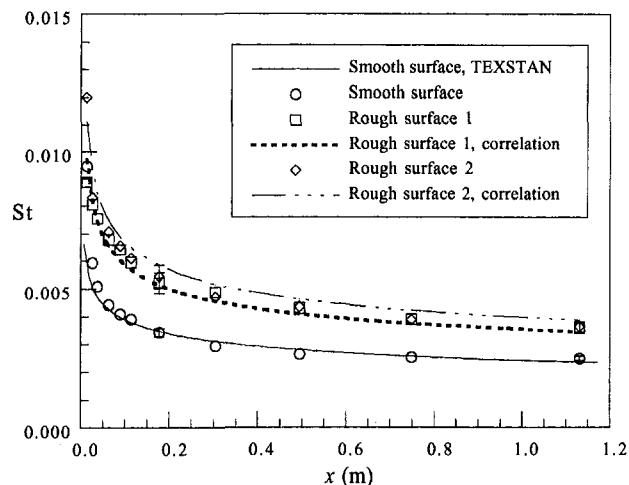


Fig. 7 Stanton number versus distance on heat flux plate for all surfaces with low free-stream turbulence

tainty for St ranged from ± 7 percent at $x = 0.2$ m to ± 5 percent at $x = 1.1$ m for both rough surfaces, and slightly less than this for the smooth surface. Precision uncertainty was determined to be ± 2 percent from a statistical analysis of the repeatability of four separate experiments.

Results of the heat transfer measurements for the smooth and rough surfaces are presented in Fig. 7 in terms of nondimensional Stanton number, St . The smooth surface data compare well with St predicted using the two-dimensional boundary layer code TEXSTAN (Kays and Crawford, 1993). The rough surface data are compared with the following correlation from Kays and Crawford (1993) for fully rough flows (fully rough flow for $Re_{ks} > 70$):

$$St = C_f/2(\text{Pr}_t + (C_f/2)^{0.5}/St_{ks})^{-1} \quad (2)$$

where St_{ks} is found from the following:

$$St_{ks} = C Re_{ks}^{-0.2} \text{Pr}^{-0.4} \quad (3)$$

The turbulent Prandtl number was taken to be $\text{Pr}_t = 0.9$, and the constant C was determined to be $C = 1.0$ by fitting to the rough surface results of Pimenta et al. (1975), who used closely packed spheres, and Hosni et al. (1991), who used hemispherical elements in ordered arrays somewhat less dense than those of the surfaces considered here. The skin friction coefficient was found using the following correlation for fully rough flows from White (1974):

$$C_f = (1.4 + 3.7 \log(x/k_s))^{-2} \quad (4)$$

This equation applies for $x/k_s > 100$. Figure 7 shows an approximately 50 percent increase in St with both rough surfaces. Predicted values based on the correlations of Eqs. (2) and (4) were in good agreement with the experimental measurements. However, the correlations predicted a distinct increase in St for rough surface #2b relative to rough surface #1, while little difference was observed in the measurements, although the differences would have been within the experimental uncertainty.

Note that the initial roughness Reynolds numbers of $Re_{ks} = 60$ and 120 for rough surfaces #1 and #2, respectively, decayed to $Re_{ks} = 40$ and 100 by the end of the test plate. Consequently surface #1 was in the transitionally rough regime (but near the fully rough regime), and surface #2 was in the fully rough regime.

The St prediction in Eq. (2) is most sensitive to C_f and only weakly dependent on St_{ks} . Consequently it is useful to note that the C_f correlation, Eq. (4), was derived by White (1974) based on sand grain roughness effects on the mean velocity profile.

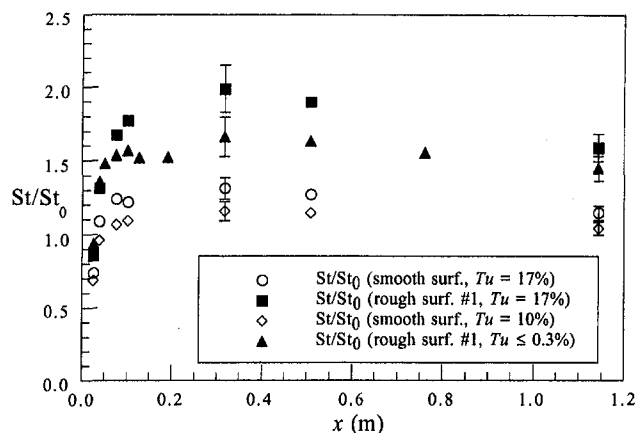


Fig. 8 Stanton number increases due to high free-stream turbulence and surface roughness relative to Stanton number for a low-free-stream turbulence, smooth wall (St_0)

The effects of high free-stream turbulence levels on measured heat transfer rates are shown in Fig. 8 in terms of St/St_0 where St_0 is the reference Stanton number measured at the same position for a smooth surface with low free-stream turbulence ($Tu < 0.3$ percent). Two levels of high free-stream turbulence were tested; $Tu = 10$ and 17 percent. These levels occurred at the start of the heat flux plate; for the $Tu = 17$ percent case the turbulence level decayed to about $Tu = 9$ percent at the end of the heat flux plate, and for the $Tu = 10$ percent case the turbulence level decayed to about $Tu = 6$ percent at the end of the heat flux plate. More details about the free-stream turbulence and associated increase in heat transfer are presented in Thole et al. (1994) and in Thole and Bogard (1995). High free-stream turbulence levels cause a maximum increase in heat transfer rates of 15 and 30 percent for $Tu = 10$ and 17 percent, respectively. This increase was distinctly less than the 60 percent increase due to the surface roughness. A key result from this experimental program was the combined effect of surface roughness and high free-stream turbulence. Figure 8 shows that increases in heat transfer rates due to surface roughness and high free-stream turbulence levels are essentially additive when surface roughness and high free-stream turbulence levels are combined. Combining rough surface #1 with a free-stream turbulence level of $Tu = 17$ percent resulted in a 100 percent increase in the heat transfer rate.

Conclusions

Analysis of two sample turbine vanes used in engines of military aircraft showed that surface roughness increased substantially after 500 hours of service, particularly on the pressure side of the vanes. Profilometer measurements provided detailed roughness profiles across the vane surfaces. The centerline average (R_a) and the average peak value, parameters typically used to characterize surface roughness, were shown to be inadequate for predicting surface roughness effects on the flow and heat transfer. Surface friction and heat transfer are correlated with the equivalent sand grain roughness, k_s , parameter. In this study k_s for the vane surface roughness was estimated using the Λ_s roughness shape/density parameter.

The vane surface roughness was simulated using a uniform array of conical elements with the appropriate size and spacing to match the R_a , k_s , and Re_{ks} parameters for the vane surface roughness. A constant heat flux surface was used for the simulated roughness test plates, and wind tunnel experiments were

conducted to determine increases in heat transfer rates due to the surface roughness. Two test surfaces with $Re_{ks} = 60$ and 120 showed about the same increase in heat transfer rates of 50 to 60 percent relative to a smooth surface. Experiments were also conducted with high free-stream turbulence levels ranging from $Tu = 10$ to 17 percent. For smooth surface these high free-stream turbulence levels caused increases in heat transfer rates from 15 to 30 percent. With combined surface roughness and high free-stream turbulence, the effects of each were additive resulting in as much as 100 percent increase in heat transfer rate. These results show the importance of accounting for the increase in surface roughness in the turbine section during the operational life of the engine, and that the effects of roughness are not diminished or overwhelmed by the high free-stream turbulence levels that exist in the turbine environment.

Acknowledgments

The authors gratefully acknowledge the support of United Technologies, Pratt & Whitney. We also are thankful for the valuable input from Mike Crawford, and appreciate Don Artieschoufsky's advice with respect to the design and construction of the rough surfaces.

References

- Acharya, M., Bornstein, J., and Escudier, M. P., 1986, "Turbulent Boundary Layers on Rough Surfaces," *Exper. In Fluids*, Vol. 4, pp. 33–47.
- Bammert, K., and Sanstede, H., 1972, "Measurements Concerning the Influence of Surface Roughness and Profile Changes on the Performance of Gas Turbine Engines," *ASME Journal of Engineering for Power*, Vol. 94, pp. 207–213.
- Bammert, K., and Sanstede, H., 1976, "Influences of Manufacturing Tolerances and Surface Roughness of Blades on the Performance of Turbines," *ASME Journal of Engineering for Power*, Vol. 98, pp. 29–36.
- Blair, M. F., 1994, "An Experimental Study of Heat Transfer in a Large-Scale Turbine Rotor Passage," *ASME JOURNAL OF TURBOMACHINERY*, Vol. 116, pp. 1–13.
- Colebrook, C. F., and White, C. M., 1937, "Experiments With Fluid Friction in Roughened Pipes," *Proc. Royal Society of London*, Vol. 161, pp. 367–381.
- Coleman, H. W., Hodge, B. K., and Taylor, R. P., 1984, "A Re-evaluation of Schlichting's Surface Experiment," *ASME Journal of Fluids Engineering*, Vol. 106, pp. 60–65.
- Forster, V. T., 1967, "Performance Loss of Modern Steam-Turbine Plant Due to Surface Roughness," *Proc. Inst. Mech. Engrs. 1966–67*, Vol. 181, Pt. 1, pp. 391–405.
- Hosni, M. H., Coleman, H. W., and Taylor, R. P., 1991, "Measurements and Calculations of Rough-Wall Heat Transfer in the Turbulent Boundary Layer," *International Journal of Heat and Mass Transfer*, Vol. 34, No. 4, pp. 1067–1082.
- Kays, W. M., and Crawford, M. E., 1993, *Convective Heat and Mass Transfer*, 3rd ed., McGraw-Hill, New York.
- Koch, C. C., and Smith, L. H., Jr., 1976, "Loss Sources and Magnitudes in Axial-Flow Compressors," *ASME Journal of Engineering for Power*, Vol. 98, pp. 411–424.
- Nikuradse, J., 1933, "Laws for Flow in Rough Pipes," *VDI-Forschungsheft*, Series B, Vol. 4, pp. 361.
- Pietrzyk, J. R., Bogard, D. G., and Crawford, M. E., 1990, "Effect of Density Ratio on the Hydrodynamics of Film Cooling," *ASME JOURNAL OF TURBOMACHINERY*, Vol. 112, pp. 437–443.
- Pimenta, M. M., Moffat, R. J., and Kays, W. M., 1975, "The Turbulent Boundary Layer: An Experimental Study of the Transport of Momentum and Heat With the Effect of Roughness," Thermoscience Division, Department of Mechanical Engineering, Stanford University, Report HMT-21.
- Schlichting, H., 1979, *Boundary Layer Theory*, 7th ed. McGraw-Hill, New York.
- Sigal, A., and Danberg, J. E., 1990, "New Correlation of Roughness Density Effects on the Turbulent Boundary Layer," *AIAA Journal*, Vol. 28, pp. 554–556.
- Speidel, L., 1954, "Influence of the Surface Roughness on the Flow Losses in Plane Blade Cascades," *Forsch. Ing.-Wes.*, Vol. 20, No. 5, pp. 129–140.
- Tarada, F., and Suzuki, M., 1993, "External Heat Transfer Enhancement to Turbine Blading Due to Surface Roughness," *ASME Paper 93-GT-74*.
- Taylor, R. P., 1990, "Surface Roughness Measurements on Gas Turbine Blades," *ASME JOURNAL OF TURBOMACHINERY*, Vol. 112, pp. 175–180.
- Thole, K. A., and Bogard, D. G., 1995, "Enhanced Heat Transfer and Shear Stress Due to High Free-Stream Turbulence," *ASME JOURNAL OF TURBOMACHINERY*, Vol. 117, pp. 418–424.
- Thole, K. A., Bogard, D. G., and Whan-Tong, J., 1994, "Generating High Freestream Turbulence Levels," *Exper. in Fluids*, Vol. 17, pp. 375–380.
- White, F. M., 1974, *Viscous Fluid Flow*, McGraw-Hill, New York.

Computational Prediction of Heat Transfer to Gas Turbine Nozzle Guide Vanes With Roughened Surfaces

S. M. Guo

T. V. Jones

Department of Engineering Science,
University of Oxford,
Oxford, United Kingdom

G. D. Lock

Department of Mechanical Engineering,
University of Bath,
Bath, United Kingdom

S. N. Dancer

Rolls-Royce plc,
Derby, United Kingdom

The local Mach number and heat transfer coefficient over the aerofoil surfaces and endwalls of a transonic gas turbine nozzle guide vane have been calculated. The computations were performed by solving the time-averaged Navier–Stokes equations using a fully three-dimensional computational code (CFDS), which is well established at Rolls-Royce. A model to predict the effects of roughness has been incorporated into CFDS and heat transfer levels have been calculated for both hydraulically smooth and transitionally rough surfaces. The roughness influences the calculations in two ways; first the mixing length at a certain height above the surface is increased; second the wall function used to reconcile the wall condition with the first grid point above the wall is also altered. The first involves a relatively straightforward shift of the origin in the van Driest damping function description, the second requires an integration of the momentum equation across the wall layer. A similar treatment applies to the energy equation. The calculations are compared with experimental contours of heat transfer coefficient obtained using both thin-film gages and the transient liquid crystal technique. Measurements were performed using both hydraulically smooth and roughened surfaces, and at engine-representative Mach and Reynolds numbers. The heat transfer results are discussed and interpreted in terms of surface-shear flow visualization using oil and dye techniques.

Introduction

The quest for increased gas turbine efficiencies and specific thrusts results in a requirement for higher turbine entry temperatures. These higher temperatures result in more severe heat transfer loads to the high-pressure components of the engine. Thus the modern aeroengine designer requires accurate computational methods to predict the heat transfer to the endwalls and aerofoil surfaces of nozzle guide vane passages. These calculations are made difficult because of the presence of highly complex secondary flows. Moreover, the nozzle guide vanes surfaces are generally not hydraulically smooth and the predictive methods should include effects of surface roughness.

There are generally two types of surface roughness that are important to the gas turbine designer. The first exists because of the deposition of dust, sand, or other particulates, and in general adversely affects the profile loss of gas turbine nozzle guide vanes and rotor blades (Schlichting, 1979; Tabakoff, 1984; Turner et al., 1985). The second type of roughness is intrinsic roughness due to the manufacturing process. Usually the latter is small ($\sim 1 \mu\text{m}$) but it may be significant if ceramic thermal barrier coating (TBC) is present. A common means of depositing TBC is by arc-plasma spraying, which tends to result in a characteristically rough surface compared to that obtained using vapor deposition.

In basic terms, the three main influences of surface roughness are as follows: (i) The point of onset of laminar-turbulent transition advances upstream with increasing roughness; (ii) the turbulent boundary layer skin friction increases with increasing roughness; and (iii) the turbulent mean heat transfer increases with increasing roughness. Hence surface roughness, whether due

to TBC or the normal erosion, corrosion, or accretion of dirt and dust that occurs in service, can have a detrimental effect on the aerodynamics and thermal characteristics of turbine blading.

This paper describes calculations of heat transfer to the end-wall and aerofoil surfaces of a nozzle guide vane with roughened surfaces using a fully three-dimensional CFD code. The method used to account for the surface roughness within the code is discussed in detail. The results of the calculations are compared with contours of isentropic Mach number and heat transfer coefficient obtained from experiments employing both smooth and roughened surfaces.

CFDS Code

The CFD code used is the Rolls-Royce Computational Fluid Dynamic System (CFDS), which is well established as a predictive method at Rolls-Royce. This CFD code is based on an algorithm described by Moore (1985) and has been applied to many turbomachinery flows (for example, Chew et al., 1996 and Northall et al., 1987). In this code the Reynolds-averaged Navier–Stokes equations are discretized by integration over a set of upwinded control volumes using linear interpolation rules. The discretized equations are integrated toward convergence using the SIMPLER algorithm as described by Patankar (1980). A mixing length is assumed with boundary layer thicknesses needed for the mixing length calculations being estimated from a vorticity based test function. The CFDS code, prior to the work reported here, had no roughness modeling.

Smooth Law of the Wall

This section will describe the law of the wall for a smooth surface. This law of the wall is used to calculate the velocity profile for the next to wall grid points in the CFDS code. The smooth law of the wall is well established and is reviewed here as a basis for the subsequent discussion concerning the modeling of surface roughness.

Contributed by the International Gas Turbine Institute and presented at the 41st International Gas Turbine and Aeroengine Congress and Exhibition, Birmingham, United Kingdom, June 10–13, 1996. Manuscript received at ASME Headquarters February 1996. Paper No. 96-GT-388. Associate Technical Editor: J. N. Shinn.

Kays and Crawford (1993) present a derivation of the law of the wall for a *hydraulically smooth* surface. The eddy diffusivity for momentum, ϵ_M , and kinematic viscosity, ν , are used to express the total apparent shear stress (molecular plus turbulent) in terms of the velocity gradient:

$$\tau = \rho(\nu + \epsilon_M) \frac{\partial \bar{u}}{\partial y}, \quad (1)$$

where \bar{u} is the mean velocity parallel to the wall, ρ is the fluid density, and y the distance from the wall. The Prandtl mixing length, l , is related to ϵ_M by

$$\epsilon_M = l^2 \left| \frac{\partial \bar{u}}{\partial y} \right|, \quad (2)$$

and to the distance from the wall by $l = \kappa y$. Here $\kappa = 0.41$.

Equation (1) is substituted into the differential momentum equation for a constant-property turbulent boundary layer. For the case of no pressure gradient and zero velocity at the wall, this momentum equation reduces to $\tau = \tau_0$ close to the wall, where the latter term is the shear stress at the wall ($y = 0$). To obtain the law of the wall, Kays and Crawford integrate Eq. (1) under this condition, i.e.,

$$\tau_0 = \rho(\nu + \epsilon_M) \frac{d\bar{u}}{dy}. \quad (3)$$

The law of the wall is expressed in terms of the nondimensional velocity, u^+ and distance (or local thickness Reynolds number), y^+ :

$$u^+ = \frac{\bar{u}}{u_\tau} \quad \text{and} \quad y^+ = \frac{y u_\tau}{\nu}, \quad (4)$$

where $u_\tau = \sqrt{\tau_0/\rho}$ is the friction, or shear velocity.

The turbulent boundary layer can be modeled to have two distinct regions: a viscous sublayer, for which $\nu \gg \epsilon_M$, and a fully turbulent region for which $\nu \ll \epsilon_M$. Either a separate law of the wall for both regions can be calculated by integrating Eq. (3) with the appropriate term neglected, or a continuous law of the wall can be obtained by using the van Driest (1956) model. In this model the Prandtl mixing length is given by the van Driest damping function, viz.,

$$l = \kappa y (1 - e^{-y^+/A^+}), \quad (5)$$

with $A^+ = 26$ for a smooth wall.

In CFDS, the following *hydraulically smooth* law of the wall (or velocity profile) is used to blend continuously between the viscous sublayer and the logarithmic region of the turbulent boundary layer (Coupland, 1995):

$$y^+ = u^+ + \frac{1}{E} \left[\exp(\beta) - 1 - \beta - \frac{1}{2}(\beta)^2 - \frac{1}{6}(\beta)^3 \right], \quad (6)$$

where $\beta = \kappa u^+$, $E = 8.8$, and again $\kappa = 0.41$. Figure 1 illustrates

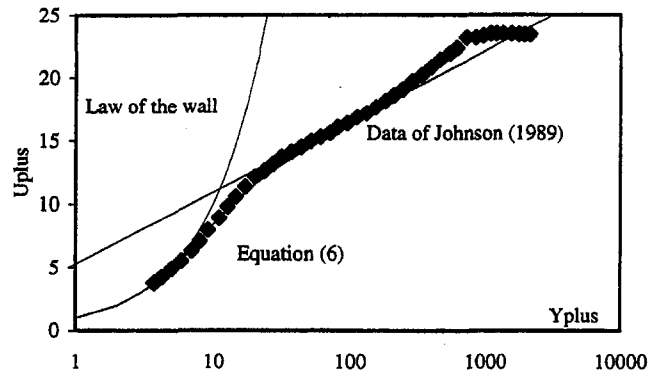


Fig. 1 Smooth law of the wall

the velocity profile predicted from Eq. (6), and compares the solution of Eq. (3) in the viscous sublayer ($u^+ = y^+$) and the fully turbulent region ($u^+ = \log(Ey^+)/\kappa$). Equation (6) has been shown to agree well with the turbulent velocity profiles measured from flat plate experiments (Johnson and Johnson, 1989), which are also shown in Fig. 1.

Law of the Roughened Wall

This section will describe the derivation of the law of the wall for a rough surface. The roughness influences the calculations in two ways; first the mixing length at a certain height above the surface is increased; second the wall function used to reconcile the wall condition with the first grid point above the wall is also altered. The first involves a relatively straightforward shift of the origin in the van Driest damping function description, the second requires an integration of the momentum equation across the wall layer. A similar treatment applies to the energy equation. This roughness modeling has been incorporated into the CFDS code by the authors.

There are several texts describing roughness modelling, e.g., Cebeci and Bradshaw (1977) or Kays and Crawford (1993). The roughness Reynolds number, $Re_k = u_\tau k_s/\nu$ is generally used as a nondimensional measure of surface roughness. The roughness element size k_s is the length dimension used by Nikuradse (1933). Three regimes can be identified from experimental data in terms of Re_k : for $Re_k \leq 5$ the surface can be considered to be hydraulically smooth; for $5 \leq Re_k \leq 70$ the surface is transitionally rough; and for $Re_k \geq 70$ the surface is considered to be fully rough.

One effect of roughness is to reduce the size of the viscous sublayer. At $Re_k = 70$ the sublayer disappears entirely. Even in this fully rough regime the surface roughness must still affect the turbulent wall shear stress. The Prandtl mixing-length model is still employed with the rough wall. The mixing length, l (and hence ϵ_M) cannot be zero at $y = 0$; otherwise there is no mechanism for transferring the shear stress to the wall.

Nomenclature

A^+ = van Driest damping constant
 E = constant for logarithmic region
 h = heat transfer coefficient
 k = roughness element size
 k_s = Nikuradse roughness element size
 l = Prandtl mixing length
 M = free-stream Mach number
 Pr = Prandtl number
 Pr_t = turbulent Prandtl number
 q = heat flux

r = recovery factor
 Re_k = roughness Reynolds number
 t = temperature
 t^+ = nondimensional temperature
 δt_0^+ = temperature displacement
 u = velocity parallel to wall
 \bar{u} = mean velocity parallel to wall
 u^+ = nondimensional velocity
 u_τ = friction or shear velocity
 y = distance from wall

y^+ = nondimensional distance
 δy = effective wall displacement
 ϵ_H = eddy diffusivity for heat transfer
 ϵ_M = eddy diffusivity for momentum
 κ = Prandtl constant
 ν = kinematic viscosity
 τ = shear stress
 τ_0 = shear stress at the wall
 ρ = density

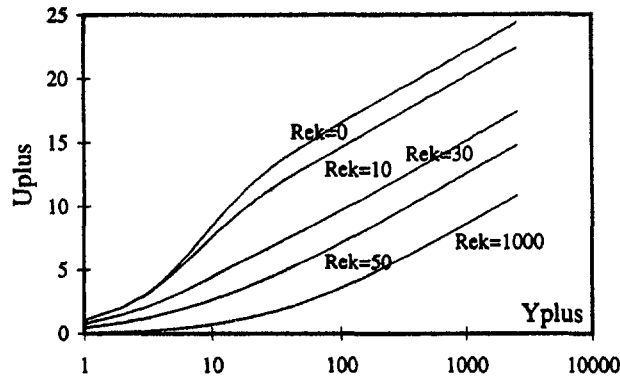


Fig. 2 Law of the wall for a roughened surface

Following Cebeci and Chang (1978), the mixing length for a rough surface is modified to

$$l = \kappa(y + \delta y)(1 - e^{-(y^+ + \delta y^+)/A^+}). \quad (7)$$

Here δy can be interpreted as an effective wall displacement. Cebeci and Chang (1978) and later Boyle (1994) define this shift in terms of the roughness Reynolds number,

$$\delta y^+ = 0.9(\sqrt{\text{Re}_k} - \text{Re}_k + e^{-\text{Re}_k/6}). \quad (8)$$

Note that this equation is only valid for $\text{Re}_k > 5$ and that if $\text{Re}_k < 5$ then $\delta y^+ = 0$.

The law of the wall for a roughened surface can be obtained by substituting Eq. (2) and the new definition of the Prandtl mixing length into Eq. (3). Then

$$\tau_0 = \rho \left[\nu + l^2 \frac{\tau_0}{\rho \nu} \left| \frac{du^+}{dy^+} \right| \right] \frac{\tau_0}{\rho \nu} \left| \frac{du^+}{dy^+} \right|, \quad (9)$$

and the substitution for the length scale in terms of nondimensional distance,

$$l = \kappa(y^+ + \delta y^+) [1 - e^{-(y^+ + \delta y^+)/A^+}] \frac{\nu}{\sqrt{\tau_0/\rho}} \quad (10)$$

leads to the nondimensional derivative as follows:

$$\frac{du^+}{dy^+} = \frac{\sqrt{1 + [2\kappa(y^+ + \delta y^+)(1 - e^{-(y^+ + \delta y^+)/A^+})]^2} - 1}{2[\kappa(y^+ + \delta y^+)(1 - e^{-(y^+ + \delta y^+)/A^+})]^2}. \quad (11)$$

The law of the wall for a roughened surface is obtained by moving the differential, dy^+ to the right-hand side of Eq. (11) and numerically integrating du^+ between zero and y^+ . It should be noted that A^+ is a function of Re_k , which complicates this integral. The value of A^+ for a smooth wall ($\text{Re}_k \leq 5$) is 26, and $A^+ = 0$ for a fully rough surface ($\text{Re}_k \geq 70$). For a transitionally rough surface A^+ is taken to vary linearly between these two limits, viz.,

$$A^+ = 26 \left(1 - \frac{\text{Re}_k}{70} \right). \quad (12)$$

This law of the wall is used to calculate the velocity profile for the grid points in the CFDS code next to the roughened wall. The variation of u^+ with y^+ , calculated using Eq. (11), for different values of Re_k can be found in Fig. 2.

Rough-Wall Temperature Profile

The law of the wall for the roughened surface affects the wall function for the temperature profile and an integration of the energy equation across the wall layer leads to the heat flux at the wall.

Kays and Crawford (1993) develop the near-wall temperature profile for a smooth surface. For the case of zero pressure gradient and zero velocity at the wall, the heat flux (turbulent plus laminar) at the wall, \dot{q}_0 , is defined as

$$\frac{\dot{q}_0}{\rho c} = - \left(\frac{\nu}{\text{Pr}} + \epsilon_H \right) \frac{dt}{dy}, \quad (13)$$

where Pr is the Prandtl number and ϵ_H is the eddy diffusivity for heat transfer. By introducing y^+ through Eq. (4) and the nondimensional temperature

$$t^+ = \frac{(t_0 - t)\sqrt{\tau_0/\rho}}{\dot{q}_0/\rho c}, \quad (14)$$

Eq. (13) can be rewritten as

$$1 = \left(\frac{1}{\text{Pr}} + \frac{\epsilon_H}{\nu} \right) \frac{dt^+}{dy^+}. \quad (15)$$

The eddy diffusivity for heat transfer and momentum are related by the turbulent Prandtl number, $\epsilon_M/\epsilon_H = \text{Pr}_t$. Using this relationship and the definition of the mixing length, Eq. (2), this equation becomes

$$\frac{\epsilon_H}{\nu} = \frac{l^{+2}}{\text{Pr}_t^2} \frac{dt^+}{dy^+}. \quad (16)$$

Here

$$l^+ = \kappa(y^+ + \delta y^+) (1 - e^{-(y^+ + \delta y^+)/A^+}), \quad (17)$$

is the van Driest form of the Prandtl mixing length scale for a roughened surface as discussed in the previous section, and δy^+ and A^+ are defined in Eqs. (8) and (12). Solving for the derivative, one obtains:

$$\frac{dt^+}{dy^+} = \frac{\sqrt{\text{Pr}^{-2} + 4l^{+2}/\text{Pr}_t^2}}{2l^{+2}/\text{Pr}_t^2}. \quad (18)$$

Equation (18) is integrated numerically to calculate the temperature profile for the next to wall grid points in the CFDS code.

Following Kays and Crawford (1993), heat can be transferred by eddy conductivity down to the plane of the roughness elements, but the actual final heat transfer to the solid surface must be through the mechanism of molecular conduction. The lower limit of t^+ is taken as a finite number, δt_0^+ rather than zero. The δt_0^+ represents the temperature difference across which heat is transferred by conduction through what may be semistagnant fluid in the roughness cavities at the surface. Kays and Crawford (1993) define this nondimensional temperature addition in terms of a roughness Stanton number St_k , i.e.,

$$\delta t_0^+ = \frac{1}{\text{St}_k} = \frac{1}{C \text{Re}_k^{-0.2} \text{Pr}^{-0.44}}. \quad (19)$$

The roughness Stanton number is a function of the type and shape of roughness and the constant C was taken as unity for the work reported here. The variation of $t^+ + \delta t_0^+$ with y^+ , calculated with Eqs. (18) and (19), for different values of Re_k is illustrated in Fig. 3.

Experimental Conditions

The results from the CFDS calculations are compared with experimental measurements in the next section. This section briefly describes the experiments performed.

The experiments were conducted in the Oxford University Cold Heat Transfer Tunnel (Martinez-Botas et al., 1993), which can achieve independent variation of Mach number and Reynolds number over a range of engine-representative conditions. The test section of the tunnel is an annular cascade of 36 nozzle

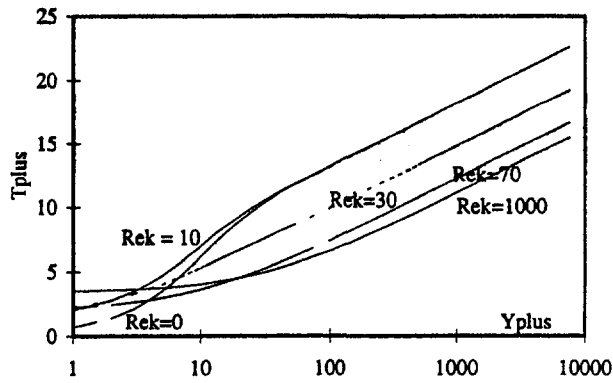


Fig. 3 Nondimensional temperature versus nondimensional distance from the wall for different roughness Reynolds number

guide vanes (NGVs) at 1.4 times larger than engine scale. At engine design conditions the exit Mach number is 0.96 and the Reynolds number (based on an axial chord of 66.4 mm) is 2×10^6 . The free-stream turbulence intensity and length scale at the NGV inlet plane were measured to be 13 percent and 21 mm, respectively (Spencer et al., 1995). The facility has a runtime of ~ 5 seconds and transient experimental techniques are employed to measure heat transfer using liquid crystals (Martinez-Botas et al., 1995; Spencer et al., 1995) or thin-film gages (Guo et al., 1995). Flow visualization tests (Martinez-Botas et al., 1995) have shown that separation occurs, in the regions of secondary flow. However, this only affects the endwalls and limited regions on the suction surface. A mixing length model should therefore be applicable at midspan. As a mixing length model has been shown to be inadequate in predicting separations, the extent of the secondary flow may be somewhat in error. The prediction of heat transfer under a given secondary flow should be reasonably predicted using a mixing length model.

Different scales of roughness can be obtained by spraying the NGV surfaces with liquid crystals and polishing them. Unpolished crystals have a maximum peak-to-peak roughness element size, measured using a *tally-surf* machine, of $k \sim 25 \mu\text{m}$. This corresponds to about $17 \mu\text{m}$ at engine scale. If the crystals are highly polished, the surfaces become very smooth. Only the two extremes of roughness were employed in the experiments reported here: The surfaces sprayed with liquid crystals were either left unpolished to create a *roughened* surface ($k = 25 \mu\text{m}$); or thin-film gages were instrumented onto flexible plastic substrates (Jones, 1995), which were adhesively bonded to the NGV, and the resulting surfaces were extremely smooth.

At engine representative conditions the roughness Reynolds number over the *rough* surface varied between 0 (at the stagnation point) to 30 (near the trailing edge), which put the NGV used in the experiments in the transitionally rough regime. On the smooth surface, Re_k was less than 5 throughout. It should be noted that typical unpolished TBC surfaces have a peak-to-peak roughness of about $55 \mu\text{m}$, which is reduced to $17 \mu\text{m}$ when polished (Watt et al., 1990). These values are of the same order as those tested experimentally. Modern plasma methods to deposit TBC can reduce this roughness to about $3 \mu\text{m}$ and typical sand grit deposition found on turbine blades is $30 \mu\text{m}$.

The effect of roughness on turbulent skin friction, aerodynamic drag, and heat transfer depends not only on the grain size but also on roughness density and shape (Schlichting, 1979). The approach usually adopted to quantify roughness is to place each surface on a scale of "equivalent sand roughness," k_s , which is based on the roughness type used by Nikuradse (1933) and for which a comprehensive body of data exists over a wide range of Reynolds numbers. The relationship between the measured roughness element size k and k_s is not

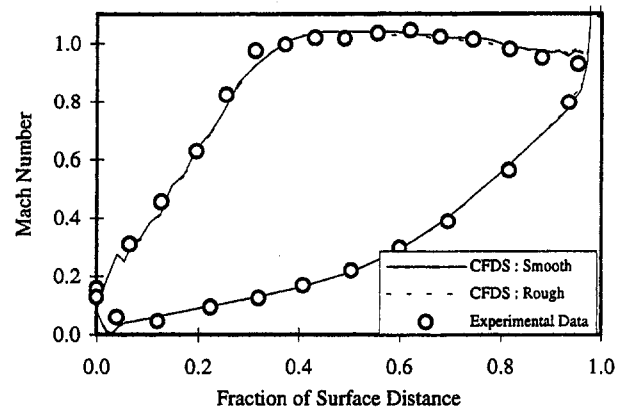


Fig. 4 Isentropic Mach number distribution around the midspan

universally established. Blair (1994) suggests that successful predictions of heat transfer from numerical codes that employ a modified mixing length model were produced using the maximum to minimum roughness value. In other words $k_s = k$ was used to evaluate the roughness Reynolds number Re_k . Boyle (1994) suggests a ratio of $k/k_s = 1$ or larger. Dunn et al. (1994) used a ratio of 0.3 for the blades they tested. As will be seen from the next section, a ratio $k/k_s \sim 1$ was found appropriate for the best comparison between experiment and calculation.

Comparing CFDS With Experiment

The isentropic Mach number distribution around the midspan of the smooth pressure and suction aerofoil surfaces at the engine design condition is illustrated in Fig. 4. The figure shows experimental measurements and compares them with the calculations for both smooth and $k = 30 \mu\text{m}$ rough surfaces. The CFDS calculations are seen to predict the pressure distribution very well and the roughness is shown to have little effect on the aerodynamics around the aerofoil.

Figures 5(a) and 5(b) are the measured isentropic Mach number contours obtained from hub and casing endwall static pressure tappings (56 and 59 tappings on the hub and casing, respectively; Spencer et al., 1995) at the engine design condition. These were obtained using hydraulically smooth surfaces. Figures 6(a) and 6(b) are the corresponding calculated contours from CFDS. The contours for the $30 \mu\text{m}$ rough surfaces were virtually identical and are not shown here. Differences between experiment and calculation are less than 5 percent. Note that in both experiment and calculation the total pressure upstream of the NGV cascade was constant.

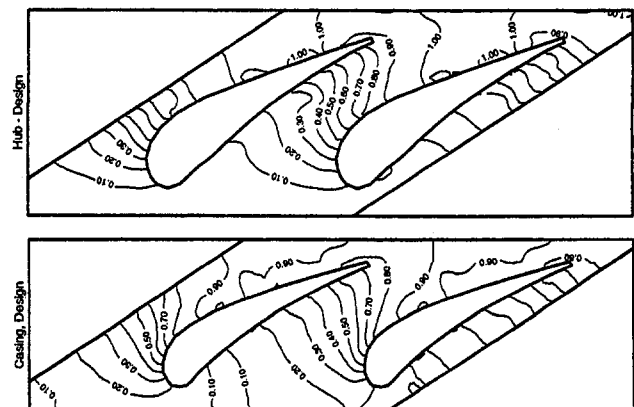


Fig. 5 Measured isentropic Mach number distribution on the endwalls

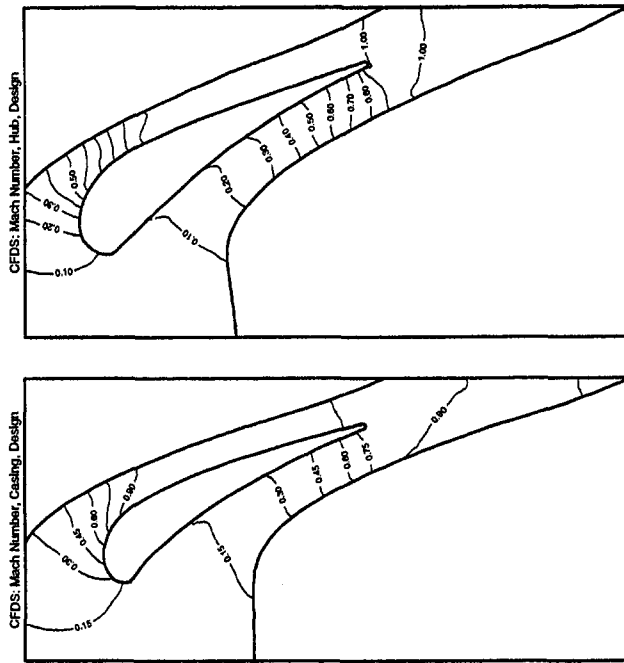


Fig. 6 Calculated isentropic Mach number distribution on the endwalls

Figure 7 compares heat transfer coefficient ($W/m^2 K$) from measurements and calculation along the midspan streamline of the aerofoil pressure and suction surfaces. It should be noted that the heat transfer coefficient is defined as the ratio of heat flux and the difference between the local wall and adiabatic wall temperatures: $h = q/(t_w - t_{aw})$. The adiabatic wall temperature is obtained by assuming a recovery factor, $r = Pr^{1/3}$, and using the relationship between the local Mach number and the local free-stream gas temperature, $t_{aw} = t_g(1 + r[(\gamma - 1)/2]M^2)$.

Measurements from both smooth and rough ($k = 25 \mu m$) surfaces are shown in Fig. 7. The experimental measurements

for the rough surface show a significant increase in heat transfer in comparison with the smooth surface, despite only a roughness equivalent to $17 \mu m$ at engine scale. At this scale of roughness Re_x is a maximum of 30 on the high Mach number regions of the suction surface and at the trailing edge region of the pressure surface. The roughness is also seen to bring the transition point forward on the suction surface despite the large levels of free-stream turbulence. These experimental observations are similar in trend to those reported by Turner et al. (1985). The heat transfer coefficient near the leading edge is quite low in comparison with other published data for nozzle guide vanes. This is a feature of this NGV and its geometry.

The CFDS predictions for the smooth surface are shown to agree reasonably well with those levels measured experimentally on both the pressure and suction surfaces. There is an overprediction on the early suction surface as the CFDS code assumes a turbulent boundary layer from the leading edge. There is also an overprediction on the early pressure surface.

The predicted levels of heat transfer are observed to increase markedly with increasing levels of roughness in a similar manner to the experimental trends. On the early suction surface, differences between the calculated and experimental heat transfer are apparent. Elsewhere on the suction surface, the experimental data is generally well predicted for levels of 20 and 30 μm roughness. On the pressure surface, CFDS generally underpredicts the experimental heat transfer levels on the roughened surfaces. On the pressure surface the roughness Reynolds number is small and it is only near the rear of the surface (at higher local velocity) that the predicted levels for 20 and 30 μm roughness reach the experimental data.

Figures 8(a) and 8(b) illustrate experimentally determined contours of the heat transfer coefficient ($W/m^2 K$) for the pressure and suction aerofoil surfaces with 25 μm roughness (Martinez-Botas et al., 1995). These were obtained using the transient liquid crystal technique, which has the advantage of providing global measurements of heat transfer. These figures are a projection of the curved aerofoil surfaces onto a two-dimensional plane (originally the plane viewed by a camera). The average uncertainty in the experimental measurements is 8 percent on the aerofoil surfaces and 8–13 percent on the endwalls. The uncertainty is dominated by the uncertainty in the thermal prop-

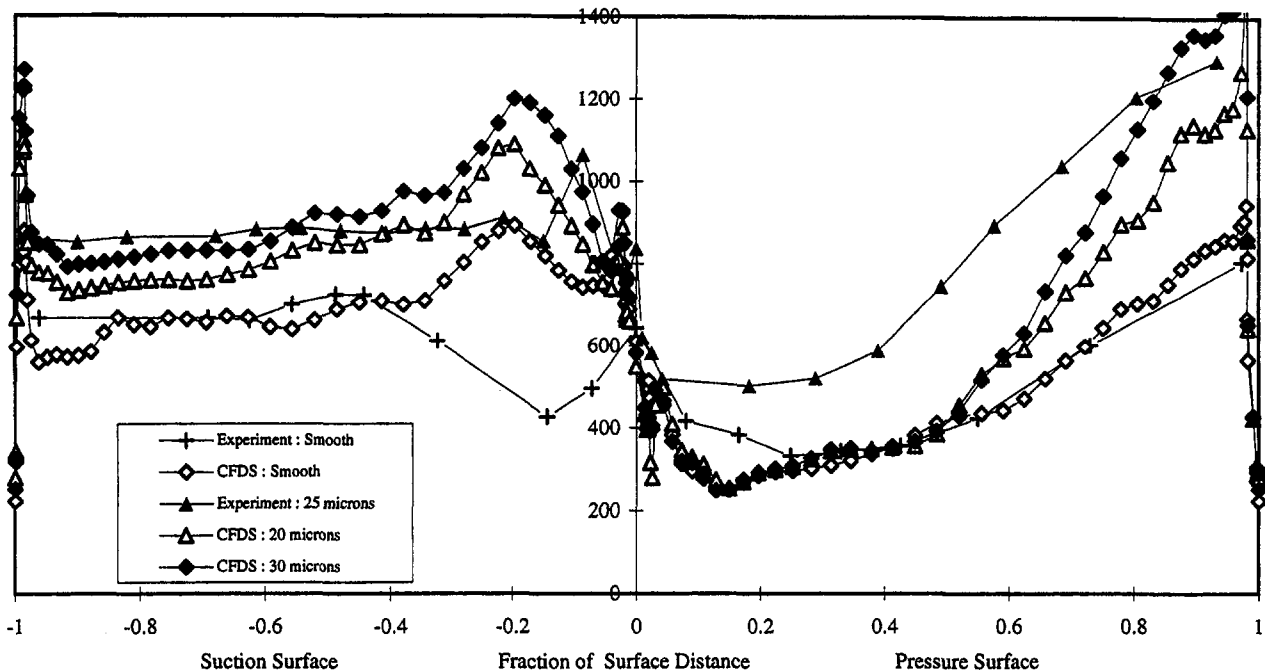


Fig. 7 Heat transfer coefficient ($W/m^2 K$) at midspan

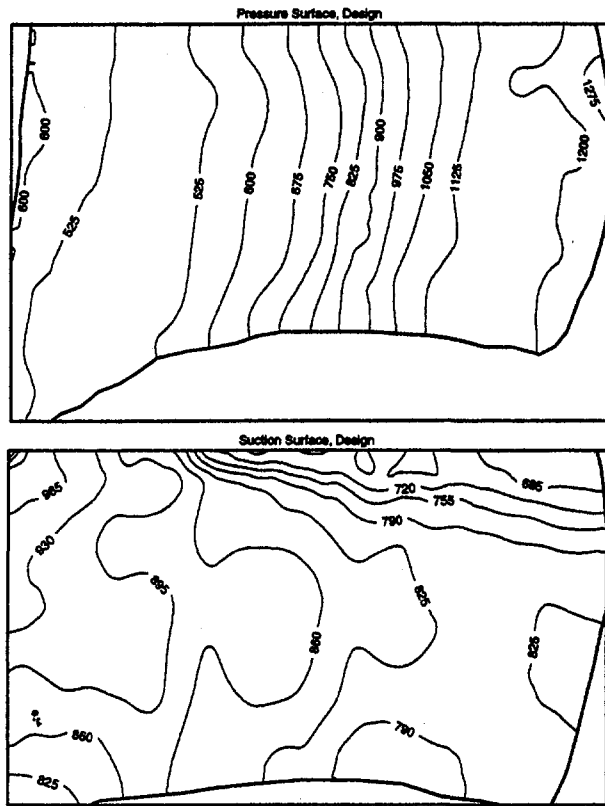


Fig. 8 Experimental contours of heat transfer coefficient ($W/m^2 K$) for the NGV aerofoil surfaces with $25 \mu m$ roughness

erties of the perspex substrate and so the relative uncertainty (used when comparing with rough versus smooth experiments) is significantly less than the absolute uncertainty. Details of the uncertainty associated with the transient liquid crystal technique are available in a paper describing the experiments (Spencer et al., 1996) and a thesis (Martinez-Botas, 1993).

The corresponding predicted contours for surfaces with $30 \mu m$ roughness is shown in Figs. 9(a) and 9(b). Both the predicted and experimental pressure surface contours are of a similar pattern. They show little variation with span position as expected from the Mach number distribution and flow visualization carried out in the tunnel (Martinez-Botas et al., 1995). CFDs is seen to underpredict the early part of the surface as discussed earlier with reference to Fig. 7.

Both the experimental and predicted contours on the suction surface show a spot of high heat transfer on the forward part of the blade near the casing. The CFDs overpredicts the heat transfer here because of the difficulty involved in locating the point of transition from laminar to turbulent flow. Both CFDs and the experiments reveal a region of low heat transfer at the casing near the trailing edge of the suction surface. This band of low heat transfer was discussed in detail by Martinez-Botas et al. (1995) and (from flow visualization experiments) was shown to be a region influenced by secondary flow with a thickened thermal boundary layer. A low heat transfer band also exists near the hub endwall but it does not migrate as far toward the midspan due to the radial pressure gradient. Figures 10(a) and 10(b) illustrate experimentally determined contours of the heat transfer coefficient ($W/m^2 K$) for the hub and casing endwall surfaces with $25 \mu m$ roughness. These were obtained using the transient liquid crystal technique at the engine design condition. It should be noted that the maximum heat transfer coefficient measured was limited to $1300 W/m^2 K$ due to restrictions on the starting process of the transient method. Generally the heat transfer coefficient contours reflect those of Mach num-

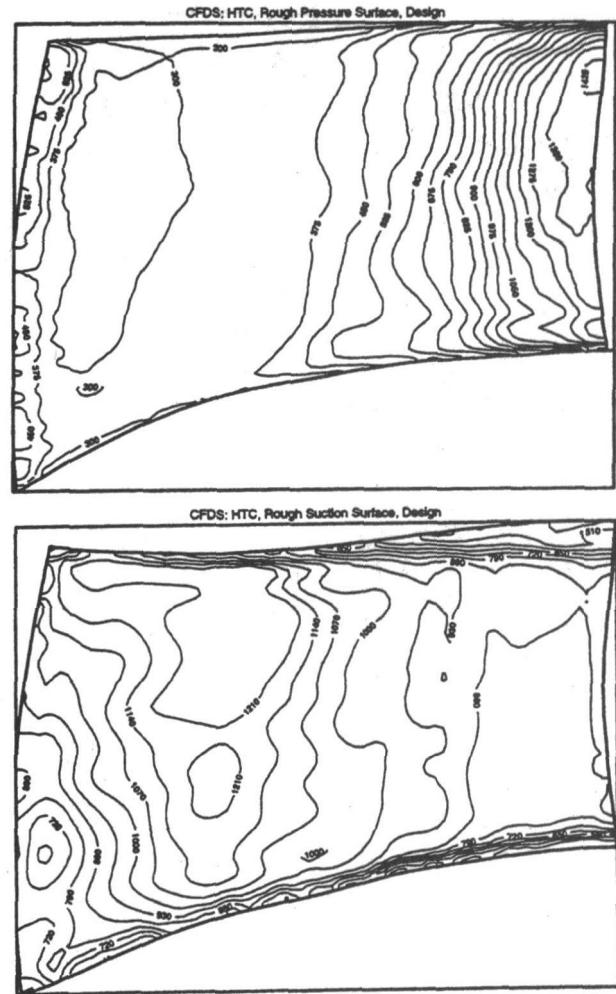


Fig. 9 Calculated contours of heat transfer coefficient ($W/m^2 K$) for the NGV aerofoil surfaces with $30 \mu m$ roughness

ber. An interpretation of these contours based on flow visualization experiments is discussed by Spencer et al. (1995, 1996). One point worthy of note here is that the casing contours illustrate an enhanced region of heat transfer on the suction surface side near the leading edge. The high heat transfer is associated with the horseshoe vortex. The horseshoe vortex does not create a spot of high heat transfer on the hub endwall because, due to

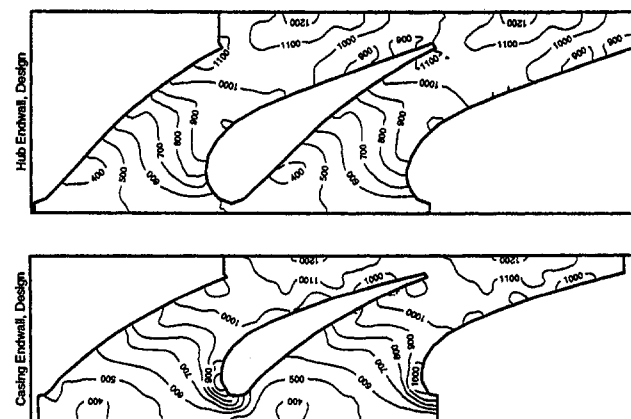


Fig. 10 Experimental contours of heat transfer coefficient ($W/m^2 K$) for the NGV endwalls with $25 \mu m$ roughness

the steep contraction at the hub, the vortex has been lifted off the endwall. The highest levels of heat transfer are observed near the casing leading edge and in the wake region downstream of the trailing edge on the pressure-surface side.

The corresponding predicted contours for smooth and 30 μm roughened surfaces are shown in Figs. 11 and 12. The roughness is shown to result in a marked increase in the level of heat transfer without significantly altering the patterns of the contours. The pattern of the predicted heat transfer contours compare well with those determined experimentally. The aforementioned region of high heat transfer near the leading edge of the casing endwall, and the absence of that enhancement on the hub, has been predicted. The CFDS has also predicted the high heat transfer in the wake regions of the endwalls. Differences between the levels determined by prediction and experiment do appear very near the suction surface toward the trailing edge. Away from this region, the heat transfer measurements generally agreed with those levels predicted with 20 and 30 μm roughness.

Conclusions

The local Mach number and heat transfer coefficient over the aerofoil surfaces and endwalls of a transonic gas turbine nozzle guide vane have been calculated using the CFDS code. A model to predict the effects of roughness has been incorporated into CFDS and heat transfer levels have been calculated for both hydraulically smooth and transitionally rough surfaces. The calculations were compared with pressure measurements and experimental contours of heat transfer coefficient obtained using both thin-film gages and the transient liquid crystal technique.

The CFD code predicted marked increases in heat transfer coefficient with increasing levels of roughness. The code predicted both the isentropic Mach number and heat transfer contour patterns very well and the levels were in reasonable agreement with the experimental measurements at similar levels of surface roughness.

In addition, the calculations identified experimentally observed features associated with secondary flows. For both

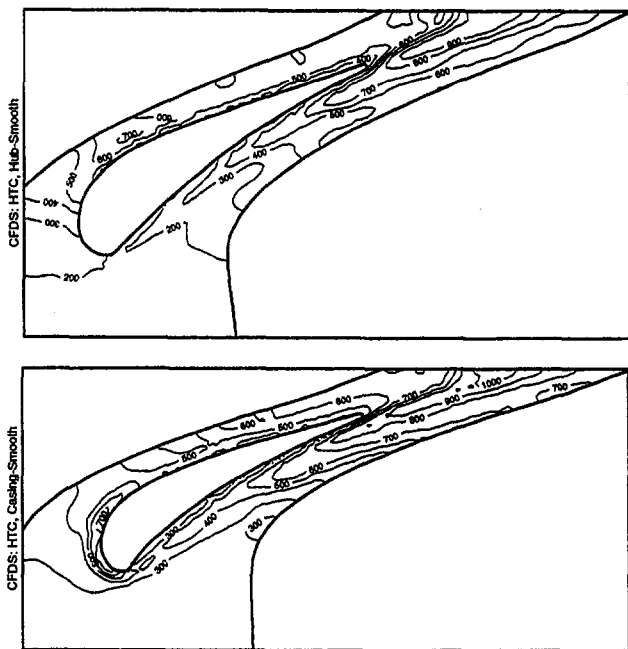


Fig. 11 Calculated contours of heat transfer coefficient ($\text{W}/\text{m}^2 \text{K}$) for the NGV smooth endwalls

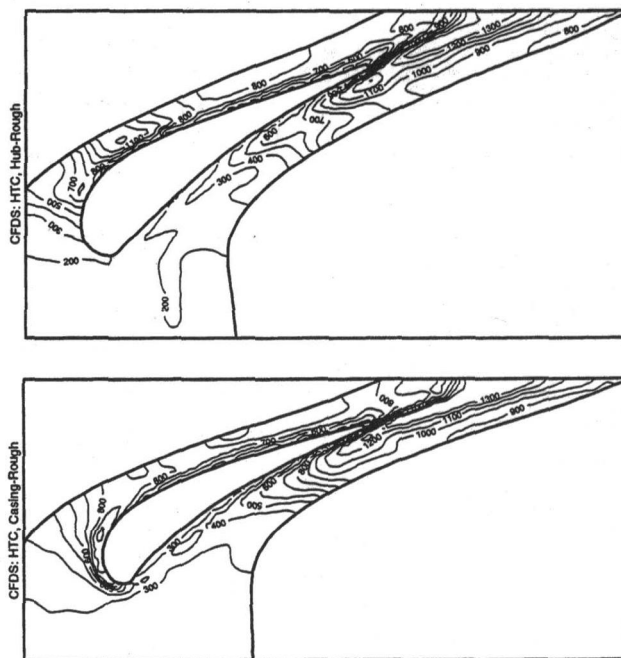


Fig. 12 Calculated contours of heat transfer coefficient ($\text{W}/\text{m}^2 \text{K}$) for the NGV endwalls with 30 μm roughness

smooth and rough conditions, CFDS captured the same heat transfer enhancement around the leading edge of the NGV on the casing endwall due to the horseshoe vortex. The absence of this vortex on the hub endwall was also correctly predicted. The low heat transfer on the late suction surface near-endwall regions due to the secondary flow was observed. Both experiment and CFDS prediction identified high heat transfer in the wake regions on the endwalls.

Acknowledgments

This work was supported by Rolls-Royce plc, the Defence Research Agency, MoD, and DTI. The authors are grateful for the assistance of M. C. Spencer, J. Chew, R. F. Martinez-Botas, and Z. Wang.

References

- Blair, M. F., 1994, "An Experimental Study of Heat Transfer in a Large-Scale Turbine Rotor Passage," *ASME JOURNAL OF TURBOMACHINERY*, Vol. 116, pp. 1–13.
- Boyle, R. J., 1994, "Prediction of Surface Roughness and Incidence Effects on Turbine Performance," *ASME JOURNAL OF TURBOMACHINERY*, Vol. 116, pp. 745–751.
- Cebeci, T., and Bradshaw, P., 1977, *Momentum Transfer in Boundary Layers*, Hemisphere, Washington, DC.
- Cebeci, T., and Chang, K. C., 1978, "Calculation of Incompressible Rough-Wall Boundary Layer Flows," *AIAA Journal*, Vol. 16, No. 7, pp. 730–735.
- Chew, J. W., Taylor, I. J., and Bonsell, J. J., 1996, "CFD Developments for Turbine Blade Heat Transfer," presented at the 3rd Int. Conf. Computers in Reciprocating Engines and Gas Turbines, I. Mech. E., London, UK.
- Coupland, J., 1995, private communication, Rolls-Royce, Derby, England.
- Dunn, M. G., Kim, J., Civinskas, K. C., and Boyle, R. J., 1994, "Time Averaged Heat Transfer and Pressure Measurements, and Comparison With Prediction for a Two-Stage Turbine," *ASME JOURNAL OF TURBOMACHINERY*, Vol. 116, pp. 14–22.
- Guo, S. M., Spencer, M. C., Lock, G. D., Jones, T. V., and Harvey, N. W., 1995, "The Application of Thin Film Gauges on Flexible Plastic Substrates to the Gas Turbine Situation," *ASME Paper No. 95-GT-357*.
- Johnson, P. L., and Johnson, J. P., 1989, *Proc. Seventh Symposium on Turbulent Shear Flows*, Stanford University, 21–23 Aug., pp. 20.2.1–20.2.6.
- Jones, T. V., 1995, "The Thin Film Gauge—A History and New Developments," Invited Lecture, 4th National UK Heat Transfer Conference, *IMEchE Conference Trans.* Manchester, pp. 1–12.

- Kays, W. M., and Crawford, M. E., 1993, *Convective Heat and Mass Transfer*, McGraw-Hill, New York.
- Martinez-Botas, R. F., Main, A. J., Lock, G. D., and Jones, T. V., 1993, "A Cold Heat Transfer Tunnel for Gas Turbine Research on an Annular Cascade," ASME Paper No. 93-GT-248.
- Martinez-Botas, R. F., 1993, "Annular Cascade Aerodynamics and Heat Transfer," DPhil Thesis, Oxford University, United Kingdom.
- Martinez-Botas, R. F., Lock, G. D., and Jones, T. V., 1995, "Heat Transfer Measurements in an Annular Cascade of Transonic Gas Turbine Blades Using the Transient Liquid Crystal Technique," ASME JOURNAL OF TURBOMACHINERY, Vol. 117, pp. 425-431 (also ASME Paper No. 94-GT-172).
- Moore, J. G., 1985, "Calculation of 3-D Flow Without Numerical Mixing," AGARD Lecture Series 140 on 3-D Computational Techniques Applied to Internal Flows in Propulsion Systems.
- Nikuradse, J., 1933, *Forsch. Arb. Ing.-Wes.*, No. 361.
- Northall, J. D., Moore, J. G., and Moore, J., 1987, "Three-Dimensional Viscous Flow Calculation for Loss Predictions in Turbine Blade Rows," *Proc. IMechE Conference on Turbomachinery—Efficiency Prediction and Improvement*.
- Patankar, S. V., 1980, *Numerical Heat Transfer and Fluid Flow*, Hemisphere, Washington, DC.
- Schlichting, H., 1979, *Boundary Layer Theory*, McGraw-Hill, New York.
- Spencer, M. C., Lock, G. D., and Jones, T. V., 1996, "Endwall Heat Transfer Measurements in an Annular Cascade of Nozzle Guide Vanes at Engine Representative Reynolds and Mach Numbers," *International Journal of Heat and Fluid Flow*, Vol. 17(2), pp. 139-147.
- Spencer, M. C., Lock, G. D., Jones, T. V., and Harvey, N. W., 1995, "Endwall Heat Transfer and Aerodynamic Measurements in an Annular Cascade of Nozzle Guide Vanes," ASME Paper No. 95-GT-356.
- Tabakoff, W., 1984, "Review—Turbomachinery Performance Deterioration Exposed to Solid Particulates Environment," ASME *Journal of Fluids Engineering*, Vol. 106, pp. 125-134.
- Turner, A. B., Tarada, F. H. A., and Bailey, F. J., 1985, "Effects of Surface Roughness on Heat Transfer to Gas Turbine Blades," AGARD-CP-390.
- van Driest, E. R., 1956, "On the Turbulent Flow Near a Wall," *Journal of Aeronautical Science*, Vol. 23, pp. 1007-1011.
- Watt, R. M., Jones, T. V., Allen, J. L., Baines, N. C., and George, M., 1990, "A Further Study of the Effects of Thermal-Barrier-Coating Surface Roughness on Gas Turbine Boundary Layers," presented at the ASME Turbo Cogen Conf., Nice.
- Wang, Z., Ireland, P. T., and Jones, T. V., 1990, "Convective Heat Transfer Measurements at Grain Roughened Surface," *Inverse Problems in Engineering*, J. V. Beck, ed., University of Michigan.

An Unsteady Velocity Formulation for the Edge of the Near-Wall Region

D. E. Wilson

A. J. Hanford

Department of Mechanical Engineering,
The University of Texas at Austin,
Austin, TX 78712

A phenomenological model is presented that relates free-stream turbulence to the augmentation of stagnation-point surface flux quantities. The model requires the turbulence intensity, the longitudinal scale of the turbulence, and the energy spectra as inputs for the unsteady velocity at the edge of the near-wall viscous region. The form of the edge velocity contains both pulsations of the incoming flow and oscillations of the streamline. Incompressible results using a single fluctuating component are presented within the stagnation region of a two-dimensional cylinder. The time-averaged Froessling number is determined from the computations. These predictions are compared to existing incompressible experimental data. Additionally, the variations in the surface flux quantities with the longitudinal scale of the incoming free-stream turbulence, the Reynolds number, and the free-stream turbulence intensity are considered.

Introduction

In general, the flow inside a gas turbine is three dimensional and highly unsteady. The unsteadiness arises from several sources, including secondary flow vortices, shock wave passing, periodic variations in the potential flow, and wake passing. It is this last source of flow unsteadiness that has attracted the most attention. The wakes form behind upstream blades and convect downstream and impinge upon other rotor blades. These wakes produce an incident flow, which is periodically unsteady in the mean velocity and contains a relatively high turbulence level. This highly turbulent, impinging wake flow significantly alters the boundary layer around the rotor blade. The two effects that are most important here are wake-induced transition on the suction surface and heat transfer augmentation in the stagnation region. It is this second effect that motivated the development of the unsteady edge model described in this paper.

The leading edge of a gas turbine airfoil represents a stagnation region with a highly unsteady (turbulent) free stream. The highest heat transfer rate is usually measured in this region even when the free stream is laminar or has a low level of turbulence. For a highly turbulent free stream the heat transfer can increase by a factor of 1.5 or 2.0. This phenomenon is of considerable importance in the gas turbine community for two basic reasons. First, an accurate prediction of heat transfer rates is a major design consideration. Second, the mechanism by which free-stream turbulence alters heat and momentum transfer within the stagnation point boundary layer is not completely understood.

The ultimate objective of this research is to develop a model that predicts enhanced stagnation region heat transfer associated with wake-generated free-stream turbulence within gas turbines. This study considers only the effect of free-stream turbulence. The relative motion and unsteady mean flow effects inherent in gas turbines are ignored in this initial formulation. Dullenkopf and Mayle (1994) have, however, developed correlations that consider both incident turbulence and moving wake effects.

The model described in this paper is intended to represent how organized vorticity patterns generally referred to as coherent structures alter the stagnation region boundary layer. These coherent structures can be generated by a number of well-known

mechanisms. Examples of generating devices include rotor blades, turbulence grids, two-dimensional cylinders, splitter plates, and free jets. The structures produced downstream of a circular cylinder due to vortex shedding have vorticity of alternating sign. If the free-stream turbulence is produced by a splitter plate with two streams of differing velocity, large-scale coherent structures of the same sign are produced. The approach adopted in this paper has two advantages. First, by eliminating the extraneous complications of the free stream, a model is developed that provides some fundamental insight into the mechanisms by which organized vorticity fluctuations alter the heat and momentum transfer inside a boundary layer. Second, a considerable experimental data base exists for relatively well-defined free-stream turbulent flows. The key features these vorticity patterns have in common that are important to the present unsteady velocity model are:

- The coherent structures are quasi-two-dimensional and the unsteadiness is quasi-periodic.
- The dominant unsteady energy is confined to a narrow spectrum, allowing its behavior to be captured by only a few frequencies or length scales.
- The vorticity axis is aligned parallel to the major axis of the downstream body, which can be represented as a cylinder.

Furthermore, we represent the effect of these unsteady structures upon the stagnation region boundary layer as a fluctuation of the stagnation point streamline and a pulsation of the incoming flow. And finally, we assume that the role of these structures on the stagnation region is to modify the time-averaged pressure gradient and velocity at the edge of the boundary layer.

Stagnation Point Heat Transfer

Laminar stagnation point theory has been successfully used to predict the heat flux when the flow conditions meet the restrictions built into the model; that is, the free stream must be laminar or at least have turbulence intensities no higher than approximately one percent.

When the flow field departs from these almost ideal conditions, the agreement between theory and experiment diverges. In particular, when spatial and temporal fluctuations are introduced into the free stream, the heat and momentum transfer in the boundary layer can become significantly enhanced. These fluctu-

Contributed by the International Gas Turbine Institute and presented at the 41st International Gas Turbine and Aeroengine Congress and Exhibition, Birmingham, United Kingdom, June 10–13, 1996. Manuscript received at ASME Headquarters February 1996. Paper No. 96-GT-478. Associate Technical Editor: J. N. Shinn.

tuations are commonly referred to as free-stream turbulence, and the phenomena are called *free-stream turbulence effects*. This notation is misleading since the fluctuations can be either vortical (turbulence) or potential (irrotational). The distinction is more than semantics, because both types of fluctuation can lead to enhanced heat and momentum transfer.

Experiments. Surface heat transfer can be correlated using the Froessling number, F_s , defined as

$$F_s \equiv \frac{Nu_D}{Re_D^{1/2} Pr^m}$$

where the exponent, m , varies between 0.33 and 0.40. For most experiments, the Prandtl number is constant and the Froessling number is shortened to $Nu Re_D^{-1/2}$.

Hanford (1994) conducted an extensive review of experimental studies, which measured the augmentation of stagnation-point surface fluxes due to turbulence generated upstream of a circular cylinder. In most of the experiments, the cylinder is placed completely across the test section. Artificially high levels of turbulence are generated upstream of the test cylinder within shear layers formed behind screens. Screens with a rectangular mesh generate shear layer vorticity oriented along both major axes of a tunnel's cross section. Screens composed of parallel rods produce vorticity, again oriented along both major axes of a tunnel's cross section. However, the vorticity component parallel to the rods is stronger than its perpendicular counterpart. The rods, and thus the stronger component of generated vorticity, may be parallel to or perpendicular to the test cylinder. The generated turbulence is greatest just downstream of the screen, decaying with distance. Further, most researchers prefer that the turbulence impinging upon the test model be homogeneous. Screen-generated turbulence is nonhomogeneous for some distance from its origin, which is a function of the mesh geometry. As such, the proximity of the model to the turbulence generator is limited by these considerations. The turbulence that reaches

the test cylinder and, therefore, the heat transfer augmentation, is a complex function of the tunnel geometry and other attributes of the flow.

Researchers have also collected data on the augmentation of surface mass transfer due to free-stream turbulence. In these studies a sublimating solid replaces the thermocouples or heat flux gages employed in heat transfer studies. Further, mass transfer studies naturally supply a constant concentration condition at the surface, which is equivalent to a constant temperature condition in heat transfer studies. Theoretically, the two types of studies may be related to each other through the Reynolds analogy for heat and mass transfer. However, this approach introduces additional uncertainties which may be significant.

Data from fourteen of these studies are displayed in Figs. 1 and 2. Data sets from studies that contained large experimental uncertainties and data taken at Reynolds numbers below 17,000 were excluded. Three curves are also included in these figures. The first is the phenomenological model developed by Smith and Kuethe (1966) for a Reynolds number of 100,000. The other two curves are empirical parabolic fits to the data of Kestin and Wood (1971), and Lowery and Vachon (1975). Froessling calculated a limiting theoretical value for $Nu_D/Re_D^{1/2}$ of 0.945 at a turbulence intensity of zero. The existing experimental results do not collapse to a single curve when correlating $Nu_D/Re_D^{1/2}$ as a function of $Tu_D Re_D^{1/2}$ alone.

Hanford (1994) reviewed these studies in detail and summarized several consensus findings. The conclusions pertinent to the model derived in this paper are given below:

- Four parameters are recognized by current researchers as being suitable for correlating local heat transfer augmentation due to free-stream unsteadiness. These parameters are Nusselt number, Reynolds number, free-stream turbulence intensity, and the nondimensional turbulence scale.
- Surface heat transfer increases for increases in either Reynolds number or turbulence intensity.

Nomenclature

a_n = pulsation parameter for frequency n	k_t = turbulent kinetic energy, m^2/s^2	$U_e = U^*/c^*b^* =$ nondimensional velocity at edge of near-wall viscous region, m/s
b^* = appropriate length scale equivalent to the half-width of the stagnation region, m	N = total number of frequencies for a_n and β_n , respectively	$V^*, v^* =$ fluid velocities perpendicular to body surface outside near-wall viscous region and within near-wall viscous region, respectively
b_n^* = oscillation parameter for frequency m , m	Nu_D = Nusselt number based on the characteristic body length, D^*	$V_e = V_e^*/(V_e^*C^*)^{1/2} =$ nondimensional velocity at edge of near-wall viscous region, m/s
c^* = inviscid strain rate (Hiemenz parameter), s^{-1}	n = nondimensional integral frequency	$X^*, Y^* =$ vertical and horizontal coordinates, respectively, using cylinder centerline as origin
C_H = strain rate constant = 3.7	\hat{n} = nondimensional integral frequency at midpoint of range of energy-containing eddies	$X_p^{**} =$ position of some particle p in terms of X^* due to local velocity fluctuations
D^* = characteristic length on the bluff body; for a circular cylinder this is the diameter, m	$P^*, p^* =$ pressure outside near-wall viscous region and within near-wall viscous region, respectively, N/m	$x^*, y^*, z^* =$ circumferential coordinate on body surface measured from mean forward stagnation line, coordinate perpendicular to body surface measured from surface, and axial or spanwise coordinate, respectively
$E^*(\kappa^*, t^*) =$ three-dimensional energy-spectrum function for the turbulence, m^3/s^2	Re_D = Reynolds number based on the characteristic body length, D^* , and the mean free-stream velocity and kinematic viscosity	
e_n = fluctuating energy at frequency n compared to total energy in fluctuations; $\sum_{n=1}^N e_n^2 = 1$; $e_{on} = e_n$ before normalization	$t^* =$ time, s ; $t = \Omega^*t^* =$ nondimensional time	
$I_u, I_v =$ turbulence intensities using only the fluctuations from the U^* component and V^* component, respectively	$Tu =$ overall turbulence intensity. In this paper, Tu (without a subscript) is equivalent to Tu_∞ .	
	$U^*, u^* =$ circumferential fluid velocities parallel to body surface outside near-wall viscous region and within near-wall viscous region, respectively	

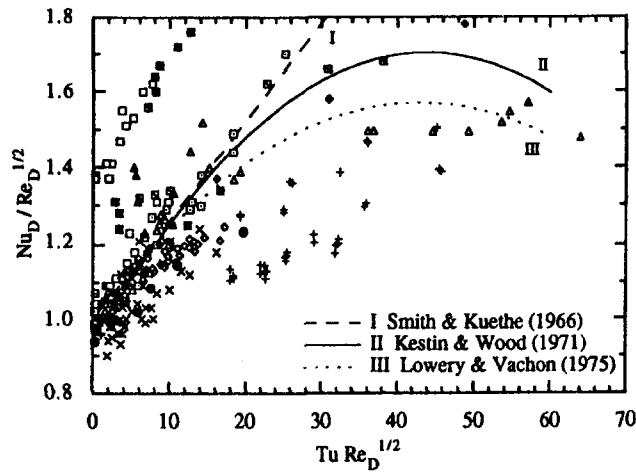


Fig. 1 The augmented stagnation-point heat transfer measurements displayed. The individual data are taken from: \square , Zapp (1950), \blacksquare , Giedt (1951), \blacktriangle , Seban (1960), \boxplus , Kestin et al. (1961), \square , Appelqvist (1965), \square , Smith and Kuethe (1966), \diamond , Kayalar (1969), \blacklozenge , Dyban et al. (1974), \bullet , Sikmanovic et al. (1974), \triangle , Lowery and Vachon (1975), \times , Yardi and Sukhatme (1978), and $+$, Ames and Moffat (1990). The correlation curves are taken from: I, Smith and Kuethe (1966), II, Kestin and Wood (1971), and III, Lowery and Vachon (1975).

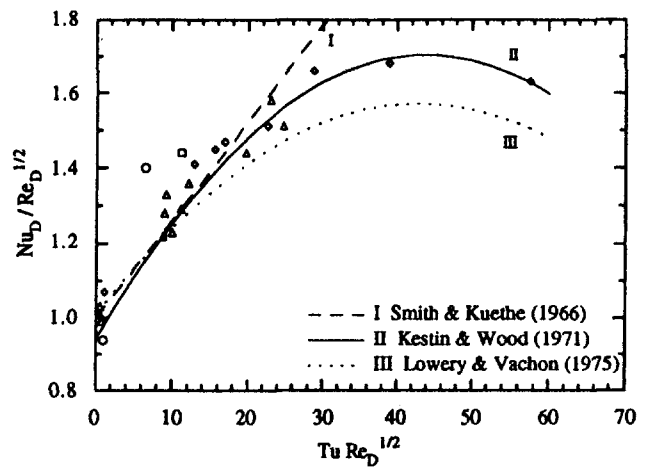


Fig. 2 The augmented stagnation-point mass-transfer measurements converted to equivalent heat transfer data and displayed. The individual data are taken from: \square , Sogin and Subramanian (1961), \circ , Brun et al. (1966), \triangle , Kestin and Wood (1971), and \diamond , Van Dresar and Mayle (1988). The curves are taken from: I, Smith and Kuethe (1966), II, Kestin and Wood (1971), and III, Lowery and Vachon (1975).

- Heat transfer is a maximum when $(\lambda_{\infty}^*/D^*) Re_D^{1/2}$ is approximately 10.
- Either turbulence parameter, $Tu Re_D$ or $Tu Re_D^{1/2}$, does equally well collapsing heat transfer data (Dyban et al., 1974). Because neither parameter includes the nondimensional scale of the free-stream turbulence, they can be used for correlating data only when the variations in the nondimensional scale of turbulence are small (Ames and Moffat, 1990).
- Recently Dullenkopf and Mayle (1995) proposed a new turbulence parameter that accounts for both turbulence intensity and length scale. This parameter, which leads to a simple heat transfer correlation, is related to the pulsation parameter in the unsteady velocity model.

Theory. Attempts at modeling the effect of free-stream turbulence in the stagnation region have been largely unsuccessful primarily because of a misunderstanding of the physical mecha-

nisms. Many researchers have attempted to “force” turbulence into laminar stagnation point theories by simply adding a turbulence transport term into the time-averaged equations. However, most boundary layers are not fully turbulent at the stagnation region and, prior to transition, they are pseudo-laminar and unsteady (Taulbee and Tran, 1988). Or, as Hoshizaki et al. (1975) state, “There seems to be no evidence from [experimental] results that the effect of free-stream turbulence is to trip the laminar boundary layer and make it turbulent. Rather, the transport in the usual laminar boundary layer seems to be augmented.”

Outside the boundary layer, both vortical (turbulence) and potential fluctuations do exist; however, their effect is felt inside the boundary layer in a manner that cannot be satisfactorily modeled by the inclusion of a classic turbulence transport term. When the fluctuations are vortical, the physical mechanism that alters the velocity and temperature profiles is primarily a modification of the time-averaged pressure gradient and boundary-

Nomenclature (cont.)

x, y = nondimensional coordinates, m ; $x = x^*/b^*$, $y = y^*(c^*/\nu_{\infty}^*)^{1/2}$

Z_U, Z_V = normalized fluctuation correlations for the $U^{*'}$ and $V^{*'}$ turbulence components, respectively

α_{Ω} = nondimensional frequency

β_n = nondimensional oscillation parameter at frequency $n = b_n^*/b^*$

β_{01}, β_{02} = constants in definition of oscillation parameter

δ_c^* = thickness of the near-wall viscous region, m

κ^* = wave number of the turbulence fluctuation, m^{-1}

$\hat{\kappa}^*$ = wave number at the center of the range of the energy containing eddies, m^{-1}

λ^* = longitudinal integral length of scale turbulence

$\lambda = \lambda_{\infty}^*/D^*$ = nondimensional integral length scale, m

λ_{1U} = value of λ for Z_{1U}

λ_{1V} = nondimensional transverse integral length scale for Z_{1V}

ν^* = kinematic viscosity, m^2/s

ρ^* = density

$\rho = \rho^*/\rho_{\infty}^*$ = nondimensional density, kg/m^3

Ω^* = characteristic frequency of large-scale, free-stream unsteadiness, rad/s

Ω_n^* = characteristic frequency at frequency $n = n\Omega^*$

Superscripts

$*$ = a dimensional quantity

$'$ = a fluctuating quantity when placed on a velocity

$-$ = a time-independent or mean quantity

$| |$ = magnitude of the quantity within

Subscripts

e = quantity evaluated at edge of near-wall viscous region

n = quantity at frequency n

t = quantity defined using a turbulent model

w = quantity evaluated at the wall

∞ = quantity evaluated at position on mean stagnation streamline just upstream of region influenced by the body in the flow; for a supersonic case, this position is downstream from any shock

layer edge condition. Hoshizaki et al. (1975) also note that, “. . . most of the boundary layer is dominated by viscous forces and that turbulence represents an additional ‘outer flow’ transport term which steepens the relevant wall gradients.”

A few researchers have solved the unsteady boundary-layer equations (Lighthill, 1954; Lin, 1957; Ishigaki, 1970). Although the mathematical analysis is generally sound, most of these studies assume arbitrary periodic flows without attempting to relate the prescribed edge velocity to realistic free-stream conditions. However, Lin (1957) did note a possible application of this work to the flow past turbine blades.

Several papers have appeared that specifically address how a particular free-stream disturbance of engineering interest might alter the stagnation-point flow field. For example, Cebeci et al. (1987) modeled a free-stream flow containing a wake passing perpendicular to the mean flow axis. Bogucz et al. (1988) considered an approaching flow which included a pair of counter-rotating vortices. Both of these studies reported significant unsteady components in the stagnation point velocity and temperature profiles. Paxson and Mayle (1991) represented the outer flow as a steady component, a periodic component from the passing wake, and a fluctuating component arising from the free-stream turbulence. They concluded that the fluctuations in the free-stream may be treated as essentially inviscid effects impressed upon the boundary layer. These investigations provide an understanding of how the spatial and temporal fluctuations of a free-stream influence stagnation-region skin friction and heat transfer.

Research Objective and Methodology

This paper helps to quantify how wake-generated free-stream turbulence alters the wall flux quantities. This approach differs from previous studies in that it relates free-stream parameters such as turbulence intensity, length scale, and energy spectra directly to the unsteady boundary layer equations.

To be useful as an engineering tool, a model must have two essential components. First, it must be relatively simple to use for a wide variety of flow field calculations. Second, the model must include the essential physics to be truly predictive. That is, it must not contain arbitrary parameters that are adjusted to reproduce experimental data accurately for some set of very specific flow conditions.

This paper presents a simple phenomenological model for the unsteady velocity at the edge of the boundary layer and then relates the characteristic free-stream turbulence parameters to this boundary layer edge velocity. It should be emphasized that the edge velocity model represents a *manifestation* of the way in which free-stream vorticity alters the boundary layer. In other words, it does not contain the time-dependent freestream vortical structures but models their *effect* insofar as the stagnation-point flow field is concerned. This simple vorticity model for the free-stream turbulence does, however, characterize the turbulence intensity, length scale effect, and energy spectra. These parameters are then directly related to the velocity edge model.

The overall methodology may be summarized by the following points:

- Model the effect of the turbulence in the near-wall, viscous region using a fluctuating *edge velocity model* containing both a pulsation of the incoming flow and an oscillation of the instantaneous stagnation point.
- Characterize the free-stream turbulence structure by a *simple vorticity model* using the parameters of turbulence intensity, energy spectra, and turbulent length scale.
- Characterize the distortion of the turbulence due to the strain field using Rapid Distortion Theory.
- Incorporate these effects into the boundary layer equations and solve both the unsteady and time-averaged equations.

The unsteady velocity model is restricted to a specialized but quite common free-stream turbulent flow. Specifically, the

model applies to wake-generated or free shear layer generated turbulence. Under these conditions, the turbulent structure is reasonably well defined. In particular, the large-scale structures are assumed to be quasi-two-dimensional and quasi-periodic. This implies that the vorticity is predominantly two dimensional and only a few length scales are necessary to quantify the unsteady behavior. With these ideas in mind, the phenomenological edge model and the simple vorticity model are presented next.

The ultimate objective of this research is a numerical technique that accurately predicts the augmentation of surface flux quantities at the stagnation point of a blunt body for compressible free-stream flows due to wake-induced fluctuations. This paper deals only with the formulation of the unsteady model. Details of the numerical solution of the mean and unsteady boundary layer equations for an incompressible flow are given by Hanford and Wilson (1994).

Unsteady Velocity Model Formulation

In previous work related to this research (Hanford and Wilson, 1994) a model for the fluctuating velocity at the edge of the near-wall viscous region was presented. This model contained the pulsation parameter, a_n , and the oscillation parameter, β_n . A crude model related the intensity of the free-stream turbulence to a_n . The oscillation parameter was determined by matching the numerical simulations with experimental data at two values of $Tu Re_D^{1/2}$. This section describes a simple vorticity model for the free-stream turbulence, which directly relates the parameters to the velocity edge model. The first subsection describes the velocity edge model and the second subsection develops the free-stream vorticity model which quantifies a_n and β_n without the use of correlations or curve fits.

Phenomenological Edge Velocity Model. At the edge of the near-wall viscous region on the mean stagnation streamline, the flow may be described as quasi-laminar. Referring to Fig. 3, the flow may be decomposed into a mean flow plus fluctuating components. These fluctuating components, without regard for their original source, will be felt at the edge of the near-wall viscous region as a series of pulsations along the mean stagnation line plus a series of oscillations about the mean stagnation line. For turbulent eddies there will be a distribution of cylindrical structures each rotating at some frequency that is characteristic of the eddy's size. The effect of this turbulence can be modeled by a finite number of cylindrical structures rotating at a finite number of discrete frequencies. This implies that the mean flow at the edge of the near-wall viscous region will contain an additional number of pulsations and a similar number of oscillations at some discrete frequencies.

On the basis of this model, the edge-velocity parallel to the wall can be written as the sum of the mean flow plus a finite number of pulsations and oscillations.

$$U_e^*(x^*, y^*, t^*) = c^* \left[1 - \sum_{n=1}^N a_n \sin(\Omega_n^* t^*) \right] \times \left[x^* - \sum_{n=1}^N b_n^* \sin(\Omega_n^* t^*) \right] \quad (1)$$

The indicated series are summed from one to some finite value. The nondimensional amplitude, a_n , is the ratio of the fluctuating velocity to the average velocity in the inviscid flow at the edge of the near-wall viscous region. Thus, the first set of terms represents the pulsation of the incoming flow and a particular component, a_n , is equal to $|V_e' / \bar{V}_e^*|$. The dimensional parameter, b_n^* , represents the displacement amplitude of the incoming stagnation streamline. Consequently, this second set of terms represents the oscillation. The parameter c^* is the inviscid strain rate.

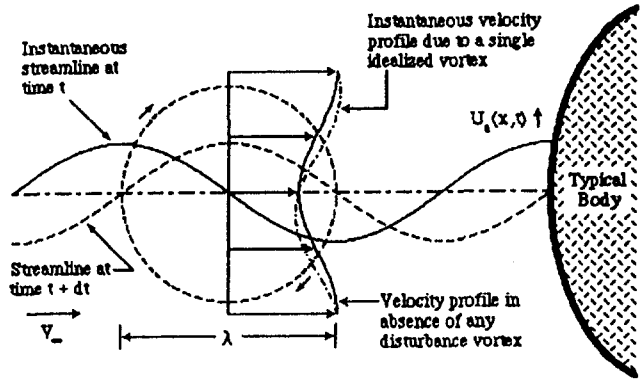


Fig. 3 Simplified vorticity model: stagnation point fluctuation due to a single wavelength vortical structure convected by the mean flow

The relationship given above assumes only N dominant frequencies are necessary to characterize the time dependence of the large-scale vortical structures. This is a valid assumption when the bulk of the fluctuating kinetic energy in the free-stream unsteadiness falls in a narrow frequency band. Fluctuating energy spectra measurements in free-stream turbulence (Britter et al., 1979) and turbulent shear layers (Driver et al., 1987) suggest this simplification to be valid.

An expression for the edge-velocity normal to the body surface may be developed based on Eq. (1) plus the continuity equation. The pulsating nature of the incoming flow is evident in the resulting equation.

$$V_e^*(x^*, y^*, t^*) = -c^*[1 - \sum_{n=1}^N a_n \sin(\Omega_n^* t^*)]y^* \quad (2)$$

In nondimensional form, the two components of the edge velocity may be expressed as

$$U_e(x, t) = [1 - \sum_{n=1}^N a_n \sin(nt)][x - \sum_{n=1}^N \beta_n \sin(nt)] \quad (3a)$$

$$V_e(y, t) = -[1 - \sum_{n=1}^N a_n \sin(nt)]y \quad (3b)$$

The corresponding pressure gradient becomes

$$\alpha_\Omega^2 \frac{\partial U_e}{\partial t} + U_e \frac{\partial U_e}{\partial x} = - \frac{p_{\text{scale}}^*}{\rho_\infty^* (c^* b^*)^2} \frac{1}{\rho_e} \frac{\partial P_e}{\partial x} \quad (4)$$

Because the pressure distribution will be impressed upon the near-wall viscous region by the outer flow, Eq. (4) reduces the governing equations within the near-wall viscous region to a boundary layer formulation. The compressible and incompressible boundary layer equations use a different p_{scale}^* . For incompressible flow $p_{\text{scale}}^* = \rho_\infty^* (c^* b^*)^2$. The pressure gradient is set once a_n , β_n , and α_Ω are known. These parameters are presented below.

Vorticity Model. As illustrated in Fig. 3, the fluctuations in the free stream may be modeled by a simple vorticity model superimposed upon a uniform mean flow. Here the coordinate system using capital letters, (X^*, Y^*) , has its origin at the center of a two-dimensional circular cylinder of diameter D^* . A second coordinate system, (x^*, y^*) , originates at the mean forward stagnation point with the coordinate x^* along the body surface in the circumferential direction. Referring to Fig. 3, the fluctuating components for a single ideal vortex in the free stream may be expressed as

$$U^{*'} = |U_\infty^{*'}| \sin \left[\frac{2\pi}{\lambda_\infty^*} (Y^* - V_\infty^* t^*) \right] \quad (5a)$$

$$V^{*'} = |V_\infty^{*'}| \sin \left[\frac{2\pi}{\lambda_\infty^*} (X^* - V_\infty^* t^*) \right] \quad (5b)$$

In general equation set (5) applies at any point along the stagnation streamline. The X^* position of a particle p at any location as a function of time can be found by noting that $U^{*'} = dX_p^{*'}/dt^*$ and integrating Eq. (5a).

$$X_p^{*'} = \frac{\lambda^*}{2\pi} \frac{|U^{*'}|}{V^*} \cos \left[\frac{2\pi}{\lambda^*} (Y^* - V^* t^*) \right] + \text{constant}$$

Taking the integration constant as zero, the amplitude, $|X_p^{*'}|$, can be written as

$$|X_p^{*'}| = \frac{\lambda^*}{2\pi} \frac{|U^{*'}|}{V^*} = \frac{\lambda^*}{2\pi} \frac{|U^{*'}|}{|U_\infty^{*'}|} \frac{|U_\infty^{*'}|}{\bar{V}_\infty^*} \frac{\bar{V}_\infty^*}{V^*} \quad (6)$$

where $V^* = \bar{V}^* + |V^{*'}|$. The components of the turbulence intensity at some station ‘‘ i ’’ and the instantaneous velocity are defined as

$$Iu_i = \frac{|U_i^{*'}|}{\bar{V}_i^*} \quad Ivi = \frac{|V_i^{*'}|}{\bar{V}_i^*} \quad Tu_i^2 = \frac{Iu_i^2 + Ivi^2}{2} \quad (7)$$

In the definitions of turbulence intensity given by expression set (7), the magnitude of the mean velocity vector is the proper denominator for the first two equations. Away from the body, however, the magnitude of the mean velocity vector may be replaced by the mean uniform velocity, \bar{V}_i^* . Then, in terms of the definitions given in Eq. (15) $|X_p^{*'}|$ becomes

$$|X_p^{*'}| = \frac{\lambda^*}{2\pi} \frac{|U^{*'}|}{|U_\infty^{*'}|} \left[Iu_\infty \left[\frac{\bar{V}^*}{\bar{V}_\infty^*} + Iu_\infty \frac{V^{*'}}{|V_\infty^{*'}|} \right]^{-1} \right] \quad (8)$$

Oscillation Parameter, β_n . To determine the oscillation parameter, a working definition of the edge of the near-wall viscous region is necessary. A sketch of this region (shown in Fig. 4) indicates the various length scales referred to in this analysis. For a laminar, or low-turbulence free stream, the edge of the boundary layer is well defined. This relation is

$$\frac{\delta_e^*}{D^*} = \frac{2.4}{C_H^{1/2}} \text{Re}_D^{-1/2} \quad (9)$$

Referring to Fig. 4, we see that $\delta_e^* = 2.4\delta_\eta^*$ where δ_η^* is the (Hiemenz) viscous length scale. However, for a highly turbulent free stream the boundary layer edge is more difficult to determine. Nevertheless, an expression is needed in order to proceed with this analysis. Based on the analysis of Taulbee and Tran (1988), the edge of the boundary layer, δ_e^* , is given by

$$\delta_e^* = 2.4(\nu_e^*/c^*)^{1/2} \quad (10)$$

where $c^* = C_H \bar{V}_\infty^*/D^*$ and ν_e^* is the ‘‘effective’’ viscosity given by $\nu_e^* = \nu^* + \nu_i^*$. Taulbee and Tran (1989) define the turbulent eddy viscosity as $\nu_i^* = 0.09k_i^{1/2}\lambda_\infty^*$, where $k_i = 1.5 (Tu_\infty \bar{V}_\infty^*)^2$. We have modified their expression by using an effective viscosity, whereas they use only the turbulent eddy viscosity in Eq. (10). Substituting these expressions into Eq. (10) yields

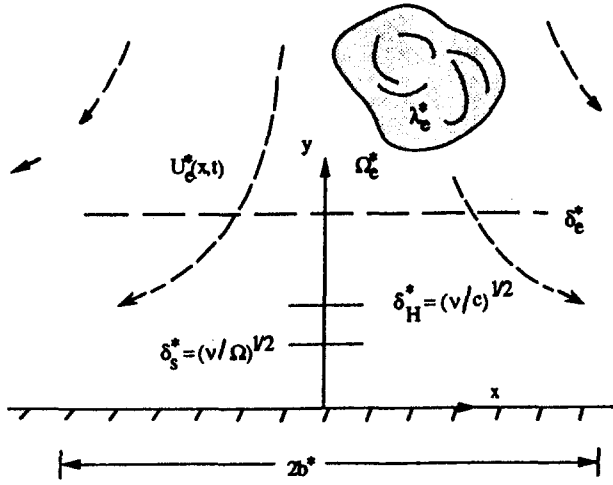


Fig. 4 Sketch of the near-wall viscous region showing a turbulent structure about to impinge on the boundary layer

$$\frac{\delta_e^*}{D^*} = \frac{2.4}{(C_H Re_D)^{1/2}} \left[1 + 0.11 Tu_\infty Re_D \frac{\lambda_\infty^*}{D^*} \right]^{1/2} \quad (11)$$

The parameter C_H has a value of 4.0 from potential flow theory. In practice C_H is approximately 3.7 (Kwon et al., 1983) for flows at high Re_D and low free-stream turbulence in facilities with negligible tunnel blockage. In general, C_H is a function of Tu_∞ , the flow blockage parameter, and Re_D . These effects are implicitly included in Eq. (11) by the terms between the brackets, thus C_H is taken as 3.7 in our analysis.

Outside the near-wall viscous region, the mean velocity is given by

$$\bar{V}_e^* = -c^* y^* \quad (12)$$

At the edge of the near-wall viscous region, y^* is equal to δ_e^* , leading to

$$\frac{\bar{V}_e^*}{V_\infty^*} = \frac{\beta_{02}}{Re_D^{1/2}} \quad (13)$$

$$\beta_{02} = 2.4 C_H^{1/2} \left[1 + 0.11 Tu_\infty Re_D \frac{\lambda_\infty^*}{D^*} \right]^{1/2} \quad (14)$$

When the free-stream Reynolds number is large relative to unity, $|X_{\beta'}^*|$ from Eq. (8) and evaluated at $y^* = \delta_e^*$ becomes

$$|X_{\beta'}^*|_e = \frac{\lambda_e^*}{2\pi} \left| \frac{U_e^{*'}}{U_\infty^{*'}} \right| \times Iu_\infty Re_D^{1/2} \left[b_{02} + Iu_\infty Re_D^{1/2} \frac{V_e^{*'}}{|V_\infty^{*'}|} \right]^{-1} \quad (15)$$

At the edge of the near-wall viscous region, $|X_{\beta'}^*|_e$ is equivalent to the magnitude of an oscillation in the velocity profile. These oscillations are included in the assumed edge velocity by the parameters b_n^* . Therefore, setting b_n^* equal to $|X_{\beta'}^*|_e$ and defining e_n as the normalized fluctuating energy for mode n yields

$$b_n^* = \frac{e_n}{2\pi} \lambda_e^* \left| \frac{U_e^{*'}}{U_\infty^{*'}} \right| Iu_\infty Re_D^{1/2} \left[\beta_{02} + Iu_\infty Re_D^{1/2} \frac{V_e^{*'}}{|V_\infty^{*'}|} \right]^{-1} \quad (16)$$

Equation (16) provides a description for the oscillation parameters based upon the simplified vortex model. However, λ_∞^* , Iu_∞ , and Iv_∞ are generally not measured in experimental studies. Two assumptions will be useful here. The first assumes the free-stream turbulence is approximately isotropic. The second assumes λ_∞^* is equal to λ_∞^* . Thus, Eq. (16) written in nondimensional form becomes

$$\beta_n = \beta_{01} e_n \left(\frac{\lambda_\infty^*}{D^*} \right) \left| \frac{U_e^{*'}}{U_\infty^{*'}} \right| \frac{Tu_\infty Re_D^{1/2} \left| \frac{V_e^{*'}}{V_\infty^{*'}} \right|}{\beta_{02} + Tu_\infty Re_D^{1/2} \left| \frac{V_e^{*'}}{V_\infty^{*'}} \right|} \quad (17)$$

where $\beta_{01} = 90/\pi$. The constant β_{01} arises from nondimensionalizing b_n^* by the scale $b^* = D^*/180$.

Pulsation Parameters, a_n . As the oscillation parameters are related to the fluctuations in the x^* direction, the pulsation parameters are related to the fluctuations in the y^* direction. Therefore, each individual fluctuation, a_n , is given by

$$a_n = e_n \frac{|V_e^{*'}|}{\bar{V}_e^*} \quad (18)$$

writing a_n as

$$a_n = e_n \frac{|V_e^{*'}|}{|V_\infty^{*'}|} \frac{|V_\infty^{*'}|}{\bar{V}_\infty^*} \frac{\bar{V}_\infty^*}{\bar{V}_e^*}$$

and using Eq. (13) yields

$$a_n = e_n \frac{Tu_\infty Re_D^{1/2}}{\beta_{02}} \left| \frac{V_e^{*'}}{V_\infty^{*'}} \right| \quad (19)$$

This final expression also assumes isotropic turbulence in the free stream. The parameter e_n again represents the percentage of the fluctuating energy in mode n compared with the total fluctuating energy.

Energy Parameters, e_n . The parameter e_n introduced above represents the amount of energy in mode n compared with the total energy in fluctuating modes. Theoretically, the summation of the e_n across the energy spectrum should be one. Therefore, e_n is a nondimensional fluctuating energy. It is the fluctuating energy at mode n divided by the total fluctuating energy.

To simplify the task of quantifying the nondimensional fluctuating energy parameters, several assumptions are useful:

- (i) The turbulence in the free stream is at least approximately isotropic.
- (ii) The free-stream turbulence modes at the highest wave numbers are dissipated before reaching the edge of the near-wall viscous region.

For an isotropic flow, Hinze (1975, p. 205) gives the turbulence intensity as a function of the three-dimensional energy-spectrum function, $E^*(\kappa^*, t^*)$:

$$\frac{3}{2} Tu^2 \bar{V}^{*2} = \int_0^\infty E^*(\kappa^*, t^*) d\kappa^* \quad (20)$$

$$\kappa^* = \frac{n\Omega^*}{\bar{V}^*}$$

Here κ^* is the dimensional wave number, t^* is the dimensional time, n is the nondimensional frequency, and Ω^* is the characteristic frequency of the freestream unsteadiness. Nondimensionally, the variables above are

$$E(\kappa, t) = \frac{\hat{\kappa}^* E^*(\kappa^*, t^*)}{\bar{V}^{*2}} \quad \kappa = \frac{\kappa^*}{\hat{\kappa}^*}$$

$$\frac{3}{2} Tu^2 = \int_0^\infty E(\kappa, t) d\kappa \quad (21)$$

The parameter $\hat{\kappa}^*$, which is at the center of the range of energy-containing eddies, is the wave number at which $E^*(\kappa^*, t^*)$ is a maximum.

Again for an isotropic flow, Hinze (1975, p. 247) presents the von Karman interpolation function for $E^*(\kappa^*, t^*)$. The von Karman function is fairly accurate at the lower wave numbers, including the range of the energy-containing eddies, but it deviates at the highest wave numbers:

$$E^*(\kappa^*, t^*) = \frac{55}{9} \frac{\Gamma(5/6)}{\sqrt{\pi} \Gamma(1/3)} \frac{Tu^2 \bar{V}^{*2}}{\hat{\kappa}^*} \frac{\left(\frac{\kappa^*}{\hat{\kappa}^*}\right)^4}{\left[1 + \left(\frac{\kappa^*}{\hat{\kappa}^*}\right)^2\right]^{17/6}}$$

$$E(\kappa, t) = 1.4528 Tu^2 \frac{\kappa^4}{[1 + \kappa^2]^{17/6}} \quad (22)$$

The gamma function is denoted by Γ . An analysis of Eq. (22) reveals that $E(\kappa, t)$ is a maximum when κ is $2\sqrt{3}/5 = 1.5492$ rather than unity as the definitions above would imply. So that $\hat{\kappa}$ will correspond to the peak value of $E(\kappa, t)$, a value of 1.5492 will be used for $\hat{\kappa}$ in the work that follows.

From the introduction above, the definition for e_n comes in two parts. From Eqs. (19) and (21), and the relation between a_n and the edge turbulence intensity presented below, e_n^2 is proportional to $E(\kappa_n, t)$. More specifically,

$$e_n \propto \frac{a_n}{Tu} \propto \frac{\sqrt{E(\kappa_n, t)}}{Tu}$$

Further, as a result of assumption (ii), the individual values of e_n^2 must, over the entire energy spectrum, sum to unity:

$$e_{on}^2 \equiv \frac{2}{3} \frac{E(\kappa_n, t)}{Tu^2} = 0.96850 \frac{\kappa_n^4}{[1 + \kappa_n^2]^{17/6}} \quad (23)$$

$$e_n^2 \equiv \frac{e_{on}^2}{\sum_i e_{oi}^2} \quad (24)$$

The normalization presented by the first equality in Eq. (23) is suggested by the integration of the three-dimensional energy spectrum function given by Eq. (21). Discretizing e_n^2 as indicated by Eq. (23) is equivalent to a numerical integration of the energy spectrum using the midpoint rule.

Because the e_n are effectively part of a numerical integration of a peaked function, $E(\kappa, t)$, an odd number of components is selected. Further, the nondimensional frequency of the component in the middle of the distribution, \hat{n} , will correspond to the wave number $\hat{\kappa}$. Therefore, an appropriate form for the wave number κ_n for use with Eq. (23) may be defined.

$$\kappa_n = \hat{\kappa} \frac{n}{\hat{n}} \quad (25)$$

For only one component in the series ($N = 1$) e_1 is unity. For a series of five components ($N = 5$) the middle component is the third, so \hat{n} is 3, and the values for e_n are tabulated in Table 1.

Distortion Effects Due to Mean Strain. The expressions for the pulsation and oscillation parameters included terms that account for the amplification and attenuation of the fluctuating components by the mean strain field as the unsteady flow ap-

Table 1 Values of e_n for an edge parameter series of five components

n/\hat{n}	κ_n	e_{on}^2	e_n^2	e_n
1/3	0.51640	0.035250	0.05478	0.23405
2/3	1.0328	0.14089	0.21894	0.46791
1	1.5492	0.17405	0.27047	0.52007
4/3	2.0656	0.15919	0.24738	0.49737
5/3	2.5820	0.13413	0.20843	0.45654
Sum		0.64351	1.00000	2.17594

proaches the stagnation region. To account for this effect, rapid distortion theory is used.

Rapid distortion theory describes the deformation of turbulence solely due to an external strain field. For turbulence convected by a flow approaching a two-dimensional stagnation point, the mean flow creates the strain field. If the turbulence is not deformed by nonlinear interactions while it is swept by the body, such as viscous dissipation, then the turbulence experiences a rapid distortion due to passing the body. Hunt (1973) developed theoretical expressions for the local stresses about a blunt body in crossflow due to a rapid distortion.

- The approaching fluid is assumed to be incompressible.
- For large eddies, when $\lambda_*^*/D^* \rightarrow \infty$, $V^{*'} decreases, $U^{*'} increases and $W^{*'} does not change. The relevant results along the mean stagnation streamline for the present model are$$$

$$\frac{U_e^{*'} U_e^{*'}}{V_*^{*'} V_*^{*'}} \cong \left(2 - \frac{\bar{V}_e^*}{\bar{V}_*^*}\right)^2 \quad \text{and} \quad \frac{\bar{V}_e^{*'} \bar{V}_e^{*'}}{\bar{V}_*^{*'} \bar{V}_*^{*'}} \cong \left(\frac{\bar{V}_e^*}{\bar{V}_*^*}\right)^2$$

- For eddies that are roughly the same size as the cylinder diameter, when λ is unity, the turbulence components generally are not amplified nor attenuated from their free-stream values.
- For small eddies, when $\lambda_*^*/D^* \rightarrow 0$, $V^{*'} increases, $U^{*'} decreases and $W^{*'} increases (by less than $V^{*'}).$$$ These results on the mean stagnation streamline are$

$$\frac{U_e^{*'} U_e^{*'}}{V_*^{*'} V_*^{*'}} \approx \frac{3}{4} \frac{\bar{V}_e^*}{\bar{V}_*^*} \left[\ln \left(\frac{4\bar{V}_*^*}{\bar{V}_e^*} \right) - 1 \right]$$

$$\frac{\bar{V}_e^{*'} \bar{V}_e^{*'}}{V_*^{*'} V_*^{*'}} \cong \frac{3}{4} \left[\frac{\bar{V}_*^*}{\bar{V}_e^*} + \frac{1}{2} \frac{\bar{V}_e^*}{\bar{V}_*^*} \ln \left(\frac{4\bar{V}_*^*}{\bar{V}_e^*} \right) \right]$$

Using the expression for \bar{V}_e^* from Eq. (13), we can summarize the results below when λ_*^*/D^* is much greater than unity:

$$\frac{U_e^{*'} U_e^{*'}}{V_*^{*'} V_*^{*'}} \cong \left(2 - \frac{\beta_{02}}{\text{Re}_D^{1/2}}\right)^2 \quad (26a)$$

$$\frac{\bar{V}_e^{*'} \bar{V}_e^{*'}}{V_*^{*'} V_*^{*'}} \cong \left(\frac{\beta_{02}}{\text{Re}_D^{1/2}}\right)^2 \quad (26b)$$

and when λ_*^*/D^* is much less than unity

$$\frac{U_e^{*'} U_e^{*'}}{V_*^{*'} V_*^{*'}} \cong \frac{3}{4} \frac{\beta_{02}}{\text{Re}_D^{1/2}} \left[\ln \left(4 \frac{\text{Re}_D^{1/2}}{\beta_{02}} \right) - 1 \right] \quad (27a)$$

$$\frac{\bar{V}_e^{*'} \bar{V}_e^{*'}}{V_*^{*'} V_*^{*'}} \cong \frac{3}{4} \left[\frac{\text{Re}_D^{1/2}}{\beta_{02}} + \frac{1}{2} \frac{\beta_{02}}{\text{Re}_D^{1/2}} \ln \left(4 \frac{\text{Re}_D^{1/2}}{\beta_{02}} \right) \right] \quad (27b)$$

While Eqs. (26) and (27) are accurate for the limiting values of λ_*^*/D^* , most real cases, including experiments, fall some-

where between these extremes. As a first approximation at expressions for any λ_{ij}^*/D^* , an exponential combination of the expressions in Eqs. (26) and (27) is suggested by the data taken by Britter et al. (1979). The basic form of the proposed interpolating function is

$$Z_j = \zeta_{ja}[1 + \zeta_{jb} \exp(\zeta_{jc}\lambda)] \quad (28)$$

In this form λ is the nondimensional integral length scale, λ_{ij}^*/D^* , Z_j is the normalized fluctuation correlation, and ζ_{ja} , ζ_{jb} , and ζ_{jc} are constants. The subscript “ j ” may be either U or V :

$$Z_U = \left| \frac{U_e^{*'}}{V_{\infty}^{*'}} \right|^2 \quad Z_V = \left| \frac{V_e^{*'}}{V_{\infty}^{*'}} \right|^2 = \frac{\overline{V_e^{*'} V_e^{*'}}}{\overline{V_{\infty}^{*'} V_{\infty}^{*'}}} \quad (29)$$

Three known values of Z_j are necessary to determine the constants in the general form Eq. (28). From the rapid distortion expressions above, Z_j is known as λ approaches zero and as λ approaches infinity. The final constant is set from experimental data using the point where Z_j is unity, λ_{1j} . From the data presented in Britter et al. (1979), λ_{1V} is approximately 1.12. Because the lateral integral length scale is roughly half of the longitudinal integral length scale within a grid-generated turbulent flow (Hinze, 1975), λ_{1U} should be one half of λ_{1V} :

$$Z_j = Z_{\infty j} + (Z_{0j} - Z_{\infty j}) \exp \left[\frac{\lambda}{\lambda_{1j}} \ln \left(\frac{Z_{1j} - Z_{\infty j}}{Z_{0j} - Z_{\infty j}} \right) \right] \quad (30)$$

The constant $Z_{\infty j}$ refers to the expressions from equation set (26), Z_{0j} refers to equation set (27), and Z_{1j} , which here is unity, refers to the values at λ_{1j} .

Nondimensional Frequency, α_{Ω} . The nondimensional frequency, α_{Ω} , which appears in Eq. (4), is defined as

$$\alpha_{\Omega}^2 \equiv \frac{\Omega^*}{c^*} = \frac{D^* \Omega^*}{c_{H1} \bar{V}_{\infty}^*} \quad (31)$$

The frequency of the large-scale unsteadiness may be expressed in terms of the local free-stream velocity and the longitudinal integral length scale, λ^* :

$$\Omega^* = 2\pi \frac{\bar{V}^*}{\lambda^*} \quad (32)$$

The magnitude of the mean velocity at the edge of the boundary layer is

$$\bar{V}_e^* = \beta_{02} \bar{V}_{\infty}^* \text{Re}_D^{-1/2} \quad (33)$$

Thus at the edge of the boundary layer where y^* is δ_e^*

$$\alpha_{\Omega}^2 = 2\pi \frac{D^*}{\lambda_e^*} \frac{\beta_{02}}{C_H \text{Re}_D^{1/2}} \quad (34)$$

Assuming $\lambda_e^*/\lambda_{\infty}^*$ is equal to 1 yields

$$\alpha_{\Omega}^2 = 7.84 \frac{D^*}{\lambda_{\infty}^*} \left[1 + 0.11 T u_{\infty} \text{Re}_D \frac{D^*}{\lambda_{\infty}^*} \right]^{1/2} \text{Re}_D^{-1/2} \quad (35)$$

Physical Interpretation of the Model. The model presented in this paper represents a first approximation for a very complex flow field. It does, however, contain what are thought to be the essential parameters necessary to describe the effect of a turbulent free stream upon the stagnation-point heat transfer rate. These parameters are the free-stream turbulence intensity, $T u_{\infty}$, the longitudinal integral length scale, λ_{∞} , and the Reynolds number, Re_D . These parameters appear naturally as part of the derivation. In this sense this analysis represents a more fundamental approach in that experimental correlations or curve fits

were not employed. This model does contain several important assumptions and approximations, which are:

- The vorticity model assumes that the free-stream turbulence is generated by a turbulent wake, or free shear layer, which is characterized by large coherent structures.
- The vortical structures are assumed to be quasi-two-dimensional with their vorticity aligned with the body's spanwise axis.
- The large-scale, coherent structures are assumed to exist only at a few discrete frequencies or length scales.
- The effect of these coherent structures modifies the edge velocity and mean pressure gradient through the pulsation parameter, a_n , the oscillation parameter, β_n , and the frequency parameter, α_{Ω} .
- The analysis ignores the existence of small-scale, random turbulence that may be entrained within the stagnation region boundary layer.

A sketch of the near-wall viscous region, Fig. 4, shows a typical coherent structure about to impinge upon the edge of the boundary layer denoted by δ_e^* which is defined in Eq. (11). For typical free-stream parameters found in a gas turbine, δ_e^*/D^* varies between 0.005 and 0.05. The width of the stagnation region is characterized by the oscillation parameter, b_n^* . In the analysis, the coordinate x^* and the oscillation parameter are scaled by $b^* = D^*/180$. From Eqs. (16) and (17), $\beta_n = b_n^*/b^*$ and is nearly independent of Re_D . Calculations confirm that β_n varies by less than 10 percent when Re_D varies from 5×10^4 to 10^6 . However, β_n varies almost linearly with λ . In most of the numerical simulations, $\beta_n \leq 1$. Its maximum value is approximately 10 when $T u_{\infty} \text{Re}_D^{1/2} = 60$ and $\lambda = 0.5$. These values correspond to an oscillation of roughly ± 10 deg about the mean stagnation point or a displacement of $\pm 0.056 D^*$. Thus, with this scaling, the edge of the unsteady boundary layer and the width of the oscillation are approximately the same.

The pulsation parameter, a_n , has a more complex behavior which is seen by writing Eq. (19) as

$$a_n = e_n \frac{T u_{\infty} \text{Re}_D^{1/2}}{2.4 C_H \left[1 + 0.11 T u_{\infty} \text{Re}_D \frac{\lambda_{\infty}^*}{D^*} \right]^{1/2}} \left| \frac{U_e^{*'}}{V_{\infty}^{*'}} \right| \quad (37)$$

For large values of $T u_{\infty} \text{Re}_D$, a_n varies inversely with λ . In most of the numerical solutions, a_n varies from approximately 2 to 5.

An important characteristic to note in this unsteady edge model is that the unsteady velocities in the stagnation region are large compared to the mean velocities. In fact, for most values typical of free-stream turbulence, $|V_e^{*'}|/|\bar{V}_e^*|$, which is equal to a_n , and $|U_e^{*'}|/|\bar{U}_e^*|$, which is proportional to β_n , are greater than unity at $x = 0$. Thus, the stagnation region boundary layer is highly unsteady.

A final point concerning the pulsation parameter can be made by evaluating a_n at $y_e = 1$, and noting that $y = y^*(c^*/\nu_{\infty}^*)^{1/2}$ and $V_e = V_e^*/(c^*/\nu_{\infty}^*)^{1/2}$. For this case, a_n becomes

$$a_n|_{y_e=1} = e_n \frac{|V_e^{*'}|}{(c^*/\nu_{\infty}^*)^{1/2}} = e_n \frac{|V_{\infty}^{*'}|}{(c^*/\nu_{\infty}^*)^{1/2}} \left| \frac{V_e^{*'}}{V_{\infty}^{*'}} \right| \quad (38)$$

In terms of the turbulence parameter, $T u_a$, defined by Dullenkopf and Mayle (1995), this expression becomes

$$a_n = e_n T u_a \left| \frac{V_e^{*'}}{V_{\infty}^{*'}} \right|$$

The effective turbulence level, $T u_{\text{eff}}$, is obtained by integrating over the energy spectrum, or in our case by summing over

the discretized spectrum. Thus Tu_{eff} defined in this manner is analogous to their Tu_λ apart from the turbulence attenuation factor $|V_e^{*'}|/|V_\infty^{*'}|$.

The final model parameter is the nondimensional frequency, α_Ω . It enters the model through the pressure gradient defined in Eq. (4). It also appears in the nondimensional form of the boundary layer equations as an important scaling parameter. Physically the nondimensional frequency measures the unsteadiness and relates the unsteady diffusion of momentum (vorticity) inside the boundary layer to the mean momentum. From Eq. (31) and Fig. 4, we see that $\alpha_\Omega^2 \propto \delta_H^*/\delta_\infty^*$.

In conclusion, a model for the effect of a specific type of free-stream turbulence is presented. It contains three nondimensional parameters. By inspecting the forms for these parameters, all three parameters are functions of Tu_∞ , Re_D , and λ_∞^*/D^* .

Results and Discussion

There are two levels at which the unsteady velocity model can and should be validated by comparing to experimental data. Obviously, from the perspective of an engineering analysis and design tool, the model must be able to predict the surface heat transfer for given free-stream turbulent parameters. But also, on a more fundamental level, the unsteady fluctuations that the turbulent free-stream imposes upon the edge of the boundary layer should be accurately represented. To validate the model at this level is difficult because most researchers do not report these components of the turbulence intensity. Further, if this information is given, the sampling location is often outside of the boundary layer for a stagnation point flow due to instrumentation limitations. Nevertheless, an attempt is presented here to quantify the model in some approximate sense at this fundamental level.

Validation of the Model Parameters, a_n and β_n . Hijikata et al. (1982) provide measurements for the amplification of the turbulence intensity as the flow approaches the stagnation region of a two-dimensional cylinder. Specifically, they measured the radial and circumferential components of turbulence intensity along the mean stagnation streamline from an upstream position where the turbulence was effectively isotropic to positions close to the cylinder surface. At a position near the cylinder but outside the boundary layer the pertinent values are:

$$Re_D = 54,000$$

$$\lambda_\infty^*/D^* = 0.09$$

$$Tu = 0.052$$

$$Tu_{e,y} = 0.42$$

$$Tu_{e,x} = 0.30$$

The pulsation parameter, a_n , in this model equals the magnitude of the fluctuating velocity divided by the average velocity normal to the stagnation point at the edge of the boundary layer. For a single component, $N = 1$, the value for a_1 is given by

$$a_1 = e_1 \frac{|V_e^{*'}|}{\bar{V}_e^*} = e_1 \frac{Tu_\infty Re_D^{1/2}}{\beta_{02}} \left| \frac{V_e^{*'}}{V_\infty^{*'}} \right|$$

Using the experimental values for Tu_∞ and Re_D and Eqs. (14) and (27b) we find $a_1 = 0.453$. This agreement is within 7 percent of the experimental value for $Tu_{e,y}$. While this agreement is excellent, it should be noted that the experimentally determined $Tu_{e,y}$ was taken at $y^*/D^* = 0.1$ while the corresponding theoretical value from Eq. (11) is $\delta_e^*/D^* = 0.03$.

The next task is finding $|U_e^{*'}|/\bar{V}_e^*$. Setting $N = 1$ and extracting the fluctuating component from U_e in Eq. (3a) gives $|U_e^{*'}| = \beta_1(c^*b^*)$. Finally, dividing by \bar{V}_e^* yields

$$\frac{|U_e^{*'}|}{\bar{V}_e^*} = \frac{C_H}{180} \frac{Re_D^{1/2}}{\beta_{02}} \beta_1 \quad (36)$$

From Eq. (17) $\beta_1 = 0.71$, thus $|U_e^{*'}|/\bar{V}_e^* = 0.14$ while the corresponding experimental value is $Tu_{e,\theta} = 0.30$. Here the cause for the poor agreement is directly related to the strong attenuation of the turbulent fluctuations very near the body's surface. Equation (27a) gives $|U_e^{*'}|/\bar{V}_e^* = 0.085$. Upon adjusting the location to $\delta_e^*/D^* = 0.1$, to be consistent with the experiment, we find that $|U_e^{*'}|/\bar{V}_e^* = 0.32$. Although this test cannot be considered as a validation of the model, it does provide some level of confidence.

Heat Transfer Predictions. The ultimate test for any theoretical model is its ability to predict quantities of engineering interest with acceptable accuracy. The key word here is "predict," since many semi-empirical models can reproduce experimentally measured quantities by proper adjustment of the model parameters. The quantity of engineering interest is surface heat transfer or its nondimensional representation given by the Nusselt number.

The local Nusselt number based on the cylinder diameter, D^* , the dimensional surface heat flux, q_w^{**} , and the thermal conductivity of the fluid, k^* , is

$$Nu_D = \frac{q_w^{**} D^*}{k^*(T_w^* - T_\infty^*)} = - \frac{D^*}{(T_w^* - T_\infty^*)} \left(\frac{\partial T^*}{\partial y^*} \right)_{y^*=0}$$

The unsteady response within the near-wall viscous region, or boundary layer, can be determined by solving the instantaneous momentum and energy equations. This solution approach analytically decomposes the nondimensional governing equations into time-independent and time-dependent expressions. The time-dependence is modeled with a few frequencies and is defined using a finite Fourier expansion in time. The individual time-dependent expressions are further simplified for the current application by using a high-frequency approximation. This model has been used successfully in both incompressible and compressible formulations.

Details of the formulation and solution of the mean (time-averaged) and unsteady boundary layer equations for an incompressible flow are given by Hanford and Wilson (1994). Interested readers should consult this reference for the details. The corresponding compressible formulation can be found in the dissertation by Hanford (1994). The incompressible code was used to predict the temperature gradient from which the Nusselt number was determined. No arbitrary parameters were adjusted in an attempt to match the experimental data. Results of the model predictions are given in Figs. 5 and 6. The general trends

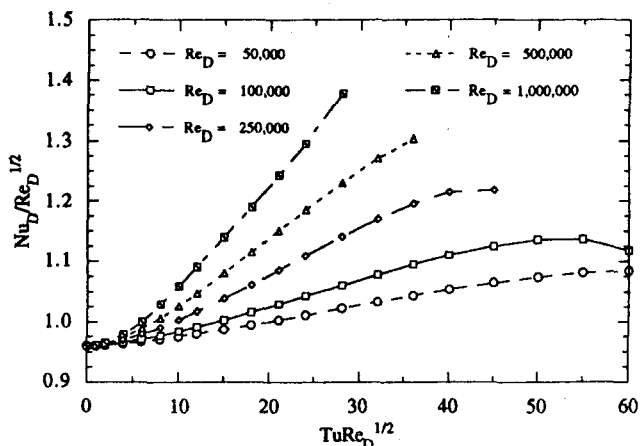


Fig. 5 Nondimensional heat transfer versus $Tu Re_D^{1/2}$ for $\lambda_\infty^*/D^* = 0.032$

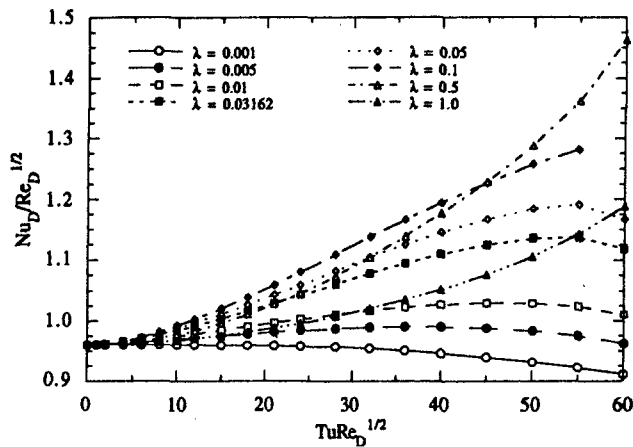


Fig. 6 Nondimensional heat transfer versus $Tu Re_D^{1/2}$ for $Re_D = 10^6$

and qualitative features of the model are discussed below and contrasted with the experimental data in Figs. 1 and 2.

The review of the literature revealed a wide range of experimental results as shown in Figs. 1 and 2. This variation arises because the correlating groups, $Nu_D/Re_D^{1/2}$ and $Tu_\infty Re_D^{1/2}$, are not completely adequate to describe the existing data. Most researchers claim that heat transfer always increases with Reynolds number, while others maintain that Reynolds number has little effect on surface heat transfer. The data in Fig. 1 do show a general trend with Reynolds number. The largest values of heat transfer occurred for the highest Reynolds number experiments and the lowest values occurred for the very low Reynolds number tests. The numerical predictions, as presented in Fig. 5, suggest that heat transfer increases as Reynolds number increases when the nondimensional scale of turbulence is constant. The value of λ in Fig. 5 was taken as 0.032.

For all but the largest Reynolds number studied, the predicted heat transfer augmentation per unit increase in turbulence intensity increases as the magnitude of the turbulence intensity increases, reaches a maximum, and then slowly decreases. This apparent saturation of the heat transfer augmentation at large turbulence intensities shown in Fig. 5 is confirmed in the experimental studies. Physically, saturation of the heat transfer represents the laminar region near the wall becoming fully disrupted by the unsteadiness convected from the outer flow. This effect is accounted for in the model because the pulsation and oscillation parameter depend upon location of the near-wall viscous region, δ_v^+ . Since δ_v^+ increases with $Tu_\infty^{1/2}$, both a_n and β_n asymptotically approach a limiting value. At a Reynolds number of 10^6 , however, the predicted surface heat transfer augmentation did not saturate at larger values of turbulence intensity. The reason for this behavior is not clear and may represent a shortcoming in the current model. Since the largest values of Reynolds number in the experimental data sets was 302,000, it would be premature to draw any definite conclusions.

The work of Yardi and Sukhatme (1978) predict a maximum in the stagnation-point heat transfer when the parameter $\lambda Re_D^{1/2}$ is roughly 10. Their experiments used Reynolds numbers from 6000 up to 100,000, nondimensional turbulence scales from 0.03 up to 0.38, and $Tu_\infty Re_D^{1/2}$ up to 20. For these values $\lambda Re_D^{1/2} = 10$. For $Re_D = 100,000$, we find that $\lambda = 0.032$. The numerical predictions for $Nu_D/Re_D^{1/2}$ as a function of λ are illustrated in Fig. 6 for a Reynolds number of 100,000. For the range of nondimensional length scales investigated, the maximum heat transfer in Fig. 6 occurs when $\lambda = 0.1$. Although this length scale is off by a factor of three compared to the experimental result, the model does confirm Yardi and Sukhatme's findings in a qualitative sense. Specifically, the model predicts that the heat transfer increases with λ , reaches a maxi-

imum value for moderate λ , then decreases as λ continues to increase. Recall that β_n increases almost linearly with λ . Large values of β_n imply large excursions of the stagnation point from its mean position. Thus, the mean heat transfer rate is expected to decrease. Additionally, a_n decreases when λ increases so that the effect is even more pronounced.

On the basis of these preliminary predictions, the model seems to have captured some of the physical mechanisms of turbulence augmented heat transfer. Its strength is that it represents the appropriate physics of the flow to a first approximation, and it does produce experimentally observed trends.

There were several approximations made in the model during the initial formulation which could be improved. Perhaps the most important one concerns the assumption that $\lambda^* = \lambda^*$. We attempted to improve this by approximating the effect of the inviscid strain field on turbulent length scale. However, the complications associated with this approach appeared to outweigh the advantage. A second source of potential error in the numerical predictions is associated with the number of individual frequencies included in the unsteady edge model. At most, we have included five discrete frequencies. In the compressible calculations we have been limited to only one due to computational limitations. An alternate numerical scheme for the boundary layer solver would remedy this limitation, and this is being considered.

Acknowledgments

This work has been supported by NASA Langley Research Center through grant NAG 1.1364. Support was also received from the Institute for Advanced Technology at the University of Texas at Austin.

References

- Ames, F. E., and Moffat, R. J., 1990, "Heat Transfer With High Intensity, Large Scale Turbulence: The Flat Plate Turbulent Boundary Layer and the Cylindrical Stagnation Point," Report HMT-44, Department of Mechanical Engineering, Stanford University, Stanford, CA.
- Appelqvist, J. D., II, 1965, "The Influence of Turbulence on the Local Heat Transfer From a Cylinder Normal to an Air Stream, Including Further Development of a Method for Local Heat Transfer Measurements," Doctoral Dissertation, Institute of Applied Thermo and Fluid Dynamics, Chalmers University of Technology, Gothenburg, Sweden.
- Bogucz, E. A., Dirik, E. A., and Lyman, F. A., 1988, "Unsteady Stagnation-Point Heat Transfer Due to the Motion of Freestream Vortices," *AIAA/ASME/SIAM/APS First National Fluid Dynamics Congress*, Vol. 3, AIAA, Washington, DC, pp. 1893-1900.
- Britter, R. E., Hunt, J. C. R., and Mumford, J. C., 1979, "The Distortion of Turbulence by a Circular Cylinder," *Journal of Fluid Mechanics*, Vol. 92, pp. 269-301.
- Brun, E. A., Diep, and Kestin, J., 1966, "Sur un nouveau type des tourbillons longitudinaux dans l'écoulement autour d'un cylindre. Influence de l'angle d'attaque et de la turbulence du courant libre," *Comptes Rendus de l'Académie des Sciences Paris*, Series A, Vol. 263, pp. 742-745 [in French].
- Cebeci, T., Kraimer, A., Simoneau, R. J., and Platzer, M. F., 1987, "A General Method for Unsteady Stagnation Region Heat Transfer and Results for Model Turbine Flows," *Proc. 1987 ASME-JSME Thermal Engineering Joint Conference*, Honolulu, HI, Vol. 2, ASME, pp. 541-646.
- Driver, D. M., Seegmiller, H. L., and Marvin, J. G., 1987, "Time-Dependent Behavior of a Reattaching Shear Layer," *AIAA Journal*, Vol. 25, pp. 914-919.
- Dullenkopf, K., and Mayle, R. E., 1994, "The Effects of Incident Turbulence and Moving Wakes on Laminar Heat Transfer in Gas Turbines," *ASME JOURNAL OF TURBOMACHINERY*, Vol. 116, pp. 23-28.
- Dullenkopf, K., and Mayle, R. E., 1995, "An Account of Free-Stream-Turbulence Length Scale on Laminar Heat Transfer," *ASME JOURNAL OF TURBOMACHINERY*, Vol. 117, pp. 401-406.
- Dyban, E. P., Epick, E. YA., and Kozlova, L. G., 1974, "Combined Influence of Turbulence Intensity and Longitudinal Scale and Air Flow Acceleration on Heat Transfer of Circular Cylinder," *FC8.4, Heat Transfer 1974: Proc. Fifth International Heat Transfer Conference*, Tokyo, Japan 1974, Vol. 2, Hemisphere Publishing Corporation, Washington, DC, pp. 310-314.
- Giedt, W. H., 1951, "Effect of Turbulence Level of Incident Air Stream on Local Heat Transfer and Skin Friction on a Cylinder," *Journal of the Aeronautical Sciences*, Vol. 18, pp. 725-730, 766.
- Hanford, A. J., 1994, "The Augmentation of Stagnation Point Heat Transfer by Quasi-Periodic Freestream Fluctuations," Doctoral Dissertation, The University of Texas at Austin, Austin, TX.

- Hanford, A. J., and Wilson, D. E., 1994, "The Effect of a Turbulent Wake on the Stagnation Point: Part II—Heat Transfer Results," *ASME JOURNAL OF TURBOMACHINERY*, Vol. 116, pp. 46–54.
- Hijikata, K., Yoshida, H., and Mori, Y., 1982, "Theoretical and Experimental Study of Turbulence Effects on Heat Transfer Around the Stagnation Point of a Cylinder," FC30, *Heat Transfer for 1982, Proceedings of the Seventh International Heat Transfer Conference*, Munich, West Germany 1982, Vol. 3, Hemisphere Publishing Corporation, Washington, DC, pp. 165–170.
- Hinze, J. O., 1975, *Turbulence*, 2nd ed., McGraw-Hill, New York.
- Hoshizaki, H., Chou, Y. S., Kulgein, N. G., and Meyer, J. W., 1975, "Critical Review of Stagnation Point Heat Transfer Theory," Technical Report AFFDL-TR-75-85, Wright-Patterson Air Force Base, Dayton, OH, pp. 1–100.
- Hunt, J. C. R., 1973, "A Theory of Turbulent Flow Round Two-Dimensional Bluff Bodies," *Journal of Fluid Mechanics*, Vol. 61, pp. 625–706.
- Ishigaki, H., 1970, "Periodic Boundary Layer Near a Two-Dimensional Stagnation Point," *Journal of Fluid Mechanics*, Vol. 43, pp. 477–486.
- Kayalar, L., 1969, "Experimentelle und theoretische Untersuchungen über den Einfluß des Turbulenzgrades auf den Wärmeübergang in der Umgebung des Staupunktes eines Kreiszyllinders," *Forschung auf dem Gebiete des Ingenieurwesens*, Vol. 35, pp. 157–167 [in German].
- Kestin, J., Maeder, P. F., and Sogin, H. H., 1961, "The Influence of Turbulence on the Transfer of Heat to Cylinders Near the Stagnation Point," *Zeitschrift für Angewandte Mathematik und Physik*, Vol. 12, pp. 115–132.
- Kestin, J., and Wood, R. T., 1971, "The Influence of Turbulence on Mass Transfer From Cylinders," *ASME Journal of Heat Transfer*, Vol. 93, pp. 321–327.
- Kwon, O. K., Turner, E. R., and Kou, Y. M., 1983, "Prediction of Stagnation Flow Heat Transfer on Turbomachinery Airfoils," AIAA Paper No. 83-1173.
- Lighthill, M. J., 1954, "The Response of Laminar Skin Friction and Heat Transfer to Fluctuations in the Stream Velocity," *Proc. Royal Society of London*, Vol. 224, pp. 1–23.
- Lin, C. C., 1957, "Motion in the Boundary Layer With a Rapidly Oscillating External Flow," *Proc. Ninth International Congress on Applied Mechanics*, Vol. 4, pp. 155–167.
- Lowery, G. W., and Vachon, R. I., 1975, "The Effect of Turbulence on Heat Transfer From Heated Cylinders," *International Journal of Heat and Mass Transfer*, Vol. 18, pp. 1229–1224.
- Paxson, D. E., and Mayle, R. E., 1991, "Laminar Boundary Layer Interaction With an Unsteady Passing Wake," *ASME JOURNAL OF TURBOMACHINERY*, Vol. 113, pp. 419–427.
- Seban, R. A., 1960, "The Influence of Free Stream Turbulence on the Local Heat Transfer From Cylinders," *ASME Journal of Heat Transfer*, Vol. 82, pp. 101–107.
- Sikmanovic, S., Oka, S., and Koncar-Djurdjevic, S., 1974, "Influence of the Structure of Turbulent Flow on Heat Transfer From a Single Cylinder in a Cross Flow," FC8.6, *Heat Transfer 1974: Proc. Fifth International Heat Transfer Conference*, Tokyo, Japan 1974, Vol. 2, Hemisphere Publishing Corporation, Washington, DC, pp. 320–324.
- Smith, M. C., and Kuethe, A. M., 1966, "Effects of Turbulence on Laminar Skin Friction and Heat Transfer," *The Physics of Fluids*, Vol. 9, pp. 2337–2344.
- Sogin, H. H., and Subramanian, V. S., 1961, "Local Mass Transfer From Circular Cylinders in Cross Flow," *ASME Journal of Heat Transfer*, Vol. 83, pp. 483–493.
- Taulbee, D. B., and Tran, L., 1988, "Stagnation Streamline Turbulence," *AIAA Journal*, Vol. 26, pp. 1011–1013.
- Van Dresar, N. T., and Mayle, R. E., 1988, "Stagnation Transfer Rates for Incident Flow With High Turbulence Intensities," *ASME Symposium on Fundamentals of Forced Convection Heat Transfer*, HTD-Vol. 101, pp. 165–172.
- Yardi, N. R., and Sukhatme, S. P., 1978, "Effects of Turbulence Intensity and Integral Length Scale of a Turbulent Free Stream on Forced Convection Heat Transfer From a Circular Cylinder in Crossflow," FC(b)-29, *Proc. Sixth International Heat Transfer Conference, Toronto, Canada 1978*, Hemisphere Publishing Company, Inc., Washington, DC, pp. 347–352.
- Zapp, G. M., 1950, "The Effect of Turbulence on Local Heat Transfer Coefficients Around a Cylinder Normal to an Air Stream," M.S. Thesis, Oregon State University, Corvallis, OR.

Convective Heat Transfer of Cubic Fin Arrays in a Narrow Channel

M. K. Chyu

Y. C. Hsing

Department of Mechanical Engineering,
Carnegie Mellon University,
Pittsburgh, PA 15213

V. Natarajan

The BOC Group,
Technical Center,
Murray Hill, NJ 07974

The present study explores the heat transfer enhancement induced by arrays of cubic fins. The fin element is either a cube or a diamond in shape. The array configurations studied include both in-line and staggered arrays of seven rows and five columns. Both cubic arrays have the same geometric parameters, i.e., $H/D = 1$, $S/D = X/D = 2.5$, which are similar to those of earlier studies on circular pin-fin arrays. The present results indicate that the cube element in either array always yields the highest heat transfer, followed by diamond and circular pin-fin. Arrays with diamond-shaped elements generally cause the greater pressure loss than those with either cubes or pin fins. For a given element shape, a staggered array generally produces higher heat transfer enhancement and pressure loss than the corresponding inline array. Cubic arrays can be viable alternatives for pedestal cooling near a blade trailing edge.

Introduction

Heat transfer associated with flow over arrays of various fin shapes has been a subject of extensive research in the past because of its importance in a wide variety of heat exchanger applications. Circular pin-fins with small height-to-diameter ratios are often used as a heat transfer augmentation device for the cooling of turbine blades and vanes, especially for internal cooling near the blade trailing edge. Significant contributions in this area have been made by groups at NASA-Lewis (VanFossen, 1982; Simoneau and VanFossen, 1984; Brigham and VanFossen, 1984) and Arizona State University (Metzger et al., 1982a, 1982b, 1984; Metzger and Haley, 1982; Metzger and Shepard, 1986), who examined the effects of pin array geometries, flow parameters, and thermal conditions. Their results for the staggered configurations were compiled by Armstrong and Winstanley (1988). More recently, Chyu (1990), Chyu and Goldstein (1991), and Chyu et al. (1993), using a mass transfer subliming system, evaluated the effects of fillets at the cylinder-endwall junction and the influence of array geometry on endwall heat transfer.

The present study explores the heat transfer enhancement induced by an alternative geometry, namely cubic fins as opposed to pin-fins. While flow characteristics near the element-endwall junction are dominated by the highly turbulent horseshoe vortex for both geometries, a recent study by Chyu and Natarajan (1995) indicated that a cubic element can produce greater heat transfer enhancement than a circular pin. Since the cubic element is a natural geometry in integrated circuit packages, most research to date pertaining to cubic array heat transfer has occurred in the domain of electronic cooling (Moffat and Ortega, 1989). Most of the earlier studies on this topic have addressed the issues concerning the gap between the element and the upper wall of the channel (Garimella and Eibeck, 1990). Recently, Chyu et al. (1993) studied the characteristics of heat transfer from cubic arrays exposed to an external boundary layer flow using an analogous mass transfer technique.

To facilitate a systematic study, the present research examines cube and diamond elements, respectively, arranged in both an in-line and staggered configuration. A diamond element is es-

entially a cube rotated 45 deg relative to the direction of the mainstream flow. In order to simulate blade cooling conditions, the test channel used in this study contains no gap between the element and the top of the channel. This marks a major difference between the current work and previous studies in electronic cooling. Figure 1 shows the top view of two sample arrays, the in-line diamond array and the staggered cube array. Each array is comprised of seven rows of five elements (five/four for the staggered array). The array geometry is determined by the aspect ratios in the transverse (S/D) and longitudinal (X/D) directions, with D being the size of the cubic element. For comparison purposes, this study uses $S/D = X/D = 2.5$, largely recognized to be the optimal geometry for pin-fin induced heat transfer enhancement. Data obtained from the study will be compared to those for pin-fins reported by Chyu (1990), which used identical array configurations and boundary conditions.

Experimental Apparatus and Procedures

The cubic fin elements, made of aluminum bar approximately 12.5 mm in length on each side, are housed in an aluminum test channel with a rectangular cross section 159 mm wide and 12.7 mm high. The initial portion of the duct serves as the hydrodynamic development section and delivers the flow to the test section. The developmental length ahead of the cube array is approximately $19D_h$, where $D_h = 23.5$ mm is the hydraulic diameter of the test channel. The distance from the last row of fin elements to the duct exit is approximately 40 mm. The forced air flow is supplied by a 50 HP compressor delivered through a filter, a pressure regulator, a control valve, and an orifice before reaching the test section.

In order to gain more accurate pin-resolved data, the present experiment uses the naphthalene sublimation technique instead of direct heat transfer measurements. The same technique has been employed in an earlier pin-fin study (Chyu, 1990). Each experiment starts with the preparation of the naphthalene coating on the cubic fin surface. This is achieved by dipping the cube, with both ends taped, into a pool of nearly boiling, molten naphthalene. During the dipping, the cube is held by tweezers at both ends and immersed in the liquid naphthalene for approximately one second. The naphthalene solidifies almost instantly after removal from the pool and forms a nearly 0.5-mm-thick layer on the cube surface. Such a coating process generally results in a quality surface, so no additional polishing or machining procedure is necessary. After the coating process, the cubes

Contributed by the International Gas Turbine Institute and presented at the 41st International Gas Turbine and Aeroengine Congress and Exhibition, Birmingham, United Kingdom, June 10–13, 1996. Manuscript received at ASME Headquarters February 1996. Paper No. 96-GT-201. Associate Technical Editor: J. N. Shinn.

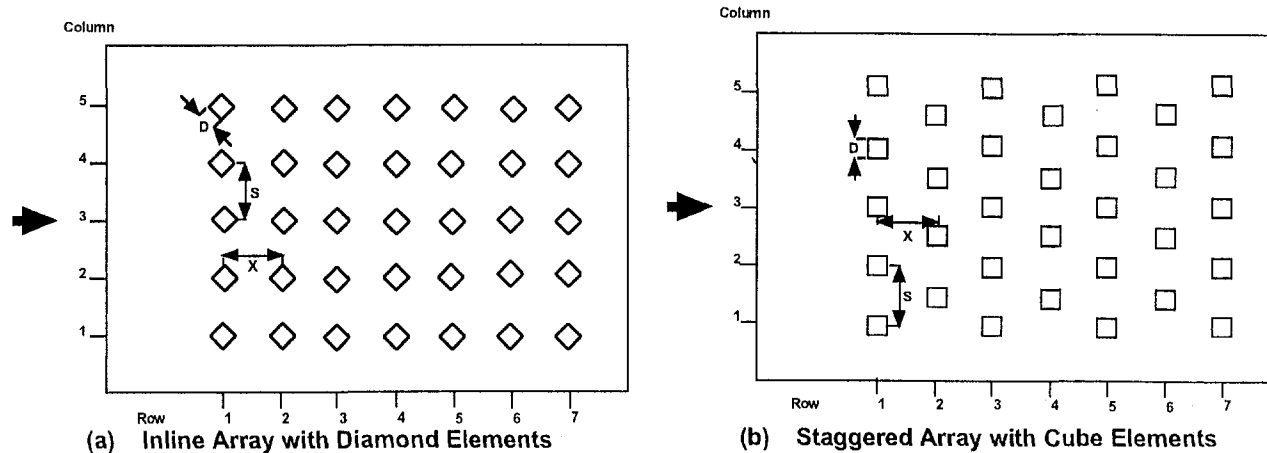


Fig. 1 Array arrangements

are stored in a tightly sealed plastic box for at least 15 hours to ensure that they attain thermal equilibrium with the surrounding air.

Before each test run, all fins are separately weighed using an electronic balance with an accuracy of 0.01 mg in a 166 g range. The cubic fins are then screw-mounted on the bottom wall of the test section, according to the array geometry desired. The entire assembly is completed when the top wall is fastened and sealed. While in place, the top wall touches the top side of each cubic fin, ensuring that no gap is present. After assembly, compressed air is forced through the channel for about 30 minutes. During the test run, the system temperature is determined by the average of the readings of four thermocouples embedded in the inner surface of the two endwalls. Such a system temperature is necessary for determining the naphthalene vapor concentration, $\rho_{v,w}$, on the fin surface, since maintaining an isothermal system is essential for the present mass transfer measurement. Test results are discarded if any two of the four thermocouple readings differ by more than 0.2C. The pressure drop is measured for each test using a manometer through a pressure tap just 2.5D in front of cubic fin array.

After the test run, all fins are unmounted from the channel and weighed again. The weight loss of the individual fins is the amount of naphthalene sublimed during the test run. The average naphthalene mass sublimed is approximately 30 mg.

As an auxiliary study, the streakline patterns on the endwall are visualized using the oil-graphite technique. Important fea-

tures revealed from the streakline patterns substantiate both the mass transfer data and interpretation of the results. To facilitate visual access, the aluminum wall on top of the test section is replaced by a transparent Plexiglas plate.

Heat/Mass Transfer Analogy and Data Reduction

The convective heat transfer coefficient, h , of each cubic fin is given by

$$h = q/(T_w - T_b) \quad (1)$$

where T_w and T_b are the element wall temperature and the bulk mean temperature in the channel, respectively. By analogy (Eckert, 1976), the mass transfer coefficient, h_m , of each cubic fin is

$$h_m = m/(\rho_{v,w} - \rho_{n,b}) \quad (2)$$

where m is the mass transfer rate per unit area, which can be calculated from the weight change of the coated cube before and after the experiment. The wall concentration, $\rho_{v,w}$, is obtained by evaluating the time-averaged naphthalene vapor pressure using the pressure-temperature correlation of Ambrose et al. (1974) in conjunction with the ideal gas law.

The increase in bulk concentration naphthalene vapor within the domain of a specific row j can be expressed as

Nomenclature

A = unobstructed area of cross section of channel	Pr = Prandtl number = ν/α	ν = kinematic viscosity of air
A_{min} = minimum cross-sectional area	Q = volumetric air flow rate	$\rho_{v,w}$ = vapor mass concentration or density of naphthalene on pin-fin surface
D = characteristic length of cubic fin = H	q = heat flux from pin-fin number	$\rho_{n,b}$ = vapor mass concentration or density of naphthalene at bulk flow
D_h = hydraulic diameter of channel	Re = Reynolds number = $U_m D/\nu$	ρ_s = density of solid naphthalene
H = height of cubic fin	S = pin spacing in spanwise direction	
h = heat transfer coefficient	Sc = naphthalene-to-air Schmidt number = ν/K	
h_m = naphthalene mass transfer coefficient	Sh = pin-resolved naphthalene mass transfer Sherwood number	
K = naphthalene-air diffusion coefficient	T = temperature	
k = thermal conductivity	t = time	
L = duct length	U = bulk mean velocity in an unobstructed duct	
m = mass transfer flux of naphthalene from pin-fin surface	U_m = mean flow in the minimum flow area	
N = number of rows in an array	X = pin spacing in streamwise direction	
Nu = Nusselt number = hD/k	α = thermal diffusivity	

$$\Delta\rho_{n,b} = M_j/Q \quad (3)$$

where M_j is the mass transfer per unit time from all fin surfaces of the entire row j , and Q is the volumetric air flow rate through the channel. Since the air flow at the channel inlet is naphthalene free, it leads to

$$\rho_{n,b} = \sum_1^{j-1} M_j/Q \quad (4)$$

As the mass transfer system is essentially isothermal, the naphthalene vapor pressure and vapor concentration at the wall are constant. In heat transfer, this is equivalent to a constant wall temperature on the fin surface. Hence the fins can be regarded as having an ideal efficiency of 100 percent.

Once h_m is evaluated, its dimensionless counterpart, the Sherwood number,

$$Sh = h_m D/K \quad (5)$$

can be determined. The naphthalene–air diffusion coefficient, K , is determined by the Schmidt number (~ 2.5)

$$Sc = \nu/K \quad (6)$$

Since naphthalene concentration in the boundary layer is extremely low, ν can be approximated by the kinematic viscosity of air under the present operating conditions.

The Sherwood number can be transformed to its heat transfer counterpart, Nusselt number (Nu), using the relation

$$Nu/Sh = (Pr/Sc)^{0.4} \quad (7)$$

where Pr is the Prandtl number. Using air ($Pr = 0.7$) as the coolant, Eq. (7) becomes

$$Nu = 0.6 Sh \quad (8)$$

The Reynolds number, Re , in the present study is defined as

$$Re = U_{max} D/\nu \quad (9)$$

and the duct Reynolds number defined as

$$Re_D = UD_h/\nu \quad (10)$$

The two Reynolds numbers are related by

$$Re_D = Re(D_h/D)(A_{min}/A) \quad (11)$$

where A_{min} is the minimum cross-sectional area with cubic elements blockage, and A is the unobstructed channel cross-sectional area.

Results and Discussion

One important feature revealed in the earlier research concerning pin-fin heat transfer in a narrow channel is the variation of the row-resolved heat transfer coefficient. According to Metzger et al. (1982a) and Chyu (1990), the maximum Nusselt number occurs at the second row and the third row for the inline and staggered arrays, respectively. Such a maximum is a result of two competing effects. Heat transfer from a fin element can be substantially promoted by direct wake shedding generated from the elements situated upstream. On the other hand, heat removed from the elements upstream elevates the bulk mean temperature in the channel, which reduces the driving potential for convective heat transfer. With this notion in mind, the highest row-resolved heat transfer should occur at the upstream-most row that is subjected to direct wake shedding. The Nusselt numbers in rows downstream from the maximum display virtually a constant value as the heat convection in the housed channel reaches a fully developed status.

Figure 2 shows the relative magnitude of mass transfer among all individual elements. The numerical value marked beside each element is the ratio of its pin-resolved Sherwood number to the mean Sherwood number of the entire array in this particular test, Sh_A . The values marked outside the figure border are the normalized row-averaged (Sh_R , top border) and column-averaged Sherwood numbers (Sh_C , right border). Although the four cases shown in Figs. 2(a) to 2(d) have different Reynolds numbers, the normalized mass transfer data revealed in each figure are very representative of the specific array geometry and are independent of the Reynolds number. A glance at these figures reveals excellent data symmetry, which attests to the quality of the present experiment.

Except for the staggered diamond array (Fig. 2(d)), the locations of the maximum Sh_R well resemble those of the corresponding pin-fin arrays; i.e., second row for the in-line and third row for the staggered, when S/D and $X/D \sim 2.5$. The maximum Sh_R for the staggered diamond array occurs at the fourth or the fifth, rather than the third, row. Compared to the pin-fin case, this deviation is attributable to the difference of wake characteristics induced by a diamond element. According to a recent study by Chyu and Natarajan (1995), the wake behind a diamond spreads much wider and longer than that behind a cylinder. A diamond element located in an array interior may be subjected to a complex pattern of wake shedding, which consists of wakes shed sideways from the adjacent elements immediately upstream and that from the element directly aligned two rows ahead. Observations reported in the same study indicated that the effect of sideways wake-shedding for the cylindrical element is relatively insignificant.

Figure 3 shows the array-averaged mass (heat) transfer results versus Reynolds number for different arrays. The ordinate of the figure uses $Sh_A/Sc^{0.4}$, which, by analogy, is equal to $Nu_A/Pr^{0.4}$ in heat transfer. Also plotted in the figure for comparison are the corresponding pin-fin data reported earlier by Chyu (1990). The results clearly indicate that the staggered cube array has the highest mass transfer overall. In fact, the cubic element in either array always produces the highest array-averaged mass transfer, followed by diamond and circular pins. In the staggered case, the average mass transfer coefficient for the cube array is about 20 to 40 percent and 30 to 80 percent higher than its diamond and pin-fin counterparts, respectively. The differences for the inline are much lower—about 10–20 percent and 10–40 percent correspondingly. These differences appear to increase with the magnitude of the Reynolds number.

The convective heat or mass transfer results may be correlated with a Reynolds number in form of power-law, i.e., $Sh_A/Sc^{0.4} = Nu_A/Pr^{0.4} = a \cdot Re^b$. Table 1 lists the best-fit values of a and b for cubic arrays. The Reynolds number dependence appears to be greater for the staggered array than for the inline array. The values of power index, b , agree well with those of the same array arrangements, but with different shapes in constituting elements. Zukauskas (1972) reported a power index of 0.63 for an in-line tube bank, and Metzger et al. (1982a) proposed a value of 0.728 for the staggered pin-fin arrays.

Heat transfer enhancement is generally accompanied by a pressure penalty. Figure 4 exhibits the pressure coefficient as a function of Reynolds number for all the six cases shown in Fig. 3. The pressure loss coefficient is defined as

$$f = 2\Delta p/(\rho U_{max}^2 N) \quad (12)$$

where Δp is the pressure drop across the entire array and N is the number of rows in an array. While the extent of pressure loss varies distinctly among different array configurations, the magnitudes of the pressure coefficient change little with Reynolds number, at least within the present test range. The staggered diamond array has the highest pressure loss among all the cases; while the cube in-line array has the lowest loss. As an interesting observation, the staggered cube array, which, as suggested in Fig. 3, has the highest heat transfer enhancement overall reveals

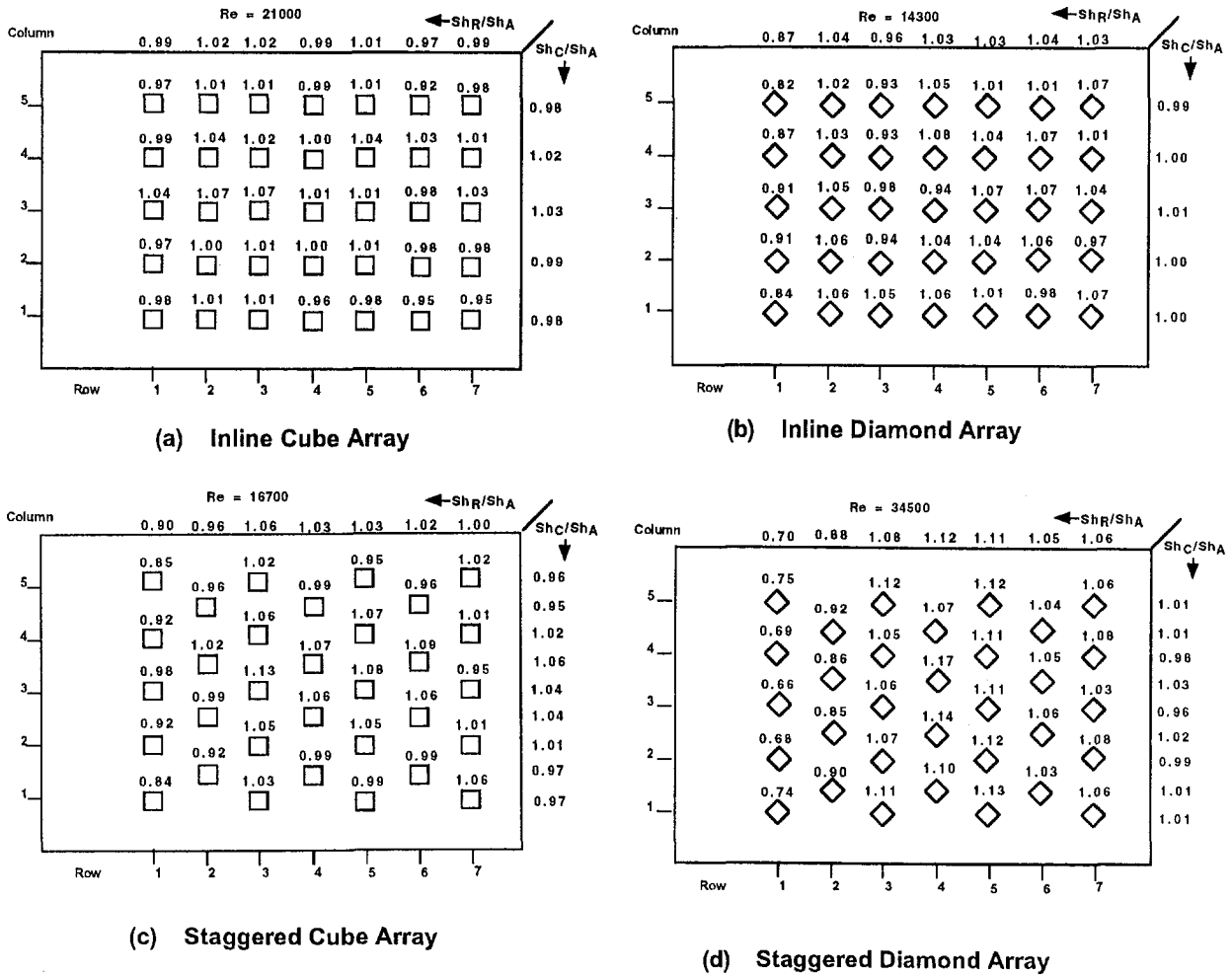


Fig. 2 Relative pin-resolved heat (mass) transfer within an array

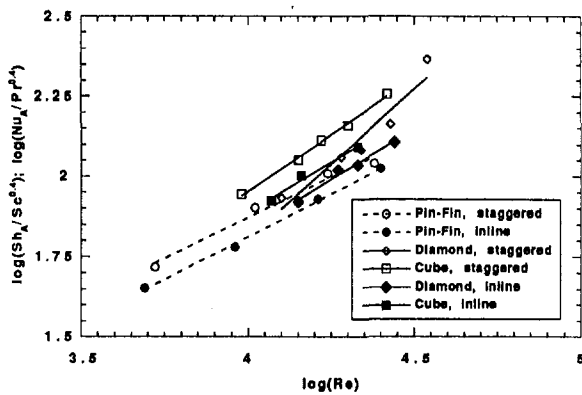


Fig. 3 Array-averaged heat (mass) transfer

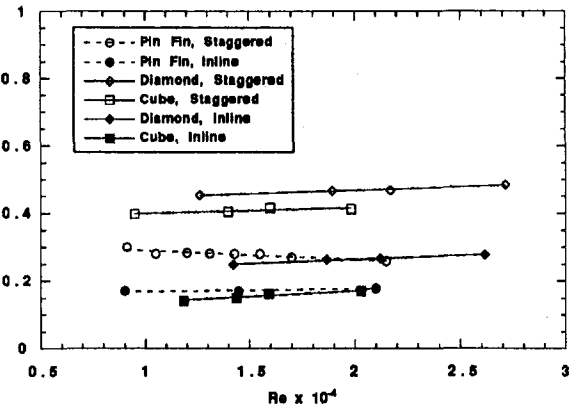


Fig. 4 Pressure loss coefficient

Table 1 Correlation coefficient

Array Configuration	Fin Shape	a	b
Inline	Cube	0.233	0.631
	Diamond	0.187	0.639
Staggered	Cube	0.138	0.704
	Diamond	0.084	0.732

a nearly 10 percent lower pressure loss than the corresponding diamond array. On the other hand, the inline circular pin-fin array that is the lowest in heat transfer enhancement shows slightly higher pressure loss than the cube inline array.

Figure 5 illustrates the relation between the array-averaged mass (heat) transfer enhancement and pressure-loss penalty. Both heat (mass) transfer and pressure loss coefficients are normalized by their smooth duct (without blockage) counterparts, Sh_0 and f_0 , respectively. The value of Sh_0 is determined from the Dittus-Boelter equation for heat transfer (Kays and Crawford, 1980)

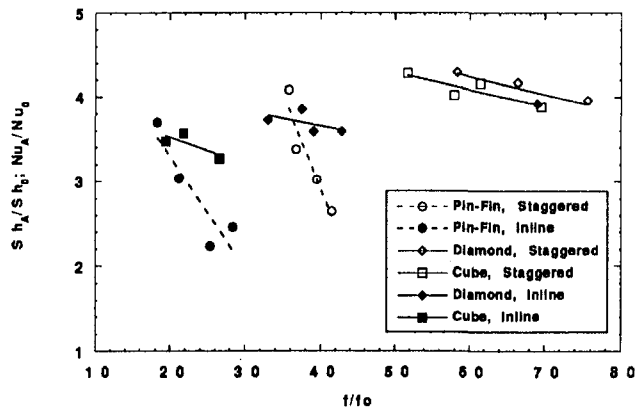


Fig. 5 Heat transfer enhancement versus pressure loss

$$\text{Nu}_{D_o}/\text{Pr}^{0.4} = 0.023 \text{Re}_D^{0.8} \quad (13)$$

where Re_D is the duct Reynolds number and Nu_{D_o} is the fully developed Nusselt number based on the duct hydraulic diameter, D_h . To be compatible with the characteristic length used for Sh , Sh_o can be expressed by

$$\text{Sh}_o/\text{Sc}^{0.4} = (D/D_h)(\text{Nu}_{D_o}/\text{Pr}^{0.4}) = 0.0124 \text{Re}_D^{0.8} \quad (14)$$

The friction factor, f_o , uses the conventional definition for fully developed turbulent flow in a smooth duct, i.e.,

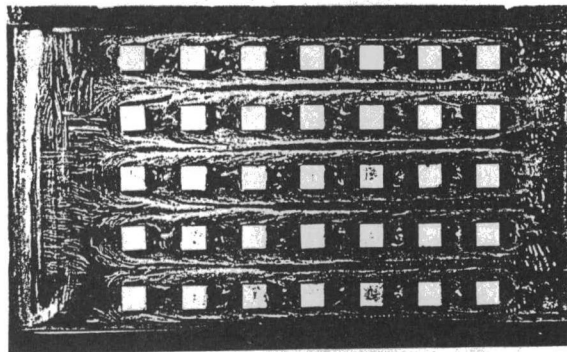
$$f_o = 2\Delta p/(\rho U^2)(D_h/L) \quad (15)$$

where L is the duct length. The value of f_o is calculated from the Blasius power-law correlation (Kays and Crawford, 1980)

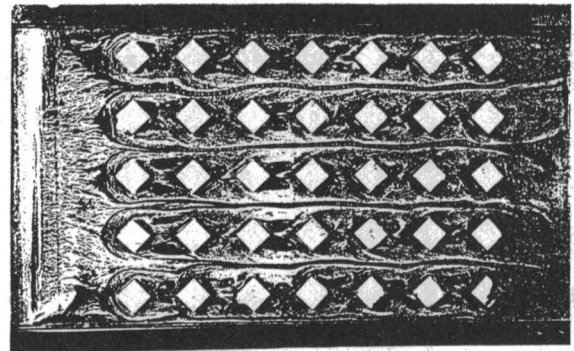
$$f_o = 0.078 \text{Re}_D^{-0.25} \quad (16)$$

One notable trend revealed in Fig. 5 is that the mass transfer enhancement Sh_A/Sh_o (or Nu_A/Nu_o) generally decreases with an increase in f/f_o . Such a decreasing trend is most significant for the circular pin-fin array and much less for the cube and diamond arrays. Since the pressure loss coefficients for all arrays, as shown in Fig. 4, are somewhat Reynolds number independent, the value of f/f_o increases with the Reynolds number. This implies that the extent of overall heat transfer enhancement induced by element blockage reduces as the Reynolds number increases. The estimated uncertainties of the present data, based on the method suggested by Moffat (1985), are 4.5 and 6 percent for the Sherwood number and pressure loss coefficient, respectively.

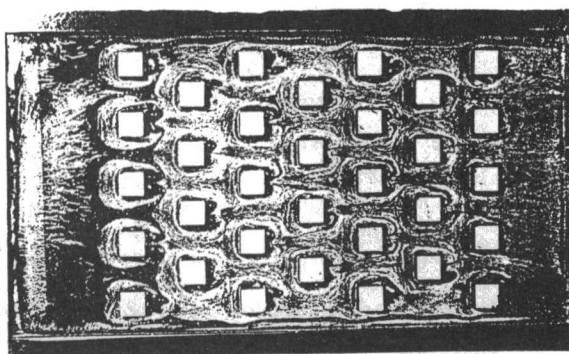
A flow visualization study, using a mixture of oil-graphite powder as the indicator, was undertaken to substantiate the results in mass transfer and pressure loss. Figures 6(a) to 6(d) show the photos of streakline pattern on the array endwall. A brighter spot in the photo generally implies higher convective transport in the region as compared to a darker spot. It is obvious that the flow through the spanwise space between neighboring elements for the in-line arrays bears a great similarity to flow in a straight channel. Such a throughflow not only induces relatively low heat or mass transfer in the region but also demotes spanwise interactions within the array. As a contrast, the wake



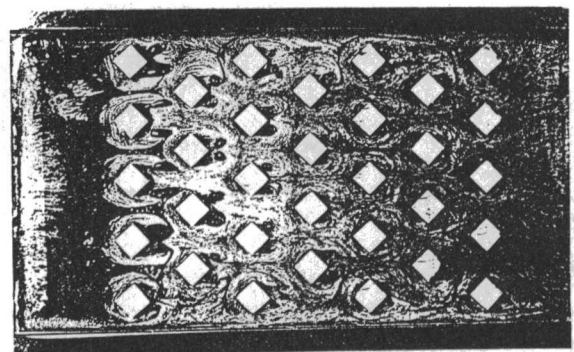
(a) Inline Cube Array



(b) Inline Diamond Array



(c) Staggered Cube Array



(d) Staggered Diamond Array

Fig. 6 Streakline pattern near array endwall

shedding and flow interaction in a staggered array appear to be strong in both streamwise and spanwise directions. The flow structure around each individual element well resembles that reported in a recent study on the endwall heat transfer by Chyu and Natarajan (1995). The area of "dead zone" (represented by dark regions) behind an element is smaller for the cube than for the diamond. To a certain extent, the size of dead zone for the staggered array is smaller than that of the inline array. As a collective result, the staggered cube array has the highest mass transfer overall.

Conclusions

The present experimental study, using a mass transfer analogy, has effectively examined the heat transfer and pressure characteristics of both inline and staggered cubic-fin arrays. Key findings are summarized below.

Row-resolved heat transfer characteristics in cubic arrays exhibit a great similarity to those of circular pin-fin arrays. The highest row-resolved heat transfer occurs at the upstream-most row subjected to direct wake shedding. For a given element geometry, a staggered array generally produces much higher heat transfer than the corresponding inline array. However, the pressure loss for the staggered array is also higher.

The cubic element in either in-line or staggered arrays always produces the highest heat transfer, followed by the diamond and circular pins. The heat transfer enhancement induced by the staggered cube array is about 20 to 40 percent and 30 to 80 percent higher than that of the staggered diamond and staggered pin-fin array, respectively. The corresponding differences are 10–20 percent and 10–40 percent for the in-line array.

The diamond element in either in-line or staggered array induces the greatest pressure loss. The loss for the staggered array is about 10 and 50 percent more than that of cube and pin-fin, respectively. The corresponding differences become approximately the same at 50 percent for the in-line arrays. The pressure loss for the in-line cube array, in fact, is the lowest overall.

In summary, cubic elements can be a viable alternative to circular pins for heat transfer enhancement, such as the pedestal cooling near a blade trailing edge. The staggered cube array appears to be one of the most attractive configurations since it produces the highest heat transfer enhancement with a moderate pressure penalty.

References

- Ambrose, D., Lawenson, I. J., and Sprake, C. H. S., 1975, "The Vapor Pressure of Naphthalene," *J. Chem. Thermo.*, pp. 1173–1176.
- Armstrong, J., and Winstanly, D., 1988, "A Review of Staggered Array Pin Fin Heat Transfer for Turbine Cooling Applications," *ASME JOURNAL OF TURBOMACHINERY*, Vol. 110, pp. 94–103.
- Brigham, B. A., and VanFossen, G. J., 1984, "Length-to-Diameter Ratio and Row Number Effects in Short Pin Fin Heat Transfer," *ASME Journal of Engineering for Gas Turbines and Power*, Vol. 106, pp. 241–246.
- Chyu, M. K., 1990, "Heat Transfer and Pressure Drop for Short Pin-Fin Arrays With Pin-Endwall," *ASME Journal of Heat Transfer*, Vol. 112, pp. 926–932.
- Chyu, M. K., and Goldstein, R. J., 1991, "Influence of Cylindrical Elements on Local Mass Transfer From a Flat Surface," *Int. J. Heat and Mass Transfer*, Vol. 34, pp. 2175–2186.
- Chyu, M. K., Natarajan, V., and Chiou, J. S., 1993, "Heat Transfer From Arrays of Cubes Exposed to an External Boundary Layer Flow," *Enhanced Cooling Techniques for Electronics Applications*, ASME HTD-Vol. 263.
- Chyu, M. K., and Natarajan, V., 1995, "Heat Transfer on the Base Surface of Three-Dimensional Protruding Elements," *Int. J. Heat and Mass Transfer*, in press.
- Eckert, E. R. G., 1976, "Analogies to Heat Transfer Processes," *Measurements in Heat Transfer*, Eckert, E. R. G., and Goldstein, R. J., eds., Hemisphere Publishing Corp., New York.
- Garimella, S. V., and Eibeck, P. A., 1990, "Heat Transfer Characteristics of an Array of Protruding Elements in Single Phase Forced Convection," *Int. J. Heat and Mass Transfer*, Vol. 33, pp. 2659–2669.
- Kays, W. M., and Crawford, M. E., 1980, *Convective Heat and Mass Transfer*, 2nd ed., McGraw-Hill, New York.
- Metzger, D. E., Berry, R. A., and Benson, J. P., 1982a, "Developing Heat Transfer in Rectangular Ducts With Staggered Arrays of Short Pin Fins," *ASME Journal of Heat Transfer*, Vol. 104, pp. 700–706.
- Metzger, D. E., and Haley, S. W., 1982, "Heat Transfer Experiments and Flow Visualization of Arrays of Short Pin Fins," ASME Paper No. 82-GT-138.
- Metzger, D. E., Fan, Z. X., Shepard, W. B., 1982b, "Pressure Loss and Heat Transfer Through Multiple Rows of Short Pin Fins," *Heat Transfer 1982*, Vol. 3, Hemisphere Publishing Corp., pp. 137–142.
- Metzger, D. E., Fan, C. S., and Haley, S. W., 1984, "Effects of Pin Shape and Array Orientation on Heat Transfer and Pressure Loss in Pin Fin Arrays," *ASME Journal of Engineering for Gas Turbines and Power*, Vol. 106, pp. 252–257.
- Metzger, D. E., and Shepard, W. B., 1986, "Row Resolved Heat Transfer Variations in Pin Fin Arrays Including Effects of Non-uniform Arrays and Flow Convergence," ASME Paper No. 86-GT-132.
- Moffat, R. J., 1985, "Using Uncertainty Analysis in the Planning of an Experiment," *ASME Journal of Fluids Engineering*, Vol. 107, pp. 173–178.
- Moffat, R. J., and Ortega, A., 1989, "Direct Air-Cooling of Electronic Components," *Advances in Thermal Modeling of Electronic Components and Systems*, Bar-Cohen, A., and Kraus, A. D., eds., Hemisphere Publication, New York.
- Simoneau, R. J., and VanFossen, G. J., 1984, "Effect of Location in an Array on Heat Transfer to a Short Cylinder in Cross Flow," *ASME Journal of Heat Transfer*, Vol. 106, pp. 42–48.
- VanFossen, G. J., 1982, "Heat Transfer Coefficient for Staggered Arrays of Short Pin Fins," *ASME Journal of Engineering for Power*, Vol. 104, pp. 268–274.
- Zukauskas, A. A., 1972, "Heat Transfer From Tubes in Cross Flow," *Advances in Heat Transfer*, Vol. 8, pp. 116–133.

The Effect of Periodic Ribs on the Local Aerodynamic and Heat Transfer Performance of a Straight Cooling Channel

G. Rau

M. Çakan

D. Moeller

T. Arts

von Karman Institute,
Rhode St. Genèse, Belgium

The local aerodynamic and heat transfer performance were measured in a rib-roughened square duct as a function of the rib pitch to height ratio. The blockage ratio of these square obstacles was 10 or 20 percent depending on whether they were placed on one single (1s) or on two opposite walls (2s). The Reynolds number, based on the channel mean velocity and hydraulic diameter, was fixed at 30,000. The aerodynamic description of the flow field was based on local pressure distributions along the ribbed and adjacent smooth walls as well as on two-dimensional LDV explorations in the channel symmetry plane and in two planes parallel to the ribbed wall(s). Local heat transfer distributions were obtained on the floor, between the ribs, and on the adjacent smooth side wall. Averaged parameters, such as friction factor and averaged heat transfer enhancement factor, were calculated from the local results and compared to correlations given in literature. This contribution showed that simple correlations derived from the law of the wall similarity and from the Reynolds analogy could not be applied for the present rib height-to-channel hydraulic diameter ratio ($e/D_h = 0.1$). The strong secondary flows resulted in a three-dimensional flow field with high gradients in the local heat transfer distributions on the smooth side walls.

Introduction

The introduction of artificial roughness elements in tubes and rectangular ducts for heat transfer enhancement is found in a wide field of applications, covering, e.g., heat exchangers, scram-jet inlets, internal cooling channels of turbine airfoils, etc.

Nikuradse (1950) developed a one-dimensional frictional analysis based on the law of the wall similarity for small sand grain roughness elements in tubes. Dipprey and Sabersky (1963) extended this analysis to a general heat transfer similarity law for roughened tubes similar to the analogy function proposed by Prandtl and Taylor for smooth tubes (see Schlichting, 1982). The effect of the pitch-to-height variation of ribs in a tube was first studied by Webb et al. (1971); their results were formulated into a correlation. In a next step, Han et al. (1978) performed measurements in a rectangular channel with an aspect ratio of 12.2 and only two ribbed walls. A comparison showed that the aforementioned similarity concept could still be applied for ribs with $e/D_h = 0.076$. Its extension to smaller aspect ratios required a description of the effect of the presence of the ribbed wall upon the friction and heat transfer characteristics along the smooth wall. This description was proposed by Han (1984) and recently verified by Chandra et al. (1997). The valid range for the application of Han's formula is, however, limited to $e/D_h \leq 0.0625$.

The larger the rib height and the closer the aspect ratio to unity, the more the flow becomes three dimensional with accelerations and decelerations in the mainstream direction combined with strong secondary flows. The simple one-dimensional similarity analysis cannot be applied any more; the complexity of the flow field requires the use of local parameters. Most of the

present efforts in numerical flow modeling are limited to two-dimensional approaches on the channel centerline (Liou et al., 1993). Further improvements in the calculation of these flows require information on the local aerodynamic and heat transfer performance. The present experimental program was designed to provide a detailed description of the aerodynamic flow field and to show some links with the local heat transfer performance. A variable heat transfer pattern results in uneven wall temperatures; the latter have to be identified by designers as they may lead to thermal failure of the material. In addition, the applicability of engineering correlations based on the friction similarity law was verified for larger rib heights. Valuable information for code validation was finally provided.

Experimental Apparatus

High spatial resolution and good optical quality of the channel walls were needed for the aerodynamic investigation, whereas limitations in the electrical power supply were imposed for the heat transfer measurements. These requirements finally resulted in the construction of two different large-scale test channels.

A Heat Transfer Measurements. A sketch of the measurement setup is shown in Fig. 1. Air at ambient pressure and room temperature was aspirated through a heated test section. This channel, made of plexiglas, had a square cross section (50 mm \times 50 mm) and a length of 1000 mm. The flow rate was controlled by measuring the wall static pressure downstream of the honeycomb.

A stationary method was used to quantify the wall heat transfer distribution. The wall temperature pattern was provided by liquid crystals. A constant heat flux boundary condition was supplied by the resistive heating of thin inconel sheets, attached to the inner channel walls by an adhesive tape. The ribs, made of plexiglas, had a cross section of 5 mm \times 5 mm, were inclined at 90 deg to the main flow direction and glued with silicone

Contributed by the International Gas Turbine Institute and presented at the 41st International Gas Turbine and Aeroengine Congress and Exhibition, Birmingham, United Kingdom, June 10–13, 1996. Manuscript received at ASME Headquarters February 1996. Paper No. 96-GT-541. Associate Technical Editor: J. N. Shinn.

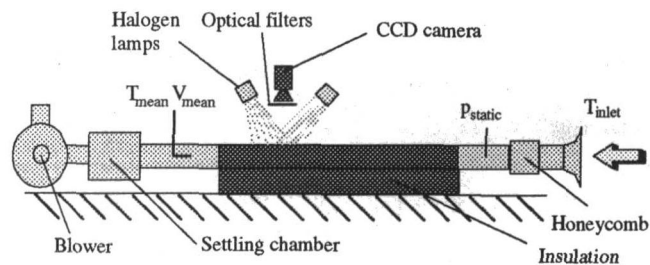


Fig. 1 Heat transfer measurement setup

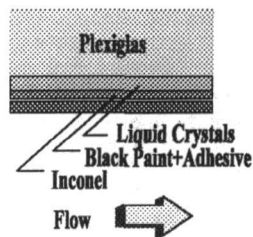


Fig. 2 Composite structure of channel walls for heat transfer measurements

adhesive on the inconel sheets. The composite structure of the walls is summarized in Fig. 2.

The different thicknesses of the layers were about $50 \mu\text{m}$ for both the liquid crystal layer and the adhesive tape, and $25 \mu\text{m}$ for the inconel sheet. Three walls were insulated by foam, the fourth one was not because of optical access.

The color pattern of the liquid crystals was recorded through sharp band optical filters and then transformed, via a calibration curve, into temperatures. This method was initially proposed by Akino et al. (1989).

The conductive heat loss was estimated, from thermocouples buried in the walls, to be around 1.5 percent of the Joule heating for the insulated walls and around 7 percent for the noninsulated one. Radiative energy exchanges in the channel were also taken into account. A streamwise linear bulk temperature distribution was assumed and experimentally verified in the test section. The enthalpy rise through the channel was calculated from a heat flux balance and compared to the results given by traversing a combined pressure/temperature probe at the exit of the test section. The detailed determination of the local Nusselt number isolines for ribbed and smooth walls required the adjustment of about four different heating regimes.

B Aerodynamic Measurements. All dimensions of the aerodynamic test section were basically scaled up by a factor of two. The cross-sectional dimensions were $100 \text{ mm} \times 100 \text{ mm}$ and the length was 1200 mm . The test section walls were made out of glass. The top wall could be removed and replaced by a plate equipped with tappings for static pressure measurements. The square rib dimensions were $10 \text{ mm} \times 10 \text{ mm}$. The

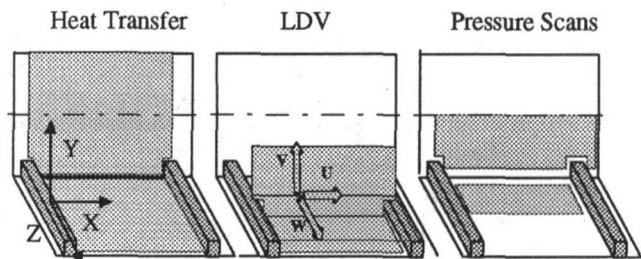


Fig. 3 Measurement planes for the three measurement methods

ambient air flow rate was controlled via a static pressure control downstream of the honeycomb.

A TSI two-dimensional LDV system was used to measure the flow field characteristics. The power output of the argon ion laser was adjusted to 2 W for all measurements. The components of the setup were described by Rau (1995). The optical probe was inclined at 5 deg to allow a close access to the walls. The length of the probe volume was 1.1 mm and its diameter 0.1 mm . The seeding consisted of propylene glycol droplets, introduced at the entrance of the wind tunnel. A comparison with the results obtained by an X -hot wire was performed at the beginning of the measurement series. The FFT analysis of the hot-wire signal demonstrated that about 800 samples per second were sufficient to capture the high-amplitude fluctuations in the flow around a single rib. The average number of samples per channel was adjusted at 6000 to minimize the statistical error on the velocity components and on their rms value. The comparison of the streamwise normal stress with the X -hot wire results further revealed that no residence-time-based velocity bias correction should be applied for this kind of flow.

The top wall was replaced by a plate with an array of 66 taps for the pressure measurements. The taps were connected via six scanivalves to two low-range (200 Pa) differential pressure transducers. The lateral density of the pressure taps was further increased by allowing a lateral displacement of this instrumented wall. The resulting grid was finally made of 119 measurement points.

C Measurement Stations and Data Analysis. In order to achieve different p/e ratios, the rib height e was kept constant while the pitch p was varied. For a constant channel length this resulted in a different number of ribs in the test section for varying p/e ratios.

The local measurements were performed in a section between two successive ribs. The last rib of the measured section was geometrically fixed at a distance of $10 * D_h$. The periodicity of the flow was verified by comparing the flow conditions up and downstream of this measurement section. The local coordinate system for the measurement section was centered on the symmetry line in the middle of the rib.

The local Nusselt number distributions were measured on the floor, between the ribs, and on the adjacent smooth side wall for all investigated p/e ratios (Fig. 3). All measured Nusselt

Nomenclature

C_p = pressure coefficient

D_h = hydraulic diameter

e = rib height

f = friction factor

f_0 = reference friction factor in smooth tube (turbulent flow)

Nu = Nusselt number

Nu_0 = reference Nusselt number in smooth tube (turbulent flow)

Δp = total pressure drop

p_s = wall static pressure

Re = Reynolds number

X, Y, Z = coordinates in streamwise, vertical, and lateral directions

U, V, W = streamwise, vertical, and lateral velocity components

X_r = separation length, measured from the edge of the rib

X_s = X -position distance from test section entry

$1s$ = ribs on one wall

$2s$ = ribs symmetric on two opposite walls

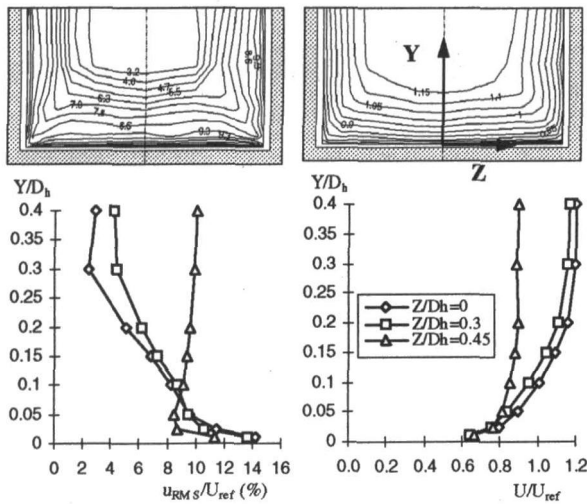


Fig. 4 Mean and fluctuation components of mainstream flow at $X_s = 2 \cdot D_h$

number distributions were normalized and presented in terms of enhancement factor with respect to the level obtained in a smooth circular tube (Dittus–Boelter equation):

$$Nu_0 = 0.023 \cdot Re^{0.8} \cdot Pr^{0.4} \quad (1)$$

Area-averaged values were calculated by means of an unstructured grid of triangular cells. The present setup did not give any information about the heat transfer on the rib itself.

The two-dimensional LDV measurements were performed in the vertical symmetry plane of the channel and in two planes parallel to the ribbed wall (Fig. 3). Velocity and normal stresses were normalized with the mean bulk velocity calculated from the flow rate.

The static pressure distribution was scanned on the floor between the ribs and on the smooth side wall up to half of the channel height. The friction factor was evaluated from the slope of the static pressure distribution measured over $5 \cdot D_h$ along the centerline of the smooth side wall. This approach takes the flow periodicity into account and reduces single reading and rib positioning errors. The definitions of the static pressure coefficient and the friction factor are given in Eqs. (2) and (3):

$$C_p = \frac{p_s - p_{Ref}}{\rho/2 \cdot \bar{U}^2} \quad (2)$$

$$f = \frac{\Delta p \cdot D_h}{2 \cdot L \cdot \rho \cdot \bar{U}^2} \quad (3)$$

All presented friction factors are normalized with the friction factor of a smooth tube, given by Blasius:

$$f_0 = 0.046 \cdot Re^{-0.2} \quad (4)$$

The uncertainties in the evaluation of the Nusselt number

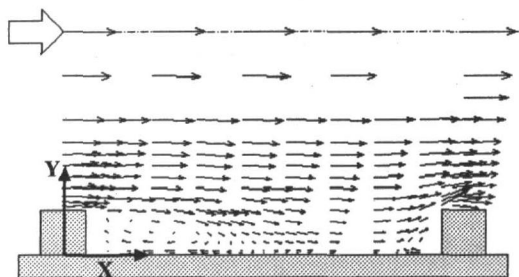
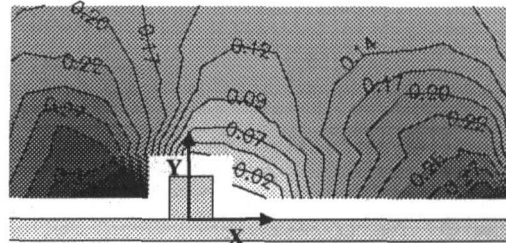


Fig. 5 Flow vectors in symmetry plane ($p/e = 9; 1s$)



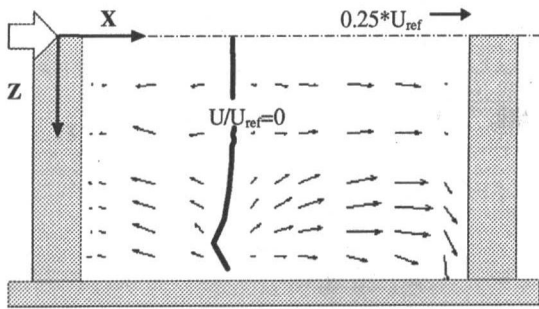


Fig. 8 Velocity vector plot at $Y/e = 0.25$ ($p/e = 9$; 1s)

pressure coefficient ΔC_p is about 0.04 while the static pressure rise in the X direction along the symmetry line is about $\Delta C_p = 0.6$. Figure 6 shows the local static pressure coefficient measured on the smooth side wall for $p/e = 9$. The reference pressure is taken at $X/e = 2$, $Y/e = 0.5$. One can essentially distinguish between a high and a low-pressure zone, respectively, in front of and behind the ribs. The low-pressure zone results from the main flow acceleration and total pressure losses due to the strong gradients in the velocity field around the ribs. The high-pressure zone is created by the impingement on the rib and the corresponding main flow deceleration in front of the rib.

The normalized U velocity isolines in a plane XZ located at $Y/e = 0.25$ are shown in Fig. 7. The maximum values are not along the symmetry line but at $Z/D_h = 0.35$. The lateral displacement of this maximum can be still seen in a XZ plane located at $Y/e = 1.5$. In this plane the maximum U values, again observed at $Z/D_h = 0.35$, are still about 10 percent higher than those measured on the symmetry line. The extension of the separation bubble in the X direction laterally decreases until $Z/D_h = 0.4$. As a result of the lateral variation it is interesting to state that for the smallest p/e ratio ($p/e = 6$) the flow clearly reattaches around $Z/D_h = 0.4$ while remaining separated in the symmetry plane.

Figure 8 shows the vector representation of the velocity components in the same plane. The entrained main stream flow is displaced by the small lateral pressure gradient towards the symmetry line and turns in front of the next rib towards the side wall.

The secondary flows in YZ cross-sectional planes were already measured for rib roughened channels by Hirota et al. (1992) and Yokosawa et al. (1989). Hirota et al. proved the existence of one large vortex cell in each half cross-sectional plane of a one-sided ribbed channel. Based on the available information and on our measurements, the three dimensional flow structure observed in a one-sided ribbed channel is sketched in Fig. 9.

The crossflow moves away from the ribbed floor along the smooth side wall and towards it in the symmetry plane. Liou

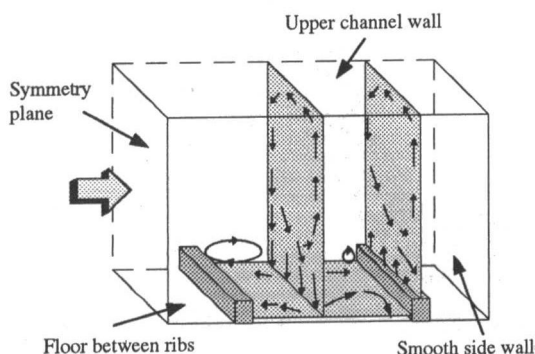


Fig. 9 Sketch of flow field in ribbed channel (1s)

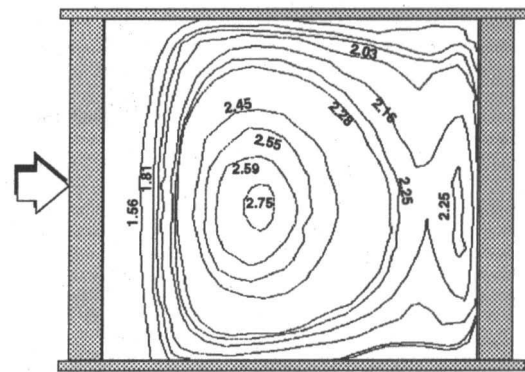


Fig. 10 Floor heat transfer enhancement factor isolines ($p/e = 12$)

et al. (1993) identified the secondary flow to be turbulence-generated (Prandtl's secondary flows of the second kind). The pressure decrease on the smooth side wall (see Fig. 6) in between the ribs clearly shows that the secondary flow has also a contribution coming from the static pressure field. The downward-directed secondary flow motion on top of the rib is deflected toward the smooth side wall by the upward-directed wall-bounded flow and the low-pressure zone on the side wall directly behind the rib. This results in a first strong impingement on the smooth side wall. A second impingement, in front of the rib, was already seen in Fig. 8.

B Nusselt Number Enhancement Pattern. The ribbed floor Nusselt number enhancement ratio isolines are given in Fig. 10.

The zone with maximum heat transfer coincides for all measured configurations with the reattachment zone. The measured normal velocity fluctuations were also maximum in this area. The two-dimensional pattern of the Nusselt number enhancement lines (Fig. 10) exhibits important lateral gradients. For higher p/e ratios ($p/e \geq 10$) a second maximum is measured in front of the ribs. The distance of this maximum from the rib corresponds to the extension of the separation zone upstream of this obstacle. An almost equivalent isoline pattern is obtained when plotting the turbulence intensity.

By looking at the Nusselt number pattern on the smooth side wall (Fig. 11) one can see high heat transfer zones in front and above the ribs. These high heat transfer zones are related to the lateral impingements previously mentioned.

C Ribs Symmetric on Two Sides. The present pattern does not change considerably for a channel with two opposite walls ribbed. The flow becomes almost symmetric with more pronounced gradients (Fig. 11(b)). Instead of one secondary flow cell per half section, one observes one cell per quadrant (see Yokosawa et al., 1989).

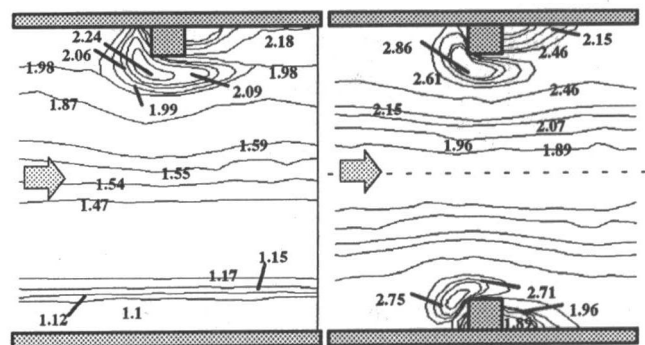


Fig. 11(a, b) Heat transfer enhancement factor isolines on smooth side wall for one and two opposite ribbed walls ($p/e = 9$)

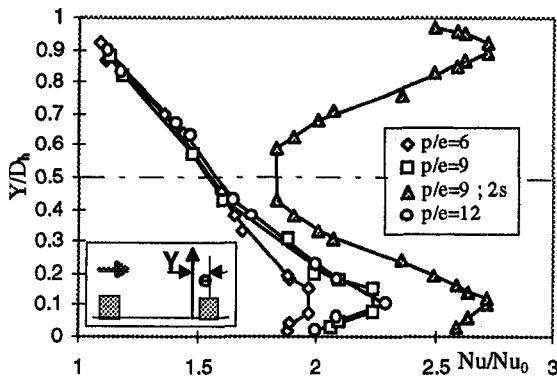


Fig. 12 Heat transfer enhancement along a vertical line on the smooth side wall

D Local Heat Transfer Performance for Three Different p/e Ratios. In the following, the variation of the local heat transfer performance and its link to the local aerodynamic parameters will be discussed for three p/e ratios (6, 9, and 12) in a one-side ribbed channel. The heat transfer and static pressure distributions show the same functional dependencies to p/e for a one and a two side ribbed channel. The two side ribbed channel results will therefore only be presented for $p/e = 9$.

D.1 Local Heat Transfer on the Lateral Wall. The local Nusselt number enhancement factor along a vertical line in front of the rib is presented in Fig. 12 for three p/e ratios.

Close to the floor, the ribs at $p/e = 9$ and 12 provide almost an equivalent enhancement, slightly superior to the case of $p/e = 6$. The location of the maximum in the Y direction is the same for all investigated p/e values ($Y/D_h = 0.1$). This maximum can be explained by the previously mentioned deflection of fluid toward the smooth side wall (see also Fig. 13). This lateral impingement becomes smaller with increasing Y/D_h ratio > 0.15 .

Above $Y/D_h = 0.4$ the heat transfer performance is independent from p/e . In this region the heat transfer is mainly influenced by turbulent momentum exchange. Note that the measured turbulence intensities on the channel centerline ($Y/D_h = 0.5$) do not change either for the three p/e ratios (Fig. 14).

The rib placement on two opposite walls leads to higher peak velocities and higher turbulence intensities so that the overall heat transfer performance is increased (Fig. 12).

The lateral W velocity was measured along a line above the rib ($Y/e = 1.5$) and close to the smooth side wall ($Z/D_h = 0.45$) (Fig. 13). The magnitude of the lateral velocities is about the same for $p/e = 9$ and 12 and smaller for $p/e = 6$. The maximum value on top of the rib is about 17 percent of the mean bulk velocity. In a parallel plane at $Y/e = 0.5$ the maximum W/U_{ref} ratio increases to about 0.22 in front of the rib (see Fig. 8).

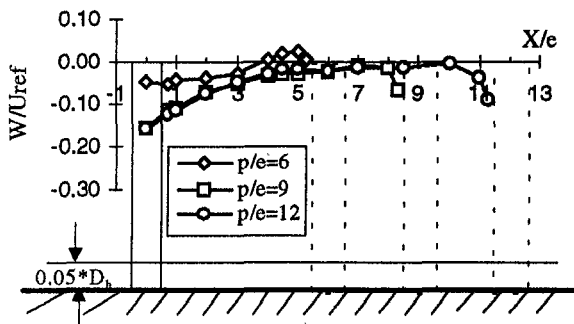


Fig. 13 Lateral normalized velocity component at $Y/e = 1.5$; $Z/D_h = 0.45$

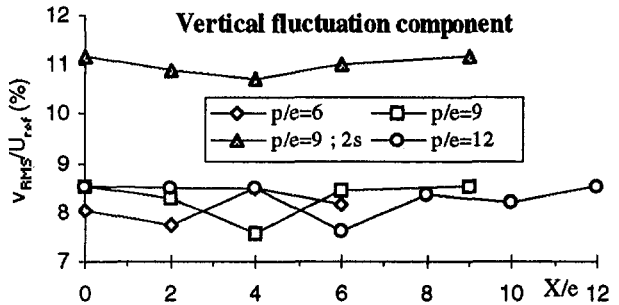
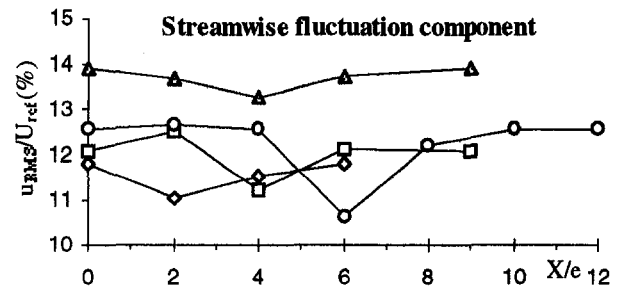


Fig. 14 Measured fluctuation components in the channel center ($Y/D_h = 0.5$; $Z/D_h = 0$)

Besides the impingement on the smooth side wall, the high turbulence intensities have a favorable effect on the heat transfer (Maciejewski et al., 1992). The measured rms values on the centerline ($Y/D_h = 0.5$, $Z/D_h = 0$) of the channel are given in Fig. 14. All curves present a minimum in between the ribs but no remarkable difference in the turbulence intensity was seen for the investigated p/e ratios. The normalized fluctuation components in X and Y directions were about 12.5 percent and 8.5 percent. The well known anisotropy in the normal stresses was observed in all measurement planes.

D.2 Local Heat Transfer Along the Symmetry Line of the Ribbed Floor. The Nusselt number enhancement factor along the symmetry line on the ribbed floor is shown in Fig. 15. The maximum value of its distribution as well as of its increase after the rib were smallest for $p/e = 6$. The p/e ratios of 9 and 12 provided about the same enhancement factor gradient but the maximum was higher for $p/e = 12$.

The location of the maximum heat transfer zone corresponded to the position of the reattachment point. The length of the separation zone downstream of the rib was measured with the LDV system at a distance of $Y/e = 0.05$ in the symmetry plane; it was defined by the interval in which the U velocity remained negative. The distance of this interval from the edge of the rib became larger for increasing p/e ratios: $3.75 < X/e < 4.0$ for $p/e = 8$, $4.0 < X/e < 4.25$ for $p/e = 9, 10, 12$, and $4.25 < X/e < 4.5$ for $p/e = 14, 16$. The same trend was also found

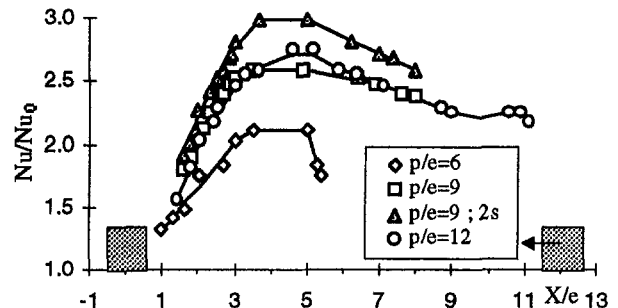


Fig. 15 Heat transfer increase along the centerline of the floor

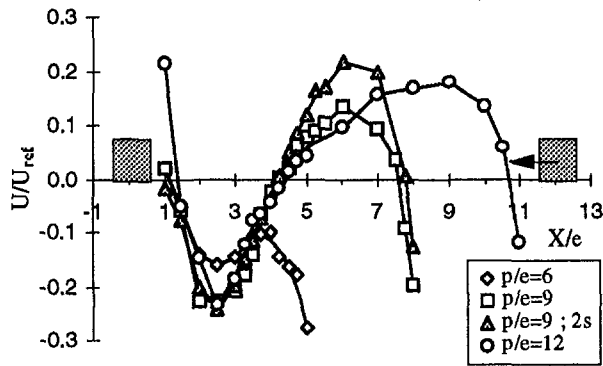


Fig. 16 U component at $Y/e = 0.1$ in the symmetry plane

by Okamoto et al. (1994). For a two-side-ribbed channel with $p/e = 9$ the reattachment distance was reduced by $\Delta X_r/e \approx 0.25$. The extension of the second separation zone in front of the rib was found to be 1–1.5 times the rib height for $p/e = 8, 9, 10, 12$ and between 0.5 and 1 times the rib height for $p/e = 14, 16$.

In between the two separation zones a new boundary layer was built up by the entrained flow. In order to overcome the pressure rise in streamwise direction the main flow above the ribs has to energize the flow in the new boundary layer through the shear layer behind the rib crest. The acceleration of this boundary layer flow is shown in Fig. 16 at a vertical distance of $Y/e = 0.1$.

In the case of a one-side-ribbed channel, the velocity gradient immediately after the reattachment was strongest for $p/e = 9$. Considering that the adverse pressure gradient was almost the same for all investigated p/e ratios leads to the conclusion that the momentum transfer through the shear layer was also maximum for this p/e ratio. A longer distance between the reattachment point and the next rib leads to a higher maximum velocity for larger p/e ratios. The vertical V velocity on this line ($Y/e = 0.1$) was slightly negative at $X/e = 4.75$ and its absolute value remained in a band of ± 1 percent (or ± 2 percent) of the mean channel velocity for the one (or two) side ribbed channel up to distance from the next rib of $\Delta X = 1.5e$.

Vogel and Eaton (1985) showed in their experiment behind a backward-facing step that the effective origin of the redeveloping thermal boundary layer lies approximately two step heights downstream of reattachment. Assuming a similar behavior for the ribbed case and considering the limited extension of the new developing boundary layer creates strong doubts about the applicability of the Reynolds analogy to the floor heat transfer for the investigated p/e ratios.

The vertical motion in the separation behind the rib, the secondary flows, and the increased cross section lead to a displace-

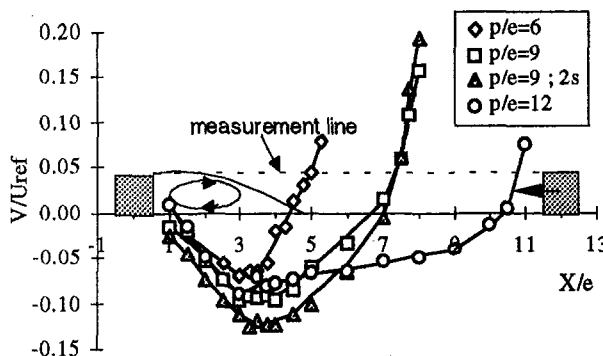


Fig. 17 Flow entrainment in between the ribs at $Y/e = 1$ in symmetry plane

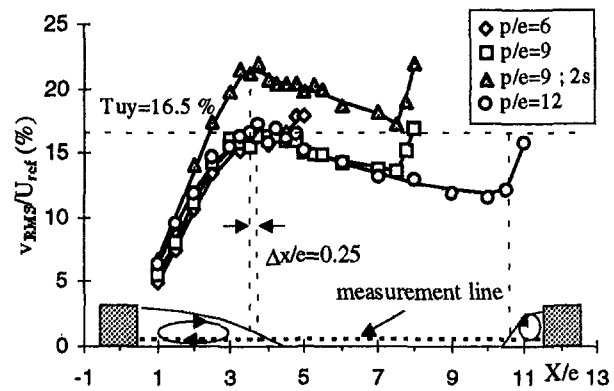


Fig. 18 Vertical fluctuation component in between the ribs at $Y/e = 0.3$ in symmetry plane

ment of cold mainstream toward the ribbed wall. This relative cold fluid reduces the local bulk temperature and consequently increases the driving temperature difference. This is shown in Fig. 17, presenting the vertical velocity component at the rib crest ($Y/e = 1$). The maximum vertical velocity was slightly higher for $p/e = 9$ compared to 6 and 12.

The rms values of the vertical velocity component at a distance of $Y/e = 0.3$ are presented in Fig. 18 as another parameter for heat transfer enhancement. The same maximum value of $Tu_y = 16.5$ percent was measured at the edge of the recirculation zones for all three p/e ratios. A shorter recirculation zone was observed for a two-side-ribbed channel ($\Delta X_r \approx 0.25 * e$). The rate of decay of these fluctuations was independent of p/e and after attaining a minimum they were again amplified by the second separation zone in front of the ribs.

In vertical direction the fluctuations were maximum in the shear layer behind the rib. For the one-side-ribbed channel the maximum values for $p/e = 6, 9, 12$ were $Tu_{x,max} = 26, 28, 28$ percent and $Tu_{y,max} = 16, 18, 18$ percent. For the two-side-ribbed channel with $p/e = 9$ they increased to $Tu_{x,max} = 35$ percent and $Tu_{y,max} = 24$ percent.

D.3 Friction Factor Analysis. While in a smooth channel the measured pressure drop can be directly linked to the shear stress at the wall, this is not true for a ribbed channel. The impingement in front of the rib leads to a local high static pressure in this zone, while the flow acceleration on top of the rib, in combination with high local total pressure losses, resulting from strong velocity gradients, gives a local low pressure zone behind the rib (Fig. 19). The resulting force is defined in the literature as form drag (Lewis, 1975).

The friction factor, calculated from the measured total pressure drop, is therefore the sum of the averaged skin friction and this rib form drag. For the application of the Reynolds analogy, it is interesting to quantify the contribution of this rib form drag on the measured total pressure drop. The rib form drag can also be easily used for numerical code validation because it contains

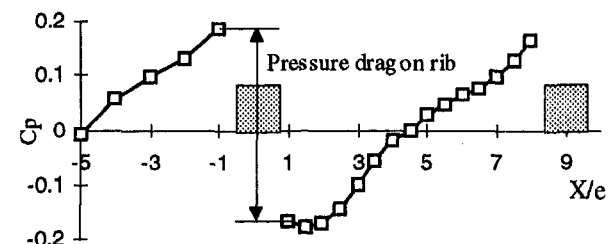


Fig. 19 Floor pressure distribution on the symmetry line ($p/e = 9; 1s$)

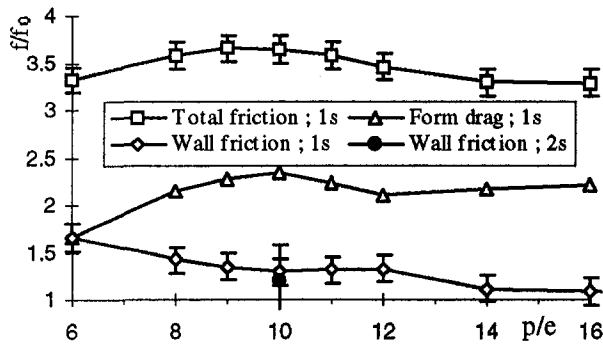


Fig. 20 Friction factor variation for one side ribbed channel

all irreversible effects that have to be modeled correctly around the rib.

In order to simplify the measurement setup a new definition of this rib form drag is proposed. This simplified rib form drag is calculated from the pressure difference between two taps on the floor centerline at a distance $0.5 * e$ before and after the rib. If the streamwise static pressure changes between these taps and the rib are negligible and if the pressure on the rib side walls is constant, this definition is equivalent to the physical rib form drag.

Figure 20 compares, for the one-side-ribbed channel, the friction factor calculated from the total pressure drop with the rib form drag. Both present a peak around $p/e = 9$. The rib form drag is the dominant contribution to the total friction factor for almost all investigated configurations.

Subtracting the form drag from the total friction factor gives the averaged skin friction factor. The results indicate that the averaged skin friction is decreasing with increasing p/e . The averaged skin friction enhancement for $p/e = 9$ is found to be about 1.3, compared to a smooth channel. The same calculation for a two-side-ribbed channel with symmetric and staggered rib arrangements gives values of respectively 1.05 and 1.2. Considering the total magnitude of the measured total friction factor enhancement of 9.5 ± 0.4 (Fig. 21), this result shows the large contribution of the rib form drag to the measured friction factor.

Furuya et al. (1976) found the same result for a flat plate roughened by two-dimensional wires. They measured the static pressure distribution on the wire itself. The subtraction of the form drag coefficient from the flow resistance coefficient gave a frictional contribution, which did not differ from that of a smooth plate. The variation of the flow resistance and pressure drag coefficient with p/e was similar to the reported results in Fig. 20 with a maximum for $p/e = 8$.

D.4 Comparison of Global Performance Parameters to Results in Literature and Correlations. The total friction factor for a two side ribbed channel is given in Fig. 21. The

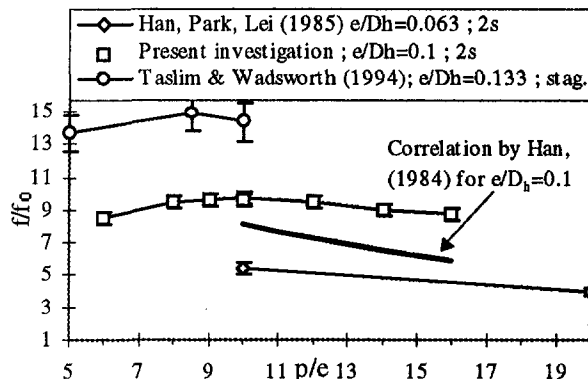


Fig. 21 Friction factor enhancement for a two-side-ribbed channel

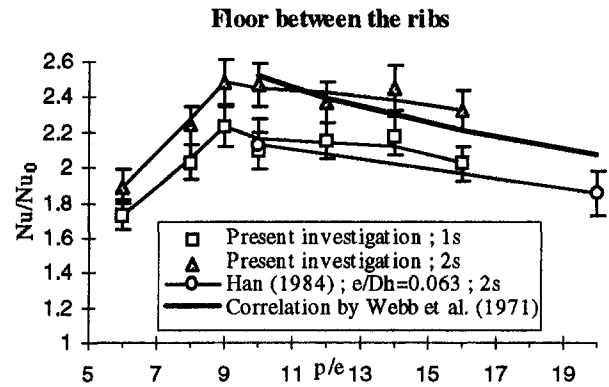


Fig. 22 Average heat transfer enhancement

comparison to the literature shows a good fit of the present data with results from previous investigations for different e/D_h ratios. The correlation, given by Han (1984), underestimates for the present e/D_h ratio of 0.1 the total pressure loss in the channel. The measured local heat transfer distributions were averaged on the floor and the smooth side wall for all investigated p/e ratios (Fig. 22).

The ratio between the averaged heat transfer enhancement on the smooth side wall and on the ribbed wall was about 70 percent for the one side ribbed channel and about 85 percent for a channel with two opposite ribbed walls. The comparison to previous investigations shows that the decrease in heat transfer performance with increasing p/e ratio was about the same for all, although the e/D_h ratio was different. It can be further seen that the increase in e/D_h ratio was more favorable for the heat transfer performance on the smooth side wall than on the ribbed wall.

The correlation of Webb et al. (1971), estimating the overall heat transfer enhancement of a ribbed tube, is also included in Fig. 22(a). His exponential fit correlated quite well with the averaged floor data of the two side ribbed channel. The approximation by Han (1984), that the overall heat transfer enhancement can be described by an area-weighted average between the results of Webb's correlation and the heat transfer of a smooth tube, is not appropriate for higher e/D_h ratios. The application of this correlation must be limited to the validated range of $0.021 \leq e/D_h \leq 0.063$ given by Han (1984).

Conclusions

Detailed aerodynamic and heat transfer measurements were performed in a square channel with ribs presenting a significant blockage ratio ($e/D_h = 0.1$). The results of the local measurements were discussed for three different p/e ratios (6, 9, 12) in a one-side-ribbed channel. The differences with a two side ribbed channel were given for $p/e = 9$.

The description of the flow characteristics showed that the flow structure is three dimensional around the rib with significant lateral velocity components and a displacement of the maximum streamwise velocity toward the smooth side wall.

The pressure field in between the ribs amplified the Reynolds-stress-induced secondary flows, while the low pressure zone on top of the rib deflected the secondary flow towards the smooth side wall. A second impingement on the smooth side wall was observed in front of the rib.

Both impingements favored the heat transfer on the smooth side wall in front and on top of the rib and a proportionality between the lateral velocity and the heat transfer enhancement was found.

The local heat transfer enhancement distribution on the symmetry line showed a slightly better performance for $p/e = 12$. The averaging over all floor data gave on the contrary a maximum for $p/e = 9$. This example indicated the difficulty of deriving general conclusions from partial information.

The maximum acceleration of new boundary layer flow for $p/e = 9$ in close proximity to the wall behind the reattachment indicated that the shear forces in the shear layer behind the rib was maximum for this p/e ratio.

Neither the turbulence intensities in the channel center nor on the symmetry line in proximity of the floor between the ribs differed significantly for varying p/e ratios.

A new definition of the rib form drag simplified the required measurement setup; its physical significance favored it for numerical code validation. The large contribution of this rib form drag to the total pressure loss emphasized the importance of the rib shape for larger e/D_h ratios and denied a direct link between the measured friction factor and the heat transfer performance via the Reynolds analogy.

The comparison of Webb's correlation and Han's approximation to the averaged measurement data showed that its range of validity could not be extended to rib height to hydraulic diameter ratios of 0.1.

The present understanding of this very complex flow field and the limitation of the existing correlations stresses the importance of further developments in numerical analysis to develop tools that are not limited to global performance estimations but capture local effects and allow to compute more realistic configurations. The presented measurement data is a contribution to the validation of these CFD codes.

Acknowledgments

The authors express their gratitude to SNECMA and TURBOMECA for the partial financial support in the present investigation.

References

- Akino, N., Ichimiya, K., Mitsushiro, K., and Ueda, M., 1989, "Improved Liquid-Crystal Thermometry Excluding Human Color Sensation," *ASME Journal of Heat Transfer*, Vol. 111, pp. 558–565.
- Chandra, P. R., Niland, M. E., and Han, J. C., 1997, "Turbulent Flow Heat Transfer and Friction in a Rectangular Channel With Varying Number of Ribbed Walls," *ASME JOURNAL OF TURBOMACHINERY*, Vol. 119, pp. 374–380.
- Dipprey, D. F., and Sabersky, R. H., 1963, "Heat and Momentum Transfer in Smooth and Rough Tubes at Various Prandtl Numbers," *Int. J. Heat Mass Transfer*, Vol. 6, pp. 329–353.
- Furuya, Y., Miyata, M., and Fujita, H., 1976, "Turbulent Boundary Layer and Flow Resistance on Plates Roughened by Wires," *ASME Journal of Fluids Engineering*, Vol. 98, pp. 635–644.
- Han, J. C., Glicksman, L. R., and Rohsenow, W. M., 1978, "An Investigation of Heat Transfer and Friction for Rib-Roughened Surfaces," *J. Heat Mass Transfer*, Vol. 121, pp. 1143–1156.
- Han, J. C., 1984, "Heat Transfer and Friction on Channels With Two Opposite Rib-Roughened Walls," *ASME Journal of Heat Transfer*, Vol. 106, pp. 774–781.
- Han, J. C., Park, J. S., and Lei, C. K., 1985, "Heat Transfer Enhancement in Channels With Turbulence Promoters," *ASME Journal of Engineering for Gas Turbines and Power*, Vol. 107, pp. 628–635.
- Hirota, M., Yokosawa, H., and Fujita, H. M., 1992, "Turbulence Kinetic Energy in Turbulent Flows Through Square Ducts With Rib-Roughened Walls," *Int. J. Heat Fluid Flow*, Vol. 13, No. 1, pp. 22–29.
- Kline, S. J., and McClintock, F. A., 1953, "Describing Uncertainty in Single-Sample Experiments," *Mechanical Engineering*, Vol. 75, Jan., pp. 3–8.
- Lewis, M. J., 1975, "An Elementary Analysis for Predicting the Momentum- and Heat-Transfer Characteristics of a Hydraulically Rough Surface," *ASME Journal of Heat Transfer*, Vol. 77, pp. 249–254.
- Liou, T.-M., Wu, Y.-Y., and Chang, Y., 1993, "LDV-Measurements of Periodic Fully Developed Main and Secondary Flows in a Channel With Rib-Disturbed Walls," *ASME Journal of Fluids Engineering*, Vol. 115, pp. 109–114.
- Maciejewski, P. K., and Moffat, R. J., 1992, "Heat Transfer With Very High Free-Stream Turbulence: Part II," *ASME Journal of Heat Transfer*, Vol. 114, pp. 834–839.
- Nikuradse, J., 1950, "Laws for Flow in Rough Pipes," NACA TM 1292.
- Okamoto, S., Tsunoda, K., Katsumata, T., Suzuki, D., and Abe, N., 1994, "Turbulent Shear Flow Over the Repeated Two-Dimensional Square Ribs on Ground Plane," presented at 7th Inter. Symp. on Appl. of Laser Techniques to Fluid Dynamics, Lisbon.
- Rau, 1995, "The Blockage Effect of Turbulators in a Rectilinear Cooling Channel," presented at VKI Lecture Series 1995-05; Brussels.
- Schlichting, H., 1982, *Grenzschicht-Theorie*, G. Braun, Karlsruhe, Germany.
- Taslim, M. E., and Wadsworth, C. M., 1997, "An Experimental Investigation of the Rib Surface-Averaged Heat Transfer Coefficient in a Rib-Roughened Square Passage," *ASME JOURNAL OF TURBOMACHINERY*, Vol. 119, pp. 381–389.
- Vogel, J. C., and Eaton, J. K., 1985, "Combined Heat Transfer and Fluid Dynamic Measurements Downstream of a Backward-Facing Step," *ASME Journal of Heat Transfer*, Vol. 107, pp. 922–929.
- Webb, R. L., Eckert, E. R. G., and Goldstein, R. J., 1971, "Heat Transfer and Friction in Tubes With Repeated-Rib Roughness," *Int. J. Heat Mass Transfer*, Vol. 14, pp. 601–617.
- Yokosawa, H., Fujita, H., Hirota, M., and Iwata, S., 1989, "Measurements of Turbulent Flow in a Square Duct With Roughened Walls on Two Opposite Sides," *Int. J. Heat Fluid Flow*, Vol. 10, No. 2, pp. 125–130.

Rib Heat Transfer Coefficient Measurements in a Rib-Roughened Square Passage

G. J. Korotky

M. E. Taslim

Mechanical Engineering Department,
Northeastern University,
Boston, MA 02165

Three staggered 90 deg rib geometries corresponding to blockage ratios of 0.133, 0.167, and 0.25 were tested for pitch-to-height ratios of 5, 8.5, and 10, and for two distinct thermal boundary conditions of heated and unheated channel walls. Comparisons were made between the surface-averaged heat transfer coefficients and friction factors for ribs with rounded corners and those with sharp corners, reported previously. Heat transfer coefficients of the furthest upstream rib and that of a typical rib located in the middle of the rib-roughened region of the passage wall were also compared. It was concluded that: (a) For the geometries tested, the rib average heat transfer coefficient was much higher than that for the area between the ribs. For the sharp-corner ribs, the rib average heat transfer coefficient increased with blockage ratio. However, when the corners were rounded, the trend depended on the level of roundness. (b) High-blockage-ratio ($e/D_h = 0.25$) ribs were insensitive to the pitch-to-height ratio. For the other two blockage ratios, the pitch-to-height ratio of 5 produced the lowest heat transfer coefficient. Results of the other two pitch-to-height ratios were very close, with the results of $S/e = 10$ slightly higher than those of $S/e = 8.5$. (c) Under otherwise identical conditions, ribs in the furthest upstream position produced lower heat transfer coefficients for all cases except that of the smallest blockage ratio with S/e of 5. In that position, for the rib geometries tested, while the sharp-corner rib average heat transfer coefficients increased with the blockage ratio, the trend of the round-corner ribs depended on the level of roundness, r/e . (d) Thermal performance decreased with the blockage ratio. While the smallest rib geometry at a pitch-to-height ratio of 10 had the highest thermal performance, thermal performance of high blockage ribs at a pitch-to-height ratio of 5 was the lowest. (e) The general effects of rounding were a decrease in heat transfer coefficient for the midstream ribs and an increase in heat transfer coefficient for ribs in the furthest upstream position.

Introduction

Various cooling methods have been developed over the years to ensure that the turbine blade metal temperatures are maintained at a level consistent with airfoil design life. The objective in turbine blade cooling is to achieve maximum internal heat transfer coefficients while minimizing the coolant flow rate. One such method is to route coolant air through serpentine channels within the airfoil and convectively remove heat from the blade. The coolant is then ejected either at the tip of the blade, through the cooling slots along the trailing edge, or film holes on the airfoil surface. Heat transfer coefficients in the cooling passages can be increased by roughening their walls. One such method, used over the past thirty years in internal cooling passages, is to mount ribs on the channel walls. These ribs, also called turbulators, increase the level of mixing of the cooler core air with the warmer air close to the channel wall, thereby enhancing the cooling capability of the passage.

Geometric parameters such as channel aspect ratio (AR), rib height-to-passage hydraulic diameter (e/D_h) or blockage ratio, rib angle of attack (α), the manner in which the ribs are positioned relative to one another (in-line, staggered, crisscross, etc.), rib pitch-to-height ratio (S/e) and rib shape (round versus sharp corners, fillets, rib aspect ratio (AR_r), and skewness toward the flow direction) have pronounced effects on both local and overall heat transfer coefficients. Some of these effects were

studied by different investigators, such as Abuaf et al. (1986), Burggraf (1970), Chandra et al. (1988), Chandra and Han (1989), Han (1984), Han et al. (1978, 1985, 1992), Metzger et al. (1983, 1988, 1990), Taslim and Spring (1988a, b), Taslim et al. (1991, 1996), Webb et al. (1971). Considerable data are available on the heat transfer coefficient on the passage surface between the ribs. However, the heat transfer coefficients on the surface of the ribs themselves have not been investigated to the same extent.

In small aircraft engines with small cooling passages and relatively large ribs, the rib surfaces comprise a large portion of the passage heat transfer area. Therefore, an accurate account of the heat transfer coefficient on the rib surfaces is critical in the overall design of the blade cooling system. The objective of this investigation was, while isolating the ribs from the wall surface thermally, to measure the overall heat transfer coefficient on the rib surface and to study the effects pitch-to-height ratio (S/e), blockage ratio (e/D_h), and rib orientation (furthest upstream position or in the middle of the channel rib-roughened portion) have on the rib surface heat transfer coefficient for a channel aspect ratio (AR) of one.

Among those investigations dealing with the measurement of heat transfer coefficients on the ribs are the following. Solntsev et al. (1973) experimentally investigated heat transfer in the vicinity of sudden two- and three-dimensional steps of circular and square cross-sectional areas mounted on a flat surface in an open channel. Enhancement in heat transfer coefficient is reported for a range of Reynolds numbers between 10^4 and 10^5 .

Berger and Hau (1979) did an experimental study of flow over square ribs in a pipe using an electrochemical analog tech-

Contributed by the International Gas Turbine Institute and presented at the 41st International Gas Turbine and Aeroengine Congress and Exhibition, Birmingham, United Kingdom, June 10–13, 1996. Manuscript received at ASME Headquarters February 1996. Paper No. 96-GT-356. Associate Technical Editor: J. N. Shinn.

nique to measure mass/heat transfer on the ribs as well as on the wall surface between them. For a blockage ratio (e/d) of 0.0364, they varied the rib pitch-to-height ratio from 3 to 10 for a range of Reynolds numbers between 10,000 and 25,000. At the Reynolds number of 10^4 , they showed enhancements, compared to smooth channels, in mass (heat) transfer on the ribs in the order of 4.4 and 5.2 for pitch-to-height ratios of 10 and 7, respectively.

Metzger et al. (1988) used a thermal transient technique to examine the contribution of the rib heat transfer to the overall heat transfer of a rib-roughened wall with variations in rib angle of attack and pitch. Square ribs representing a blockage ratio of 0.14 were mounted on only one wider side of a 0.154 aspect ratio rectangular channel. The main conclusions were that heat transfer on the rib surface significantly contributed to the overall rib-roughened wall heat transfer and this contribution mainly depended on the rib pitch-to-height spacing, with very little effect from the rib angle.

Lockett and Collins (1990) used a holographic interferometry technique to measure heat transfer coefficient in a 0.25 aspect ratio rectangular channel. Square ribs with sharp as well as round top corners representing a blockage ratio, e/D_h , of 0.067 and a pitch-to-height ratio of 7.2 were mounted on one of the wider sides of the channel, perpendicular to the flow direction. They reported overall enhancements in heat transfer of up to 2.24 for the Reynolds number of 7400.

Liou et al. (1991) performed numerical as well as experimental investigation of turbulent flow in a 4:1 aspect ratio rectangular channel roughened on two opposite wider sides with square ribs in an in-line arrangement perpendicular to the flow direction. The rib blockage ratio, e/D_h , was 0.081 and four pitch-to-height ratios of 5, 10, 15, and 20 were examined at a fixed Reynolds number of 33,000. Two-dimensional Navier–Stokes equations in elliptic form in conjunction with the $k-\epsilon$ turbulence model were solved numerically and a holographic interferometry technique was used in the experimental part. They reported an enhancement in heat transfer on the rib surface of 3.1.

Sato et al. (1992) investigated the flow characteristics and heat transfer in a rectangular channel with a total of 20 square ribs on two opposite walls in staggered, in-line, and quarter-pitch-shift arrangements. The channel aspect ratio was 0.2 and the ribs, mounted on the two wider sides of the channel, had a blockage ratio of 0.12. Details of the flow and heat transfer

over a typical rib-roughened section (including the rib surface) well downstream of the first rib were presented. They concluded that the staggered arrangement had a better heat transfer performance than the other two arrangements.

Dawes (1994) solved the three-dimensional Navier–Stokes equations in a rotating serpentine coolant passage of cylindrical geometry roughened with square ribs. Rib blockage, e/d , and pitch-to-height ratios were 0.2 and 10, respectively. Results of this work were compared with other numerical and experimental works.

Liou and Hwang (1993) also used the holographic interferometry technique to measure the heat transfer coefficient and friction factor in a 0.25 aspect ratio rectangular channel with three rib shapes including a square rib geometry mounted on two opposite wider sides in an in-line arrangement perpendicular to the flow direction. For a blockage ratio of 0.08, they tested four rib pitch-to-height ratios of 8, 10, 15, and 20 for a range of Reynolds numbers between 7800 and 50,000. The heat transfer coefficient was measured over the ribs as well as the wall surfaces between the ribs. They reported overall heat transfer coefficient enhancements on the order of 2.2 and 2.7 for semi-cylindrical and square ribs, respectively.

Taslim and Wadsworth (1997) reported on the rib surface-averaged heat transfer coefficients in a square channel. Thirteen rib geometries including three blockage ratios and four pitch-to-height ratios were tested. Sharp corner ribs were mounted on two opposite walls of the channel at a 90 deg angle with respect to the flow direction in a staggered arrangement. A major conclusion of their study was that the rib surface-average heat transfer coefficient was much higher than that for the area between the ribs (h_{floor}). Therefore, the contribution of the ribs to the overall heat transfer in a rib-roughened passage is significant. They showed that for a typical rib arrangement the $h_{\text{rib}}A_{\text{rib}}$ can be as high as 33 to 53 percent of $h_{\text{overall}}A_{\text{total}}$. Other conclusions were that (a) for sharp-edged ribs, a pitch-to-height ratio of 8.5 produced the highest heat transfer coefficient, and (b) heat transfer coefficient on ribs in the furthest upstream position was lower than that on the midchannel ribs.

This work, which is a continuation of the above-mentioned work, studies the effects of the rounded rib corners on the heat transfer and friction in a rib-roughened channel. It addresses an important problem facing the designer of the turbine blade cooling cavities, namely, relatively sharp-edged ribs, cast at the

Nomenclature

a = channel height (Fig. 1)	h_{overall} = overall average heat transfer coefficient on a rib and on the wall surface between a pair of ribs	r = rib top corner radius
b = channel width (Fig. 1)	h_{rib} = rib average heat transfer coefficient = $q/(T_s - T_m)$	S = rib pitch (center-to-center)
A = channel cross-sectional area without ribs = ab	i = current through the heater inside the copper rib	T_f = film temperature = $0.5(T_s + T_m)$
A_{floor} = wall heat transfer area between two ribs	k = air thermal conductivity	T_m = air mixed mean temperature at copper rib location
A_{rib} = rib total heat transfer area (three sides)	L = length of the rib-roughened portion of the test section	T_s = copper rib surface temperature
A_{total} = total heat transfer area = $A_{\text{rib}} + A_{\text{floor}}$	\dot{m} = air mass flow rate	U_m = air mean velocity
AR = channel aspect ratio = b/a	Nu = rib average Nusselt number = $h_{\text{rib}}D_h/k$	v = voltage drop across the heater inside the copper rib
AR_r = rib aspect ratio = e/w	Nu_s = average Nusselt number in a smooth channel	w = rib width
D_h = hydraulic diameter based on the smooth cross section = $4A/P = a$	P = channel perimeter without ribs	X = distance between the instrumented rib and test section entrance (Fig. 1)
e = rib height	Pr = Prandtl number	α = angle of attack
\bar{f} = Darcy friction factor = $\Delta P(D_h/L)/(1/2\rho U_m^2)$	q = net heat flux from the copper rib three surfaces = $(vi - Q_{\text{loss}})/A_{\text{rib}}$	μ = air dynamic viscosity
\bar{f}_s = Darcy friction factor in an all-smooth-wall channel	Q_{loss} = heat losses from the copper rib by radiation and conduction	ΔP = pressure drop across the rib-roughened portion of the test section
h_{floor} = average heat transfer coefficient on the wall surface between a pair of ribs	Re = Reynolds number	ρ = air density

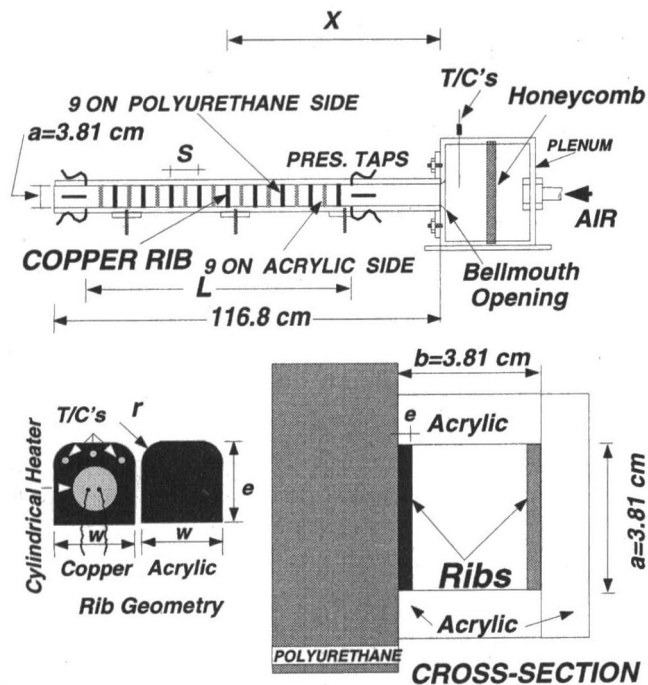


Fig. 1 Schematic of a typical test section

beginning of a core die life span, gradually deteriorate to round-corner ribs as the die wears. This change in rib profile will affect the flow pattern, which in turn decreases the heat transfer performance of the rib accompanied with a decrease in the pressure drop. It is the main objective of the present work to investigate these effects.

Test Sections

Figure 1 shows schematically the layout and cross-sectional area of a typical test section. Rib geometry details are shown in Table 1. All test sections, with a length of 116.84 cm, had a square 3.81 cm by 3.81 cm cross-sectional area. Three walls of these channels were made of 1.27-cm-thick clear acrylic plastic. The fourth wall, on which the surface heaters and instrumented copper rib were mounted and all measurements were taken, was made of a 7.62-cm-thick machinable polyurethane slab. Eighteen ribs of square cross section with round top corners were symmetrically staggered on the polyurethane wall and its opposite acrylic wall (nine on each) at 90 deg angle of attack to the air flow. The entrance region of all test sections was left smooth to simulate the cooling passage in the dovetail region of a gas turbine blade. All ribs but one were machined out of acrylic plastic and were mounted on the walls using a special double-stick 0.05-mm-thick tape with minimal temperature deformation characteristics. The instrumented rib on which all measurements were taken was machined out of copper. Inside this copper rib, a 60-Ohm cylindrical electric heater was installed using a highly conductive silver glue. The heater, which ran the full length of the rib, was mounted as centrally as possible. Also installed in the copper rib were three calibrated thermocouples to measure the surface temperature. These three thermocouples were equally spaced over the length of the rib with their beads close to the rib surface. Their temperature readings were found to be the same within a fraction of a degree. For data reduction, the average of the three temperatures was used. Copper rib surfaces were polished to minimize the radiational heat losses from the copper rib to the unheated wall. Rib heat transfer coefficient measurements were performed for two distinct rib locations. First, the copper rib was mounted in the middle of the rib-roughened portion of the channel (fifth rib) and other eight acrylic plastic ribs were arranged on each side with the desired rib pitch-

to-height ratio. Second, the copper rib was moved to the furthest upstream position and the other eight ribs were mounted downstream of it. Table 1 shows the rib location from the channel entrance, X , for each geometry. Two 3.81 cm by 27.94 cm custom-made etched-foil heaters with a thickness of 0.15 mm were placed on the polyurethane wall abutting both sides of the copper rib using the same special double-stick tape. The test section was covered on all sides by 5-cm-thick styrofoam sheets to minimize the heat losses to the environment. Surface heat flux in the test section was generated by the heaters through a custom-designed power supply unit. Each heater was individually controlled by a variable transformer.

Before testing, thermocouples were calibrated using ice water and boiling water reference points and calibration curves were constructed for minor deviations (within a fraction of a degree). For a typical test run, the Reynolds number was set by precisely fixing the mass flow rate. The heat flux was induced by adjusting heater power until the copper rib reached the desired temperature. Enough time was given so that the system came to thermal equilibrium, at which time data was recorded. Power to the copper rib was then increased to gather data at a higher surface temperature. This procedure was repeated for all copper temperatures and flow rates.

Static pressure taps were mounted on all three acrylic plastic walls of the test section to measure the pressure drop across the rib-roughened portion of the test section. A contact micromanometer with an accuracy of 0.025 mm of water column measured the pressure differences between the static pressure taps. A critical venturimeter, with choked flow for all cases tested, measured the total mass flow rate entering the test section. The reported friction factor is the overall passage average, \bar{f} , and not just the rib-roughened surfaces. Details of the experimental apparatus and test procedures are reported by Korotky (1994).

The radiational heat loss from the heated rib (and wall) to the unheated walls as well as losses to ambient air were taken into consideration when heat transfer coefficients were calculated. The reported heat transfer coefficients are the averages over the rib surfaces and not that of wall surfaces between the ribs. The heat transfer coefficients on the roughened walls for various geometries are reported by those investigators mentioned in the Introduction section. Experimental uncertainties, following the method of Kline and McClintock (1953), were determined to be ± 8 and ± 6 percent for the heat transfer coefficient and friction factor, respectively.

Results and Discussion

Heat transfer as well as friction factor results for the twelve round corner rib geometries are compared with those of sharp edge ribs in Figs. 3–6 and 8–16. The Dittus–Boelter (1930)

Table 1 Specifications

Test	e (mm)	r/e	e/Dh	S/e	X (cm)	X/Dh	Remarks
1	9.525	0.25	0.25	5	57.4	15	Midstream
2	9.525	0.25	0.25	8.5	57.4	15	Midstream
3	9.525	0.25	0.25	10	57.4	15	Midstream
4	9.525	0.25	0.25	8.5	24.89	10.4	Upstream
5	6.35	0.25	0.167	5	57.4	15	Midstream
6	6.35	0.25	0.167	8.5	57.4	15	Midstream
7	6.35	0.25	0.167	10	57.4	15	Midstream
8	6.35	0.25	0.167	8.5	35.81	9.4	Upstream
9	5.08	0.197	0.133	5	57.15	15	Midstream
10	5.08	0.197	0.133	8.5	57.15	15	Midstream
11	5.08	0.197	0.133	10	57.15	15	Midstream
12	5.08	0.197	0.133	8.5	39.62	10.4	Upstream

AR = 1, AR_t = e/w = 1, $\alpha = 90^\circ$ Staggered for all Geometries

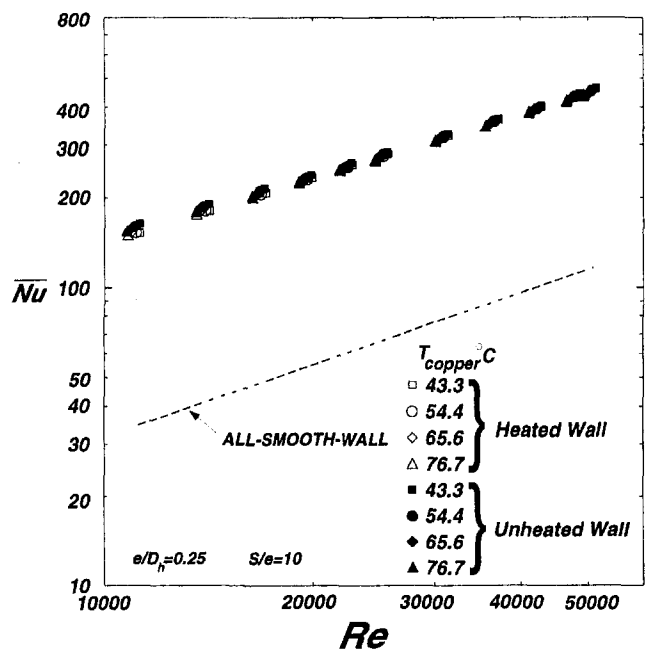


Fig. 2 Rib average Nusselt number for a range of rib surface temperatures

correlation for an all-smooth-wall channel ($\overline{Nu}_s = 0.023Re^{0.8} Pr^{0.4}$) is plotted in Fig. 2. With this correlation, the enhancement (relative to smooth walls) in rib-roughened heat transfer coefficients is readily evaluated. The thermal performance based on the same pumping power was derived by Gee and Webb (1980) as $(\overline{Nu}/\overline{Nu}_s)/(\overline{f}/\overline{f}_s)^{1/3}$, where \overline{f}_s is the all-smooth-wall friction factor from Moody (1944). It should be noted that the thermal performances reported here do not include the contribution of the heat transfer coefficient on the surface area between the ribs, h_{floor} . Thermal performance data for the surface area between the ribs are reported by the second author (Taslim et al., 1996) and can be combined with the present data to determine the overall thermal performances. Air properties for Nusselt and Reynolds number calculations are based on the local film temperature, T_f , for all cases.

Figure 2 shows the Nusselt versus Reynolds numbers for the first rib geometry corresponding to a blockage ratio, e/D_h , of 0.25 and a pitch-to-height ratio, S/e , of 10. Copper rib temperature is varied from 43.3°C to 76.7°C with no change in the measured heat transfer coefficient. This lack of effect of the copper surface temperature on heat transfer coefficient continued for all geometries examined. Furthermore, this insensitivity of the measured heat transfer coefficient to the rib surface temperature supports the accuracy of our accounting for the heat losses to the ambient air and radiational losses from the heated copper rib to the unheated surrounding walls.

To investigate the effects pitch-to-height ratio have on rib heat transfer and channel overall friction factor, the same rib geometry was tested for three pitch-to-height ratios of 5, 8.5, and 10 (geometries 1–3 in Table 1) the results of which are shown in Fig. 3. Also shown in Fig. 3 are the rib heat transfer results for an S/e of 8.5 when the instrumented copper rib was mounted in the furthest upstream position (geometry 4 in Table 1). Several observations are made. First, the heat transfer coefficient for the furthest upstream rib was considerably lower than that for the rib in the middle of the rib-roughened region, indicating that upstream ribs and those staggered on the opposite wall contribute significantly to the very high level of heat transfer enhancement of downstream ribs by interrupting the flow and diverting its direction thus promoting high levels of mixing. Second, round-corner ribs produced lower Nusselt numbers than

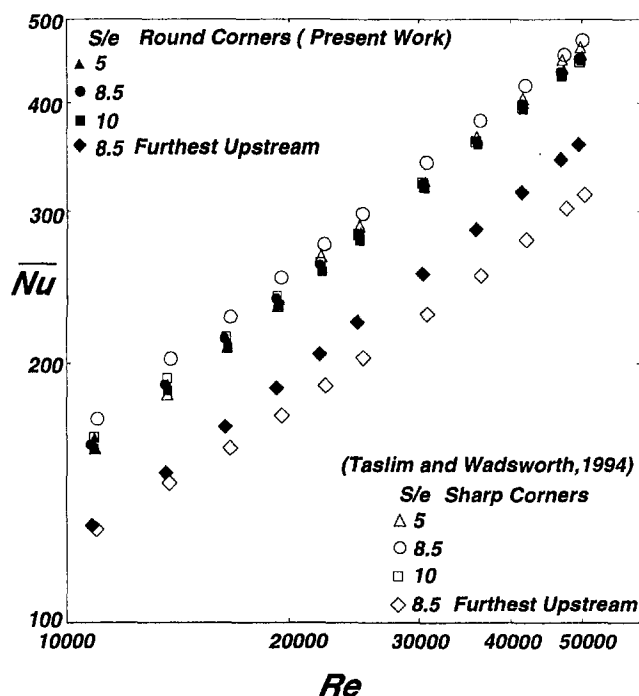


Fig. 3 Rib average Nusselt number for a range of pitch-to-height ratios for $e/D_h = 0.25$

sharp-edged ribs in the midstream position. This was expected, especially for high blockage ratio ribs such as these. Reported data by the second author (Taslim and Spring, 1994) and other investigators have shown that, when the rib corners are rounded, the heat transfer coefficient on the surface between the ribs reduces due to lower levels of mixing of the warmer near-wall air with the core air. At the same time, the contribution of the round-corner ribs on the opposite wall to the flow interruption is somewhat reduced. It is speculated that, for the same reasons, the heat transfer coefficients on the rib surfaces also decrease when rib corners are rounded. However, the round-corner ribs in the furthest upstream position produced Nusselt numbers higher than those by sharp-edged ribs. This behavior, which is consistent for other blockage ratios, could be attributed to the formation of recirculating bubbles on top and directly behind the sharp edged rib in the furthest upstream position, thus reducing the core flow contact with the rib surface. Rounding of the sharp corners, on the other hand, enhances the flow adherence to the rib surfaces (Lockett and Collins, 1990), which, in turn, increases the heat transfer coefficient. Third, for round-corner ribs, the middle position Nusselt numbers was insensitive to the pitch-to-height ratio. This could also be attributed to a better adherence of the flow to round-corner ribs. Effects of rib spacing on Nusselt number for this rib and the other two geometries for a typical Reynolds number are shown in Fig. 17. It is noted that the heat transfer coefficients for the smaller ribs are sensitive to the rib spacing. Friction factors for these geometries are shown in Fig. 4. As one would expect, the round-edge ribs produce lower pressure drops and consequently lower friction factors compared to sharp edged ribs. However, S/e of 5 represented a reversed trend for round-edge ribs. Following the discussion of the heat transfer results, better adherence of flow to the round-edge rib surfaces can produce higher skin friction while in case of sharp-edge ribs, if ribs are positioned too close to each other, with the formation of a recirculating bubble in the cavity between the ribs the flow may totally skip that cavity, thus producing a lower friction factor.

The next series of four tests, shown in Fig. 5, corresponded to a rib blockage ratio of 0.167, three of which (test geometries 5–8 in Table 1) were performed for pitch-to-height ratios of

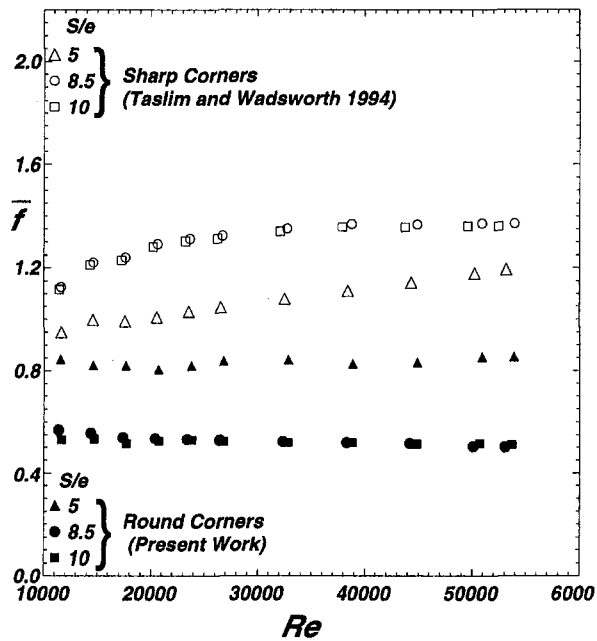


Fig. 4 Channel average friction factor for a range of pitch-to-height ratios, $e/D_h = 0.25$

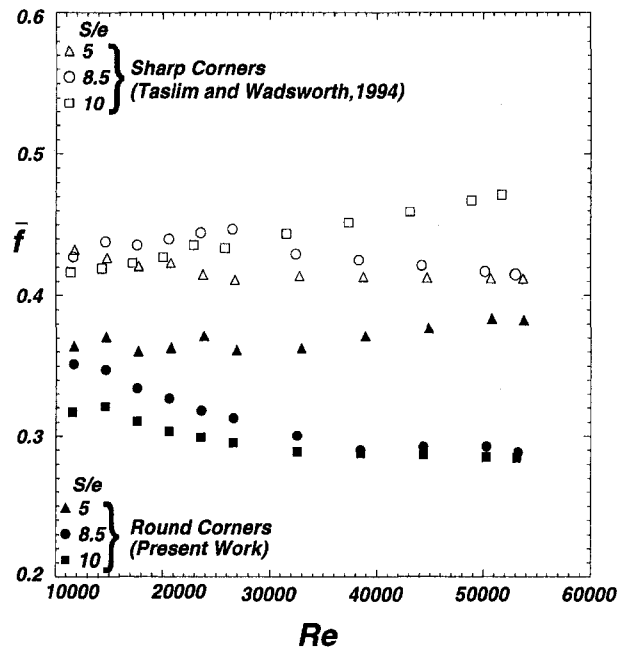


Fig. 6 Channel average friction for a range of pitch-to-height ratios for $e/D_h = 0.167$

10, 8.5, and 5 with the instrumented copper rib mounted in the middle of the rib-roughened region. The fourth test represents the heat transfer results when copper rib was mounted in the furthest upstream position (geometry 8 in Table 1). Again, midstream sharp-edged ribs produced higher Nusselt numbers than round-edge ribs and the trend was reversed for the furthest upstream ribs similar to the previous case of 0.25 blockage ratio. The round-edge rib heat transfer results for the pitch-to-height ratio of 10 were higher than those of $S/e = 5$ and 8.5. For the sharp-edged ribs, however, a pitch-to-height ratio of 8.5 produced the highest heat transfer coefficient. Also, heat transfer enhancement for the furthest upstream rib was lower than that for midstream ribs, although not as much lower as it was for

the blockage ratio of 0.25 as seen in Fig. 3. We will see that this difference further reduced for a still lower blockage ratio test. The friction factors for these tests are shown in Fig. 6 and trends are similar to that of Fig. 4, i.e., (a) lower pressure drops (friction factors) for round-corner ribs and (b) for round-corner ribs, S/e of 5 producing a higher friction factor than those of $S/e = 8.5$ and 10.

Figure 7 shows the results of two tests of identical geometries for which the foil heaters were on and off, respectively. A maximum difference of 6 percent was measured for the lowest tested Reynolds number. At higher Reynolds numbers, however, the difference was well below the experimental uncertainties, indicating that, for most test points, the thermal boundary

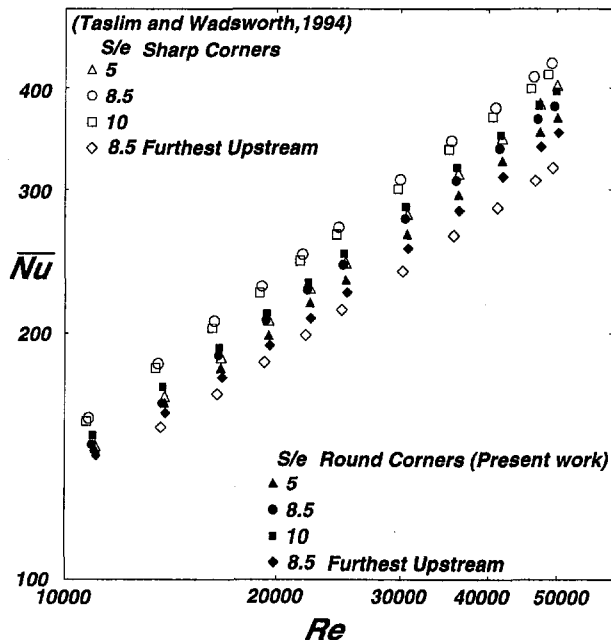


Fig. 5 Rib average Nusselt number for a range of pitch-to-height ratios for $e/D_h = 0.167$

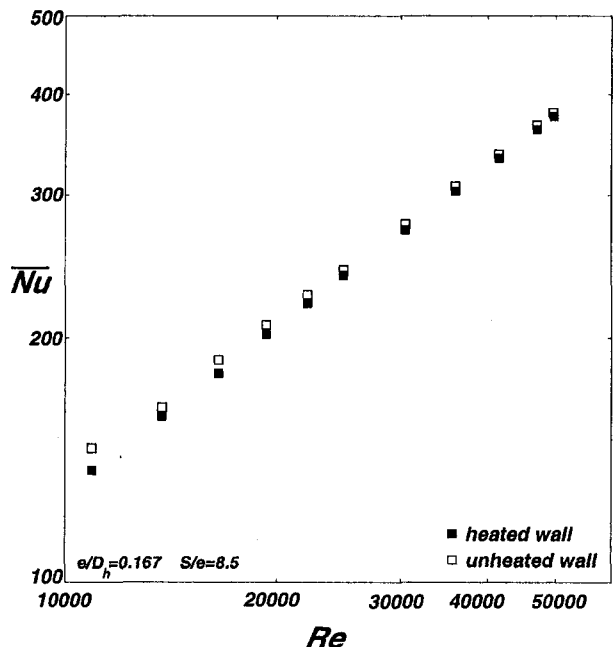


Fig. 7 Comparison of rib average Nusselt numbers for heated and unheated walls

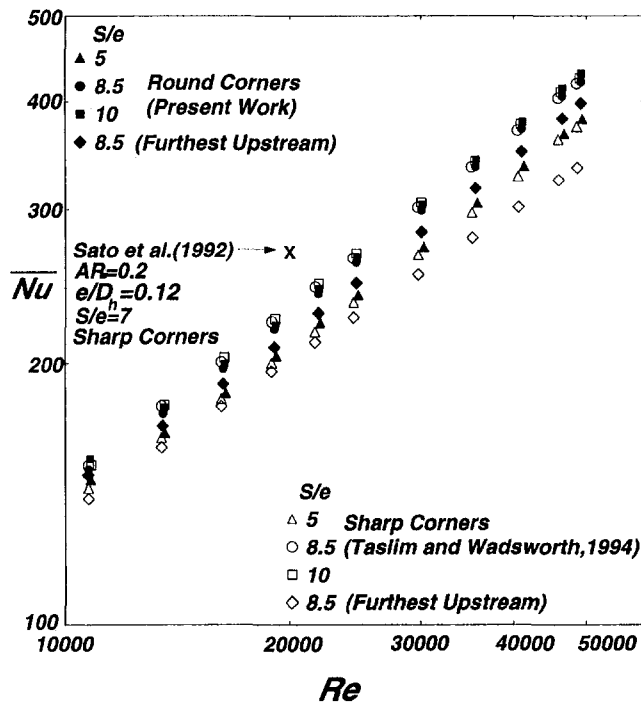


Fig. 8 Rib average Nusselt number for a range of pitch-to-height ratios, $e/D_h = 0.133$

layer, being interrupted repeatedly by the ribs, did not affect the heat transfer. It would appear that the mixing phenomenon was the dominant driving force for the high levels of heat transfer coefficient. As for having only one heated wall, it is noted that an experimental investigation by El-Husayni et al. (1994) on heat transfer in a rib-roughened channel with one, two, and four heated walls showed that, in a stationary roughened channel, the heat transfer coefficient was not significantly sensitive to the number of heated walls, i.e., the variation in heat transfer coefficient was within the reported experimental uncertainty of ± 8 percent.

The next four tests, shown in Fig. 8, corresponded to a yet smaller rib blockage ratio of 0.133. The first three tests (geometries 9–11 in Table 1) were performed for pitch-to-height ratios of 10, 8.5, and 5 with the instrumented copper rib mounted in the middle of the rib-roughened region. The fourth test represents the heat transfer results for the copper rib mounted in the furthest upstream position (geometry 12 in Table 1). A data point from Sato et al. (1992) is also plotted for sharp corner staggered ribs in a small aspect ratio channel ($AR = 0.2$) for a rib blockage ratio of 0.12 and a pitch-to-height ratio of 7. This geometry was the closest to the present geometry that could be found in the open literature. The higher heat transfer coefficient is attributed to a very small channel aspect ratio, which brings the ribs on the two opposite walls very close to each other. Several other observations are made. Round-corner rib results for this small blockage ratio are relatively close to those of sharp-edged ribs since (a) the rib radius-to-height ratio, r/e (Table 1) was smaller than that for the other two rib geometries, and (b) several investigators, including the second author, have shown that the rounding effects on heat transfer coefficient are less pronounced for low blockage ratio ribs. Again, the round-corner rib in the furthest upstream position produced a higher heat transfer coefficient than that of a sharp-edged rib in the same position. In contrast with the above-mentioned cases of higher blockage ratios, the heat transfer enhancements for the furthest upstream rib were comparable to those of midstream ribs at low Reynolds numbers, and only at higher Reynolds numbers did they start to deviate. This is an indication that the

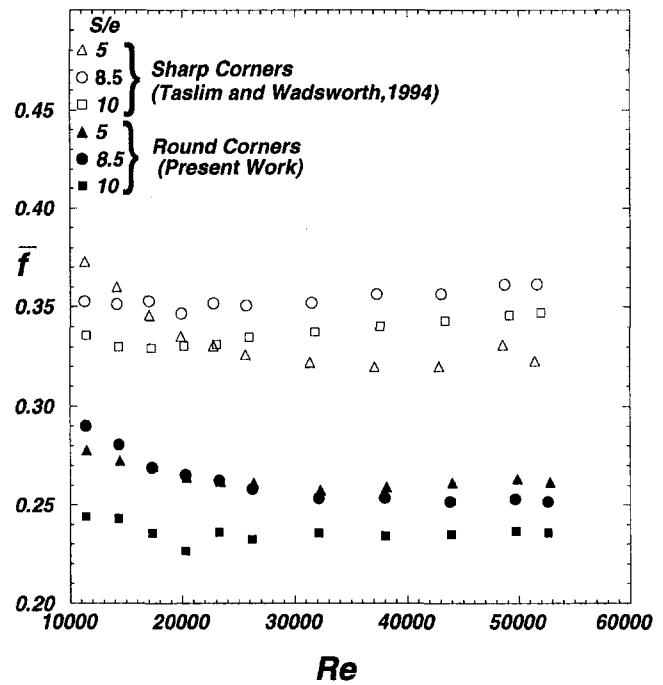


Fig. 9 Channel average friction factor for a range of pitch-to-height ratios, for $e/D_h = 0.133$

contribution of the staggered ribs on the opposite wall to the copper rib heat transfer coefficient, caused by the diversion of flow toward the ribs on the opposite wall, is more significant for higher blockage ratios and at higher Reynolds numbers. For the round-corner ribs, the Nusselt numbers corresponding to the pitch-to-height ratio of 5 fell below the furthest upstream rib results indicating a poor thermal communication between the ribs on opposite walls and a low level of mixing for these low blockage ratio ribs. The rounding effects on the friction factor are more significant than those on the heat transfer as they are shown in Fig. 9. This behavior is also observed on the surface between the ribs by other investigators.

Figure 10 combines the results of all three rib geometries in the furthest upstream position at S/e of 8.5. It is seen that smaller ribs produce higher heat transfer coefficients. Not benefiting from the effects of the ribs on the opposite wall, it is speculated that this behavior is due to the change of flow pattern over different ribs. In other words, for the sharp-edged ribs in the extreme case, recirculating bubbles may form on both the back and top surfaces of the big rib, reducing the contribution of the rib top surface to heat transfer, known to be major for square ribs with sharp corners by all investigators mentioned above. For round-corner ribs and the smallest sharp-edged rib, however, the top surface is in contact with the core air; thus higher heat transfer coefficients are produced.

Figures 11 and 12 compare the midchannel rib heat transfer coefficient and channel friction factors for three blockage ratios at one pitch-to-height ratio of 10. In contrast with the heat transfer coefficient on the area between a pair of ribs, which is highly affected by the blockage ratio, the rib heat transfer coefficient did not show as strong a dependence on blockage ratio for $S/e = 10$. However, as ribs were brought closer to each other by reducing the pitch-to-height ratio, rib heat transfer coefficient was more and more affected by the blockage ratio (Figs. 13 and 15). It is noted that for all pitch-to-height ratios (Figs. 11, 13, and 15) the round-corner rib with the blockage ratio of 0.133 produced higher heat transfer coefficients than that with a blockage ratio of 0.167. This was not the case for the sharp-corner ribs. The reason for this behavior is the higher roundness of r/e for the bigger rib, indicating the significant

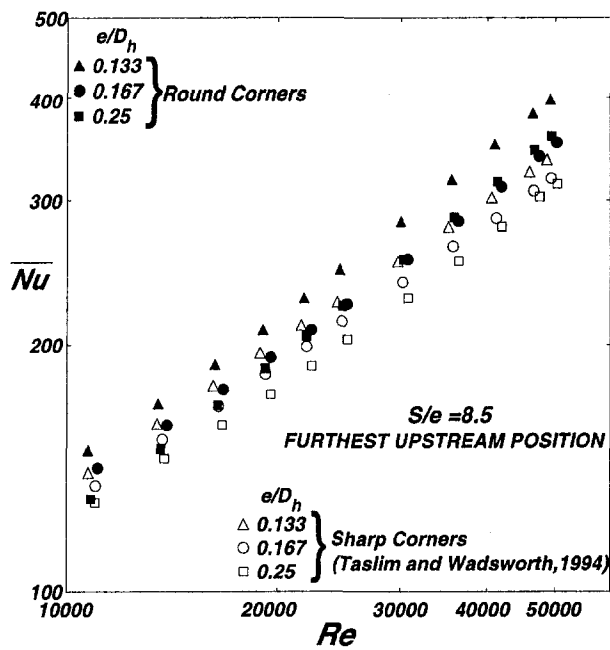


Fig. 10 Rib average Nusselt number of the furthest upstream rib for a range of blockage ratios

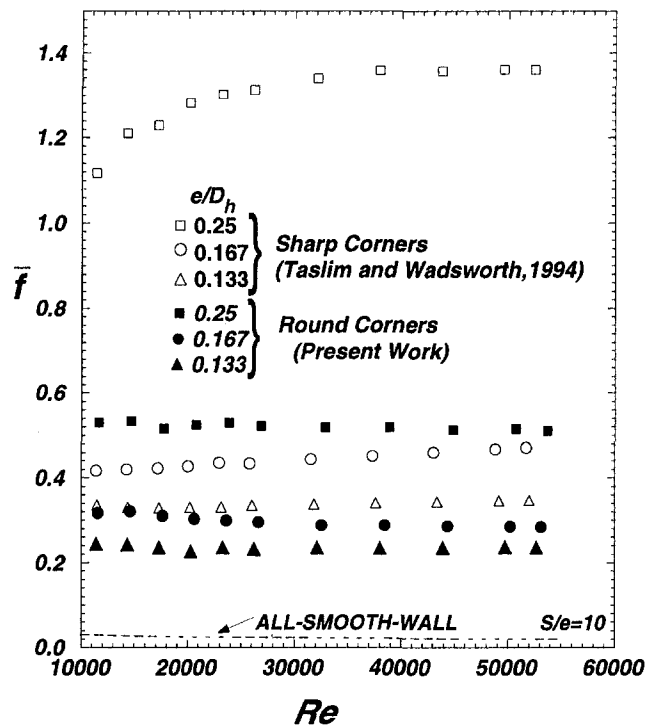


Fig. 12 Channel average friction factor for a range of blockage ratios, $S/e = 10$

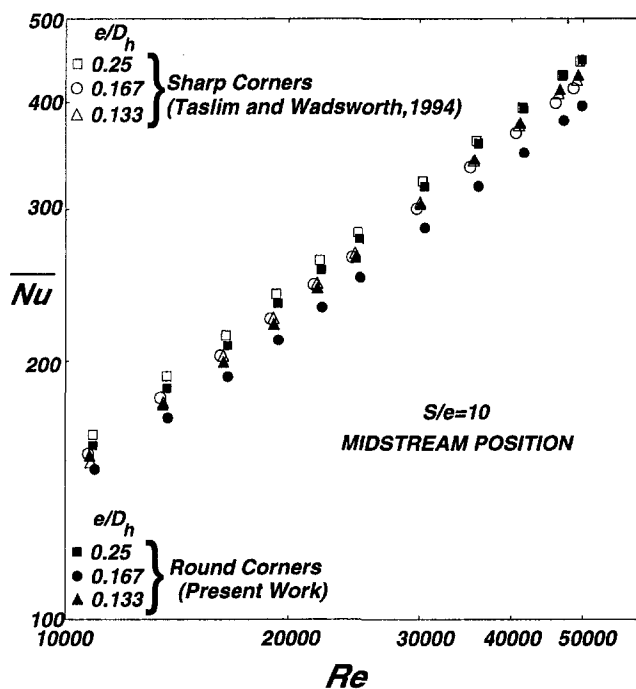


Fig. 11 Rib average Nusselt number for a range of blockage ratios, $S/e = 10$

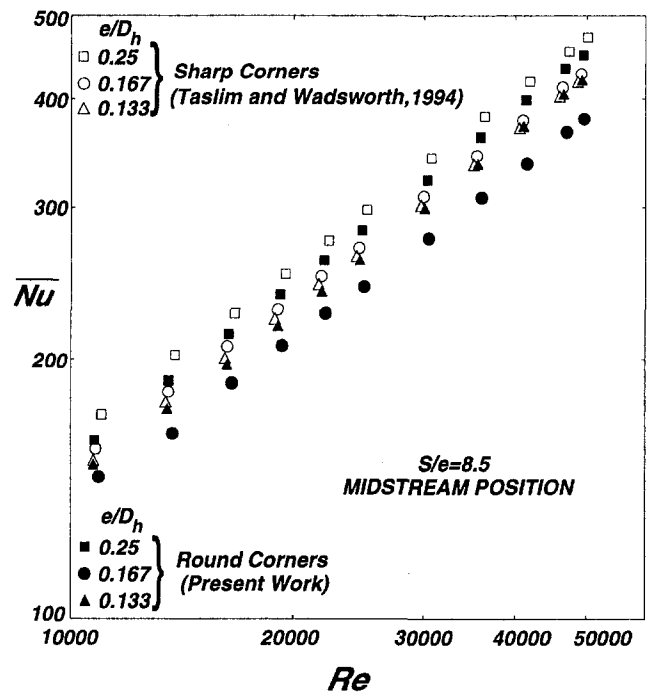


Fig. 13 Rib average Nusselt number for a range of blockage ratios, $S/e = 8.5$

effect of rounding on rib heat transfer coefficient. The corresponding friction factors for S/e of 8.5 and 5 are shown in Figs. 14 and 16.

Figure 17 shows the variation of Nusselt number with the rib spacing for the three rib geometries tested. The results are for a typical Reynolds number of 30,000 and for the ribs in the midstream position. Nusselt number increases with the pitch-to-height ratio for the two smaller ribs while the rib with the highest blockage ratio shows a slight decrease. In contrast with the sharp-corner ribs for which a pitch-to-height ratio of 8.5 was determined to be an optimum, it appears that for the round-

corner ribs, especially the two smaller geometries, the optimum spacing is 10 and possibly greater. Low rib spacing resembles a cavity-driven flow between the ribs that causes a decrease in the heat transfer coefficient (Metzger et al., 1988).

Finally, the thermal performances of all geometries tested are compared in Fig. 18. It is seen that as the blockage ratio increases, the rib thermal performance decreases. For the blockage ratios of 0.167 and 0.25, the furthest upstream ribs had the

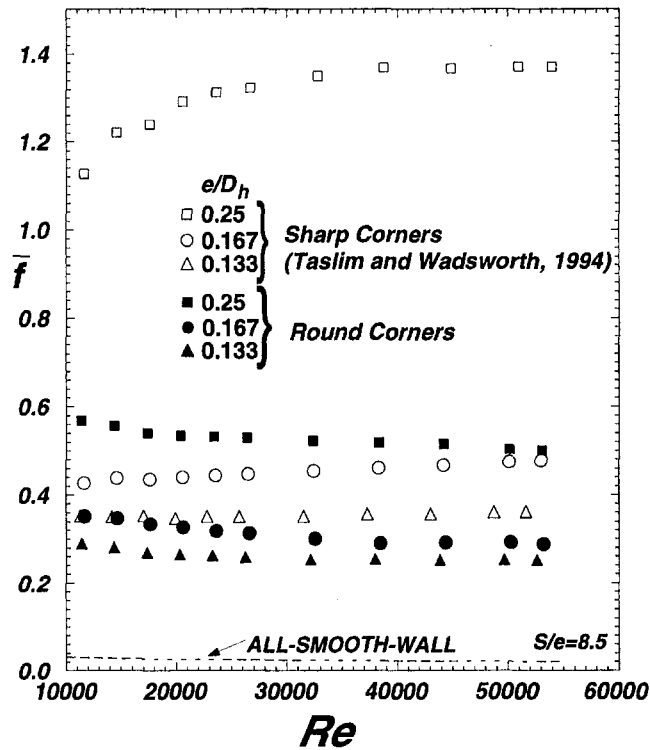


Fig. 14 Channel average friction factor for a range of blockage ratios, $S/e = 8.5$

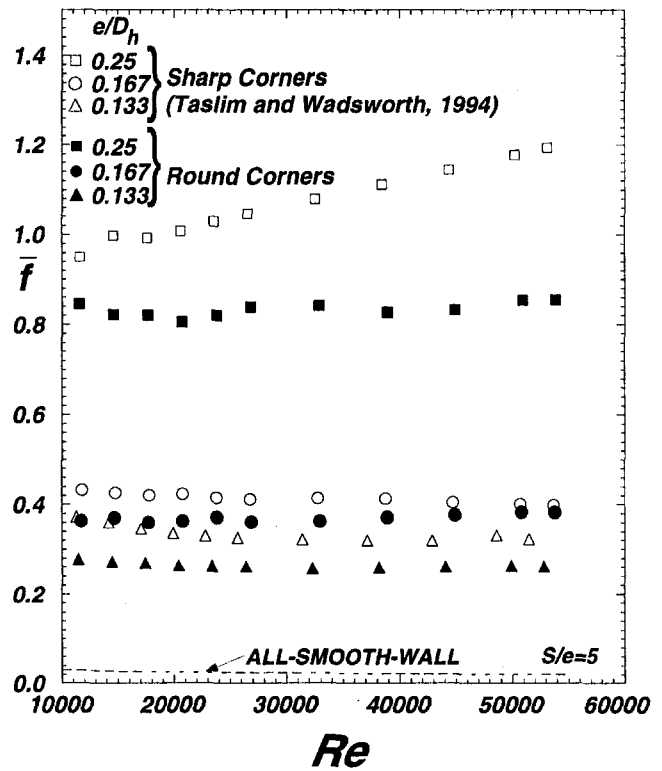


Fig. 16 Channel average friction factor for a range of blockage ratios, $S/e = 5$

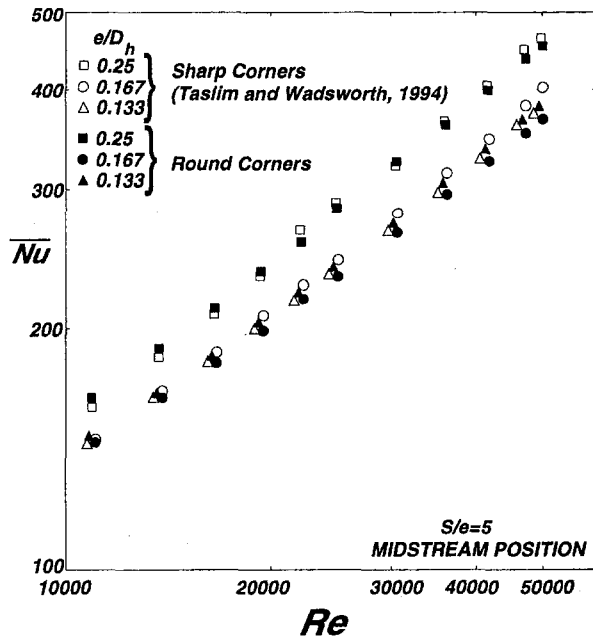


Fig. 15 Rib average Nusselt number for a range of blockage ratios, $S/e = 5.0$

lowest thermal performances. This was expected since, for the same channel average friction factor, the furthest upstream rib had a lower heat transfer coefficient than that in the middle of the rib-roughened region. For the small ribs, however, the pitch-to-height ratio of 5 showed the lowest thermal performance.

Conclusions

A total of twelve round-corner rib geometries representing three blockage ratios in a practical range for small aircraft en-

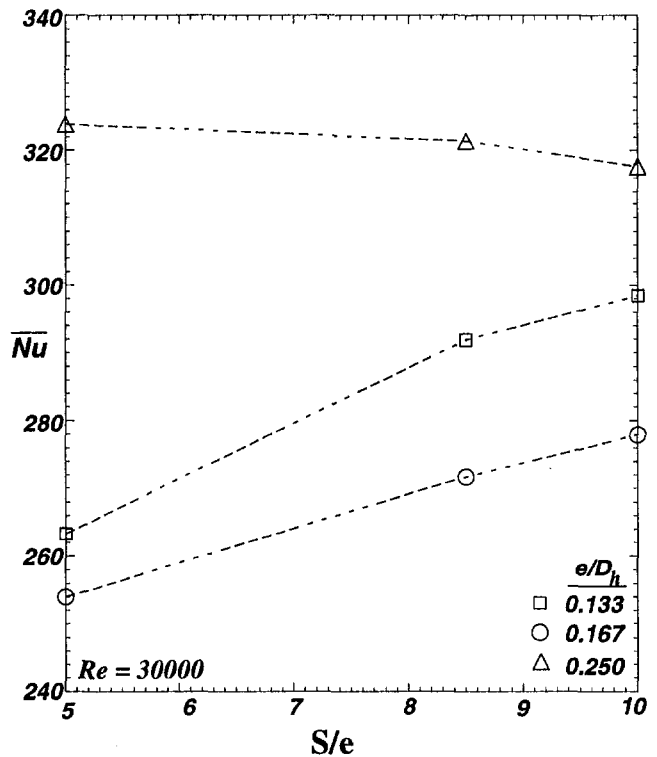


Fig. 17 Rib average Nusselt number versus pitch-to-height ratio for all blockage ratios

gines and at three pitch-to-height ratios were tested for heat transfer and pressure loss variations. The results were compared with those of sharp-edge ribs reported previously. From this study, it was concluded that:

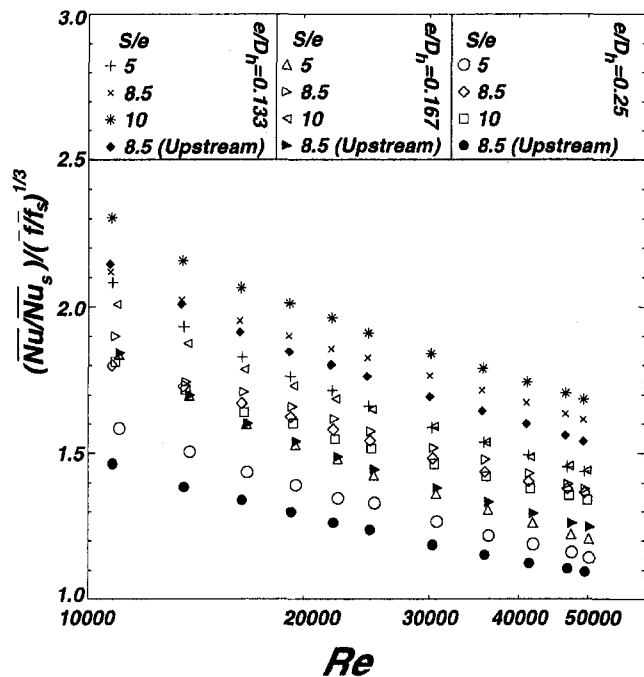


Fig. 18 Rib thermal performances of the twelve geometries

1 For the geometries tested, the rib average heat transfer coefficient was much higher than that for the area between the ribs. For high blockage ribs with large heat transfer areas, commonly used in small gas turbines, the rib heat transfer is a significant portion of the overall heat transfer in the cooling passages. For the sharp-corner ribs, the rib average heat transfer coefficient increased with the blockage ratio. However, when the corners were rounded, the trend depended on the level of roundness, r/e .

2 High blockage ratio ($e/D_h = 0.25$) ribs were insensitive to the pitch-to-height ratio. For the other two blockage ratios, the pitch-to-height ratio of 5 produced the lowest heat transfer coefficient. Results of the other two pitch-to-height ratios were very close, with the results of $S/e = 10$ slightly higher than those of $S/e = 8.5$.

3 Under otherwise identical conditions, ribs in the furthest upstream position produced lower heat transfer coefficients for all cases except that of the smallest blockage ratio with S/e of 5. In that position, for the rib geometries tested, while the sharp-corner rib average heat transfer coefficients increased with the blockage ratio, the trend of round-corner ribs depended on the level of roundness, r/e .

4 The thermal performance decreased with the blockage ratio. While the smallest rib geometry at a pitch-to-height ratio of 10 had the highest thermal performance, thermal performance of high blockage ribs at a pitch-to-height ratio of 5 was the lowest.

5 The general effect of rounding was a decrease in the heat transfer coefficient for midstream ribs and an increase for the ribs in the furthest upstream position.

References

Abuaf, N., Gibbs, R., and Baum, R., 1986, "Pressure Drop and Heat Transfer Coefficient Distributions in Serpentine Passages With and Without Turbulence Promoters," *Eighth International Heat Transfer Conference*, C. L. Tien, V. P. Carey, and J. K. Ferrel, eds., pp. 2837-2845.

Berger, F. P., and Hau, K. F., F. L., 1979, "Local Mass/Heat Transfer Distribution on Surfaces Roughened With Small Square Ribs," *Int. J. Heat Mass Transfer*, Vol. 22, pp. 1645-1656.

Burggraf, F., 1970, "Experimental Heat Transfer and Pressure Drop With Two Dimensional Turbulence Promoters Applied to Two Opposite Walls of a Square

Tube," *Augmentation of Convective Heat and Mass Transfer*, by A. E. Bergles and R. L. Webb, eds., ASME, pp. 70-79.

Chandra, P. R., Han, J. C., and Lau, S. C., 1988, "Effect of Rib Angle on Local Heat/Mass Transfer Distribution in a Two Pass Rib-Roughened Channel," *ASME JOURNAL OF TURBOMACHINERY*, Vol. 110, pp. 233-241.

Chandra, P. R., and Han, J. C., 1989, "Pressure Drop and Mass Transfer in Two-Pass Ribbed Channels," *AIAA Journal of Thermophysics*, Vol. 3, No. 3, pp. 315-319.

Colburn, A. P., 1933, "A Method of Correlating Forced Convection Heat Transfer Data and a Comparison With Fluid Friction," *TRANS. AICHE*, Vol. 29, pp. 174-210.

Dawes, W. N., 1994, "The Solution-Adaptive Numerical Simulation of the 3D Viscous Flow in the Serpentine Coolant Passage of a Radial Inflow Turbine Blade," *ASME JOURNAL OF TURBOMACHINERY*, Vol. 116, pp. 141-148.

Dittus, F. W., and Boelter, L. M. K., 1930, *Publications in Engineering*, University of California, Berkeley, CA, Vol. 2, p. 443.

El-Husayni, H. A., Taslim, M. E., and Kercher, D. M., 1994, "An Experimental Investigation of Heat Transfer Coefficients in a Spanwise Rotating Channel With Two Opposite Rib-Roughened Walls," *ASME JOURNAL OF TURBOMACHINERY*, Vol. 113, pp. 75-82.

Gee, D. L., and Webb, R. L., 1980, "Forced Convection Heat Transfer in Helically Rib-Roughened Tubes," *Int. J. Heat Mass Transfer*, Vol. 23, pp. 1127-1136.

Han, J. C., Glicksman, L. R., and Rohsenow, W. M., 1978, "An Investigation of Heat Transfer and Friction for Rib Roughened Surfaces," *International Journal of Heat Mass Transfer*, Vol. 21, pp. 1143-1156.

Han, J. C., 1984, "Heat Transfer and Friction in Channels With Two Opposite Rib-Roughened Walls," *ASME Journal of Heat Transfer*, Vol. 106, No. 4, pp. 774-781.

Han, J. C., Park, J. S., and Lei, C. K., 1985, "Heat Transfer Enhancement in Channels With Turbulence Promoters," *ASME Journal of Engineering for Gas Turbines and Power*, Vol. 107, pp. 628-635.

Han, J. C., Zhang, Y. M., and Lee, C. P., 1992, "Influence of Surface Heat Flux Ratio on Heat Transfer Augmentation in Square Channels With Parallel, Crossed, and V-Shaped Angled Ribs," *JOURNAL OF TURBOMACHINERY*, Vol. 114, pp. 872-880.

Kline, S. J., and McClintock, F. A., 1953, "Describing Uncertainty in Single-Sample Experiments," *Mechanical Engineering*, Vol. 75, Jan., pp. 3-8.

Korotky, G. J., 1994, "An Experimental Investigation of the Rib Surface-Averaged Heat Transfer Coefficient in a Square Passage Roughened With Rounded Ribs of Two Aspect Ratios," MS Thesis, Mechanical Engineering Dept., Northeastern University, Boston, MA.

Liou, T. M., Hwang, J. J., and Chen, S. H., 1991, "Turbulent Heat Transfer and Fluid Flow in a Channel With Repeated Rib Pairs," *Proc. ASME/JSME Thermal Eng.*, Vol. 3, pp. 205-212.

Liou, T. M., and Hwang, J. J., 1993, "Effects of Ridge Shapes on Turbulent Heat Transfer and Friction in a Rectangular Channel," *Int. J. Heat Mass Transfer*, Vol. 36, pp. 931-940.

Lockett, J. F., and Collins, M. W., 1990, "Holographic Interferometry Applied to Rib-Roughness Heat Transfer in Turbulent Flow," *Int. J. of Heat Mass Transfer*, Vol. 33, pp. 2439-2449.

Metzger, D. E., Fan, C. S., and Pennington, J. W., 1983, "Heat Transfer and Flow Friction Characteristics of Very Rough Transverse Ribbed Surfaces With and Without Pin Fins," *Proc. ASME-JSME Thermal Engineering Joint Conference*, Vol. 1, pp. 429-436.

Metzger, D. E., Chyu, M. K., and Bunker, R. S., 1988, "The Contribution of On-Rib Heat Transfer Coefficients to Total Heat Transfer From Rib-Roughened Surfaces," *Transport Phenomena in Rotating Machinery*, J. H. Kim, ed., Hemisphere Publishing Co.

Metzger, D. E., Fan, C. S., and Yu, Y., 1990, "Effects of Rib Angle and Orientation on Local Heat Transfer in Square Channels With Angled Roughness Ribs," *Compact Heat Exchangers: A Festschrift for A. L. London*, Hemisphere Publishing Co., pp. 151-167.

Moody, L. F., 1944, "Friction Factors for Pipe Flow," *Transactions of ASME*, Vol. 66, p. 671.

Sato, H., Hishida, K., and Maeda, M., 1992, "Characteristics of Turbulent Flow and Heat Transfer in a Rectangular Channel With Repeated Rib Roughness," *Exp. Heat Transfer*, Vol. 5, pp. 1-16.

Solntsev, V. P., Luzhanskii, B. E., and Kryukov, V. N., 1973, "An Investigation of Heat Transfer in the Turbulent Separation Zones in the Vicinity of Sudden Steps," *Heat Transfer—Society Research*, Vol. 5, No. 2, pp. 122-128.

Taslim, M. E., and Spring, S. D., 1988a, "An Experimental Investigation of Heat Transfer Coefficients and Friction Factors in Passages of Different Aspect Ratio Roughened With 45° Turbulators," *Proc. ASME National Heat Conference*, Houston, TX.

Taslim, M. E., and Spring, S. D., 1988b, "Experimental Heat Transfer and Friction Factors in Turbulated Cooling Passages of Different Aspect Ratios, Where Turbulators Are Staggered," Paper No. AIAA-88-3014.

Taslim, M. E., Rahman, A., and Spring, S. D., 1991a, "An Experimental Investigation of Heat Transfer Coefficients in a Spanwise Rotating Channel With Two Opposite Rib-Roughened Walls," *ASME JOURNAL OF TURBOMACHINERY*, Vol. 113, pp. 75-82.

Taslim, M. E., Bondi, L. A., and Kercher, D. M., 1991b, "An Experimental Investigation of Heat Transfer in an Orthogonally Rotating Channel Roughened With 45° Criss-Cross Ribs on Two Opposite Walls," *ASME JOURNAL OF TURBOMACHINERY*, Vol. 113, pp. 346-353.

Taslim, M. E., and Spring, S. D., 1994, "Effects of Turbulator Profile and Spacing on Heat Transfer and Friction in a Channel," *AIAA J. Thermophysics and Heat Transfer*, Vol. 8, No. 3, pp. 555–562.

Taslim, M. E., Li, T., and Kercher, D. M., 1996, "Experimental Heat Transfer and Friction in Channels Roughened With Angled, V-Shaped, and Discrete Ribs on Two Opposite Walls," *ASME JOURNAL OF TURBOMACHINERY*, Vol. 118, pp. 1–9.

Taslim, M. E., and Wadsworth, C. M., 1997, "An Experimental Investigation of the Rib Surface-Averaged Heat Transfer Coefficient in a Rib-Roughened Square Passage," *ASME JOURNAL OF TURBOMACHINERY*, Vol. 119, pp. 381–389.

Webb, R. L., Eckert, E. R. G., and Goldstein, R. J., 1971, "Heat Transfer and Friction in Tubes With Repeated-Rib-Roughness," *Int. J. Heat Mass Transfer*, Vol. 14, pp. 601–617.

LDA Study of the Flow Development Through an Orthogonally Rotating U-Bend of Strong Curvature and Rib-Roughened Walls

H. Iacovides

D. C. Jackson

H. Ji

G. Kelemenis

B. E. Launder

K. Nikas

Department of Mechanical Engineering,
UMIST,
P.O. Box 88,
Manchester M60 1QD, United Kingdom

This paper reports laser-Doppler anemometry (LDA) and wall pressure measurements of turbulent flow in a square-sectioned, rotating U-bend, typical of coolant passages employed in modern gas turbine blades. In the upstream and downstream tangents, the pressure and suction (inner and outer) surfaces are roughened with discrete square-sectioned ribs in a staggered arrangement for a rib-height to duct-diameter ratio of 0.1. Three cases have been examined at a passage Reynolds number of 10^5 : a stationary case; a case of positive rotation (the pressure side coinciding with the outer side of the U-bend) at a rotation number ($Ro \equiv \Omega D/U_m$) of 0.2; and a case of negative rotation at $Ro = -0.2$. Measurements have been obtained along the symmetry plane of the duct. In the upstream section, the separation bubble behind each rib is about 2.5 rib heights long. Rotation displaces the high-momentum fluid toward the pressure side, enhances turbulence along the pressure side, and suppresses turbulence along the suction side. The introduction of ribs in the straight sections reduces the size of the separation bubble along the inner wall of the U-bend, by raising turbulence levels at the bend entry; it also causes the formation of an additional separation bubble over the first rib interval along the outer wall, downstream of the bend exit. Rotation also modifies the mean flow development within the U-bend, with negative rotation speeding up the flow along the inner wall and causing a wider inner-wall separation bubble at exit. Turbulence levels within the bend are generally increased by rotation and, over the first two diameters downstream of the bend, negative rotation increases turbulence while positive rotation on the whole has the opposite effect.

1 Introduction

Flow and heat transfer in U-bends of strong curvature are of direct relevance to the internal cooling of gas turbine blades. In modern gas turbines, relatively cool air, extracted from the compressor stages of the engine, is circulated through internal cooling passages inside the turbine rotor blades, in order to maintain the operating temperature of the blades at safe levels. Flow and heat transfer inside these cooling channels are affected by the presence of sharp U-bends, the rotation of the blades giving rise to Coriolis and rotational buoyancy forces, and the presence of heat-transfer-enhancing ribs.

In three-dimensional flows through either curved or rotating passages, both the Coriolis force and curvature induce strong secondary motions (see, for example, Moon, 1964; Taylor et al., 1982; Chang et al., 1983). In blade cooling passages, space constraints dictate that the U-bend must be so tight that flow separation occurs downstream of the bend and also possibly at the bend entry. The flow thus becomes considerably more complex, even in the absence of ribs and rotation. The combined effects of strong curvature and orthogonal rotation have been examined in our earlier experimental study (Cheah et al., 1996), in which detailed LDA data were collected for flow through a U-bend of square cross section and of curvature ratio (R_c/D) of 0.65 that was either stationary or rotating about an axis

parallel to the axis of curvature. In that study the inlet and exit tangent ducts were smooth and the rotation and bend-curvature axes were parallel. While this configuration differs from gas turbine practice it has the advantage that, in principle, the flow is symmetric about the plane orthogonal to the rotation axis passing through the centre plane of the duct. Moreover, it is a condition for which convective heat transfer data have already been obtained (Wagner et al., 1989).

Here the results of a subsequent investigation are reported in which the effects of discrete roughness elements have been included. As shown in Fig. 1, square ribs have been added to the straight sections of the square-sectioned U-bend, in a staggered arrangement along the inner and outer walls. The objective is to generate detailed mean and turbulent flow data that reveal how the ribs modify the flow development within the U-bend under both stationary and rotating conditions. Such data should not only improve our understanding of blade cooling flows, but would also provide challenging test cases for further assessment of turbulence models used in the computation of blade-cooling flows.

2 Experimental Apparatus and Procedure

As described in Cheah et al. (1996), the rig consists of a motor-driven turntable mounted in a 1.22-m-dia water tank. A rib-roughened U-bend of 0.05-m-square cross section and of curvature ratio $R_c/D = 0.65$, shown in Fig. 1, is mounted on a turntable so that the curvature axis of the duct is parallel to the axis rotation of Fig. 2. This mode of rotation was selected

Contributed by the International Gas Turbine Institute and presented at the 41st International Gas Turbine and Aeroengine Congress and Exhibition, Birmingham, United Kingdom, June 10–13, 1996. Manuscript received at ASME Headquarters February 1996. Paper No. 96-GT-476. Associate Technical Editor: J. N. Shimm.

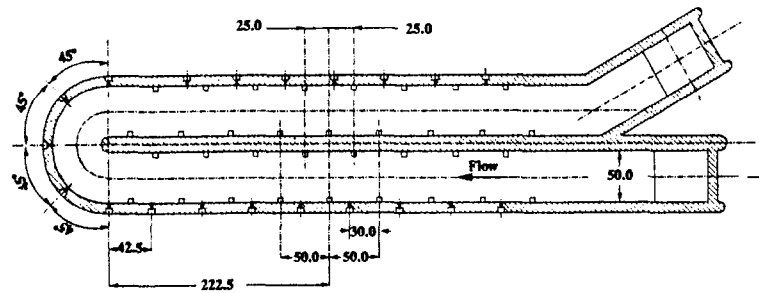


Fig. 1 Experimental model

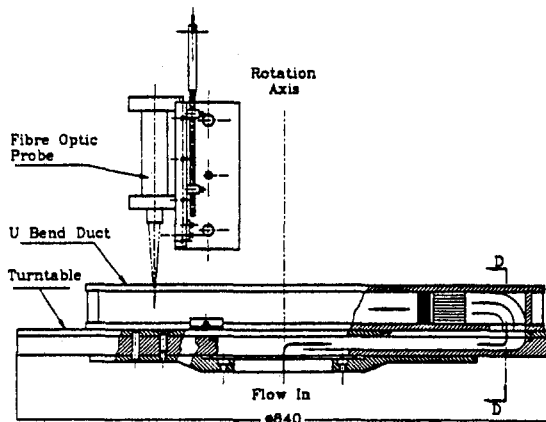


Fig. 2 Experimental apparatus

because the geometric plane of symmetry of the U-bend still remains the hydrodynamic plane of symmetry. The inner and outer duct walls of the upstream and downstream sections are artificially roughened using ribs of square cross section in a staggered arrangement. The ribs are oriented normal to the duct axis. The rib-height-to-duct-diameter ratio h/D is 0.1 and the pitch-to-height ratio, P/h , is 10. The closing side walls of the duct are smooth. The axial throughflow to the test rig is fed into the square duct through a passage that is built into the rotating turntable and the outflow is exhausted into the open water tank. A combination of fine wire meshes and a honeycomb section are located downstream of the flow entrance to the duct to provide uniform and symmetric flow into the U-bend section. The test section is made of 0.01-m-thick perspex to facilitate optical access by LDA laser beams.

The rotor/turntable could be driven at any speed up to 250 rpm in either direction. A feedback control circuit utilizes the input signals from a shaft rotary encoder to control precisely the rotational speed.

The LDA system employed was a TSI two-channel, four-beam fiber-optic system with frequency shifting on both the blue and the green channels. A 4-W argon-ion laser was used to power the system and two counter processors (TSI 1980B) were used for signal validation. Subsequent data processing was done through a Zech data acquisition card on a PC. LDA measurements have so far been collected along the duct symmetry plane. A fiber-optic probe, of focal length 0.135 m, was

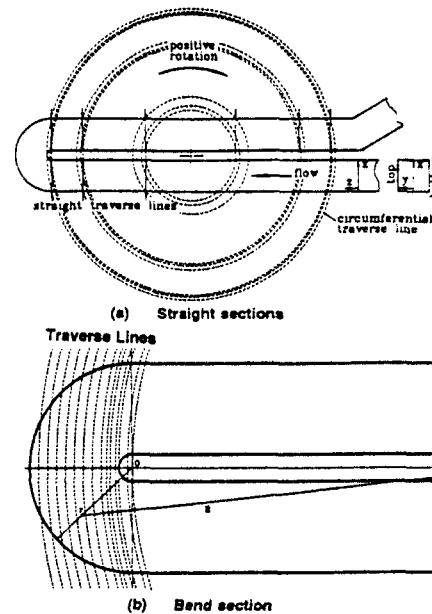


Fig. 3 LDA traverse paths

mounted in a stationary position above the turntable as seen in Fig. 2. The laser beams entered the top wall of the duct, with the LDA measurements being taken as the rotating duct swept across the beams. Simultaneous two-component velocity measurements were collected, with a coincidence window of $20 \mu\text{s}$, at several selected radial locations. The position of each data point in the flow was indexed by an incremental rotary encoder mounted on the rotating drive-shaft. Measurements from each discrete angular location were then recorded in separate data bins. The stationary probe was thus able to collect rotating flow data along circumferential lines as shown in Fig. 3(a). A $\frac{1}{8}$ -deg resolution produced 2880 data bins per traverse line. A total of 60,000–80,000 data points was gathered in each traverse. The maximum circumferential length of a data bin was 0.6 mm and the average closer to 0.3 mm. For the turbulence quantities, data from up to three adjacent bins were combined to produce a sufficiently large sample at each angular position. To obtain profiles along straight traverse lines across the duct, three circumferential traverses were performed along three close radial

Nomenclature

C_p = pressure coefficient $\equiv (P - P_{\text{ref}}) / (0.5\rho U_m^2)$

D = duct hydraulic diameter

h = rib height

P = rib pitch

R_c = bend mean curvature

Re = flow Reynolds number $\rho U_m D / \nu$

Ro = Rotation number $\equiv \Omega D / U_m$

U_m = bulk velocity

U_x = cross-duct velocity

U_z = streamwise velocity

x = cross-duct direction

z = streamwise direction

ν = kinematic viscosity

Ω = angular velocity of rotating duct

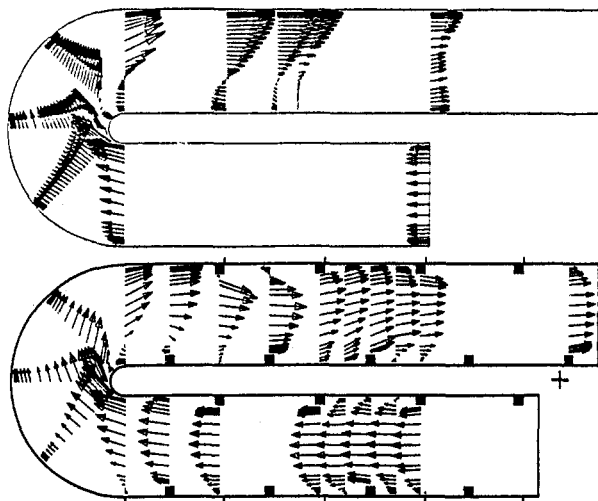


Fig. 4 Mean flow comparisons for stationary U-bends

positions, so as to envelop the required cross-duct line as shown in Fig. 3(a). The corresponding straight-line profiles were then obtained through interpolation. Measurements within the U-bend were obtained along eleven equispaced radial traverses shown in Fig. 3(b). Bilinear interpolation was then used to construct profiles along radial lines. For the stationary case manual traverses were carried out.

In addition to the LDA data, wall static pressure measurements were also collected through a series of static pressure taps along the top (flat) wall. The pressure taps were connected to pressure transducers attached to the rotating model and, through slip-rings, the transducer output was transmitted to a data-processing PC.

The fluid temperature was maintained at a uniform level within 0.2°C. The mass flow rate was monitored by an orifice run installed in ducting preceding the U-bend.

The overall estimated uncertainties for the streamwise and cross-duct velocity components U_z and U_x , respectively, and of the corresponding turbulence quantities are:

$$\begin{aligned} U_z &\leq 0.02U_m & \sqrt{u_z^2} &\leq 0.02U_m \\ U_x &\leq 0.03U_m & \sqrt{u_x^2} &\leq 0.02U_m \\ \overline{u_x u_z} &\leq 0.004U_m^2 \end{aligned}$$

3 Presentation and Discussion of Results

Three cases have been investigated in this study, all for a flow Reynolds number of 100,000: a stationary U-bend, a case for a U-bend rotating positively at $Ro = 0.2$, and one with negative rotation at $Ro = -0.2$. In all cases traverses have been carried out both within the U-bend and also within the upstream and downstream straight sections. These traverses yielded measurements of the mean velocity components in the streamwise and cross-duct directions, measurements of the corresponding turbulence intensities and shear stress, and also measurements of the four triple correlations associated with this plane.

The vector plots of Fig. 4 present a comparison between the mean flow development through a stationary U-bend with smooth walls, obtained earlier (Cheah et al., 1996), and the corresponding flow development for the ribbed U-bend, obtained in the present study. Within the straight upstream section, the present measurements show that the flow is fully developed, with the same flow pattern being repeated over successive rib intervals. The separation bubble downstream of each rib is about 0.25 diameters long, or 2.5 rib heights. The effects of the U-bend appear to extend to only about one hydraulic diameter upstream of the bend entry. There, the adverse pressure gradient

along the outer wall extends the length of the separation bubble downstream of the last rib to over five rib heights. Thus, in contrast to the smooth wall case, there is now a small region of flow separation along the outer wall at the bend entry. Along the inner wall, the introduction of ribs appears to delay flow separation, which now occurs after the 90 deg plane. The subsequent separation bubble is not as wide as that formed in the absence of ribs. Reattachment occurs at about one diameter downstream of the bend exit, whereas for the smooth U-bend reattachment occurs at about 2.2 diameters. It is interesting to note that the first downstream rib along the inner wall, 0.45 diameters after the bend exit, is within the separation bubble. Along the outer wall, as in the smooth U-bend, the favorable pressure gradient initially causes a strong flow acceleration at the bend exit. The first downstream rib along the outer wall, 0.95 diameters from the bend exit, consequently poses a greater obstacle to the flow, leading to a large region of flow separation over the first rib interval, which displaces the high momentum fluid toward the duct centre. In contrast (and in consequence), over the second rib interval, there is almost no flow separation along the outer wall. By about six diameters downstream of the bend exit, fully periodic flow conditions are restored.

The effects of rotation on the mean flow are shown in the vector plots of Fig. 5 and the mean velocity profiles of Fig. 6. In the upstream section where repeating flow conditions are again in evidence, positive rotation displaces the faster fluid toward the outer wall, which is also the pressure side of the rotating duct, while negative rotation has the opposite effect. This is a consequence of the rotation-induced secondary flow. Rotation also has a noticeable effect on the flow development within the U-bend. As can be more clearly seen in Fig. 6, positive rotation leads to a more uniform velocity distribution within the bend, by lowering velocities along the inner side, whereas with negative rotation, the high-momentum fluid remains closer to the inner side. These effects are consistent with the rotation effects observed in flow through smooth U-bends (Cheah et al., 1996). The Coriolis-induced secondary motion convects the high-momentum fluid toward the pressure side of the rotating duct. Negative rotation increases the width of the inner wall separation bubble over the first downstream rib and, again, positive rotation has the opposite effect. Because with negative rotation the inner side fluid has a higher momentum, it is less able to follow the curvature of the inner wall. As it comes out of the U-bend, the fluid is thus directed to the outer side, leaving a larger separation bubble along the inner wall. The enlarged separation bubble over the first rib interval along the outer wall is still present with both modes of rotation. The influences of rotation on the mean flow development in a rib-roughened U-bend are at least as strong as those observed in flows through similar U-bends with smooth walls.

Figure 7 shows profiles of the turbulent stresses measured within a rib interval which is far enough downstream of the bend for periodic flow conditions to prevail. As expected, the levels of turbulence are considerably higher than those observed in the straight sections of the U-bend with smooth walls (Cheah et al., 1996). Turbulence levels become higher over the ribs, and also in the near-wall regions downstream of the ribs, where the flow is separated. Streamwise turbulence levels are generally higher than the cross-duct levels in the near-wall regions. Rotation appears to increase the streamwise turbulence intensities along the pressure side (which for positive rotation is the outer side and for negative rotation the inner side) of the duct. Moreover, due to the onset of secondary motion, rotation also leads to an overall increase in the levels of the cross-duct turbulence intensities. The effects of rotation on turbulence are also evident in the turbulent shear stress profiles of Fig. 7(c). Along the pressure side, rotation increases shear stress levels while, along the suction side, levels are suppressed relative to their stationary duct values.

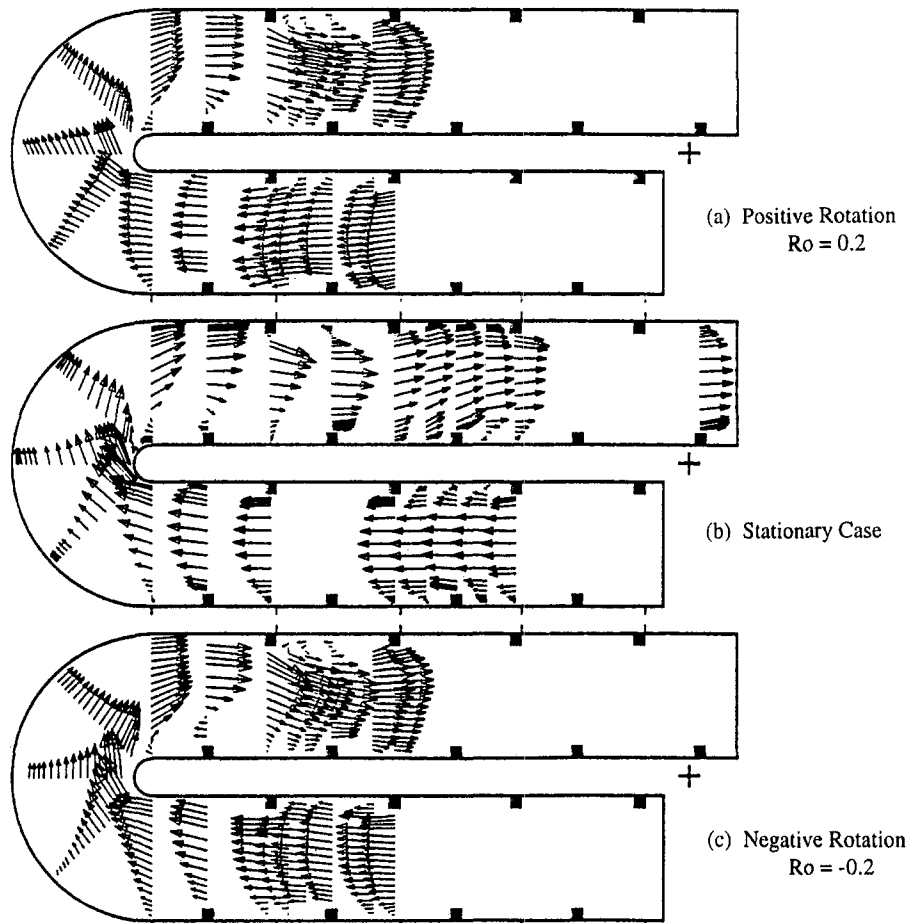


Fig. 5 Comparison of mean velocity fields for ribbed U-bend

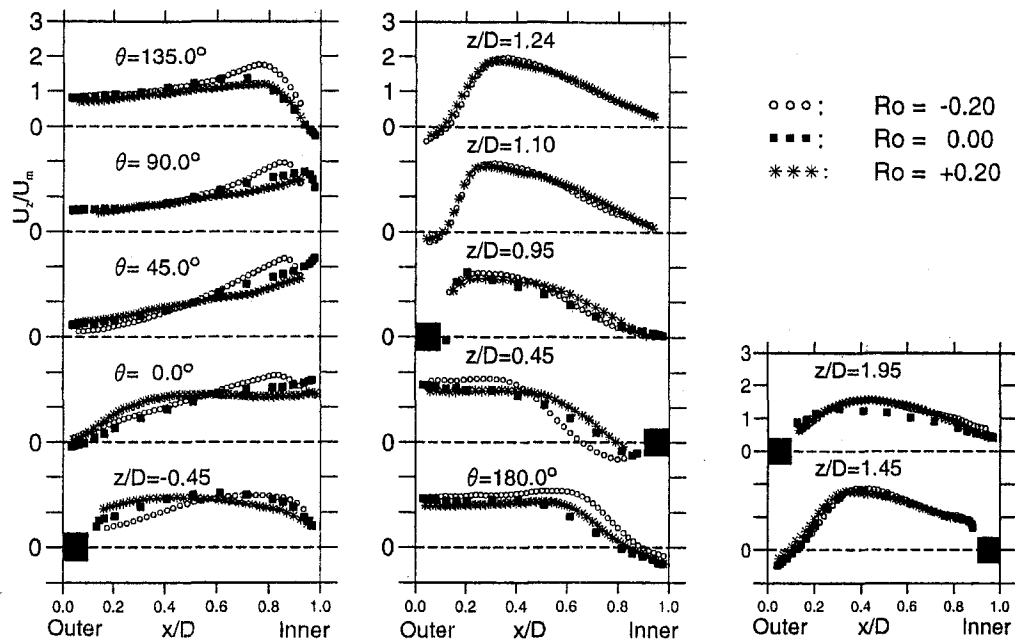


Fig. 6 Profiles of streamwise velocity

Figure 8 shows profiles of streamwise turbulence intensities in the vicinity of the U-bend. Because of the ribs in the upstream section, the flow is highly turbulent at the bend entry, especially along the outer wall, due to the adverse pressure gradient. These

higher turbulence levels at the bend entry are responsible for the delayed flow separation along the inner wall and the smaller subsequent separation bubble. Over the second half of the bend, where a separation bubble is formed along the inner wall, there

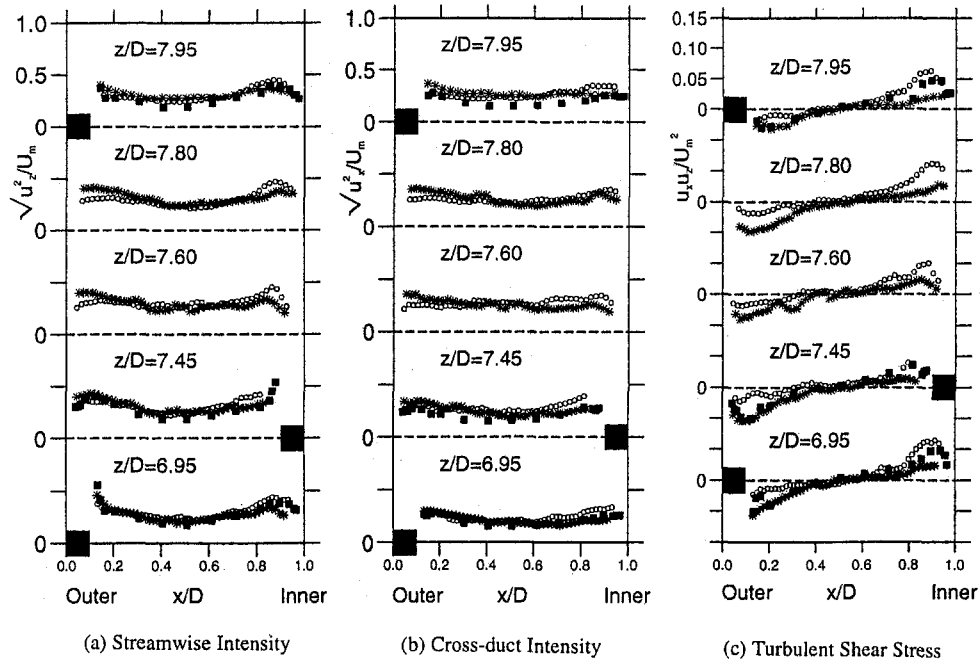


Fig. 7 Turbulence profiles for fully developed flow in the straight sections

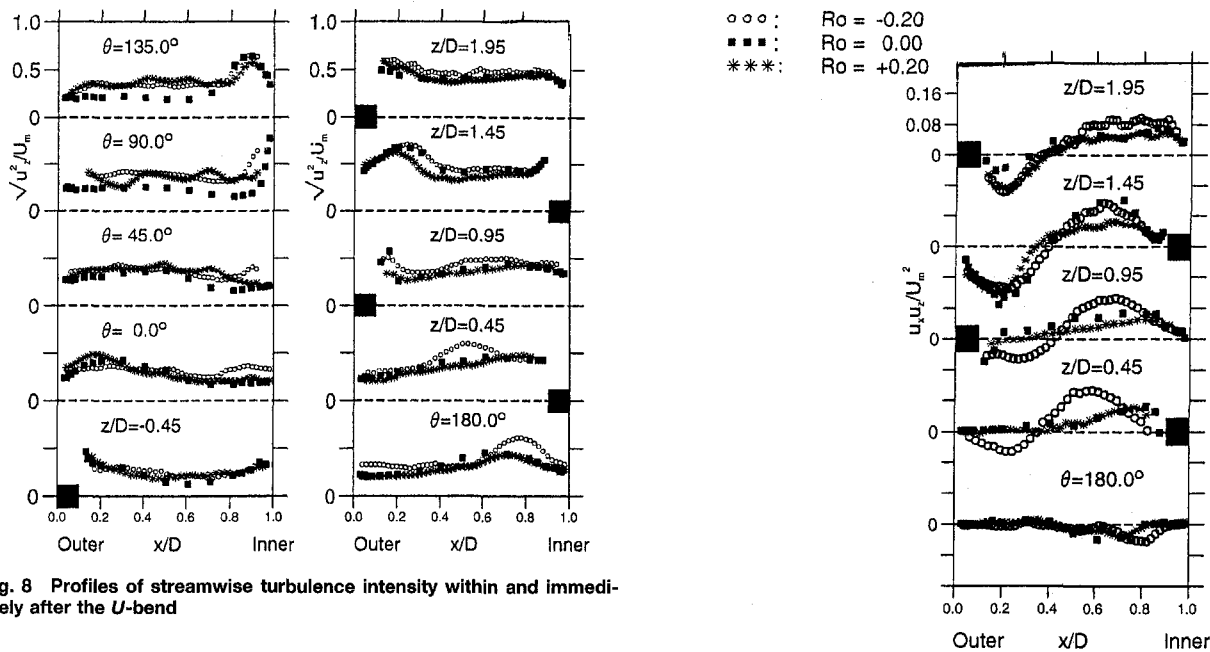


Fig. 8 Profiles of streamwise turbulence intensity within and immediately after the U-bend

is a marked increase in near-wall turbulence levels and, as the separation bubble grows further downstream, the high turbulence levels move toward the duct center. The main characteristic downstream of the U-bend, is the strong rise in turbulence levels along the outer wall over the first rib-interval. This is caused by the large separation bubble formed over this region, shown in Figs. 4, 5, and 6. Both positive and negative rotation enhance core turbulence within the U-bend. Downstream of the bend, as also noted in our earlier study (Cheah et al., 1996), negative rotation generally leads to higher levels of turbulence. The effects of rotation on turbulence within and downstream of the U-bend are not, however, as strong as those observed in the corresponding study of the smooth U-bend (Cheah et al., 1996). Figure 9 indicates that, in the region immediately downstream of the bend exit, there is a substantial rise in the turbulent shear stress. This increase is more noticeable after the first outer-

Fig. 9 Turbulent shear stress profiles immediately after the U-bend

wall rib. Negative rotation appears generally to augment the turbulent shear stress in the downstream region, whereas positive rotation tends to attenuate it.

Finally Fig. 10 shows the variation in static pressure along the top (flat) wall, for both a smooth and a ribbed U-bend. The smooth duct data indicate that in the upstream section, frictional losses are not significantly affected by rotation. For the stationary and positively rotating U-bends there is a small rise in static pressure within the bend whereas, for the case of negative rotation, where as shown in Cheah et al. (1996), there is flow separation at the bend entry, there is a drop in static pressure within the bend. A strong drop in static pressure occurs at the bend exit, where of course, a large separation bubble is present.

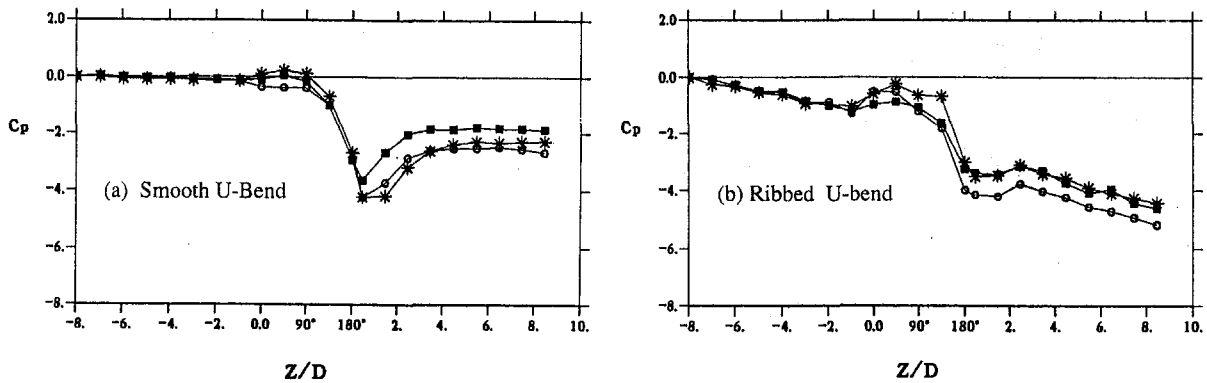


Fig. 10 Static pressure variation along the top (flat) wall: ■: stationary U-bend, *: $Ro = +0.2$, ○: $Ro = -0.2$

This decrease in pressure is greater for the two rotating cases. A partial recovery begins about two diameters after the bend exit for the stationary and negatively rotating U-bends, whereas for positive rotation, where the separation bubble is longer, recovery begins one diameter further downstream. Negative rotation, which increases turbulence levels within and downstream of the bend, also leads to greater loss in static pressure.

For the case of the ribbed U-bend, frictional losses within the straight upstream section are much greater than those in the corresponding smooth sections. In the straight upstream section, where curvature effects are negligible, frictional losses are again not significantly affected by rotation, at least not for Ro values of 0.2. Over the bend entry the pressure rise is least for the stationary case because of the presence of separation at the entry. The decrease in pressure at the bend exit is not as strong as in the smooth U-bend, possibly because the separation bubble along the inner wall is not as large, but the subsequent recovery is also weaker in the ribbed downstream section. The U-bend thus causes a similar pressure loss in the ribbed test model as in the smooth, but there are greater frictional losses in the upstream and downstream ribbed sections. Again negative rotation leads to a greater overall loss in static pressure.

4 Concluding Remarks

The reported measurements provide insight into the flow structure within a rotating hairpin bend roughened with discrete ribs for a rotation number of 0.20, similar to that encountered in internal cooling passages of gas turbine blades. Comparisons with our recent analogous studies of flow through a smooth U-bend reveal that:

- In the fully developed sections, away from the bend influence, resistance to streamwise flow arising from the ribs results in the flow pattern and pressure drop.
- The ribs also reduce the region of bend influence to about one diameter ahead of and six diameters downstream of the U-bend.
- At entry to the bend, the upstream ribbing along the outer-bend wall coupled with the adverse pressure gradient leads to separated or nearly separated flow on this wall; in consequence, the flow near the inner wall is stronger.

- Principally because of the much higher turbulence levels with the ribbed wall, separation from the inner wall is delayed somewhat and the separation bubble is thinner than for the smooth duct; nevertheless, the first inner-wall rib downstream of the U-bend actually lies within the separated flow zone.
- The flow acceleration at exit near the outer-wall means that the first rib on that surface imposes a greater blockage than elsewhere and a recirculating flow that extends to the next rib.

Further measurements are in progress close to the smooth side walls, which will give a more complete picture than the center-plane measurements reported here. Measurements are also being made with the first downstream rib removed to discern the effects that this has on the flow downstream of and, indeed, within the U-bend. Even the present data should, however, provide a very challenging data set for those wishing to assess the capabilities for their CFD codes for blade cooling applications.

Acknowledgments

This research has been supported by ABB (Switzerland), Electricité de France, European Gas Turbines, Rolls-Royce plc and the Defence Research Agency (Pyestock). Outstanding technical assistance has been provided by Mr. J. Hosker and Mr. D. Cooper. Authors' names are listed alphabetically.

References

- Chang, S. M., Humphrey, J. A. C., and Modavi, A., 1983, "Turbulent Flow in a Strongly Curved U-Bend and Downstream Tangent of Square Cross-Section," *Physico-Chemical Hydrodynamics*, Vol. 4, p. 243.
- Cheah, S. C., Iacovides, H., Jackson, D. C., Ji, H., and Launder, B. E., 1996, "LDA Investigation of the Flow Development Through Rotating U-ducts," *ASME JOURNAL OF TURBOMACHINERY*, Vol. 118, pp. 590–596.
- Moon, I. M., 1964, "Effects of Coriolis Force on the Turbulent Boundary Layer in Rotating Fluid Machines," MIT Gas-Turbine Laboratory, Report No. 74.
- Moore, J., 1967, "Effects of Coriolis on Turbulent Flow in Rotating Rectangular Channels," MIT Gas-Turbine Laboratory, Report No. 89.
- Taylor, A. M. K. P., Whitelaw, J. H., and Yianneskis, M. J., 1982, "Curved Ducts With Strong Secondary Motion: Velocity Measurements of Developing Laminar and Turbulent Flow," *ASME JOURNAL OF FLUIDS ENGINEERING*, Vol. 104, pp. 350–359.
- Wagner, J. H., Johnson, B. V., and Hajek, T. J., 1991, "Heat Transfer in Rotating Passages With Smooth Walls and Radial Outward Flow," *ASME JOURNAL OF TURBOMACHINERY*, Vol. 113, pp. 42–51.